Hybrid-Electric Aircraft with Over-the-Wing Distributed Propulsion
Aerodynamic Performance and Conceptual Design

de Vries, R.

DOI
10.4233/uuid:ef87dc11-e7b2-4726-a41f-28588d64c58d

Publication date
2022

Document Version
Final published version

Citation (APA)
de Vries, R. (2022). *Hybrid-Electric Aircraft with Over-the-Wing Distributed Propulsion: Aerodynamic Performance and Conceptual Design*. [Dissertation (TU Delft), Delft University of Technology]. https://doi.org/10.4233/uuid:ef87dc11-e7b2-4726-a41f-28588d64c58d

Important note
To cite this publication, please use the final published version (if applicable).
Please check the document version above.

Hybrid-Electric Aircraft with Over-the-Wing Distributed Propulsion

Aerodynamic Performance and Conceptual Design

Hybrid-Electric Aircraft with Over-the-Wing Distributed Propulsion

Aerodynamic Performance and Conceptual Design

Dissertation

for the purpose of obtaining the degree of doctor
at Delft University of Technology
by the authority of the Rector Magnificus prof. dr. ir. T.H.J.J. van der Hagen,
Chair of the Board for Doctorates,
to be defended publicly on
Monday 17 January 2022 at 15:00 o'clock

by

Reynard de Vries

Master of Science in Aerospace Engineering,
Delft University of Technology, the Netherlands

born in Amsterdam, the Netherlands.

This dissertation has been approved by the promotor.

Composition of the doctoral committee:

Rector Magnificus	chairperson
Prof. dr. ir. L. L. M. Veldhuis	Delft University of Technology, *promotor*
Dr. ir. R. Vos	Delft University of Technology, *copromotor*
Independent members:	
Prof. Dr.-Ing. G. Eitelberg	Delft University of Technology
Prof. Dr.-Ing. R. Radespiel	Technische Universität Braunschweig, Germany
Prof. dr. L. P. Ruiz Calavera	Universidad Politécnica de Madrid, Spain
Prof. dr. B. J. German	Georgia Institute of Technology, USA
Dr. habil. A. T. Isikveren	Safran S. A., France
Prof. dr. ir. C. Simão Ferreira	Delft University of Technology, *reserve member*

This research was funded by the European Union's Horizon 2020 Clean Sky 2 Large Passenger Aircraft program (CS2-LPA-GAM 2017-2021) under grant agreement numbers 807097 and 945583.

Keywords: hybrid-electric propulsion, distributed propulsion, propulsion integration, propeller aerodynamics, over-the-wing propellers, conceptual aircraft design, aircraft performance, wind-tunnel testing

ISBN 978-94-6384-287-7

An electronic version of this dissertation is available at
`http://repository.tudelft.nl/`.

SUMMARY

Recent developments in the field of hybrid-electric propulsion (HEP) have opened the door to a wide range of novel aircraft configurations with improved energy efficiency. These electrically-driven powertrains enable "distributed propulsion" configurations, in which the aerodynamic interaction between the propulsive devices and the airframe is exploited to enhance the aero-propulsive efficiency of the aircraft. In this context, the present research focuses specifically on over-the-wing distributed propulsion (OTWDP) for regional propeller aircraft. Over-the-wing (OTW) propellers are particularly promising because they can significantly enhance the lift-to-drag ratio of the wing, as well as reduce flyover noise due to shielding by the wing. Thus, a hybrid-electric aircraft with OTWDP can potentially constitute a low-noise, high-efficiency alternative for the future regional aircraft market.

The objective of this research is therefore to quantify the impact of OTWDP on the energy efficiency of hybrid-electric aircraft. However, to do this, research is required on multiple fronts. On one hand, the fundamental aerodynamic interaction between an OTW propeller and the surrounding elements is not clearly understood. Consequently, it is not known what the actual aerodynamic or propulsive-efficiency benefits of an OTWDP system are, or how they are affected by different operating conditions and design parameters. On the other hand, there are no HEP aircraft design methods which can systematically translate these subsystem-level performance characteristics into aircraft-level performance characteristics. To address these challenges, this research is divided into three main parts. First, a sizing method for hybrid-electric distributed-propulsion (HEDP) aircraft is developed, independently of where the propellers are positioned with respect to the airframe. Second, the aerodynamic interaction effects and performance characteristics of OTWDP systems are investigated, independently of the type of powertrain used to drive the propellers. And third, the sizing method and aerodynamic performance estimates of the previous two points are combined to assess the effect of hybrid-electric OTWDP on aircraft-level performance metrics.

The preliminary sizing method formulated in the first part shows that HEDP can be accounted for by modifying the traditional sizing methods for wing area, installed power, and aircraft weight in two ways. First, the flight-performance equations are adapted to include a series of "delta" terms that represent the propulsion-airframe interaction effects (ΔC_L, ΔC_D, $\Delta \eta_\mathrm{p}$). Then, a simplified powertrain representation is used to compute the power flows across a generic HEP architecture, using three power-control parameters. This leads to a series of component-oriented power-loading diagrams, which are combined with a mission analysis and a simplified weight estimation to compute the weight and energy consumption of the aircraft. A verification study shows that this new sizing method provides values which deviate by less than 5% from reference aircraft data and the results of an independent HEP sizing method, in terms of take-off mass and energy consumption. Then, to illustrate the effect of distributed-propulsion on the sizing

process, a regional aircraft with leading-edge distributed propulsion (LEDP) is sized and compared to a conventional twin-prop reference aircraft. This shows that LEDP can increase the wing loading by more than 50%, leading to a 6% increase in lift-to-drag ratio for the particular mission. These results demonstrate that the aerodynamic interaction effects can have a decisive influence on aircraft performance, and therefore further investigation is required to understand and model these effects in the case of OTWDP.

For this reason, the second part of this research focuses on the interaction phenomena between an OTW propeller and surrounding elements such as the wing, duct, or adjacent propellers. Due to the three-dimensional, unsteady, and viscous nature of the interaction mechanisms, a predominantly experimental approach is taken. These experiments are complemented with Reynolds-Averaged Navier Stokes (RANS) simulations to provide additional insight into the flow field, and a low-order numerical method to analyze the effect of some key design variables.

The investigations reveal that the effect of an OTW propeller on the wing pressure distribution can be decomposed into an effective angle-of-attack increase, and a local change in surface pressure directly beneath the propeller. Simultaneously, the wing disturbs the inflow velocities to the propeller disk, leading to a strong non-uniform loading. For three propellers placed side-by-side above a rectangular wing, at 80% chord and with a diameter-to-chord ratio of 0.67, these interaction effects are found to locally increase the wing lift-to-drag ratio by 45% in cruise conditions. This benefit comes at the expense of a 12% reduction in propulsive efficiency. However, these performance changes are highly dependent on the geometry of the system—especially in high-lift conditions. If the propeller is placed above the flap hinge, the adverse pressure gradient induced by the propeller triggers flow separation over the flap. The unsteady interaction between the tip vortices and wing boundary layer only play a minor role in this propeller-induced separation. If, on the other hand, the propeller is placed half a radius further upstream, then a Coandă effect is created which delays flow separation. Similarly, if the propeller is deflected together with the flap, then the flow separation is postponed.

The performance of the OTW propeller is also affected by the adjacent propellers and, if present, the duct. Since a priori it is unknown whether a duct is required, or what the optimal shape would be, two simplified limit cases are investigated numerically for a single propeller: a square duct, and a conventional, circular duct. The flow fields show that the propeller-induced pressure gradients lead to flow separation in the corners of the square duct at high thrust settings. The varying end-plate effect also leads to unsteady blade loading. Consequently, for a given advance ratio and (sub-optimal) blade pitch angle, the square ducted system is found to be 4.5% less efficient than the circular one, and both systems are found to produce 7% less thrust than an isolated propeller. Based on these results, and considering the two-dimensional velocity field above an unswept wing, an unducted OTWDP system or an OTWDP system with an envelope duct are considered the most promising solutions—depending on the axial position of the propellers. However, in either of those configurations, each propeller interacts with its neighbors. An experimental investigation shows that, in that case, the velocities induced by each propeller's vortex system lead to additional unsteady blade loading. Furthermore, the propeller efficiency is found to reduce by 1.5% due to the presence of the adjacent propellers and their nacelles, for a tip clearance equal to 4% of the radius.

The third and final part of this research combines the aircraft sizing method, the qualitative design considerations identified in the detailed aerodynamic analyses, and the quantitative performance estimates of a lower-order numerical model to evaluate the potential of OTWDP at aircraft level. For this, first a design-space exploration is performed. This shows that a partial-turboelectric powertrain is the most promising HEP architecture for regional aircraft with distributed propulsion. In such a configuration, the benefits of distributed propulsion increase with range, decrease with cruise Mach number, and are independent of the payload weight. The results also reflect that a 15% energy reduction due to HEDP is unlikely in the mid-term (circa 2035), since this would require an average aero-propulsive efficiency increase of 17%–23% with a "power split" of just 20%, which is extremely challenging to attain in practice. For a partial-turboelectric aircraft with two aft-mounted propellers and an OTWDP system consisting of 38 propellers, a diameter-to-chord ratio of 0.19, and a covered wing span fraction of 0.53, the average aero-propulsive efficiency increase is found to be 9% for a 1500 nmi mission. Roughly 4% of this benefit is required to offset the power losses in the electrical drivetrain. This leads to an overall energy reduction of 5% relative to a conventional twin-turboprop configuration, with an uncertainty margin of ±5% due to uncertainty in the aerodynamic modeling alone. In this case, the OTWDP and the conventional configurations present a comparable take-off mass.

These energy-efficiency benefits are insufficient to justify a radical change in the layout of the aircraft, especially considering that they have been obtained with a preliminary sizing method which neglects aspects such as tail sizing or trim drag. Nevertheless, the results show that the substantial aerodynamic benefits of OTW propellers at subsystem level also lead to an aero-propulsive benefit at aircraft level. Thus, OTWDP systems can present a strong case if, additionally, the noise-shielding capabilities can be proven, or if the aero-propulsive benefits are further increased by, for example, integrating the control surfaces with a duct or by producing a full-span OTWDP system. Other market segments, such as small, fully-electric aircraft for general aviation purposes should also be explored in order to mature the technology. Such investigations, along with the sizing method and detailed aerodynamic interaction studies provided in this research, will contribute towards the development of the next generation of energy-efficient passenger aircraft.

SAMENVATTING

Recente ontwikkelingen op het gebied van hybride-elektrische voortstuwing (*hybrid-electric propulsion*, HEP) hebben de deur geopend voor een groot aantal nieuwe vliegtuigconfiguraties met verbeterde energie-efficiëntie. Deze elektrische aandrijflijnen maken configuraties met verdeelde voortstuwing (*distributed propulsion*) mogelijk, waarbij de aerodynamische interactie tussen de propellers en andere elementen van het vliegtuig wordt gebruikt om de aerodynamische en voortstuwingsefficiëntie van het vliegtuig te verbeteren. In deze context richt dit onderzoek zich specifiek op *over-the-wing distributed propulsion* (OTWDP) voor regionale propellervliegtuigen, waar de propellers boven de vleugel worden geplaatst. *Over-the-wing* (OTW)-propellers zijn veelbelovend omdat ze de lift-over-weerstandsverhouding van de vleugel aanzienlijk kunnen verbeteren, en het flyover-geluid als gevolg van afscherming door de vleugel kunnen verminderen. Een hybride-elektrisch vliegtuig met OTWDP kan dus potentieel een geluidsarme, hoogrenderende optie zijn voor de toekomstige markt voor regionale vliegtuigen.

Het doel van dit onderzoek is om de impact van OTWDP op de energie-efficiëntie van hybride-elektrische vliegtuigen te kwantificeren. Hiervoor is echter onderzoek nodig op meerdere fronten. Aan de ene kant is de fundamentele aerodynamische interactie tussen een OTW-propeller en de omliggende elementen onduidelijk. Verder is het niet bekend wat de werkelijke aerodynamische of voortstuwingsefficiëntievoordelen van een OTWDP-systeem zijn, of hoe deze worden beïnvloed door verschillende omstandigheden en ontwerpparameters. Aan de andere kant zijn er geen ontwerpmethoden voor HEP vliegtuigen die deze prestatiekenmerken op subsysteemniveau systematisch kunnen omrekenen naar prestatiekenmerken op vliegtuigniveau. Om deze uitdagingen aan te gaan, is dit onderzoek opgesplitst in drie delen. Ten eerste wordt een ontwerpmethode ontwikkeld voor vliegtuigen met hybride-elektrische verdeelde voorstuwing (*hybrid-electric distributed propulsion*, HEDP), onafhankelijk van waar de propellers zijn geplaatst op het vliegtuig. Ten tweede worden de aerodynamische interactie-effecten en prestatiekenmerken van OTWDP-systemen onderzocht, onafhankelijk van het type aandrijflijn dat wordt gebruikt voor de propellers. Ten derde worden de ontwerpmethode en aerodynamische prestatieschattingen van de vorige twee punten gecombineerd om het effect van hybride-elektrische OTWDP op vliegtuigniveau te beoordelen.

De conceptuele ontwerpmethode die in het eerste deel van dit onderzoek wordt geformuleerd laat zien dat HEDP in het ontwerpproces kan worden meegenomen door de traditionele ontwerpmethoden op twee manieren aan te passen. Eerst worden de vluchtprestatievergelijkingen aangepast om een reeks "delta" termen op te nemen die de interactie-effecten tussen propeller en vleugel beschrijven (ΔC_L, ΔC_D, $\Delta \eta_\mathrm{p}$). Vervolgens wordt een vereenvoudigde representatie van de aandrijflijn gebruikt om de vermogensstromen door een generieke HEP-architectuur te berekenen, met behulp van drie regelparameters. Dit leidt tot een aantal componentgerichte *power-loading* diagram-

men, die worden gecombineerd met een analyse van de missie en een vereenvoudigde gewichtsschatting om het gewicht en energieverbruik van het vliegtuig te berekenen. Uit een verificatiestudie blijkt dat deze nieuwe methode waardes oplevert in termen van startmassa en energieverbruik die minder dan 5% afwijken van de referentiedata en de resultaten van een aparte HEP-ontwerpmethode. Om het effect van verdeelde voortstuwing op het ontwerpproces te illustreren, wordt vervolgens een regionaal vliegtuig met verdeelde voortstuwing aan de voorrand van de vleugel (*leading-edge distributed propulsion*, LEDP) vergeleken met een conventioneel referentievliegtuig met twee propellers. Dit toont aan dat LEDP de vleugelbelasting met meer dan 50% kan verhogen, wat tot een toename van de lift-over-weerstandsverhouding van 6% leidt voor de specifieke missie. Deze resultaten tonen aan dat de aerodynamische interactie-effecten een beslissende invloed kunnen hebben op de prestaties van het vliegtuig, en daarom is verder onderzoek nodig om deze effecten te begrijpen en te modelleren in het geval van OTWDP.

Om deze reden richt het tweede deel van dit onderzoek zich op de aerodynamische fenomenen die optreden vanwege de interactie tussen een OTW-propeller en componenten in de nabijheid zoals de vleugel, de gondel, of aangrenzende propellers. Vanwege de driedimensionale, tijdsafhankelijke en viskeuze aard van de interactiemechanismen, wordt er grotendeels voor een experimentele benadering gekozen. Deze experimenten worden aangevuld met *Reynolds-Averaged Navier Stokes* (RANS)-simulaties om meer inzicht te krijgen in het stromingsveld, en een lage-orde numerieke methode om het effect van verschillende ontwerpvariabelen te analyseren.

Uit het onderzoek blijkt dat het effect van een OTW-propeller op de drukverdeling van de vleugel kan worden opgesplitst in een effectieve toename van de invalshoek en een lokale verandering in oppervlaktedruk direct onder de propeller. Tegelijkertijd verstoort de vleugel de instroming naar de propeller, wat een sterke niet-uniforme belasting op de propellerschijf genereert. Voor drie propellers boven een rechte vleugel, met een axiale positie van 80% van de vleugelkoorde en een diameter–koorde verhouding van 0.67, blijkt dat deze interactie-effecten de lift-over-weerstandsverhouding van de vleugel lokaal met 45% verhogen voor de kruisvlucht. Dit voordeel gaat ten koste van een vermindering van 12% van de voortstuwingsefficiëntie van de propellers. Deze prestatieveranderingen zijn echter sterk afhankelijk van de geometrie van het systeem—vooral in hoge-lift condities. Als de propeller boven het scharnierpunt van een uitgeklapte klep wordt geplaatst, veroorzaakt de drukgradiënt onder de propeller loslating van de stroming over de klep. De tijdsafhankelijke interactie tussen de tipwervels van de propeller en de grenslaag van de vleugel speelt maar een kleine rol bij deze propellergeïnduceerde loslating. Integendeel, als de propeller een halve radius verder stroomopwaarts wordt geplaatst, ontstaat er een Coandă-effect dat de loslating voorkomt. Evenzo, als de propeller samen met de flap wordt geroteerd, wordt de loslating van de stroming uitgesteld.

De prestaties van de OTW-propeller worden ook beïnvloed door de aangrenzende propellers en, indien aanwezig, de mantel (of *duct*). Omdat het a priori niet bekend is of een mantel nodig is, of wat de optimale vorm daarvan zou zijn, worden twee vereenvoudigde geometrieën numeriek onderzocht voor een enkele propeller: een vierkante mantel en een conventionele, circulaire mantel. De stromingsvelden laten zien dat de propeller-geïnduceerde drukgradiënten tot loslating leiden in de hoeken van de

vierkante mantel bij hoge trekkrachtscoëfficiënten. Het variërende eindplaateffect leidt ook tot een tijdsafhankelijke belasting op de bladen. Als gevolg hiervan blijkt het systeem met een vierkante mantel 4.5% minder efficiënt te zijn dan het cirkelvormige systeem voor een gegeven advance ratio en (sub-optimale) bladhoek, terwijl beide systemen 7% minder stuwkracht produceren dan een propeller zonder mantel. Op basis van deze resultaten, en rekening houdend met het tweedimensionale snelheidsveld boven een vleugel zonder pijlhoek, worden een OTWDP-systeem zonder mantel of een OTWDP-systeem met een tweedimensionale "envelop" mantel beschouwd als de meest belovende oplossingen—afhankelijk van de axiale positie van de propellers. In beide deze gevallen is er echter een interactie tussen aangrenzende propellers. Een experimenteel onderzoek toont aan dat in dat geval de snelheden die door het wervelsysteem van elke propeller worden geïnduceerd tot extra tijdsafhankelijke belastingen op het blad leiden. Bovendien wordt het propellerrendement met 1.5% verminderd vanwege de aanwezigheid van de aangrenzende propellers en hun gondels, voor een propeller tipafstand gelijk aan 4% van de radius.

Het derde en laatste deel van dit onderzoek combineert de vliegtuigontwerpmethode, de kwalitatieve ontwerpoverwegingen geïdentificeerd in de gedetailleerde aerodynamische analyses, en de kwantitatieve prestatieschattingen van een lage-orde numerieke model om het potentieel van OTWDP op vliegtuigniveau te evalueren. Hiervoor wordt eerst een gevoeligheidsanalyse uitgevoerd. Dit toont aan dat een gedeeltelijk-turbo-elektrische aandrijflijn de beste HEP-architectuur is voor regionale vliegtuigen met verdeelde voortstuwing. In die configuratie nemen de voordelen van verdeelde voortstuwing toe met het vliegbereik, nemen deze af met het cruise Mach-getal, en zijn deze onafhankelijk van het gewicht van de lading. De resultaten laten ook zien dat een energiereductie van 15% als gevolg van HEDP op middellange termijn (circa 2035) onwaarschijnlijk is, aangezien dit een gemiddelde verhoging van de aerodynamische en voortstuwingsefficiëntie van 17%–23% zou vereisen met een "*power split*" van slechts 20%, wat in de praktijk bijna onmogelijk is. Voor een gedeeltelijk-turbo-elektrisch vliegtuig met twee op de staart gemonteerde propellers en een OTWDP-systeem bestaande uit 38 propellers, een diameter–koordeverhouding van 0.19, en een spanwijdte van 53% van de vleugel, blijkt de gemiddelde toename van de aerodynamische en voortstuwingsefficiëntie 9% te zijn voor een missie van 1500 nmi. Ongeveer 4% van dit voordeel is nodig om de vermogensverliezen in de elektrische aandrijflijn te compenseren. Dit leidt tot een totale energiereductie van 5% ten opzichte van een conventionele twinturbopropconfiguratie, met een onzekerheidsmarge van $\pm$5% vanwege onzekerheid in de aerodynamische modellering. In dat geval hebben de OTWDP en de conventionele configuraties een vergelijkbare startmassa.

Deze verbeteringen van de energie-efficiëntie zijn onvoldoende om een radicale verandering in de lay-out van het vliegtuig te rechtvaardigen, vooral gezien het feit dat ze zijn berekend met een conceptuele ontwerpmethode die aspecten zoals staartontwerp of trimweerstand niet meeneemt. Toch laten de resultaten zien dat de substantiële aerodynamische voordelen van OTW-propellers op subsysteemniveau ook tot een aerodynamisch voordeel op vliegtuigniveau kunnen leiden. OTWDP-systemen hebben dus een grote potentie, vooral indien een geluidsreductie kan worden bewezen, of als de aerodynamische of voortstuwingsvoordelen verder worden vergroot door bijvoorbeeld de stu-

urvlakken te integreren met de mantel, of door een OTWDP systeem te produceren die de hele spanwijdte van de vleugel dekt. Andere marktsegmenten, zoals kleine, volledig elektrische vliegtuigen, moeten ook worden onderzocht om de technologie te laten ontwikkelen. Dergelijke onderzoeken, samen met de ontwerpmethode en aerodynamische interactiestudies die in dit onderzoek worden gepresenteerd, zullen bijdragen aan de ontwikkeling van de volgende generatie van duurzame passagiersvliegtuigen.

RESUMEN

Los avances recientes en el campo de la propulsión híbrida-eléctrica (*hybrid-electric propulsion*, HEP) para aeronaves han abierto la puerta a una amplia gama de configuraciones con mayor eficiencia energética. Estos trenes de propulsión eléctricos permiten configuraciones con propulsión distribuida (*distributed propulsion*), en las que la interacción aerodinámica entre los propulsores y el resto del avión se aprovecha para mejorar la eficiencia aeropropulsiva del vehículo. En este contexto, esta investigación se centra específicamente en la propulsión distribuida sobre el ala (*over-the-wing distributed propulsion*, OTWDP) en aviones de hélice regionales. Las hélices instaladas encima del ala (*over-the-wing*, OTW) son especialmente prometedoras porque pueden mejorar significativamente la eficiencia aerodinámica del ala, así como reducir el ruido de sobrevuelo debido al apantallamiento del ala. Por tanto, un avión híbrido-eléctrico con OTWDP puede posicionarse como una alternativa de bajo ruido y alta eficiencia para el futuro mercado de aviones regionales.

El objetivo de esta investigación es, por tanto, cuantificar el impacto de OTWDP sobre la eficiencia energética de los aviones híbridos-eléctricos. Sin embargo, para ello es necesario investigar diferentes aspectos. Por un lado, a día de hoy se desconocen los detalles de la interacción aerodinámica entre una hélice OTW y los elementos que la rodean. Como consecuencia, se desconoce el beneficio real que se puede obtener con un sistema OTWDP en términos de eficiencia aerodinámica o rendimiento propulsivo, y cómo este beneficio se vería afectado por las diferentes condiciones de funcionamiento y parámetros de diseño del sistema. Por otra parte, no existen métodos de diseño de aeronaves HEP que puedan relacionar sistemáticamente estas características de rendimiento del subsistema con el rendimiento de la aeronave. Para abordar estos retos, esta investigación se divide en tres partes principales. En primer lugar, se desarrolla un método de diseño para aeronaves de propulsión híbrida-eléctrica y distribuida (*hybrid-electric distributed propulsion*, HEDP), independientemente de la posición de las hélices con respecto al ala o fuselaje. En segundo lugar, se investigan la interacción aerodinámica y el rendimiento de los sistemas OTWDP, independientemente del tipo de tren motriz utilizado para mover las hélices. Y en tercer lugar, el método de diseño y las estimaciones de rendimiento aerodinámico de los dos puntos anteriores se combinan para evaluar el efecto de OTWDP a nivel global de la aeronave.

El método de diseño preliminar formulado en la primera parte incorpora HEDP modificando los métodos de diseño tradicionales de dos maneras. En primer lugar, las ecuaciones de movimiento de la aeronave se adaptan para incluir una serie de términos "delta" que representan la interacción aerodinámica entre los propulsores y el resto de la aeronave (ΔC_L, ΔC_D, $\Delta \eta_\mathrm{p}$). En segundo lugar, se utiliza una representación simplificada de la cadena cinemática para calcular los flujos de potencia para una configuración HEP genérica, utilizando tres parámetros de control. Esto conduce a una serie de diagramas de *power loading* que representan cada componente del sistema de propulsión,

los cuales se combinan con un análisis de la misión y una estimación simplificada del peso de los componentes para calcular el peso de despegue y consumo energético de la aeronave. Un estudio de verificación muestra que este nuevo método proporciona valores que se desvían menos de un 5% de la aeronave de referencia y de los resultados producidos por otro método de diseño HEP independiente, en términos de peso de despegue y consumo de energía. A continuación, para ilustrar el efecto de la propulsión distribuida en el proceso de diseño, se dimensiona un avión regional con hélices distribuidas en el borde de ataque (*leading edge distributed propulsion*, LEDP) y se compara con un avión turbohélice de referencia. Esta comparación demuestra que LEDP puede aumentar la carga del ala (*wing loading*) más de un 50%, lo que conlleva un aumento del 6% de la eficiencia aerodinámica para la misión en cuestión. Estos resultados demuestran que los efectos de interacción aerodinámica pueden tener una influencia decisiva en el rendimiento de la aeronave, por lo que es necesario seguir investigando para comprender y modelar estos efectos en el caso de OTWDP.

Por esta razón, la segunda parte de esta investigación se centra en los fenómenos de la interacción aerodinámica entre una hélice OTW y otros elementos como el ala, el carenado o las hélices adyacentes. Debido a la naturaleza tridimensional, viscosa y no estacionaria de los mecanismos de interacción, se opta por un enfoque predominantemente experimental. Estos experimentos se complementan con simulaciones numéricas RANS (*Reynolds-Averaged Navier Stokes*) para proporcionar información adicional del flujo, y un método numérico simplificado para analizar el efecto de los principales parámetros de diseño.

Los resultados revelan que el efecto de una hélice OTW sobre la distribución de presión del ala puede descomponerse en un aumento del ángulo de ataque efectivo y un cambio local en la presión sobre la superficie directamente debajo de la hélice. Simultáneamente, el ala perturba las velocidades que percibe la hélice, lo que provoca una distribución de carga no uniforme sobre la hélice. En el caso de tres hélices adyacentes colocadas sobre un ala rectangular, con una posición axial del 80% de la cuerda y una relación diámetro-cuerda de 0.67, se observa que la interacción aumenta la eficiencia aerodinámica seccional del ala en un 45% en condiciones de crucero. Este beneficio se produce a expensas de una reducción del 12% del rendimiento propulsivo de las hélices. Sin embargo, estos cambios de rendimiento dependen en gran medida de la geometría del sistema, especialmente en condiciones de alta sustentación. Si la hélice se sitúa por encima del eje de un flap desplegado, el gradiente de presión adverso inducido por la hélice provoca la separación del flujo sobre el flap. La interacción no estacionaria entre los vórtices de punta de las palas y la capa límite del ala sólo tiene un papel menor en esta separación inducida por la hélice. Si, por el contrario, la hélice se adelanta una distancia de medio radio (aguas arriba), se crea un efecto Coandă que retrasa la separación del flujo. Del mismo modo, si la hélice se despliega junto con el flap, entonces la separación del flujo se pospone.

El rendimiento de una hélice OTW también se ve afectado por las hélices adyacentes y, si está presente, por el carenado (*duct*) de la hélice. Dado que a priori se desconoce si es necesario un carenado, o cuál sería su geometría óptima, se investigan numéricamente dos casos límite para una sola hélice: un carenado cuadrado y un carenado circular convencional. Los resultados muestran que, con altos coeficientes de tracción,

los gradientes de presión generados por la hélice conducen a la separación del flujo en las esquinas del carenado cuadrado. La holgura variable entre la punta de las palas y el carenado también conduce a una carga oscilatoria en las palas. En consecuencia, para un determinado parámetro de avance y paso (subóptimo) de la hélice, el sistema con carenado cuadrado resulta ser un 4.5% menos eficiente que el circular, y ambos sistemas producen un 7% menos de empuje que una hélice sin carenado. Basado en estos resultados, y teniendo en cuenta el flujo bidimensional que se produce encima de un ala sin flecha, un sistema OTWDP sin carenado o un sistema OTWDP con un carenado bidimensional se consideran las soluciones más prometedoras, dependiendo de la posición axial de las hélices. Sin embargo, en ambas configuraciones cada hélice interactúa con las hélices adyacentes. Una investigación experimental muestra que, en ese caso, las velocidades inducidas por el sistema de vórtices de cada hélice generan una carga adicional no estacionaria. Además, se observa que el rendimiento propulsivo de la hélice se reduce en un 1.5% debido a la presencia de las hélices adyacentes y sus góndolas, para una distancia de separación igual al 4% del radio.

Para evaluar el potencial de OTWDP a nivel de aeronave, la tercera y última parte de esta investigación combina el método de diseño preliminar de la aeronave, las consideraciones cualitativas identificadas en los análisis aerodinámicos, y las predicciones de rendimiento obtenidos con un método numérico simplificado. Para ello, primero se realiza un estudio de sensibilidad para explorar el espacio de diseño. Esto muestra que un sistema de propulsión parcialmente turboeléctrico es la configuración HEP más prometedora para aviones regionales con propulsión distribuida. En esta configuración, las ventajas de la propulsión distribuida aumentan con el alcance, disminuyen con el número de Mach de crucero, y son independientes de la carga de pago. Los resultados también reflejan que una reducción del consumo energía del 15% gracias a HEDP es improbable a medio plazo (alrededor del año 2035), ya que esto requeriría un aumento promedio de la eficiencia aeropropulsiva en torno al 17%–23% con una "hibridización" de sólo el 20%, lo cual es extremadamente difícil de conseguir en la práctica. En el caso de un avión parcialmente turboeléctrico con dos hélices montadas en la parte trasera del fuselaje y un sistema OTWDP compuesto por 38 hélices, una relación diámetro-cuerda de 0.19, y una fracción de envergadura cubierta de 0.53, el aumento promedio de la eficiencia aeropropulsiva es del 9% para una misión de 1500 millas náuticas. Aproximadamente el 4% de este beneficio es necesario para compensar las pérdidas de energía en el tren de transmisión eléctrico. Esto lleva a una reducción de consumo de energía del 5% respecto a una turbohélice convencional, con un margen de incertidumbre de $\pm$5% debido a la incertidumbre en el modelado aerodinámico. En este caso, la configuración OTWDP y configuración convencional de referencia presentan un peso de despegue comparable.

Estos beneficios en la eficiencia energética son insuficientes para justificar un cambio radical en la configuración del avión, sobre todo teniendo en cuenta que se han obtenido con un método de diseño preliminar que no tiene en cuenta aspectos como el dimensionamiento de la cola. No obstante, los resultados demuestran que los beneficios aerodinámicos de las hélices OTW a nivel de subsistema también conllevan un beneficio aeropropulsivo a nivel de aeronave. Por lo tanto, los sistemas OTWDP pueden constituir una configuración prometedora si, además, se puede demostrar la capacidad

de apantallamiento del ruido, o si los beneficios aeropropulsivos se incrementan por encima de los valores obtenidos en este estudio—por ejemplo, integrando las superficies de control con un carenado, o produciendo un sistema OTWDP que cubra la envergadura completa del ala. También deberían explorarse otros segmentos de mercado con el fin de madurar la tecnología, como los pequeños aviones eléctricos para la aviación general. Estas investigaciones, junto con el método de diseño y los detallados estudios de interacción aerodinámica proporcionados en esta tesis, contribuirán al desarrollo de la próxima generación de aeronaves sostenibles.

CONTENTS

NOMENCLATURE

SYMBOLS

a	=	Speed of sound [m/s], axial induction factor $\Delta u / V_\infty$ [-]
a_0, b_0, c_0, m_0, n_0	=	Dummy variables
A	=	Aspect ratio b/c [-], coefficient matrix [-]
b	=	Span [m], right-hand-side of linear equation
b_{dp}	=	Wing span covered by distributed-propulsion system [m]
B	=	Number of blades [-]
BPF	=	Blade-passage frequency nB [-]
c	=	Chord length [m], climb rate [m/s]
c_d	=	Sectional drag coefficient $d/(q_\infty c)$ [-]
c_l	=	Sectional lift coefficient $l/(q_\infty c)$ [-]
C_D	=	Drag coefficient $D/(q_\infty S_{\text{ref}})$ [-]
$C_{D\text{i}}$	=	Induced drag coefficient [-]
C_{D0}	=	Zero-lift drag coefficient [-]
$C_{D\text{min}}$	=	Minimum drag coefficient [-]
C_{f}	=	Skin friction coefficient τ_{w}/q_∞ [-]
C_L	=	Lift coefficient $L/(q_\infty S_{\text{ref}})$ [-]
$C_{L\text{max}}$	=	Maximum lift coefficient [-]
$C_{L\text{min}D}$	=	Minimum-drag lift coefficient [-]
C_p	=	Pressure coefficient $(p - p_\infty)/q_\infty$ [-]
$C_{p\text{t}}$	=	Total pressure coefficient $(p_{\text{t}} - p_{\text{t}\infty})/q_\infty + 1$ [-]
C_N	=	Normal-force coefficient $N/(\rho_\infty n^2 D_{\text{p}}^4)$ [-]
C_P	=	Power coefficient $P_{\text{s}}/(\rho_\infty n^3 D_{\text{p}}^5)$ [-]
C_Q	=	Torque coefficient $Q/(\rho_\infty n^2 D_{\text{p}}^5)$ [-]
C_T	=	Thrust coefficient $T/(\rho_\infty n^2 D_{\text{p}}^4)$ [-]
C_ω	=	Vorticity coefficient $\omega/(2\Omega)$ [-]
CSP	=	Combined specific power [kW/kg]
d	=	Tip clearance between propellers [m], sectional drag [N/m]
D	=	Drag [N], diameter [m]
D_{i}	=	Induced drag [N]
D_{p}	=	Propeller diameter [m]
D_0	=	Zero-lift drag [N]
DOH	=	Degree-of-hybridization of energy $E_{0,\text{bat}}/(E_{0,\text{bat}} + E_{0,\text{f}})$ [-]
e	=	Oswald factor [-], specific energy [Wh/kg]
$\vec{e}_x, \vec{e}_y, \vec{e}_z$	=	Unitary basis vectors of Cartesian grid [m]
E	=	Energy [J], complete elliptic integral of the second kind [-]
E_{jk}	=	Exponent of the k-th variable of the j-th monomial [-]
f	=	Frequency [Hz]
f_W	=	Aircraft weight fraction W/W_{TO} [-]
F	=	Force [N]

F^*_{xc}	=	Horizontal force coefficient $F_x/(q_\infty S_{\text{ref}})$ [-]
F^*_{zc}	=	Vertical force coefficient $F_z/(q_\infty S_{\text{ref}})$ [-]
g	=	Gravitational acceleration [m/s^2]
h	=	Altitude [ft], cell size [m]
H_P	=	Hybridization factor [-]
i_{P}	=	Propeller incidence angle [deg]
J	=	Advance ratio $V_\infty/(nD_{\text{P}})$ [-]
k	=	Turbulent kinetic energy [m^2/s^2]
$k_0, k_1, k_2, k_{\text{P}}$	=	Constants [-]
K	=	Complete elliptic integral of the first kind [-]
l	=	Reference length [m], sectional lift [N/m]
L	=	Lift [N]
m	=	Mass [kg], number of monomials [-]
$\dot{m}$	=	Mass flow rate [kg/s]
M	=	Mach number V/a [-]
n	=	Rotational speed [Hz], load factor [-], number of data points [-]
N	=	Propeller normal force [N], number of elements or variables [-]
N_{c}	=	Normal-force coefficient $N/(q_\infty S_{\text{P}})$ [-]
N^*_{c}	=	Normal-force coefficient $N/(q_\infty S_{\text{ref}})$ [-]
p	=	Static pressure [Pa], helix pitch [m], observed order of grid conver. [-]
p^*	=	Theoretical order of grid convergence [-]
p_{t}	=	Total pressure [Pa]
P	=	Power [W], order of polynomial fit [-]
PREE	=	Payload-range energy efficiency $(W_{\text{PL}}R)/E_{\text{miss}}$ [-]
q	=	Dynamic pressure $0.5\rho V^2$ [Pa]
Q	=	Torque [Nm]
Q_{c}	=	Torque coefficient $Q/(q_\infty S_{\text{P}}R)$ [-]
r	=	Radial coordinate [m]
R	=	(Propeller) radius [m], range [nmi]
R^2	=	Coefficient of determination [-]
Re	=	Reynolds number $(\rho V l)/\mu$ [-]
RSS	=	Residual sum of squares
S	=	Area [m^2], propeller side force [N]
S_{c}	=	Side-force coefficient $S/(q_\infty S_{\text{P}})$ [-]
S^*_{c}	=	Side-force coefficient $S/(q_\infty S_{\text{ref}})$ [-]
S_{P}	=	Propeller disk area πR^2 [m^2]
S_{w}	=	Wing reference area $b \cdot c$ [m^2]
SP	=	Specific power [kW/kg]
t	=	Time [s], thickness [m]
T	=	Thrust [N], temperature [$^{\text{o}}$C]
T_{c}	=	Thrust coefficient $T/(q_\infty S_{\text{P}})$ [-]
T^*_{c}	=	Thrust coefficient $T/(q_\infty S_{\text{ref}})$ [-]
u, v, w	=	Velocity components in local reference frame [m/s]
u_τ	=	Friction velocity $(\tau_{\text{w}}/\rho)^{0.5}$ [m/s]
U	=	Uncertainty (95% confidence interval)
v_r	=	Radial velocity component [m/s]

v_θ	=	Azimuthal velocity component [m/s]
V	=	Velocity magnitude [m/s]
V_s	=	Stall speed [m/s]
V_P	=	Velocity magnitude at propeller location [m/s]
V_2	=	Take-off safety speed [m/s]
W	=	Weight $m \cdot g$ [N], weighting function [-]
$x_1, x_2, \ldots$	=	Independent variables
$X_1, X_2, \ldots$	=	Monomials
x, y, z	=	Cartesian coordinates in local reference frame [m]
X, Y, Z	=	Cart. coord. in inertial ref. frame, rotated by γ around Y' axis [m]
X', Y', Z'	=	Cartesian coordinates in inertial reference frame [m]
$y_1, y_2, \ldots$	=	Dependent variables
y^+	=	Non-dimensional wall distance $(\rho u_\tau y)/\mu$ [-]
α	=	Angle of attack [deg], constant factor in grid UQ, vortex velocity ratio [-]
α_P	=	Propeller angle-of-attack w.r.t. local inflow [deg]
β	=	Blade pitch angle [deg], coefficient of surrogate model
γ	=	Flight path angle [deg]
Γ	=	Circulation [m^2/s]
δ_f	=	Flap deflection angle [deg]
δ_P	=	Thrust-vectoring deflection angle [deg]
δ_{99}	=	Boundary-layer thickness [m]
$\delta(\ )$	=	Change w.r.t. single-propeller configuration
$\Delta(\ )$	=	Change w.r.t. isolated configuration or w.r.t. reference configuration
$\Delta x, \Delta y, \Delta z$	=	Displacement or spacing along Cartesian coordinates [m]
$\Delta\phi$	=	Relative blade phase angle [deg]
Δ_ϕ	=	Maximum difference observed among ϕ values in grid UQ
ϵ	=	Error
ε	=	Tip clearance w.r.t. wing surface [m]
ζ	=	Overall efficiency parameter $\eta_\mathrm{p}\eta_\mathrm{PT}(L/D)$ [-]
η	=	Conversion or transmission efficiency [-]
η_dp	=	Propulsive efficiency of distributed-propulsion system [-]
η_p	=	Propulsive efficiency $(-F_X V_\infty)/P_\mathrm{s}$ [-]
$\eta_\mathrm{p1}, \eta_\mathrm{p2}$	=	Propulsive efficiency of primary/secondary propulsion system [-]
η_P	=	Propeller efficiency $(TV_\infty)/P_\mathrm{s}$ [-]
η_1, η_2, η_3	=	Powertrain branch efficiencies [-]
θ	=	Azimuthal coordinate [deg]
$\Lambda_{c/2}$	=	Half-chord wing-sweep angle [deg]
μ	=	Dynamic viscosity [Pa·s], bank angle [deg]
ξ	=	Throttle setting [-]
ρ	=	Density [kg/m^3]
σ	=	Standard deviation
τ_w	=	Wall shear stress $\mu(\partial u/\partial y)_{y=0}$ [Pa]
ϕ	=	Blade phase angle [deg], dummy variable for grid UQ
ϕ_l	=	Azimuthal coordinate along square duct $l/(4b_\mathrm{duct})$ [-]
φ	=	Shaft power ratio $P_{s2}/(P_{s1}+P_{s2})$ [-]
Φ	=	Supplied power ratio $P_\mathrm{bat}/(P_\mathrm{f}+P_\mathrm{bat})$ [-]

χ	=	Thrust ratio of distributed-propulsion system T_{dp}/T [-]
ω	=	Vorticity [1/s], specific dissipation rate [1/s]
ω^*	=	Normalized vorticity $(\omega D_{\text{P}})/u_{\text{eff}}$ [-]
Ω	=	Angular velocity $2\pi n$ [rad/s]

ADDITIONAL SUB- AND SUPERSCRIPTS

airframe	=	Airframe-only contribution
b	=	Blade
bat	=	Battery
bL	=	Balked landing
cI	=	One-engine-inoperative ceiling
conv	=	Conventional, convective
cr	=	Cruise
div	=	Diversion mission
dp	=	Of distributed-propulsion system
e	=	Electrical (path)
eff	=	Effective
eq	=	Equilibrium
f	=	Friction contribution, fuel
FP	=	Equivalent flat plate
gb	=	Gearbox (path)
gt	=	Gas turbine (path)
ind	=	Induced
inst	=	Installed
invisc	=	Inviscid
iso	=	Isolated conditions
L	=	Landing, lower bound
max	=	Maximum
mean	=	Spatially- or temporally-averaged value
miss	=	Nominal mission
OE	=	Operative empty
OE'	=	Operative empty excluding wing and powertrain
off	=	Propeller-off conditions
on	=	Propeller-on conditions
opt	=	Optimal
p	=	Propulsive
p→w	=	Induced by propeller on wing
p	=	Pressure contribution
P	=	Propeller
PH	=	Parallel hybrid
PL	=	Payload
PT	=	Powertrain
q	=	Query location/instance
ref	=	Reference
rms	=	Root-mean-square
s	=	Shaft
SH	=	Serial hybrid

side	=	Relative to side propeller
SLS	=	Sea-level static conditions
ssc	=	Second-segment climb
tip	=	Blade tip
tot	=	Total
tr	=	Transition
TO	=	Take-off
U	=	Upper bound
visc	=	Viscous
vx	=	Vortex
w	=	Wing
w→p	=	Induced by wing on propeller
θ	=	Tangential component
0	=	At start of mission
1, 2	=	Primary/secondary powertrain branch, start/end of mission segment
$0.7R$	=	At radial station $r/R = 0.7$
$0.75R$	=	At radial station $r/R = 0.75$
∞	=	Freestream quantity
$\sim$	=	Phase-averaged quantity
$'$	=	Unsteady quantity (i.e. mean value subtracted)
$\breve{}$	=	Scaled value
$\hat{}$	=	Estimated value

ACRONYMS

AC	=	Alternating current
AD	=	Actuator disk
AEO	=	All-engines operative
BAT	=	Battery
BEM	=	Blade element method
BL	=	Balked landing, Boundary layer
BLI	=	Boundary-layer ingestion
BSFC	=	Brake-specific fuel consumption
CFD	=	Computational fluid dynamics
CFL	=	Courant-Friedrichs-Lewy number
CNC	=	Computer numerical control
CST	=	Class-function/shape-function transformation
CTOL	=	Conventional take-off and landing
DC	=	Direct current
DNW	=	German-Dutch Wind Tunnels
DoE	=	Design of experiments
DP	=	Distributed propulsion
EARSM	=	Explicit algebraic Reynolds stress model
EIS	=	(Year of) entry into service
EM	=	Electrical machine
ESC	=	Electronic speed controller
EU	=	European Union
F	=	Fuel

FB	=	Full blade
FOV	=	Field of view
GB	=	Gearbox
GDP	=	Gross domestic product
GEN	=	Generator
GT	=	Gas turbine
HEDP	=	Hybrid-electric distributed propulsion
HEP	=	Hybrid-electric propulsion
IR	=	Infrared
LEDP	=	Leading-edge distributed propulsion
LHS	=	Latin-hypercube sampling
LLM	=	Lifting line method
LST	=	Low-speed tunnel
LTT	=	Low-turbulence tunnel
MEA	=	More-electric aircraft
MRF	=	Multiple reference frame
MTOM	=	Maximum take-off mass
MUSCL	=	Monotonic upstream-centered scheme for conservation laws
NACA	=	National Advisory Committee for Aeronautics
NASA	=	National Aeronautics and Space Administration
OEI	=	One-engine inoperative
OEM	=	Operative empty mass
OEW	=	Operative empty weight
OJF	=	Open-jet facility
OTW	=	Over-the-wing
OTWDP	=	Over-the-wing distributed propulsion
P	=	Propulsor or Propeller
PE	=	Propulsive empennage
PIV	=	Particle-image velocimetry
PM	=	Panel method
PMAD	=	Power management & distribution system
PTE	=	Partial-turboelectric
RANS	=	Reynolds-averaged Navier-Stokes
ROC	=	Rate of climb
RSB	=	Rotating shaft balance
SL	=	Sea level
SM	=	Surrogate model
sPD	=	Small propeller domain
SPPH	=	Serial/parallel partial hybrid
SST	=	Shear-stress transport
STOL	=	Short take-off and landing
TOM	=	Take-off mass
TOW	=	Take-off weight
UQ	=	Uncertainty quantification
VTOL	=	Vertical take-off and landing
WT	=	Wind tunnel

Part I

Background

1

INTRODUCTION

The world population will continue to grow in the coming years and is currently expected to reach between 9 and 11 billion human beings towards the end of the century [1, 2]. Moreover, although more than 8% of the world population still lives in conditions of extreme poverty as of 2019 [3], the average gross domestic product (GDP) per capita has increased exponentially over the past century [4]. This growth is accompanied by an increase in the amount of kilometers traveled per capita, which is expected to increase by 54% by 2050, relative to the year 2020 [5]. Furthermore, the cost of air travel per passenger kilometer has reduced significantly in the past decades [6, 7]. Therefore, not only the total amount of kilometers traveled is increasing, but also the fraction covered using air transport is on the rise [5, 6]. Consequently, the air transport sector has grown at a much higher rate than the world economy: between 1970 and 2010, the world's GDP increased three-fold, while the amount of scheduled revenue passenger-kilometers covered worldwide by air increased ten-fold [7]. Although this growth can be negatively affected at times by crises such as the COVID-19 pandemic, the aviation industry is expected to keep on expanding in the long term [8, 9].

While this growth is both a driver and a consequence of globalization, it also entails significant challenges regarding the sustainability of the system. The aviation industry contributes to global warming through the emission of carbon dioxide (CO_2), nitrous oxides (NO_x), and contrail and cirrus formation, among other factors [10]. It is currently responsible for approximately 2.4% of the total anthropogenic CO_2 emissions and 3.5% of the effective radiative forcing [11]. For practically all future scenarios investigated, this relative impact of the aviation sector on global warming is predicted to rise in the coming decades [12–14]. Moreover, though the pandemic in 2020 showed that a temporary reduction in flights directly translates into a non-negligible reduction in anthropogenic emissions [15, 16], the effects of aviation on the atmosphere can last for tens or hundreds of years [14], and thus reductions in emissions today will only slow down global temperature change in several decades [17]. Consequently, institutions such as the European Commission (EC) [18] and the National Aeronautics and Space Administration (NASA) [19] have set strict sustainability goals to reduce the climate impact of aviation as soon as possible. As an example, the Flightpath 2050 goals target a 75% reduction in CO_2 emissions and a 90% reduction in NO_x emissions, relative to the year 2000 [18].

One way to meet these targets is to improve the efficiency of the propulsion system and its integration with the airframe [20–22]. A key consideration in this sense is the use of alternative energy sources, such as liquified natural gas [23], hydrogen [24, 25], sustainable aviation fuels [26, 27], or batteries for (hybrid-) electric propulsion [22, 24]. Of these energy sources, especially battery-based propulsion has gained traction in recent years, with the first fully-electric commercial flight taking place in 2019 [28], and the first type certificate for a fully-electric aircraft being awarded in 2020 [29]. The use of such aircraft for commercial purposes could reduce the aviation sector's CO_2 emissions, especially if the electricity were produced using renewable energy sources [30, 31]. Therefore the question is not *if* electrical power should be used for aircraft propulsion, but *how*.

1.1. HYBRID-ELECTRIC PROPULSION

The aforementioned milestones were achieved for small, general-aviation aircraft. However, the largest fraction of fuel consumption of the aviation sector comes from the narrow-body and wide-body markets [32]. These market segments—especially the narrow-body market—are also the ones which are projected to grow the most in the coming decade [33]. For these large passenger aircraft, fully-electric propulsion is not viable without unrealistically high battery specific-energies [32, 34–36]. Thus, hybrid solutions with only a modest degree of "electrification" are required instead [37]. In these *hybrid-electric propulsion* (HEP) systems, (part of) the power obtained from the energy source(s) is transmitted to the propulsors as electrical power. This can improve aircraft efficiency in two main ways.

The first aims to improve the powertrain efficiency, i.e., to improve the transmission efficiency from the energy sources to the shaft of the propulsive device. This can be achieved by directly exploiting the high conversion efficiency of electrical machines to drive the propulsors [38], or by using them to down-size or improve the off-design performance [39, 40] and surge margins [41] of the combustion engine. This design strategy requires the use of batteries, and is typically applied in a parallel architecture (see e.g. Refs. [40, 42–46]), without significant modifications to the airframe. The use of batteries can provide additional "more-electric aircraft" (MEA) benefits, such as electric taxiing, engine starting capabilities, or the elimination of hydraulic or bleed air systems for environmental control and control-surface actuation [47].

The second design strategy aims to improve the aero-propulsive efficiency of the aircraft, i.e., to increase the lift-to-drag ratio of the airframe or the thrust-to-power ratio of the propulsive devices. This approach does not necessarily require batteries, but takes advantage of the scalability of electrical machines and the versatility of electrical power distribution to place the propulsive devices at beneficial locations on the airframe. This strategy is referred to as *distributed propulsion* (DP), and leads to noticeable changes in the external layout of the aircraft. Several examples of such aircraft configurations are depicted in Fig. 1.1. Spreading the thrust over multiple, electrically-driven propulsors can also provide short take-off and landing (STOL) operations [48, 49], reduced yawing moments in case of component failure, and effective thrust-vectoring capabilities which may reduce the required tail size [50, 51]. Furthermore, the increased design freedom in terms of the number, size, and location of the propulsors can enable new low-noise configurations with reduced blade tip-Mach numbers or improved noise shielding.

(a) NASA X-57 Maxwell [48]: tip-mounted and leading-edge distributed propulsion. Credits: NASA Langley/Advanced Concepts Lab, AMA, Inc.

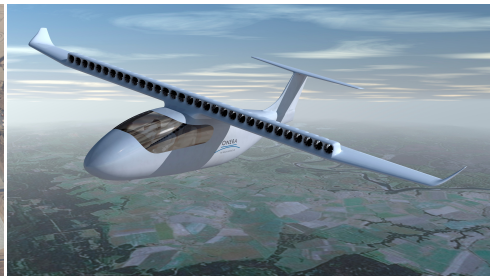

(b) Onera Ampere [52]: over-the-wing distributed propulsion. © Onera, reproduced with permission.

(c) Onera DRAGON [53]: under-the-wing distributed propulsion. © Onera, reproduced with permission.

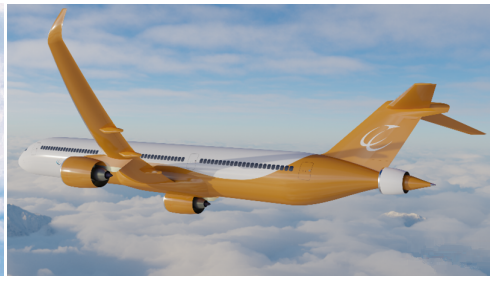

(d) Centerline propulsive-fuselage concept: boundary-layer ingestion. Adapted from Seitz et al. [54].

Figure 1.1: Examples of (hybrid-) electric aircraft concepts with distributed propulsion.

The research presented in this dissertation focuses on the second approach, that is, on the use of HEP to increase the aero-propulsive efficiency of the aircraft. More specifically, the research focuses on the lower-speed variants of passenger transport aircraft: the regional turboprop market. There are several reasons for this. Firstly, the lower flight speed allows for the use of propeller propulsion. This is inherently more efficient than turbofan or turbojet propulsion [55] and, moreover, propellers can be installed more easily at different locations on the aircraft. This makes it possible to exploit synergistic aerodynamic interaction effects with the airframe, which is much more problematic at higher flight speeds due to the local appearance of supersonic velocities and the challenges involved in integrating ducts and nozzles with the airframe. Secondly, as the technology readiness-level of high power-density electrical machines gradually scales up, the use of such technologies is likely to become feasible earlier for turboprop aircraft than for transonic aircraft, which require more powerful engines. And thirdly, when analyzing the range flown by scheduled passenger flights, the mode is approximately 1000 km [56, 57], with more than 60% of all available seat kilometers corresponding to mission ranges below this value, and more than 90% to ranges below 2000 km [58]. Narrow-body [59], or even wide-body [60] turbofan aircraft are often used to cover such ranges, despite having a design range which is several times higher. These ranges can be covered by existing turboprop aircraft without a significant increase in door-to-door travel time. Although this would lead to an appreciable reduction in fuel consumption, a shift towards turboprop aircraft for these missions has generally been hindered by the associ-

ated cabin noise levels and the reduced passenger acceptance for propeller propulsion [58]. However, both these factors can likely be mitigated with distributed-propulsion systems. Therefore, substituting this market segment with high-efficiency, distributed-propulsion aircraft could imply a significant reduction in the environmental footprint of the aviation sector.

The use of electrically-distributed propulsion for such missions opens the design space to a wide range of configurations which are unpractical with conventional combustion engines. Hence, additional questions arise: How many propellers should be used? How will they be powered? Where should they be installed? In this sense, multiple configurations can be considered which would enhance the aerodynamic performance of the aircraft, such as leading-edge distributed propellers [61, 62], over-the-wing propellers [52, 63], boundary-layer ingesting propellers [54, 64], or tip-mounted propellers [65, 66] (see Fig. 1.1). Though many of these configurations have been investigated to a greater or lesser extent at subsystem level, it is unclear which one would provide the largest benefit at aircraft level.

1.2. OVER-THE-WING PROPULSION

Of the different propeller arrangements, the over-the-wing (OTW) propeller is particularly interesting for regional transport aircraft. First, because it can significantly increase the wing lift-to-drag ratio in both cruise [63] and high-lift [67] conditions. In this sense, OTW propellers present a clear advantage over tractor propellers, because they allow for a "clean" wing. Tractor propellers, on the other hand, create strong spanwise gradients in the wing lift distribution [68, 69], which leads to induced drag, and additionally cause part of the boundary layer to transition from laminar to turbulent [70]. Additionally, the high-lift capabilities of the wing can be increased with OTW propellers if the propeller or its slipstream are deflected, similarly to the configurations analyzed in e.g. Refs. [71, 72]. Furthermore, due to the shielding effects of the wing, flyover noise can be reduced [73, 74]. This also constitutes an advantage over tractor and, especially, pusher propellers.

The OTW propeller is not a new concept. A well-known example of OTW propulsion, shown in Fig. 1.2, is the Dornier Do-X. This 50-ton seaplane, which featured twelve propellers driven by 525 hp piston engines, flew for the first time in 1929 [75]. However, despite the aforementioned advantages, the vast majority of planes produced over the past century do not feature OTW propellers, and research on these configurations is equally scarce. This can largely be attributed to the associated propulsive-efficiency penalty observed in some studies [76], the need for large pylons to support the propeller above the wing, and potentially to a large thrust-induced, nose-down pitching moment. However, these drawbacks may be reduced if a single, large propeller is substituted by multiple, smaller ones, similarly Fig. 1.1b. Over-the-wing propulsion and hybrid-electric propulsion therefore present a synergy: the benefit of combining these two technologies is likely to exceed the summation of the benefits provided by the two separately. While historically this has not been feasible due to the low power- and energy-density of electrical components, in the future an aircraft with over-the-wing distributed propulsion (OTWDP) may constitute a low-noise, high-efficiency alternative for the regional turboprop market.

Figure 1.2: The Dornier Do-X: an early application of (distributed) over-the-wing propellers.
Credits: San Diego Air and Space Museum.

However, much research is needed to understand the true potential of OTWDP systems, and to find out whether it offsets the complexity and weight penalty typically associated to HEP powertrains (see e.g. Refs. [77–79]). Such research is required on multiple fronts. On one hand, the aerodynamic characteristics of both over-the-wing and distributed propeller systems are not readily understood. This is evidenced by the contradictions observed in literature: while some authors have found moderate [67] to drastic [68] reductions in propulsive efficiency with OTW propellers, others have found an increase in propulsive efficiency [63]. Analogously, most authors conclude that OTW propellers reduce the drag of the wing [63, 68], but for some configurations it has been found to increase [80]. This makes it difficult to extrapolate the findings of these studies to distributed-propulsion configurations, where the complexity of the flowfield is further increased due to additional elements such as ducts or adjacent propellers. On the other hand, even if these aerodynamic characteristics could be understood, and subsequently modeled, there are no conceptual design methods which systematically incorporate these effects in the aircraft sizing process. Hence, it is currently extremely challenging to compare the aircraft performance of different distributed-propulsion configurations under equal assumptions with the appropriate levels of fidelity.

Several of these gaps have been identified in recent investigations of the research infrastructure within the European Union (EU). These investigations highlight the need for wind-tunnel testing, ground testing, and scaled-flight testing to mature hybrid-electric and distributed-propulsion technologies [81]. Multiple EU initiatives, such as the NOVAIR research project [37, 44, 82, 83], aim to shed a light on these challenges. More specifically, one of the key objectives of NOVAIR [84] is to perform the "preliminary design of radical aircraft configurations, optimized for the integration of Hybrid Electric Propulsion (HEP) systems [...] with a focus towards propulsion integration and propulsion system architecture development." The research presented in this dissertation aims to support this objective by, for the first time, bridging the two aforementioned gaps: the aerodynamic characterization and the conceptual design of hybrid-electric aircraft with OTW distributed propulsion.

1.3. RESEARCH OBJECTIVES

At the start of this research project, in 2017, a review of the state-of-the-art was performed. This analysis revealed that:

- A large number of hybrid-electric aircraft concepts are currently being investigated, and prototypes have been built and tested.
- A meagre amount of information is available regarding the design process of these concepts, and no systematic design procedure is followed.
- Hybrid-electric powertrains are widely researched at component level, and component sizing methods have been developed.
- Analyses of the aerodynamic performance of over-the-wing or distributed-propulsion systems exist, but are limited in number and generally lack detail.
- No unsteady or off-design aero-propulsive interaction studies have been found for distributed-propulsion layouts.
- The findings of detailed aero-propulsive interaction studies are rarely, if ever, linked to their impact at vehicular level.

Based on this synopsis, the main research question of this project is formulated:

What are the effects of over-the-wing distributed-propulsion on the energy efficiency of hybrid-electric aircraft?

To be able to answer this question, several objectives must be met. These objectives are:

1. To understand the dominant steady and unsteady aerodynamic interaction effects that take place in over-the-wing distributed-propulsion systems from a phenomenological point of view.
2. To establish how these interaction mechanisms affect the aerodynamic performance of the system (i.e., propulsors plus wing).
3. To develop a sizing method capable of including these effects in the design process of hybrid-electric aircraft.
4. To assess the impact of incorporating over-the-wing distributed-propulsion systems on the overall performance of the aircraft.

1.4. SCOPE & LIMITATIONS

The objectives defined above already suggest that the research entangles different disciplines (aerodynamics, aircraft design, flight performance) and different levels of system complexity (single propeller, multiple propellers, propellers plus wing, complete aircraft). It is therefore necessary to limit the scope of this research, such that it can be performed within the time and resources available. Two key limitations have to be considered in this sense: limitations in the applicability of the aircraft design approach, and limitations in the representativeness and scalability of the aerodynamic analyses.

REGARDING THE AIRCRAFT DESIGN APPROACH

As discussed previously, the research presented in this dissertation focuses on passenger transport aircraft. Therefore, the sizing methods, design cases, and discussions focus on subsonic, fixed-wing aircraft of the commuter (CS-23/FAR Part 23) and large aeroplanes (CS-25/FAR Part 25) categories, with conventional or short take-off and landing capabilities (CTOL and STOL, respectively). Thus, in general, the methods presented are not applicable to vertical take-off and landing (VTOL) aircraft, rotorcraft, or lighter-than-air vehicles. Moreover, the methods are intended for conventional tube-and-wing configurations. In this way, the effect of hybrid-electric and distributed propulsion can be assessed by comparing to existing conventional aircraft, without superimposing the effect of additional radical technologies. If this is done successfully, then the methods and findings of this dissertation can be expanded in future work to account for less conventional morphologies such as blended wing bodies or flying wings.

Furthermore, the level of detail of the design process is limited to the preliminary sizing phase, which is the first step of aircraft conceptual design [85]. There are three reasons for this. First, because the sizing method has to remain generic, such that different configurations can be compared without knowing the details of the aircraft layout. Second, because in this way it is possible to trace the effects of distributed propulsion and gain a conceptual understanding of the key implications, without getting lost in details. And third, because implementing a detailed design method which can account for hybrid-electric distributed propulsion would require an unrealistically large amount of time. This implies that topics such as stability and control are not investigated in this research.

Moreover, the purpose of this exploratory research is to investigate the *aerodynamic performance* characteristics of over-the-wing distributed propulsion, and determine what effect they have at aircraft level. Hence, the design methods emphasize on the aerodynamic implications of distributed propulsion, and do not investigate other aspects (e.g. structural implications) in detail. Analogously, hybrid-electric propulsion is treated as a means to an end; that is, as an enabling technology for over-the-wing distributed propulsion. Thus, the level of fidelity of the hybrid-electric powertrain models are kept to a minimum, while ensuring that the key sensitivities are accounted for—such that a fair quantitative comparison can be made between different configurations. This implies that many components of the HEP system are simplified and treated as "black boxes". Detailed studies of these powertrains and the "black boxes" that constitute them can be found in the work of others, as discussed in Chapter 2.

Finally, when assessing the impact of these new technologies, different configurations are compared in terms of vehicle-level metrics such as the maximum take-off mass and energy consumption. These metrics serve as indicators of the costs and emissions of the aircraft, and are sufficient to determine whether one configuration is better than another in the preliminary sizing phase. However, the costs and emissions are not calculated explicitly. Likewise, fleet-level implications, as well as potential changes in maintenance procedures, operations, or infrastructure requirements, are considered beyond the scope of this research.

1

REGARDING THE AERODYNAMIC ANALYSES

In a generic sense, an over-the-wing distributed-propulsion system comprises numerous elements (wing, high-lift device(s), rotors, ducts, nacelles, pylons,...) installed in close proximity, each of which has an aerodynamic effect on all the others. However, given that such systems have not been practical until the recent appearance of high-efficiency electrical machines, there is only a limited amount of research on these aerodynamic interaction effects. It is therefore unknown how the flow field evolves in such a system, or what the optimal design would look like. Consequently, this research does not focus directly on the aerodynamic performance of a complete OTWDP system but, instead, takes a step back and first attempts to understand the aerodynamic interaction between individual components. Special attention is paid to the components that act as lifting surfaces: the wing, blades, and—to a lesser extent—the duct. Secondary elements such as the nacelles, spinners, or pylons are not looked into in detail.

Central to this investigation is the rotational device that converts shaft power into momentum of the flow: a rotor, fan, or propeller. Although there is no clear-cut distinction between these three concepts, when talking about the propulsive devices of an aircraft, generally a "rotor" refers to a device which lifts or propels the aircraft in hover conditions (i.e., without a significant axial inflow velocity). A "propeller", on the other hand, is intended for use in forward flight[1]. Finally, a "fan" can be used for both hover and forward flight, but generally has a high number of blades and a duct. Since the OTWDP concept is primarily intended for forward flight, and given that it is unclear whether the duct is even necessary, the propulsive device will be treated as a propeller in this research. This implies that the propulsive device will have a "typical" propeller geometry, and not present a geometry optimized specifically for OTWDP. The same can be said for other elements such as the duct or wing. These geometries are selected to represent an OTWDP system as closely as possible, but a priori it is unknown what their optimal shape looks like. Hence, the phenomena and trends observed in this research are representative of what one could encounter in an OTWDP system, but the quantitative performance data will not match those of an actual "optimized" design.

The propellers of the OTWDP system produce a three-dimensional and unsteady flow field. This flow field interacts with the surrounding elements, which can be stationary (wings, duct) or rotating (adjacent propellers). Some of these interaction effects are inviscid in nature, while others present significant viscous effects. Moreover, the effect of different design parameters and operating conditions on these interaction effects is unclear. The complexity of the flow field, combined with the large amount of variables involved, makes most numerical methods unsuitable or inefficient to study the detailed interaction phenomena. Hence, in this research, a predominantly experimental approach is taken. The disadvantage of this approach is that scaled-down versions of the components have to be investigated, given the available wind-tunnel facilities, hardware, and resources. Therefore, the models and test matrices are designed such that most non-dimensional parameters, such as the diameter-to-chord ratio, advance ratio, or aerodynamic force coefficients, are representative of the full-scale application.

[1] Highly-loaded, unducted propellers with swept blades for high-subsonic flight are also known as "propfans" [86] or "open rotors" [87]. The term "open rotor" is common especially for contra-rotating configurations.

However, since the wind tunnels operate at ambient conditions (pressure, temperature, density), a limitation in model size and freestream velocity implies that the Reynolds number and Mach number of the experiments do not match those of the full-scale aircraft. To illustrate these differences, Table 1.1 presents the maximum Reynolds and Mach numbers tested experimentally in this research, and compares them to typical values that can be expected from a full-scale aircraft application. The table shows that the freestream and blade-tip Mach numbers achieved in the experiments are approximately one third of the values of the full-scale aircraft in cruise. For the wing performance, this is not a major limitation, since in any case the flow is subsonic for the aircraft configurations studied in this research. However, the propeller blades of an OTWDP system could reach transonic speeds on a full-scale aircraft. In that case, the loading distribution on the propeller disk changes due to compressibility effects, and the propeller efficiency is reduced (see e.g. Refs. [88, 89]). This does not significantly alter the interaction phenomena observed in this study, but does significantly change the optimal propeller design of the full-scale system.

Table 1.1: Comparison of typical operating conditions of the experimental campaigns performed in this research and a full-scale, ATR72-like aircraft. Values with asterisks are assumed. Propeller blade chord assumed to be $c_{0.7R} = 0.15R$.

	Wind tunnel (max)	**Full-scale turboprop (cruise)**	**Full-scale OTWDP (cruise)**	**Full-scale OTWDP (approach)**
Diameter over chord D_P/c	0.2	1.7	0.2*	0.2*
Advance ratio J	0.8	1.5*	1.8*	1.0*
Freestream Mach M_∞	0.12	0.45	0.45	0.17
Prop. tip Mach M_{tip}	0.36	1.00	0.87	0.57
Wing Reynolds Re_c	$1.6{\cdot}10^6$	$1.3{\cdot}10^7$	$1.3{\cdot}10^7$	$9.0{\cdot}10^6$
Prop. blade Reynolds $Re_{0.7R}$	$9.0{\cdot}10^4$	$3.6{\cdot}10^6$	$3.7{\cdot}10^5$	$3.3{\cdot}10^5$

Regarding the Reynolds-number effects, Table 1.1 shows that the wing-chord-based and blade-chord-based Reynolds numbers are nearly one order of magnitude lower in the experiments than in the full-scale OTWDP aircraft. Hence, the actual values of the performance metrics obtained in this study differ from those in real flight. This is especially the case for the propeller, since the low blade Reynolds number ($Re_{0.7R} < 10^5$) makes the performance of the propeller sensitive to laminar-flow effects—as evidenced in recent investigations [90]. Nevertheless, as explained in the following chapters, the most important interaction effects in terms of wing and propeller performance are inviscid in nature. Hence, the effect of the lower Reynolds number on the *changes* in performance due to interaction is of secondary importance. One exception in this regard is the effect of Reynolds number on the interaction between the propeller and the wing boundary-layer. In that case, the Reynolds number not only has a small quantitative effect (i.e. it changes the lift or drag values), but could also have a large qualitative effect (i.e. it changes the type of flow separation on the wing). Thus, special care has to be taken when interpreting the results, and the effect of Reynolds number has to be addressed explicitly. For this reason, this interaction is discussed separately from the other interaction effects in a dedicated chapter (Ch. 7).

1

1.5. RESEARCH OUTLINE

The research project is divided into four main parts, as shown in Fig. 1.3. **Part I** establishes the research plan and context. This includes the present introductory chapter, where the objectives are defined along with the scope of the project, and a second chapter which provides a review of some of the concepts used throughout the dissertation.

Part II then presents how aero-propulsive interaction effects can be accounted for in the preliminary sizing process of hybrid-electric aircraft, *independently of the type of propulsors used to generate thrust.* Part II therefore aims to fulfill **Objective 3** (see Sec. 1.3). For this, a preliminary sizing method is formulated in Chapter 3 based on elementary physics-based relations, and proven semi-empirical methods. This method is validated for hybrid electric aircraft in Chapter 4, without considering any aero-propulsive interaction effects. Then, in Chapter 5, the consequences of incorporating these interaction effects are demonstrated by sizing an aircraft with (leading-edge) distributed propulsion. These chapters provide an understanding of the relation between aero-propulsive interaction effects and aircraft-level performance metrics, laying the foundation for the subsequent investigation into the interaction effects of OTWDP systems.

Consequently, **Part III** looks into the aerodynamic interaction effects of OTWDP systems, *independently of the type of drivetrain used to power the shafts.* Given the large amount of aerodynamic surfaces involved, a large portion of this Part is dedicated to understanding the interaction between individual components from a phenomenological perspective (**Objective 1**). Hence, experimental and numerical setups with simplified geometries are used. To this end, Chapter 6 studies the aerodynamic interaction between a single OTW propeller and the wing (Sec. 6.1), between a single propeller and a simplified duct (Sec. 6.2), and between multiple propellers (Sec. 6.3). These investigations show that, with the exception of possible flow separation in duct corners, the most important flow phenomena in terms of system performance are inviscid effects. Subsequently, Chapter 7 is dedicated to the interaction between the propeller and the wing boundary-layer. This interaction has a dedicated chapter because viscous effects play an important role, and thus the findings cannot be scaled up directly to actual aircraft applications. Once the key flow phenomena have been investigated, Chapter 8 looks into the performance of the OTWDP system in cruise conditions, and how to model it (**Objective 2**). It is important to emphasize that the performance model obtained corresponds to a simplified geometry, as discussed in Sec. 1.4, and not to a fully-optimized, case-specific design of an OTWDP system.

Finally, **Part IV** combines the sizing method of Part II with the qualitative design considerations and simplified performance models of Part III to estimate the impact of OTWDP on the performance of a hybrid-electric aircraft (**Objective 4**). For this, first a series of sensitivity studies is conducted in Chapter 9, to understand the impact of different HEP and OTWDP design parameters, technology assumptions, and mission requirements on aircraft-level performance metrics. Since, chronologically, this design-space exploration phase was performed before most of the aerodynamic studies of Part III, only rudimentary aerodynamic models are used. The lessons learned are then applied in Chapter 10, where a HEP aircraft with OTWDP is sized using the aerodynamic model of Chapter 8. This design study concludes the main body of the dissertation, and is followed by the conclusions & recommendations for future research in Chapter 11.

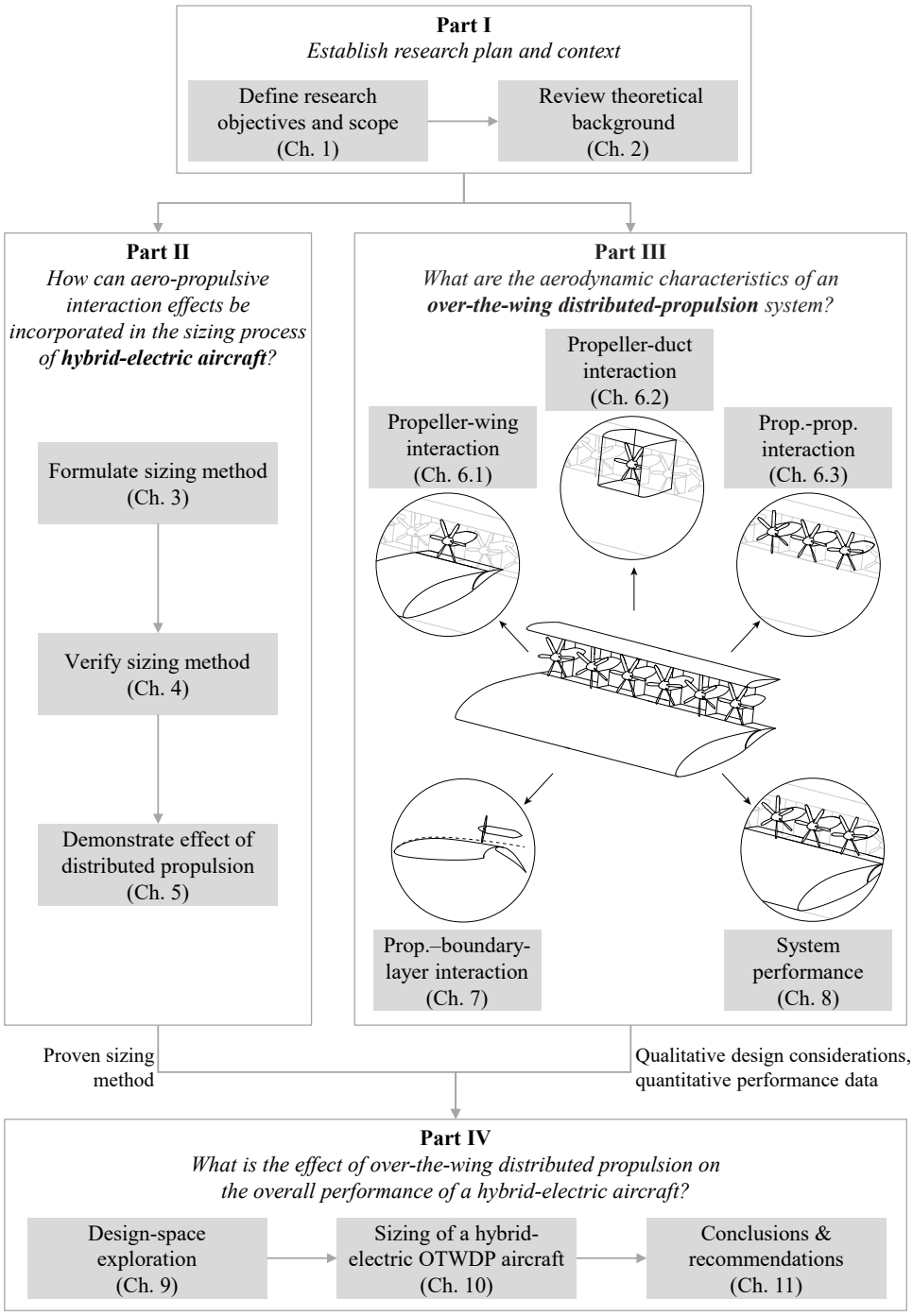

Figure 1.3: General outline of the research presented in this dissertation.

2

THEORETICAL BACKGROUND

This chapter provides a brief overview of some of the fundamentals of hybrid-electric aircraft sizing (Sec. 2.1) and propeller propulsion (Sec. 2.2), which serves as a basis for the research presented in this dissertation. Although the discussions focus only on the aspects that are relevant for the present work, some key references are provided in case the reader is looking for additional background information.

2.1. CONCEPTUAL DESIGN OF HYBRID-ELECTRIC AIRCRAFT

The aircraft design process comprises three main phases, as shown in Fig. 2.1: conceptual design, preliminary design, and detailed design. This research focuses on the conceptual *design* phase, with special attention being paid to the preliminary *sizing* process since it provides the first quantitative estimates of top-level aircraft parameters such as the take-off mass (TOM) or energy consumption. The conceptual design of tube-and-wing aircraft with conventional propulsion systems can be performed following classical aircraft design books such as the works of Torenbeek [91], Roskam [85], or Raymer [92].

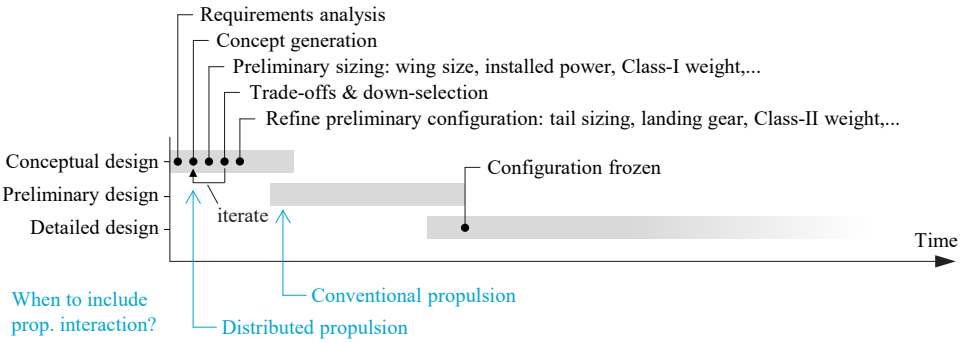

Figure 2.1: Overview of the different phases of the aircraft design process.

Due to the multidisciplinary, iterative, and semi-empirical nature of the design process, there is no single universal "design theory". The differences among the various design approaches become even more pronounced when incorporating a technology such as hybrid-electric propulsion, for which no extensive empirical data or knowledge base exist. To provide a starting point, Sec. 2.1.1 provides a brief summary of existing HEP aircraft sizing methods, and shows how the traditional sizing methods must be expanded to account for hybrid-electric and distributed propulsion. Subsequently, Sec. 2.1.2 presents several figures of merit that can be used to assess the benefit of distributed propulsion and compare the energy efficiency of different configurations.

2.1.1. SIZING METHODS

Several authors have developed sizing methods specifically for hybrid-electric aircraft [93–101], of which the works of Isikveren [102, 103] and Finger [104] are particularly relevant for the present work. Numerous other HEP aircraft design studies have been performed using case-specific sizing approaches, maintaining take-off mass constant[1], or without clearly specifying the sizing approach. An overview of many of these studies can be found in Refs. [105, 106]. Definitions of the main parameters used in such studies are given in Ref. [107]. In general, the aero-propulsive interaction effects are not included in a systematic and generic manner in these studies. Moreover, while all methods account for the presence of a hybrid-electric powertrain, they do so in varying levels of fidelity and flexibility. A particularly important aspect in this regard is the so-called power split between the "consumable" (i.e., variable weight: fuel) and non-consumable (i.e., constant weight: battery) energy source, which can be a constant throughout the mission, a design variable throughout the mission, or follow a predefined strategy (e.g. "peak shaving", see Ref. [108]). These strategies have a large impact on the vehicle sizing [109], and therefore different sizing approaches are likely to provide substantially different designs for the same set of requirements.

This shows that two key modifications have to be made to the traditional sizing methods in order to size hybrid-electric configurations with distributed propulsion. First, due to the strong coupling between lift, drag, and thrust in the case of highly-integrated propulsion systems, the effect of the aerodynamic interaction between the airframe and the distributed propulsors must be accounted for [110]. In conventional aircraft configurations, this coupling is relatively weak compared to the absolute forces generated by the wing and propulsors, and therefore the aerodynamic interaction can be neglected until the tail-sizing process or later in the design process. However, for distributed-propulsion configurations, the interaction effects can have a direct impact on the wing sizing and power requirements [48], and therefore they must be included already in the preliminary sizing phase, as reflected in Fig. 2.1. For this, the basic flight-performance equations of the aircraft must be modified, as shown in Ch. 3. This implicitly assumes that future airworthiness regulations will change such that the performance requirements can be met in powered conditions, instead of in engine-idle conditions. Although this change is subject to debate [111], it should be kept in mind that some of the envisioned benefits of distributed-propulsion systems cannot be achieved with the current regulations.

[1] Note that such "retrofit" studies are not actual design studies, since the aircraft is not actively sized to meet a predefined set of requirements.

The second main modification that has to be made to the traditional sizing methods is to include the components of the electric drivetrain. These components are conceptually shown in the example of Fig. 2.2, which represents a hypothetical HEP configuration with a primary aft-mounted propulsor system, and a secondary OTWDP system. The figure also indicates some of the potential secondary applications of the electrical power. Components such as switches, electric actuators, cooling elements, or redundant connections in case of component failure are not shown. A more detailed example of such elements in provided in Ref. [112]. From a preliminary sizing perspective, the batteries, electrical machines (motors and generators), converters, inverters, and rectifiers used to produce propulsive power are the most important to account for, since they are not present in conventional propulsion systems, but can constitute an appreciable fraction of the aircraft weight [113–115].

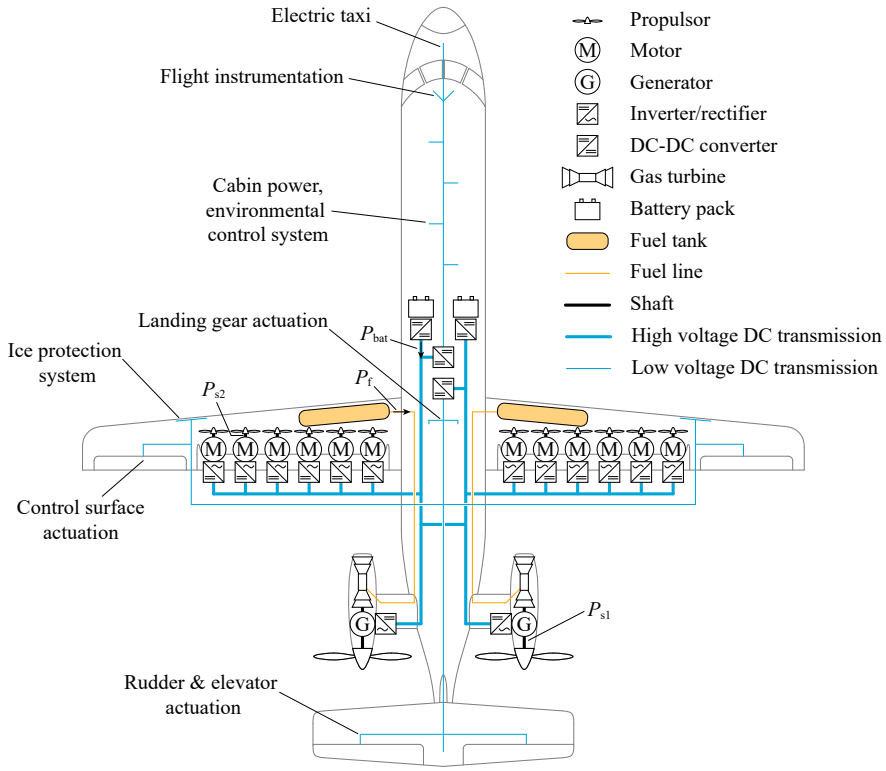

Figure 2.2: Simplified overview of the main components of a hypothetical HEP system, including potential MEA applications. Component size and position not drawn to scale.

However, at the start of the design process, little is known regarding the aircraft, and hence the level of detail of the powertrain modeling must be kept to a bare minimum. Therefore, the batteries and electrical machines (with their associated rectifiers/converters) are treated as "black boxes" in the present research, characterized by a transmission or conversion efficiency η, and a gravimetric specific energy (e, in J/kg

or Wh/kg) or specific power (SP, kW/kg), while the volumetric constraints are neglected. Other components such as cables and switches are gathered in a "power-management and distribution" (PMAD) box. When assuming values of e and SP for batteries, it is important to make a distinction between cell-level and pack-level values, since the cells typically constitute between 30% and 80% of the total battery-pack weight [36]. Moreover, a minimum state-of-charge must be assumed for the batteries (generally around 20% [78]) to avoid detrimental effects on battery life, and the combination of specific energy and specific power should correspond to realistic C-rates. References [116–118] provide an overview of current and projected specific-energy values for various battery chemistries. Given the general uncertainty of such projections, it is important to assume a year of entry-into-service (EIS) of the aircraft, and additionally perform a sensitivity study with respect to the battery technology level (see Chapters 4 and 9).

Regarding the electrical machines and power converters, several projections of specific power and efficiency can be found in Refs. [106, 119]. Important considerations when evaluating such projections are the system voltage, machine topology, and thermal management. For additional information on these topics, the reader is referred to Refs. [120–123]. However, since these considerations are beyond the preliminary sizing phase, in subsequent chapters a fixed weight penalty is assumed for the power distribution and thermal management systems. The level-of-fidelity of the component modeling can also be increased by using simplified physics-based or empirical models to represent the behavior of the electrical components. Given that this is considered beyond the scope of the present research, the reader is referred to Refs. [104, 124–126] for simplified battery, electrical machine, or power converter models .

2.1.2. AIRCRAFT PERFORMANCE INDICATORS

Several figures of merit are required to compare the overall performance of hybrid-electric aircraft to conventional reference aircraft for the same set of mission requirements and EIS. The first figure of merit is the maximum take-off mass (MTOM) of the aircraft. This parameter is often used for comparison in aircraft design studies, since it gives an indication of the "size" of the aircraft and has a direct impact on power requirements, energy requirements, and production and maintenance costs [92]. Moreover, it determines the certification category of the aircraft.

A second figure of merit is required to quantify the energy efficiency of the aircraft. The energy consumption of the aircraft is an important metric because, in addition to being tightly related to the operating costs, it determines the emissions generated by the aircraft[1]. Several such performance metrics exist for conventional aircraft, such as the payload-range efficiency (PRE = $W_{\mathrm{PL}}R/W_{\mathrm{f}}$) [127], or the payload-fuel energy efficiency (PFEE = $W_{\mathrm{PL}}R/E_{\mathrm{f}}$) [128]. Alternative metrics have also been used for hybrid-electric aircraft, such as the energy-specific air range (ESAR = $\mathrm{d}R/\mathrm{d}E$) [129], the cost-specific air range (COSAR) [94], or the productivity-specific energy consumption (PSEC = $E/(m_{\mathrm{PL}}R)$) [130], where the energy consumed E includes both fuel and bat-

[1] If the electrical power used to charge the batteries comes from a renewable energy grid, the fuel consumption may be a more indicative parameter of aircraft emissions than the total energy consumption. However, given the low degrees of hybridization analyzed in this study and the fact that state-of-art electrical power grids obtain energy predominantly from non-renewable energy sources, this distinction is ignored.

tery energy. However, when quantifying the overall "efficiency" of the aircraft in terms of energy consumption, only the energy consumed during the nominal mission E_{miss} must be considered, and not the reserves. Although the reserves affect the MTOM of the aircraft—and therefore, indirectly, the energy consumption—they do not directly define the energy consumed during its day-to-day operation. Since the aforementioned metrics are not directly applicable to hybrid-electric aircraft, do not consider the amount of payload carried, or do not take into account exclusively the energy consumed during the nominal mission, a different definition is used. This figure of merit, the *payload-range energy efficiency* [131], is an adaption of the existing metrics and can be expressed as

$$\text{PREE} = \frac{W_{\text{PL}} R}{E_{\text{miss}}}, \tag{2.1}$$

that is, as the payload weight times the harmonic range of the aircraft and divided by the total energy consumed during the nominal mission (excluding reserves). This dimensionless parameter represents how many joules of "useful work", interpreted as the work required to displace a unit of payload weight over a unit of distance, are extracted per joule of energy consumed by the system. PREE can be larger than one, and should not be interpreted as a thermal or mechanical efficiency η.

To understand why the use of distributed propulsion does or does not lead to a reduction in energy consumption, it is useful to monitor different efficiency metrics of the aircraft. Two important factors in this regard are the aerodynamic efficiency, characterized by the lift-to-drag ratio L/D, and propulsive efficiency η_{p}. In this research, the latter is defined as

$$\eta_{\text{p}} = \frac{-F_x V_\infty}{P_{\text{s}}}, \tag{2.2}$$

where V_∞ equals the speed of the aircraft, P_{s} is the shaft power of the propulsor, and F_x is the net axial force generated by the propulsor, which is positive in downstream direction. For a propulsor aligned with the freestream direction, $-F_x$ equals the thrust component, T (see Fig. 2.6). Note that η_{p} is commonly defined using Eq. 2.2 from an aircraft-design perspective. However, in the field of fluid mechanics, the "propulsive efficiency" generally refers to the ratio between TV_∞ and the increase in kinetic of the fluid, $\dot{m}(V_{\text{jet}}^2/2 - V_\infty^2/2)$, while Eq. 2.2 is considered the "overall propulsor efficiency" [132].

The product of the propulsive efficiency and lift-to-drag ratio constitutes the so-called aero-propulsive efficiency, $\eta_{\text{p}}(L/D)$. The purpose of most DP applications is precisely to enhance this factor. However, in some cases—particularly in turboelectric configurations—this benefit comes at the expense of a reduction in powertrain efficiency, since additional electrical elements are required to distribute power from the gas turbine to the electrical motors. The overall powertrain efficiency η_{PT} can be defined as the ratio between the total shaft power produced by all propulsors (see e.g. Fig. 2.2), and the total power extracted from the energy sources, that is,

$$\eta_{\text{PT}} = \frac{\sum P_{\text{s}}}{P_{\text{f}} + P_{\text{bat}}}, \tag{2.3}$$

since in the case of HEP two power sources can be present: fuel ($P_f = \dot{m}_f e_f$) and batteries (P_{bat}). Note that, for some powertrain architectures and operating conditions, the powertrain efficiency can also be higher than in a conventional propulsion system, due to the high transmission efficiency of electrical machines compared to combustion engines.

Finally, an "overall efficiency parameter" (also known as the global chain efficiency [107]) of the aircraft system can be defined as

$$\zeta = \eta_p \eta_{PT} (L/D). \tag{2.4}$$

For steady, level flight, $L/D = W/T$, and hence $\zeta = (W V_\infty)/(P_f + P_{bat})$. The parameter ζ is therefore inversely proportional to the amount of power required from the energy sources to displace an aircraft of weight W at a velocity V_∞. It is conceptually equivalent to the "range parameter" of fuel-based aircraft (see e.g. Ref. [133], Ch. 4), but is expressed in terms of HEP-related parameters instead of the specific fuel consumption of a conventional engine. The parameter appears indirectly in the range equation (see Appendix B), and is a useful metric for the comparison of HEDP configurations since, for a given MTOM, a reduction in energy consumption with respect to a conventional reference aircraft can only be achieved if $\zeta_{DP} > \zeta_{conv}$.

2.2. PROPELLER AERODYNAMICS

Of the various components that constitute an OTWDP system, the wing and propellers are responsible for the largest aerodynamic loads: lift and thrust. The flow fields induced by these components affect each other, and as a consequence of this *aerodynamic interaction*, the forces generated by the system differ from the summation of the forces generated by each isolated component separately. However, while the aerodynamics of wings is generally well-established in the aerospace community, the aerodynamics of propellers is not always understood clearly. As stated by Betz [134] in the 1920s,

> *The reason why the comprehension of what occurs in the vicinity of a propeller is commonly regarded as especially difficult, does not lie so much in the complexity of the hydrodynamical phenomena as in our limited ability of geometrical presentation, which sometimes fails us, even in simple cases, when these have a spiral form. [...] Aside from the above inconveniences, which are not inherent to the nature of the phenomena, the propeller offers no greater difficulties than the majority of other hydrodynamic problems.*

Although the theory of propellers has advanced considerably in the past century, it is beneficial to briefly revisit some concepts here, since the research presented in Chapters 6–8 focuses on propeller interaction effects. For this purpose, some of the fundamentals of isolated propellers are described in Sec. 2.2.1. This helps to understand how the propeller affects and is affected by the wing (Sec. 2.2.2) and surrounding propellers and ducts (Sec. 2.2.3).

2.2.1. FUNDAMENTALS OF ISOLATED PROPELLERS

Three main theoretical models can be used to understand the basic aerodynamic characteristics of propellers: actuator disk theory (also known as momentum theory), blade-element theory, and vortex theory. Overviews of these theories, including historical per-

spectives, are given by van Kuik et al. [135], Okulov et al. [136], and Wald [137]. The actuator disk and blade-element models are not extensively used in the present research and are therefore not described here—although they are referred to when explaining some of the propeller interaction effects. More information on these theories can be found in e.g. Durand [138] and Veldhuis [68]. Likewise, although propeller aeroacoustics is not the focus of this research, some design considerations and discussions in the following chapters rely on a basic understanding of propeller noise. For this, the reviews of Marte and Kurtz [139] and Magliozzi et al. [140] are recommended.

A. FLOW FIELD INDUCED BY A PROPELLER

Understanding the propeller vortex system is particularly relevant for over-the-wing propellers. For tractor propellers, the propeller slipstream impinges on the wing and therefore the dynamic-pressure and swirl distributions inside the slipstream determine the loading distribution on the downstream wing. Extensive research on tractor propellers—the effect of which on wing sizing is briefly analyzed in Ch. 5—can be found in the works of Veldhuis [68] and Sinnige [141], among others. For OTW propellers, on the other hand, the wing is located outside the slipstream. The flow field induced by the propeller outside its slipstream can be understood by analyzing the different components of the associated vortex system, shown in Fig. 2.3.

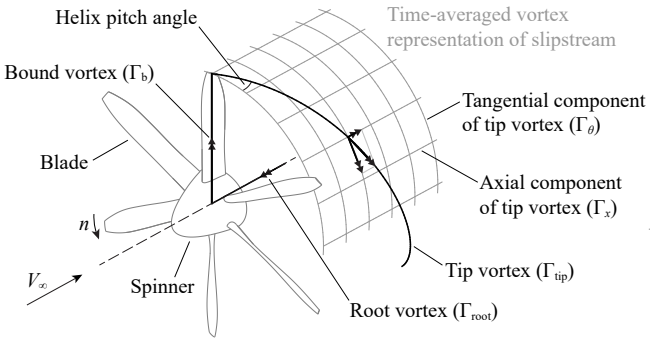

Figure 2.3: Simplified representation of the propeller vortex-system components. The sketch assumes constant bound circulation and neglects slipstream contraction.

Analogously to a finite wing, the bound vortex of a propeller blade cannot end in a fluid, and therefore emanates from the blade root and tip until infinity or the starting vortex of the propeller. The tip vortex forms a helix of pitch p due to the combined axial and rotational motion of the blade tip relative to the fluid. The root vortex, on the other hand, has a much larger pitch angle: in Fig. 2.3 it is drawn along the propeller axis for simplicity ($p = \infty$), although in practice it would emanate from the blade root at the spinner surface ($r/R > 0$), and would therefore follow a helicoidal path as well. Moreover, a propeller blade generally has a variable loading distribution in radial direction. Hence, a helical sheet of trailing vorticity would be generated, rather than discrete vortices at the tip and root. However, in practice, the trailing vorticity rapidly rolls up into the root and tip vortices, and a clearly distinguishable tip vortex can be observed directly behind the propeller blade.

The vorticity of the tip vortices—which in a time-averaged sense form the edge of the slipstream—can be decomposed into an axial and tangential component. Consequently, the time-averaged slipstream of a propeller with uniform loading can be represented by a series of axial vorticity lines and tangential vorticity rings [142, 143], as shown in Fig. 2.3. It can be shown that, of the various vorticity components, only the tangential one (Γ_θ) induces axial and radial velocities in the flow field, while the bound (Γ_b) and axial (Γ_x, Γ_{root}) components only contribute to the swirl velocity behind the propeller disk [68]. This is evidenced in Fig. 2.4, which presents the velocity distribution induced by a series of discretized vortex elements representing the propeller vortex system, calculated

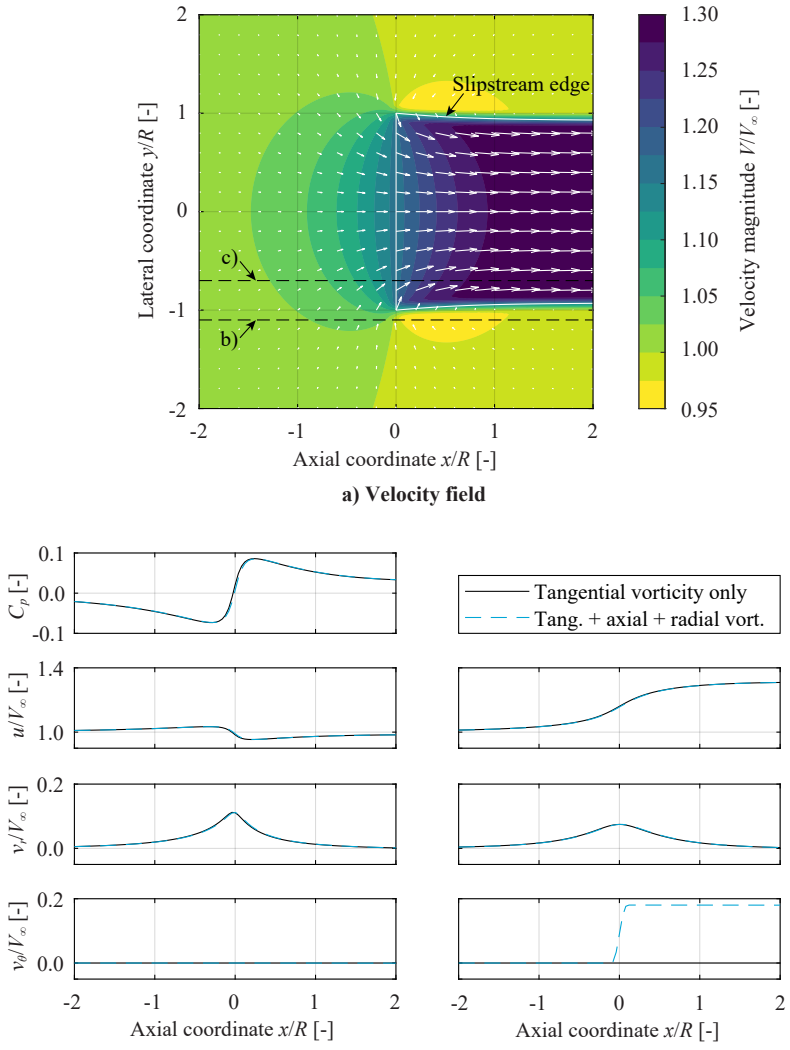

Figure 2.4: Velocity components induced by the vortex system of an isolated propeller with constant circulation, including propeller-induced velocity vectors ($u - V_\infty$, v) in subplot a) ($T_c = 1.0$).

using the Biot-Savart law. The velocity profiles extracted at two radial locations (Figs. 2.4b and 2.4c) compare the velocity distribution induced by all vorticity components shown in Fig. 2.3 to the velocity distribution induced by only the tangential component of the tip vortices. These profiles show that, indeed, the radial vorticity component on the propeller blades and the axial vorticity components of the root and tip vortices only affect the swirl velocity v_θ inside the slipstream.

The axial velocity inside the slipstream ($r/R = 0.7$, Fig. 2.4c) gradually increases as described in actuator disk theory, reaching a determined $\Delta u_P = aV_\infty$ at the propeller location, and $2\Delta u_P$ far downstream. The flow immediately outside the slipstream ($r/R = 1.1$, Fig. 2.4b), on the other hand, presents a different evolution. Here, the axial velocity is first increased upstream of the propeller disk, and then decreased downstream of it. The associated slipstream contraction is also evident in the radial velocity v_r, which presents a maximum at the propeller location. Since the total pressure is constant outside the slipstream, the Bernoulli priciple can be used to estimate the static pressure coefficient C_p. The C_p profiles of Fig. 2.4b show that, outside the slipstream, the static pressure first decreases, then sharply increases at the location of the propeller disk, and eventually tends back to freestream values. Inside the slipstream, the pressure rise at the disk location would represent a discontinuity in the case of an ideal actuator disk. These changes in static pressure in the vicinity of the propeller disk are recognizable in the wing pressure distribution of OTW configurations (see Chapters. 6–8).

Figure 2.4 represents an idealized case without unsteady effects, viscous effects, or variable circulation distributions along the propeller blade. In practice, the flow field induced by the propeller is more complex, as shown in Fig. 2.5. The time-averaged velocity

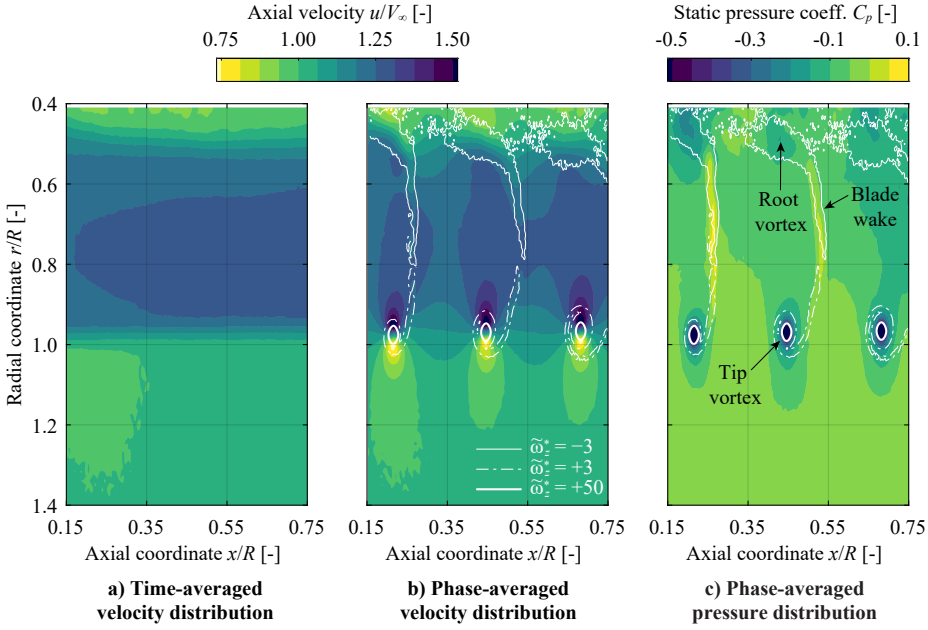

Figure 2.5: Velocity and pressure distributions in an isolated propeller slipstream at a moderate thrust setting, based on experimental data. Figure adapted from Ref. [144].

distribution of Fig. 2.5a shows a higher velocity near the region of highest blade loading ($r/R \sim 0.8$), and reduced velocities near the nacelle surface ($r/R < 0.5$). Moreover, the blade wakes and tip vortices associated with each blade passage are clearly visible in the out-of-plane vorticity contours $\tilde{\omega}_z^*$ of the phase-averaged flow field. Figure 2.5b shows how the tip vortices locally increase the axial velocity on the inboard side ($r/R < 1$) and locally reduce it on the outboard side ($r/R \geq 1$). Furthermore, a strong suction peak exists in the vortex cores due to the centrifugal forces, as reflected in Fig. 2.5c. In an OTW configuration, these localized gradients interact with the wing boundary layer and create pressure fluctuations on the wing surface, as discussed in Ch. 7.

B. PROPELLER PERFORMANCE COEFFICIENTS

When assessing the performance of an isolated or installed propeller, it is of interest to express the forces on the propeller as non-dimensional coefficients in order to make the performance characteristics scalable. These performance coefficients are often expressed as a function of the advance ratio,

$$J = \frac{V_\infty}{nD_\mathrm{P}}. \tag{2.5}$$

The advance ratio is a measure of the rotational speed of the propeller relative to the freestream velocity, and is proportional to the pitch of the helical path followed by the blade tips, p. The propeller thrust T is defined as the force generated on the propeller blades and spinner in the direction of the propeller axis. The thrust is commonly normalized in different ways, depending on the application. The first propeller thrust coefficient C_T is defined as

$$C_T = \frac{T}{\rho n^2 D_\mathrm{P}^4}. \tag{2.6}$$

The thrust coefficient C_T presents two advantages: first, it is (almost) linear with advance ratio when the blades are not stalled ($C_T \propto J$). Second, it presents a finite value at zero forward velocity. A second propeller thrust coefficient can also be defined by dividing the thrust by the dynamic pressure $q_\infty = 0.5\rho V_\infty^2$ and propeller disk area[1]:

$$T_\mathrm{c} = \frac{T}{q_\infty \pi R^2}. \tag{2.7}$$

This definition of the thrust coefficient is useful because it removes the rotational speed from the non-dimensionalization. It is related to the definition of Eq. 2.6 through $T_\mathrm{c} = 8C_T/(\pi J^2)$ and is inversely proportional to the advance ratio, $T_\mathrm{c} \propto J^{-1}$. Finally, when comparing the forces generated by the propeller to the forces generated by the wing or other elements of the airframe, it is often beneficial to normalize the thrust coefficient using the same reference area as the lift or drag coefficients [68], namely

$$T_\mathrm{c}^* = \frac{T}{q_\infty S_\mathrm{ref}}. \tag{2.8}$$

[1] Note that the thrust coefficient T_c is defined by some authors as $T/(\rho V_\infty^2 D_\mathrm{P}^2)$. Different symbols can also be used; e.g. in marine propulsion it is common to represent C_T and T_c as K_T and C_T, respectively [145].

The side-force and normal-force coefficients can be defined similarly to Eqs. 2.6–2.8 (see Nomenclature list, page xxiii). Analogously, the torque and power coefficients can be expressed as

$$C_Q = \frac{Q}{\rho n^2 D_\mathrm{P}^5}, \tag{2.9}$$

$$C_P = \frac{P_\mathrm{s}}{\rho n^3 D_\mathrm{P}^5}. \tag{2.10}$$

Finally, the propeller efficiency is defined as

$$\eta_\mathrm{P} = \frac{T V_\infty}{P_\mathrm{s}}. \tag{2.11}$$

Equation 2.11 is similar to Eq. 2.2; in fact, if the propulsive device is an isolated propeller at zero angle of attack, then the propeller efficiency and propulsive efficiency are identical. For this reason, some works on isolated propellers (see e.g. Ref. [146]) use the two terms interchangeably. However, in the present work, the propulsive efficiency is based on the force component in the direction of flight and is considered applicable to any propulsive device, while the propeller efficiency is defined using the thrust along the propeller axis. Given that the shaft power is related to the torque through $P_\mathrm{s} = 2\pi n Q$, the propeller efficiency can also be expressed as a function of the performance coefficients using

$$\eta_\mathrm{P} = \frac{C_T}{C_Q}\frac{J}{2\pi}. \tag{2.12}$$

From a conceptual aircraft design perspective, it can be useful to obtain a preliminary estimate of the propeller efficiency as a function of the thrust setting, without knowing the propeller geometry beforehand. The propeller efficiency can be approximated by

$$\eta_\mathrm{P} = k_\mathrm{P}\left(\frac{2}{1+\sqrt{1+T_\mathrm{c}}}\right), \tag{2.13}$$

where the term in parenthesis is the propulsive efficiency of an ideal actuator disk (i.e., the Froude efficiency, $\eta_\mathrm{p} = 1/(1+a)$), and the factor $k_\mathrm{P} < 1$ accounts for swirl, viscous, and induced losses. Given that Eq. 2.13 assumes that the slipstream contraction is negligible and that k_P is independent of the thrust setting, it is inaccurate at zero thrust and at very high thrust ($T_\mathrm{c} \gg 1$) settings. However, given that such conditions only occur for a short duration during a typical mission of fixed-wing aircraft, Eq. 2.13 can be used to provide a first estimate. The equation is more accurate for variable-pitch propellers, since they present a relatively constant efficiency over a wider range of thrust coefficients.

2.2.2. OVER-THE-WING PROPELLERS

The aerodynamic interaction effects in OTW propeller systems are not fully understood, partially because only a limited number of research groups have investigated the aerodynamic characteristics of such systems. The main works focusing on a single propeller

placed above a planar wing are those of Johnson and White [63], Cooper et al. [80], Müller et al. [67, 69], and Veldhuis [68]. However, some additional insight can be gained from configurations that present comparable interaction phenomena:

- Channel-wing propellers: the earliest works encountered on OTW propellers focus on this configuration [147, 148], where the vertical position of the propeller is lowered and the wing follows a circular contour beneath the propeller. Numerical simulations have been performed by Müller et al. [67, 69, 76, 149] and Wang et al. [150, 151]. These show that the lift enhancement is larger for channel-wing configurations than for planar-wing configurations, although this is accompanied by an increased propulsive-efficiency penalty.
- OTWDP on high-aspect-ratio wings: several authors have investigated configurations with small, distributed OTW ducted fans [52, 152–154]. While these concepts closely resemble the layouts investigated in the present work, the analyses of these integral propulsion systems with generic three-dimensional geometries provides no clear breakdown of the interaction mechanisms.
- OTWDP on blended-wing-bodies: these configurations are intended for transonic conditions and present several ducted fans placed side-by-side near the trailing edge [155, 156]. Due to the low diameter-to-chord ratios, the investigations focus on the effect of boundary-layer ingestion on fan and engine performance, rather than looking into the effect of the propulsors on the wing.
- OTW turbofans: conceptually, the upstream effect of a fan on the wing surface is comparable to the upstream effect of a propeller. However, the pressure distributions obtained in OTW turbofan investigations [157–159] show that the governing interaction mechanisms are different from OTW propeller configurations, due to the dominant influence of the nacelle and the transonic operating conditions for which these systems are intended.
- Upper-surface blown wings: the interaction between the slipstream and the wing surface downstream of an OTW propeller presents some similarity with earlier jet-wing interaction studies focusing on high-lift conditions [160, 161]. However, in these studies, the momentum increase is produced closer to the surface, leading to a Coandă effect which is likely to increase system lift more than in an OTW propeller configuration.

These studies provide a preliminary understanding of some of the aerodynamic interaction effects present in OTW propeller systems. The following two subsections discuss these interaction effects for cruise conditions and high-lift conditions, respectively, and highlight some of the challenges and shortcomings identified in the existing literature.

A. AERODYNAMIC INTERACTION IN CRUISE CONDITIONS

When a propeller is placed above a wing, the propeller-induced velocity field described in Sec. 2.2.1 affects both the time-averaged and the unsteady loading distribution on the wing. Reciprocally, the velocity field induced by the wing alters the inflow conditions to the propeller. Compared to an isolated propeller at zero angle of attack, the associated

non-uniform loading leads to the appearance of in-plane propeller forces and an unsteady blade-loading component. Figure 2.6, which provides a side view of a propeller placed at a generic location over a wing, shows how the various force components are defined.

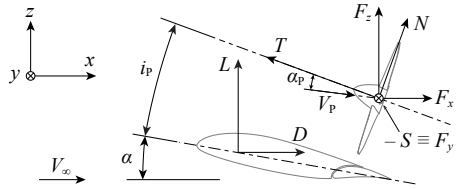

Figure 2.6: Definition of force components on the wing and propeller.

The velocities induced by the wing on the propeller can conceptually by decomposed into four contributions, as shown in Fig. 2.7a. The average increase in axial velocity leads to an increase in the effective advance ratio of the propeller, while the vertical velocities induced by the wing on average lead to a change in the effective angle of attack. The non-uniform velocity profile that remains after subtracting these mean effects can, in turn, be decomposed into two contributions: inviscid and viscous. The latter is caused by the ingestion of the boundary layer at the bottom of the disk, although for single-OTW propeller applications this does not significantly affect the loading distribution on the propeller [67, 69]. However, the disturbed inflow to the propeller leads to a thrust reduction, especially in the bottom part of the propeller disk. This generally leads to signif-

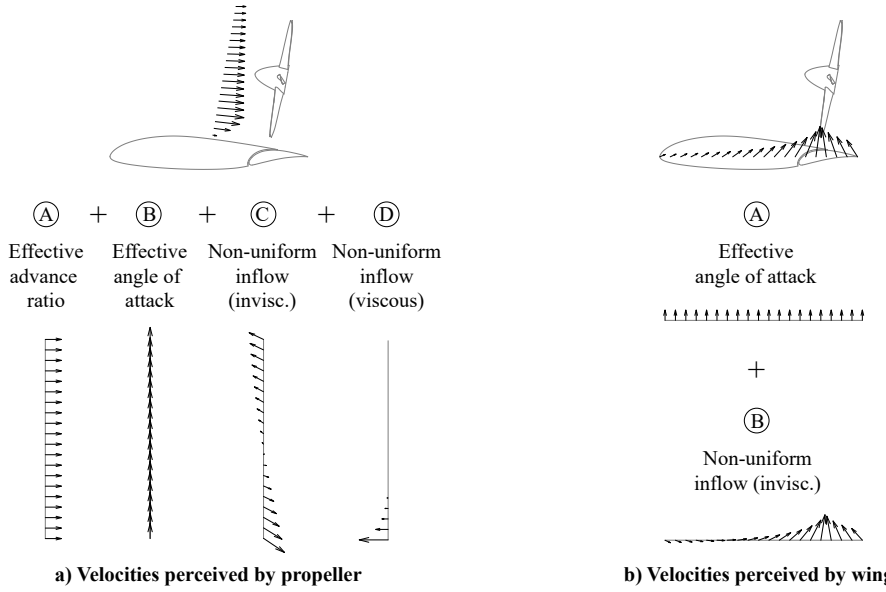

Figure 2.7: Conceptual interpretation of the different velocity components contributing to a change in wing and propeller performance in cruise conditions.

icant propeller-efficiency penalties, with some studies finding η_P reductions of over 20% [68, 69]. However, others show an increase of more than 10% in cruise conditions [63]. These apparent contradictions suggest that the effect on propeller efficiency is highly dependent on the design and operating conditions of the system.

The velocities induced by the propeller vortex system at the wing location (see Fig. 2.4b) can also be decomposed into two contributions, as reflected in Fig. 2.7b. On one hand, the radially-induced velocities increase the effective angle of attack of the airfoil. The streamwise variations in induced axial and radial velocities, on the other hand, decrease the wing surface pressure ahead of the propeller location, while increasing the pressure downstream of it [63, 80]. In low-lift conditions, this leads to an offset in the wing lift polar [154]. Experimental studies suggest that the lift increase is maximum for a propeller placed near the trailing edge [68, 80], though in some numerical investigations it has been found to be maximum near the mid-chord [68]. The reason for this lift increase is fundamentally different from tractor propellers, where the dynamic pressure of the wing sections in the propeller slipstream is increased, leading to an increase in the lift-curve slope [68]. As a consequence of the propeller-induced pressure distribution and the change in the effective angle of attack, the wing drag is also reduced. This drag reduction is maximum for a propeller placed near the location of maximum airfoil thickness [63, 68, 80]. Contrary to tractor propellers, where the slipstream impingement leads to strong dynamic pressure and angle-of-attack variations along the wing span, OTW propellers generate much weaker spanwise lift and drag gradients [69]. Overall, this can lead to lift-to-drag ratio benefits of over 50%, relative to a tractor configuration [69].

B. AERODYNAMIC INTERACTION IN HIGH-LIFT CONDITIONS

The lift benefit of OTW propellers is also present in high-lift conditions, when the flaps are deflected. The Reynolds-Averaged Navier-Stokes (RANS) simulations performed by Müller et al. [67] showed that this lift increment is lower for an OTW propeller ($\Delta C_{L,\text{OTW}} = 0.24$) than for a tractor propeller ($\Delta C_{L,\text{tractor}} = 0.66$), although in the case of the OTW propeller it is accompanied by a drag reduction ($\Delta C_{D,\text{OTW}} = -0.101$) instead of a drag increase ($\Delta C_{D,\text{tractor}} = +0.223$). On one hand, this indicates that—in the absence of additional high-lift enhancement strategies such as propeller deflection or a propeller-induced Coandă effect—a tractor propeller is likely to outperform an OTW propeller in approach conditions. On the other hand, the drag reduction of the OTW system can be beneficial in take-off conditions, which often determine the powertrain size.

However, additional investigations are required to confirm this. Subsequent work by Müller et al. [149] showed that steady RANS simulations are, in fact, insufficient to accurately predict the aerodynamic interaction between an OTW propeller and the wing when the flap is deflected. The authors identified the unsteady interaction between the propeller tip-vortices and the wing boundary-layer as a possible cause of flow separation over the flap, which was not captured in steady analyses. A schematic representation of the velocities induced by the tip vortices in the vicinity of the wing surface is sown in Fig. 2.8. Although the tip vortices are helical, they are closest to the wall directly beneath the propeller axis, where they are tangent to the wing surface, and approximately perpendicular to the freestream direction (depending on the advance ratio). In this region, the problem can conceptually be treated as a quasi-2D flow field. Figure 2.8 shows how, in

that case, the tip vortex—together with the image vortex required to maintain zero normal velocity at the wall—induces velocities in upstream direction at the wing surface. This locally reduces the wall-normal velocity gradient and makes the boundary-layer more prone to separation. Both theoretical [162] and experimental [163] studies confirm that vortex–boundary-layer interaction significantly affects the displacement thickness of the boundary layer, and that it can indeed lead to local flow separation [164, 165]. Even in the inviscid limit, a rectilinear vortex convected parallel to a wall can lead to reverse flow, depending on the ratio between the self-induced vortex speed and the uniform flow speed [166].

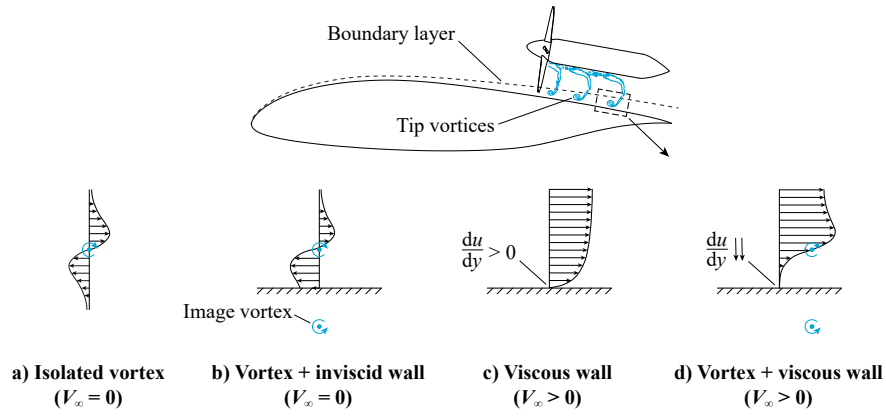

Figure 2.8: Simplified 2D representation of the velocities induced by the tip vortices in the vicinity of the wing surface beneath the propeller axis.

These vortex–boundary-layer interaction studies do not consider the presence of a rotor close to the wall, which imposes additional pressure gradients and three-dimensional effects. The experiments of Murray et al. [167] show that, in that case, flow reversal can occur locally beneath the rotor and that additional unsteady vortical structures are formed, comparable to the ground-vortex effect on propeller aircraft [168] or propeller-hull interaction effects in marine applications [169, 170]. Moreover, if the tip-clearance between rotor and the wall is small, the local thrust increases not only due to the local reduction in inflow velocity, but also due to the end-plate effect [171]. This leads to local variations in blade loading [149] and tip-vortex strength. Furthermore, additional complications arise when the propeller is positioned above a wing. In that case, the wing curvature introduces an additional streamwise pressure gradient in the boundary layer, which changes its receptivity to the perturbations of the propeller. It is therefore unclear how the interaction between the propeller blades and the wing boundary-layer affects flow separation, especially when an additional pressure gradient is generated by a trailing-edge high-lift device. For this reason, Ch. 7 aims to provide some insight into these interaction phenomena.

2.2.3. DISTRIBUTED PROPELLERS

In an OTWDP system, several propellers are installed side-by-side in close proximity to each other. In most—if not all—recent OTWDP concepts, the array of propulsors is ducted [52, 71, 152, 153, 172]. While the duct can offer several advantages in terms of aerodynamic performance, safety, or noise production, it is currently unclear whether a duct is necessary for subsonic OTWDP configurations. Existing literature has shown that, in the case of a single propeller with an axisymmetric duct, the loading is increased near the blade tip due to an end-plate effect [171]. Moreover, at high thrust settings, the duct itself can substantially contribute to the total thrust of the system [173]. However, at high speeds and low thrust settings (i.e., in cruise conditions), the drag of the duct may outweigh its benefits [174]. Nevertheless, in an OTW configuration it may also provide benefits in cruise conditions if it can tailor the inflow to the propellers in order to reduce the non-uniformity. In such a configuration the duct may also reduce the noise of the system since, in addition to its noise shielding capabilities [175, 176], it would reduce the unsteady loading on the propeller.

Three generic OTWDP layouts are depicted in Fig. 2.9. In the first, the duct has a circular cross-section at the propeller location. The propellers therefore maintain a constant tip clearance in this configuration, which is beneficial for the unsteady blade loading. The envelope duct, on the other hand, is structurally simpler, has significantly less wetted area, and is most likely sufficient to reduce the non-uniformity of the propeller inflow, since the spanwise inflow-velocity gradients are small in the case of an unswept wing. However, in this case, the tip clearance of the propeller blades varies as they approach and retreat from the duct and wing surfaces. Furthermore, in both the envelope-duct and the unducted configurations, each propeller interacts with its neighbor. In these cases, the propeller–duct interaction and propeller–propeller interaction both have an impact on the unsteady and time-averaged loads of the propellers, as discussed in Ch. 6.

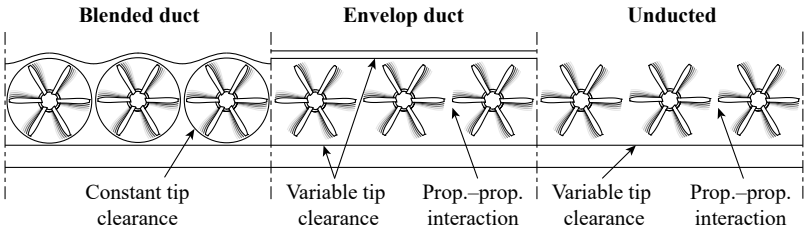

Figure 2.9: Front view of three hypothetical OTWDP system layouts, indicating elements that the blade tips interact with throughout a revolution.

The literature on propeller–propeller interaction in forward flight is scarce. However, this topic has recently gained interest due to the appearance of numerous urban-air mobility concepts with distributed propellers. In this context, Stokkermans [177, 178] has investigated the aerodynamic interaction of side-by-side and one-after-another propellers, with and without overlap. Moreover, a significant amount of literature is avail-

able regarding the aerodynamic interaction between two or more rotors in the case of tandem helicopters [179, 180], tiltrotors [181, 182], and small unmanned aerial vehicles (UAVs or "drones") [183–192]. Based on these studies, where the "propellers" operate at or near to zero forward velocity, it becomes evident that the aerodynamic interaction between adjacent propellers is relevant in three main ways:

1. The performance of the rotors themselves is affected. When placed close to each other without overlap, the thrust produced at a given rotational speed typically drops by 2% – 8% [183, 184, 186, 192], depending on the configuration, and the efficiency is reduced [179]. For propellers in forward flight, this penalty would increase with sideslip [178]. Moreover, the interaction leads to an appreciable unsteady loading on the propeller blades [183, 185, 187].

2. The streamwise development of the slipstream changes, which affects the aerodynamic loads on downstream elements such as the tail or trailing-edge high-lift devices. In a twin-rotor configuration, the slipstream deforms and loses its circular cross-section [188], and a recirculation zone may be generated between the slipstreams [189]. Moreover, the interaction between vortical structures in the slipstream leads to an earlier breakdown of the blade wakes and tip vortices [183].

3. The noise production of the system changes. When the separation distance between the rotors is reduced, in general an increase in noise with respect to the isolated rotors is observed [183, 185, 188]. Furthermore, the aerodynamic and acoustic interference between the different rotors significantly changes the noise directivity pattern of the system [193–195]. This directivity pattern can be manipulated by controlling the relative phase of the noise sources, that is, by regulating the relative blade phase angles of the propellers [196, 197]. This approach is similar to the synchrophasing technique employed in turboprop aircraft to reduce cabin noise [198, 199]. But, in the case of electrically-driven propellers, the motor can be used to actively control the relative phase angles, thereby adapting the directivity pattern as desired throughout the mission. However, the potential local noise reduction due to active phase control rapidly deteriorates if the rotational speed and blade phase angles of the propellers are not controlled accurately [197, 200], which remains challenging to do in practice [191, 201, 202].

Part II

Preliminary Sizing of Hybrid-Electric Aircraft

3

AIRCRAFT SIZING METHOD

Despite the large amount of ongoing research related to hybrid-electric distributed propulsion (HEDP), little information is available regarding the clean-sheet design process of such aircraft. As discussed in Ch. 2, several design studies analyze the hybrid-electric powertrain in detail starting from a predefined aircraft configuration [45, 66], often maintaining the take-off weight constant [113, 204, 205]. Other studies have formulated more generalized conceptual sizing methods for HEP aircraft [94–98, 102–104], but do not integrate the aero-propulsive interaction effects in the process. These effects cannot be neglected for DP configurations, since they have a large impact on wing and powertrain sizing [48, 61] and, hence, on the overall design of the aircraft. Thus, there is a need to establish a systematic sizing method capable of rapidly exploring the design space and performing trade-off studies and sensitivity analyses for such configurations.

To this end, the traditional preliminary sizing methods [85, 91, 92] are expanded to account for both the hybrid-electric powertrain and the aero-propulsive effects of the associated propulsion system. The approach consists of four steps, as shown in Fig. 3.1. First, the conventional thrust, lift, and drag decompositions of the aircraft are modified to account for the aerodynamic interaction between the airframe and the propulsors. This leads to a set of modified flight-performance constraint equations, which are collected in a propulsive power-loading diagram, as explained in Sec. 3.1. Second, a powertrain model is formulated which converts the propulsive power-loading diagram into a series of powertrain component-oriented power-loading diagrams. The powertrain model is described in Sec. 3.2. Based on these constraint diagrams, the designer must select a design point in terms of wing loading and power loading. Third, the battery and fuel energy requirements are calculated for an assumed take-off mass (TOM) by analyzing the mission for a set of power-control profiles specified by the designer (Sec. 3.3). And fourth, with the power requirements obtained from the constraint diagrams and the energy requirements obtained from the mission analysis, the aircraft mass is estimated using a modified Class-I weight breakdown (Sec. 3.4). The mission analysis and weight estimation modules are then evaluated iteratively until the TOM converges.

Parts of this Chapter have been published in Ref. [203].

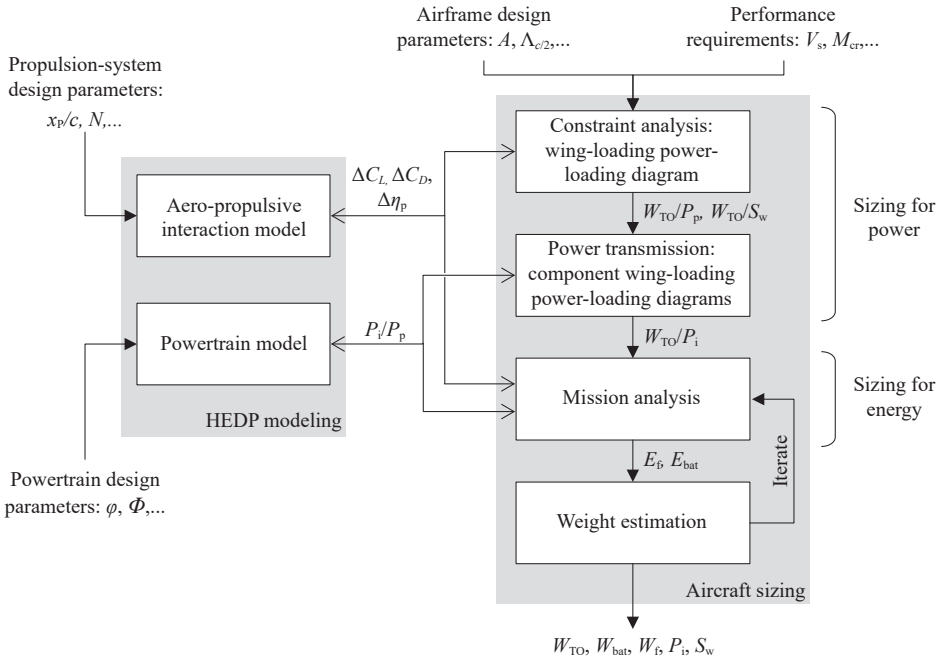

Figure 3.1: Simplified flowchart of the proposed design methodology, indicating the sizing modules, HEDP models, and main input/output parameters.

3.1. SIZING FOR POWER: PERFORMANCE CONSTRAINTS

The first step in the sizing process is to determine the design wing-loading and power loading of the HEDP aircraft. These aircraft can feature multiple propulsion systems. In this context, a "propulsion system" is defined as a set of identical propulsive elements which have an equal impact on aircraft performance, such as for example an array of propellers distributed along the leading edge of the wing, or a pair of ducted fans. The propulsive elements are generally propellers, jets, or fans, and are indistinctly referred to as "propulsors" in this study. In many cases, at least one of the propulsion systems has an appreciable effect on the aerodynamic performance of the airframe or vice versa. This effect must be considered in the lift and drag decomposition of the aircraft (Sec. 3.1.1), which affects the performance equations (Sec. 3.1.2) and the resulting constraint diagram (Sec. 3.1.3).

3.1.1. THRUST, LIFT AND DRAG DECOMPOSITION

Due to the aero-propulsive interaction that takes place between the propulsors and the airframe, the aerodynamic performance of the system differs from the combined performance of the two individual components. For highly-integrated propulsion-systems such as distributed propulsion, it is necessary to estimate the forces generated by the installed system, or, more specifically, to estimate the difference between these forces and the ones that the airframe and propulsors would generate separately. Although the

rationale followed in the following paragraphs can be extended to a generic number of propulsion systems, for simplicity here it is assumed that the aircraft features a maximum of two types of propulsion system. In this case, the total thrust of the aircraft T can be expressed as

$$T = T_{\text{conv}} + T_{\text{dp}}, \tag{3.1}$$

where T_{conv} is the thrust generated by a propulsion system that has no appreciable impact on airframe performance, and T_{dp} is the thrust generated by a (distributed) propulsion system which presents strong interaction effects with the airframe. If the aircraft only has one set of propulsors, then one of the two terms is zero. The "thrust' is defined here as the propulsor force component in the direction of flight. If the propulsors can be deflected for thrust vectoring, then this corresponds to the thrust direction in the retracted configuration ($\delta_{\text{P}} = 0^{\text{o}}$). In other words, if the propulsors are deflected an angle δ_{P}, then the thrust vector forms an angle δ_{P} with the velocity vector V (see Fig. 3.2). The normal (i.e., vertical) forces created by the propulsor, meanwhile, can be included in the lift "delta" discussed in subsequent paragraphs.

Since the distributed-propulsion system is placed at a finite distance from the rest of the airframe, there is an aerodynamic coupling. Thus, in a general sense, an aerodynamic property y (for example, lift) depends on a series of parameters $x_{1,\text{iso}}, x_{2,\text{iso}}, \ldots$ which would affect the system even without aerodynamic coupling (for example, angle of attack), and a series of parameters $x_{1,\text{inst}}, x_{2,\text{inst}}, \ldots$ inherent to the specific type of installation of the propulsion system on the airframe (for example, propeller position relative to the wing):

$$y = f(x_{1,\text{iso}}, x_{2,\text{iso}}, \ldots, x_{1,\text{inst}}, x_{2,\text{inst}}, \ldots), \tag{3.2}$$

For conceptual design purposes, it is beneficial to decompose the dependency f into two contributions. The first represents the aerodynamic forces (or other properties) that would exist on the isolated airframe or propulsor, and does not depend on $x_{1,\text{inst}}, x_{2,\text{inst}}, \ldots$. The other represents the change in aerodynamic properties as a result of the installation, i.e.

$$y = f_{\text{iso}}(x_{1,\text{iso}}, x_{2,\text{iso}}, \ldots) + f_{\Delta}(x_{1,\text{iso}}, x_{2,\text{iso}}, \ldots, x_{1,\text{inst}}, x_{2,\text{inst}}, \ldots). \tag{3.3}$$

Traditionally, only the first term of Eq. 3.3 is included in the conceptual design process, since it is often the dominant term. However, to assess the effects of distributed propulsion, the second contribution must be included as well. In such highly-integrated propulsion systems, this so-called "Delta" term is not necessarily small relative to the isolated-component contribution. However, it is also much more complex to quantify because it depends on additional parameters. In the following paragraphs, Eq. 3.3 is applied more specifically to the lift, drag, and propulsive efficiency. While the dependency of f_{iso} on $x_{1,\text{iso}}, x_{2,\text{iso}}, \ldots$ is not explicitly shown in subsequent equations to improve readability, it should be noted that f_{iso} is not a constant.

The airframe lift can be related to the total lift generated by the aircraft L through

$$L = L_{\text{airframe}} + \Delta L(T_{\text{dp}}, L_{\text{airframe}}, S, ...), \tag{3.4}$$

where ΔL is the increase in aircraft lift due to the thrust generated by the propulsors. ΔL depends on thrust of the distributed propulsion system and other operational and geometrical parameters of the aircraft, and does not include the effective lift increase due to thrust vectoring.

Analogously, the effect of aero-propulsive interaction on the overall drag of the aircraft is included as follows:

$$D = D_0 + \Delta D_0(T_{\text{dp}}, S_{\text{w}}, ...) + D_{\text{i}}(L_{\text{airframe}}) + \Delta D_{\text{i}}(T_{\text{dp}}, L_{\text{airframe}}, S_{\text{w}}, ...), \tag{3.5}$$

where D_0 is the zero-lift drag of the aircraft when no DP system is present, and ΔD_0 is the increase in zero-lift drag due to the DP system. This increase can be caused by interaction of the airframe with jets or slipstreams at zero lift, by variations in angle of attack in order to maintain zero lift, or by changes in wetted area due to pylons, nacelles, and other external elements of the propulsion-system installation. Additionally, D_{i} is the lift-induced drag of the airframe without propulsion system, and ΔD_{i} is the change in lift-induced drag due to thrust, that is, the difference between the drag of the complete aircraft with the propulsor at a determined thrust setting, and the drag that would exist at $T_{\text{dp}} = 0$ for the same total lift value. For the lift-induced drag coefficient of the airframe, a parabolic lift polar is assumed (i.e., $C_{D_i} = C_{L_{\text{airframe}}}^2 / (\pi Ae)$). Although different drag breakdowns exist, this simplified approach has been taken because it clearly identifies the contribution of the installation effects.

Finally, there are several ways to account for the effect of the airframe on propulsor performance. The first is to evaluate the changes in propulsor thrust due to the presence of different elements such as the wing, nacelle, fuselage, and so on [206]. For configurations with significant inflow distortion such as boundary-layer ingestion, on the other hand, an integral system-level approach is required, using for example the power-saving coefficient [132, 207] or power-balance methods [208, 209]. In any case, since the hybrid-electric powertrain is modeled in terms of power balances (see Sec. 3.2), it is preferable to express the interaction effects in terms of the propulsive efficiency of the distributed-propulsion system η_{dp}:

$$\eta_{\text{dp}} = \frac{T_{\text{dp}} V}{P_{\text{s,dp}}} = \eta_{\text{dp,iso}} + \Delta\eta_{\text{dp}}(T_{\text{dp}}, L_{\text{airframe}}, S_{\text{w}}, ...). \tag{3.6}$$

Here $\eta_{\text{dp,iso}}$ is the propulsive efficiency that these propulsors would have in absence of any other body, and $\Delta\eta_{\text{dp}}$ refers to the change in propulsive efficiency when installed on the aircraft. Note that flight speed V is employed in Eq. 3.6 instead of the freestream velocity V_∞ used in Eq. 2.2 to be consistent with the nomenclature used in the following sections. However, $V = V_\infty$, since the flight speed in the inertial reference frame equals the velocity of the incoming airflow in the aircraft reference frame. Moreover, as mentioned earlier in this section, the thrust component is assumed to be aligned with the direction of flight ($-F_{x,\text{dp}} = T_{\text{dp}}$). The factor $\Delta\eta_{\text{dp}}$ may depend on geometrical parameters of the wing such as its reference area, as well as on aerodynamic parameters such

as L_{airframe}, which is the lift that would be generated by the aircraft in the same flight condition (V, α, etc.) if no thrust were produced.

In order to incorporate the aero-propulsive interaction effects in the sizing process, these "Delta" terms (lift, drag, and propulsive efficiency) have to be estimated. Since an accurate estimation of the Delta components requires detailed aerodynamic analyses, they are often only included in the later stages of the design loop. For DP systems and other novel propulsion-system layouts, these effects cannot be neglected, and therefore simplified aerodynamic models or surrogate models are required. Two examples of how this can be done for wing-mounted distributed propellers are provided in Appendix C.

3.1.2. DERIVATION OF POINT PERFORMANCE EQUATIONS

The main forces acting on the aircraft are represented in Fig. 3.2. Here it is assumed that T_{conv} is always aligned with the velocity vector for simplicity, while the thrust vector of the DP system can be deflected an angle δ_{P} if, for example, the propulsors are installed on a flap, or if the jet or slipstream is deflected. Note that the X, Y, Z axes are equal to the X', Y', Z' axes of the ground reference frame, but rotated around the Y' axis such that the X axis is aligned with the velocity vector. They are therefore not the body axes of the aircraft, since they do not follow the angle of attack or bank angle of the aircraft. By applying Newton's second law along the X, Y and Z axes respectively, one obtains the following equilibrium equations:

$$T_{\text{conv}} + T_{\text{dp}} \cos\delta_{\text{P}} - W \sin\gamma - D = \frac{W}{g}\frac{\mathrm{d}V_X}{\mathrm{d}t}, \tag{3.7a}$$

$$L \sin\mu + T_{\text{dp}} \sin\delta_{\text{P}} \sin\mu = \frac{W}{g}\frac{\mathrm{d}V_Y}{\mathrm{d}t}, \tag{3.7b}$$

$$L \cos\mu + T_{\text{dp}} \sin\delta_{\text{P}} \cos\mu - W \cos\gamma = \frac{W}{g}\frac{\mathrm{d}V_Z}{\mathrm{d}t}, \tag{3.7c}$$

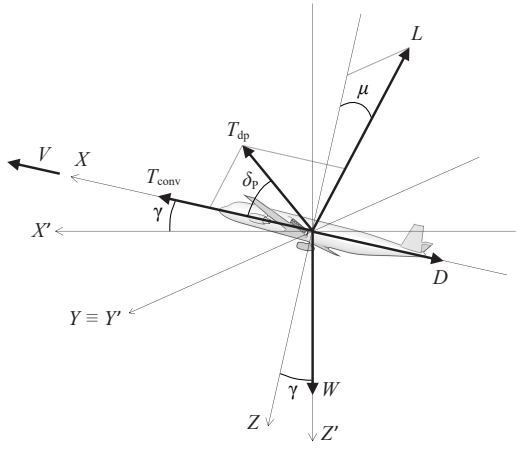

Figure 3.2: Schematic representation of the forces acting on the aircraft point model.

where the flight path angle γ of the aircraft can be related to the climb rate $c = \mathrm{d}h/\mathrm{d}t$ through

$$\sin\gamma = \frac{c}{V}. \tag{3.8}$$

Defining the ratio between the thrust of the DP array and the total thrust of the aircraft as $\chi = T_{\mathrm{dp}}/T$, the force equilibrium along the X axis (Eq. 3.7a) can be expressed as

$$\frac{T}{W} = \frac{1}{1-\chi(1-\cos\delta_{\mathrm{P}})}\left(\frac{D}{W} + \frac{c}{V} + \frac{1}{g}\frac{\mathrm{d}V}{\mathrm{d}t}\right), \tag{3.9}$$

where the term on left hand side of the equation is the total thrust-to-weight ratio of the aircraft. By reorganizing terms, applying the lift and drag breakdowns given by Eqs. 3.4 and 3.5, and expressing the contributions as non-dimensional coefficients, the equilibrium of forces along the X and Z axes can be expressed as:

$$\frac{T}{W} = \frac{\dfrac{q_\infty}{(W/S_{\mathrm{w}})}\left[C_{D_0} + \Delta C_{D_0}\left(\chi\dfrac{T}{W}, \dfrac{W}{S_{\mathrm{w}}}, \ldots\right) + \dfrac{C^2_{L_{\mathrm{airframe}}}}{\pi Ae} + \Delta C_{D_{\mathrm{i}}}\left(\chi\dfrac{T}{W}, C_{L_{\mathrm{airframe}}}, \dfrac{W}{S_{\mathrm{w}}}, \ldots\right)\right] + \dfrac{c}{V} + \dfrac{1}{g}\dfrac{\mathrm{d}V}{\mathrm{d}t}}{1-\chi(1-\cos\delta_{\mathrm{P}})}, \tag{3.10}$$

$$\frac{W}{S_{\mathrm{w}}} = \frac{q_\infty\cos\mu\left[C_{L_{\mathrm{airframe}}} + \Delta C_L\left(\chi\dfrac{T}{W}, C_{L_{\mathrm{airframe}}}, \dfrac{W}{S_{\mathrm{w}}}, \ldots\right)\right]}{\sqrt{1-\left(\dfrac{c}{V}\right)^2} - \chi\left(\dfrac{T}{W}\right)\sin\delta_{\mathrm{P}}\cos\mu + \dfrac{1}{g}\dfrac{\mathrm{d}V_Z}{\mathrm{d}t}}. \tag{3.11}$$

Equations 3.10 and 3.11 constitute the point performance equations used to construct the constraint diagram of a HEDP aircraft. Since performance constraints are typically evaluated for steady symmetric flight or coordinated turns in the horizontal plane, the terms $\mathrm{d}V/\mathrm{d}t$ and $\mathrm{d}V_Z/\mathrm{d}t$ are generally equal to zero. Sustained-turn maneuvers can be solved directly using Equations 3.10 and 3.11 if the bank angle is known. However, if the turn radius of the maneuver is given as a performance requirement instead, the bank angle has to be computed from the equilibrium of forces along the Y axis. In this case, $\mathrm{d}V_Y/\mathrm{d}t$ represents the centrifugal acceleration of the aircraft, and Eq. 3.7b can be rewritten as

$$\sin\mu = \frac{\dfrac{1}{g}\dfrac{V^2}{R_{\mathrm{turn}}}}{\dfrac{q_\infty}{W/S_{\mathrm{w}}}\left[C_{L_{\mathrm{airframe}}} + \Delta C_L\left(\chi\dfrac{T}{W}, C_{L_{\mathrm{airframe}}}, \dfrac{W}{S_{\mathrm{w}}}, \ldots\right)\right] + \chi\sin\delta_{\mathrm{P}}\left(\dfrac{T}{W}\right)}. \tag{3.12}$$

If, on the other hand, the turn rate or load factor of the maneuver are specified, these can be related to the turn radius through $\Omega = V/R_{\mathrm{turn}}$ and $n = \sqrt{1+(V^2/gR_{\mathrm{turn}})^2}$, respectively.

Given that the aircraft size is unknown at this stage, it is important to express the "Delta" terms as a function of normalized variables such as the thrust coefficient T_{c}

or aerodynamic force coefficients. These can in turn be related to T/W and W/S_w (see Appendix C.1), and thus the performance equations can be solved without knowing the actual weight of the aircraft. For conventional aircraft, the "Delta" terms are zero and the airframe lift coefficient can be related to wing loading directly through $C_{L_{\text{airframe}}} = (W/S_w)/q_\infty$, and therefore T/W can explicitly be computed as a function of wing loading for a given flight condition. However, when the aero-propulsive effects are considered during equilibrium flight, lift depends on thrust and vice versa. Hence, given that $\Delta C_L, \Delta C_{D_0}, \Delta C_{D_i} = f\left(\chi(T/W), C_{L_{\text{airframe}}}, (W/S_w), ...\right)$ can be arbitrarily complicated functions, Eqs. 3.10 and 3.11 must be solved iteratively.

3.1.3. CONSTRUCTING THE PERFORMANCE CONSTRAINT DIAGRAM

For a given flight condition and airframe lift coefficient, Eqs. 3.10 and 3.11 generate the two solid curves shown Fig. 3.3. The intersection of these curves gives the equilibrium flight point $[(W/S_w)_{eq},(T/W)_{eq}]$, that is, the combination of T/W and W/S_w where the required flight condition is satisfied without any additional accelerations. Along the "Z-equilibrium" curve, the aircraft presents no acceleration in Z direction, and thus it can climb or accelerate in X direction if the excess power is positive ($T/W > (T/W)_{eq}$), or descend or decelerate if it is negative ($T/W < (T/W)_{eq}$). Analogously, the "X-equilibrium" curve represents the loci of points of zero excess power. Along this curve, the aircraft accelerates in the negative Z direction if $T/W > (T/W)_{eq}$, or in positive Z direction if $T/W < (T/W)_{eq}$. The potential benefit of distributed propulsion can clearly be identified in Fig. 3.3: for a given airframe lift coefficient, the wing loading of the aircraft can be increased from $(W/S_w)_{T_{dp}=0}$ to $(W/S_w)_{eq}$, if $\Delta C_L > 0$.

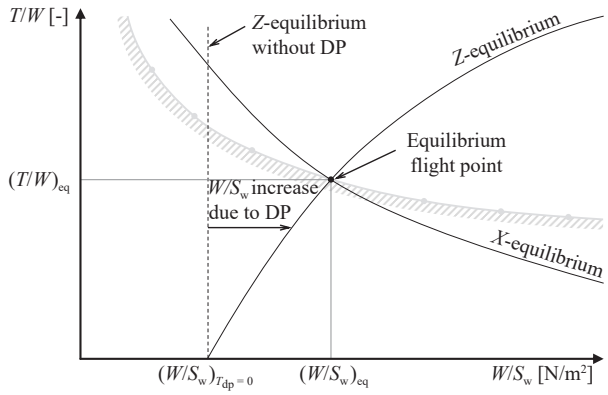

Figure 3.3: Notional wing-loading versus thrust-to-weight-ratio diagram indicating the curves obtained from the equilibrium of forces along the X axis (Eq. 3.10) and Z axis (Eq. 3.11).

The solution of Eqs. 3.10 and 3.11 provides a single point in the diagram. By parametrically varying one of the variables, the equations can be solved to obtain a constraint curve, as indicated by the gray, hashed curve in Fig. 3.3. For most constraints, either the airframe lift coefficient or the flight speed are varied to obtain the points of this curve. Taking this into consideration, four types of performance constraints can be distinguished:

- Constraints at constant flight speed. As the assumed airframe lift coefficient increases while keeping the flight speed constant, a smaller wing (i.e. higher wing loading) is required to generate the same total lift.
- Constraints at constant airframe lift coefficient. This occurs when a stall margin has to be maintained. For example, if a climb gradient requirement must be met at 1.4 times the reference stall speed, then the aircraft must be able to fly at $C_{L_{\max}}/1.4^2$, where $C_{L_{\max}}$ is the total maximum lift coefficient (including aeropropulsive effects). In this case, the resulting velocity at which the maneuver must be performed increases with increasing wing loading.
- Constraints at fixed flight speed and airframe lift coefficient. An aircraft must be able to, for example, achieve a determined stall speed at $C_{L_{\max}}$. Since both the velocity and lift coefficient are fixed, a single point in the diagram is obtained. This implies that the maximum wing loading can only be reached at a single thrust-to-weight ratio. If the pilot were to decrease the thrust setting at maximum wing loading, the aircraft would stall not only due to its deceleration, but also because the change in lift due to thrust (ΔC_L) would decrease. Since the thrust required for this performance constraint is, in general, not a sizing condition, the engines must be set to a predetermined thrust setting once the powertrain has been sized by one of the other, more limiting constraints. Thus, for resemblance with conventional wing-loading diagrams, in this research a vertical line is drawn at the wing loading corresponding to the point obtained. However, if the DP system is sized in landing conditions—as may be the case for concepts comparable to e.g. the X-57 demonstrator [48]—then the installed thrust must correspond exactly to the T/W obtained at this point. In that case, the designer can still opt for a lower wing loading ($C_L < C_{L_{\max}}$), but then the performance requirement becomes a constant-flight-speed constraint.
- Semi-empirical constraints. During take-off and landing, Eqs. 3.7a, 3.7b and 3.7c are not applicable due to the forces exerted on the runway surface. Hence, semi-empirical methods [91, 92] are used to determine the take-off distance and landing distance constraints.

For HEDP aircraft, a power-loading diagram is preferred over a thrust-to-weight ratio diagram, since the powertrain components are modeled in terms of power (see Sec. 3.2). The thrust-to-weight ratios obtained from Eqs. 3.10 and 3.11 can be expressed as power-loading (W/P_{p}) values using:

$$\frac{W}{P_{\mathrm{p}}} = \frac{1}{V(T/W)}. \tag{3.13}$$

Since the constraints can correspond to different points along the mission with different aircraft weights ($W \leq W_{\mathrm{TO}}$), each curve has to be corrected to take-off weight (TOW), in order to compare the different constraints in equal conditions. To this end, a weight fraction f_W is assumed for each flight condition, such that $(W_{\mathrm{TO}}/P) = (W/P)/f_W$. After applying this weight correction, the *propulsive* power-loading diagram is obtained. In traditional power-loading diagrams, the *shaft* power is used on the Y-axis of the power-loading diagram, since this determines the size of the gas turbine. However, for HEP

aircraft, multiple components exist, each of which can be sized by different requirements. Therefore, the propulsive power-loading diagram must be translated into a series of component-oriented power-loading diagrams, creating one power-loading diagram per component of the powertrain.

3.2. HYBRID-ELECTRIC POWERTRAIN MODELING

This section presents a simplified analytical model used to compute the power required from any element of the powertrain for a given propulsive-power requirement and power-control strategy. Several prerequisites are considered for the model:

- It must require only a limited amount of input variables, which are known in the preliminary sizing phase.
- It has to be applicable to different powertrain architectures, including those which present two distinct propulsion systems.
- It must account for component failure, and be compatible with the charging of batteries, as well as energy harvesting.
- it should be sensitive to a series of basic power-control parameters which allow a posterior analysis and optimization of power settings along the mission.

To meet all these prerequisites simultaneously, a series of simplifications are required. The system is treated as steady-state, and a constant conversion/transmission efficiency is assumed per component. Additionally, the effect of battery state-of-charge on the maximum power output of the batteries is not considered. Furthermore, the cables and thermal management systems are not explicitly included in the model. Although these simplifications limit the accuracy and applicability of the model, confidence in the results can be maintained by assuming conservative values for the efficiency, specific power, or specific energy of the electrical machines and batteries, such that a margin for unaccounted components is included. This approach is considered sensitive enough for the preliminary sizing phase, since the effect of such simplifications on aircraft-level performance metrics is expected to be well within the typical $\epsilon < \pm 10\%$ error margin associated to Class-I sizing methods.

3.2.1. HYBRID-ELECTRIC POWERTRAIN ARCHITECTURES

This study considers a set of predefined powertrain architectures, based on the classification of the National Academy of Engineering [22]. These architectures are shown in the first six figures of Fig. 3.4, also including a conventional powertrain for reference. The simplified representations include energy sources, nodes, components which transform one type of power into another, and the power paths that connect these elements. Fuel cells are not considered in this study, although a similar rationale can be followed to expand the method and make Fig. 3.4 applicable to fuel-cell-based architectures. It is also assumed that the thrust produced by the gas-turbine core exhaust is small compared to the total thrust, and therefore the thrust produced by the nozzle is not explicitly accounted for. Components such as converters or transformers are not explicitly modeled, since they do not change the type of power transmitted. Nevertheless, the effect of con-

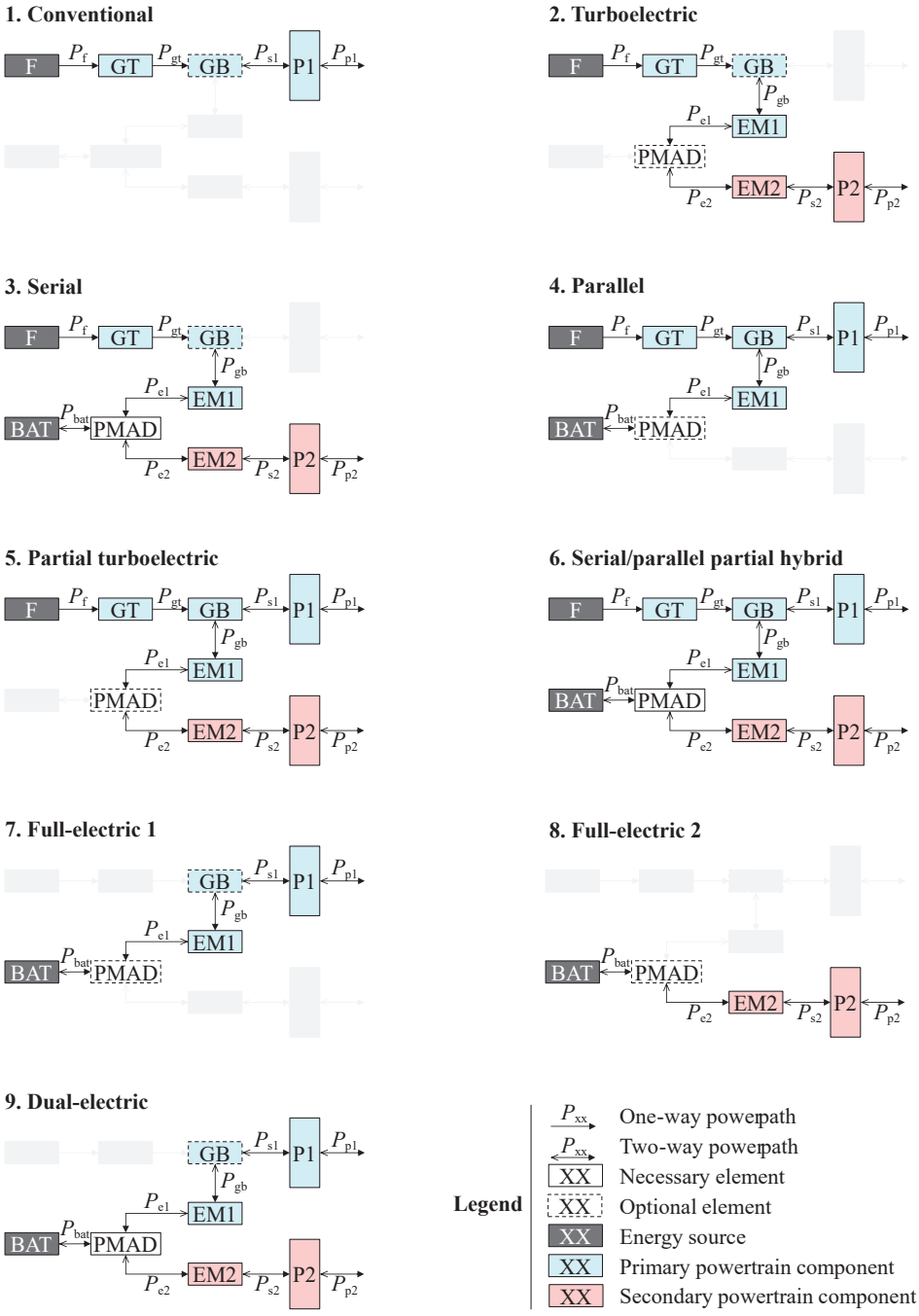

Figure 3.4: Simplified models of the nine powertrain architectures considered in this study. Filled arrowheads indicate the transmission direction corresponding to positive power values.

verters (i.e., inverters and rectifiers) can be accounted for by including their weight correlations and efficiency losses in the associated electrical machine (EM) elements. Similarly, in first approximation, the weight and efficiency of other elements of the electrical grid can be grouped in the power management and distribution (PMAD) element. The components are divided into the elements which constitute the "primary" powertrain, and those that constitute the "secondary" powertrain. The primary components are, directly or indirectly, mechanically coupled to the gas turbine. The secondary components include the devices which power the electrically-driven propulsion system. The primary and secondary branches of the powertrain contain N_1 and N_2 identical instances of each component, respectively.

Closer inspection of the first six powertrain configurations shown in Fig. 3.4 reveals that the first five are, in essence, limit cases of the sixth (the serial/parallel partial hybrid, SPPH). Therefore, with the correct parametrization, the SPPH architecture can be used as a generic model which can be solved for any other architecture as well. In other words, independently of the chosen architecture, the same set of equations can be used to compute component powers, and no architecture-specific equations have to be derived like in other sizing methods [94]. After a more detailed analysis of the SPPH, three additional limit cases are identified (Configurations 7–9), which do not use fuel. Thus, the model is applicable to conventional, hybrid-electric, and fully-electric powertrains. Consequently, the term "hybrid-electric propulsion" is in fact used here to refer to the complete spectrum of propulsion-system architectures, with conventional combustion-based systems at one end of the spectrum, and fully-electric systems at the other end—contrary to some other authors which make a distinction between hybrid-electric (electrical and non-electrical energy storage) and turboelectric (only non-electrical energy storage) propulsion [105].

3.2.2. DEFINITION OF POWER CONTROL PARAMETERS

The SPPH architecture contains two nodes: a gearbox and a PMAD system. Therefore, one can already anticipate that two parameters are necessary in order to completely define the power shares of the system, in addition to one extensive parameter which dictates how much power the system must actually produce. The authors of previous studies [45, 102, 109, 210] have used different parameters to describe the powertrain, and it appears no consensus has been reached with respect to the nomenclature and definition of these variables. Consequently, the parameters proposed here are based on previous definitions, but have been modified such that specific combinations of the power-control parameters can define the powertrain architecture.

The first parameter is the *supplied power ratio*, which was originally defined by Isikveren et al. [102] and can be expressed as

$$\Phi = \frac{P_{\text{bat}}}{P_{\text{bat}} + P_{\text{f}}}. \tag{3.14}$$

The supplied power ratio represents the amount of power drawn from the electrical energy source (batteries) with respect to the total amount of power drawn from all energy sources (battery plus fuel, in this case) for a given point along the mission. Hence, this parameter is only non-zero for powertrains containing batteries (configurations 3, 4 and

6–9). In normal operation, the battery is discharging and thus $\Phi \in [0,1]$. However, if the battery is being charged ($P_{\text{bat}} < 0$), this parameter is negative or greater than one.

The second power-control parameter is the *shaft power ratio*, which represents the amount of shaft power produced by the (one or more) secondary electrical machines, EM2, with respect to the total amount of shaft power produced in a given flight condition:

$$\varphi = \frac{P_{s2}}{P_{s2} + P_{s1}}. \tag{3.15}$$

Analogously to the supplied power ratio, the shaft power ratio belongs to the interval $\varphi \in [0,1]$ during normal operation (when both propulsion systems are generating thrust), but is negative or greater than 1 if one or both of the propulsion systems are windmilling (i.e., extracting energy from the flow). The relations between the two power-control parameters and the nine powertrain layouts considered are collected in Table 3.1.

Table 3.1: Supplied power ratio and shaft power ratio values associated to each architecture. A dot (·) indicates any value can be used.

Configuration	Φ	φ
1. Conventional	0	0
2. Turboelectric	0	1
3. Serial	·	1
4. Parallel	·	0
5. Partial TE	0	·
6. S/P partial hybrid	·	·
7. Full-electric 1	1	0
8. Full-electric 2	1	1
9. Dual-electric	1	·

In addition to the architectures listed in Table 3.1, a tenth "limit case" of the SPPH powertrain corresponds to a situation where the batteries and electrically-driven propulsors operate completely independently from the primary powertrain for all flight conditions. This is the case of an aircraft which has two fully-decoupled propulsion systems, one fuel based, and one battery based. In this architecture, which is considered a variant of the parallel architecture by some authors [211], the powers P_{gb} and P_{e1} are zero. Though this architecture is not explicitly shown in Fig. 3.4, it can be modeled using the same approach if Φ and φ satisfy the following relation:

$$\frac{\Phi}{1-\Phi} k_0 = \frac{\varphi}{1-\varphi}, \tag{3.16}$$

where the constant k_0 equals $1/(\eta_{\text{EM2}}\eta_{\text{PM}}\eta_{\text{GB}}\eta_{\text{GT}})$ or $(\eta_{\text{EM2}}\eta_{\text{PM}})/(\eta_{\text{GB}}\eta_{\text{GT}})$, depending on whether the battery is charging ($\Phi, \varphi < 0$) or discharging ($\Phi, \varphi > 0$), respectively.

Apart from the power control parameters Φ and φ, the conventional gas-turbine throttle is defined as

$$\xi_{\text{GT}} = \frac{P_{\text{GT}}}{P_{\text{GT,max}}}, \tag{3.17}$$

which represents the power produced by the gas turbine with respect to the maximum power it can produce in the given flight condition. This power can in turn be related to the installed sea-level static power of the gas turbine $P_{\mathrm{GT,max,SLS}}$ by means of an altitude and velocity lapse. In the studies presented in Chapters 5, 9, and 10, the altitude lapse provided by Ruijgrok [212] is applied, and the velocity lapse is neglected. For the fully-electric architectures (Configurations 7–9), where no gas turbine is used, an analogous "electrical machine throttle" is used instead:

$$\xi_{\mathrm{EM}} = \frac{P_{\mathrm{EM}}}{P_{\mathrm{EM,max}}}. \tag{3.18}$$

In Eqs. 3.17 and 3.18 the subscripts contain upper-case letters. These refer to a *component* of the powertrain, while lower-case letters refer to a *power path* (indicated by arrows in Fig. 3.4). Although the "installed" gas turbine power evidently refers to the shaft power it can produce (i.e. $P_{\mathrm{GT}} = P_{\mathrm{gt}}$), for an electrical machine this distinction is necessary. For example, the "installed" electrical machine power P_{EM2} could either be equal to P_{e2} or P_{s2}, depending on whether it is acting as an electric motor or as a generator.

Finally, it is necessary to link the power-control parameters to the performance constraint equations derived in Sec. 3.1.2. In this process, two thrust sources were assumed, T_{conv} and T_{dp}. Logically, the use of two thrust sources is only compatible with powertrain architectures that present two types of propulsion system (i.e., configurations 5, 6, and 9). For the other architectures, either T_{conv} or T_{dp} has to be zero. If the aircraft does present two propulsion systems, then the thrust ratio χ can be related to the shaft power ratio φ through

$$\chi = \begin{cases} \dfrac{1}{1 + \dfrac{\eta_{\mathrm{p2}}}{\eta_{\mathrm{p1}}}\left(\dfrac{\varphi}{1-\varphi}\right)}, & \text{if the DP system belongs to the primary powertrain branch,} \\ \dfrac{1}{1 + \dfrac{\eta_{\mathrm{p1}}}{\eta_{\mathrm{p2}}}\left(\dfrac{1-\varphi}{\varphi}\right)}, & \text{if the DP system belongs to the secondary powertrain branch,} \end{cases} \tag{3.19}$$

where η_{p1} and η_{p2} are the propulsive efficiencies of the propulsors of the primary and secondary powertrain branches, respectively. The propulsive efficiency given by Eq. 3.6 corresponds to either η_{p1} or η_{p2}, depending on whether the DP system is installed on the primary or secondary powertrain branch. With Eq. 3.19 it is evident that χ and φ represent the same degree of freedom, but χ refers to the *propulsive* power share of the DP system (which can correspond to either the primary or secondary powertrain branch), while φ refers to the *shaft* power share of the secondary, electrically-driven, propulsor system. Thus, if φ is not in the interval [0,1] because one or both of the propulsion systems are harvesting energy, then χ is also negative or greater than one. Consequently, the thrust-to-weight ratio obtained from the performance equations will change accordingly. Furthermore, the average propulsive efficiency of the aircraft, which is used to define the aero-propulsive efficiency, can be calculated from

$$\eta_{\mathrm{p}} = (1-\varphi)\eta_{\mathrm{p1}} + \varphi\eta_{\mathrm{p2}}. \tag{3.20}$$

3.2.3. SOLVING THE POWERTRAIN EQUATIONS

The powertrain model has ten unknowns, corresponding to the ten power paths shown in Fig. 3.4-6. Thus, ten equations are necessary to solve the system. The first seven can be obtained by applying a power balance across each component. For a generic component, this equation is expressed as:

$$\sum P_{\text{out}} = \eta \sum P_{\text{in}}, \tag{3.21}$$

where the left-hand side indicates the summation of power paths flowing "out" of the component, and the right-hand side represents the summation of power paths flowing "in" to the component, multiplied by the conversion efficiency of the component, η.

Three additional equations or values are required. This ties in to the discussion of Sec. 3.2.2, which stated that three parameters have to be specified in order to define the complete behavior of the powertrain. For example, Φ (which relates P_{bat} to P_{f}), φ (which relates P_{s1} to P_{s2}), and the total required propulsive power $P_{\text{p}} = P_{\text{p1}} + P_{\text{p2}}$ can be specified. The set of linear equations can then be expressed as

$$\begin{bmatrix} -\eta_{\text{GT}} & 1 & 0 & 0 & 0 & 0 & 0 & 0 & 0 & 0 \\ 0 & -\eta_{\text{GB}} & 1 & 1 & 0 & 0 & 0 & 0 & 0 & 0 \\ 0 & 0 & 0 & -\eta_{\text{P1}} & 0 & 0 & 0 & 0 & 1 & 0 \\ 0 & 0 & -\eta_{\text{EM1}} & 0 & 1 & 0 & 0 & 0 & 0 & 0 \\ 0 & 0 & 0 & 0 & -\eta_{\text{PMAD}} & -\eta_{\text{PMAD}} & 1 & 0 & 0 & 0 \\ 0 & 0 & 0 & 0 & 0 & 0 & -\eta_{\text{EM2}} & 1 & 0 & 0 \\ 0 & 0 & 0 & 0 & 0 & 0 & 0 & -\eta_{\text{P2}} & 0 & 1 \\ \Phi & 0 & 0 & 0 & 0 & (\Phi-1) & 0 & 0 & 0 & 0 \\ 0 & 0 & 0 & \varphi & 0 & 0 & 0 & (\varphi-1) & 0 & 0 \\ 0 & 0 & 0 & 0 & 0 & 0 & 0 & 0 & 1 & 1 \end{bmatrix} \cdot \begin{bmatrix} P_{\text{f}} \\ P_{\text{gt}} \\ P_{\text{gb}} \\ P_{\text{s1}} \\ P_{\text{e1}} \\ P_{\text{bat}} \\ P_{\text{e2}} \\ P_{\text{s2}} \\ P_{\text{p1}} \\ P_{\text{p2}} \end{bmatrix} = \begin{bmatrix} 0 \\ 0 \\ 0 \\ 0 \\ 0 \\ 0 \\ 0 \\ 0 \\ 0 \\ P_{\text{p}} \end{bmatrix} \tag{3.22}$$

In Eq. 3.22, the first seven rows of the coefficient matrix correspond to the power balance equations across the gas turbine, gearbox, primary propulsor, primary electrical machine, PMAD, secondary electrical machine, and secondary propulsor, respectively. The last three rows correspond to the additional information provided. These three rows can be replaced by different equations, depending on what the designer wants to specify as input to the problem. For example, during the mission analysis, the three power-control parameters can be specified as input, and the resulting propulsive power produced by the aircraft can be computed (see Appendix A). However, if a configuration different than the SPPH is selected, then one or two of these equations will be fixed by Φ and/or φ (see Table 3.1). For example, if a turboelectric configuration is selected, then $\Phi = 0$ and $\varphi = 1$. In this case, rows 8 and 9 of Eq. 3.22 are readily determined, and the remaining degree of freedom must be specified in the last row.

The signs of the coefficients in Eq. 3.22 assume that the powers flow as indicated by the filled arrowheads in Fig. 3.4.6. If, for example, the primary electrical machine acts as an electric motor, providing power to the primary system, then P_{e1} and P_{gb} are negative. Under these conditions, the criteria of which power paths flow "in" and "out" of the component in Eq. 3.21 change. Therefore, the efficiency factor will appear in a

different column of the coefficient matrix. This implies that the values in the coefficient matrix are not actually constants, but depend on the direction of the power flows, that is, on the sign of the solution variables. One possibility would be to assume a given direction of power flows and to solve the system iteratively, updating the coefficient matrix based on the sign of the solution of the previous iteration. However, this should be done with caution, since the solution presents discontinuities in gradient, and Φ and φ tend to infinity as $P_f \rightarrow -P_{bat}$ and $P_{s1} \rightarrow -P_{s2}$, respectively. A more effective approach is to assume a given direction of power flow, to construct and solve the corresponding matrix, and to verify the assumption thereafter. Closer inspection of the SPPH architecture reveals that in total nine possible operating modes exist. This conclusion can be drawn by considering that the gas turbine can only produce positive power, and that not all power paths connected to a given component can simultaneously flow in or out of that component. Appendix A provides the coefficient matrices corresponding to these nine operating modes. Although in the most generic sense all the different solutions have to be probed, in most practical applications the designer decides beforehand under which conditions the powertrain is operating. Moreover, the other, more simple powertrain architectures contain less possible operating modes, and thus only a limited number of these combinations have to be evaluated.

3.2.4. SIZING FOR COMPONENT FAILURE

When applying the powertrain model to the propulsive power-loading diagram, the inverse of power loading, $1/(W/P_p)$, can be used. In other words, the powers are computed per unit weight of the aircraft. However, some of the constraints in the diagram must be met in "one-engine-inoperative" (OEI) conditions. OEI is interpreted here as the failure of any one component of the powertrain. An exception is the PMAD, which is assumed to contain redundant buses, such that the failure of a component of the primary powertrain branch does not affect the secondary powertrain branch and vice versa. Thus, the effect of a single component failure can be accounted for by over-sizing all components of the branch where the failure occurs by a factor $N_1/(N_1-1)$ or $N_2/(N_2-1)$, depending on whether the failure occurs in the primary or secondary powertrain branch, respectively. This implies that a single propulsive-power constraint leads to two constraints in the component-power-loading diagrams in OEI conditions, depending on the powertrain branch in which the failure occurs.

The previous paragraph assumes that a single component of the powertrain will fail, as is traditionally assumed for conventional aircraft. However, in the case of DP systems, multiple instances of the components may be powered by the same source. As an example, consider a HEP aircraft with twelve electrically-driven fans, clustered in groups of three, such that if a connection fails in the PMAD, three electrical machines are lost simultaneously. In this case, the "OEI" sizing constraint must over-size each element of that powertrain branch by a factor $N_2/(N_2-3)$. It becomes evident that, in general, accurately sizing the electrical powertrain for all possible failure modes is a complicated and case-specific task, and is therefore not treated in depth in this preliminary sizing method. A designer can use this method as basis and gradually increase the fidelity of the modeling as the system architecture becomes more defined. Similarly, the effect of battery pack failure is not addressed in this study. Although a simple correction can be

applied by multiplying the battery's power requirements by a fraction $N_{\text{bat}}/(N_{\text{bat}}-1)$, where N_{bat} is the number of independent battery packs, an accurate evaluation of battery failure would require a more detailed design and analysis of the electrical system.

Another important characteristic of powertrains with two energy sources is the ability to divert power from one branch to the other in case of component failure. For example, if one of two gas turbines fails, the other will not have to be over-sized by a factor 2, if the battery can supply additional power. This would, in essence, change the supplied power ratio during that flight condition. Therefore, although the re-routing of power in case of component failure is not explicitly included in the present method, it can be accounted for by correctly selecting the independent variables φ and Φ. The designer can do so through trial-and-error, or by means of an external optimization loop. Finally, it is worth noting that in case of component failure, the same total thrust is maintained in order to meet the performance requirement, and thus the aero-propulsive effects are assumed to remain unaffected. This is a valid assumption if ΔC_L, ΔC_D, and $\Delta\eta_{\text{p}}$ vary linearly with thrust. However, if the failure of a determined powertrain component has a significant impact on the aero-propulsive effects, then the delta terms of Eqs. 3.6–3.5 must include additional dependencies to reflect this.

3.3. SIZING FOR ENERGY

This step of the sizing process calculates the fuel and battery energy required for an assumed mission profile and take-off weight. Since, at this stage, the power-loading of each component has been determined, the installed power can readily be obtained with an assumed TOW value. For conventional aircraft, the fuel mass is commonly determined in the preliminary sizing phase Breguet range equation for the cruise phase, and constant fuel fractions for the non-energy-intensive mission phases [85, 91]. An analytical range equation can also be derived for hybrid-electric aircraft if constant power-control parameters are assumed (Sec. 3.3.1). However, the power-control profiles have a strong impact on block energy consumption [102], and thus the energy sizing method must be applicable for generic power-control profiles. Therefore, already in the preliminary sizing phase of hybrid-electric aircraft, a time-stepping mission analysis is recommended (Sec. 3.3.2).

3.3.1. RANGE EQUATION

If constant power-control parameters are assumed and the cruise phase is dominant for the overall energy consumption, then an analytical equation can be used to estimate the energy required for a mission of a determined range R. In Appendix B, a range equation for hybrid-electric aircraft with a single propulsion system is derived, leading to:

$$R = \eta_3 \frac{e_{\text{f}}}{g}\left(\frac{L}{D}\right)\left(\eta_1 + \eta_2 \frac{\Phi}{1-\Phi}\right)\ln\left[\frac{W_{\text{OE}} + W_{\text{PL}} + \dfrac{g}{e_{\text{bat}}}E_{0,\text{tot}}\left(\Phi + \dfrac{e_{\text{bat}}}{e_{\text{f}}}(1-\Phi)\right)}{W_{\text{OE}} + W_{\text{PL}} + \dfrac{g}{e_{\text{bat}}}\Phi E_{0,\text{tot}}}\right]. \tag{3.23}$$

The range equation given by Eq. 3.23 is valid for conventional, serial, parallel, turbo-electric, and fully-electric architectures, as long as the supplied power ratio, flight speed,

lift-to-drag ratio, and transmission efficiencies are constant. An approach similar to the one in Appendix B can be followed to derive the equivalent expression for powertrains with two propulsion systems (partial-turboelectrc, SPPH), although in that case also the shaft power ratio must be constant. Although Eq. 3.23 is straightforward to apply, it should be used with some caution. For example, it can be used to compute the total energy required for a given harmonic range only if most of the energy is consumed in the cruise phase, e.g. for long-haul flights. If not, Eq. B.15 should be used instead to compute the energy requirements of specific mission segments. However, both formulations are inaccurate for climb and descent phases, since they assume a small flight-path angle ($\gamma \ll 1$). Furthermore, given that (hybrid-) electric configurations typically have much higher empty-weight fractions than conventional fuel-based aircraft—due to the increased powertrain weight—it is important to assume appropriate empty-weight values when comparing different aircraft configurations.

3.3.2. MISSION ANALYSIS

In this approach, a numerical quasi-steady point-model is used, which analyses the instantaneous point performance of the aircraft at suitably small time intervals along the mission. For this, the mission is divided into different segments, such as climb, cruise, descent, or loiter. For each time step, performance is assumed constant and thus the battery energy and fuel energy consumed in the interval i can be estimated by multiplying P_{bat} and P_{f} by the duration of the time interval Δt_i:

$$E_{\text{f},i} = P_{\text{f},i} \cdot \Delta t_i, \tag{3.24a}$$

$$E_{\text{bat},i} = P_{\text{bat},i} \cdot \Delta t_i, \tag{3.24b}$$

The power consumption at the energy sources is in turn related to the total propulsive power through the powertrain model described in Sec. 3.2. Depending on the mission segment, the designer can either specify the required propulsive power and compute the necessary power-control parameters, or specify all three power-control parameters and compute the resulting excess power used to change altitude or velocity (see Appendix A). The total propulsive power can be calculated as a function of the flight condition using Eqs. 3.10, 3.11 and 3.13. In this way, the aero-propulsive interaction effects are taken into account. Then, for the subsequent time step, the aircraft weight must be updated to account for the reduction in fuel weight (which is zero if $\Phi = 1$),

$$W_{i+1} = W_i - \frac{g E_{\text{f},i}}{e_{\text{f}}}. \tag{3.25}$$

Finally, the total energy requirements are computed by integrating the energy consumption per time interval along the entire mission.

3.4. WEIGHT ESTIMATION

For hybrid-electric aircraft, the operative empty weight (OEW) cannot be estimated using the traditional Class-I empirical correlations, since there is no weight database for HEP aircraft. The weight breakdown of these aircraft differs appreciably from conventional aircraft for several reasons. First of all, the battery weight has to be included in the

total aircraft weight. Secondly, the weight of the powertrain is considerably higher for hybrid-electric propulsion systems (see for example Refs. [77–79, 113–115]). Furthermore, in some cases, the wing loading can be significantly higher for HEP concepts [48], and therefore the wing weight fraction will not be comparable to conventional aircraft. Taking this into account, the TOW of the aircraft can be expressed as:

$$W_{TO} = W_{OE} + W_{PL} + W_f + W_{bat}, \tag{3.26}$$

where the fuel weight W_f is obtained from the mission analysis.

The weight of the batteries W_{bat} is not included in the "empty weight" term because it is not accounted for in traditional empty-weight correlations, can constitute a significant fraction of the overall aircraft weight, and may—in some applications—be a variable weight term if, for example, interchangeable battery packs are used in varying quantities depending on the mission. The required battery weight for a determined mission can be limited by either energy or power requirements. Both should be evaluated in the sizing process, so as to assure both requirements are met. In terms of energy requirements, the total battery energy computed in the mission analysis can be divided by the specific energy of the batteries at pack level, e_{bat}, in order to obtain the battery mass. To this amount, a minimum SOC margin (typically around 20%; see Sec. 2.1.1) should be added to avoid limited power output or reducing the batteries' cycle life. The maximum power requirement, on the other hand, can be obtained from the design power-loading value obtained in the battery-power-loading diagram, together with an initial guess of the TOW, i.e. $P_{bat} = W_{TO}/(W_{TO}/P_{bat})$. This can then be converted into a minimum battery mass requirement if the battery's specific power at pack level is known. The specific energy and power at pack level can in turn be related to more accurate descriptors such as cell voltage, maximum discharge rate, or packaging efficiency if a battery model is available.

The OEW term of Eq. 3.26 should be further decomposed in order to distinguish the contribution of the powertrain W_{pt}, as evidenced in earlier studies [78, 213, 214]. Furthermore, as discussed previously, the contribution of the wing weight W_w should be isolated:

$$W_{OE} = W_{OE'} + W_w + W_{PT}. \tag{3.27}$$

In Eq. 3.27, $W_{OE'}$ is the operating empty weight excluding the powertrain and wing. This component can be estimated by calculating the OEW of a conventional reference aircraft using empirical correlations, and subtracting the weight that the wing and powerplant would have on that aircraft, i.e. $W_{OE'} = W_{OE,ref} - W_{w,ref} - W_{PT,ref}$. This assumes that the rest of the airframe is not significantly affected by incorporating a HEP or DP system. Although the accuracy of this assumption is debatable, more detail would imply going to a complete Class-II weight estimation, for which a more extensive description of the design would be required. The empirical correlations used in this research for the wing, turboshaft, and operating empty weight of conventional aircraft are based on the books of Torenbeek [91], Roskam [85], and Raymer [92], respectively. The wing-loading value used to compute $W_{w,ref}$ is estimated by evaluating the stall speed constraint in absence of aero-propulsive interaction effects, in which case $(W/S_w)_{ref} = q_\infty C_{L_{max,airframe}}$.

Finally, the weight of the powertrain has to be estimated. If the specific power (kW/kg) or a power-to-weight correlation of each component of the corresponding powertrain architecture is known, then the complete powertrain weight can be estimated for a given TOW value, since the power required from each component is determined by its respective power-loading diagram. Since most of the mentioned component weights depend on the TOW of the aircraft, an iterative calculation is required, as indicated in Fig. 3.1. After converging on the TOW in the weight estimation module, the mission analysis can be employed to recompute the fuel and battery energy requirements, repeating the process until converging on a final TOW.

4

VERIFICATION OF SIZING METHOD

The preliminary sizing method described in the previous chapter should be validated to ensure that no critical considerations have been overlooked in the formulation of the method and its assumptions, and that no mistakes have been made in the derivation and numerical implementation of the equations. However, since only a limited number of manned hybrid-electric aircraft have been flight tested, no validation data is available. Therefore, a formal validation process is not possible, and the procedure outlined in Fig. 4.1 is followed instead.

The first step of Fig. 4.1 is to validate the sub-modules of the method, such as the weight-estimation module or the aerodynamic model. However, since the proposed sizing method is limited to Class-I sizing, no complex sub-modules which require a dedicated validation are used. The weight-estimation methods are based on proven statisti-

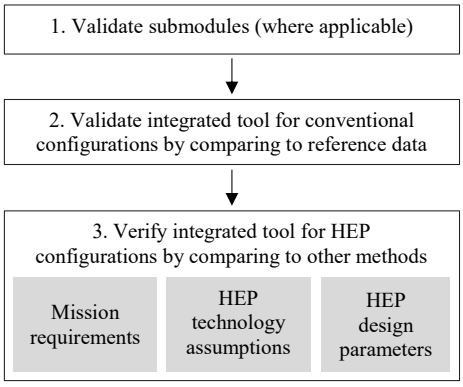

Figure 4.1: Main steps of the verification & validation procedure.

The studies presented in this Chapter were performed in collaboration with D. F. Finger [104] and have been published in Ref. [215]

cal correlations, while the aerodynamic polar is based on assumed variables such as the Oswald factor and zero-lift drag coefficient, which are again chosen based on empirical values. One exception is the aero-propulsive model, which can be arbitrarily complex. If such a model is incorporated in the sizing process—which is not the case in this initial validation exercise—then it must first be validated separately. The aero-propulsive models used in this dissertation are validated in Ch. 8 and Appendix C. In the second step of Fig. 4.1, the method is used to size a conventional reference aircraft, for which sufficient validation data is available. This step confirms that reasonable input values (e.g. drag polar characteristics) have been assumed, and that the method is applicable to conventional aircraft configurations.

If the submodules have been validated individually and the method is validated for conventional aircraft configurations, then it is also applicable to HEDP aircraft, as long as the simplified HEP powertrain representation and the incorporation of the aero-propulsive effects are correct. Although no validation can be performed as such, these modules are based on elementary physical relationships (Eqs. 3.7a–3.7c: "force equals mass times acceleration", Eq. 3.21: "power out equals power in times transmission efficiency"). Thus, a verification study is considered sufficient to gain confidence in the accuracy of the overall sizing method for HEP configurations. To maximize this confidence in the sizing method, the impact of the parameters which have the largest influence on the aircraft figures of merit, or those that present the largest uncertainty, should be analyzed. Although the influence of each parameter depends on the configuration, in general, at least the following three sets of parameters should be considered: mission requirements (e.g. range), technology assumptions (e.g. battery specific energy), and HEP-specific design parameters (e.g., supplied power ratio).

For this verification procedure, the method proposed in the previous chapter is compared to an independently-developed sizing method. This benchmark method is described in the following section. Since the reference method was not developed to account for aero-propulsive interaction effects, these are not included in the verification study. The two methods are then used to size a conventional reference aircraft and a series of hybrid-electric variants in Secs. 4.2 and 4.3, respectively.

4.1. BENCHMARK SIZING METHOD

The method used for cross-validation was developed by Finger [104] at FH Aachen. This methodology was conceived for the design of general-aviation aircraft, with special focus on the ability to analyze VTOL aircraft. The methodology of the sizing process is documented in Refs. [104, 211]. Analogous to the method described in Ch. 3, the methodology is separated into two major parts: point performance, also referred to as the constraint diagram, and mission performance, also known as the mass estimation. The mission is broken into a several segments and simulated in a time-stepping manner, using an energy-based approach. To cover the mix of consumable (fuel) and non-consumable (batteries) energy sources, the masses are not treated as fractions, but as absolute values. Based on a first estimate for the MTOM, all masses that make up the total mass are calculated. This can be done using both Class-I and Class-II mass estimation methods from the traditional aircraft design methods. Based on the new MTOM, the next iteration step can be started.

This reference sizing method is applicable to conventional, parallel, serial, and fully-electric powertrains with one type of propulsor. For serial and parallel powertrains, a "hybridization factor" H_P is defined to specify the split of power coming from the two energy sources, analogous to the supplied power ratio defined in the previous chapter. This hybridization of power is expressed differently for parallel hybrid (PH) and serial hybrid (SH) architectures and, for the conventions used in Fig.3.4, is defined as:

$$H_{P,\mathrm{PH}} = \frac{-P_{\mathrm{gb}}}{P_{\mathrm{gt}} - P_{\mathrm{gb}}}, \tag{4.1}$$

$$H_{P,\mathrm{SH}} = \frac{P_{\mathrm{bat}}}{P_{\mathrm{bat}} + P_{\mathrm{e1}}}. \tag{4.2}$$

The variable H_P therefore governs the power split at the node (i.e., the gearbox for the parallel architecture, or the electrical node for the serial architecture), while the supplied power ratio Φ specifies the power split at the energy sources. The two parameters can be linked through:

$$\Phi = \begin{cases} \dfrac{1}{1 - \dfrac{\eta_{\mathrm{gb}}}{\eta_{\mathrm{gt}}} \dfrac{\left(1 - H_{P,\mathrm{PH}}\right)}{H_{P,\mathrm{PH}}}}, \text{ for parallel architectures,} \\ \\ \dfrac{1}{1 + \dfrac{1}{\eta_{\mathrm{gt}}\eta_{\mathrm{e1}}} \dfrac{\left(1 - H_{P,\mathrm{SH}}\right)}{H_{P,\mathrm{SH}}}}, \text{ for serial architectures.} \end{cases} \tag{4.3}$$

In both formulations, a fully-electrical powertrain is achieved if the power split is equal to one ($H_P = 1 \leftrightarrow \Phi = 1$) for all mission segments and performance constraints of the sizing process. In that case, the power required from the gas turbine is zero independently of the architecture considered. Therefore, in both sizing methods, the fully-electrical architecture can automatically be obtained as a limit case.

In the text that follows, "**Method A**" will be used to refer to the benchmark method of FH Aachen, while "**Method B**" will be used to refer to the method described in this dissertation. Although both methods stem from the well-known Class-I design methods, there are differences in the assumptions, constraint analysis, mission analysis, and systems analysis. In addition to the different parametrization approach described above, one important difference is the calculation and interpretation of the power-loading diagrams, which is discussed in Sec. 4.3.2. For a more exhaustive explanation of the differences, the reader is referred to Ref. [215].

4.2. REFERENCE AIRCRAFT

In this section, a baseline reference aircraft is sized for a given set of top-level requirements. For this study, a 19-seat, CS-23 commuter aircraft is selected. Commuter class aircraft (up to 8618 kg) are larger than the general aviation category (up to 5760 kg), for which Method A is designed, and smaller than the CS-25 transport aircraft, for which Method B is typically used. In this way, it is possible to verify that the approaches are

generic enough for the sizing of hybrid-electric aircraft in general, and not just limited to the aircraft category for which they were initially intended. The results are subsequently used as a baseline for the hybridization studies of Sec. 4.3.

4.2.1. TOP-LEVEL REQUIREMENTS AND ASSUMPTIONS

The reference aircraft is based closely on the Dornier/RUAG Do 228NG, a twin-turboprop STOL utility aircraft [216]. This aircraft has been analyzed in previous hybrid-electric aircraft studies (see e.g. Refs. [217, 218]). Moreover, performance data of the aircraft is available from multiple sources [216, 219–221], and therefore it is well-suited as a reference configuration. For propulsion, Honeywell TPE331 engines are used. They are flat-rated at 579 kW when installed on the Do 228 [220], but are designed to produce up to 701 kW [221]. The reference aircraft is sized for a typical commuter mission, including diversion, 30 minutes of loiter, and additional contingency fuel reserves, as specified by the regulations [222]. The mission specification and top-level design requirements are shown in Table 4.1. The selected aircraft performance requirements are based on information given in Refs. [216, 220], while the propulsion system data is obtained from manufacturer data and the Do 228's pilot's operating handbook [219]. Moreover, the mission requirements are extracted from the payload-range diagram of the aircraft, presented in Fig. 4.2.

Table 4.1: Mission and performance requirements of the baseline aircraft used in the validation study.

Parameter	Value	Parameter	Value
Take-off distance [m]	793	Diversion speed V_{div} [m/s]	85
Taxi/Take-off altitude h_{TO} [m]	0	AEO ROC at SL [m/s]	8
Cruise altitude h_{cr} [m]	3000	OEI ROC at SL [m/s]	2
Landing/Taxi altitude h_{L} [m]	0	Range (baseline) R [km]	396
Diversion altitude h_{div} [m]	1000	Diversion range R_{div} [km]	270
Loiter altitude h_{loiter} [m]	450	Loiter time [min]	30
Cruise speed V_{cr} [m/s]	115	Contingency fuel [%]	5
Stall speed V_{s} [m/s]	34.5	Payload (baseline) m_{PL} [kg]	1960

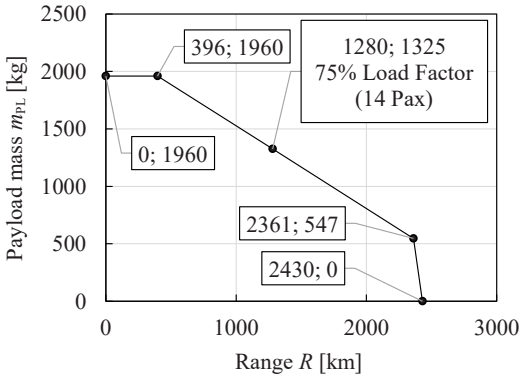

Figure 4.2: Payload-range diagram of the Do 228NG. Data taken from Ref. [220].

The values of the design parameters and additional input assumptions selected to meet these top-level requirements are included in Appendix D.1 for traceability. For the aerodynamic characteristics of the Do 228NG, no data was found in the public domain, and therefore a drag polar had to be assumed. A two-term drag polar was used, as indicated in Eq. 4.4, for which it is assumed that the quadratic term is inversely proportional to the Oswald factor, as normally defined in a symmetric drag polar. The assumed aerodynamic properties, which were based on preliminary CFD simulations of a simplified Do 228NG geometry [215], are gathered in Table 4.2. The designs were found to be especially sensitive to the aerodynamic modeling of the aircraft and to the performance characteristics of the turboshaft engine. For the power lapse and or thermal efficiency of the engine, a surrogate model was built based on the TPE331 performance data provided in Ref. [221]. Due to the flat-rating of the TPE331 used on the Do228, the engine was found to be able to produce maximum power at all combinations of flight speed and altitude considered in this study. The specific fuel consumption of the engine, meanwhile, is computed as a function of flight speed and altitude using the surrogate model, and additionally corrected for part-throttle, as mentioned in the previous section.

$$C_D = C_{D,\min} + \frac{(C_L - C_{L,\min D})^2}{\pi A e} \tag{4.4}$$

Table 4.2: Drag polar characteristics assumed for the verification study.

Parameter	Value
Aspect ratio A [-]	9
Minimum drag coefficient $C_{D,\min}$ [-]	0.029
Minimum-drag lift coefficient $C_{L,\min D}$ [-]	0.17
Oswald factor e [-]	0.63

4.2.2. SIZING FOR BASELINE MISSIONS

The first step of the sizing process is to determine the wing loading and power-loading or power-to-weight ratio of the aircraft. To this end, the results obtained from both methods for the Do 228 is shown in Fig. 4.3. For completeness, all additional performance requirements specified by the regulations (Refs. [223, 224]) have been included in grey lines. However, these additional constraints were found to not actively constrain the design space, and are therefore not discussed in further detail.

The agreement of both methods is good, although slight variations can be observed in the diagram. The most glaring disparity is the take-off distance constraint. Method A uses Gudmundsson's approach [225], which correlates $W_{\text{TO}}/S_{\text{w}}$ and $P_{\text{s}}/W_{\text{TO}}$ in a non-linear fashion. Method B uses Raymer's linear regression approach [92], which gives more optimistic values at high wing loading. The one-engine inoperative (OEI) rate-of-climb (ROC) constraint at sea level (SL) is found to differ slightly due to the different flight speeds assumed in the two methods [215], with Method B being slightly more conservative. The all-engines operating (AEO) ROC constraint and the stall speed constraint, which determine the design point, are found to show a good agreement between the two methods, as well as the cruise speed constraint. Consequently, the design points obtained from both methods are practically identical and differ less than 1% from the design point of the Do 228, as shown in Table 4.3.

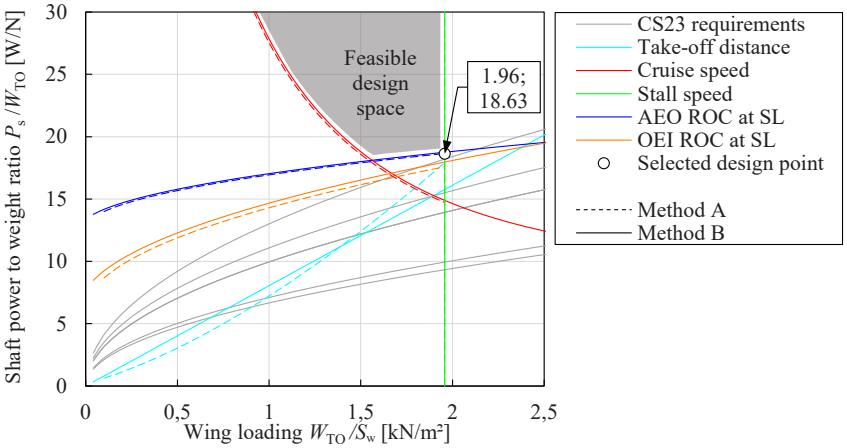

Figure 4.3: Performance constraint diagram of the reference aircraft configuration, corrected to maximum throttle.

Table 4.3: Mission and performance requirements of the baseline aircraft used in the validation study.

	Do 228	**Method A**		**Method B**	
	Ref. data	Value	Difference	Value	Difference
W_{TO}/S [N/m^2]	1962	1957	-0.3%	1958	-0.2%
P_s/W_{TO} [W/N]	18.44	18.65	+1.1%	18.63	+1.0%

Using the P_s/W_{TO} and W_{TO}/S_w data from the constraint diagrams, the mission performance analysis is carried out to determine the energy requirements of the desired mission. This is conducted for three different points of the Do 228 payload-range diagram: a short-range mission with maximum payload, a medium-range mission with 75% load factor, and a long-range mission that corresponds to maximum fuel and minimum payload (see Fig. 4.2). Since these three missions lie on the envelope of the payload-range diagram, the sizing methods should also return the same take-off mass for each of the points. The sizing results of these missions are shown in Table 4.4 for both methods. The difference in MTOM between the reference aircraft and the sizing results of the numerical methods is less than 4%. This is a relatively accurate result, considering that these methods are intended for conceptual design studies, and the fidelity of the modeling is relatively low. As a general trend, Method A seems to over-estimate MTOM (+0.5 to +3.8%), but no clear trend regarding the influence of the design range can be seen. Method B gets an excellent result (+0.3%) for the short mission, but slightly underpredicts MTOM for longer ranges (up to -3.3%). Furthermore, to verify that the MTOM estimation of the aircraft is correct and not an artifact of counteracting effects in the component mass estimation, the component masses of both methods for each mission are compared to reference data in Fig. 4.4. This figure shows that, apart from the fuel mass, both methods are capable of sizing the different components with reasonable accuracy.

Table 4.4: Mission and performance requirements of the baseline aircraft used in the validation study.

Mission		Reference	Method A		Method B	
R [km]	m_{PL} [t]	MTOM [t]	MTOM [t]	Diff.	MTOM [t]	Diff.
396	1.96	6.40	6.64	+3.8%	6.42	+0.3%
1280	1.33	6.40	6.43	+0.5%	6.40	0.0%
2361	0.55	6.40	6.49	+1.4%	6.19	-3.3%

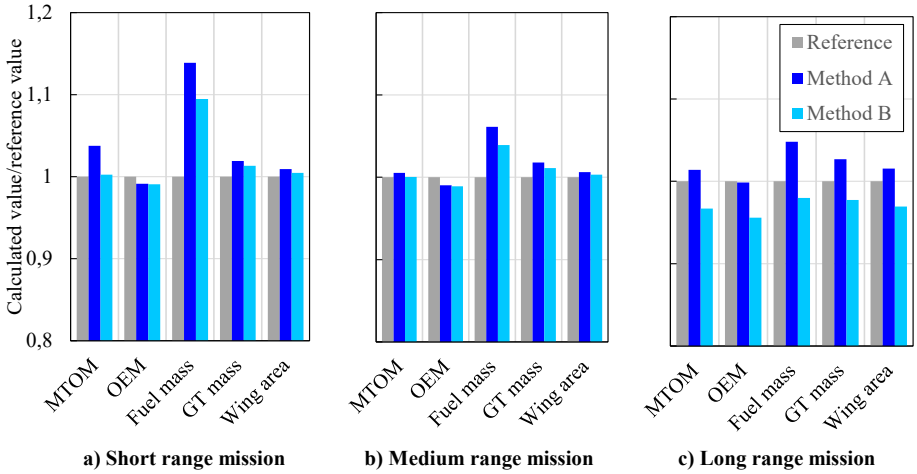

Figure 4.4: Comparison between results obtained from the two sizing methods and reference aircraft data.

Figure 4.4 shows that the largest discrepancy between the reference and the results of both methods is found for the fuel mass. Fuel mass is directly connected to the overall efficiency of the aircraft, and almost all modeling errors manifest themselves in an increase or decrease in fuel burn. The sensitivity of fuel burn to the aerodynamic characteristics of the aircraft and to the performance map of the turboshaft engine make the discrepancy hard to trace back to a specific assumption or modeling error. The largest relative difference is found for the short-range mission, which also has the lowest absolute fuel mass. Consequently, the relative deviation from the reference data is the largest, even though the fuel mass is only over-predicted by approximately 60 kg (see Appendix D.1). The larger error for shorter missions also suggests that different reserve-fuel requirements might play a role. For example, the actual diversion range of the reference aircraft might be lower than assumed here.

The inherent differences of the mission analyses of both methods play a factor as well: the taxi, take-off, and landing fuel fractions are calculated differently, a different climb and descent strategy is used, and the variable turboshaft efficiency is implemented differently, as discussed in Ref. [215]. Especially the last two points have an important effect for the shorter missions, as a larger fraction of the mission is spent in off-design conditions, instead of in cruise flight. To further investigate possible differences in the mission analysis, Fig. 4.5 shows the mission profile obtained by the two sizing methods

for the short-range mission. Note that, for such a short mission, the reserves play an important role in determining the total fuel weight. Although no mission data is available for the reference aircraft, Fig. 4.5 shows that the two methods produce similar mission profiles. The climb and descent profiles of Method B are smoother but lead to slightly higher energy consumption, as discussed earlier. Moreover, Method A explicitly models the taxi-out, take-off, landing, and taxi-in phases, while Method B does not. For Method B, the nominal mission starts at take-off speed and ends at the approach speed. Finally, Method A always accelerates/decelerates and climbs/descends between mission phases, while Method B presents a discontinuity at the beginning and end of the loiter phase, for which no transition phases are modeled. However, despite these differences, the block fuel consumption computed by the two methods does not differ significantly, as reflected in Fig. 4.4.

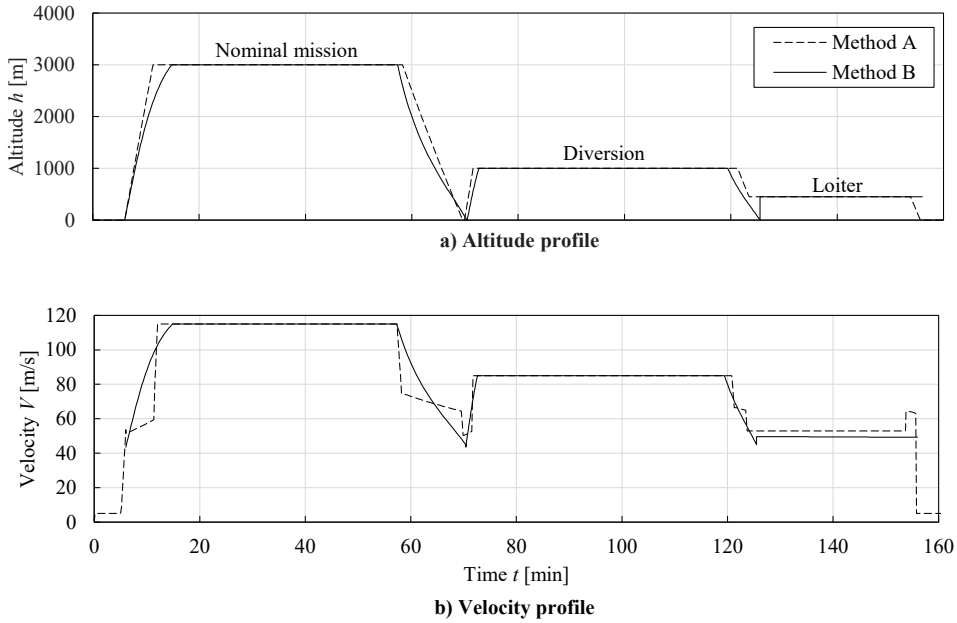

Figure 4.5: Reference aircraft altitude (top) and velocity (bottom) profiles for the short-range mission.

4.3. HYBRID-ELECTRIC AIRCRAFT

In this section, the conventional, parallel-hybrid, serial-hybrid, and fully electric aircraft obtained from the two methods are compared with each other. The differences observed with the conventional baseline aircraft in Sec. 4.2.2 can largely be attributed to different modeling approaches for the mission reserves and powertrain components. To exclude these differences—which are not inherent to the formulation of the two sizing methods—several additional simplifications are made for the comparison of hybrid-electric aircraft. In this way, the additional discrepancies due to the incorporation of hybrid-electric propulsion can be isolated. These simplifications are described in Sec. 4.3.1. Sections 4.3.2 and 4.3.3 then present the results for the baseline mission and the parameter sweeps, respectively.

4.3.1. ASSUMPTIONS

For conventional 19-seater aircraft, a 5% contingency fuel reserve has to be maintained [222]. Given that for HEP aircraft it is unclear whether these energy reserves should be accounted for in the fuel energy, battery energy, or both, this 5% contribution to total energy is not included in the following analyses. Thus, the fuel mass is reduced compared to the conventional short-range results. Moreover, for the serial and parallel powertrains, a constant power split of $H_P = 0.1$ is assumed throughout the mission and for all performance constraints. Furthermore, for the comparison of (hybrid-) electric concepts, the thermal efficiency of the gas turbines is fixed, independently of the throttle setting or flight condition, and assumed to be $\eta_{GT} = 0.21$. This corresponds to a BSFC[1] of 398 g/kWh, and is applied to both the (hybrid-) electric concepts and the conventional fuel-based reference aircraft, which is re-evaluated for this comparison. This value is obtained by calculating the average efficiency of the short-range mission, including the ground and diversion phases of the mission.

The values of specific power and transmission efficiency assumed for the electrical machines (EM) and inverters/rectifiers are based on the state-of-the-art research goals presented in Ref. [119] and are gathered in Table 4.5. The EMs are assumed to achieve 13 kW/kg, and the specific power of the power converters is assumed to be 19 kW/kg. Note that these values do not correspond to technology existing today, but are projected values based on state-of-the-art research goals. Since a thermal management system and additional elements of the power management and distribution (PMAD) system can significantly increase this system's mass, the total mass of the electrical systems is increased by 30%. This generic mass penalty is assumed due to a lack of information in the preliminary sizing phase for an accurate estimation of the mass of components such as cooling systems or cables. Thus, the equivalent specific EM mass is assumed to be 5.92 kW/kg. To describe the losses of the electrical system, a constant equivalent motor efficiency of 95% is used, and all other component's efficiencies are set to 100%.

Table 4.5: Characteristics assumed for electrical drivetrain components in the verification study.

Parameter	Value
Turboshaft specific power SP_{GT} [kW/kg]	3.31
Turboshaft efficiency η_{GT} [-]	0.21
EM specific power (equivalent) SP_{EM1}, SP_{EM2} [kW/kg]	5.92
EM efficiency (equivalent) η_{EM1}, η_{EM2} [-]	0.95
Battery specific energy e_{bat} [Wh/kg]	1500[a]
Battery specific power SP_{bat} [kW/kg]	6.0 ($= 4C$)
Battery efficiency η_{bat} [-]	1.0
Minimum battery state-of-charge [-]	20%

[a] This value is selected to obtain converged designs for longer mission ranges, for verification purposes only. It is not supposed to represent a realistic value for any particular year of EIS.

[1] Note that BSFC = $1/(\eta_{GT} e_f)$.

The battery system is modeled using a rudimentary "energy in a box" approach. Thus, an idealized constant potential battery is assumed. The internal resistance and other losses are assumed to be zero, and consequently, the efficiency of the battery is 100% (see Table 4.5). To preserve battery life and to account for energy reserves, a 20% state-of-charge margin is used. For the sake of comparison, futuristic technology assumptions are used, to allow for convergence of aircraft with high levels of hybridization and fully electric aircraft. With a specific energy e_{bat} = 1500 Wh/kg and a 4C discharge rate, reasonable MTOM values could be achieved over the range of input parameters evaluated in Sec. 4.3.3. The selection of more realistic, near-term battery technology would have resulted in many unconverged design points in the parameter sweeps. However, it is important to stress that these technology values assumed for the batteries at pack level must be considered beyond optimistic. The maximum theoretical specific energy of typical Li-Ion batteries (lithium cobalt oxide cells) at cell level is 387 Wh/kg [116]. Lithium-sulfur or lithium-air batteries could reach specific energy levels over 2500 Wh/kg in theory but are far from being usable in practical, high-power applications [116].

4.3.2. SIZING FOR BASELINE MISSIONS

In this section, the HEP variants are sized for the three reference missions presented in Sec 4.2.1. Both methods differ in their approach to constructing the constraint diagram, which is the first step of the sizing process. To illustrate the difference, Fig. 4.6 presents a series of constraint diagrams obtained from Method A and Method B. For both methods, only the five driving constraints (as discussed in Sec. 4.2.2) are presented; other constraints from the certification specifications are neglected. As this example is only meant to further illustrate the different approaches of the methods, the constraint diagrams are only shown for the parallel architecture.

Method A attempts to simplify the power-sizing process as much as possible. The constraint diagram is constructed with all constraints at the same hybridization factor H_P, corrected to maximum throttle at sea level and maximum take-off mass, and subsequently, the design point is selected. In Fig. 4.6 , the design point is 18.63 W/N at a wing loading of 1.96 kN/m². To find the power required for a predetermined hybridization ratio, the total power-to-weight ratio, P_s/W_{TO}, is split by the hybridization ratio. For the example in Fig. 4.6, a P_s/W_{TO} of 16.76 W/N is obtained for the gas turbine, while the remaining difference between gas turbine power and total installed power is provided by the electric power system. In other words, since a hybridization of 10% is used, $P_{\text{gt}}/W_{\text{TO}}$ = 16.76, and $P_{\text{EM}}/W_{\text{TO}}$ = 1.87 (where the electric motor power is $P_{\text{EM}} = -P_{\text{gb}}$, following the convention of Fig. 3.4). Because the normalization to maximum gas-turbine throttle at sea level is applied to the total shaft power, the electric powertrain components are slightly oversized.

Method B, on the other hand, allows the designer to specify different power-control parameters (i.e., throttle and supplied power ratio) for each performance constraint. Hence, different components can be sized by different constraints, and none of the components is over-sized. For example, if the batteries and electromotor were only used during climb, then they would be actively sized in that condition, while the gas-turbine would have to provide only part-power, and would, therefore, be sized by a different

constraint such as take-off or cruise. However, compared to Method A, this requires the designer to specify additional control settings, leading to a more complex interpretation of the constraint diagrams, as evidenced in the bottom half of Fig. 4.6. This figure shows how first the shaft power-loading diagram is constructed (Fig. 4.6.B.1), based on

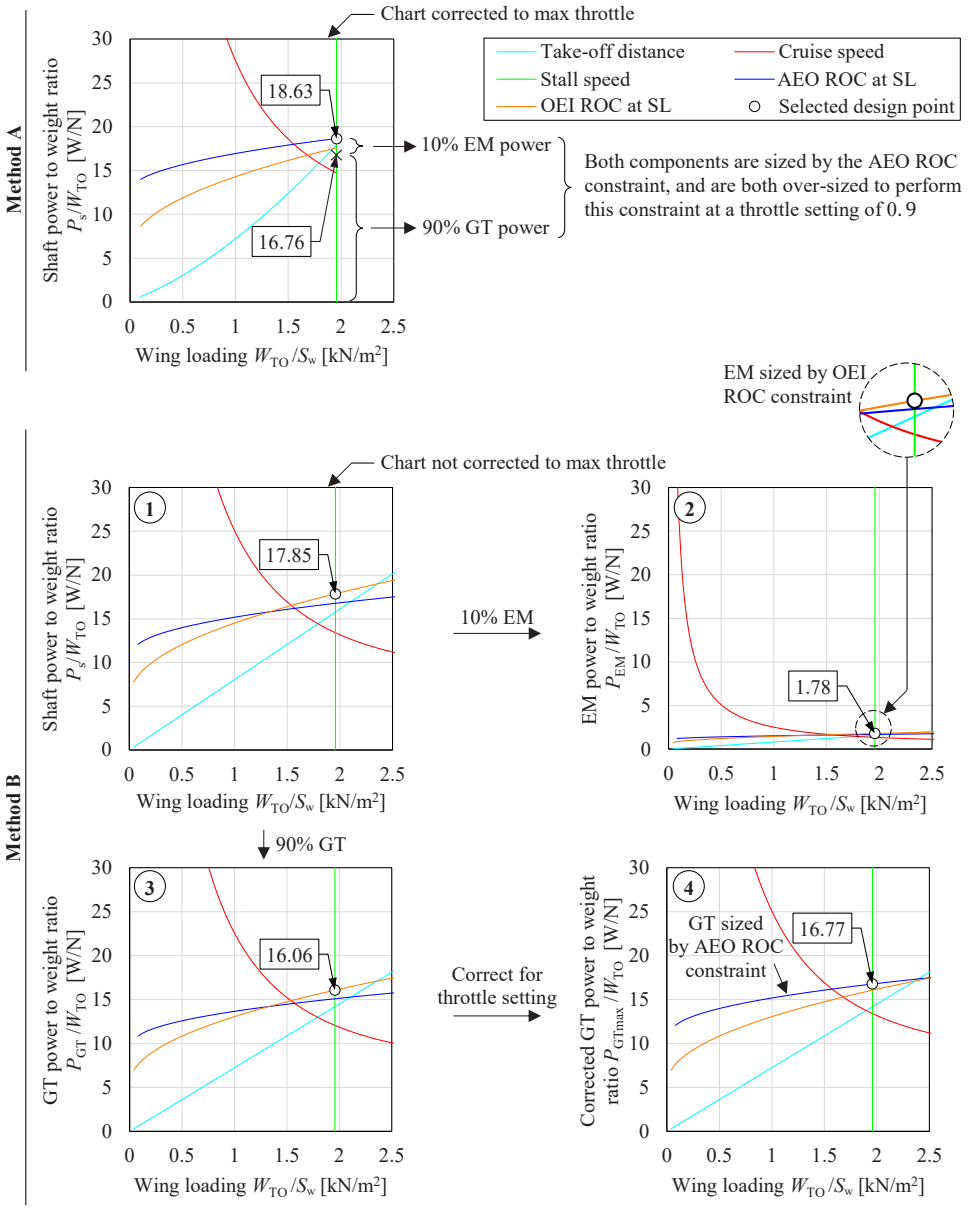

Figure 4.6: Overview of how the constraint diagrams of Method A (top) and Method B (bottom) are used in the design process. Diagrams obtained for the parallel powertrain configuration.

which the constraint diagrams of the remaining elements of the powertrain are computed for a given supplied power ratio. Since the power split is kept constant for all performance constraints in this study ($H_P = 0.1$), the relative positions of the constraints do not change much, although the power-to-weight ratio required from the electric motors is much lower than the gas turbine, as visible in Figs. 4.6.B.2 and 4.6.B.3. Given that different throttle settings are used for different constraints (see Appendix D.1), the gas turbine has a different active constraint than the electric motors. Note that only the gas turbine is corrected for throttle setting, as shown in Fig. 4.6.B.4. Nevertheless, even though the two methods use fundamentally different approaches for the matching diagrams, the resulting design points are comparable. The gas-turbine power-to-weight ratio is virtually the same for both cases (P_{GT}/W_{TO} = 16.76 and 16.77 for Methods A and B, respectively). The power-to-weight ratio obtained for the electrical motors is approximately 5% lower for Method B (P_{EM}/W_{TO} = 1.87 and 1.78 for Methods A and B, respectively) since it is not throttle-corrected.

Using the P/W_{TO} and W_{TO}/S_w data from the constraint diagrams, the mission performance analysis is carried out, and the aircraft's size is matched to the required mission performance. The resulting MTOM predicted by the two methods is presented in Table 4.6, including the difference of Method B with respect to Method A, which is calculated as ($MTOM_B$-$MTOM_A$)/$MTOM_A$. Additionally, the MTOM breakdown obtained for the short-range mission is shown in Fig. 4.7. In all cases, the differences between the two methods are considered acceptable for a Class-I sizing process. The most important conclusions that can be drawn are summarized in the following paragraphs.

A. CONVENTIONAL POWERTRAIN

The results for the conventional powertrain configuration (shown in Table 4.6) differ slightly from the results shown in Sec. 4.2.2, due to the simplified modeling approach taken for the HEP comparison. The discrepancy is larger for the short- and long-range

Table 4.6: Maximum-take off mass values calculated for the conventional, parallel, serial, and fully-electric powertrain configurations. "N/A" indicates that no converged design was obtained.

Powertrain	R [km]	m_{PL} [t]	Method A MTOM [t]	Method B MTOM [t]	Difference
Conventional	396	1.96	6.22	6.26	+0.7%
	1280	1.33	6.36	6.45	+1.3%
	2361	0.55	7.08	7.18	+1.4%
Parallel	396	1.96	6.36	6.39	+0.4%
	1280	1.33	7.06	7.10	+0.6%
	2361	0.55	13.47	13.36	-0.8%
Serial	396	1.96	8.30	8.25	-0.6%
	1280	1.33	12.52	12.35	-1.3%
	2361	0.55	N/A	N/A	N/A
Electric	396	1.96	8.17	8.29	+1.5%
	1280	1.33	N/A	N/A	N/A
	2361	0.55	N/A	N/A	N/A

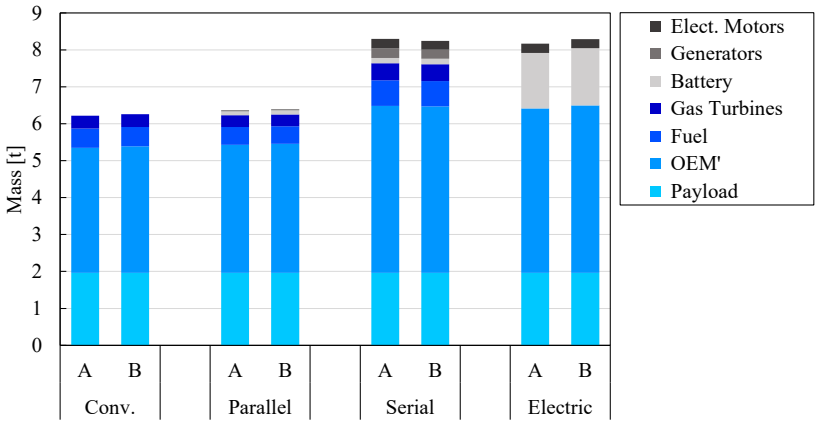

Figure 4.7: Mass breakdown of the four powertrain configurations obtained using Method A and Method B, for the short-range mission ($R = 396$ km, $m_{PL} = 1.96$ t).

missions than for the medium-range mission. For both methods, the MTOM obtained for the short-range mission is lower than in Sec. 4.2.2, because the average gas-turbine efficiency is accurate, but the fuel reserves are neglected. The MTOM obtained for the long-range mission, to the contrary, is over-predicted because, in this case, the exclusion of contingency fuel has a relatively lower impact, while the assumed gas-turbine efficiency is lower than in practice, due to the long cruise segment. Nevertheless, the agreement between both methods is good. The maximum difference in MTOM between method A and method B is less than 1.5%.

B. PARALLEL POWERTRAIN

The results for the parallel hybrid powertrain show excellent agreement, with a difference of less than 1% between both methods. The level of hybridization is fixed at 10%, which means that the propeller is always supplied by 1 part electric-motor power and 9 parts gas-turbine power, joined through a gearbox with 100% efficiency. A converged design is obtained for all three missions, even though the long-range aircraft is more than twice as heavy as the short-range aircraft. Considering the very advanced technology assumptions that are made, this result indicates that efficient long-range flying with hybrid-electric propulsion systems is not a straightforward task. However, the detailed results for the short-range mission (Fig. 4.7) show that the fuel mass is reduced, when comparing against the conventional propulsion layout, even though MTOM increases.

C. SERIAL POWERTRAIN

For this study, none of the prospective advantages of serial-hybrid designs (aero-propulsive interaction, distributed propulsion, etc.) are taken into account. The serial powertrain is therefore expected to perform worse than the conventional or parallel-hybrid configurations. This is supported by the results presented in Table 4.6. Only the short- and medium-range mission have converged. For the long-range mission, the powertrain is too heavy and inefficient to converge—even with the highly optimistic

technology assumptions. The results are very close (0.6% difference) for the short-range mission, and still provide an acceptable agreement (1.6% difference) for the medium-range mission. It is worth noting that, as for the parallel-hybrid powertrain, the level of hybridization is fixed at 10%. This means that the electric motor is always supplied by 1 part battery power and 9 parts generator power.

D. FULLY-ELECTRIC POWERTRAIN

The final analysis is conducted for the fully electric powertrain configuration. Even with the highly optimistic technology assumptions, only the short-range mission converges for this powertrain architecture, as shown in Table 4.6. The medium and long-range missions require an MTOM above 50 tons, which is infeasible for a CS-23 aircraft. Yet, both methods converged within 1.5% for the short-range mission. For this specific set of requirements and technology assumptions, the serial-hybrid short-range aircraft and the electric short-range aircraft converge to almost the same MTOM. In Fig. 4.7 it can be observed that the additional mass required by the batteries for the fully-electric configuration completely compensates the weight reduction due to the absence of gas turbines, fuel, and generators. However, while Method A predicts a higher MTOM than Method B for the serial-hybrid short-range case, it predicts a lower MTOM for the electric short-range case. Therefore, no clear conclusion can be drawn regarding which of the two methods is more or less conservative.

4.3.3. PARAMETER SWEEPS

As a final step of this verification study, the design methods are evaluated regarding their ability to properly account for changes in key input parameters. The reader is reminded that the aim is to compare the data and gradients obtained with the two methods, and not to study the impact of these parameters on the performance of an actual hybrid-electric aircraft. In this process, the impact of three parameters is analyzed while keeping all other parameters constant: range, battery specific energy, and the hybridization ratio. The baseline point for the parameter sweeps is the short-range mission. Thus, payload is fixed at 1.96 t, and the design range is fixed at 396 km. The baseline technology assumptions are the same as in Sec. 4.3. The results of the parameter sweeps are shown in Fig. 4.8 for two measures of merit: maximum take-off mass (MTOM) and payload-range energy efficiency (PREE) (as discussed in Sec. 2.1.2).

A. RANGE

The design range is varied from 100 km to 2500 km in steps of 100 km. Thus, short-range missions of just 15 min flight time are covered at the low end, while the longest flight would last 6 hours. The variables in Figs. 4.8a and 4.8b show a good agreement between the two methods. The MTOM plots show an exponential relationship for increasing ranges. When analyzing the MTOM results, the conventional aircraft shows to be less sensitive to an increase in range, when compared to the other designs. The serial and parallel designs show a similar slope but present an offset. This can be attributed to the mass increase, which is inherent to the hybrid propulsion systems. The fully electric design shows the highest slope. This behavior is expected, due to the much lower specific energy of batteries, compared to fossil fuels. PREE shows an almost linear relationship

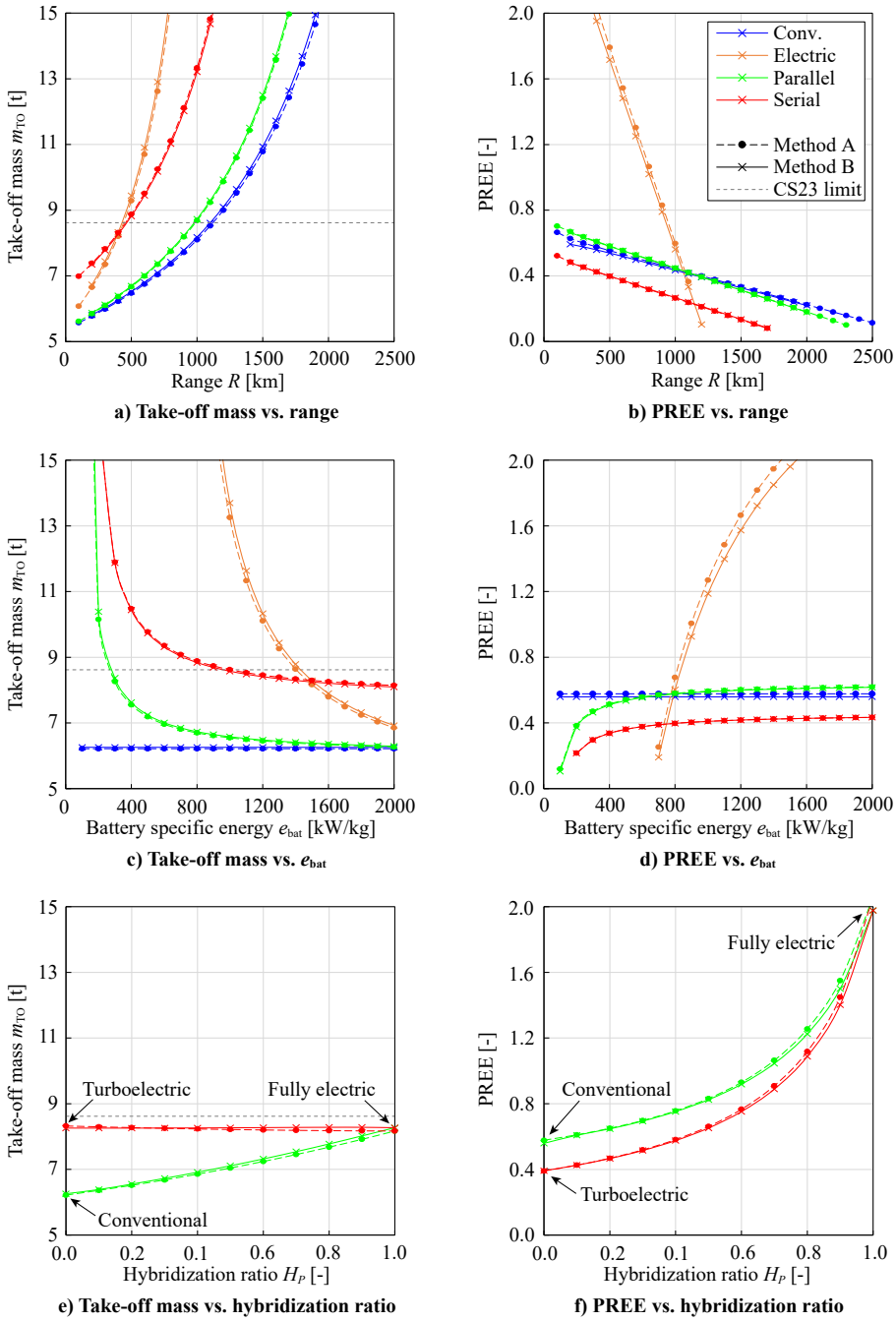

Figure 4.8: Maximum take-off mass and PREE obtained for different mission ranges, battery specific energies, and hybridization ratios ($R = 396$ km, $e_{bat} = 1500$ Wh/kg, $H_P = 0.1$, unless indicated otherwise).

with range. Again, the highest sensitivity is observed for the fully electric aircraft, and the lowest sensitivity is observed for the conventional design. When results for Methods A and B are compared, they show only subtle differences for PREE. Method A slightly overpredicts PREE, when compared to Method B. This is expected because the definition of E_{miss} is slightly different between the methods, as described previously. The difference is more pronounced at the lower ranges because the relative time spent for landing and taxi-in is larger.

If the CS-23 commuter mass limit of 8618 kg (19000 lb) would be enforced, then the maximum range of the fully electric and serial hybrid designs would be limited to less than 450 km—even with the highly optimistic battery-technology assumptions—while the conventional aircraft could achieve ranges of 1100 km. However, even though the conventional aircraft is the lightest, its PREE is inferior to the electric and parallel hybrid design at ranges up to 1100 km. This matches the trends observed in literature, which show that electric and hybrid-electric aircraft can be more efficient for short-distance flights, while longer ranges are most likely to be carried out by conventional aircraft [213]. However, these are un-optimized designs with extremely optimistic technology assumptions, and thus no quantitative conclusions should be drawn from this data.

B. BATTERY TECHNOLOGY LEVEL

The specific energy e_{bat} of the batteries is varied from 100 Wh/kg to 2000 Wh/kg. The reader is reminded that the extremely high specific-energy levels of this study are far beyond the capabilities of practical batteries and are only used parametrically to show the corresponding sensitivities. At the same time, the specific power SP_{bat} is varied to maintain a constant discharge rate of 4C. Thus, SP_{bat} = 0.4 kW/kg at 100 Wh/kg, while SP_{bat} = 8 kW/kg at 2000 Wh/kg. e_{bat} is varied in steps of 100 Wh/kg, and the results of the sweep are presented in Figs. 4.8c and 4.8d. For the 4C discharge rate limit assumed, the battery mass was found to be sized by energy requirements in all cases, and not by power requirements. Thus, all missions are completed with a 20% state-of-charge remaining.

Again, the MTOM and PREE plots show a good agreement for all propulsion-system architectures. The trends expected based on previous studies are captured, with battery technology having no influence on conventional designs. For the other configurations, improving battery performance yields lighter aircraft, which are also more efficient. The absolute differences in MTOM between methods A and B are more pronounced at lower technology levels because the aircraft become heavier. Method A again slightly overpredicts PREE, when compared to Method B. For this analysis, the relative error of the PREE calculation remains nearly constant across the sweep, because the mission range is not varied. The difference in PREE is more evident for the fully electric configuration (approximately 5% for the baseline e_{bat} = 1500 Wh/kg) and is also reflected in the MTOM comparison. This discrepancy is more prominent for the fully-electric configuration due to the higher battery weight fraction and subsequent higher sensitivity to battery specific energy.

Figure 4.8c shows that the CS-23 mass limit requires an e_{bat} of at least 1450 Wh/kg to allow for a fully-electric design. This indicates that electric propulsion systems will not be a drop-in replacement for conventional propulsion systems in the near future, for the missions considered. However, a design with such kind of batteries would reach

three times the PREE of the conventional aircraft. Benefits in terms of PREE can already be observed for batteries that exceed 800 Wh/kg. However, these aircraft would be four times heavier than comparable conventional aircraft, due to the snowball effect of the sizing process. Finally, Fig. 4.8d also shows that parallel architectures can present minor improvements in PREE if the battery specific energy is increased beyond 700 Wh/kg. Serial powertrains, on the other hand, are always outperformed by conventional fuel-based powertrains, since no potential improvements in aero-propulsive efficiency or gas-turbine efficiency are included in this comparison.

C. HYBRIDIZATION RATIO

The hybridization ratio of the propulsion system is varied from 0% to 100% in steps of 10%. Note that the hybridization ratio is defined differently for serial and parallel powertrains, as discussed in Sec. 4.1. In both cases, a hybridization ratio of 100% corresponds to a fully electric aircraft, which exclusively uses batteries. However, for a serial architecture, a hybridization of 0% corresponds to a turbo-electric aircraft, while for a parallel architecture, the powertrain is reduced to a conventional fuel-based engine. Consequently, Figs. 4.8e and 4.8f shows the results of the parameter sweeps for the serial and parallel powertrains, while the conventional and fully-electric configurations are obtained as limit cases of these two sweeps.

Once more, the results show a good agreement between the methods for both propulsion-system architectures. The parallel hybrid with a hybridization ratio of 0% corresponds to a conventional aircraft and is, therefore, the lightest solution for the given mission. As the hybridization ratio is increased, the weight fraction of the electric power systems of the aircraft increases. However, as MTOM increases, so does PREE. At 100% hybridization, the fully electric configuration is reached. The serial hybrid with a hybridization of 0% corresponds to a turbo-electric propulsion configuration that uses no buffer battery. As H_P increases, the gas turbine size is reduced, and batteries are added until the fully electric configuration is reached at $H_P = 1.0$. The data points at $H_P = 0.0$, 0.1, and 1.0 can also be found in the previous diagrams. Figure 4.8e shows that, for the serial powertrain, the MTOM is practically insensitive to the hybridization ratio, while PREE improves with increasing hybridization. This almost constant relationship between H_P and MTOM is specific for this set of input parameters, and not a trend inherent to the type of propulsion system in general. This was confirmed by performing the sweep for a different value of e_{bat}. Therefore, the practically zero gradient is a coincidence: for the selected input parameters, the increase in battery mass as H_P increases compensates the decrease in engine, generator, and fuel mass.

4.4. CONCLUDING REMARKS

The previous sections have verified the implementation of the sizing method described in Ch. 3 by comparing results to an independently-developed sizing method. A 19-seater, fuel-based reference aircraft is first sized for three points of the payload-range diagram. The results obtained from the two methods deviate from the reference data by approximately 1% in terms of power-to-weight ratio, and by less than 4% in terms of MTOM. The discrepancy in MTOM is predominantly attributed to uncertainties in component modeling and variations in the mission profile. The two methods are then

used to evaluate parallel, serial, and fully-electric configurations. When comparing the different powertrain architectures for the three payload-range combinations selected, a difference in MTOM of less than 2% is observed between the two methods. Additionally, three parameter sweeps are performed, in order to analyze the sensitivity of MTOM and PREE to mission range, battery specific energy, and the hybridization ratio of the aircraft. The results of these sweeps show an excellent agreement in both slope and offset between the two methods. The largest deviations are observed for the fully-electric configuration, due to the sensitivity of the battery-weight fraction to energy consumption. This leads to a PREE difference between the two methods of approximately 5% for the baseline mission requirements and technology assumptions.

These differences lie well within the uncertainty of the Class-I sizing process and confirm the correct implementation of the two methods. Although this does not necessarily guarantee that the formulation of the methods is flawless—since both methods might coincidentally be based on the same, inaccurate assumption—the agreement of results significantly increases the confidence in these two formulations. This is further evidenced by the trends observed in the parameters sweeps, which coincide with those expected from literature. Based on this it is concluded that, if the sub-modules have been individually validated, then the method described in Ch. 3 can indeed be used for the preliminary sizing of hybrid-electric aircraft. However, when applying the method, it should be noted that these indicative uncertainty margins, which are of the order of a few percent, do not account for uncertainty in the input variables. For example, the assumed battery specific energy, gas-turbine efficiency, or zero-lift drag coefficient may differ by more than just a few percent from the actual value attained in practice. Consequently, also the predicted aircraft characteristics may differ from the final product by more than the 2%~5% uncertainty observed in this study. To minimize such biases, it is important to draw conclusions based exclusively on the differences between the hybrid-electric aircraft and a reference aircraft sized with the same input parameters, and not based on a comparison to existing aircraft data.

5

CASE STUDY: EFFECT OF DISTRIBUTED PROPULSION ON AIRCRAFT SIZING

The derivations presented so far are applicable to HEP aircraft with generic propulsion-system layouts. This section demonstrates how the method can be applied to tube-and-wing aircraft featuring leading-edge distributed-propulsion systems. The purpose of this demonstration is to understand how the incorporation of aero-propulsive interaction effects impacts the wing size, installed power, weight, and energy consumption of the aircraft. A leading-edge distributed propulsion (LEDP) configuration is analyzed because, a priori, no aero-propulsive model is available for over-the-wing configurations, and LEDP configurations are comparable in the sense that they present a series of propellers installed along the wing which significantly affect its aerodynamic properties. Since the aerodynamic characteristics of LEDP are not the focus of this Dissertation, the reader is referred to Refs. [49, 61, 226] for additional information on this topic. For this design study, the simplified LEDP aerodynamic interaction model described in Appendix C.2 is used. First, a set of hypothetical top-level requirements is defined in Sec. 5.1, together with the assumed aircraft characteristics and design parameters. Then, a power control strategy is chosen and discussed in Sec. 5.2. Finally, in Sec. 5.3 a conventional configuration is compared to reference aircraft data and two hybrid-electric concepts, showing the potential benefits and penalties of these HEDP aircraft.

5.1. TOP-LEVEL REQUIREMENTS AND ASSUMPTIONS

A regional transport aircraft comparable to the ATR 72-600 is considered, with a harmonic range of R = 1528 km (825 nautical miles) and a payload of 7500 kg. The aircraft has a cruise speed of M_{cr} = 0.41 at a cruise altitude of 5486 m (18,000 ft), and the approach speed must be no greater than 59 m/s (115 kts). In the case of a balked landing,

Parts of this Chapter have been published in Ref. [203].

the aircraft must be able to attain a climb gradient of 2.1% at 1.4 times the reference stall speed with one engine inoperative [227]. Furthermore, a diversion range of 370 km (200 nm) is required, for which a diversion altitude and Mach number of 3048 m (10,000 ft) and 0.3 are assumed, respectively. Finally, the aircraft must be able to take off with a field length of less than 1333 m. In this demonstration case, the take-off-parameter (TOP) described by Raymer [92] is used for the take-off distance constraint. The aircraft requirements are collected in Table 5.1. The design parameters selected to meet these requirements are given in Table 5.2. Several of the values shown in these tables are based on ATR 72-600 reference data [228]. Three powertrain architectures are examined as candidates: a conventional turboprop, a serial powertrain with DP, and a partial-turboelectric (PTE) powertrain with DP.

Table 5.1: Top-level aircraft requirements.

Requirement	**Value**
Payload, m_{PL} [t]	7.5
Cruise altitude, h_{cr} [m]	5486
Cruise Mach number, M_{cr} [-]	0.41
Range, R [km]	1528
Approach speed [m/s]	59
OEI BL climb gradient [%]	2.1
OEI BL stall speed margin [-]	1.4
Diversion altitude, h_{div} [m]	3048
Diversion Mach number, M_{div} [-]	0.3
Diversion range, R_{div} [km]	370
Take-off field length [m]	1333

Table 5.2: Selected design parameter values.

Parameter	**Value**
Aspect ratio, A [-]	12
Half-chord sweep, $\Lambda_{c/2}$ [rad]	0
Taper ratio [-]	0.62
Root thickness-to-chord ratio, t/c [-]	0.18
N$^{\text{o}}$ of primary propulsors, N_1 [-]	2
N$^{\text{o}}$ of secondary propulsors, N_2 [-]	12
DP span fraction, b_{dp}/b [-]	0.6
Spacing between DP propulsors, d/D_{P} [-]	0.01
Axial position of DP propulsors, x_{P}/c [-]	0.2

Regarding the assumed aircraft properties, the parameters which depend on the aircraft configuration (clean, take-off, or landing) are shown in Table 5.3. These parameters are presented per performance constraint. For all three design concepts, no thrust vectoring is considered, i.e. $\delta_{\text{P}} = 0^{\text{o}}$. Furthermore, lower propulsive-efficiency values are assumed for the secondary propulsors of the serial architecture than for the PTE archi-

tecture. While the latter presents two propulsion systems, in the serial configuration all thrust has to be produced by the DP system. Consequently, it requires higher disk-loading values, and hence the associated propulsive efficiency is lower.

Additionally, several assumptions related to the hybrid-electric powertrain are gathered in Table 5.4. The weights of the gearbox, PMAD and propulsors are neglected. The efficiency and specific power of the electrical machines are based on the technology goals presented by Jansen et al. [119], and include both the electrical machine itself and the associated inverter or rectifier. The values assumed are comparable to those assumed in Ch. 4. For the batteries, a specific energy of 500 Wh/kg at pack level is selected, which is considered an optimistic value for the 2035 timeframe, close to the theoretical limits of lithium-ion batteries at cell level [45, 93, 116, 117]. Moreover, a specific power of 1 kW/kg is assumed at pack level. Given the importance of cycle life, failure rate, and failure containment for aerospace applications, a pack-level value of $e_{\text{bat}} = 500$ Wh/kg will almost surely require cell chemistries other than lithium-ion, and therefore the feasibility of such specific-energy values for an EIS of 2035 is debatable. However, projec-

Table 5.3: Assumed aerodynamic and mission properties per constraint. All parameters are non-dimensional.

	Cruise speed	**Approach speed**	**Take-off distance**	**OEI climb gradient**
Flap configuration	clean	landing	take-off	landing
Landing gear position	retracted	extended	extended	retracted
Zero-lift drag coefficient, C_{D_0}	0.022	0.087	0.037	0.067
Oswald factor, e	0.8	0.95	0.9	0.95
Maximum lift coeff., $C_{L_{\text{max,airframe}}}$	-	2.7	2.1	2.7
Prop. efficiency (primary), η_{p1}	0.85	0.8	0.75	0.8
Prop. eff. (secondary, serial), η_{p2}	0.8	0.6	0.7	0.7
Prop. eff. (secondary, PTE), η_{p2}	0.85	0.65	0.75	0.8
Aircraft weight fraction, f_W	0.98	0.95	1	0.95
Gas turbine throttle, ξ_{GT}	0.8	0.5	1	1
Supplied power ratio (serial), Φ	0.05	0	0.1	0.1
Shaft power ratio (PTE), φ	0.1	0.8	0.4	0.4

Table 5.4: Assumed HEP component technology levels for the 2035 timeframe.

Parameter	**Value**
Battery pack specific energy, e_{bat} [Wh/kg]	500
Battery pack specific power, SP_{bat} [kW/kg]	1
Minimum SOC [%]	20
EM specific power, SP_{EM1}, SP_{EM2} [kW/kg]	7.7
EM efficiency, η_{EM1}, η_{EM2} [-]	0.96
PMAD efficiency, η_{PMAD} [-]	0.99
Gearbox efficiency, η_{GB} [-]	0.96
Gas turbine efficiency, η_{GT} [-]	0.3

tions for the coming decades estimate values of this order for automotive applications [116, 117], and thus this value is assumed here for illustrative purposes, to demonstrate the effect that the batteries would have on aircraft weight and energy consumption in these conditions.

5.2. POWER-CONTROL STRATEGIES

The designer must specify the values of the power-control parameters defined in Sec. 3.2.2 for each performance constraint and mission segment included in the sizing process. For conventional aircraft, this is limited to the gas-turbine throttle. However, for hybrid-electric aircraft, up to two additional design parameters (Φ and φ; see Eqs. 3.14 and 3.15) have to be specified per constraint and mission segment. For this demonstration case, a simplified mission profile is assumed which includes the climb, cruise, and descent phases for both the nominal mission and a diversion. The take-off and landing segments are neglected in the mission analysis, although their power requirements are included in the power-loading diagrams. During climb and descent, all power-control parameters are specified as input, while during cruise, the flight condition is completely specified in terms of speed and altitude, and thus one control parameter is a dependent variable. Note that consistent power-control values must be used if the power requirements of a determined mission segment appear as a performance constraint in the power-loading diagrams, such as a cruise-speed constraint.

In this study, the power-control strategy is selected based on a series of qualitative arguments, although a systematic optimization study could have a large impact on the resulting design [109]. The values of ξ_{GT}, Φ, and φ used for each performance constraint can be found in Table 5.2. The power-control profiles chosen for the mission analysis are shown for the three designs with thin lines in Fig. 5.1. In this example, ξ_{GT}, Φ, and and φ are assumed to vary linearly with altitude during climb and descent, and to vary linearly with range during cruise. The thick lines are a result of applying the point model for a fixed flight condition during the mission analysis and are therefore not known a priori, although they have been included here for completeness. Note that the throttle values obtained during cruise do not necessarily coincide with the values specified in Table 5.2, since the cruise-speed constraint may not be actively limiting the installed power of the powertrain components (see Sec. 5.3). Only the climb, cruise and descent phases of the nominal mission are included in Fig. 5.1. Similar control strategies are applied for the diversion phase, though with reduced throttle to compensate the decrease in aircraft weight.

For the conventional architecture (Fig. 5.1a), the throttle values are specified as input during climb and descent, with the cruise throttle decreasing over time to compensate the reduction in aircraft weight. For the serial architecture (Fig. 5.1b), throttle is specified during cruise, while the supplied power ratio is adapted to compensate the changes in thrust requirements. Consequently, the gas turbine operates near its sizing condition for a large part of the mission. This can improve its efficiency [210, 229], although sensitivity to this benefit has not been included here. During descent, a negative supplied power ratio is specified, such that the power produced by the gas turbine in idle conditions is used to recharge the batteries. This extra battery energy can be used for the diversion phase, or to reduce charging time on the ground.

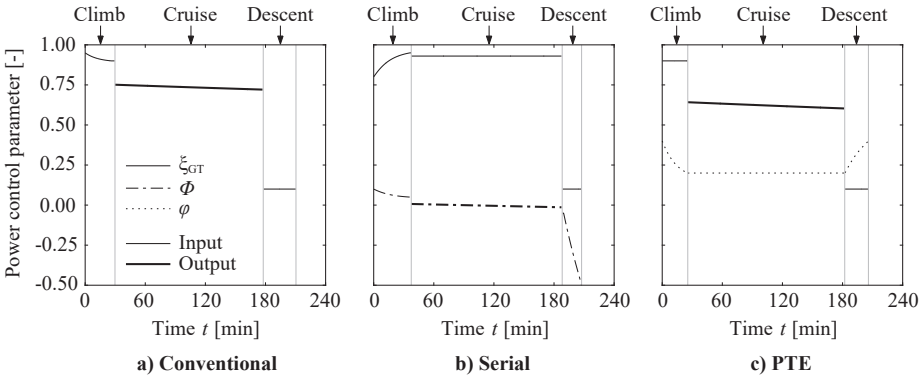

Figure 5.1: Power-control profiles throughout the nominal mission of the three powertrain architectures.

Finally, for the PTE architecture (Fig. 5.1c), a φ profile is specified throughout the mission in order to maximize aero-propulsive performance, while the throttle is varied accordingly. The control strategy was selected as follows. During take-off, the power is shared equally between the primary and secondary propulsors (see Table 5.3). This spreads the loads over a larger area for a given primary-propulsor size, or reduces its size for a given disk loading. The first option would increase propulsive efficiency with respect to a conventional configuration, while the second would entail secondary benefits such as reduced landing gear length, both of which are only quantified in later stages of the design process. During cruise, low φ values are used since the distributed propellers decrease the lift-to-drag ratio of the wing in this flight condition. This does not, however, imply that the aircraft would present a lower L/D than the conventional configuration if φ were increased: the use of DP in low-speed conditions can increase the maximum wing loading (see Sec. 5.3.2), which in turn increases the lift-to-drag ratio. Finally, during approach, the gas turbine throttle is reduced but most power is diverted to the DP system, thus enhancing lift and increasing the maximum wing-loading. These relations between the power-control strategy and the aero-propulsive effects highlight the importance of understanding and incorporating both aspects early in the design process.

5.3. RESULTS

5.3.1. COMPARISON TO REFERENCE DATA

In this section the results of the conventional configuration are compared to reference data of the ATR 72-600 at maximum payload [228], in order to verify that the assumed aerodynamic properties and mission requirements are representative of a regional turboprop application. For this, Table 5.5 presents the traditional Class-I results of the conventional configuration and reference aircraft. The TOM is underestimated by 3.8%, mainly due to an underestimation of the operative empty mass (OEM), which is calculated using the Class-I empirical correlation of Raymer [92]. The fuel mass, on the other hand, is slightly over-estimated, indicating that the assumed aerodynamic properties and component efficiencies may differ from the reference aircraft. Nonetheless, the deviations are within the accuracy expected from a preliminary sizing method, and therefore the method is deemed applicable for comparing different propulsion-system architectures under equal assumptions.

Table 5.5: Comparison between a reference ATR 72-600 and the sized conventional configuration.

	Reference[a]	Conv.	Difference
m_{TO} [t]	22.8	21.9	−3.8%
m_{OE} [t]	13.3	12.3	−7.4%
m_f [t]	2.0	2.1	+6.6%
W_{TO}/S_w [kN/m^2]	3.67	3.60	−1.8%
$W_{TO}/P_{GT,max,SLS}$ [N/W]	0.058	0.055	−5.2%

[a]Since the reference data provides P_{s1} instead of P_{gt}, the reference power-loading has been multiplied by η_{GB} in order to compare $W_{TO}/P_{GT,max,SLS}$ in equal conditions.

5.3.2. DESIGN WING LOADING AND POWER LOADING

The power-loading diagrams obtained for the three different powertrain architectures are shown in Fig. 5.2. Only the most instructive component diagrams are included for brevity, although in practice one diagram exists per component included in the powertrain model. In these diagrams, the feasible design space, shaded in gray, represents the combinations of wing loading and power loading which generate an aircraft capable of satisfying all performance requirements. The designer must analyze these diagrams and select the aircraft's wing-loading. Then, for each component, a power-loading value must be selected. Generally, the maximum power-loading allowed at the chosen wing-loading is selected for each component, since this leads to a minimum component weight. The diagrams also show which performance requirement is actively constraining the maximum allowable power-loading of each component. This maximum power loading can be varied by, for example, changing the power-control variables of the limiting constraint.

Figure 5.2 clearly shows an increase in maximum wing loading due to DP. For the conventional architecture, no aero-propulsive effects have been included. In this way, the diagram of Fig. 5.2a can be compared with the reference aircraft, and the effect of including the aero-propulsive interaction in the sizing process can be distinguished. However, in practice, this configuration also presents appreciable interaction effects between the propeller and the wing. Thus, the actual increase in wing loading due to DP is slightly lower than suggested by Fig. 5.2. The increase in wing loading is higher for the serial architecture than for the PTE architecture, since for the latter the shaft power ratio is $\varphi = 0.8$ in landing conditions (see Table 5.3), and thus not all the power is used to enhance lift. For the PTE architecture, a shaft power ratio lower than unity was selected in landing conditions because, for the aerodynamic characteristics assumed, using all thrust to enhance lift in landing conditions leads to an excessively high wing-loading, with a negative impact on cruise performance. In practice this would imply that a smaller, less complex high-lift system could be used during landing, compensating the decrease in $C_{L_{max,airframe}}$ by increasing the shaft power ratio.

Several possible design points are included in Fig. 5.2. These show how the optimum design point in terms of one component generally does not coincide with the optimum size of other components. In this study, the design point for maximum wing loading is selected, which for conventional aircraft often corresponds to the smallest wing size. However, due to the large impact of the powertrain on TOM, for HEP aircraft it may be

more beneficial to select a different design point, as demonstrated in the work of Finger et al. [230]. At the design point corresponding to maximum wing loading, all components in Fig. 5.2 are sized by the take-off constraint, except for the gas turbine of the serial architecture, which is sized by the cruise constraint. This is a result of the battery-assisted take-off. In all three cases, the OEI balked landing constraint is inactive but close to the design point of the gas turbine. The secondary electrical machines, on the other hand, can easily satisfy the OEI constraint. This highlights the benefit of having

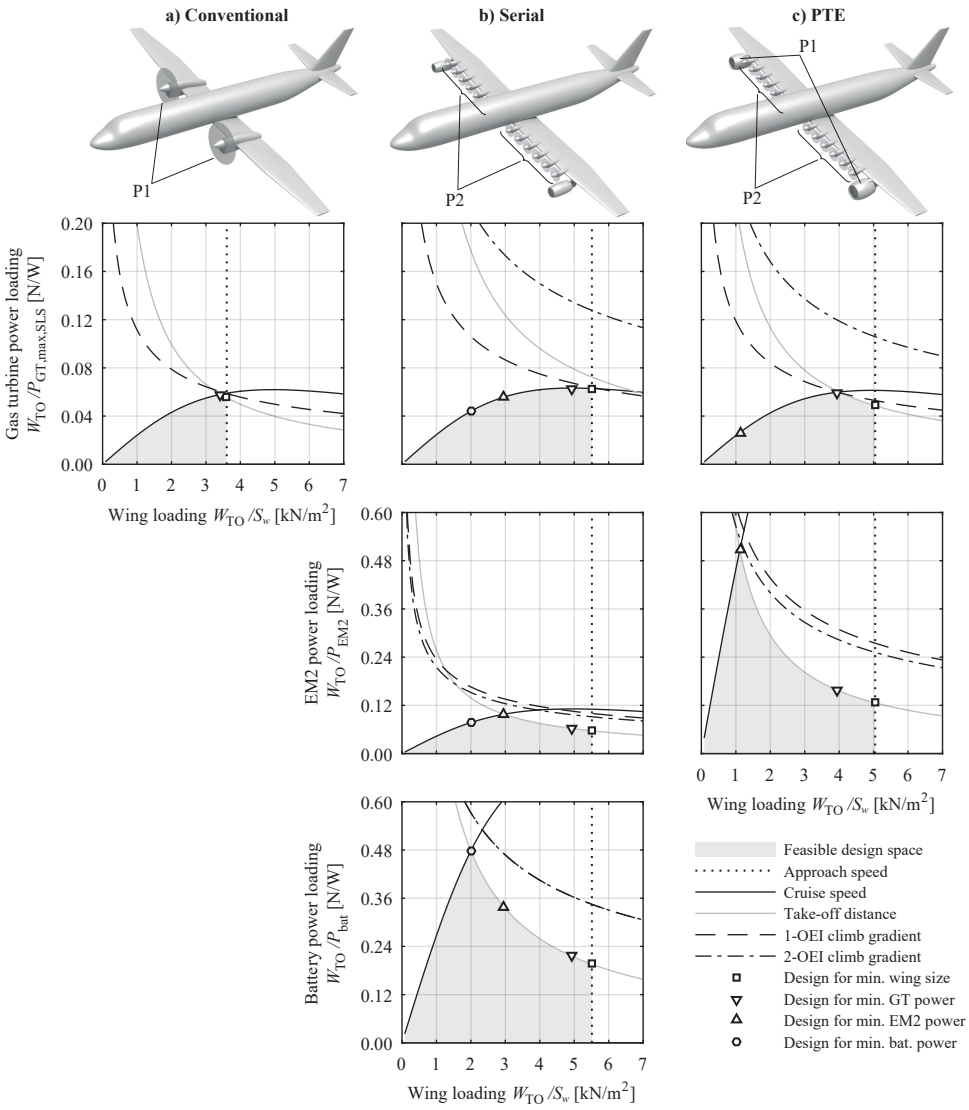

Figure 5.2: Component power-loading diagrams for the (a) conventional, (b) serial, and (c) PTE powertrain architectures, including a notional representation of the propulsion system layout at the top.

redundant propulsors in DP systems: while a failure in the primary powertrain branch requires the components of that branch to be over-sized by a factor 2, a failure in the secondary powertrain branch only requires the corresponding components to be over-sized by a factor 12/11. Moreover, when comparing the serial and PTE architectures, one can observe that a higher electrical-machine power-loading is achieved for the latter, since during take-off part of the propulsive power is generated by the primary propulsors. In any case, the highest power-loading values are obtained in the battery power-loading diagram of Fig. 5.2b. Given the sensitivity of TOM to battery energy and power requirements [45, 79, 113, 172], higher battery power-loading values are required to avoid an excessively high TOM.

5.3.3. WEIGHT BREAKDOWN AND ENERGY CONSUMPTION

Table 5.6 collects the main results of the three designs. Despite the higher wing-loading values obtained for the two HEP concepts, the serial configuration is 26% heavier than the conventional configuration, while the PTE configuration is 2% heavier. Nonetheless, the increased wing loading leads to a reduced wing area for both the serial (−18%) and PTE (−27%) configurations. The corresponding L/D increase is not large enough to offset the increase in aircraft weight, leading to increased energy consumption with respect to the conventional concept. This directly translates into a reduction in PREE, which is 28% and 3% lower for the serial and PTE configurations, respectively. The cruise lift-to-drag ratio of the PTE architecture is slightly higher than for the serial configuration, even though the latter presents a higher wing-loading. This is because, for the serial architecture, the lift coefficient during cruise is too high, exceeding the value corresponding to optimum L/D.

Table 5.6: Summary of results obtained for the three architectures evaluated. Lift-to-drag ratio is presented as the average of the cruise phase.

	Conv.	Serial	PTE
m_{TO} [t]	21.9	27.7	22.4
W_{TO}/S [kN/m^2]	3.60	5.51	5.04
$W_{TO}/P_{GT,max,SLS}$ [N/W]	0.055	0.063	0.049
S_w [m^2]	60	49	44
$E_{f,miss}$ [GJ]	73.8	103.0	75.8
$E_{bat,miss}$ [GJ]	0	1.7	0
$(L/D)_{cr}$ [-]	17.5	18.4	18.5
PREE [-]	1.52	1.09	1.48

The differences in TOM of the three concepts are further clarified in the breakdowns presented in Fig. 5.3. The wing mass fraction is lower for the two HEP concepts, due to the increased wing loading. Figure 5.3 also shows that not only the fuel mass, but also the fuel fraction is slightly higher for the serial architecture than for the conventional concept. This indicates that, for the given mission, the increase in L/D does not offset the lower propulsive efficiency assumed for the DP system (see Table 5.3) and the power lost in the conversion from mechanical energy to electrical energy and vice versa. Figure

5.3 also shows that the total powertrain weight fractions of the serial (13%) and PTE (8%) architectures exceed the weight fraction of the conventional one (5%). Although in the serial architecture the gas-turbine weight fraction is reduced, this does not compensate the increase in weight due to the electrical components. The reduction in gas-turbine weight fraction is a consequence of the increased gas-turbine power-loading at the design point. This increase in power-loading is attributed to increased wing-loading due to aero-propulsive effects on one hand (see Fig. 5.2), and to the addition of battery power during take-off on the other. However, since all power has to be transmitted through the electrical components, the weight of the electrical machines is substantially higher than for the PTE architecture. Finally, even though Table 5.6 shows that the battery accounts for just 1.6% of the total energy consumed by the serial architecture during the nominal mission, it represents 5% of the total aircraft weight, thus having a substantial impact on TOM.

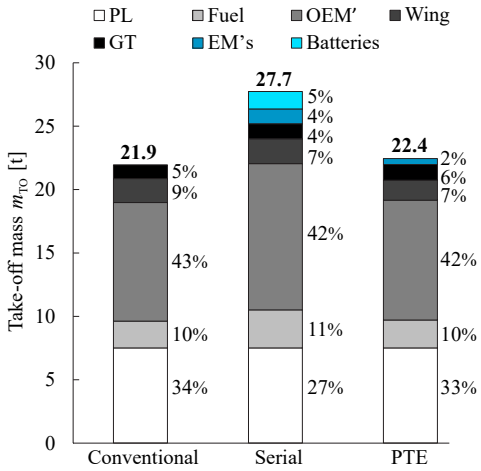

Figure 5.3: Mass breakdown of the three configurations evaluated. Values are expressed in metric tons and as a percentage of take-off mass.

5.4. ANALYSIS OF FINDINGS & DISCUSSION

The results indicate that the two HEP concepts present no benefit with respect to a conventional powertrain. This is in line with the findings of previous studies, which show that either more optimistic e_{bat} values [45, 78, 79, 119] or reduced ranges [66, 115, 204, 205, 213] are required for the HEP concepts to be competitive. However, the results obtained in this study are conservative for several reasons. Firstly, the wing area of the HEP concepts was reduced at constant aspect ratio, instead of at constant span. If the latter approach had been taken, the lift-to-drag benefit due to DP would further increase. Secondly, the wing-loading increase enabled by DP would improve the short take-off and landing (STOL) capabilities of the aircraft, without significantly penalizing cruise performance. Thirdly, the potential increase in propulsive efficiency due to reduced disk

loading has not been included in this demonstration case. Moreover, these results have been obtained for range, altitude, and Mach numbers for which the reference aircraft is optimized, without carrying out any systematic sensitivity or optimization studies for the hybrid-electric concepts. For example, for the assumed mission, the PTE concept consumes approximately 3% more energy than the conventional one, but presents a 6% higher lift-to-drag ratio. This indicates that this hybrid-electric concept is likely to be advantageous for longer ranges, such that the benefit in aero-propulsive efficiency can lead to a fuel weight reduction which offsets the powertrain weight penalty. For the serial configuration, on the other hand, no significant benefits are expected. Apart from the detrimental effect of batteries on aircraft weight, there are two additional reasons for this. Firstly, since all power has to be diverted to the secondary propulsors during take-off, the weight of the electrical machines is much higher than for the PTE configuration. Secondly, since the disk loading is higher for the serial configuration, lower propulsive efficiencies are achievable. Thus, powertrain layouts with two propulsion systems should not be discarded a priori due to their complexity or weight penalty, since they can be used in a much more beneficial manner throughout the mission. These claims are analyzed in more detail in Ch. 9.

The sizing method is found to be flexible and sensitive to the relevant top-level design parameters, and can therefore be easily applied to evaluate a wide range of configurations. It can be used in sensitivity or optimization studies to determine more optimal mission and power-control profiles, as well as to rapidly evaluate different combinations of mission requirements, powertrain architectures, and technology-level assumptions. The results also provide valuable insight into possible areas of improvement for a particular design. For example, the power-loading diagrams show which performance requirements are constraining for each component of each powertrain architecture, clearly indicating in which flight condition the aerodynamic or operational characteristics must be improved in order to obtain a benefit at aircraft level. In this sense, it provides a quick and visually-evident way of relating the findings of higher-fidelity propulsion-system studies to their impact at aircraft level.

Nevertheless, although the method constitutes a solid basis for more elaborate conceptual-design frameworks, multiple improvements can be incorporated to increase its accuracy. Most importantly, the powertrain model can be improved by, for example, incorporating the effect of battery state-of-charge, variable gas-turbine efficiency, and the thermal management system. Furthermore, additional aero-propulsive models should be developed for highly-integrated propulsion systems such as leading-edge distributed-propulsion, over-the-wing distributed-propulsion, tip-mounted propulsion, or boundary-layer ingestion, based on detailed aerodynamic studies. The implementation of different aero-propulsive models will broaden the applicability of the method and enable the rapid design-space exploration of a wide range of aircraft configurations.

Part III

Aerodynamic Characterization of Over-the-Wing Distributed Propulsion

6

PROPELLER INTERACTION EFFECTS

The theoretical background presented in Ch. 2 revealed that the literature on the aerodynamic performance of over-the-wing propellers is scarce and, on occasions, contradictory. The earlier studies show that OTW propellers can significantly increase the lift-to-drag ratio [69]; however, while some studies encounter propeller-efficiency penalties [68, 69], others find an efficiency increase [63]. The optimum axial propeller position in terms of lift increase also differs among the various studies. Moreover, no detailed studies were encountered regarding the interaction between adjacent propellers in forward flight, or the interaction between propellers and non-circular ducts. Consequently, it is currently not clear which aerodynamic interaction phenomena are dominant in OTWDP systems, or how they affect the performance of the system.

The purpose of this chapter is therefore to analyze the aerodynamic interaction that occurs among the different elements of an OTWDP system. An overview of these elements is given in Fig. 6.1, which represents a fraction of a hypothetical OTWDP system with a simple envelope duct. The OTWDP system comprises five main components: wing (potentially with a flap), duct, propellers, nacelles, and pylons. The scope of the present research is limited to the first three elements, which are responsible for the largest aerodynamic forces. Thus, this chapter focuses on how a propeller interacts with the wing (Sec. 6.1), the duct (Sec. 6.2), and the adjacent propellers (Sec. 6.3). Since a priori it is unclear what shape the duct should have (see Fig. 2.9), or whether it is required in the first place, a simplified limit case is studied in Sec. 6.2, namely the interaction between a single propeller and a square duct. This step is considered "qualitative" because, although *quantitative* data is presented, the purpose of the investigation is to provide a *qualitative* understanding of the physical phenomena using a simplified geometry. The qualitative understanding helps to establish design guidelines, and indicates which effects must be incorporated in performance estimates, which ones can be neglected, or what the consequences are of neglecting a determined interaction effect. The interaction between the propeller and the wing or adjacent propellers, on the other hand, is studied both qualitatively and quantitatively, in the sense that the measured changes in

Parts of this Chapter have been published in Refs. [231–233].

forces and efficiency are representative of what would be encountered in more realistic designs. The qualitative understanding obtained in this chapter is then used to produce a quantitative performance model in Ch. 8 and to justify a series of design choices in Ch. 10. Given that each interaction problem presents different elements and aerodynamic phenomena, different experimental and numerical approaches are used in the following sections.

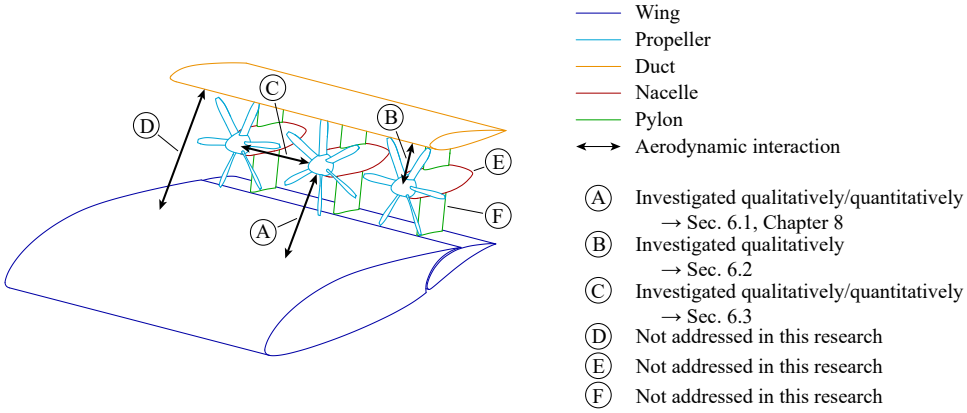

Figure 6.1: Schematic overview of the components and the aerodynamic interactions between those components that are investigated or neglected in the present research.

6.1. PROPELLER–WING INTERACTION

This section focuses on the interaction between a wing and a single OTW propeller, to gain a physical understanding of the effect of the wing on the propeller and vice versa, without the superimposed effect of any adjacent propellers. Given the discrepancies observed between lower-order numerical methods and experimental data in earlier studies [68, 80] and the computational cost of performing high-fidelity simulations, an experimental approach was selected to be able to efficiently analyze different different thrust settings (i.e., advance ratios). Thus, two exploratory wind-tunnel campaigns were performed. The purpose of the first campaign was to investigate the effect of the propeller on the pressure distributions on the wing surface and in the wake of the system. The wing pressure distributions were analyzed to understand how the propeller affects the wing lift and drag, and to provide additional insight into some of the discrepancies observed in literature in terms of lift and drag changes. The wake pressure distributions were analyzed to determine how the slipstream deforms due to the presence of the wing, and whether this is relevant from a performance-modeling perspective. The purpose of the second campaign, on the other hand, was to analyze the effect of the wing on the propeller forces and efficiency. These experimental setups are described in Sec. 6.1.1. The main effects of the propeller on the wing and vice-versa are subsequently presented in Secs. 6.1.2 and 6.1.3, respectively. The interaction effects discussed in the process serve as a basis for the high-lift and performance-oriented investigations of Chapters 7 and 8, respectively.

The experimental campaigns of Sec. 6.1 were performed together with E. A. P. Marcus as a part of an MSc thesis research project [234].

6.1.1. EXPERIMENTAL SETUP

The two aforementioned experiments were performed in the low-turbulence tunnel (LTT) and the open-jet facility (OJF), respectively. Rather than designing a completely new setup, existing available hardware was used in these initial campaigns. Therefore, the two tests employed different models and measurement techniques, which are described in the following subsections. Furthermore, for these preliminary tests, no systematic uncertainty quantification was performed. However, repeated measurements were performed in both campaigns. The differences among these repeated measurements were confirmed to be small when compared to the effects of the propeller on the wing and vice versa.

A. EXPERIMENT 1: LTT

The first wind tunnel (WT) campaign was carried out in low-turbulence tunnel at the Delft University of Technology, which has a cross-section of 1.8 m × 1.25 m. This wind tunnel has a maximum velocity of 120 m/s and freestream turbulence limited to a level of 0.02% for velocities below 40 m/s [235].

Model Description

In order to simulate an OTW propeller configuration, a propeller was positioned on the suction side of a wing mounted vertically in the wind-tunnel test section, as depicted in Figures 6.2 and 6.3. The wing spanned the full height of the test section and was placed on a turntable, which could be rotated to change the angle of attack. It featured a chord of 0.6 m and an NLF-MOD22B airfoil designed at Delft University of Technology for low-speed applications [236]. The airfoil presents a maximum thickness-to-chord ratio of 0.17 at 35% chord and a Fowler flap of 30% chord length. The main dimensions are indicated in Figure 6.2. Additional information regarding the experimental setup can be found in Ref. [234].

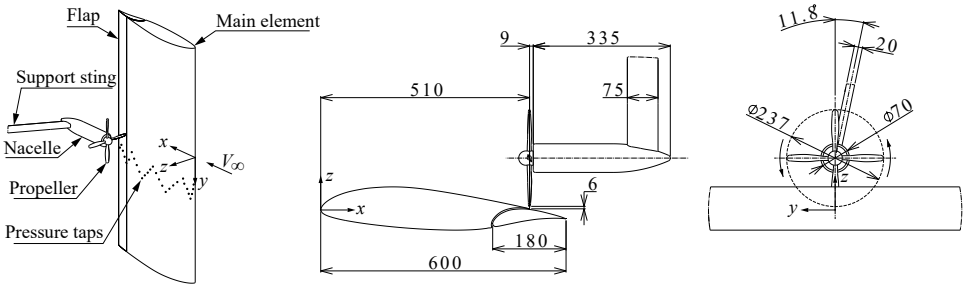

Figure 6.2: Isometric (left), top (middle) and front (right) views of the wind tunnel setup, including component designation, coordinate system and direction of rotation of the propeller. All dimensions in mm.

The four-bladed propeller model has a diameter of $D_P = 0.237$ m ($D_P/c = 0.395$), a blade chord of 7.8% of the propeller diameter, and a pitch angle of 23° at 75% of the propeller radius. More detailed characteristics of the propeller can be found in Refs. [141, 237]. The propeller was driven by a 7.5 hp three-phase induction motor housed in a nacelle of 0.07 m diameter, positioned by means of a support sting which could be

traversed along all three axes. The support sting was installed under a small inclination angle as depicted in Figure 6.2, in order to position the propeller axis at the spanwise location of the pressure ports when the traverse mechanism was set at its neutral position along the y-axis.

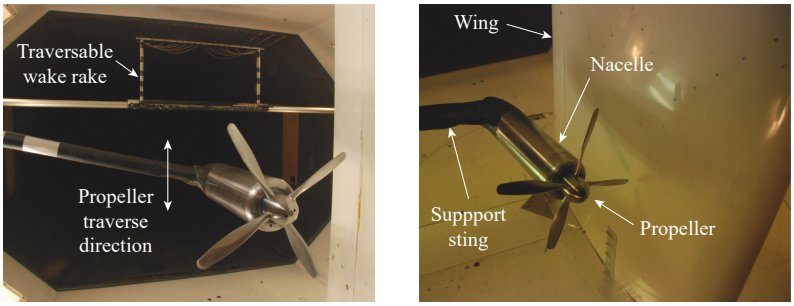

Figure 6.3: Photos of the wind tunnel setup, indicating main components.

Measurement Techniques

In the experiment two main variables were measured: the pressure distribution on the wing surface and the total pressure distribution in a wake plane (a yz-plane downstream of the model). Additionally, an Optris PI640 infrared (IR) camera was installed during all measurements to observe the location of boundary-layer transition. In order to obtain the surface pressure distribution, the wing model featured 54 static pressure ports on the main element and 27 on the flap, distributed over the pressure and suction sides. The ports were located along a zigzag path extending over a spanwise interval of 100 mm, as indicated in Figure 6.2. For each configuration, the propeller was traversed in spanwise direction to resolve the 2D wing pressure distribution, covering a span of $1.5D_P$. Trailing-edge pressures were extrapolated on the suction and pressure sides of the wing, based on the values obtained from the two pressure ports located closest to the trailing edge. The resulting lift and pressure-drag coefficients were corrected for streamline curvature, wake blockage, and wing blockage [238]—but not for slipstream blockage, since the propeller disk area represented only 2% of the cross-sectional area of the wind tunnel.

Wake plane pressure measurements were performed with a horizontal wake rake located 1.25 chord-lengths downstream of the wing trailing edge. The wake rake probes had a spacing of 3 mm at the center, with decreasing density up to a separation of 24 mm at the outer edges. The full span of the rake was $2.1D_P$, which was insufficient to capture the propeller slipstream and wing wake with acceptable resolution in a single traverse along the Y-axis. Accordingly, for each measurement configuration the wake rake was traversed along the wing span twice, centering the rake once around the propeller slipstream and once around the wing wake. Each traverse covered a spanwise interval of $1.7D_P$, centered around the vertical position of the propeller axis.

Test conditions

The wing was set to an angle of attack which was representative of cruise conditions ($C_L \approx 0.5$) and had been evaluated in earlier experiments [236], $\alpha = 2.08°$. To simulate high-lift conditions, the maximum possible flap deflection of $\delta_f = 23°$ was selected,

which was limited by the geometry of the support sting. For the selected deflection angle, the values of flap gap and overlap (defined in Figure 6.4) were selected to be of 3.9% and 3.5% chord length respectively, based on earlier reports [236].

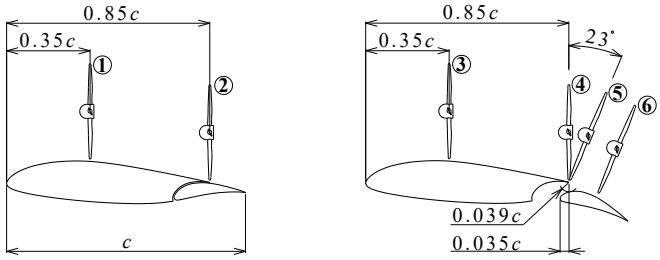

Figure 6.4: Side view of the six configurations analyzed, separated into flap retracted (left) and flap deflected (right) cases.

Figure 6.4 shows the selected configurations. For the cruise conditions (flap nested), two axial propeller positions were evaluated: the location of maximum airfoil thickness (Configuration 1, at 35% chord) and the trailing edge of the main element (Configuration 2, at 85% chord). These locations were selected based on the observations of earlier studies [63, 68, 80], which indicate that the axial position of maximum wing drag reduction and lift increase are close to the thickest point and the trailing edge respectively. However, the trailing edge of the flap was not considered due to the structural complications that would arise in real applications and the potential reduction of noise shielding effects. The separation between the propeller blade tips and wing surface was chosen as low as possible[1], since the drag reduction has been found to be larger for smaller clearances [63], which is desirable for potential OTW applications. The propeller axis was aligned with the freestream direction for simplicity.

For the high-lift conditions (flap deflected), two additional propeller positions were evaluated. The first features a propeller that is located at 85% chord in cruise conditions (Configuration 2) but is rotated 23° around the main element's trailing edge when the flap is deflected (Configuration 5). The second corresponds to the position that the propeller would attain if it were physically connected to the flap (Configuration 6). These configurations were analyzed to investigate whether deflecting the propeller to increase system lift through thrust-vectoring had any adverse effects on the wing performance.

Advance ratios of 0.7, 0.8 and 0.9 were selected for the current experiment, based on isolated propeller data obtained in earlier experiments [65]. These values correspond to isolated-propeller thrust coefficients of $C_T = 0.12$, 0.10 and 0.06, respectively [239]. The isolated-propeller thrust measurements were performed at a wing-chord based Reynolds number of 1.65 million, and thus this Reynolds number was selected for the test campaign, corresponding to a freestream velocity of approximately 41 m/s. For each setup, a measurement was also taken with the propeller removed and replaced by a dummy hub for reference. A summary of the tested parameters is given in Table 6.1.

[1] For safety reasons, this was considered to be 6 mm, i.e. 1% chord.

Table 6.1: Summary of test conditions evaluated in Experiment 1 (LTT).

Parameter	Test values
Freestream velocity V_∞ [m/s]	41
Blade pitch angle $\beta_{0.75R}$ [deg]	23
Reynolds number Re_c [-]	$1.65{\cdot}10^6$
Wing angle of attack α [deg]	2.08
Flap deflection δ_f [deg]	0, 23
Propeller advance ratio J [-]	0.7, 0.8, 0.9
Diameter-to-chord ratio D_p/c [-]	0.395
Propeller axial positions x_p/c [-]	See Fig. 6.4.
Propeller tip clearance ε/c [-]	0.01

B. EXPERIMENT 2: OJF

The second wind tunnel campaign was performed int he Open-Jet Facility (OJF) of Delft University of Technology. This open-jet, closed-circuit wind tunnel has a contraction outlet of 2.8 m ×2.8 m, as shown in Figs. 6.5 and 6.6. The tunnel presents a maximum freestream velocity of 30 m/s and a freestream turbulence level below 0.5%. The purpose of this experimental campaign was to obtain a preliminary understanding of the effect of an OTW propeller's position on its thrust, torque, and propeller efficiency.

Model Description

For this experiment, a propeller of diameter D_p = 0.4064 m was installed in the center plane of the wind tunnel at zero degrees angle of attack. The propeller was installed 0.5 m (2.5R) above the ground table by means of a pylon of 300 mm (1.5R) chord, as shown in Fig. 6.6. The six-bladed, carbon fiber "XPROP" propeller presented a blade pitch of $\beta_{0.7}$ = 30^o and was driven by a TDI 1999 pneumatic motor. Additional information regarding the geometry of the propeller can be found in Refs. [240, 241].

A wing of 1.25 m span and c = 0.74 m chord was installed vertically on the starboard side of the propeller, to produce a inflow velocity distribution to the propeller that was representative of an OTW application. To reduce the tip effects on this low aspect-ratio wing (A = 1.7), an end plate was attached on the top side, as indicated in Figs. 6.5 and 6.6. The wing featured a generic low-speed airfoil and was installed at an angle of attack of 4^o. At this angle-of-attack, the lift coefficient of the wing was estimated to be C_L = 0.61, based on a 3D panel-method analysis [234]. Therefore, although the setup was not representative of a 2D wing due to the low aspect ratio and the presence of the pylon, the inflow velocity profile generated at the propeller location (see Fig. 2.7a) was considered comparable to the typical conditions that an OTW propeller could encounter in cruise conditions. By fixing the wing at different locations on the ground table and support structure, the position of the propeller relative to the wing could be varied.

Measurement Techniques

The propeller was instrumented with a custom-built, six-component rotating shaft balance (RSB) to measure the propeller forces and efficiency. This balance features a measurement range of ±350 N and ±30 Nm for the thrust and torque components, respec-

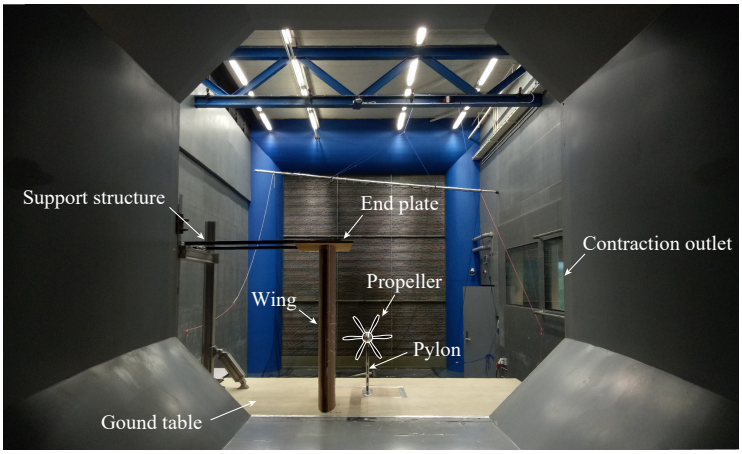

Figure 6.5: Downstream view of the main components involved in the OJF experiment, viewed from the settling chamber.

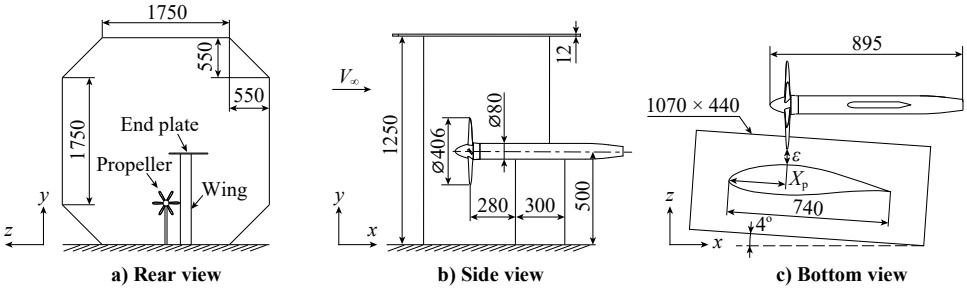

Figure 6.6: Approximate dimensions of the test setup used in the OJF experiment. All dimensions in mm. Figure adapted from Ref. [234].

tively. Calibrations with static loads showed that the error for these force components is below 0.25% of the full-scale measurement range [242]. For each measurement run, data were acquired at various advance ratios in random order by varying the rotational speed of the propeller while maintaining the freestream velocity constant. For each measurement point, the data were recorded at 10 kHz and averaged over 30 seconds. Repeated measurement runs were performed to confirm that the spread in the data was small compared to the changes in performance due to the effect of the wing at each location. No wind-tunnel corrections were applied, since their effect on the propeller performance was considered small compared to the general uncertainty of the inflow velocity created by the three-dimensional setup. Therefore, they would not affect the main takeaways of this exploratory test.

Test conditions

Measurements were performed at $V_\infty = 20$ m/s, since isolated-propeller reference data was available at that freestream velocity. The corresponding wing-chord-based Reynolds

number is approximately 10^6. Although this value is roughly one order of magnitude lower than the Reynolds numbers expected in full-scale applications (see Table 1.1), the changes in induced velocities at the propeller location due to changes in the boundary-layer thickness at higher Reynolds numbers are considered of secondary importance, compared to the inviscid effect of the wing. The propeller was operated in an advance ratio range of $0.4 < J < 1.2$, which corresponds to thrust coefficients ranging from approximately $C_T = 0$ to $C_T = 0.35$, blade Reynolds numbers between $Re_{0.7R} = 8 \cdot 10^4$ and $Re_{0.7R} = 2.3 \cdot 10^5$, and blade-tip Mach numbers between $M_{\text{tip}} = 0.16$ and $M_{\text{tip}} = 0.47$. Moreover, three axial propeller positions (35%, 60%, and 85% chord) and three propeller tip-clearance values (1%, 5%, and 10% chord) were evaluated. An overview of these test conditions is provided in Table 6.2.

Table 6.2: Summary of test conditions evaluated in Experiment 2 (OJF).

Parameter	**Test values**
Freestream velocity V_∞ [m/s]	20
Blade pitch angle $\beta_{0.7R}$ [deg]	30
Reynolds number Re_c [-]	10^6
Wing angle of attack α [deg]	4
Flap deflection δ_f [deg]	0
Propeller advance ratio J [-]	0.4–1.2
Diameter-to-chord ratio D_p/c [-]	0.55
Propeller axial position x_p/c [-]	0.35, 0.60, 0.85
Propeller tip clearance ε/c [-]	0.01, 0.05, 0.10

6.1.2. EFFECT OF PROPELLER ON WING

The findings of the LTT experiment are explained in the following subsections. The results are divided into two categories: in cruise-lift conditions (flap retracted), and high-lift conditions (flap deflected). In both cases, the wing characteristics are expressed as a "delta" with respect to propeller-off conditions. For reference, the isolated-wing pressure distributions are given in Fig. 6.7. The corresponding wing lift and pressure-drag coefficients are collected along with those of the propeller-off configurations in Table 6.3.

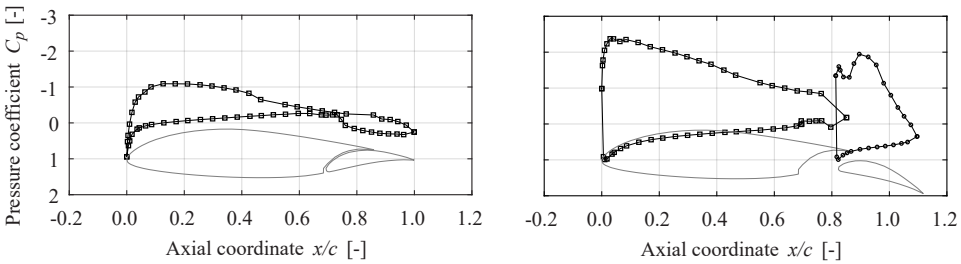

a) Flap retracted **b) Flap deflected**

Figure 6.7: Isolated-wing pressure distributions with and without flap deflection (Experiment 1).

Table 6.3: Propeller-off and isolated wing lift and drag coefficients obtained in Experiment 1.

Configuration	δ_f [deg]	C_L [-]	C_{Dp} [-]
Isolated wing (cruise)	0	0.47	0.006
Configuration 1	0	0.47	0.013
Configuration 2	0	0.44	0.008
Isolated wing (high lift)	23	1.63	0.020
Configuration 3	23	1.64	0.032
Configuration 4	23	1.61	0.026
Configuration 5	23	1.60	0.025
Configuration 6	23	1.60	0.023

A. CRUISE-LIFT CONDITIONS

To demonstrate the effect of the propeller on the pressure distribution over the wing surface, Figure 6.8 presents the pressure coefficient difference between the propeller-on and propeller-off measurements, i.e. $\Delta C_p = C_{p,\text{on}} - C_{p,\text{off}}$, for Configurations 1 and 2. The results are presented for moderate lift coefficient values ($C_L \approx 0.5$), which are representative of the cruise phase. In these conditions, the flap is retracted, and the performance of the wing should be optimized in terms of lift-to-drag ratio. The results are presented as an increase with respect to propeller-off measurements because this study focuses on the effect of the propeller, and not the installation effects of a nacelle and support structure of arbitrary geometry. In Figure 6.8 the flow goes from left to right, and the spanwise coordinate $y/D_P = 0$ corresponds to the location of the propeller axis.

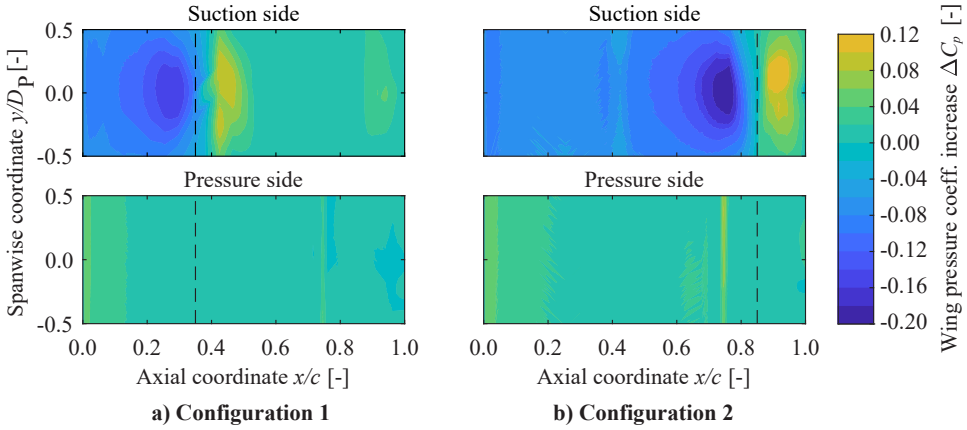

Figure 6.8: Wing pressure distributions with the flap retracted at advance ratio $J = 0.7$ (Experiment 1). Dashed lines indicate the projection of the propeller disk onto the wing surface.

Figure 6.8 shows that, on the suction side, pressure is reduced in front of the propeller and increased behind it for both configurations. This is attributed to the acceleration of the flow ahead of the propeller, while behind the propeller disk a region of flow diverging from the wing surface is created by the contraction of the slipstream. Results at advance

ratios $J = 0.8$ and $J = 0.9$ (which are not presented here) confirmed that the magnitude of the pressure differences diminishes with increasing advance ratio. More pronounced pressure effects of the propeller on the wing are observed for Configuration 2 than for Configuration 1. This is a consequence of the higher effective advance ratio in Configuration 1, since the wing-induced velocities are higher at 35% chord than at the main element's trailing edge (see Figure 6.7a[1]). In both cases, the pressure distributions are nearly symmetrical with respect to $y/D_P = 0$. On the pressure side of Configuration 2 (Fig. 6.8b), a minor increase in pressure coefficient is observed near the flap slot, due to the increased pressure behind the propeller disk which is propagated through the slot.

The findings of Johnson and White [63], who stated that an OTW propeller had no effect on viscous drag, is further assessed by analyzing the IR images. These show that, for the aft-mounted position (Configuration 2), the boundary-layer transition location is not noticeably affected by the propeller, despite the effective angle-of-attack increase induced by the propeller (see Fig. 2.7). For Configuration 1, on the other hand, local changes in transition location are observed. These observations are shown in Figure 6.9. In the propeller-off case of Configuration 1 (Figure 6.9a), the transition location moved aft due to the favorable pressure gradient generated by the nacelle. However, with the propeller operating ahead of the transition line (Figure 6.9), the transition location moves forward. There are two reasons for this. Firstly, an adverse pressure gradient is generated directly beneath the propeller disk, as visible in Figure 6.8. Secondly, the interaction between the tip vortices and the boundary layer introduces instabilities in the flow [149]. These effects are discussed in more detail in Ch. 7, but in any case the IR images indicate that the propeller only has a measurable impact on boundary-layer transition if it is installed close to or ahead of the transition location.

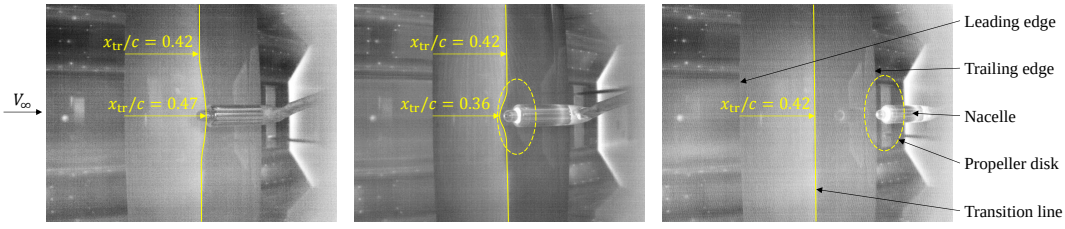

a) Configuration 1, Prop off **b) Configuration 1, $J = 0.7$** **c) Configuration 2, $J = 0.7$**

Figure 6.9: Infrared images showing the effect of the propeller on boundary layer transition (Experiment 1).

By integrating the pressure distributions, wing lift and pressure drag are obtained. Note that for the computation of these coefficients the reference area considered spans one propeller diameter, that is, forces are evaluated over an area of $S_{ref} = c \cdot D_P$, and not over the entire wing. For reference, Table 6.3 presents the isolated wing and propeller-off lift and drag coefficients. The propeller-off pressure measurements differ from those in Figure 6.7 due to the blockage effect of the nacelle and support sting, and showed that upstream of the nacelle the static pressure was increased, whereas it decreased directly

[1]The isolated-wing pressure distributions give an indication of the local velocity magnitude. For steady, incompressible, inviscid flow the local flow velocity can be expressed as $V = V_\infty \sqrt{1 - C_p}$.

beneath the nacelle [234]. This generally led to additional pressure drag in all configurations, given that the nacelle was situated above the rearwards-facing part of the wing surface. Nevertheless, as discussed earlier, the primary interest of this study lies in the effect of the propeller, and not of the installation elements. Accordingly, Figure 6.10 shows the lift and drag coefficients as a difference between propeller-off and propeller-on conditions. The wing lift is shown to increase with decreasing advance ratio (increased thrust) as expected from theory. This can be attributed to the region of low pressure generated in front of the propeller, which becomes stronger with increasing propeller thrust. For this particular diameter-to-chord ratio and system geometry, the lift of the wing is increased by approximately 4% at a low thrust setting, and by 15% at a high thrust setting, for a propeller positioned at 85% of the chord (Configuration 2).

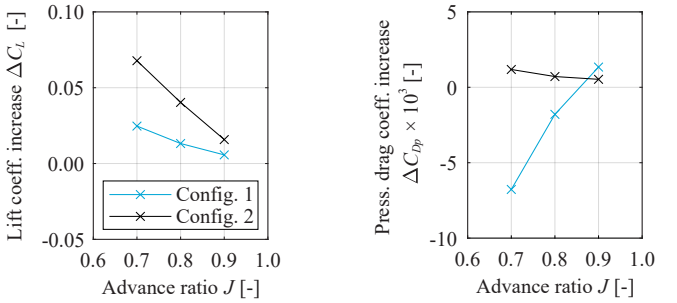

Figure 6.10: Wing lift and pressure drag increase with respect to propeller-off conditions, as a function of advance ratio (Experiment 1, flap retracted).

Regarding the pressure drag of the wing, Figure 6.10 shows that it decreased with decreasing advance ratio for Configuration 1, leading to a significant drag reduction at high thrust settings. The magnitude of this drag reduction exceeds the pressure drag of the clean wing, and occurs due to increased suction ahead of the thickest point of the wing. In Configuration 2, it appears the pressure variations upstream and downstream of the thickest point scaled equally with advance ratio, leading to an approximately constant pressure drag. In this configuration, the pressure drag is increased with respect to the propeller-off case. Since the friction drag of the wing cannot be obtained from the experimental data, the changes in lift-to-drag ratio cannot be quantified exactly. However, if the airfoil is evaluated in a viscous 2D panel method (XFOIL [243]) at the same angle of attack and Reynolds number, then a sectional friction-drag coefficient of $c_{df} \approx 0.0047$ is obtained. If that were the case, and the friction drag were not significantly affected by the presence of the propeller (as suggested by Fig. 6.9 and Ref. [244]), then for Configuration 1 the lift-to-drag of the wing segment of span D_P would be increased by 74% and decreased by 8% relative to propeller-off conditions at high ($J = 0.7$) and low ($J = 0.9$) thrust settings, respectively. For Configuration 2, the changes in L/D would be +0.1% and -3% at high and low thrust settings, respectively. Although these values are only indicative, and the comparison is not performed at constant lift or constant thrust, they show that the pressure-drag reduction due to OTW propellers can substantially increase the L/D. Hence, this aerodynamic interaction must be accounted for in performance predictions for OTWDP systems.

B. HIGH-LIFT CONDITIONS

In this section, the results are presented for high-lift conditions. These conditions are representative of the climb segment, when the flap is deflected ($C_L \approx 1.6$) and wing lift should be maximized. The pressure-coefficient distributions on the wing, ΔC_p, are presented in Figure 6.11 for high-lift Configurations 3 to 6 at advance ratio $J = 0.7$. Again, wing pressures are decreased and increased in front of and behind the propeller respectively, except in Configuration 3. In this configuration, the effective advance ratio is exceptionally high and, accordingly, propeller effects on the wing are weak. When the propeller is inclined at 23° (Configuration 5), the suction on the main element is decreased, while the pressure on the flap is increased. The pressure variations are even more prominent in Configuration 6, due to an improved alignment between the propeller axis and the local flow direction and reduced distance between the flap surface and the propeller.

Strips of increased pressure can be observed in Figure 6.11 on the suction side at $x/c = 0.3$ for all configurations. Additional IR images, not shown here, revealed that this location corresponded to the chordwise location of boundary-layer transition. Since the transition location was upstream of the propeller for all high-lift configurations, no appreciable changes in transition location were observed. However, a pressure tap was located exactly beneath the transition location, causing a slight movement to show up very prominently.

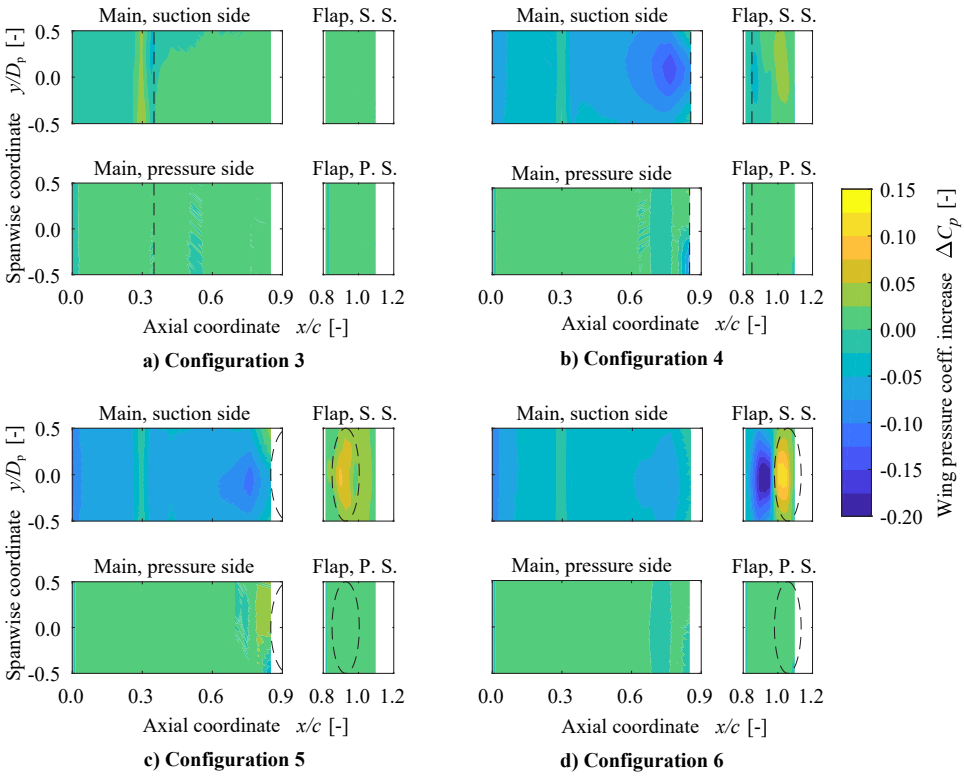

Figure 6.11: Wing pressure distributions with the flap deflected (Experiment 1, $J = 0.7$). Dashed lines indicate projection of propeller disk onto the wing surface. Note that the contour levels differ from those in Figure 6.8.

Figure 6.12 shows the lift and drag coefficients as a difference between propeller-on and propeller-off measurements. Figure 6.12a indicates an increase in lift with decreasing advance ratio, comparable to the effect seen for cruise configurations. From Figure 6.12 it is evident that at high advance ratios, the propeller is operating in windmilling conditions close to the wing surface, leading to decreased lift and increased pressure drag. This effect was confirmed with the wake-plane pressure distributions, and is more pronounced in Configuration 3 due to the large inflow velocities perceived by the propeller towards the leading edge of the wing. Again, as the advance ratio is decreased, the pressure drag also reduces, due to the increased suction in front of the wing location with maximum thickness. For the inclined-propeller positions (Configurations 5 and 6), the pressure drag is found to reduce significantly, while the lift is comparable to the configuration without propeller inclination (Configuration 4).

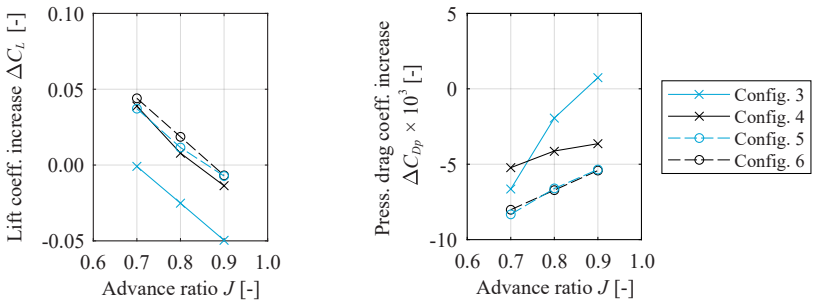

Figure 6.12: Wing lift and pressure drag increase with respect to propeller-off conditions in high-lift configurations, as a function of advance ratio (Experiment 1, flap deflected).

6.1.3. EFFECT OF WING ON PROPELLER

The following paragraphs describe how the slipstream loading distribution and propeller performance are affected by the presence of the wing. The effects are described in the following two subsections, using data of the LTT (Experiment 1) and OJF (Experiment 2) tests, respectively. Therefore, the two subsections correspond to different geometries and operating conditions, and any key takeaways should be qualitative in nature.

A. SLIPSTREAM TOTAL-PRESSURE DISTRIBUTIONS

The total-pressure distributions in the wake plane are shown in Figure 6.13. The decreased total pressure in the wake of the support sting, nacelle and wing can be clearly distinguished. Although the annular propeller slipstream is also clearly distinguishable, it is deformed and displaced in vertical direction due to the downwash of the wing. At the bottom of the slipstream, lobes of increased total pressure are observed due to the interaction with the wing wake. Two important effects regarding the propeller loading distribution are observed in Figure 6.13. First, for the same advance ratio, the slipstream total pressure is lower in Configuration 1 (Fig. 6.13a) than in Configuration 2 (Fig. 6.13b), due to the increased axial velocities at that propeller location. Second, the non-uniform

inflow conditions lead to azimuthal loading variations in both configurations. In Configuration 1, the strong vertical gradient of axial velocity above the wing is the main source of non-uniform loading. This leads to a low disk loading near the wing, where inflow velocities are highest. In Configuration 2, however, the wing-induced velocities have a negative w-component at the location of the propeller disk, generating the highest loads on the upward-going blade, which experiences a higher angle of attack. This can be inferred from Figs. 6.13a and 6.13b if the pressure distributions are rotated approximately 30^o in counter-clockwise direction to account for the swirl in the slipstream, such that the low-pressure region in the slipstream due to the support-sting wake is aligned with the support-sting wake outside the slipstream. This observation is also supported by the numerical analyses of Ref. [234]. From this it can be concluded that, while the effect of the propeller on the wing pressure distribution is approximately symmetric with respect to $y/D_P = 0$, the effect of the wing on propeller loading is quasi-symmetric in Configuration 1, and asymmetric in Configuration 2.

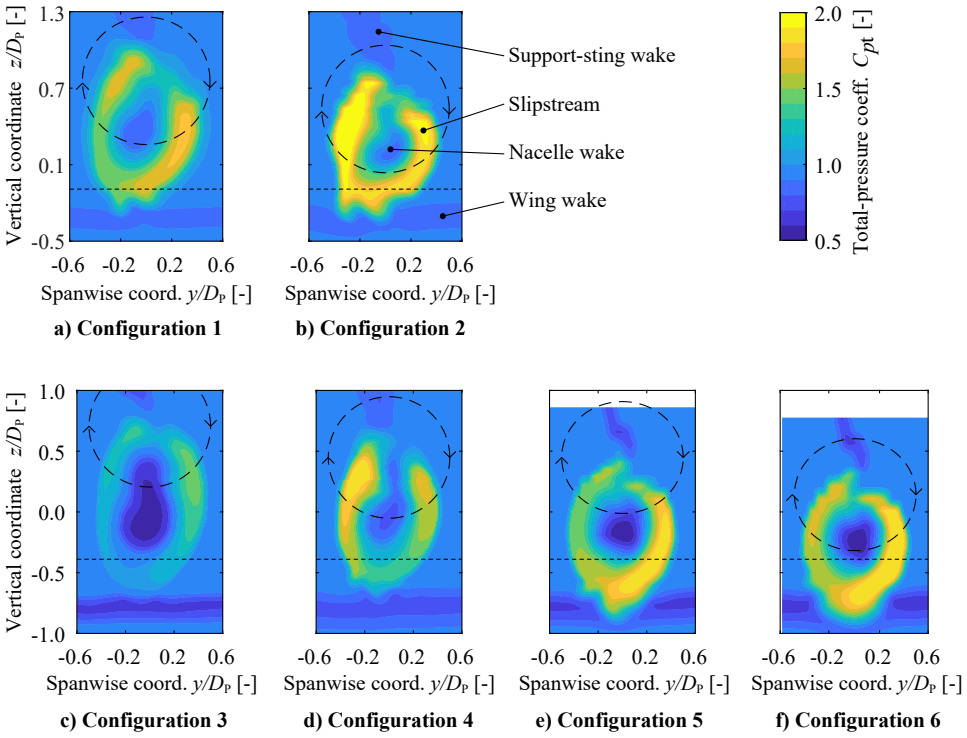

Figure 6.13: Wake-plane total pressures 1.25c downstream of the wing trailing edge in cruise (top) and climb (bottom) conditions at $J = 0.7$ (Experiment 1). Dashed and dotted lines indicate projections of propeller disk and wing trailing edge, respectively.

Results of the total-pressure measurements in the wake plane for the climb configurations are shown in Figs. 6.13c–6.13f. Additional wake-plane results showed that, in for example Configuration 3, $J = 0.8$, the total pressure coefficients in the slipstream were

lower than in the freestream, indicating that the propeller was extracting energy from the flow over the complete disk. This implies that in Configuration 3 the propeller is windmilling for advance ratios above 0.8, even though the isolated propeller generates thrust up till $J = 1$. This explains the lift decrease observed in Figure 6.12. Since flow velocities above the wing decrease as the distance to the wing surface increases, in some cases only the bottom fraction of the propeller was windmilling, while the top part, which had a lower effective advance ratio, was generating thrust, as reflected in Figure 6.13a. For the same reason, when comparing Figures 6.13a, 6.13c and 6.13d, it can be seen that the thrust is reduced more in Configuration 3 than in Configurations 1 and 4, since the flow velocities above the wing are higher with the flap deflected and at 35% instead of 85% chord-length.

In Figure 6.13d (Configuration 4), the up-going blade experiences a higher loading than the down-going blade. This is due to the downward-oriented wing-induced velocities, which follow the local inclination of the airfoil surface. If, on the other hand, the propeller is deflected 23° (Configurations 5 and 6), the angle of attack perceived by the blades is highest on the down-going side. In both Configurations 5 and 6, the slipstream presents a large vertical displacement due to the inclination of the propeller, and penetrates the wing wake. The total pressure values are higher in Configuration 6 than in Configuration 5, since the propeller is ingesting lower-velocity flow. The fact that Configurations 5 and 6 present higher momentum in the slipstream when compared to Configuration 4 indicates that deflecting the propeller together with the flap leads to increased thrust at a given advance ratio. However, the strong differences in loading between the up- and down-going blade sides show that a significant unsteady blade loading is generated.

B. PROPELLER PERFORMANCE

The propeller thrust, torque, and efficiency obtained from the OJF experiment are presented in Fig. 6.14. Figures 6.14a and 6.14b show how the propeller thrust and torque are both reduced for a given advance ratio in the OTW configuration, when compared to the isolated propeller. The reduction is more pronounced for more forward propeller positions. Moreover, a change in slope is observed for $J \approx 0.9$, potentially due to the onset of blade trailing-edge flow separation at lower advance ratios [241]. Overall, the non-uniform inflow leads to a reduction in propeller efficiency, as shown in Fig. 6.14c. Note that, according to the definitions of Eqs. 2.2 and 2.11, the propeller efficiency equals the propulsive efficiency of the OTW system in this case, since the propeller axis is aligned with the freestream. The propeller-efficiency penalty is more pronounced a higher advance ratios because the wing-induced velocities become more dominant, compared to the propeller's self-induced velocities. Moreover, due to the increase in local advance ratio above the wing, the (freestream-based) advance-ratio values corresponding to maximum efficiency and zero thrust are lower than in the isolated-propeller configuration.

From a conceptual aircraft-design perspective, it is more informative to remove the influence of the rotational speed from the normalization and present the propeller efficiency versus the thrust coefficient T_c instead. This is shown in Fig. 6.14d, which indicates that the propeller-efficiency penalty is highest near the thrust setting corresponding to maximum efficiency. Furthermore, if the aircraft is assumed to use a variable-pitch

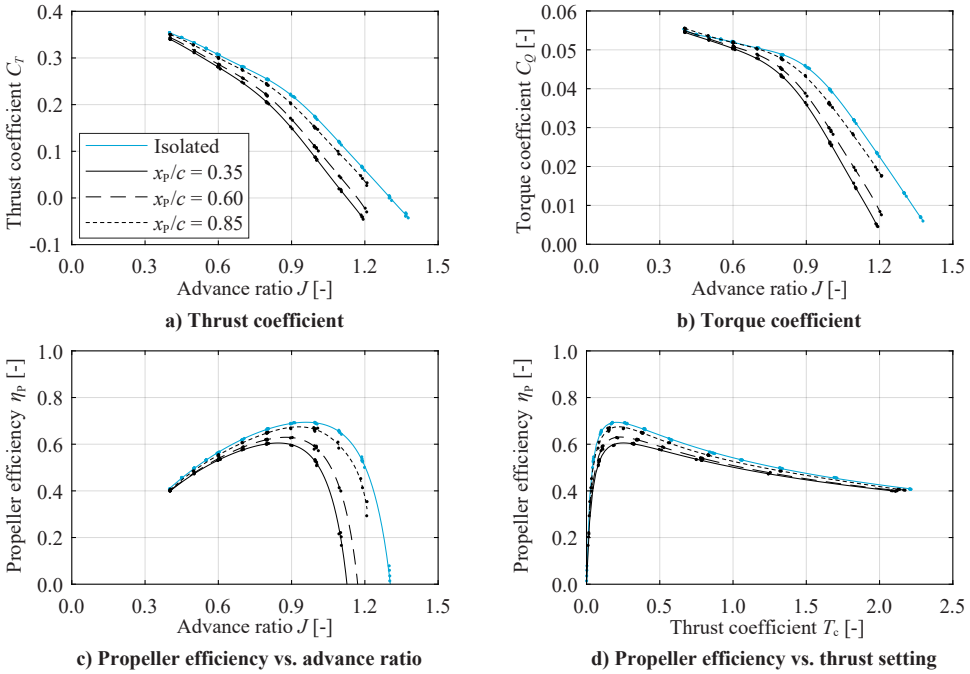

Figure 6.14: Propeller performance curves obtained in Experiment 2 for different axial OTW propeller positions. Dots indicate individual measurements. Isolated-propeller data provided by T. Sinnige [141].

propeller, or a propeller whose pitch is optimized for the OTW installation, then the difference between the maximum propeller efficiencies observed in the isolated and OTW configurations is a more representative indicator of the propeller-efficiency penalty. The maximum propeller efficiency of the different OTW propeller positions is presented as a fraction of the isolated-propeller's maximum efficiency in Fig. 6.15. Figure 6.15a shows that the propeller-efficiency reduction grows from 3%–4% at $x_P/c = 0.85$ to 10%–13% at $x_P/c = 0.35$. The slope is steeper for a smaller tip clearance. In fact, Fig. 6.15b shows that, at $x_P/c = 0.35$, the propeller efficiency increases as the tip clearance is increased, while for $x_P/c = 0.85$ it decreases with increasing tip clearance. This occurs because, for more aft propeller locations, the axial velocity increase over the wing surface reduces, until it eventually stagnates at the trailing edge. Therefore, for propellers placed near the trailing edge, other effects such as a change in the effective angle of attack play a more important role, and the propeller efficiency may actually be higher for smaller tip clearances. These effects are investigated in more detail using a lower-order method in the performance studies of Ch. 8. In any case, the propeller-efficiency losses of the order of 10% observed in Fig. 6.15a show that a duct may indeed be beneficial to reduce the non-uniform inflow for propellers placed at more forward locations, while for propellers placed near the trailing edge the duct is most likely unnecessary from an aerodynamic-performance perspective. To analyze the additional benefits or drawbacks that such a duct may present, the following section analyzes how a propeller interacts with a simplified duct.

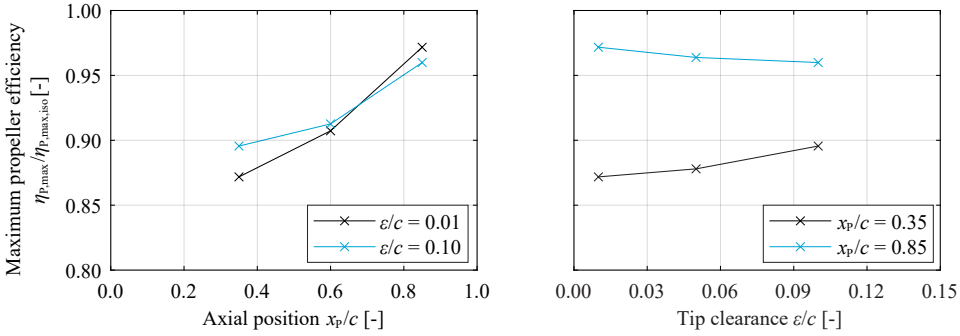

a) Effect of axial propeller position **b) Effect of propeller tip clearance**

Figure 6.15: Effect of OTW propeller axial position and tip clearance on the maximum propeller efficiency for a given blade pitch (Experiment 2), as a fraction of the maximum efficiency of the isolated propeller.

6.2. PROPELLER–DUCT INTERACTION

For the distributed-propulsion array, multiple duct designs can be envisioned, such as an array of circular ducts, a two-dimensional "envelope" duct, an array of square ducts, or a combination thereof—as discussed in Sec. 2.2.3 (see Fig. 2.9). The aerodynamic interaction effects present in these unconventional designs can be understood by analyzing two simplified limit cases: a circular ducted rotor, and a square ducted rotor, as shown in Fig. 6.16. However, as discussed in Ch. 2, the studies found in literature regarding the aerodynamic performance of ducted propellers only refer to circular ducts [171, 173–175]. While aerodynamic phenomena present in uninstalled square ducts can, to a certain extent, be inferred from corner flow studies [246, 247], it is unclear how these phenomena are affected by the presence of a rotor. The goal of this section is therefore to analyze the aerodynamic interaction phenomena present in unconventional ducted propeller systems, and to understand how these phenomena affect the performance of the system. Although determining the optimal duct shape is considered beyond the scope of this research, a basic understanding of these interaction effects provides a basis for the design choices and modeling assumptions made in subsequent chapters. Since corner-flow effects are expected to be relevant, an experimental approach is discarded due to the limited physical and optical access to the flow field inside the duct. Thus, numerical (RANS) simulations are performed to obtain detailed flow-field information of the two idealized limit cases of duct shape. The numerical methods and models used are described in Sec. 6.2.1. Afterwards, Sec. 6.2.2 describes the most relevant interaction phenomena observed in the ducted propeller systems. Subsequently, Sec. 6.2.3 discusses the main effects of the interaction between the propeller and each duct on the forces produced the system.

The numerical simulations of Sec. 6.2 were performed by H. F. M. Bento as a part of an MSc thesis research project [245].

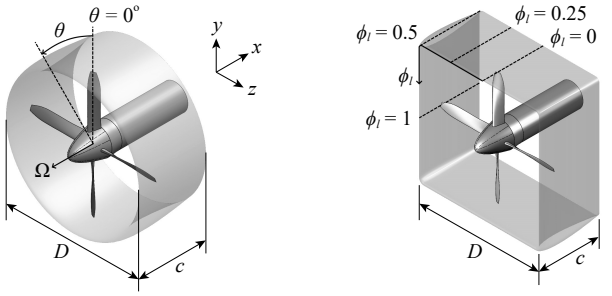

a) Circular ducted propeller **b) Square ducted propeller**

Figure 6.16: Definition of coordinates for the circular and square ducted propellers.

6.2.1. NUMERICAL SETUP

The following subsections present the geometries, solver, domains, boundary conditions, and grid used in the numerical study. Furthermore, the grid convergence and validation study is briefly discussed. The discussion here is a summary of the original work; for more details regarding the numerical setup, the reader is referred to Refs. [232, 245].

A. GEOMETRY

The circular and square ducted propeller geometries shown in Fig. 6.16 were studied. To compare the sectional pressure distributions to data from literature, the NACA0012 airfoil was selected for the ducts. The ducts have an aspect ratio $A = D/c = 2$, where D is the diameter of the circular duct, which is equal to the square duct's span. In order to improve the convergence of the simulations, the corners of the square duct were slightly rounded, so that the minimum corner radius (at the airfoils' thickest point) would be 1% of the propeller radius, R. The minimum gap between the propeller tips and duct surface (or tip clearance) was maintained at 0.3% of the propeller radius, leading to a duct chord of approximately 0.217 m. The propeller, whose blade size and geometry corresponds to the XPROP used in the OJF experiment of the previous section, presents a radius of $R = 0.2032$ m. In this study, the blade pitch $\beta_{0.7R}$, was kept at 30°. The number of propeller blades was reduced to 4 so that only one quarter of the domain had to be solved, using periodic boundary conditions. The axial location of the propeller was set to 30% duct chord, which is the location of maximum thickness of the NACA 0012 airfoil. Figure 6.16 also shows the axis system used, and how the azimuthal location, θ, and the spanwise location, $\phi_l = l/D$, were defined. l is the length along the duct's span, starting at the top surface's mid-span. The propeller rotates in counter-clockwise direction when viewed from the front, as indicated by the angular velocity vector Ω in Fig. 6.16.

B. SOLVER SETUP

The CFD simulations were performed using the solver ANSYS Fluent 18.2, and were based on the solution of steady and unsteady RANS equations. The RANS equations were discretized using the 3rd order MUSCL scheme (Monotonic Upstream-centered Scheme for Conservation Laws) [248], which was developed from the original MUSCL scheme (introduced by van Leer [249]). As the solver ANSYS Fluent is cell-centered, the values of pressure at the cell faces were calculated by interpolation considering the values of pressure at the center of the cells [248], with a 2nd order scheme. The unsteady calculations

were made using a 2nd order implicit temporal discretization. The isolated ducts were analyzed as steady simulations, whereas for the computations with the propeller both steady and unsteady flowfields were calculated. The fluid (air) was modelled as an ideal gas in order to take into account compressibility effects. Furthermore, turbulence was modelled using the two-equation k-ω shear-stress transport (SST) turbulence model, which was developed by Menter [250]. This model has been used previously in several propeller-related studies [251–254]. Besides, the k-ω SST model has been concluded to be relatively accurate for a wide range of flowfield problems, when compared against other one or two equation turbulence models (which yield similar computational costs) [255]. However, the results should be analyzed while keeping in mind that the model also has drawbacks. As an example, the k-ω SST model experiences difficulties at predicting separated flows [256].

C. PROPELLER MODELING METHODS

Two different methods were used to model the propeller: a full blade (FB) model and an actuator disk (AD) model. The full blade model was used for the isolated and installed simulations with the propeller. For the isolated propeller computations, both steady and unsteady simulations were performed. The steady simulations were performed using a Multiple Reference Frame approach (MRF), so that the propeller blades remain stationary. The MRF approach is valid when the flowfield is steady is the reference frame of the rotating body (e.g. a propeller). In the unsteady simulation, the rotation of the blades was modelled using a sliding mesh technique. For the ducted propeller installed cases, the FB model was only used to obtain unsteady solutions. The actuator disk model was used to estimate time-averaged interaction effects, for the installed configurations. The AD model applied in this study has been subjected to a validation study in Ref. [257]. The AD imposes an axial momentum, tangential momentum and energy jump at the propeller location, as described in Ref. [257]. Thus, the AD requires the thrust and torque of the propeller as inputs. In this research, the inputs of the AD were obtained from FB simulations of the isolated propeller.

D. DOMAIN AND OPERATING CONDITIONS

The domain used for the simulation of the square ducted propeller is presented (with the FB model) in Fig. 6.17. This domain is equal to the domain used in the circular ducted propeller simulation. Figure 6.17a shows that the domain was reduced to one quarter (to a 90^o domain) by using periodic boundary conditions. Far upstream of the geometry, the flow direction and the total pressure and temperature were specified at the inlet. The inlet values were calculated in order to result in a free-stream velocity, V_∞, of 30m/s, at sea-level conditions. In the far-field boundary, the flow direction, the static pressure and temperature and the Mach number were specified in order to impose equivalent free-stream conditions. Besides, the free-stream values of turbulent kinetic energy, k_∞, and specific dissipation rate, ω_∞, were specified at the inlet and far-field boundaries. The values of k_∞ and ω_∞ were chosen according to the recommendations of Ref. [258]. The decay of k and ω from the inlet to the studied geometries was avoided by placing sources for these quantities inside the domain, also in agreement with the recommendations found in Ref. [258]. At the outlet, the static pressure was prescribed.

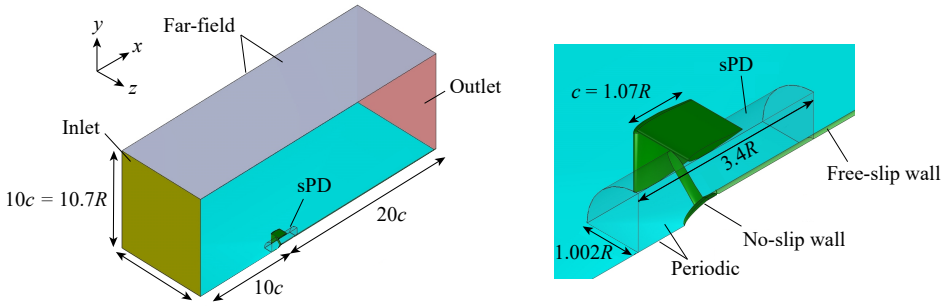

a) Square ducted propeller simulation domains

b) Close-up view of the small propeller domain (sPD) case

Figure 6.17: Domains and boundary conditions used for the simulation of the square duct with propeller.

Figure 6.17b shows how the duct surface, the propeller blade and the spinner were modelled as no-slip walls, whereas the remaining part of the nacelle (which was extended until the outlet) was modelled as a free-slip boundary. The remaining simulations were made with similar domains. For the AD simulations, the propeller blade was not included and the spinner was also modelled as a free-slip wall. The inputs for the AD model were obtained from the simulation of the isolated propeller at three operating conditions: $J = 0.7$, $J = 0.8$ and $J = 0.9$. For the simulation of the isolated propeller, the steady simulations were performed with a propeller domain considerably larger (in the radial direction) than the small propeller domain, sPD, shown in 6.17b. With a sPD, a steady solution calculated with the MRF approach leads to unphysical results [245], and thus only unsteady simulations were performed with the sPD. In the specific case of the computation of the isolated circular duct flowfield, an additional 2D simulation was performed, using an axisymmetic boundary condition in the duct's axis. The 2D simulation was used in the verification and validation process of the isolated duct computations. A summary of the operating conditions considered in this study can be found in Table 6.4. The free-stream values of density, pressure and temperature, which are omitted in the table, correspond to sea-level conditions. The advance ratio tested in the installed FB simulations, $J = 0.7$, is representative of climb conditions, as this value corresponds to a high thrust setting.

Table 6.4: Operating conditions used in the ducted propeller simulations.

Configuration	V_∞ [m/s]	α [deg]	k_∞ [m^2/s^2]	ω_∞ [s^{-1}]	$\beta_{0.7R}$ [deg]	J [-]
Uninstalled ducts	30	0	9×10^{-4}	695	30	-
Uninstalled prop. (FB)						0.7, 0.8, 0.9
Ducted prop. (AD)						0.7, 0.8, 0.9
Ducted prop. (FB)						0.7

E. GRID

The grids used in this research were generated with ANSYS Meshing software. In most regions, an unstructured mesh was used. However, near no-slip walls, inflation layers were generated. The inflation layers allow for the specification of the first layer height, which was set in all surfaces in order to achieve in a maximum y^+ lower than 1. Besides, the prism-shaped inflation layers resemble a structured mesh, allowing the elements to be more aligned with the (expected) main local flow direction. This improves convergence, even though the solver ANSYS Fluent always reads the mesh as unstructured. Furthermore, the surface mesh over no-slip walls was also specified as a structured-like mesh. However, in critical regions, exceptions had to be made and the surface mesh was also set as unstructured. The unstructured surface mesh was used in the square duct's corner and in the regions of the ducts' surface in close proximity to the blade tips. Due to the complexity of the grids generated for the installed configurations with the FB model, the resultant mesh sizes led to large increases in the computational cost of the unsteady installed calculations.

F. GRID CONVERGENCE STUDY

A grid convergence study was performed to estimate the discretization error, which is commonly the strongest source of numerical error in CFD simulations [259]. The convergence study is not described in detail here to improve readability, but is provided in Appendix E.1 for transparency. Based on this study, meshes of 8 million, 12.6 million, and 20 million cells were selected for the isolated propeller, circular ducted propeller, and square ducted propeller configurations, respectively. The drag, thrust and torque-coefficient uncertainties due to discretization were estimated to be below 1.7% for all cases, based on the procedure of Ref. [259]. However, while this is considered an acceptable margin for the overall C_D uncertainty, the pressure and friction-drag components of the ducts were found to decrease and increase with increasing grid refinement, respectively. In fact, the uncertainty-quantification (UQ) procedure predicted uncertainties of the order of 20% for these two components individually. To determine whether this was a result of an inaccurate UQ procedure or an under-resolved flow field, the pressure distributions and boundary-layer thickness of the various meshes were compared, and the convergence behavior of the isolated circular duct was compared to a 2D axisymmetric simulation of the duct [245]. The results of these comparisons were physically consistent and presented only minor differences between the various grids. Therefore, the high uncertainty of the friction and pressure-drag components was attributed to a conservative UQ procedure, potentially due to the limited number of meshes evaluated in the UQ.

G. COMPARISON WITH EXPERIMENTAL STUDIES

In this section, the simulation results are compared to existing experimental data. Although the geometries and operating conditions of these data differ slightly from the ones analyzed in this study, a qualitative comparison is performed to increase the confidence in the numerical results.

Isolated circular duct

The estimated values of the circular duct's drag coefficient were compared against results found in literature of similar geometries. Figure 6.18 shows the sectional drag co-

efficients of a 2D NACA 0012 profile for various Reynolds numbers [260], and the drag coefficient of the circular duct analyzed by Traub [261]—which has the same airfoil and aspect ratio as the one analyzed in this study. The drag coefficients obtained in this study for both the axisymmetric 2D and the 3D simulations are also included. The two CFD solutions show a very good agreement, as expected. The results from the 2D experiments indicate that the sectional drag coefficient, c_d, of the NACA 0012 profile decreases with the chord based Reynolds number, Re_c, from $\mathrm{Re}_c = 0.17 \times 10^6$ to $\mathrm{Re}_c = 0.33 \times 10^6$. In the experimental studies [260, 261], the Re_c influences the transition location over the airfoil sections, which does not occur in the fully-turbulent numerical simulations. From $\mathrm{Re}_c = 0.33 \times 10^6$ to $\mathrm{Re}_c = 0.66 \times 10^6$, the c_d of the NACA 0012 airfoil remains almost constant, according to Ref. [260]. Traub also studied the circular duct in the wind tunnel at $\mathrm{Re}_c = 0.17 \times 10^6$. This duct's c_d is higher than the c_d of the 2D NACA 0012 airfoil at the same Re_c. This a result of the increased velocities inside the duct due to the conservation of mass of the streamtube, which leads to increased suction inside the duct, when compared to the 2D airfoil at $\alpha = 0^o$. The flow acceleration in the duct is further increased due to the presence of a support structure in the experimental setup of Ref. [261]. Consequently, the lower c_d obtained in the RANS simulations is a result of the higher Re_c, and of the absence of a support structure in the computational approach.

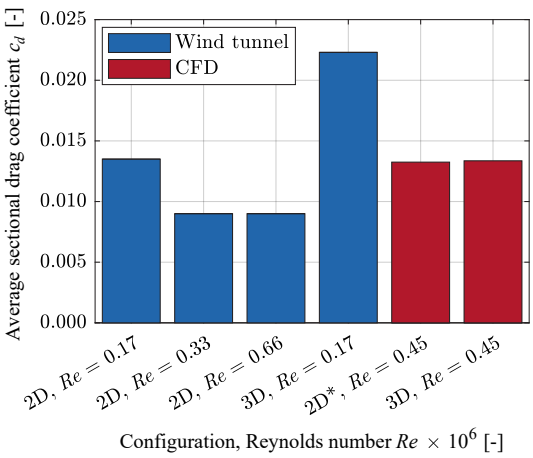

Figure 6.18: Comparison of the sectional drag coefficient obtained from CFD with the experimental data of Refs. [260, 261], for a NACA 0012 profile. "2D" = two-dimensional wing in Cartesian coordinates (infinite wing), "2D*" = two-dimensional wing in cylindrical coordinates (ring wing), and "3D" = complete circular duct (ring wing).

Isolated propeller

The only data available for validation of the propeller CFD results consist of experimental data obtained at the Open-Jet Facility (OJF) at Delft University of Technology. These data were provided via internal communication by T. Sinnige [141], who acquired the data using the same experimental setup as Li [240]. The data consists of thrust and torque measurements, performed with a rotating shaft balance at the same free-stream velocity

and advance ratios as the ones tested in the CFD simulations. Several factors can lead to discrepancies between the wind tunnel and CFD results, such as the boundary conditions of an open-jet tunnel, the simplification of the nacelle geometry and boundary conditions in the CFD simulations, the exclusion of the forces on the spinner in the CFD results, and the turbulence modeling of the computational approach. However, most importantly, the propeller used in the experimental campaign had 6 blades, whereas the propeller used in the CFD computations had its number of blades reduced to 4. Since the thrust produced by a propeller does not scale linearly with the number of blades, the wind-tunnel data could not be compared to the CFD directly. Therefore, it was decided to compare both high-fidelity results to a lower-order method capable of analyzing different numbers of blades. To this end, the program XROTOR [262] was selected to analyse the performance of the propeller geometries with both 4 and 6 blades. XROTOR is a program based on the lifting line method (LLM). Since XROTOR receives airfoil properties as an input, these were obtained for each radial location using XFOIL [243].

The CFD results of the propeller simulation were compared against the wind tunnel and LLM results at $V_\infty = 30$ m/s for three different advance ratios: $J = 0.7$, $J = 0.8$, and $J = 0.9$. Figure 6.19 shows the thrust and torque coefficients obtained per blade (i.e., $T_{c,\mathrm{b}} = T_c/B$ and $Q_{c,\mathrm{b}} = Q_c/B$), as well as the resulting propeller efficiency. When comparing the T_c results of the wind-tunnel experiment with CFD in Fig. 6.19a, similar trends are observed, although the curves present an offset. The thrust obtained per blade for the 4-bladed (CFD) case is higher than the thrust obtained per blade for the 6-bladed (WT) case, which is expected since a higher total thrust of the 6-bladed propeller leads to a higher induced axial velocity at the propeller disk, and thus to a lower effective angle of attack at each blade section. This can be confirmed by comparing the results obtained for four and six blades using the LLM, which show a comparable offset. The same effect is seen for the torque coefficient (Fig. 6.19b) and, in both cases, the lifting-line method over-predicts the loads, when compared to the wind tunnel or CFD data. Moreover, the LLM predicts a linear variation of propeller efficiency (Fig. 6.19c) with advance ratio, while the higher-fidelity methods predict a lower efficiency at high

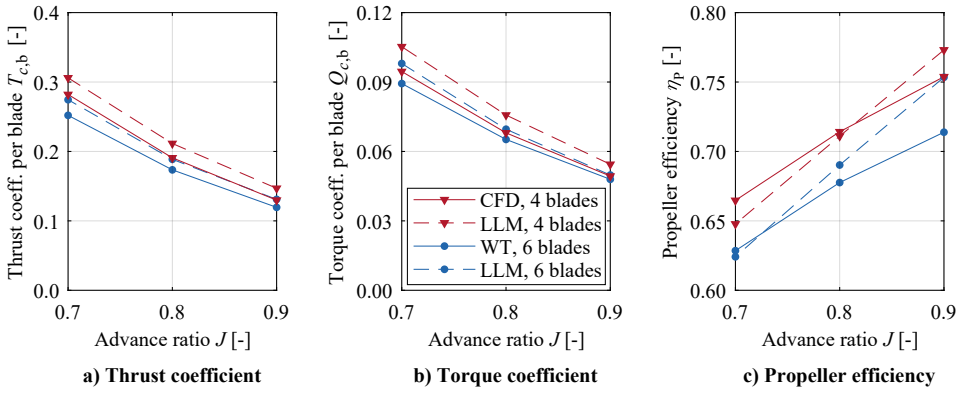

Figure 6.19: Comparison of isolated propeller performance with wind tunnel (WT) data and a lifting-line method (LLM). Note that forces are expressed per propeller blade.

advance ratios. There are several assumptions used in the LLM calculations which may lead to discrepancies with respect to the results obtained with higher fidelity methods; for example, given that XROTOR only accepts a limited number of airfoil characteristics as input, the airfoil polars considered in XROTOR lose accuracy. In any case, the qualitative agreement of the three methods indicates that the isolated propeller performance is captured correctly by the CFD simulations.

6.2.2. AERODYNAMIC INTERACTION PHENOMENA

The following section describes the most relevant aerodynamic phenomena caused by the interaction between the propeller and each duct. First, the circular ducted propeller case is discussed, followed by the square ducted propeller.

A. CIRCULAR DUCT

Existing literature indicates that a circular duct is able to produce thrust, in the installed configuration, provided that the thrust coefficient, T_c, of the propeller is high enough [173, 263, 264]. A high T_c leads to a higher slipstream contraction of the flow upstream of the propeller. The upstream slipstream contraction causes a change in the effective angle of attack of the duct sections, which then leads to the production of thrust by the duct. To confirm this, the pressure distribution at the surface of the circular duct is evaluated and compared in propeller-on and propeller-off conditions in Fig. 6.20. Figure 6.20c shows that a strong suction peak occurs at the inner surface of the installed duct, which is indicative of the change in effective angle of attack caused by the propeller. The region of increased suction is maintained up till the location of the propeller, where a sudden increase in static pressure is generated across the propeller disk. Figure 6.20c also presents the force vectors calculated from the average C_p chordwise distribution for the installed case. The force vectors show how the change in effective α and the consequent leading edge suction peak result in the production of thrust by the duct.

The instantaneous pressure distribution of Fig. 6.20d shows that the pressure is lowered everywhere along the leading edge of the duct, but more prominently closer to the propeller blade. The figure also indicates the presence of a strip of lower pressure at the duct surface, trailing from the blade tip. At the same location, the axial friction coefficient C_{fx} shown in Fig. 6.20e is negative, which indicates reversed flow. Therefore, the results indicate that, near the blade tip, the strong pressure jump across the blade causes flow separation in the axial direction at the duct's surface. The vorticity isosurface of Fig. 6.20e also indicates that the blade tip vortex continues to interact with the duct's boundary layer after the blade has passed. However, since the chordwise length of the reversed flow region is relatively short, this phenomenon does not have a strong effect on the overall propulsive performance of the system. The dominant effect of the propeller on duct performance is, therefore, the increased leading-edge suction. The drag produced by the duct is further reduced because the propeller is placed at the position of maximum thickness. Therefore, the increased pressure behind the propeller blades, visible in Fig. 6.20d, acts on a backwards-facing surface, while the increased suction ahead of the propeller acts on a forwards-facing surface. This leads to an additional net axial force which increases duct thrust.

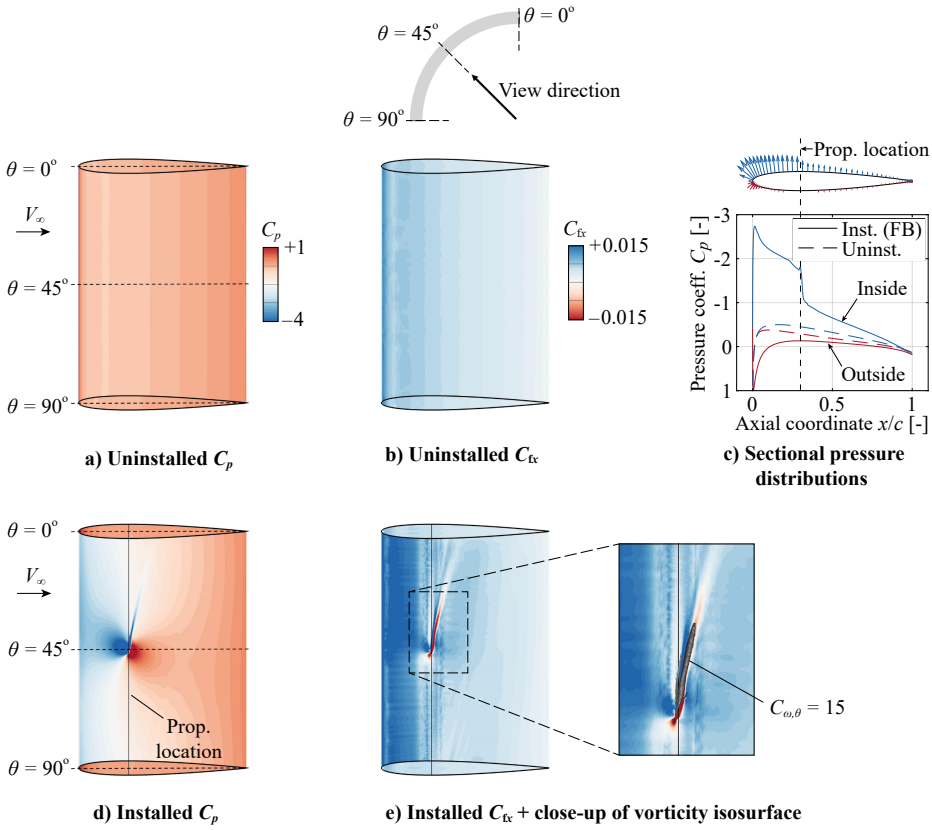

Figure 6.20: Pressure (left) and axial skin-friction (center) coefficient contours on the circular duct's inner surface. Tangential-vorticity isosurface of subplot e) only shown for $0.95 < r/R_p < 1$. Unsteady results obtained from FB model shown in the installed case ($\theta_b = 45^o$, $J = 0.7$, $T_{c_{FB}} = 0.87$).

B. SQUARE DUCT

The flowfield generated by the square ducted propeller is more complex than the flowfield of the circular ducted propeller case, since the geometry is no longer axisymmetric. Therefore, the steady results of the AD simulation are analyzed first, followed by the results of the FB simulation, to understand which additional unsteady phenomena occur.

Time-Averaged Effects (AD Simulation)

The steady results of the installed square duct simulation are relevant to understand the effect of the duct corners on the performance of the system. For this, Figs. 6.21a and 6.21b show the pressure and skin-friction coefficient distributions inside the duct. A small region of reverse flow ($C_{f_x} < 0$) is observed in the vicinity of the duct's corner, which is an indicator of flow separation. Moreover, Figs. 6.21c and 6.21d show that, in the installed case, the region of reverse flow is considerably larger, starting approximately at the axial position of the propeller, 30% duct chord. Fig. 6.21c also shows that, for the installed case, the static pressure recovers to higher values at the trailing edge for the spanwise locations far from the corner. Furthermore, Fig. 6.21c shows two regions of low C_p located symmetrically on either side of the corner, at the duct's trailing edge.

This is created by a pair of corner vortices, which are clearly visible in the surface streaklines. Literature also indicates that corners can be prone to the formation of vortices. Rubin and Grossman [246], who studied the flow over at the corner between two flat plates and also found "swirling flow in the corner", even though in their results "a closed vortical pattern is not established". However, in the present study, the propeller induces adverse pressure gradients which increase the magnitude of flow separation. This effect is also comparable to the flow separation that occurs at wing-body junctions at higher angles of attack [265], although the effective increase in angle of attack is, in this case, a consequence of slipstream contraction.

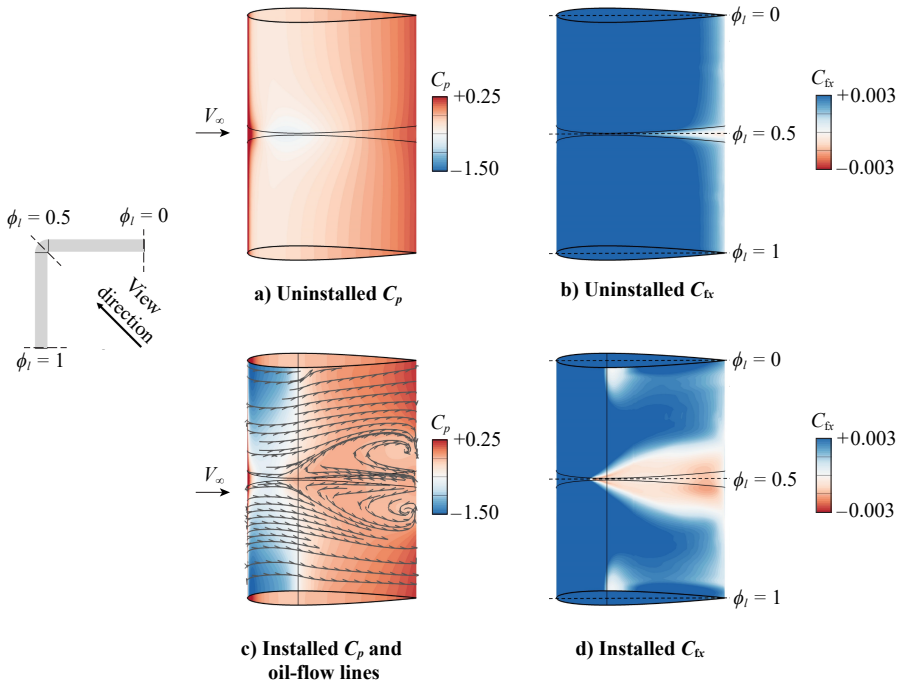

Figure 6.21: Pressure (left) and axial skin-friction (right) coefficient contours on the square duct's inner surface. Installed case (bottom) simulated with AD propeller model ($J = 0.7$, $T_{c_{AD}} = 1.13$).

In order to further investigate the flowfield at the square duct's corner, the flow's axial vorticity is shown in Fig. 6.22 for three planes: $x/c = 0.3$ (plane of the propeller disk), $x/c = 1$ (at the duct's trailing edge) and $x/c = 1.5$ (downstream of the duct). In Fig. 6.22, the in-plane velocity vectors are also shown. The uninstalled vorticity contours indicate that the axial vorticity in the duct's boundary layer grows towards the trailing edge, which is associated with a minor spanwise movement of the flow towards (inner surface) or away from (outer surface) the corner. This is caused by the increased suction on the inside of the corner of the duct (see Fig. 6.21c), and reduced suction on the outside of the corner due to 3D-relief effects. Figure 6.22b also shows the influence of the small separated region at the corner in the vorticity distribution, although in the wake of the system (Fig. 6.22c), no significant swirl is observed.

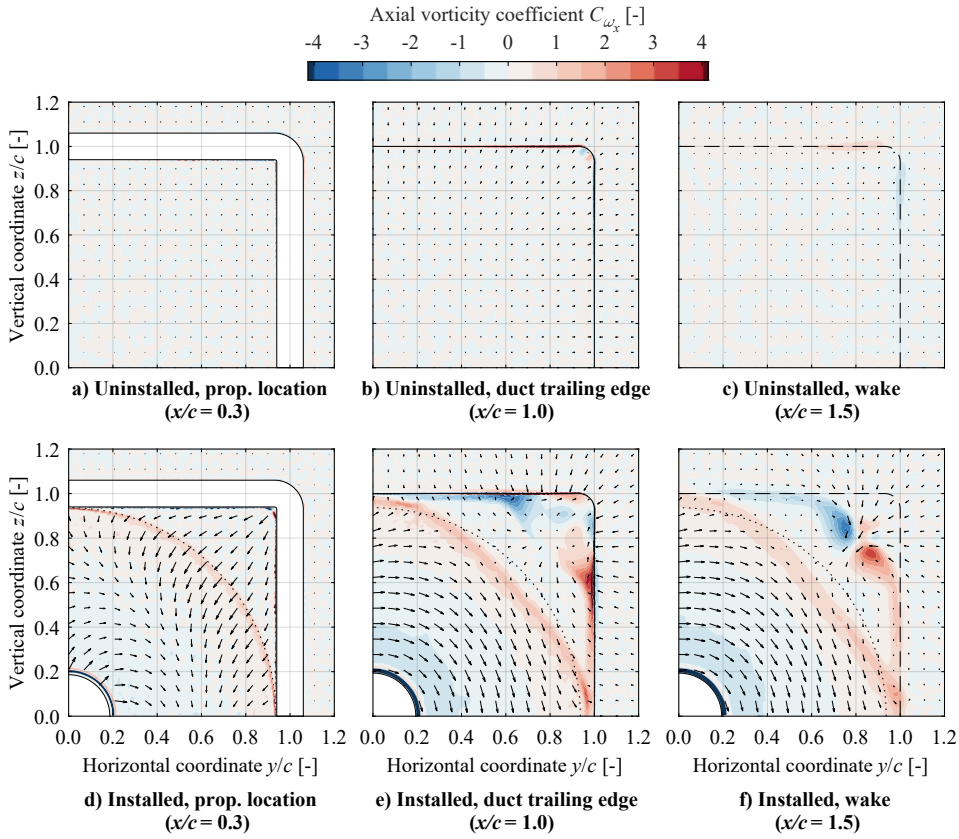

Figure 6.22: Axial vorticity contours and in-plane velocity vectors around the corner of the square duct, at three axial locations. Installed cases simulated with AD model ($J = 0.7$, $T_{c_{\mathrm{AD}}} = 1.13$).

When the propeller is installed, several additional phenomena are visible. Firstly, Fig. 6.22d shows the swirl imposed by the AD. This leads to a generation of axial vorticity at the inner and outer radius of the AD model, due to the shear that occurs with the surrounding flow. In practice, this vorticity is concentrated in the root and tip vortices of the propeller, respectively. Figure 6.22d also shows a significant slipstream contraction at the location of the actuator disk, as the velocity vectors are directed away from the corner, in the direction of the AD. This effect can, in fact, contribute towards the strong separation which occurs inside the square duct under these operating conditions, as shown in Figs. 6.22e and 6.22f. These figures show how, towards the trailing edge, there is a spanwise flow along the duct surface towards the corners, in line with Fig. 6.21c. Near the corner, flow reversal occurs, and the flow separates from the wall, moving inwards towards the propeller axis along the bisector of the duct quadrant. Consequently, downstream of the duct (Fig. 6.22f), two distinct regions of concentrated vorticity of opposite sign are observed. Therefore, both Figs. 6.21 and 6.22 indicate the generation of vortices by the square ducted propeller. This phenomenon constitutes a disadvantage of the square duct, as the vortices also contribute towards a higher pressure drag of the system.

Unsteady Effects (Full-Blade Simulation)
Since the corner vortices can have a strong detrimental effect on the performance of the square ducted system, it is important to analyze how this phenomenon is affected by the unsteady excitation of the propeller blades. Figure 6.23 shows axial vorticity coefficient, C_{ω_x}, isosurfaces for the installed simulations with the AD (Fig. 6.23a) and with the FB model (Fig. 6.23b). Figure 6.23 shows that the corner vortices generated in the AD simulation are also present in the FB case, although they appear to be weaker. This is an artifact of the lower thrust of the FB with respect to the thrust of the AD model, at the same advance ratio. The thrust of the AD was set to be equal to the thrust of the isolated propeller for each of the three advance ratios considered. The differences in thrust between the isolated and ducted propeller cases are discussed with more detail in the next section. Figure 6.23a also shows streaks of increased positive vorticity generated near the mid-section of each duct edge. This vorticity is a consequence of the high shear that occurs between the slipstream edge and the duct boundary-layer. In an unsteady sense (Fig. 6.23b), this region of increased vorticity manifests itself as periodic patches of increased vorticity, generated during each blade passage. Figure 6.23b also shows the tip vortices present in the propeller slipstream, although they do not form clear helical filaments as occurs for unshrouded propellers. This is due to the cyclic loading that the blade undergoes every 90°, as discussed in the following section.

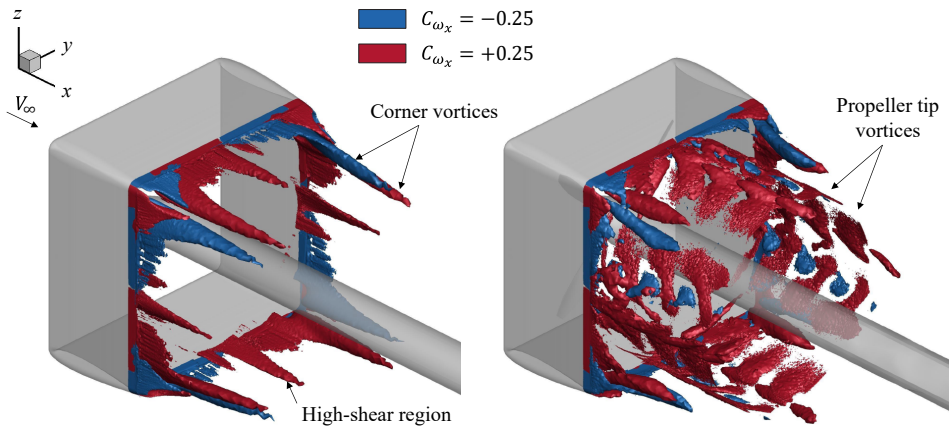

a) AD propeller model **b) FB propeller model**

Figure 6.23: Axial vorticity coefficient isosurfaces from the installed square duct simulations ($J = 0.7$), with AD (left) and FB (right) models. Isosurfaces are only shown for axial locations downstream of the duct trailing edge ($x/c > 1$), and for $r/R > 0.5$.

6.2.3. PROPELLER AND DUCT LOADS

After having analyzed the main aerodynamic interaction phenomena present in the ducted propeller systems, the main performance parameters are discussed in the following subsections. First, the loading distributions on the propeller are presented, followed by the loading distributions on the ducts. Finally, combined performance of the propeller and duct is discussed.

A. BLADE LOADING DISTRIBUTIONS

The radial thrust and torque distributions over a propeller blade obtained from the FB simulations are shown in Fig. 6.24. For the ducted propeller simulations, Fig. 6.24 shows both the average and the spread of the radial distributions considering all the recorded time steps. The average distributions reveal that the propeller operates at a higher loading for the isolated case, followed by the square duct case. The propeller therefore operates at the lowest loading when installed with the circular duct. The main reason for the differences in averaged thrust and torque are the inflow velocities at the propeller disk. The effective inflow velocity is highest for the circular duct, since the circular duct causes a higher contraction of the streamtube passing through the duct than the square duct, for the same duct airfoil thickness. The effective inflow velocity is lowest for the isolated propeller, which perceives undisturbed free-stream flow. However, near the blade tip ($r/R \rightarrow 1$), the circular ducted propeller generates the highest thrust and torque. This is due to the constant low tip-clearance for the circular ducted propeller. The low tip clearance reduces the tip loss effect and the strength of the blade tip-vortex, thus increasing the loading at large radial locations.

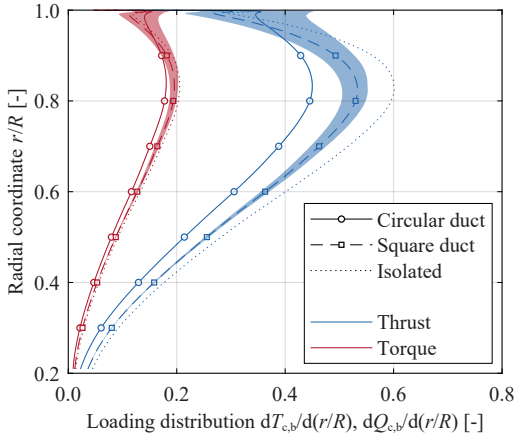

Figure 6.24: Radial propeller loading distributions in the isolated and installed (FB) configurations, with the propeller operating at $J = 0.7$. Shaded area indicates the spread in loading throughout a propeller revolution.

A comparison of the spread of the thrust and torque distributions for the two ducted cases reveals that the radial variations of T and Q are signficant for the square ducted propeller, while practically no variations in loading can be observed for the circular duct, as expected. In the square duct, the amplitude of the thrust fluctuations at the radial location of maximum loading ($r/R = 0.85$) equals 9% of the mean thrust at that location. The amplitude of this unsteady loading increases towards the tip, exceeding 70% of the mean thrust at $r/R = 0.99$, partially due to the lower mean thrust levels at that location. The blade experiences these loading variations for two reasons. Firstly, the inflow velocities at the propeller disk location depend on the azimuthal position of the blade, since the blockage effect of the duct is not axisymmetric. Secondly, the tip clearance of the blade is not uniform inside the square duct, which leads to temporal variations of the tip-loss reduction felt by the propeller blade. Consequently, the variations in blade load-

ing are highest near the tip and, while on average the blade tip-loading is highest for the circular duct, for determined phase angles, the tip-loading is higher in the square duct. This is detrimental for both the noise emissions and fatigue life of the propeller.

B. DUCT LOADING DISTRIBUTIONS

The spanwise distributions of thrust at the circular and square ducts, from the installed FB simulations, were analyzed in order to understand which configuration enables a better propulsive performance of the duct. Figure 6.25 shows the thrust coefficient distributions along the duct perimeter. The thrust coefficient, T_c, is decomposed into a pressure contribution, T_{cp}, and a friction contribution, T_{cf}. In Fig. 6.25a, which presents the circular duct, the distributions are show versus the azimuthal coordinate of the duct section with respect to the nearest blade. The figure indicates that T_{cf} is approximately constant with respect to the spanwise location, whereas T_{cp} sees large variations. T_{cp} is largest for the duct sections near the blade, which was already expected from the analysis of Fig. 6.20. Furthermore, Fig. 6.25a also indicates that, in a reference frame that rotates with the propeller, the temporal variation of the spanwise distributions of thrust at the duct is relatively small.

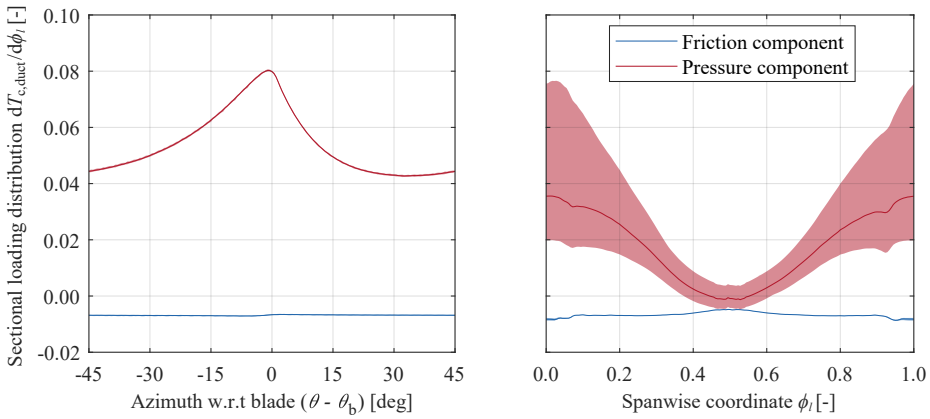

a) Circular duct **b) Square duct**

Figure 6.25: Spanwise thrust coefficient distributions along the duct perimeter in the installed configurations (FB, $J = 0.7$). Shaded area indicates the spread in loading throughout a propeller revolution. Note that the x-axes are expressed in the propeller and duct reference frame for subplots (a) and (b), respectively.

Figure 6.25b shows the thrust distributions for the square duct with respect to the spanwise location ϕ_l. The figure indicates that the spanwise variation of the friction thrust coefficient is also smaller than the spanwise variation of the pressure thrust coefficient for the square duct. Still, T_{cf} is higher (less negative) at the corner, where $\phi_l = 0.5$, than for spanwise locations far from the corner. This is due to the reverse flow region near the corner, identified previously in Fig. 6.21. Figure 6.25b also shows that the temporal variation of T_{cf} for each duct section is negligible, which indicates that the flow separation in the corner does not vary significantly with the blade position. In other words, the increased separation in the corner of the duct is a consequence of the slipstream contraction observed in Fig. 6.22, and not an unsteady phenomenon which is

excited at the blade-passage frequency. The T_{cp} distribution, on the other hand, shows large fluctuations with the periodic passage of the propeller blades. On average, the duct produces more pressure thrust at the locations far from the corner. Towards the corner of the square duct, T_{cp} reduces due to two main reasons. Firstly, due to the larger distance between the corner sections and the propeller disk, the effect of slipstream contraction on the local angle of attack perceived by the corner sections reduces. Secondly, the corner's axial flow separation and the associated corner vortices also contribute towards the generation of drag at the duct. The comparison of Figs. 6.25a and 6.25b also indicate that the circular duct is able to produce more thrust than the square duct, for the same rotational speed of the propeller, even though the propeller itself produces more thrust when placed inside the square duct.

C. SYSTEM THRUST AND EFFICIENCY

In this section, the loading distributions are integrated to understand how the thrust produced by the different systems compares, as well as their efficiency. For the installed systems, the propulsive efficiency is defined as $\eta_{\text{p,system}} = V_\infty T_{\text{system}} / P_{\text{s}}$, where $T_{\text{system}} = T_{\text{P}} + T_{\text{duct}}$. Firstly, Fig. 6.26 shows the ratio of duct thrust to system thrust obtained from the installed AD simulations, for both ducts and for the three operating conditions tested, $J = 0.9$, $J = 0.8$ and $J = 0.7$. The figure indicates that both ducts contribute more towards the system's thrust as the thrust setting increases, as expected from literature [173]. This is due to the higher slipstream contraction that is perceived by the duct when the thrust setting increases. Besides, Fig. 6.26 also shows that the thrust of the circular duct with respect to the system's thrust (15% at $T_{\text{c,system}} \approx 1.0$) is higher than the square duct's contribution (2.5% at $T_{\text{c,system}} \approx 1.0$), for all operating conditions tested. This result is consistent with the discussion of the previous section. For the square duct at the lowest thrust setting, the pressure drag in the corners of the duct and friction drag outweigh the suction generated on the leading edge due to slipstream contraction, leading to a negative thrust contribution.

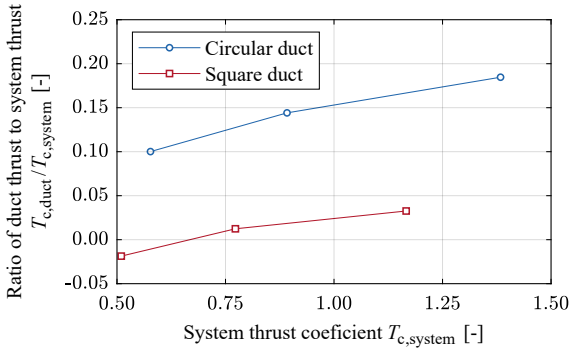

Figure 6.26: Ratio of duct thrust to total system (i.e., propeller + duct) thrust obtained from the AD simulations for three propeller thrust settings.

Finally, Fig. 6.27 shows the time-averaged thrust coefficient and efficiency of the three systems studied with the FB propeller model. Figure 6.27 shows that the isolated propeller is the propulsion system which produces more thrust, for the chosen advance

ratio. The main reason for this is the lower axial velocity of the flow at the propeller disk, when compared to the ducted configurations. However, even though the isolated propeller produces approximately 7% more thrust than the ducted configurations, the efficiency of the circular ducted system is higher than the efficiency of the isolated propeller ($\Delta\eta_{p,system} = +0.03$). This is primarily because the isolated propeller operates at a lower effective advance ratio than in the circular duct, and therefore operates at a less optimal point along the efficiency curve of the propeller (see Fig. 6.19c).

As discussed previously, the propeller produces more thrust inside the square duct than inside the circular duct (at a fixed J setting), whereas the circular duct produces the more thrust than the square one. At the operating conditions tested, both ducted systems produce the same net thrust (with a difference of only 0.4%), as visible in Fig. 6.27. At the same system thrust, the circular ducted propeller is estimated to be 4.5% more efficient than the square ducted propeller. However, this value has to be interpreted with caution since, for the same system thrust, the propeller produces more thrust inside the square duct. This occurs because the propeller operates at a lower effective advance ratio, since the average inflow velocity to the propeller disk is lower for the square duct than for the circular duct. Therefore, it is at a less efficient operating point along its efficiency curve (see Fig. 6.19c), and for a fair comparison, the blade pitch of both ducted systems would have to be adapted to maximize efficiency at the same total system thrust. This would decrease the efficiency penalty of the square ducted system. In any case, the aerodynamic phenomena discussed in the previous sections confirm that, for a single propeller at a high thrust setting, a circular ducted system is more efficient than a square one.

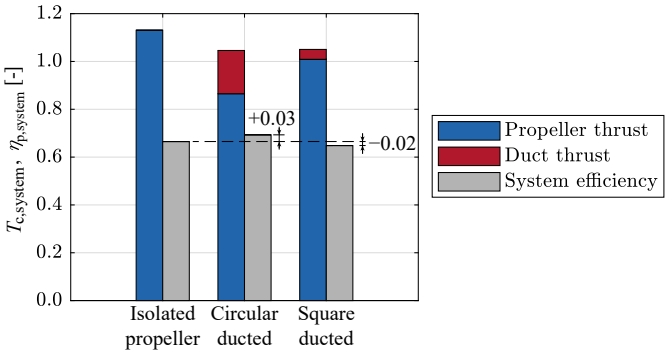

Figure 6.27: Thrust coefficient and system efficiency of the three propulsion systems, obtained from the FB model for $J = 0.7$.

6.2.4. IMPLICATIONS FOR DISTRIBUTED-PROPELLER SYSTEMS

These findings show that the circular ducted propeller is the best solution for a single propeller operating at a high thrust setting in uniform inflow. However, several differences have to be taken into account for an actual OTWDP application:

- The wing replaces the lower part of the duct. Thus, the contribution of the duct to the net axial force is lower for an OTW propeller than for an uninstalled propeller. However, the changes in wing performance due to the presence of the duct must also be accounted for.

- For most OTW propeller positions, the velocity field induced by the wing degrades the propeller efficiency (see Sec. 6.1). Since the duct can reduce this non-uniformity at the propeller location, the effect of the duct on the propeller efficiency is more positive for an OTW propeller than for an uninstalled propeller.

- The average thrust setting throughout a typical mission is significantly lower than the ones investigated analyzed in this section ($T_{c,mean} \approx 0.1$; see Ch. 10). Therefore, the relative impact of friction drag increases and the duct-thrust benefit, especially of the circular duct, is lower or negative.

- Multiple adjacent propellers are used in an OTWDP array. While a single circular duct presents less wetted area than a single square duct, this may not be the case for an array of $N \gg 1$ adjacent propellers. This is reflected in Fig. 6.28, which plots the wetted area of the duct, normalized with the duct chord c and the propeller diameter D, versus the number of propellers it has to cover. If an infinitely thin duct wall is assumed, then an array of square ducts sharing one wall with each neighbor presents a lower wetted area than the circular-duct equivalent for $N > 7$. If a "2D" envelop duct is considered instead, then the wetted area is lower than the circular and square options for $N \geq 2$, since the additional wall between each propeller is removed.

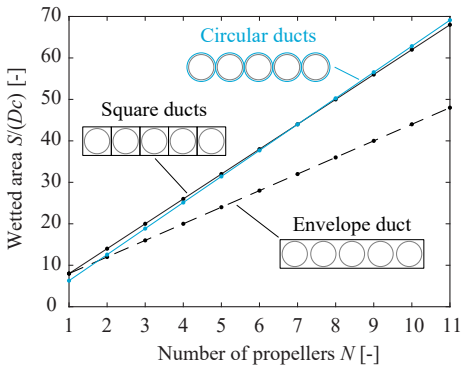

Figure 6.28: Wetted area of circular, square, and envelope ducts of chord c for N propellers of diameter D, assuming infinitely thin duct walls and zero tip clearance.

Based on this qualitative discussion and the detailed numerical investigation of the interaction effects, it appears that each configuration has its advantages, and therefore the best solution depends on the operating conditions and design objectives of the OTWDP system. In summary:

- Unducted OTW propellers are beneficial for aerodynamic performance if the propellers are placed near the trailing edge, where the propulsive-efficiency penalty is small (see Sec. 6.1 and Ch. 8). In that case, a duct would increase the drag during most of the mission.
- Circular duct arrays are beneficial if propeller noise and fatigue life are a limiting factor, since they reduce the unsteady loading more than square ducted propellers. Circular ducts can also be beneficial from a performance perspective if the thrust coefficient is high during a large part of the mission, or during a heavily-sizing performance constraint.
- Envelope ducts are beneficial for the aerodynamic performance if the propellers are placed far from the trailing edge. They are the most effective to mitigate the 2D velocity disturbance above an unswept wing, and present significantly less wetted area than circular or square duct arrays (Fig. 6.28). The motor pylons can also be used to support the envelope duct (see Fig. 6.1), and part of their friction drag can be offset by the swirl-recovery effect [240].
- Square ducted arrays do not present any aerodynamic advantages over the envelope duct, due to the increased wetted area and corner-flow effects. They may, however, be more beneficial than an envelop duct from a acoustic perspective, if the propeller-propeller interaction were to lead to significant noise penalties (see Sec. 6.3). A hybrid variant, with a square entrance and gradual transition to a circular cross-section at the propeller location (see e.g. Refs. [52, 71, 153]), is also expected to further reduce the unsteady loads and noise of the propellers.

Since the optimum duct shape is not known at this stage, its effect on system performance is cannot accurately be accounted for in the following chapters. In this research, the objective of the OTWDP system is to maximize the aero-propulsive efficiency. Therefore, neglecting the duct can be considered a conservative approach, since a duct would only be included if it further enhanced the aero-propulsive efficiency of the system. If, however, noise or fatigue constraints drive the design of the system, then a duct which degrades the aero-propulsive efficiency may be required. Especially in that case, additional research is required to analyze the effect of the duct geometry on system performance.

6.3. PROPELLER–PROPELLER INTERACTION

If an OTWDP system presents no duct, or if it uses an envelope duct as suggested in the previous section, then each propeller interacts with the adjacent one(s). However, contrary to the aerodynamic interaction between multiple rotors in hover conditions, the effects in forward flight remain relatively unexplored (see Ch. 2). It is unclear which interaction mechanisms lead to a loss of thrust in forward flight, or what effect they have on the propulsive efficiency, if any. Furthermore, the influence of many design parameters, such as rotation direction, axial separation, incidence angle, or relative blade phase angle, is unknown. These shortcomings indicate that a more in-depth understanding of the flow field is required before design guidelines and mitigation strategies can be established to improve the efficiency and noise characteristics of the system.

The objective of this section is therefore to analyze the aerodynamic interaction between multiple propellers operating in close proximity in forward flight, to understand how this affects the performance and wake evolution of the system. Due to the potential relevance of unsteady effects (e.g. blade-blade interaction), a numerical simulation of the interaction between N propellers would require computationally intensive simulations with meshes of $N \cdot B$ blades, which is ineffective to explore the large parameter space. Therefore, an experimental approach is selected. Three side-by-side propellers, without wing, are studied in order to simplify the problem as much as possible, and focus on how a determined propeller is affected by the interaction with its neighbors. In most measurements, the propellers are placed in very close proximity, since previous studies show that the effects on propeller performance increase exponentially as the separation distance is reduced [183, 184, 187]. Although the interaction could be minimized by increasing the separation, this reduces the benefits produced by the propeller on the wing (see Ch. 8), and therefore it is of interest to study the limit case of propellers with minimum separation. The experimental setup employed for this is described in Sec. 6.3.1. Section 6.3.2 then discusses how the flow field upstream and downstream of the propeller is affected by the adjacent ones, and what effect this has on propeller performance. Subsequently, Sec. 6.3.3 presents how these interaction effects vary with different parameters such as the rotation direction, angle of attack, axial position, relative blade-phase angle, or differential-thrust settings.

6.3.1. EXPERIMENTAL SETUP

A. FACILITY AND MODEL DESCRIPTION

The experiments were performed at the low-speed, low-turbulence tunnel (LTT) at Delft University of Technology, similarly to Experiment 1 of Sec. 6.1. An overview of the experimental setup is provided in Fig. 6.29, with the main dimensions and configurations presented in Fig. 6.30. An array of three propellers was used in the setup, so that the flow conditions perceived by the middle propeller were representative of a distributed-propulsion configuration. Since the influence of one propeller on another decreases rapidly with separation distance, the influence of additional, more distant propellers on the middle propeller is a second-order effect, and thus the quasi-periodicity condition

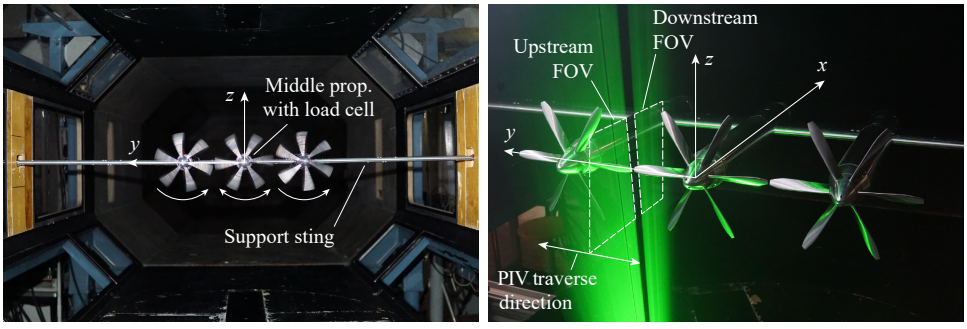

a) Test section (viewed from front) **b) Close-up view of propellers**

Figure 6.29: Photographs of the experimental setup in the wind tunnel, indicating main components and the illumination plane of the PIV setup.

can be approximated by placing just one propeller on each side. These six-bladed, steel propellers have a radius of $R = 101.6$ mm and are known as the "XPROP-S" propellers, whose blade chord and pitch distributions are given in Fig. 6.31. These propellers are a 1:2 scaled model of the propeller used in Experiment 2 of Sec. 6.1, with a modified trailing-edge thickness for manufacturability reasons. Additional characteristics of the propellers can be found in Refs. [90, 266]. Additionally, a fourth, mirrored version of the propeller was used to be able to change the rotation direction of the middle propeller and replicate a counter-rotating configuration (Fig. 6.30b). These propellers were installed on a straight, untapered support sting consisting of a NACA 0020 profile with an original airfoil chord of 100 mm, but with the last two millimeters truncated to facilitate the manufacturing process. The leading edge was located approximately $3R$ downstream of the propeller disks to limit the upstream influence on the propellers.

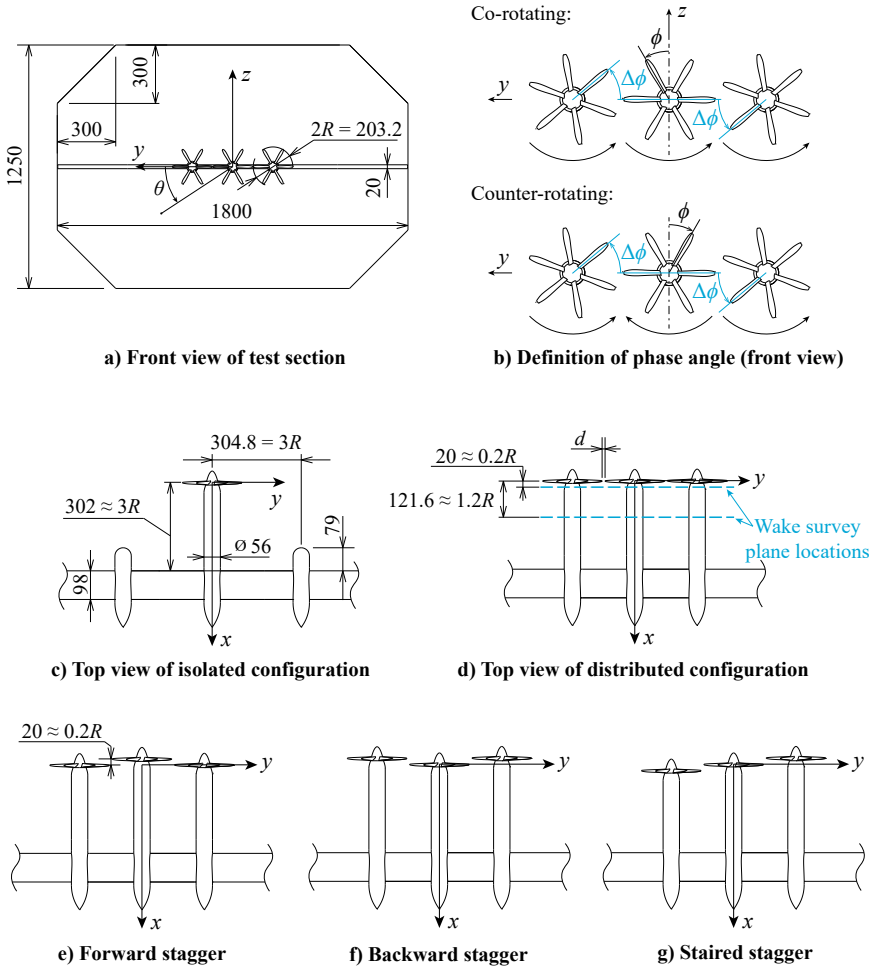

a) Front view of test section

b) Definition of phase angle (front view)

c) Top view of isolated configuration

d) Top view of distributed configuration

e) Forward stagger

f) Backward stagger

g) Staired stagger

Figure 6.30: Overview of test setup, indicating main dimensions, reference systems, and configurations. Dimensions in mm.

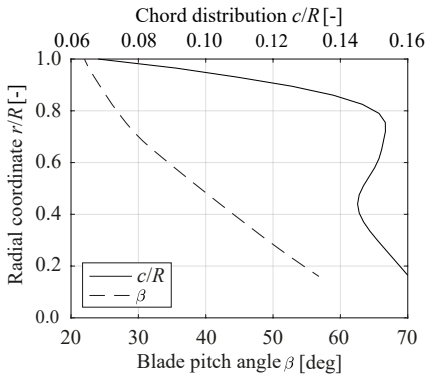

Figure 6.31: Blade chord and pitch distributions of the six-bladed XPROP-S propeller. Figure adapted from Ref. [90].

The propellers were driven by brushless DC electrical motors, each powered by a dedicated PWM-controlled trapezoidal electronic speed controller (ESC) and an externally programmable 5 kW DC power supply. The electrical motors were housed inside an aluminum nacelle, which could be fixed at different spanwise locations on the support sting in order to vary the separation distance between the propellers. The left and right nacelles could be removed and replaced with caps to minimize the influence on the middle propeller during "isolated" propeller measurements, as shown in Fig. 6.30c. Moreover, several inserts could be installed in the nacelles to vary their length and therewith change the stagger of the propellers; that is, to change their relative axial position (Figs. 6.30d-6.30g).

B. TEST CONDITIONS & CONFIGURATIONS

Measurements were performed at a nominal freestream velocity of $V_\infty = 30$ m/s, with a propeller blade pitch of $30^o \pm 0.05^o$ at 70% of the blade radius. The blade pitch angle is such that the maximum efficiency is obtained at a high thrust setting, and is therefore more representative of take-off conditions than of cruise conditions. This setting was preferred over larger pitch angles since higher thrust coefficients and blade tip Mach numbers could be achieved, which made both the aerodynamic and acoustic interaction effects more clearly identifiable in the experiment. The propellers were evaluated for advance ratios ranging from $J = 0.8$ (184.5 Hz) to $J = 1.35$ (109.3 Hz), as reflected in Table 6.5. This corresponds to thrust coefficients T_c between 0 and 1.1, blade tip Mach numbers ranging from 0.22 to 0.36, and a blade Reynolds number at 70% radius ranging from approximately $3.8 \cdot 10^4$ to $6.0 \cdot 10^4$. In addition to testing the "distributed" and "isolated" propeller configurations, several measurements were performed with a single propeller installed on one of the three nacelles, to distinguish the interaction with adjacent propellers from the interaction with adjacent nacelles.

The rotational speed of the propellers was controlled with custom-made software, achieving a standard deviation of the rotational speed of 0.1 Hz during random-phase measurements, and of 0.05 Hz during phase-controlled measurements. The random-phase measurements were performed by increasing the rotational speed of the two outer propellers by 0.03 Hz relative to the center propeller, such that the relative blade angles

between the propellers $\Delta\phi$ would cover approximately one blade passage (0^o to 60^o) throughout the acquisition time of each measurement point. Thus, the averaged reading represents a phase-random measurement. This offset in rotational speed corresponded to a change in advance ratio below 0.03%, and therefore had a negligible effect on (isolated) propeller performance. In the phase-controlled measurements, the blade position of the two outer propellers was controlled relative to the blade position of the middle propeller, and the performance and noise production of the system was evaluated in steps of 10^o (see Table 6.5). The standard deviation of the relative blade-phase angle during these measurements was below 0.3^o. Therefore, the controller was sufficiently accurate to study the effect of the relative blade-phase angles on noise production without any appreciable loss in coherence of the noise sources [197].

Additionally, the angle of attack, rotation direction, tip clearance, and stagger of the propellers was varied. The angle of attack α could be set with an accuracy of $\pm 0.1^o$, which was the maximum difference in installation angle observed among the three propellers and the horizontal axis (at $\alpha = 0^o$) in repeated installation procedures. Regarding the tip clearance between adjacent propellers, most measurements were performed at a small separation distance ($d/R = 0.04$), since numerous previous studies have already shown that the interaction effects are strongest at small separation distances, and rapidly reduce as the separation distance increases [184, 186, 187]. Repeated installation procedures showed that the tip clearance varied by less than ± 0.5 mm ($d/R \pm 0.005$) among the different measurements of a determined d/R setting. Finally, the relative axial position of the propellers could be accurately changed by including one or more inserts of 20 mm length in each nacelle. These inserts were used to simulate the three configurations shown in Figs. 6.30e–6.30g, in addition to the baseline, zero-stagger configuration. A summary of these parameters is given in Table 6.5. The results discussed in Secs. 6.3.2 and 6.3.3 are presented for the baseline parameter values, unless explicitly mentioned otherwise.

Table 6.5: Overview of test conditions. Baseline values indicated in bold.

Parameter	**Values**
Freestream velocity V_∞ [m/s]	**30**
Blade pitch at $r/R = 0.7$ [deg]	**30**
Advance ratio J [-]	$0.80 < J < 1.35$ (**1.00**)
Thrust coefficient T_c [-]	$0 < T_c < 1.1$ (**0.45**)
(P)ropeller/(N)acelle configuration	**3P + 3N** ("distributed"), 1P + 3N, 1P + 1N ("isolated")
Relative blade-phase angle $\Delta\phi$ [deg]	**random**, 0, 10, 20, 30, 40, 50, 60
Rotation direction	**co-rotating**, counter-rotating
Angle of attack α [deg]	**0**, 5
Tip clearance d/R [-]	**0.04**, 1.00
Stagger $\Delta x/R$ (left, mid, right) [-]	**in-line (0, 0, 0)**, forward (0, 0.2, 0), backward (0.2, 0, 0.2), staired (0, 0.2, 0.4)

C. MEASUREMENT TECHNIQUES

This section describes the three types of measurement performed. For the normalization of the recorded performance and flow-field parameters, the effective freestream velocity was corrected for nacelle, support-sting, and slipstream blockage. The blockage effect of the nacelles and support sting at the center of the middle propeller was estimated numerically by representing them as a distribution of point sources and placing image sources to mimic the wind-tunnel walls, as recommended in Ref. [267]. Glauert's slipstream blockage correction was applied to account for propeller thrust. Combined, the effect of blockage was found to range between −0.5% and +1.0% of the nominal freestream velocity, depending on the configuration and thrust setting. In addition to the measurements described here, microphone measurements were performed to gain a preliminary understanding of the changes in noise due to aerodynamic interaction. For the description and results of those measurements, the reader is referred to Ref. [233].

Load Measurements

The middle propeller was instrumented with an ATI MINI-40E six-component force sensor to measure forces and moments on the propeller (i.e., on the blades and spinner). The force sensor was calibrated for a full-scale load range of 60 N, 20 N, and 1 Nm for thrust, in-plane forces, and torque, respectively. For each configuration, propeller forces were measured for several advance ratios (see Table 6.5). Data were sampled at 10 kHz and averaged over 5 seconds. In every measurement run, each advance-ratio setpoint was measured at least four times, and the measurement sequence was randomized to convert potential systematic errors within a measurement run (i.e., drifts) into random error. Additionally, repeated measurements were performed after several days and configuration changes for selected cases to verify the reproducibility of results. The differences between repeated measurement runs were found to be comparable to the scatter observed within a single run. Third-order polynomial fits were made through the thrust and torque curves to model the propeller response over the considered J range.

The variations in motor temperature were found to appreciably affect the load-cell readings, and therefore a linear temperature calibration was applied, similarly to Ref. [266]. The temperature-calibration process was verified by comparing thrust measurements to the data obtained from an external balance, as detailed in Ref. [233]. The uncertainty of the performance curves was estimated taking into account potential misalignments in propeller angle-of-attack, errors in the temperature-calibration factors, and random error in the data due to e.g. variations in operating conditions. The resulting errorbars are included in performance curves of the results section. These errorbars present the 95% confidence interval for a determined propeller geometry. They do not include potential errors due to deviations in blade geometry from the theoretical blade shape, or misalignments in blade-pitch angle. A comparison of the four, theoretically identical propellers showed deviations of approximately $T_c \pm 0.005$ and $Q_c \pm 0.0005$ between each other. This error has a second-order, negligible effect on the *changes* in performance reported here, but should be taken into account when comparing the absolute performance of the propeller to numerical simulations with idealized geometries.

Wake-Pressure Measurements

The total-pressure distribution behind the propellers was measured at two locations: close to the propeller ($x/R = 0.2$), which reflects the non-uniform loading distribution on

the propeller disk, and further downstream ($x/R = 1.2$), to determine whether the slipstreams had deformed significantly at a typical wing leading-edge location. The wake pressures were measured for the configurations shown in Figs. 6.30c–6.30f, and the position of the two survey planes is shown in Fig. 6.30d. For this, two types of probes were used. Firstly, a single Pitot probe was traversed horizontally in the y-direction ($z/R = 0$) directly behind the propeller, with a spatial resolution ranging from 3 mm in the inboard region to 0.5 mm in the blade-tip region. This provided an appropriately resolved total-pressure distribution and location of the slipstream edge. Secondly, a vertical wake rake containing 74 total-pressure probes, separated 3 mm, was traversed in y-direction behind the propellers, also in steps of 3 mm. This provided a 2D pressure distribution of the flow field, though with reduced resolution compared to the single probe.

The pressure ports were connected to an electronic pressure scanner. The pressure sensors present an uncertainty of ±4 Pa on the full-scale measurement range, corresponding to ±0.7% of the freestream dynamic pressure. Repeated measurements showed only minor quantitative differences (±2 Pa), and no qualitative differences. Each data point was averaged over 10 seconds measurement time, at an acquisition frequency of 10 Hz.

Particle-Image Velocimetry

A stereoscopic particle-image velocimetry (PIV) setup was used to obtain the velocity distributions upstream and downstream of the propellers. For this, a query plane was set up parallel to the xz plane in between two of the propellers, as shown in Fig. 6.29b. A mixture of diethylene-glycol and water was used for flow seeding, obtaining tracer particles with an average diameter and relaxation time below 1 μm and 1 μs, respectively. A 200 mJ Nd:YAG laser was used for illumination, positioned beneath the test section. The light was directed through a plexiglass plate in the wind-tunnel floor, generating a laser sheet of approximately 2 mm thickness upstream and downstream of the propellers. Four 16-bit LaVision Imager sCMOS cameras were used for image acquisition, two for the field-of-view (FOV) upstream of the propellers, and two for the FOV downstream of the propellers. These cameras feature a 2560 × 2160 pixel sensor with a pixel size of 6.5 μm, and were equipped with 105 mm lenses at f/11 aperture.

For each measurement, 500 uncorrelated images were acquired at 15 Hz. By traversing the cameras and laser in y direction, multiple parallel planes were sampled, evaluating a total of 26 planes in steps of 1.8 mm (in the tip region) to 5 mm (at the more inboard blade locations). A combination of these planes provided volumetric information of the time-averaged velocity field upstream and downstream of the propellers. A summary of the characteristics of the setup is provided in Table 6.6. The table also includes the uncertainty of the velocity field, computed following the method outlined in Ref. [268]. Note that this uncertainty does not included potential errors due to misalignment of the illumination plane relative to the model, or possible deviations from the nominal test conditions established in Table 6.5. An inspection of the flow field immediately upstream of the isolated propeller, which in theory should be symmetric with respect to the $z = 0$ plane, showed differences of up to 2% of the freestream velocity between the upper and lower halves of the FOV. This indicative error band should be taken into account when comparing the results to independent numerical or experimental analyses.

Table 6.6: Main characteristics of the PIV setup.

FOV	Upstream	Downstream
Field of view $x \times z$ [mm^2]	100×120	100×160
Number of (uncorrelated) images [-]	500	
Number of parallel planes [-]	26	
Plane locations [mm]	$y \in [51.6, 145.2]$	
Focal length [mm]	105	
Pixel shift [pixel] (at V_∞)	10	
Imaging resolution [pixel/mm]	16.8	
Window size [pixel^2]	64×64	
Overlap factor [%]	50	
Vector spacing [mm]	1.9	
Instantaneous velocity uncertainty [%]	1.3[a]	3.7[b]
Mean velocity uncertainty [%]	0.1[a]	0.2[b]

[a] Average value upstream of propeller disk, as a percentage of V_∞.
[b] Average value in tip-vortex region, as a percentage of V_∞.

6.3.2. INTERACTION EFFECTS IN BASELINE CONFIGURATION

This section describes the time-averaged aerodynamic interaction observed between the three propellers in the baseline configuration, without stagger or angle-of-attack effects. First, the effect of this interaction on the performance of the propellers is presented. Then, the changes in velocity and pressure fields relative to the isolated-propeller case are described, to explain the changes in propeller loading and slipstream development.

A. PROPELLER PERFORMANCE

To understand the impact of the aerodynamic interaction on propeller performance, Fig. 6.32 presents the thrust coefficient, torque coefficient, and efficiency of the middle propeller versus advance ratio, for the isolated and distributed-propeller cases. The figure shows a slight reduction in thrust in the distributed-propeller configuration for all advance ratios, which outweighs the reduction in torque and, overall, leads to a drop in propeller efficiency. The efficiency loss is especially evident at high advance ratios. This occurs because the performance loss is predominantly caused by a local variation in effective advance ratio (see following subsections), and the propeller efficiency is more sensitive to variations in advance ratio near the zero-thrust condition.

Figure 6.32 indicates that, for a fixed-pitch propeller, a significant performance loss can occur due to propeller–propeller interaction at low thrust settings. However, in practice, a propeller typically operates at the advance ratio corresponding to maximum efficiency in cruise conditions, and to the left of that (i.e., at lower advance ratios) in take-off or climb conditions. Therefore, the appreciable efficiency loss visible in Fig. 6.32 for $J > 1.2$ can be avoided by selecting an appropriate blade-pitch setting. For a variable-pitch propeller, the loss in propeller efficiency at the thrust setting corresponding to maximum efficiency ($T_c \approx 0.38$, in this case) is more representative of the performance loss due to propeller–propeller interaction. In Fig. 6.32, the propeller-efficiency penalty

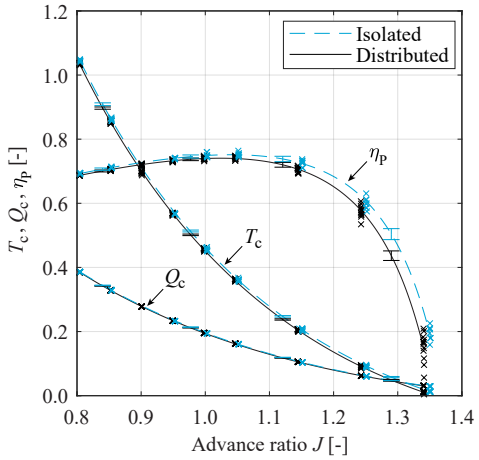

Figure 6.32: Performance of the middle propeller in the baseline isolated and distributed configurations. Markers indicate individual measurements.

at this thrust setting is approximately 1.5% of the isolated-propeller efficiency. The cause of this performance loss is described in the following section.

B. FLOW-FIELD CHARACTERIZATION

The presence of additional propellers alters the inflow conditions to each propeller, thus changing the loading distribution on the propeller blades. This variation in loading affects the velocity and pressure field downstream of the propeller, which is also simultaneously affected by adjacent propeller slipstreams. In order to understand this aerodynamic coupling, the following subsection first describes the flow field upstream of the propellers, and subsequently the evolution of the flow field downstream of the propellers is described.

Inflow Conditions

Figure 6.33 shows how the velocity field ahead of the middle propeller is affected by the presence of adjacent propellers. The velocity distributions are obtained from the ensemble-averaged PIV data, and only a part of the FOV is shown. In this figure, the velocity vectors indicate the in-plane velocities induced by the propellers and nacelles; i.e. the freestream velocity has been subtracted from the axial component. The slipstream contraction is evident in the horizontal plane of the isolated-propeller case (Fig. 6.33a). Near the radial position of maximum loading ($y/R \approx 0.7$), the radial velocity is zero, while further outboard, the slipstream contracts. Inboard of $y/R = 0.7$, on the other hand, the radial flow is outward-oriented. This outward-oriented flow is caused predominantly by the spinner. The trailing vorticity in the inboard region of the blade also plays a minor role, since it is opposite in sign compared to the tip region, and induces radial velocities which cause the streamtube to expand rather than to contract.

When additional propellers are placed on the side (Fig. 6.33b), two main differences can be observed. Firstly, the velocity magnitude has increased, as can be seen by com-

paring the contour levels of Figs. 6.33a and 6.33b. Secondly, near the propeller tip, the spanwise velocity component v is reduced to practically zero. This is especially evident in the close-up view, where the distributed-propeller velocity vectors (black) are practically aligned in streamwise direction, while the isolated-propeller velocity vectors (red) present a significant spanwise component. Above the horizontal plane ($z > 0$), the reduction in spanwise velocity is accompanied by an increase in the magnitude of the vertical velocity component w, leading to the reorientation of the velocity vectors indicated in Fig. 6.33b.

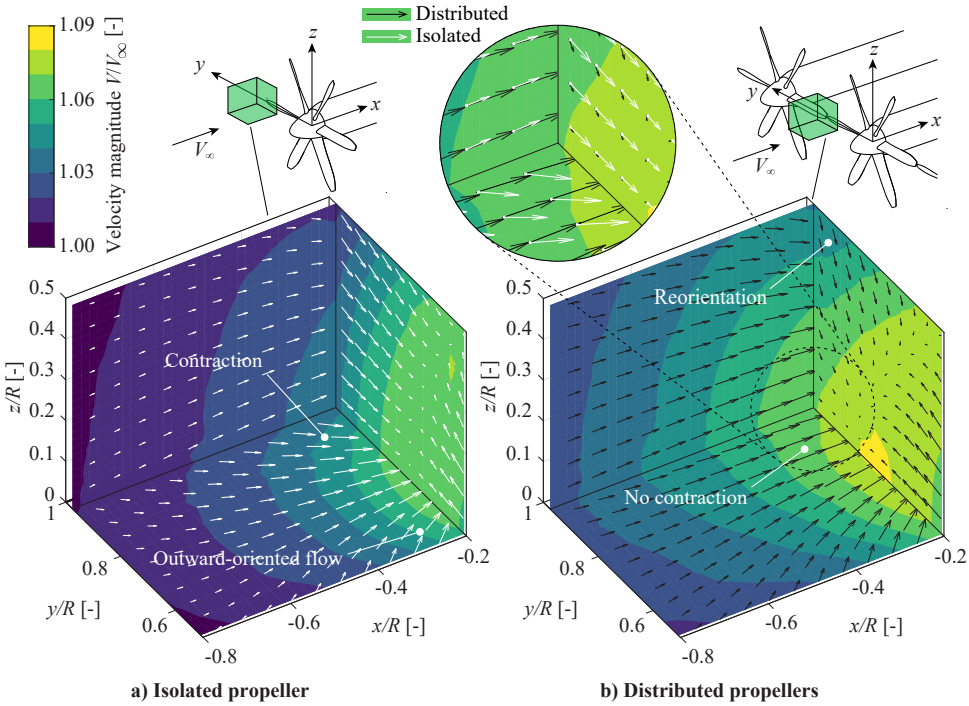

Figure 6.33: Inflow velocity distributions upstream of the middle propeller, obtained from PIV measurements in isolated and distributed configurations.

To analyze these differences in more detail, Fig. 6.34 displays the axial and tangential velocity profiles extracted from the cross-flow plane upstream of the propeller disk at $x/R = -0.2$, for three azimuthal locations. The axial velocity profiles (Fig. 6.34a) show that the inflow velocity is higher in the distributed configuration than in the isolated configuration, especially along the centerline ($\theta = 0^o$). The tangential velocity profiles, on the other hand, show no significant swirl at $\theta = 0^o$ in Fig. 6.34b. This is expected since, in a time-averaged sense, a propeller does not induce swirl upstream of the propeller disk. However, as the blade approaches this horizontal position, it perceives a tangential inflow in the same direction as the blade rotation direction ($\theta = -30^o$). On the other hand, once it passes this horizontal position, it perceives a negative tangential inflow ($\theta = +30^o$).

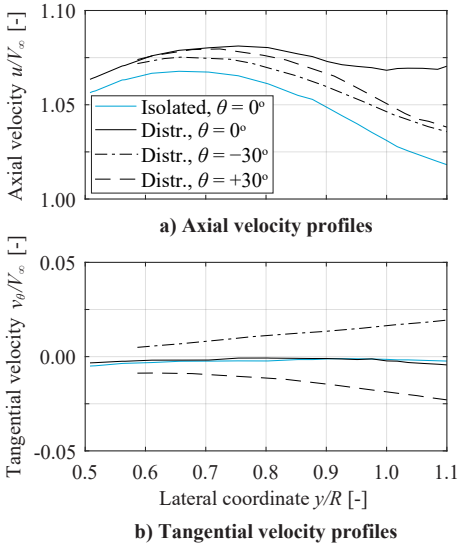

Figure 6.34: Axial and tangential velocity profiles upstream of the middle propeller ($x/R = -0.2$), at three azimuthal locations: approaching side ($\theta = -30^o$), horizontal position ($\theta = 0^o$), and retreating side ($\theta = +30^o$).

The changes in inflow conditions can be explained by considering the velocities induced by the propeller vortex system. The vortex associated to an idealized single blade without spinner contains three segments: the root vortex (axial), the bound vortex (radial), and the tip vortex (helical), as shown in Fig. 6.35. As discussed in Sec. 2.2.1, of the various vorticity components that constitute the propeller slipstream, only the tangential one induces axial and radial velocities outside the slipstream. Therefore, the changes in inflow conditions observed in Figs. 6.33 and 6.34 can be understood by representing the propeller as a semi-infinite series of ring vortices, starting at the propeller disk location. The velocity field induced by such a semi-infinite distribution of ring vortices is notionally shown in the lower left corner of Fig. 6.35. For this illustration, it is assumed that all tangential vorticity is concentrated in the tip (i.e., that the blade loading is constant), and the Biot-Savart law is applied to discretized vortex segments. The illustration shows how the radial velocities are highest at the start of the vortex tube, while decaying to zero in upstream and downstream directions. Inside the vortex tube, the axial velocity gradually increases in streamwise direction, in line with actuator disk theory. Outside the vortex tube, the axial velocity is increased upstream of the propeller disk, decreased downstream of the disk, and is not affected at the disk location. Therefore, a propeller induces both axial and radial velocities ahead of the adjacent propellers.

These induced velocities are shown by the vectors sketched on the two gray planes of Fig. 6.35, where the black arrows represent the velocity components induced by the middle propeller, and the blue arrows on the left- and right-hand sides represent the velocity components induced by the starboard and port propellers, respectively. The effect of the port and starboard propellers on the opposite sides is neglected for simplicity, since the increased distance makes it a second-order effect. For a point on the horizontal plane halfway between two propellers (right-hand side of Fig. 6.35), the induced

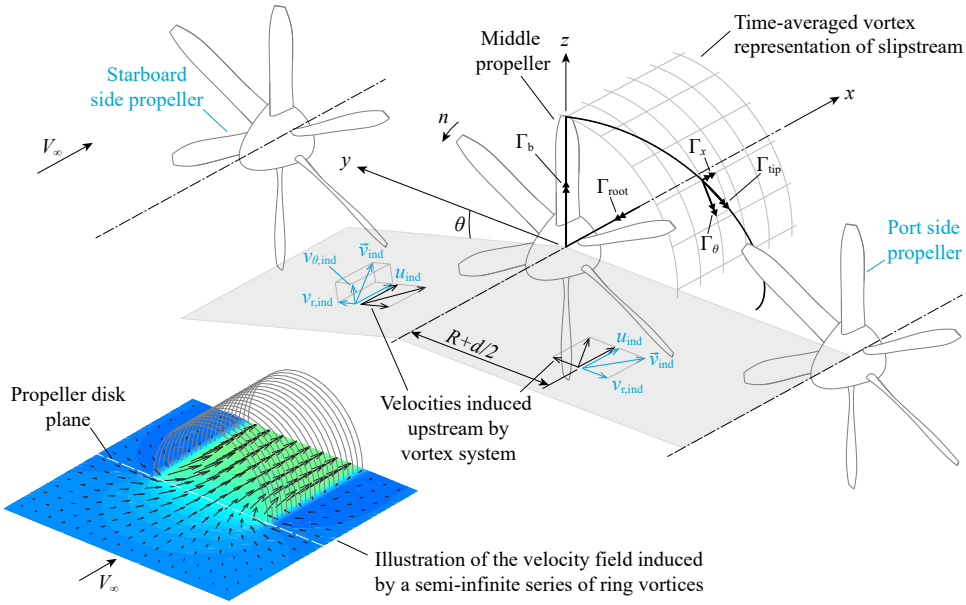

Figure 6.35: Conceptual sketch of the propeller vortex system, the velocities it induces, and its effect on the inflow to adjacent propellers.

axial velocities u_{ind} add up, while the radial components $v_{r,\text{ind}}$ oppose each other. This is the cause for the axial velocity increase observed in Fig. 6.34a, and the reduction in spanwise velocity observed in Fig. 6.33b. If a generic azimuthal location θ is analyzed instead (left-hand side of Fig. 6.35), the velocity induced by the side propeller not only affects the axial and radial inflow components, but additionally creates an out-of-plane component, $v_{\theta,\text{ind}}$. This tangential component is reflected in the profiles of Fig. 6.34b.

The increase in axial velocity observed upstream of the propeller disk is, however, not the main cause for the loss of thrust in the distributed-propeller configuration: at the propeller disk location, the axial velocity induced by adjacent vortex systems is approximately zero (see illustration in Fig. 6.35). The tangential inflow component is also not responsible for the thrust loss, since it is symmetric with respect to the $z = 0$ plane and would, on average, lead to a negligible thrust increase, similar to a propeller at a small angle of attack. Therefore, the thrust reduction is caused by the nacelles. This effect is conceptually indicated in Figs. 6.36a and 6.36b. When additional nacelles are installed next to the middle propeller, the inflow velocity increases as a result of the blockage of the nacelles. This was confirmed by comparing thrust measurements with one propeller and three nacelles (not shown here) to those of the isolated propeller. The comparison showed that the majority of the thrust loss occurred when the additional nacelles were installed, while the incorporation of the adjacent propellers themselves had a much smaller effect. For this reason, the two T_c curves of Fig. 6.32 present a relatively constant offset, rather than a difference in slope. Since the effect of the nacelles decays with the distance to the nacelle axis, the thrust offset also decreases gradually as the propeller separation distance is increased, as seen in earlier studies [183, 184].

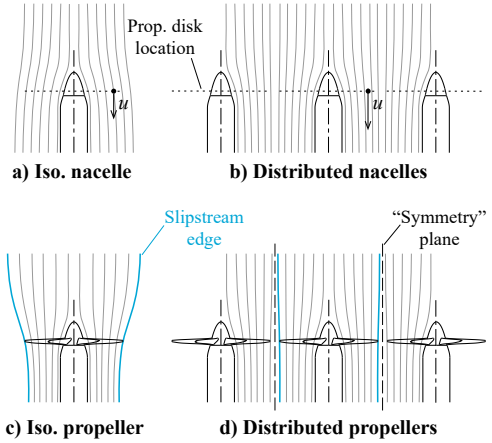

Figure 6.36: Conceptual interpretation of the effect of nacelles and propellers on the streamlines in the horizontal plane ($z = 0$).

Although the adjacent propellers' vortex systems do not significantly affect the thrust of the middle propeller, they do lead to unsteady loading. While the inflow conditions of an isolated propeller are axisymmetric, the velocities induced by adjacent propellers break this axisymmetry and create a (quasi-)symmetry plane between each pair of propellers instead, as shown in Figs. 6.36c and 6.36d. In a time-averaged sense, this "boundary condition" would represent a perfect symmetry condition if an array of infinite propellers were considered, in which case the spanwise velocity would be exactly zero halfway between each propeller. The associated reorientation of the in-plane Cartesian velocity components (v, w) in the propeller disk leads to the tangential component observed in Fig. 6.34b, causing a twice-per-revolution excitation on the blades of the middle propeller. It is worth nothing that, while the axial velocity induced by the propellers outside the slipstream is zero in the plane of the propeller disk (see bottom left of Fig. 6.35), the induced radial velocities are highest at that axial location. Therefore, the use of stagger not only affects the time-averaged loading on the propellers, but also the unsteady loading. It is also important to note that this unsteady loading exists in the blade reference frame purely as a consequence of the time-averaged influence of the adjacent slipstreams, and does not yet consider additional unsteady effects due to the perturbations produced by discrete blades passages (see Sec. 6.3.3).

Slipstream Characteristics

The asymmetric inflow conditions lead to non-uniform loading on the propeller disk in the distributed configuration. This is reflected in the total-pressure distribution immediately behind the propeller disk ($x/R = 0.2$), shown in Fig. 6.37. These distributions do not directly represent the loading distribution on the propeller disk, due to slipstream contraction, swirl, and diffusion and dissipation in the blade wakes and tip vortices. However, they provide a qualitative description of the loading on the disk itself. The total-pressure distribution in the baseline, co-rotating configuration (Fig. 6.37a) shows that, overall, the propeller loading is still relatively axisymmetric. However, the interaction

effects become more prominent when analyzing the changes in loading due to the presence of adjacent propellers, shown in Figs. 6.37b and 6.37c. These figures show the difference in C_{pt} between the distributed configuration and a three-nacelles, one-propeller configuration. The differences are not expressed relative to the isolated propeller, to decouple the effect of the adjacent propellers on the unsteady loading from the effect of the nacelles. Moreover, in this way, it is possible to install a single propeller on the side nacelle, and register the "deltas" on the side propeller (Fig. 6.37b) as well. The differences in total pressure, δC_{pt}, are normalized with the propeller thrust coefficient T_c to express the changes as a percentage of the average loading on the propeller disk[1]. Figure 6.37c shows that the loading is reduced when approaching the horizontal position, especially near the radial location of highest loading ($r/R \approx 0.7$). When the blade retreats from the horizontal axis, the loading increases, especially in the outboard portion of the blade. This is consistent with the trends in blade loading observed in earlier studies [185], and

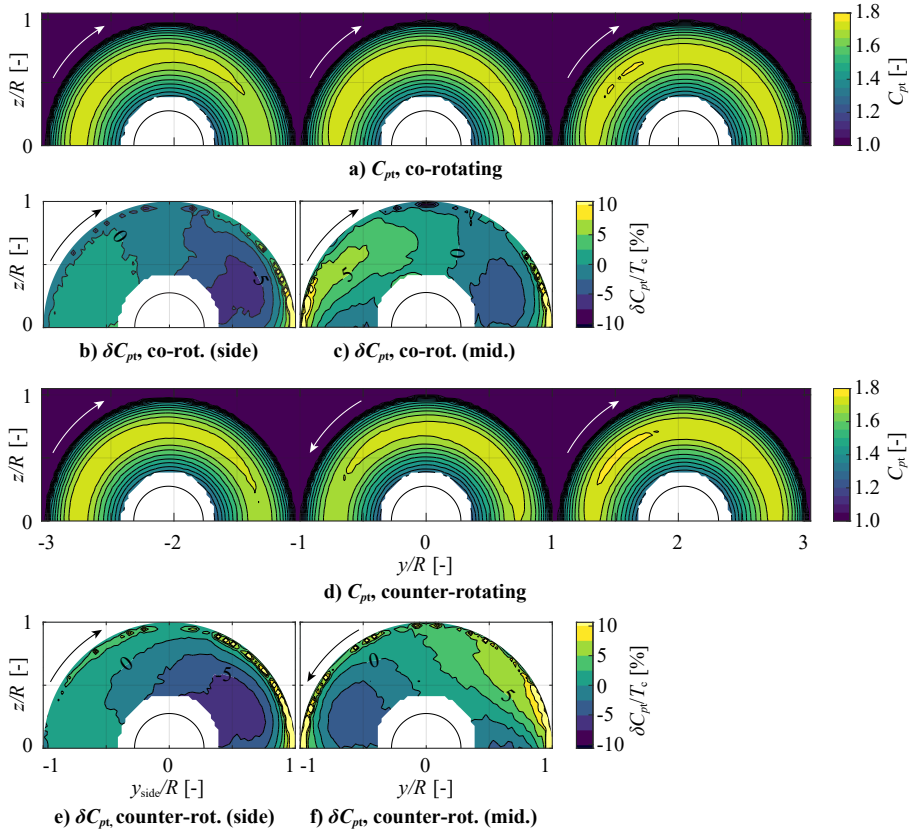

Figure 6.37: Total-pressure distributions measured $0.2R$ downstream of the propellers, viewed from behind.

[1] If the swirl component is neglected, the average total-pressure increase across the propeller is equal to its thrust coefficient: $T_c = C_{pt,mean} - C_{pt,\infty} = C_{pt,mean} - 1$.

is a consequence of the tangential inflow velocities seen in Fig. 6.34b. The magnitude of the changes in momentum is of the order of ±5% of the propeller thrust coefficient. On the side propeller (Fig. 6.37b), the same effect is observed when the blades approach the middle propeller. In this case, no significant loading changes exist in the left-hand side of the figure, since there is no adjacent propeller. In the counter-rotating case (Figs. 6.37d-6.37f), the effects on the middle propeller are mirrored, as discussed in Sec. 6.3.3.

It should be noted that the large changes in loading at the edges of the slipstream in Figs. 6.37b and 6.37c are not representative of local changes in blade loading. Although the loading at the blade tips might locally increase when approaching a blade or tip vortex of the adjacent propellers (see Sec. 6.3.3), this effect cannot be quantified with these measurements. Instead, these sharp gradients at the edge of the slipstream are mainly an artifact of the changes in slipstream contraction between the distributed-propeller and single-propeller configurations. This is shown in Fig. 6.38, which represents the total-pressure distribution measured in the Y-direction at $Z = 0$ with increased spatial resolution near the slipstream edge. The dashed lines show how the slipstream edge is closer to the propeller axis when a single propeller is installed on either the middle or side nacelle. However, in the distributed configuration, the quasi-symmetry condition discussed previously prevents slipstream contraction from occurring in the horizontal plane, and thus the edges of the slipstreams are closer to each other.

Figure 6.37a shows that, at $x/R = 0.2$, the slipstreams are practically circular in cross section. Additional total-pressure distributions, not shown here, indicated that the slipstream deformation was also minor at more downstream locations. To verify the impact of this minor slipstream deformation on the inflow to a downstream wing, Fig. 6.39 shows the axial-velocity and flow-angle distributions in the horizontal plane at $x/R = 1.2$, which can be considered a typical position of the wing leading edge. Figure 6.39 shows that the maximum axial velocity in the slipstream is reduced with respect to isolated conditions. This is caused by the reduction in thrust on one hand, and the widening of the slipstream on the other. The latter is visible toward the edge of the slipstream ($y/R \rightarrow 1$), where the velocity in the slipstream tends to freestream values faster in the isolated propeller case than in the distributed-propeller case. This distributes the momentum imparted by the propeller over a wider area. Moreover, no significant changes

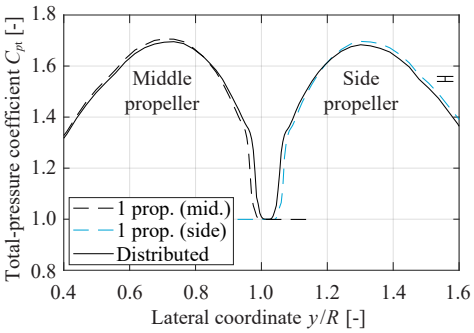

Figure 6.38: Total-pressure profiles measured in the horizontal plane ($z = 0$), $0.2R$ behind the propellers, comparing the single-propeller (with three nacelles) and distributed ($\Delta\phi = 0^o$) configurations.

in inflow angle due to slipstream swirl (Fig. 6.39b) are observed. Therefore, the effect of propeller-propeller interaction on the integral lift of a downstream wing is expected to be minor.

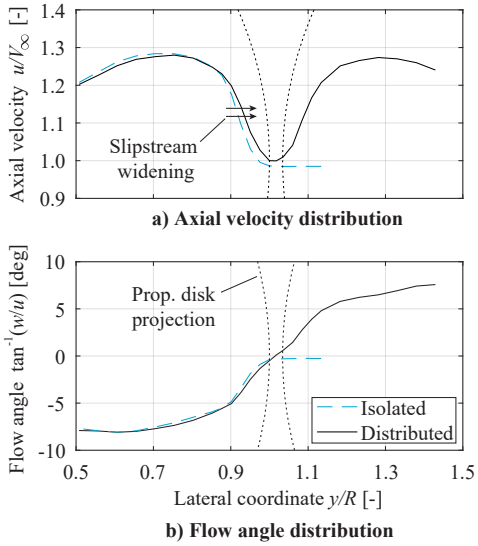

Figure 6.39: Axial velocity and flow-angle profiles obtained from PIV measurements in the horizontal plane ($z = 0$), $1.2R$ downstream of the propellers.

6.3.3. INFLUENCE OF DESIGN PARAMETERS & OPERATING CONDITIONS

Now that the main interaction phenomena and their effect on the time-averaged performance of the propeller have been presented, this section describes how these phenomena are affected by different operating conditions or design choices. The influence of rotation direction, angle of attack, stagger, differential thrust, and relative phase angle is described in the following subsections, respectively.

A. ROTATION DIRECTION

To determine whether the rotation direction has a significant effect on the performance of distributed propellers, Fig. 6.40 presents the changes in propeller performance due to interaction for the co- and counter-rotating cases. The plots indicate the change in thrust or efficiency as a percentage of the isolated propeller's thrust or efficiency, respectively, versus the thrust setting of the isolated propeller. Note that the error bars are significant at low thrust settings, since the force uncertainty is large relative to the absolute forces, and ΔT_c and $\Delta\eta_P$ are affected by the uncertainty of both the installed measurements and the isolated-propeller measurements used as reference. In all cases, there is a drop in propeller thrust and efficiency due to the interaction, which is more pronounced at lower thrust settings. This occurs because the adjacent nacelles are the main cause of the thrust reduction in the distributed configuration (see Sec. 6.3.2), and their relative contribution to the overall propeller performance is larger at lower thrust settings. The asymptotic behavior at $T_{c,iso} \rightarrow 0$ is a result of a finite change in thrust due to interaction

at the advance ratio corresponding to zero isolated-propeller thrust, as can be extrapolated from Fig. 6.32. For both rotation directions, the efficiency loss is approximately 1.5% at the thrust setting of maximum efficiency, $T_c = 0.38$. However, considerably lower thrust coefficients ($T_c < 0.2$) are obtained in cruise conditions of distributed-propeller aircraft (see Chapter 10). Figure 6.40 shows that the efficiency loss is significantly larger in those conditions, exceeding 5%. Nonetheless, as mentioned earlier, this is a result of this specific blade-pitch setting, and can be avoided in practice by selecting a blade pitch which presents the maximum efficiency at the cruise thrust setting instead.

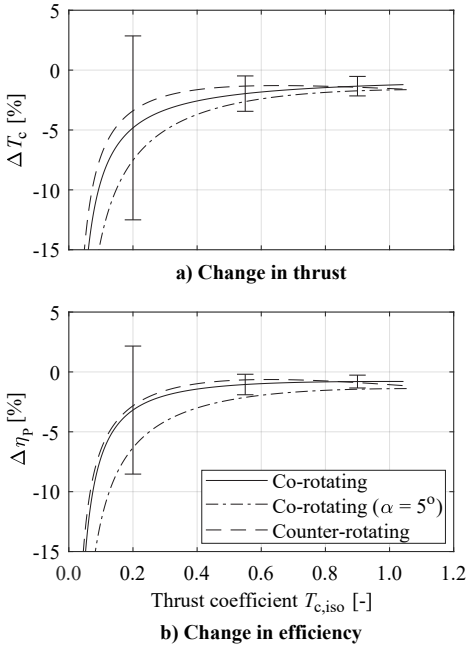

Figure 6.40: Effect of rotation direction and angle of attack on the change in propeller thrust and efficiency due to interaction. Error bars are only shown for the baseline configuration, but are indicative for all cases.

When comparing the co- and counter-rotating cases in Fig. 6.40, the differences lie well within the 95% confidence interval, and are most likely related to the uncertainty of the fit and minor differences between the geometries of the two mirrored propeller models. Therefore, the effect of rotation direction on the performance penalty is negligible. This reaffirms the interpretation of the time-averaged effects described in Sec. 6.3.2, according to which the rotation direction should not affect the performance of the adjacent propeller. This is further confirmed in the wake-pressure distributions, displayed in Fig. 6.37. When changing the rotation direction of the middle propeller, the changes in loading distribution are mirrored, and no significant change in the amplitude or extent of the peaks is observed. The loading distributions on the side propellers, meanwhile, are barely affected by the rotation direction of the middle propeller.

B. ANGLE OF ATTACK

Figure 6.40 shows that the performance loss due to interaction at $\alpha = 5^o$ is comparable to $\alpha = 0^o$, though slightly more pronounced. For $\alpha = 5^o$, the efficiency loss at $T_c = 0.38$ is approximately 3%. A more pronounced difference can be seen in the normal-force coefficient, presented in Fig. 6.41. This figure shows that the normal force coefficient C_N (normalized with the rotational speed of the propeller) increases linearly with advance ratio, presenting an additional offset in the distributed configuration. This constant offset indicates that the increase in normal-force coefficient is not dependent on the slipstream contraction of the adjacent propellers. Instead, it is attributed to the presence of the adjacent nacelles, which induce an additional upwash and increase the effective angle of attack of the propeller. At the advance ratio corresponding to maximum efficiency ($J = 1.04$, $T_c \approx 0.38$), the normal force is approximately 11% higher in the distributed configuration, for an angle of attack of 5^o. Therefore, the derivative $\partial C_N/\partial\alpha$ is higher in the distributed configuration, which affects aircraft stability.

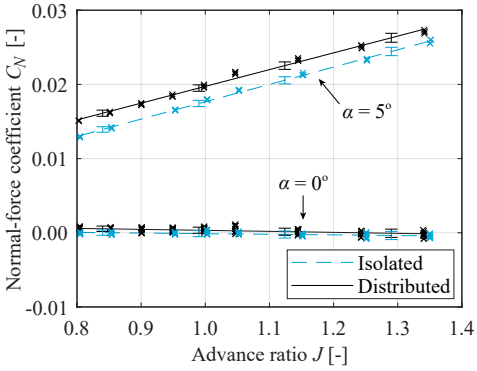

Figure 6.41: Influence of interaction effects on propeller normal force in the baseline configuration, at two angles of attack. Markers indicate individual measurements.

The normal force is a consequence of the differences in loading between the up-going and down-going blade sides. This loading difference is reflected in the wake-pressure distributions downstream of the propeller, shown in Fig. 6.42. The figures show a clear non-uniform loading due to the angle of attack, where the loading is increased on the down-going blade side, and reduced on the up-going side. Given that the survey plane is relatively far downstream ($x/R = 1.2$), the azimuthal regions with highest and lowest loading have been shifted in the direction of propeller rotation, due to the swirl in the slipstream on one hand, and the phase delay in unsteady blade forces on the other. Moreover, the side and middle propellers exhibit a similar loading distribution, indicating that the non-uniform loading due to the positive angle of attack is dominant over the interaction effects with neighboring propellers. Analogously to $\alpha = 0^o$, at $\alpha = 5^o$ a change in the rotation direction of the middle propeller leads to a mirrored loading distribution, and the slipstreams remain practically undeformed.

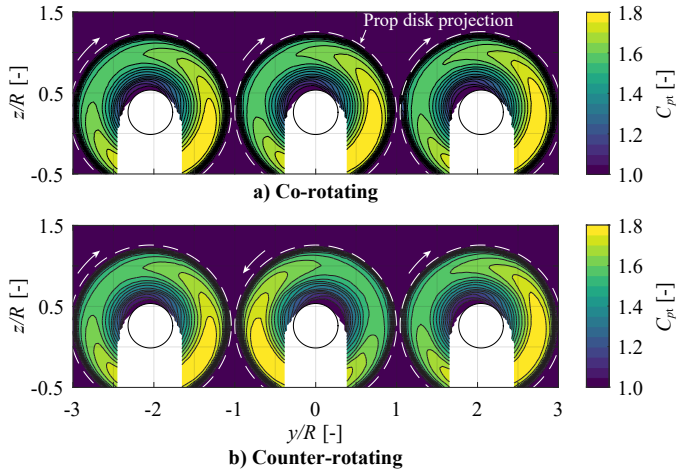

Figure 6.42: Wake total-pressure distributions measured at $\alpha = 5^{o}$ ($x/R = 1.2$), viewed from behind. Note that the z-coordinate is expressed relative to default reference system with propeller at $\alpha = 0^{o}$.

C. STAGGER

When the propellers are placed at different axial locations, the quasi-symmetry condition described in Sec. 6.3.2 is lost. In this case, the inflow to the propeller depends, among other factors, on whether it is placed behind or ahead of adjacent propellers. This is shown in Fig. 6.43, which presents the velocity distributions upstream of the propellers in a forward stagger configuration, i.e. where the middle propeller is placed further forward at $x/R = -0.2$, while the side propellers remain at $x/R = 0$ (see Fig. 6.30e). Figure 6.43a shows that the inflow to the middle is comparable to the baseline configuration without stagger (Fig. 6.33b). However, the contours show a slightly higher velocity magnitude, due to the axial velocity induced upstream by the adjacent propellers (see Fig. 6.35). Moreover, the velocity vectors near the $y/R = 1$ plane present a weak lateral velocity component. This occurs because, for $x/R < -0.4$, the radial velocities induced by the middle propeller's vortex system dominate over the radial velocities produced by the adjacent vortex systems, since the middle propeller is placed more upstream. The downstream (side) propeller, on the other hand, experiences a significantly different inflow (Fig. 6.43b). Firstly, the inflow velocity magnitude is reduced. Secondly, there is a strong lateral velocity component upstream of the propeller, opposite to the usual slipstream contraction. This is visible in the horizontal plane of Fig. 6.43b and occurs because, upstream of the side propeller, the flowfield is dominated by the contraction of the middle (forward) propeller. This is also evident in the xz plane, where a local region of increased velocity magnitude is visible around $x/R = -0.4$.

The resulting variations in propeller loading are illustrated by the total-pressure distributions of Figs. 6.44a–6.44f. Note that the forward propellers are installed $0.2R$ further upstream than in the baseline configuration, while the wake survey plane remains at the same location, as reflected in Fig. 6.30. Therefore, the measured total-pressure distribution deviates slightly more from the actual loading on the propeller disk, due to

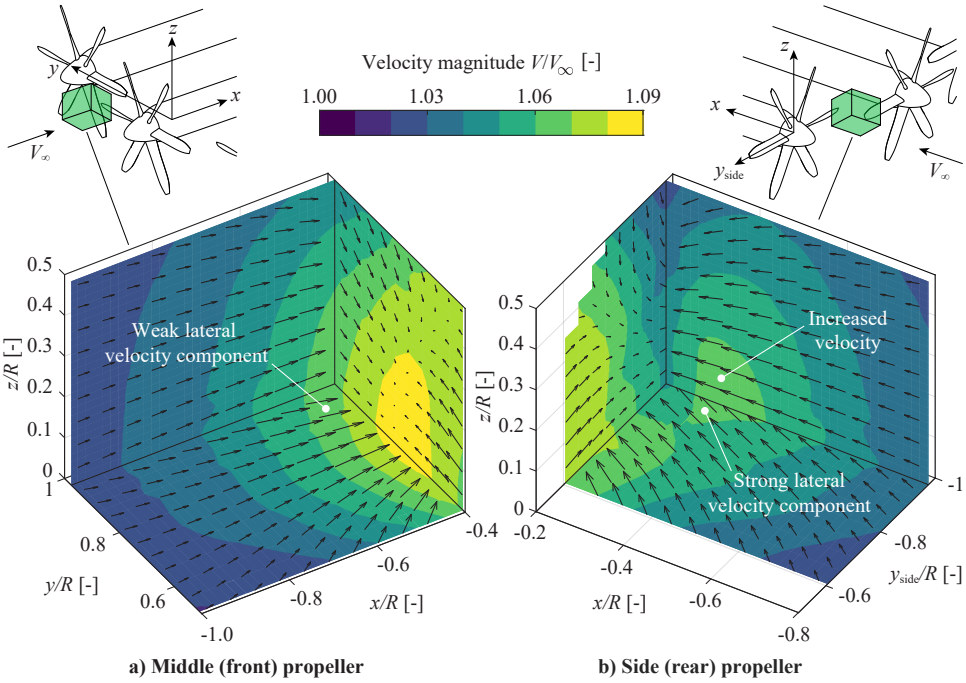

Figure 6.43: Inflow velocity distributions ahead of the middle (front) propeller and side (rear) propeller, obtained from PIV measurements in the forward-stagger configuration.

the dissipation, diffusion, and slipstream rotation that takes place between the propeller plane and the measurement plane. Again, when computing δC_{pt}, the three-nacelles, one-propeller measurement is taken as reference instead of the isolated propeller. When comparing the δC_{pt} distributions of the middle propeller in the forward (Fig. 6.44a, 6.44c) and backward (Fig. 6.44d, 6.44f) stagger configurations, it appears that on average the former presents less total-pressure rise than the latter. The opposite is observed for the side propellers. These observations reinforce the interpretation of Fig. 6.35, which shows that propellers positioned upstream of their neighbors perceive an increased axial inflow velocity, while the opposite occurs for propellers placed downstream of their neighbors.

However, the total-pressure distributions should be interpreted with caution, since the slipstream contraction is different between the distributed and single-propeller configurations. This is evident in Figs. 6.44c and 6.44e, which show high total-pressure values at the edge of the slipstream. These streaks appear because in the distributed case, the slipstream of the upstream propeller first contracts, and is subsequently widened due to the contraction of the adjacent propellers. Hence, the slipstream is wider than in the isolated case, and therefore the "delta" between the two appears as highly positive in the contour maps around $y/R = \pm 1$. It is interesting to note that the opposite does not occur on the top side of the slipstream; i.e. the slipstream widens while maintaining a constant height, rather than widening while maintaining a constant cross-sectional

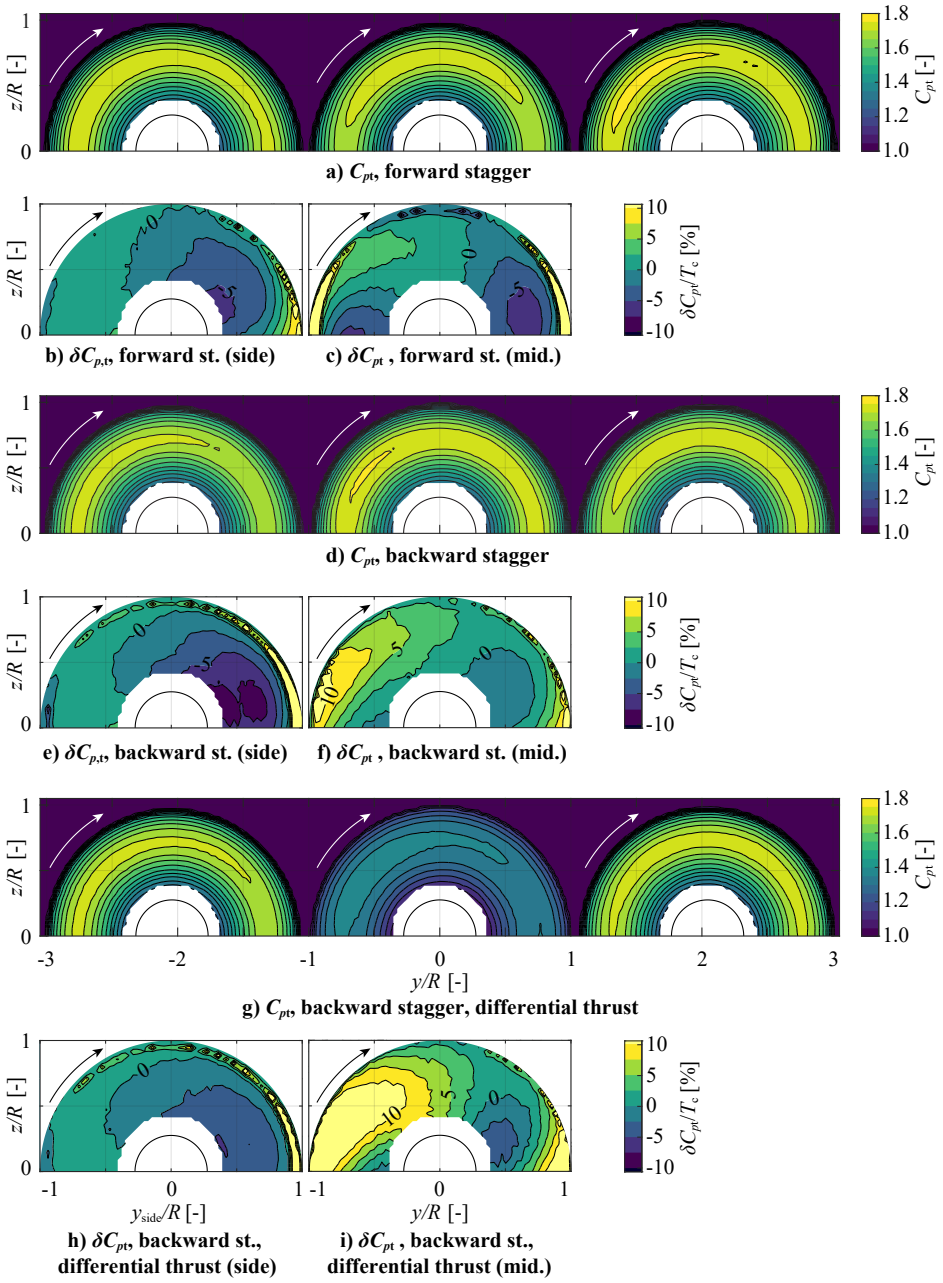

Figure 6.44: Slipstream total-pressure distributions measured at $x/R = 0.2$ with forward and backward stagger ($J = 1.00$, $J_{\text{differential thrust}} = 1.15$).

area. Furthermore, in the backward-staggered case (Fig. 6.44f), the width of the slipstream is comparable to the single-propeller case, and an increase in loading of approximately 10% of the propeller thrust is observed on the left-hand side. This indicates that the unsteady loading is higher than in the case without stagger (Fig. 6.37c), even though the propeller blades are further away from the ones of the adjacent propellers.

The corresponding changes in propeller thrust and efficiency are shown for the different stagger configurations in Fig. 6.45. The differences among the various stagger configurations are comparable to the uncertainty band, and are therefore small and cannot be quantified accurately. Nonetheless, the trends are consistent with the observations made in Figs. 6.43 and 6.44. The thrust reduction of the middle propeller is largest in the forward-stagger configuration ($\Delta T_c = -4.5\%$ at $T_{c,iso} = 0.38$), due to the axial velocities induced upstream by the side propellers. The thrust and efficiency penalties of the middle propeller in the backward-staggered case are comparable to the baseline configuration, since the negative axial velocities induced by the adjacent vortex systems are partially compensated by the velocity increase due to blockage of the adjacent nacelles. Note that the effect would be opposite when staggered propellers are installed with an overlap, in which case the thrust of the downstream propeller is significantly reduced [178]. Finally, in the staired configuration, the performance loss is halfway between the forward- and backward-staggered configurations, since the effects on the two sides of the propeller compensate each other.

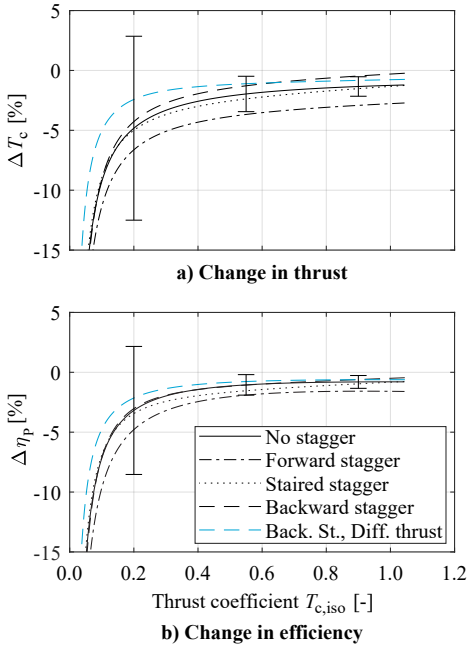

Figure 6.45: Effect of stagger and differential thrust on the change in propeller thrust and efficiency due to interaction. Error bars are only shown for the baseline configuration, but are indicative for all cases.

D. DIFFERENTIAL THRUST

In specific situations, the thrust setting of adjacent propellers may not be equal; for example, if a failure occurs in one of the motors, or if thrust vectoring is used to control the attitude of the aircraft. In this case, the propellers which operate at a higher thrust setting will create a slipstream which acts as a dominating boundary condition for propellers at lower thrust. This can be seen in Figs. 6.44g–6.44i, which present the total-pressure distribution in the backward-stagger configuration when the middle propeller operates at a lower thrust setting. During the wind-tunnel campaign, the impact of differential thrust was only evaluated for the backward-stagger configuration, since the interaction effects were expected to be most critical in that condition. In this case, the change in disk loading relative to the single-propeller configuration is much larger than in the equal-thrust case, as shown in Fig. 6.44i. This leads to an increased ratio between the unsteady and steady blade loads, and occurs because the influence of the middle propeller on the flowfield is relatively weak, and thus its inflow conditions are governed by the adjacent vortex systems. For the backward-staggered configuration, this leads to deceleration of the axial inflow velocity to the middle propeller. However, the average loading on the propeller is not significantly affected, as reflected in the propeller thrust curves that are obtained when the advance ratio of the propeller is varied while maintaining the advance ratio of the side propellers constant ($J = 1.0$). This is visible in Fig. 6.45, which shows a small increase in thrust at low thrust settings, when compared to the backward-staggered configuration at equal thrust. At high thrust settings, the opposite occurs, since in that case the thrust of the middle propeller is higher than the thrust of the side propellers.

E. RELATIVE PHASE ANGLE

The relative blade phase angle between adjacent propellers, $\Delta\phi$, has an important effect on noise production [197]. However, Fig. 6.46 shows that the effect on the time-averaged propeller performance is negligible. In both the co- and counter-rotating cases, the variation in propeller thrust with $\Delta\phi$ is less than 0.5% of the mean thrust. However, in the counter-rotating case, a weak sinusoidal trend can be observed. Two observations can be made in this regard. Firstly, the maximum and minimum thrust are not generated when the blades present the minimum (0^o) or maximum (30^o) phase difference, but at 10^o and 40^o. This phase delay is attributed to the evolution of the trailing vorticity that emanates from the adjacent propellers' blades, which requires some time to concentrate in the tip (and root) vortices. Secondly, the trend is only distinguishable in the counter-rotating case. This is likely due to the fact that, for this rotation direction, the blades of neighboring propellers locally move in the same direction. Thus, the velocities induced by one blade affect the blade of the neighboring propeller for a larger part of the rotation cycle.

The relative phase angle also affects the slipstream evolution in the tip region between each pair of propellers, as reflected in Fig. 6.47. In the co-rotating case, the slipstream edges are deformed, being practically mirrored in the $\Delta\phi = 10^o$ and $\Delta\phi = 40^o$ cases. In the counter-rotating case, on the other hand, there are no noticeable local variations in the slipstream radius, although the slipstream edges are located more towards the left and right in the $\Delta\phi = 10^o$ and $\Delta\phi = 40^o$ cases, respectively. It is interesting to note that while the effect of relative phase-angle on propeller performance is more pronounced in the counter-rotating case, its effect on slipstream deformation is more pro-

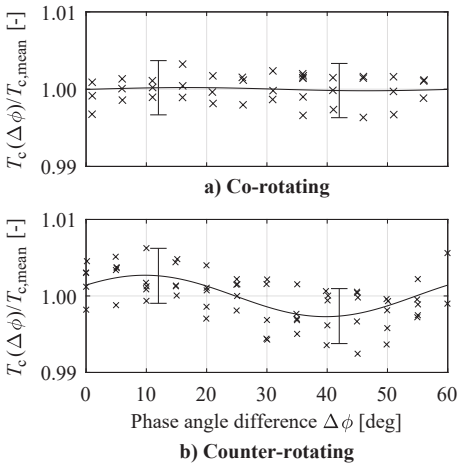

Figure 6.46: Effect of relative blade-phase angle on propeller thrust. Markers indicate individual measurements.

nounced in the co-rotating case. This is hypothesized to be due to the orientation of the helical tip vortices of adjacent propellers, which are locally parallel in the counter-rotating case, while being locally oblique in the co-rotating case—as shown in Fig. 6.48. In the counter-rotating case, the velocity induced locally by an initially undisturbed vortex Γ_1 at a point P_2 on the adjacent vortex ($\vec{v}_{\text{ind},1\to2}$) is perpendicular to that adjacent vortex Γ_2. The reciprocal effect of Γ_2 on Γ_1 induces a velocity $\vec{v}_{\text{ind},2\to1}$ of the same magnitude and direction, and therefore each tip vortex locally reduces the swirl velocity of the adjacent slipstream equally. To the contrary, in the co-rotating case, the velocities induced by each vortex on the other form an oblique angle, and are not perpendicular to the vortex filament. Compared to the isolated propeller, this changes the local direction of the flow and causes a shear in the vortex filaments which, on average, leads to the distorted slipstream edge observed in Figs. 6.47a and 6.47b. Furthermore, these induced

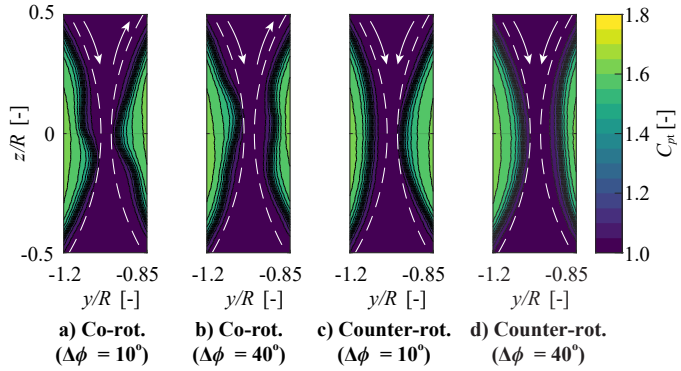

Figure 6.47: Comparison of slipstream deformation for different relative phase angles ($X/R = 1.2$).

velocities will change the loading at the blade tips throughout each blade passage. This effect is highly localized and therefore has no appreciable effect on the performance of the propeller, as evidenced in Fig. 6.46. However, it may lead to a noise increase due to impulsive changes in loading. This source of unsteady loading is different from the unsteady loading due to the time-averaged tangential inflow velocities discussed in Sec. 6.3.2, which would also exist if the adjacent propeller were an idealized actuator disk with infinite blades. This impulsive loading on the blade tips, on the other hand, is a consequence of a repeated exposure to the same part of the unsteady flowfield induced by a finite number of blades on the adjacent propeller, rotating at a synchronized phase angle. Additional high-fidelity numerical analysis or high-resolution, unsteady measurements would be required to quantify this effect and determine how much it is affected by the relative phase angle.

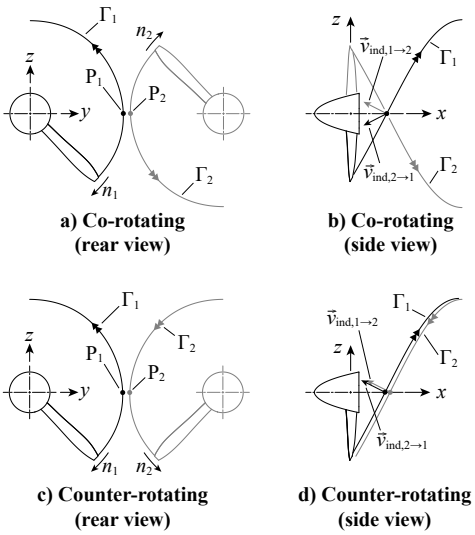

Figure 6.48: Conceptual sketch of the influence of rotation direction on the velocities induced by one vortex system on the other, when the relative phase angle is kept constant ($\Delta\phi = 0^o$).

6.4. SUMMARY OF KEY FINDINGS

The studies presented in this chapter have investigated how a propeller of an OTWDP system interact with the wing, duct, and adjacent propellers. The purpose of these investigations was not to provide a realistic performance estimate of OTWDP systems, but to understand the aerodynamic interaction mechanisms that potentially affect the performance. This understanding is used in subsequent chapters to justify design choices and performance-modeling approaches. To conclude this analysis, the main findings are summarized in the following paragraphs.

PROPELLER–WING INTERACTION

Two exploratory wind-tunnel campaigns were performed to analyze the aerodynamic interaction between an OTW propeller and the wing. The results confirm that the propeller decreases the pressure on the wing surface upstream of the propeller disk, while decreasing the pressure behind it. Overall, this leads to an increase in lift and, for a propeller placed at 35% chord, a reduction in pressure drag. For a propeller placed at 85% chord, the pressure drag is increased slightly. When the flap is deflected, the lift increase is reduced, and the pressure-drag reduction is enhanced.

When the propeller operates above a wing, the blades experience a significant unsteady loading. The loading is highest and lowest at the top and bottom halves of the propeller disk, respectively, for a propeller placed near the location of maximum airfoil thickness. Conversely, the loading is highest and lowest on the up-going and down-going blade sides, respectively, for a propeller placed near the trailing edge. This non-uniform loading is evident in the propeller slipstream, which deforms due to the wing-induced velocities and the interaction with the wing wake. The increased axial component and non-uniformity of the inflow velocities to the propeller disk lead to a reduction in propeller thrust, torque, and efficiency, for a given advance ratio. The reduction in maximum propeller efficiency for a given blade pitch setting is found to decrease by several percent for a propeller placed near the trailing edge, and by more than 10% for a propeller placed at 35% chord. However, these values correspond to a determined geometry, propeller size, and incidence angle. The effect of such parameters on the overall performance of the system is assessed in more detail in Ch. 8.

PROPELLER–DUCT INTERACTION

Numerical (steady and unsteady RANS) simulations have been performed to understand the aerodynamic interaction mechanisms that occur in propellers with unconventional duct shapes, as is the case for OTWDP systems. To simplify the problem to two limit cases, a propeller at a high thrust setting was simulated in a circular duct, and in a square duct. For the same advance ratio, the circular duct is found to generate more thrust than the square duct. This occurs due to two main reasons. Firstly, in the circular duct configuration the propeller is always close to the duct surface, which means that the slipstream contraction caused by the propeller has a strong effect on the loads on the circular duct. On the other hand, for the square duct case, the propeller blades have a weaker effect on the performance of the duct when these are pointing at the corner, due to the larger distance between blades and duct surface. Secondly, in the installed configurations, flow separation occurs at the corner of the square duct, generating a pair of counter-rotating vortices in each corner. However, the propeller produces more thrust inside the square duct than inside the circular duct, for the same advance ratio. This is due to a lower axial inflow velocity at the propeller disk inside the square duct. The non-axisymmetric inflow inside the square duct also leads to significant cyclic loading variations on the propeller blades. The higher thrust of the propeller when placed inside the square duct compensates for the lower amount of thrust generated by the duct itself, when compared to a circular duct. Thus, at the operating conditions tested, both the circular and the square ducted-propeller propulsion systems were found to produce approximately the same thrust. In these high-thrust conditions, the efficiency of the circular ducted propeller is approximately 4.5% higher than the efficiency of the square ducted propeller.

Based on the physical effects observed in these simulations and a rudimentary qualitative analysis of the differences between a single ducted propeller and an OTWDP system, it is concluded that the optimum duct type depends on the operating conditions and design objectives of the system. From an aerodynamic performance perspective, an propeller array without duct or with an envelope duct are considered the most beneficial, depending on the axial location and average thrust setting of the propellers. However, if the design is driven by noise or fatigue constraints, then an array of circular ducts may be beneficial, due to the reduced unsteady blade loading.

PROPELLER–PROPELLER INTERACTION

Finally, an experimental investigation has been performed to study the interaction effects that arise when multiple propellers operate in close proximity in forward flight. The results show that, for a given rotational speed, the propeller thrust and efficiency are slightly reduced in the distributed-propeller configuration, when compared to an isolated propeller. In this study, the propeller-efficiency loss due to the interaction was 1.5% at the thrust setting corresponding to maximum efficiency, for a tip-clearance equal to 4% of the propeller radius. The performance reduction is predominantly caused by the blockage effect of the adjacent nacelles. For a given blade-pitch angle, this performance penalty is larger at lower thrust settings, at higher angles of attack, or a more forward position of the propeller relative to its neighbors, while being independent of the rotation direction of the propellers or the relative blade phase angle.

The velocities induced by the propeller blades and slipstream do not significantly affect the time-averaged performance of the adjacent propellers, although they induce an in-plane velocity component which leads to loading variations across the propeller disk of 5%–10% of the average pressure jump. Therefore, the unsteady blade loading observed in earlier propeller–propeller interaction studies exists not only due to the unsteady interaction between discrete blade tips and tip vortices, but also due to the time-averaged velocities induced by the adjacent propellers' vortex system. Moreover, the interaction between propellers does not appreciably modify the streamwise development of the slipstream.

7

BOUNDARY-LAYER INTERACTION IN HIGH-LIFT CONDITIONS

The previous chapter analyzed the aerodynamic interaction between a propeller and the surrounding elements of an OTWDP system. The majority of the effects were inviscid in nature, while viscous effects only played a secondary role. However, in high-lift conditions, the interaction with the viscous boundary layer can significantly affect the high-lift performance of the wing [149]. Therefore, a dedicated study is required to understand viscous interaction between the propeller and the wing boundary-layer. To allow for a more fundamental breakdown of the interaction effects, a simplified wing geometry with controllable pressure gradients is analyzed.

Two steps are taken in this process. First, an experimental study is performed to gain an understanding of the flow phenomena involved, with and without pressure gradients on the wing. It becomes evident that, if a flap is deflected behind the propeller, the propeller can trigger flow separation. Therefore, in the second step, a mitigation strategy for this flow separation is investigated, namely to deflect the propeller with the flap. The effect of propeller inclination is analyzed using unsteady RANS simulations, to obtain additional information regarding the flow field. Given the difficulty of modeling the three-dimensional, unsteady, and viscous interaction that leads to flow separation, the results are first compared to experimental data to asses the limitations of the numerical approach. The numerical and experimental approaches are presented in Sec. 7.1. Section 7.2 then describes how a propeller interacts with a boundary layer of a flat wall (i.e., without external pressure gradients). Subsequently, the interaction between the propeller and the boundary layer in the case of flap deflection (i.e., with external pressure gradients) is analyzed in Sec. 7.3. Finally, propeller inclination is investigated as a potential mitigation strategy for propeller-induced flow separation in Sec. 7.4.

Parts of this Chapter have been published in Refs. [269, 270]. The numerical simulations were performed by S. A. Bölk as a part of an MSc thesis research project [271].

7.1. ANALYSIS METHODS

Wind-tunnel experiments were performed to analyze the interaction between the propeller and boundary layer in two configurations: flat wall (without pressure gradients), and flap deflected (with pressure gradients). Both cases were analyzed without propeller inclination. The numerical simulations were also performed for two configurations: with and without propeller inclination. In this case, both configurations were analyzed with the flap deflected. The geometry of the wind-tunnel setup was analyzed in the numerical simulations, such that a direct comparison could be performed for validation purposes. These experimental and numerical setups are described in Secs. 7.1.1 and 7.1.2, respectively.

7.1.1. EXPERIMENTAL SETUP

A. WIND TUNNEL FACILITY AND MODELS

The experiments were performed in the closed-circuit, low-speed, low-turbulence tunnel (LTT) at Delft University of Technology. This is the same tunnel as the one employed in Sec. 6.3. A propeller was positioned in close proximity to the suction-side surface of a straight, untapered wing by means of a support sting, as shown in Fig. 7.1. The support sting was mounted on an external balance during propeller force measurements, and on a three-axes traversing system for all other measurements.

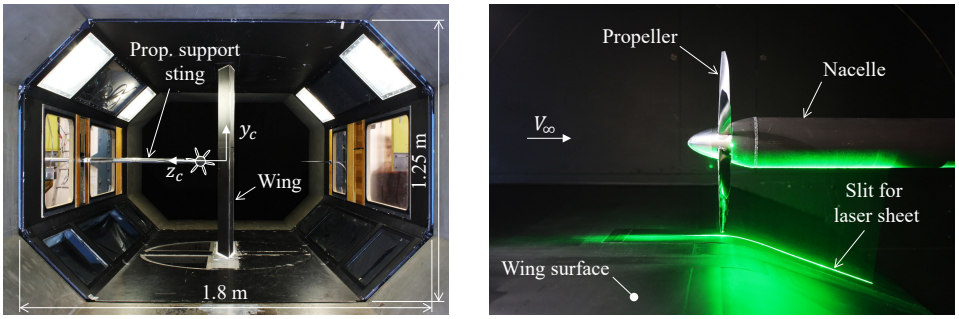

a) Test section (viewed from behind) **b) Close-up of propeller installation**

Figure 7.1: Overview of wind-tunnel setup, showing position of wing model and installation of propeller relative to the wing.

Wing Geometry and Operating Conditions

The wing profile was designed such that, close to the propeller, it is representative of a quasi-flat-plate configuration when the flap is retracted ($\delta_f = 0^o$). The resulting profile, shown in Fig. 7.2b, presents a chord[1] of $c = 1.02$ m, and a thickness-to-chord ratio of 11%. The leading-edge geometry follows a modified super-ellipse of aspect ratio 6 up to 32% chord, in order to provide a smooth transition to the flat upper and lower surfaces [272]. Both the suction and pressure sides are then extended parallel to the wing chordline up to 80% chord, which corresponds to the axial position of the flap hinge. The flap

[1] In the experiment the reference chord-length is taken as the length of the profile when the flap is retracted ($\delta_f = 0^o$). Since the upper surface of the flap translates when it is deflected, the true chord varies.

hinge is located near the pressure side, generating a tangent circular arc with a radius of curvature equal to 10% chord on the suction side of the flap, which is approximately equal to the propeller radius. Behind the arc, the flap surface extends the remaining 20% of the chord to the trailing edge. The upper and lower surfaces of the flap can be split and aligned in axial direction in order to elongate the flat surface of the wing. In this way, by placing an additional body of the same thickness as the wing in the test section (see Fig. 7.2a), the pressure gradient surrounding the flap region is removed.

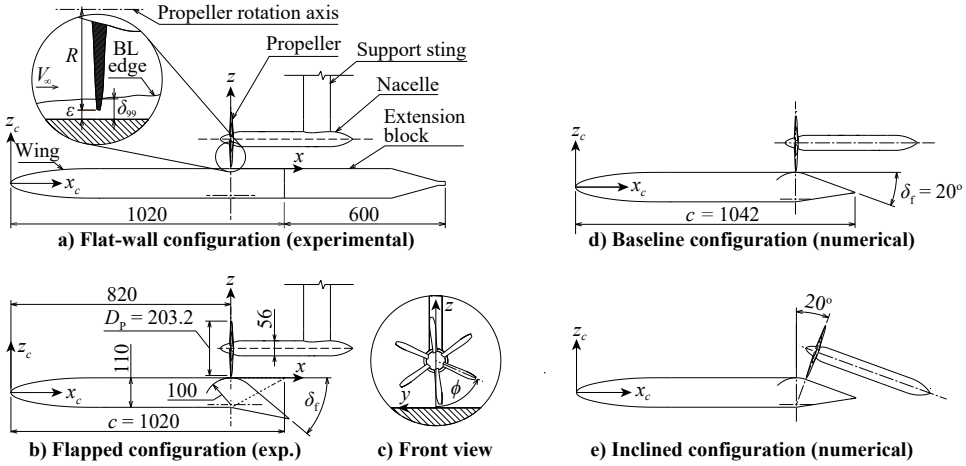

Figure 7.2: Main characteristics of the experimental setup (left), and the simplified geometry analyzed in the numerical simulations of Sec. 7.1.2 (right). Dimensions expressed in mm. Origin of the local reference frame (x, y, z) corresponds to $(x_c, y_c, z_c) = (820, 55, 0)$ mm in the wing-based reference frame.

Measurements were carried out at $\alpha = 0^o$ and $V_\infty = 40 \pm 0.05$ m/s in order to maximize the Reynolds number ($Re_c = 2.76 \cdot 10^6$) without exceeding the maximum input level of the microphones or the maximum power of the electrical motor that drove the propeller, and at $V_\infty = 20 \pm 0.05$ m/s ($Re_c = 1.38 \cdot 10^6$), in order to increase the maximum thrust coefficient. Two boundary-layer configurations were tested, to vary the equivalent Reynolds number of the boundary layer at the propeller location and verify whether there were any significant scaling effects that may be overlooked when using a scaled-down wind-tunnel model. The first, named "BL_1", corresponded to the turbulent boundary-layer obtained with a 3 mm wide trip-strip of distributed roughness elements with an average diameter of 530 µm (carborundum particles of grit size 36) located at 7.5% chord on both sides of the wing. The second, "BL_2", was a thicker turbulent boundary-layer obtained by applying sandpaper of grit size 36 from 7.5% chord to 32% chord on the suction side. This was done to increase the boundary-layer thickness at the downstream propeller location without significantly changing the boundary-layer profile, as discussed at the end of this section. After analyzing multiple flap deflection angles, an angle of $\delta_f = 20^o$ was selected to study the interaction phenomena in more detail, since for this deflection angle, the flow remained attached over the flap hinge but started to separate towards the trailing edge of the isolated wing (i.e., without propeller installed).

Propeller Geometry and Operating Conditions

For the majority of the measurements, the propeller was positioned above the flap hinge ($x_P/c = 0.8$). , which was identified as an axial location with a good compromise between lift gain, drag reduction, and propeller-efficiency loss in Sec. 6.1. The installation was designed such that the propeller axis was located at the mid-span of the wing when connected to the balance. The same six-bladed propeller of Sec. 6.3 was used ($D_P = 0.2032$ m, $D_P/c = 0.2$), though with the blade pitch set to $\beta_{0.7R} = 45^o \pm 0.05^o$. The propeller was operated at advance ratios between $J = 1.7$ and $J = 2.3$ at $V_\infty = 40$ m/s, and between $J = 1.0$ and $J = 2.0$ at $V_\infty = 20$ m/s, in order to obtain thrust coefficients and slipstream characteristics comparable to full-scale aircraft. For the baseline measurement conditions ($V_\infty = 20$ m/s, $J \approx 1.1$), this corresponds to approximately 5,300 rpm, a tip Mach-number of $M_{tip} = 0.18$, and a blade Reynolds-number of $Re_{0.7R} = 4.2 \cdot 10^4$. Previous numerical and experimental analyses of the propeller [90] showed that the radial loading distribution varies slightly with Mach number and that the integral thrust increases with Reynolds number, but without any qualitative changes in the behavior of the propeller. Therefore, although the quantitative results may vary, the conceptual interpretation of the phenomena observed in the experiment were considered applicable to a full-scale distributed-propeller configuration in take-off or landing conditions. The rotational speed of the propeller was controlled with an accuracy of ±0.1 Hz which, together with the velocity uncertainty, corresponds to fluctuations in advance ratio below ±0.5%. Furthermore, the clearance between the propeller blade tips and the wing surface, ε, was varied in order to analyze the impact of tip clearance on the interaction effects. Finally, a subset of measurements were taken with the propeller at $x_P/c = 0.75$, in order to determine the influence of the propeller's axial position on flow separation.

B. MEASUREMENT TECHNIQUES

The following subsections provide an overview of the measurement techniques used during the experiment. The measured velocities and pressures were corrected for wind-tunnel blockage caused by the wing, following the image method described in Ref. [267]. Lift interference corrections were not applied, since only low lift coefficients were attained ($c_l \approx 0.1$). Propeller slipstream and support-sting blockage corrections were neglected, since their combined effect on the velocity was estimated to be below 0.9%.

External Balance

The propeller was installed on an external six-component balance to measure propeller thrust. The balance presented an uncertainty of ±0.02 N in the range of forces measured in the experiment, which corresponds to approximately 0.4% at high thrust ($C_T = 0.35$) and 1.2% at medium thrust ($C_T = 0.2$). Data was acquired at 10 Hz and each measurement point was averaged over 30 seconds. Several measurements were repeated twice to verify the reproducibility of results. In order to obtain the net forces generated by the propeller blades and spinner, all measurements were carried out both with the propeller on (indicated with the subscript "on"), and with the propeller removed and replaced by a dummy spinner (indicated with the subscript "off"). The net thrust, T, is then defined as $T = T_{on} - T_{off}$. It should be noted that the thrust force therefore includes the change in drag on the nacelle and support sting due to the propeller slipstream.

The uncertainty of the thrust measurements was calculated taking into account uncertainties in the blade pitch angle, propeller alignment, and balance readings, as well as the data spread of repeated measurements due to, for example, variations in operating conditions. For this, the sensitivity of propeller thrust to blade pitch angle ($\partial T/\partial \beta$) and angle-of-attack ($\partial T/\partial \alpha$) were obtained from experimental and numerical data of the isolated propeller [90]. The resulting thrust-coefficient uncertainty was below 1% at high thrust ($C_T = 0.35$) and below 3% at medium thrust ($C_T = 0.2$).

Total Pressure Probe

A pressure probe was traversed in z-direction at $x_c/c = 0.8$ to determine the boundary-layer profiles of the isolated wing at the axial position of the propeller disk. The measurement sweep started at 0.5 mm ($0.005R$) clearance from the wing surface, and was traversed up to 240.5 mm ($2.37R$) clearance. The pressure was measured at 57 locations for each of the three spanwise positions sampled ($y/R = 0, -0.9$, and $+0.9$), with a higher resolution in the vicinity of the wing surface. Pressure data were acquired at 10 Hz and averaged over 30 seconds for each point, using a DTC-Initium pressure scanner. The measurement uncertainty of the total pressure sensors (± 4 Pa) and the spread in data due to spanwise variations in the boundary-layer profile led to a total-pressure coefficient uncertainty below 2% of the freestream value. The boundary layer thickness, δ_{99}, was determined as the distance from the surface where the total pressure reached 0.99^2 times the total pressure of the freestream, that is, where $C_{pt} = 0.98$.

Wing Surface Pressure Taps

The wing was instrumented with 81 static pressure taps in order to evaluate the time-average impact of the propeller on the wing pressure distribution. These taps were distributed with a higher density near the leading edge and near the flap hinge. The holes were located along a zig-zag pattern at $y = \pm 15$ mm, i.e., 15 mm above or below the mid-span location of the wing. Due to the geometrical constraints surrounding the flap mechanism, no zig-zag pattern was followed in this region, as visible in Fig. 7.3. Data were acquired at 10 Hz and averaged over 30 seconds acquisition time per measurement point. A subset of measurements were repeated at the start and the end of the experiment to verify the reproducibility of results. The spread in the data of the repeated measurements, along with the uncertainty of the static-pressure sensors of the pressure scanner (± 1 Pa), contribute to a pressure-coefficient uncertainty of approximately ± 0.025.

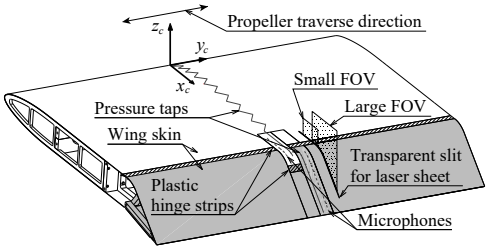

Figure 7.3: Axonometric view of the suction side of the wing model, indicating the location of pressure taps, microphones, and PIV plane. Elements that constitute the flap are shaded in gray. "FOV" = field of view.

Two types of static pressure measurements were taken. In the first, the propeller was installed on an external traversing system and moved in y-direction, mapping the pressure response on the wing surface below the propeller. For these measurements, the propeller was traversed 150 mm in each direction ($y/R = \pm 1.5$), sampling at 51 spanwise locations in total. In the second type of measurement, the propeller—connected to the balance—was positioned at the mid-span of the wing, and the pressure distribution was recorded along the line of pressure taps. In this case, the resulting pressure distribution did not correspond exactly to the mid-section of the wing, due to the zig-zag pattern. The difference was quantified by analyzing the spanwise pressure distribution obtained during the y-sweeps, and included as uncertainty in the results.

Wing Surface Microphones

The wing was instrumented with nineteen Sonion 8044 microphones, in order to map the unsteady pressure response on the wing surface below the propeller slipstream. Twelve microphones were installed on the flap (at $y = 35$ mm), and seven on the main wing immediately upstream of the flap (at $Z = -35$ mm), as indicated in Fig. 7.3. The microphones measured in a frequency range of 20 Hz–15 kHz, with a maximum input level of 123.5 dB (ref $20 \cdot 10^{-6}$ Pa) at 1 kHz and an equivalent noise level of 35 dBA. A frequency-dependent calibration was carried out using a LinearX M53 reference microphone, which was in turn calibrated by means of a GRAS 42AA piston phone.

Microphone data were acquired synchronously with the propeller encoder's once-per-revolution trigger signal using an array of National Instruments 9234 DAQ modules. The microphone data were recorded in tandem with the wing pressure data during the y-sweeps of the propeller. At each point, the signals were measured at a sampling frequency of 51.2 kHz during 30 seconds, which corresponds to approximately 1,500 to 3,500 propeller revolutions (i.e., 9,000 to 21,000 blade passages), depending on the rotational speed of the propeller. Although no quantitative uncertainty analysis was carried out, a comparison of repeated measurements showed that the amplitude of the tonal components differed by less then 1 dB. Furthermore, the levels recorded during the measurements were verified to be at least 25 dB, typically 45 dB, above the background noise levels recorded with the wind tunnel off.

Particle-Image Velocimetry

A stereoscopic PIV setup was used to analyze the velocity field in the propeller slipstream and wing boundary-layer. Two fields-of-view were considered. The main, large field-of-view (FOV) was set up downstream of the flap hinge—i.e., downstream of the propeller disk location—as shown in Fig. 7.3. A second, high-resolution FOV focused on the region surrounding the blade tips. The same light source, seeding, and cameras as in Sec. 6.3.1 were used. The light was directed through the wing with a dedicated slit in the wing and flap skin (see Fig. 7.1b), generating a laser sheet of 2 mm thickness. Both slits were covered with a transparent plastic sheet of 0.2 mm thickness to prevent the through-flow of air. The cameras were employed with 105 mm $f/8$ and 200 mm $f/8$ lenses for the large and small FOVs, respectively. For installed propeller measurements, 600 uncorrelated images were acquired, in addition to 300 phase-locked images at selected phase angles and 300 images with the propeller blades removed (i.e., wing and nacelle only). The main characteristics of the PIV setup are gathered in Table 7.1.

Table 7.1: Main parameters of the PIV setup.

FOV	Large	Small
Focal length [mm]	105	200
Field of view [mm^2]	100 × 150	50 × 65
Pixel shift [pixel] (at V_∞)	9.5	8.2
Imaging resolution [pixel/mm]	19	41
Window size [pixel^2]	24	24
Overlap factor [%]	50	50
Vector spacing [mm]	0.6	0.3
Velocity uncertainty [%]	2.5	2.75

For two measurement cases, phase-locked PIV data were acquired at different y-locations relative to the propeller, by positioning the propeller at different spanwise locations along the wing. The resulting velocity fields were combined to obtain a volumetric data set which provides three-dimensional information of the flow field. The distance between adjacent measurement planes varied from 2.5 to 10 mm, which constituted a relatively low spanwise resolution. Thus, during the post-processing, the velocity fields were interpolated on additional planes between each pair of measurement planes to improve the visualization of the blade wakes and tip vortices, as described in Appendix F.2.

C. DETERMINATION OF TIP-CLEARANCES: ISOLATED-WING CHARACTERISTICS

This section describes the aerodynamic characteristics of the isolated wing, to establish the conditions under which the interaction effects are studied in subsequent sections. Figure 7.4 shows the pressure-coefficient distributions obtained on the wing surface, with the propeller and support sting removed. When the flap is deflected by $\delta_f = 20^o$, an appreciable pressure peak is generated over the flap, as shown in Fig. 7.4. The pressure gradient on the suction side tends towards zero near $x_c/c = 1$, indicating that the flow has separated at the trailing edge. A suction peak is also generated on the pressure side, since the surface is convex near the flap hinge. Together, this leads to a low sectional lift coefficient of $c_l = 0.1$. Moreover, a small pressure peak is generated around $x_c/c = 0.08$

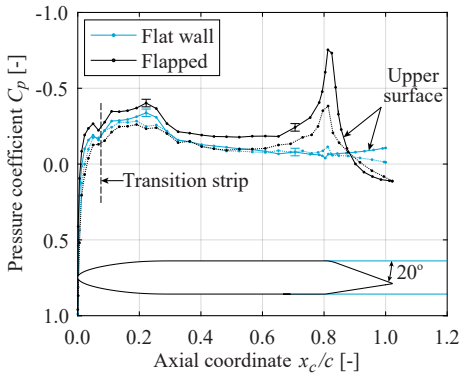

Figure 7.4: Isolated-wing C_p distributions in the flat-wall and flapped configurations ($V_\infty = 20$ m/s, BL$_1$).

by the trip strip, while additional suction is generated around $x_c/c = 0.22$ due to a flaw in the curvature of the wing skin. However, these peaks occur relatively far (approximately six radii) upstream of the propeller location, and therefore have a negligible impact on the interaction phenomena.

In the flat-wall configuration, the difference between the pressure and suction sides of the wing is negligible, and the pressure gradient is small for $x_c/c > 0.4$. However, several imperfections are visible. Firstly, small pressure peaks are generated around $x_c/c = 0.8$, due to steps in the surface geometry at the overlap from the main element to the flap. Secondly, towards the trailing edge, the difference between the pressure side and suction side increases, indicating that the flap surfaces—which were aligned with the downstream extension block (see Fig. 7.2)—were not perfectly parallel. These imperfections may affect the development of the boundary layer, and therefore it is necessary to determine the boundary-layer profiles inherent to this experimental setup. Nevertheless, the average pressure-coefficient increase across the propeller disk, which can be calculated by dividing the propeller thrust by the disk area, ranges from approximately 0.2 at medium thrust to 0.6 at high thrust. Thus, the local pressure variations due to surface imperfections are small, and the interaction phenomena are dominated by the effect of the propeller.

The boundary-layer profiles are presented for different configurations and operating conditions in Fig. 7.5. The effect of an increase in equivalent surface roughness can be observed by comparing the two flat-wall profiles at $V_\infty = 40$ m/s: when the boundary layer is tripped (BL_1), the boundary-layer thickness is $\delta_{99}/R = 0.14$, while with an increase in surface roughness (BL_2), the thickness increases to $\delta_{99}/R = 0.20$. This 43% increase in boundary-layer thickness corresponds to an increase in the equivalent turbulent flat-plate Reynolds number[1] from $Re_{FP} = 1.8 \cdot 10^6$ to $Re_{FP} = 2.8 \cdot 10^6$. The measurements at $V_\infty = 20$ m/s, on the other hand, both correspond to BL_1. Under those

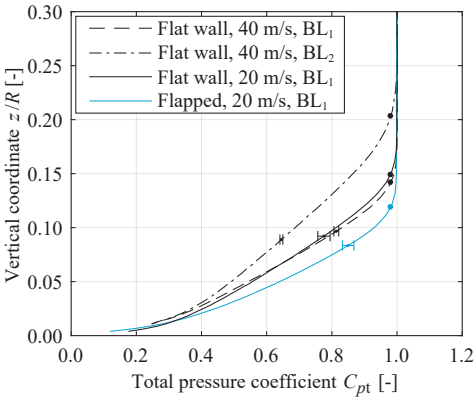

Figure 7.5: Boundary-layer profiles on the wing surface at $x_c/c = 0.8$, with the propeller and support sting removed. Round markers indicate the vertical coordinate corresponding to δ_{99}.

[1] The equivalent turbulent flat-plate Reynolds number is defined as $Re_{FP} = (\rho_\infty V_\infty X_{FP})/\mu$, where X_{FP} is the distance to the virtual origin of the equivalent flat plate, computed using $\delta_{99} = 0.37 X_{FP} \left(\rho_\infty V_\infty X_{FP}/\mu\right)^{-1/5}$ [273].

conditions, the flat-wall boundary-layer is thicker than the one obtained with the flap deflected, due to the increased velocity over the wing in the flap-deflected case. When comparing the flat-wall boundary-layers (BL_1) at 20 m/s and 40 m/s, it appears that the former is thicker, as expected, but also presents a fuller profile than the latter. This suggests that the surface geometry was altered between the two measurements, most likely due to changes in the plastic hinge strips (see Fig. 7.3), which are situated near the measurement location.

The values of δ_{99} are summarized in Table 7.2. The propeller tip-clearances analyzed throughout this Chapter are selected as fractions or integer multiples of these values. Note that, when the flap is deflected, the propeller tip-clearance is still selected as a fraction or multiple of the flat-wall boundary-layer thickness. In this way, the same absolute separation between the blade tips and the wing surface (ε/R) was kept, and thus the time-average pressure effect of the propeller on the wing is maintained.

Table 7.2: Summary of the measured boundary-layer configurations and propeller tip-clearance values.

Configuration	δ_{99}/R	ε/R
Flat wall, BL_1 (40 m/s)	0.14	0.07 (½BL_1)
		0.14 (1BL_1)
		0.28 (2BL_1)
Flat wall, BL_2 (40 m/s)	0.20	0.10 (½BL_2)
		0.20 (1BL_2)
		0.40 (2BL_2)
Flat wall, BL_1 (20 m/s)	0.15	0.037 (¼BL_1)
		0.07 (½BL_1)
		0.15 (1BL_1)
$\delta_f = 20^o$, BL_1 (20 m/s)	0.12	0.037 (¼BL_1)
		0.07 (½BL_1)
		0.15 (1BL_1)
		0.44 (3BL_1)

7.1.2. NUMERICAL SETUP

In the following sections, the computational set up is explained, starting with the geometry of the wing and propeller models, and followed by the solver setup, computational domain, operating conditions, and propeller modeling technique. Finally, the effect of the overset mesh and a grid convergence study are discussed to assess the numerical uncertainty. A comparison to experimental data is performed in Sec. 7.3.3. A more detailed description of the numerical setup is provided in Ref. [271].

A. GEOMETRY AND OPERATING CONDITIONS

The wing and propeller geometries of the experimental investigation described in Sec. 7.1.1 are used, such that a validation study can be performed. Since only the flap-deflected configuration is analyzed, the true chord with flap deflected, $c = 1.042$, is used as reference chord in the numerical simulations. The inclined OTW propeller position is

derived from the baseline configuration by rotating the propeller around the flap hinge by the flap-deflection angle, $\delta_f = 20°$, as shown in Fig. 7.2. Consequently, the inclined propeller is positioned behind the flap curvature, closer to the trailing edge than the baseline propeller, and the axis of the inclined propeller is parallel to the suction side of the flap. This configuration would be obtained if the propeller were physically attached to the flap mechanism. The gap between the propeller tips and the wing surface, ε, is 7.5 mm ($\varepsilon/R = 0.0738$) in both configurations. This corresponds to the ½BL$_1$ configuration defined in the previous section. The simulations are also performed at the same freestream velocity ($U_\infty = 20$ m/s, $Re = 1.4 \cdot 10^6$). An advance ratio of $J = 1.13$ is simulated, which corresponds to high thrust in uninstalled conditions ($C_T = 0.35$), being representative of a typical take-off thrust setting.

B. COMPUTATIONAL DOMAIN

The computational domain of the isolated propeller simulations is shown in Fig. 7.6a. The working fluid is air and is treated as a compressible, ideal, gas, where Sutherland's Law is used to calculate the dynamic viscosity. The walls of the propeller blade, spinner, and nacelle are modeled as no-slip walls with a first layer height below $y^+ = 1$. The total gauge pressure and total temperature are specified at the inlet whereas, at the outlet, the pressure is prescribed to be the ambient, standard, sea-level pressure. Values for the turbulence quantities k and ω are chosen based on the recommendations by Spalart and Rumsey [258], and source terms are used in the flow to prevent their decay from the inlet to the model. Only one blade with periodic boundary conditions is modeled in the domain to reduce the required calculation time. At the top boundary, a pressure far-field condition is used with a prescribed Mach number, static pressure, and static temperature corresponding with the inlet condition. The mesh is locally refined in areas close to the propeller geometry, as well as upstream and downstream of the propeller, as shown in Fig. 7.6b.

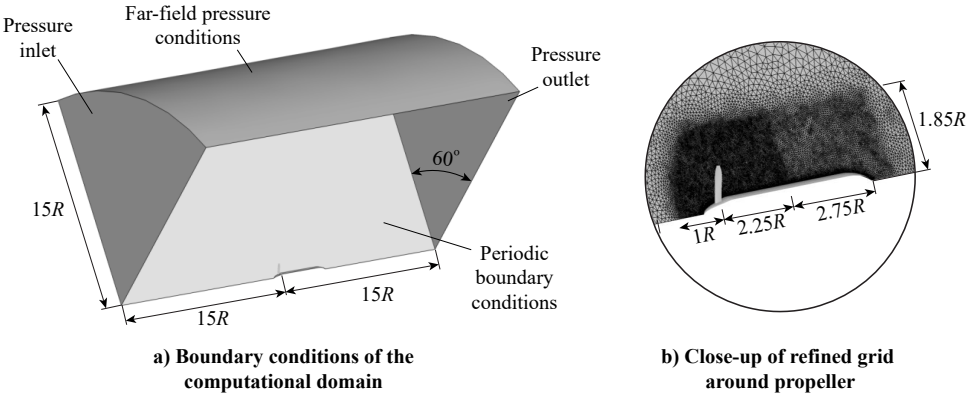

Figure 7.6: Computational domain of the isolated propeller.

The dimensions of the isolated wing and its domain are identical to the ones of the installed OTW simulations, except for the volume where the propeller mesh is added with the overset technique. Therefore, only the domain of the OTW configuration is shown in

Fig. 7.7. An overset approach was selected in the installed propeller simulations for two reasons: to reduce the number of cells required, and to simulate the two configurations without having to completely redefine the mesh. The comparison of the numerical to the experimental results is done for the baseline configuration with wind tunnel walls, shown in Figs. 7.7a and 7.7c, where the cross-section in Fig. 7.7a has the same dimensions as the test-section of the experiment.

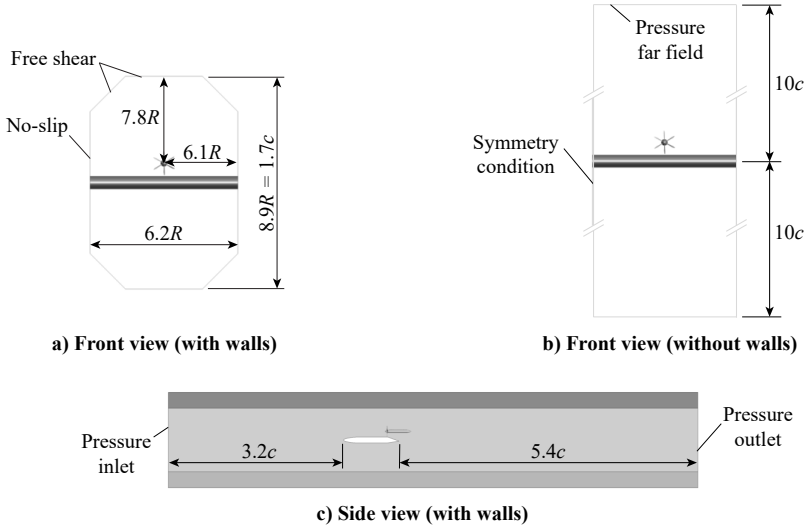

Figure 7.7: Computational domain of the configurations with (a, c) and without (b) wind-tunnel walls.

The domain extends approximately three chords upstream and five chords downstream of the wing. For the comparison to experimental data, the sidewalls of the wind tunnel that intersect with the wing model are modeled as a no-slip boundary condition to account for the interaction of the wing with the wind-tunnel boundary-layer. To reduce the computational effort, however, a wall-function approach is used at these sidewalls, contrary to the resolved boundary-layer with $y^+ < 1$ on the wing. All other walls of the wind tunnel are set as free-slip walls. In the remaining studies (Sec. 7.4), the influence of the wind tunnel walls is removed by changing the sidewalls to symmetry boundary conditions and extending the top and bottom of the domain with far-field pressure boundary conditions ten chord lengths away, as shown in Fig. 7.7b. The length and width of the domain is not changed, and all other solver settings are kept constant, compared to the domain with wind tunnel walls.

C. SOLVER SETUP

The simulations are performed as unsteady, compressible, Reynolds-Averaged Navier–Stokes (RANS) calculations with the commercial, cell-centered, finite volume ANSYS Fluent 19.1 solver. Unsteady RANS simulations are chosen based on the findings in Ref. [149]. To improve the accuracy of predicting flows with a strong adverse pressure gradient, the k-ω based Explicit Algebraic Reynolds Stress Model (EARSM) by Wallin and Johansson [274] is used to model turbulence. This model is reported to predict effects of

rotation, and the separation behavior of boundary-layers in adverse pressure gradients better than two-equation models due to a more realistic representation of the anisotropy in the flow [274]. The pressure and momentum coupling algorithm by Rhie-Chow [275] is used, where spatial discretization is achieved by second-order upwind schemes and a first-order implicit transient formulation is employed. The unsteady calculations of the installed configurations are performed with a time-step that is equal to two degrees of propeller rotation, with 30 inner iterations. The isolated wing and propeller simulations, however, are performed as steady simulations with a Courant-Friedrichs-Lewy (CFL) condition of CFL = 2. A moving reference-frame approach is used for the isolated propeller calculation, where only one blade is simulated using periodic boundary conditions.

D. VERIFICATION & UNCERTAINTY QUANTIFICATION

A verification study is performed to assess the effect of the overset mesh and to quantify the uncertainty due to convergence error and discretization error. This verification study is not discussed in detail here to improve readability, although it is included in Appendix E.2 for traceability. Based on the mesh refinement study, a wing mesh of approximately 80,000 cells and a propeller mesh of approximately 3.9 million cells are selected. For the propeller mesh, the thrust and torque uncertainties due to discretization error are estimated to be 1%, based on the procedure of Ref. [276]. For the wing mesh, the lift and drag uncertainties are estimated to be 4% and 6%, respectively. Moreover, the iterative error is confirmed to be small compared to the discretization error. However, a comparison of the boundary-layer profiles with and without an empty overset mesh show that the interpolation procedure in the overlap region of the wing and propeller mesh leads to a minor kink in the velocity distribution near the wing surface, effectively creating a slightly fuller boundary-layer profile. Although this does not appreciably affect the overall lift and drag values of the wing, it should be taken into account when interpreting the results, and is discussed in more detail in the validation study of Sec. 7.3.3 .

7.2. AERODYNAMIC INTERACTION WITH A FLAT-WALL BOUNDARY LAYER

This section describes how the propeller interacts with the boundary layer developing over a wing without axial pressure gradients. In this configuration, the boundary-layer thickness and propeller tip-clearance were found to have a negligible effect on propeller thrust, as reflected in Fig. 7.8. The interaction effects are decomposed into a steady and unsteady component in the following subsections. In both cases, the phenomena are presented for high thrust and low tip clearance (BL_1, $V_\infty = 20$ m/s, $C_T = 0.35$, $\varepsilon/R = 0.037$), unless explicitly mentioned otherwise.

7.2.1. TIME-AVERAGED FLOW PHENOMENA

The velocity distributions between the nacelle and the wing surface in the flat-wall configuration are shown in Fig. 7.9. In propeller-off conditions, the axial velocity in this region is slightly higher than the freestream velocity due to the presence of the nacelle and wing (Fig. 7.9a). When the propeller is installed and operated at a high thrust setting (Fig.

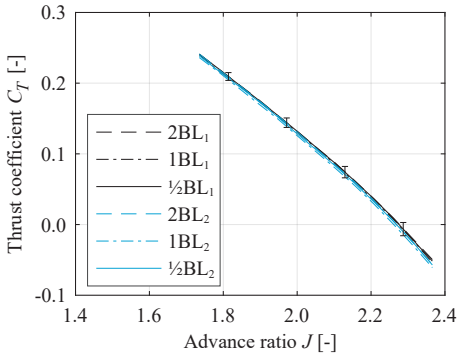

Figure 7.8: Propeller thrust curves, measured for different tip clearances and boundary-layer thicknesses in the flat-wall configuration (V_∞ = 40 m/s).

7.9b), the axial velocity in the slipstream is increased, especially near the radial location of highest loading ($r/R \approx 0.7$). Immediately downstream of the propeller disk, near the surface, a region of low axial velocity is observed. The low-velocity region is originated directly beneath the propeller disk due to slipstream contraction close to the wall, and persists until the flow has convected approximately half a propeller radius downstream. Beyond that point, the slipstream approaches the wall and the velocity near the surface increases. This effect is further evidenced in Figs. 7.9c and 7.9d. At $x/R = 0.2$, the flow velocity near the wall is lower than in the propeller-off case, although no reverse flow is observed. The swirl angle, however, is opposed to the swirl inside the slipstream. At $x/R = 0.8$, on the other hand, the velocity is higher near the wall. Moreover, a significant swirl angle remains in the vicinity of the wall. This indicates that the edge of the slipstream has approached the wall, since, in a time-averaged sense, swirl is only generated inside the propeller slipstream. The cause of this vertical displacement is described in subsequent subsections.

The corresponding surface-pressure field induced by the propeller is shown in Fig. 7.10. In this figure, the static pressure measured in the propeller-off case has been subtracted (i.e., $\Delta C_p = C_{p,\text{on}} - C_{p,\text{off}}$), to remove the effect of the nacelle. The static-pressure jump created across the propeller disk leads to a decrease in pressure on the wall upstream of the propeller, and an increase in pressure downstream of it. Although at low thrust settings and large tip-clearances the effect on the wing surface is weak, at higher thrust settings and smaller clearances, more pronounced pressure peaks are observed. The suction peak generated ahead of the propeller is nearly symmetric with respect to $y/R = 0$, as expected from earlier studies [167, 277] and the findings of Sec. 6.1. The pressure peak created downstream of the propeller, however, is not. This is due to the tangential momentum imparted to the flow by the propeller, which leads to a spanwise velocity component near the wall, as reflected in Fig. 7.9d.

Between the two pressure peaks observed in Fig. 7.10, a strong adverse pressure gradient is generated. The magnitude of this adverse pressure gradient is directly proportional to the propeller's thrust, since it is governed by the pressure jump across the disk. This is shown in Fig. 7.11, where the parameter $C_T/J^2 \propto T_c$ is used on the x-axis to exclude the effect of rotational speed from the non-dimensionalization. It should

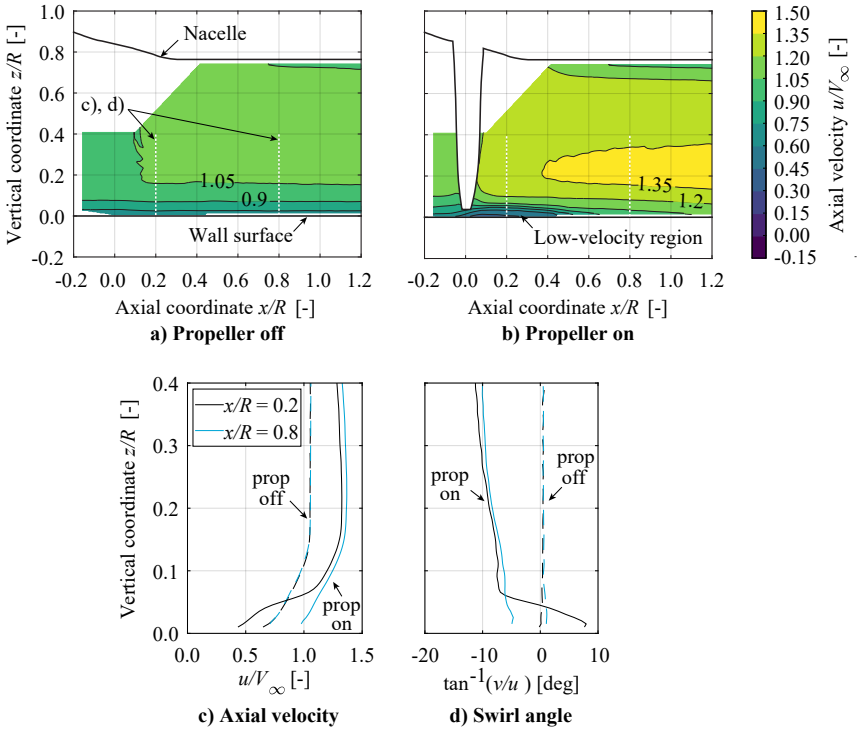

Figure 7.9: Time-averaged velocity distributions between nacelle and flat wall (experimental data, $y/R = 0$).

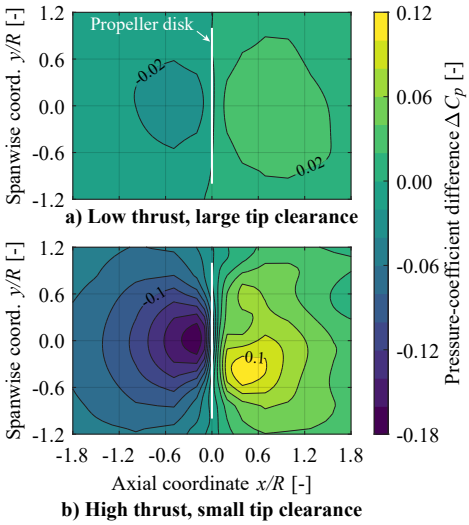

Figure 7.10: Wing surface-pressure distribution induced by the propeller in the flat-wall configuration. Measurements at a) $V_\infty = 40$ m/s, $C_T = 0.2$, $\varepsilon/R = 0.14$, and b) $V_\infty = 20$ m/s, $C_T = 0.35$, $\varepsilon/R = 0.037$.

be noted that these measurements were performed at 40 m/s and therefore do not reach the high thrust coefficients of Figs. 7.9b or 7.10b ($C_T < 0.25$). The slopes of the curves increase with decreasing tip-clearance, while showing no significant dependency on the boundary-layer thickness—although additional measurements at constant tip-clearance and different boundary-layer thicknesses would be required to quantify this. This suggests that the time-averaged adverse pressure gradient generated beneath the propeller can be captured by lower-order methods such as actuator disk models.

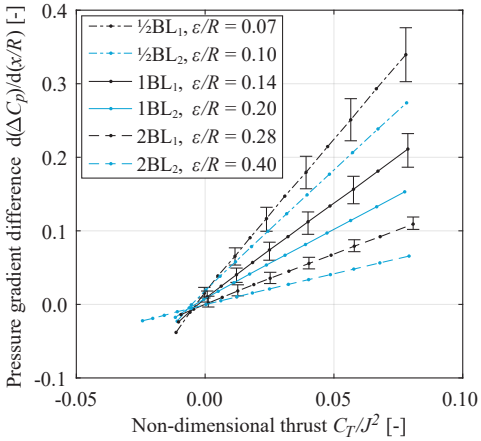

Figure 7.11: Non-dimensional pressure gradient measured on the wing surface below the propeller disk in the flat-wall configuration ($V_\infty = 40$ m/s).

7.2.2. UNSTEADY FLOW PHENOMENA

Additional insight into the interaction mechanisms can be gained by analyzing the unsteady flow structures in the propeller slipstream. To this end, the aerodynamic interaction between the tip vortices and the wing boundary-layer is first assessed by analyzing the local velocity fields. The pressure fluctuations generated on the wing surface by these flow structures are then described, and finally the velocity and pressure distributions are combined to provide a volumetric description of the evolution of the tip vortices.

A. VORTEX–BOUNDARY-LAYER INTERACTION

Figure 7.12 presents the phase-averaged spanwise vorticity distribution in the $y/R = 0$ plane, for three different phase angles. The non-dimensional vorticity is defined as $\tilde{\omega}_y^* = \tilde{\omega}_y D/u_{\text{eff}}$, where u_{eff} is the theoretical velocity at the propeller disk, as obtained from actuator-disk theory for a given thrust coefficient [138]. For this measurement, the thrust coefficient corresponds to an effective velocity of $u_{\text{eff}} = 1.13 V_\infty$. The propeller tip vortices appear in Fig. 7.12 as regions of highly concentrated (negative) spanwise vorticity. The vorticity contained in the blade wakes, on the other hand, switches sign in accordance with the spanwise loading gradient along the propeller blade. The negative vorticity in the boundary layer is also visible near the wall. When comparing the three time instances, it becomes evident that the tip vortices initially move away from the wall and subsequently, beyond $x/R \approx 0.25$, start to approach the wall again. The trajectory followed by each tip vortex delimits the low-speed region observed in Fig. 7.9.

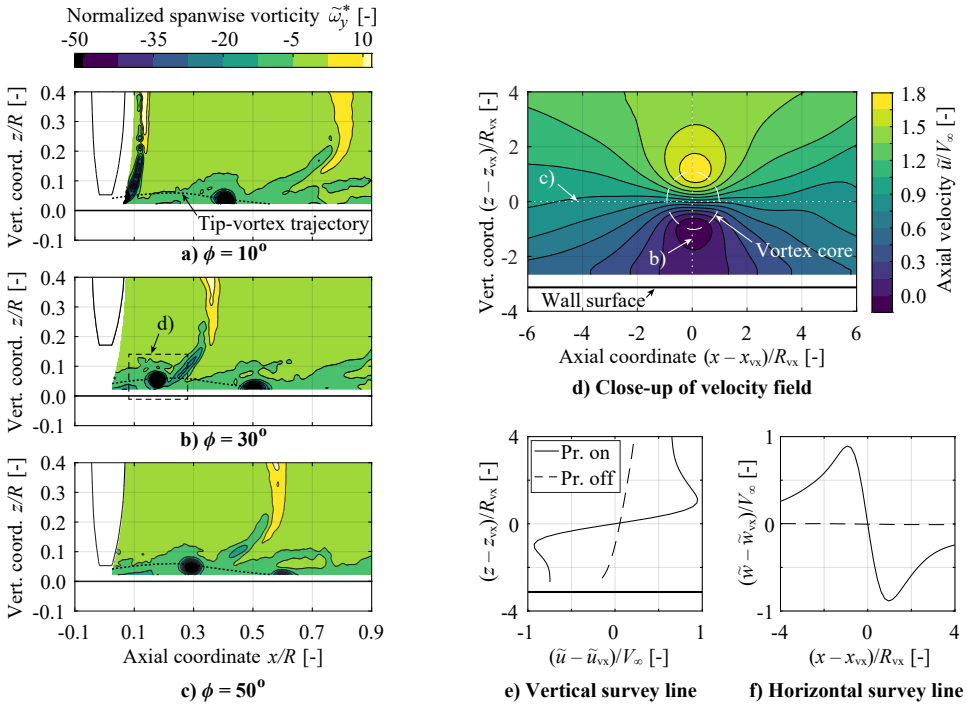

Figure 7.12: Phase-averaged spanwise vorticity (left) and velocity (right) distributions in propeller slipstream, obtained from PIV measurements.

The velocity field surrounding the vortex indicated in Fig. 7.12b is analyzed in more detail in Fig. 7.12d, to verify whether the viscous shear between the boundary layer and the vortices is responsible for their downwards displacement. The axes of Fig. 7.12d are expressed relative to the center of the vortex core, for which the point of maximum out-of-plane vorticity $\tilde{\omega}_y$ is selected. Figure 7.12d also indicates the boundaries of the vortex core, defined by the radial coordinate where the tangential velocity with respect to the center of the vortex is maximum. The average distance to the vortex center is then taken as the vortex radius, R_{vx}. It is worth noting that this "phase-averaged vortex core" is larger than the vortex core that would be identified in an instantaneous velocity field. This occurs because, for the same phase angle, the tip vortices are located at slightly different positions from one blade passage to another, due to the random interaction with the turbulent eddies in the boundary layer. This random behavior was confirmed by comparing the instantaneous velocity fields obtained from PIV (not shown here). The flow field of Fig. 7.12d shows that, on average, a region of negative velocity is induced beneath the vortex, although at the wall no flow reversal is observed.

More insight can be gained by extracting two survey lines, shown in Figs. 7.12e and 7.12f. These plots present two velocity profiles, expressed relative to the velocity at which the vortex core is convected ($\tilde{u}_{vx}$, $\tilde{v}_{vx}$). Figure 7.12e shows that the axial velocity profiles above and below the vortex center are roughly anti-symmetric, but that the top half tends

asymptotically to a higher absolute axial velocity than the lower half. This is due to the superimposed effect of the boundary-layer profile and image vortex. The vertical velocity on the horizontal survey line (Fig. 7.12f), on the other hand, tends towards the zero on either side of the vortex core. The shear stresses on either side of the vortex therefore counteract each other, which suggests that no appreciable net vertical force is exerted on the vortex core. These findings are in line with the predictions of Doligalski and Walker [166] and Chuang and Conlisk [165], who studied the response of a convecting rectilinear vortex near a wall and defined the ratio between the convection speed of the vortex core and the uniform inflow velocity[1], α, as

$$\alpha = \frac{u_{\mathrm{vx}}}{u_\infty} = 1 + \frac{u_{\mathrm{ind}}}{u_\infty}, \tag{7.1}$$

where u_{ind} is the velocity induced by the image vortex, such that $u_{\mathrm{vx}} = u_\infty + u_{\mathrm{ind}}$. The velocity induced by the image vortex accounts for both the vortex strength Γ_{vx} and distance to the wall $\varepsilon_{\mathrm{vx}}$, since $u_{\mathrm{ind}} = \Gamma_{\mathrm{vx}}/(2\pi(2\varepsilon_{\mathrm{vx}}))$. The circulation of the vortex core can be obtained by integrating the vorticity inside the core ($\Gamma_{\mathrm{vx,core}} = -0.19\ \mathrm{m}^2/\mathrm{s}$). By assuming that this is approximately equal to the total circulation of the vortex ($\Gamma_{\mathrm{vx}} \approx \Gamma_{\mathrm{vx,core}}$) and extracting the convective velocity and vortex position from Fig. 7.12d, a velocity ratio of $\alpha = 0.85$ is obtained from Eq. 7.1. For this value, the interaction with the boundary layer has a negligible effect on the vertical position of the vortex [165]. Moreover, in the inviscid limit, no flow reversal should occur near the wall for $\alpha > 0.75$ [166], which is consistent with the velocity field of Fig. 7.12d. Although the exact limit differs for viscous flow [166], the velocity ratio obtained in this experiment appears to be beyond this limit. This confirms that the vertical displacement of the tip vortices is not caused by viscous interaction with the boundary layer, but by additional effects that are not captured in this simplified analysis, such as pressure gradients or three-dimensional effects.

B. PROPELLER-INDUCED SURFACE PRESSURE FLUCTUATIONS

The vortex cores are not visible downstream of $x/R \approx 0.6$ in the FOV of Fig. 7.12. To further investigate this effect, the rms of the surface-pressure fluctuations is shown in Fig. 7.13. Directly beneath the propeller, at the locations indicated with crosses, the maximum excitation amplitude of the microphones was exceeded. Therefore, the values in this region are conservative, and no quantitative comparisons should be made. Nevertheless, several important qualitative observations can be made based on the unsteady pressure distributions. With these observations it is possible to distinguish three different regions of pressure fluctuations, as indicated in the bottom part of Fig. 7.13.

Firstly, the rms of the surface-pressure fluctuations is larger than the time-averaged surface-pressure difference induced by the propeller (see Fig. 7.10). This indicates that the discrete blade passages generate large differences between the maximum and minimum surface pressures, which could be reduced by producing the same thrust with a higher number of blades. Secondly, two distinct regions of pressure fluctuations can be observed in Fig. 7.13: fluctuations induced by the propeller blades (bound vorticity and volume displacement), and fluctuations induced by the tip vortices (trailing vorticity). Upstream of the propeller, the surface-pressure fluctuations are dominated by the

[1] Note that the local "effective" uniform inflow velocity at the vortex location is unknown, since it is affected by the presence of both the boundary layer and the propeller slipstream ($u_\infty \neq V_\infty$).

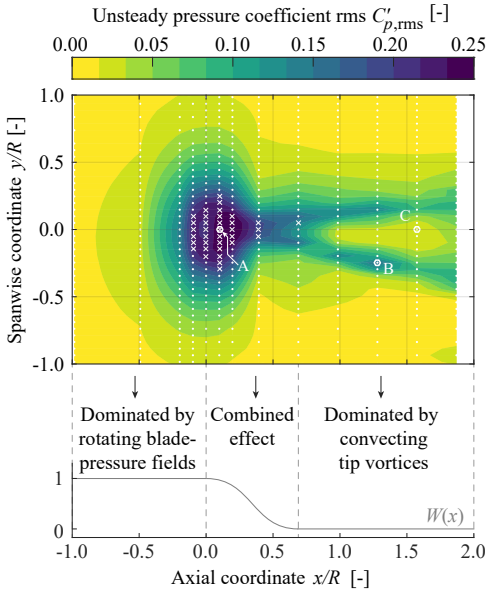

Figure 7.13: Unsteady pressure-coefficient rms contours on the wall surface. Dots indicate measurement locations, while crosses indicate locations where the maximum input level of the microphone was exceeded.

static-pressure fields surrounding each propeller blade, which are approximately constant in a rotating reference frame, but lead to periodic perturbations in an inertial reference frame. "Far" downstream of the propeller, the surface-pressure fluctuations are dominated by the flow structures convected in the slipstream. Between these two regions, the two contributions are superimposed. Moreover, although Fig. 7.12 indicates that the blades' trailing vorticity rapidly concentrates in the tip vortices, Fig. 7.13 shows that the surface-pressure fluctuations produced by the propeller blades are larger than the ones produced further downstream by the tip vortices. This occurs because, at the propeller location, the surface pressure is affected by the trailing vorticity, the bound vorticity, and the volume displacement of the blades. Far downstream, the surface pressure is only affected by the trailing vorticity. The relative importance of the three contributions directly beneath the propeller disk could not be established with the current data set. Although this does not affect the conclusions drawn in this chapter, a more detailed investigation into the flow field surrounding the blade tip and its effect on the unsteady surface-pressure distributions can be recommended for future research.

Figure 7.13 also shows that, downstream of the propeller, the streak of high-amplitude fluctuations splits in two. The pressure spectra recorded at locations B and C, shown in Fig. 7.14, indicate that the region of low rms between the two streaks only presents a weak tonal component at the blade passage frequency. However, in the streak of increased rms—as well as at point A—the pressure spectrum is dominated by high-amplitude peaks at the blade passage frequency and multiple harmonics. Therefore, while at locations A and B sharp waveforms are generated by the passage of the propeller blades and tip vortices, respectively, at point C these excitations are barely perceived.

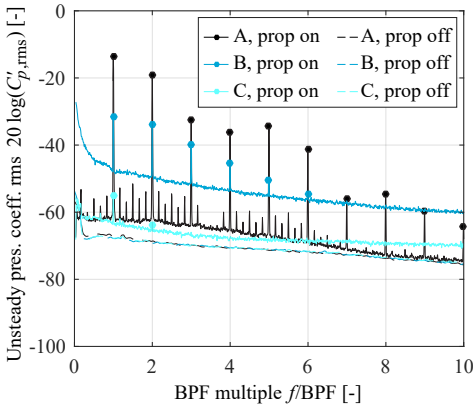

Figure 7.14: Surface-pressure spectra recorded at the locations indicated in Fig. 7.13. Note that the maximum excitation amplitude of the microphone was exceeded at location A in the propeller-on case. BPF = 482 Hz.

The mechanism that causes the high-rms region to divide in two can be understood by analyzing the interaction of the tip vortices with the solid surface. However, the axial measurement resolution is relatively low, being of the same order-of-magnitude as the wavelength of the dominant excitation in this region. Hence, the axial plotting resolution is artificially increased by reconstructing the pressure history between subsequent axial measurement locations, as described in Appendix F.3. Given that not all measurements were acquired synchronously, only the phased-averaged waveforms are reconstructed. Figure 7.14 shows that the tonal excitations are dominant, and thus only a negligible amount of information is lost by removing the broadband component of the fluctuations. Moreover, since these pressure perturbations are hydrodynamic in nature, they propagate according to the local flow and boundary conditions, and not as acoustic waves. Upstream of the propeller ($x/R < 0$), the tonal pressure fluctuations displace in negative y-direction, following the local movement of the blades. Far downstream of the propeller ($x/R > 0.7$), the pressure fluctuations displace mainly in axial direction, convected at the local flow velocity. Finally, for the interpolation procedure, a sigmoid weighting function $W(xX)$ is applied in the overlap region ($0 < x/R < 0.7$) to provide a smooth transition between the two excitation sources, as shown in Fig. 7.13.

The pressure-reconstruction process presents some uncertainty for several reasons, such as outliers in the estimated convective-velocity distribution, and the arbitrary choice of a sigmoid weighting function. Therefore, for validation, the instantaneous pressure distributions are compared to the phase-locked vorticity field obtained from the PIV measurements in Fig. 7.15. This figure shows the spanwise vorticity distribution in the $y/R = 0$ plane together with the phase-averaged surface-pressure distribution, for a phase angle of $\phi = 35^{\circ}$. The pressure distribution contains both the time-averaged component acquired with the pressure taps, and the unsteady component acquired with the microphones. Beneath the tip vortices, whose location can be clearly identified in the vorticity field, regions of low pressure are observed. Peaks of low pressure are also induced ahead of the propeller blades, which are responsible for the low-pressure area shown upstream of the propeller disk in Fig. 7.10. A time-resolved animation showed

that the location of the suction peaks on the surface is consistent with the position of the propeller blades and tip vortices, for all phase angles. This indicates that the pressure reconstruction is, at least qualitatively, correct. Moreover, a comparison of different phase angles shows how the suction peaks created ahead of the propeller are strongest when the blade tip is closest to the wall ($\phi \approx 0^o$). The strength of the pressure fluctuations induced by the tip vortices decreases as they are convected downstream, especially in the $y/R = 0$ plane.

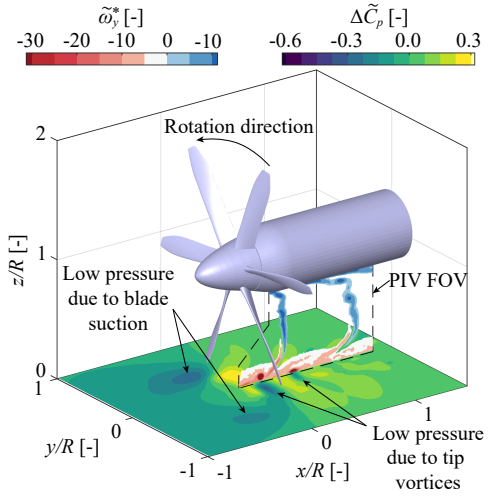

Figure 7.15: Comparison of phase-averaged surface-pressure and slipstream-vorticity distributions for $\phi = 35^o$. Vorticity contours only shown for $|\tilde{\omega}_y^*| > 2$. Figure based on experimental data.

7

C. TIP-VORTEX DEFORMATION

To determine how the slipstream structures evolve outside the $y/R = 0$ plane, Fig. 7.16 presents a close-up view of the blade-tip region for a phase angle of $\phi = 5^o$. The vortex trailing behind the blade tip is clearly identifiable in the vorticity field. The figure confirms that the low-pressure region generated beneath the tip vortices is also captured outside of the $y/R = 0$ plane. For this blade angle, a strong suction peak is generated on the wall ahead of the suction side of the blade. Downstream of the propeller blade, a $\tilde{\omega}_y^* = -15$ isosurface is present near the wall, due to the strong vertical gradient of axial velocity in the boundary layer. At this location the pressure at the wall has increased, due to the increased static pressure behind the blade and the associated slipstream contraction.

In Fig. 7.16, the projection of the downstream tip vortex onto the wall is curved and suggests that the vortex filament has deformed. This can be confirmed by analyzing the unsteady pressure distribution on the wall for a determined phase angle, as shown in Fig. 7.17. This figure includes the projection of the tip vortices, which are drawn based on the $\Delta\tilde{C}_p$ distribution and on the data presented in Figs. 7.12 and 7.13. In an undisturbed slipstream, the tip vortices follow a helical path, and thus these projections would locally appear as oblique lines positioned at an angle equal to the pitch of the helix, with a weak inflection point at $y/R = 0$. However, due to the presence of the wall, the vortex segments

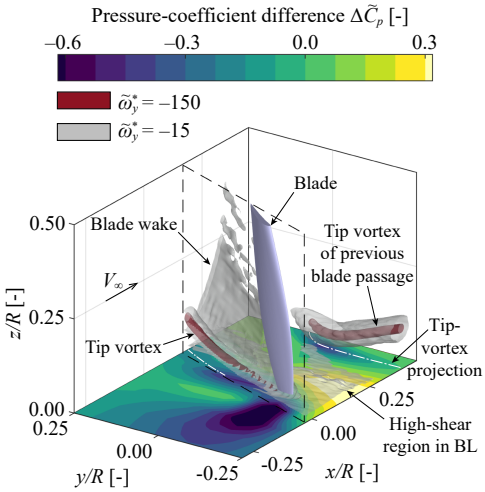

Figure 7.16: Phase-averaged surface-pressure distribution and vorticity isosurfaces in the vicinity of the propeller blade-tip for $\phi = 5^o$. Vorticity isosurfaces only shown downstream of the plane indicated by dashed black lines. Figure based on experimental data.

closest to the wall are convected at a lower axial velocity. Consequently, the segments below the propeller axis ($y/R = 0$) start to lag, and the vortices deform. This is clearly visible for the second vortex ("Vx. 2") in Fig. 7.17. Due to the downwards displacement of the slipstream, the central part of the vortex filament eventually approaches the wall and splits in two, as can be seen for the third and fourth vortex.

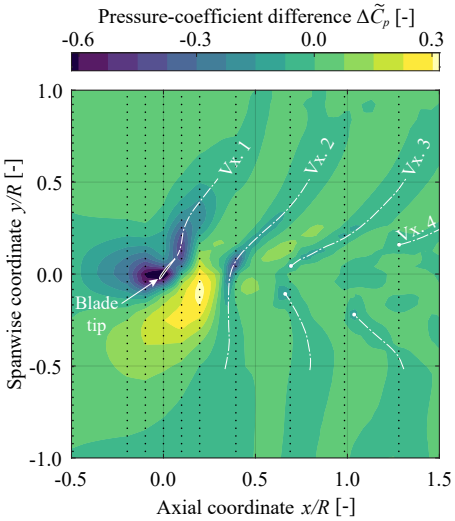

Figure 7.17: Phase-averaged surface pressure-coefficient distribution beneath the propeller slipstream for $\phi = 0^o$. Data based on microphone measurements, i.e., mean pressure is not included.

Finally, a schematic representation of the phenomena observed in Figs. 7.10–7.17 is drawn in Fig. 7.18 to explain the downwards displacement of the slipstream. When the

tip vortex is originally formed behind the blade, it follows a helical path (point A). Due to the strong pressure jump across the propeller disk, the slipstream contracts and the tip vortex moves away from the wall (Point B). However, the pressure increase behind the disk also leads to a spanwise pressure gradient on the wall. The spanwise gradient accelerates the flow away from the $y/R = 0$ plane. This in turn creates a mass deficit near the wall in the $y/R = 0$ plane, which leads to fluid entrainment from the slipstream above. Since the slipstream contraction rate rapidly diminishes downstream of the disk (as known from actuator disk theory; see e.g. Ref. [138]), beyond a determined point B, the effect of the spanwise gradient becomes dominant and causes the slipstream to move downwards. Simultaneously, the vortex filament is deformed due to the lower convective velocity near the wall. For the thrust coefficient and advance ratios studied in this experiment, an undisturbed helical vortex would constitute a stable structure which only self-induces axial velocities [278]. However, due to the local deformation of the tip vortex, this equilibrium is lost, and the vortex filament self-induces a velocity in the negative z-direction in the $y/R = 0$ plane (point C). This further contributes to the downwards displacement of the slipstream. Eventually, the tip vortex comes in very close proximity to the wall, where the axial velocity tends to zero due to the no-slip condition. The associated deformation and dissipation causes the central segment of the filament to split in two (point D). Since at the wall no normal velocities can be induced, the vorticity vector must reorient, and the two extremities of the vortex filament must be perpendicular to the wall. These two ends gradually separate from each other as they convect downstream, as shown in Fig. 7.13. The distance between the propeller disk and point D, x_D, increases with increasing tip-clearance or decreasing thrust coefficient. As this distance increases, the velocity deficit beneath the slipstream reduces, until eventually the point of slipstream adherence to the wall disappears ($x_D \to \infty$), leaving a relatively undisturbed channel between the slipstream edge and the wall surface. This is reflected in Table 7.3, which provides the approximate location of point D for different thrust settings and tip clearances, based on additional PIV data.

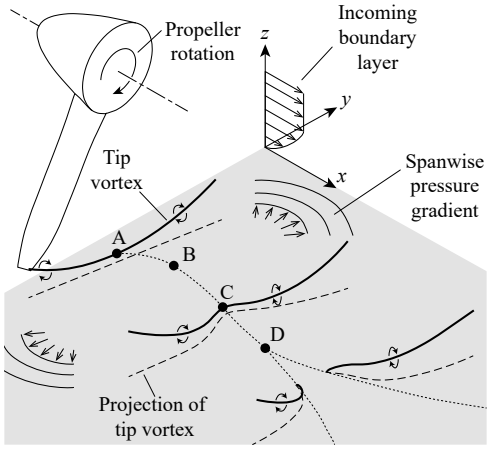

Figure 7.18: Notional interpretation of the evolution of the tip vortices. The dotted line represents the trajectory of the lowest point of the vortex filament.

Table 7.3: Approximate location of point D (see Fig. 7.18), for different thrust settings and tip clearances.

Constant thrust ($C_T = 0.35$)		**Constant clearance ($\varepsilon/R = 0.037$)**	
ε/R	x_D/R	C_T	x_D/R
0.037	0.6	0.35	0.6
0.07	1.5	0.20	0.8
0.15	∞	0.10	∞

7.3. AERODYNAMIC INTERACTION WITH EXTERNAL PRESSURE GRADIENTS

When the propeller is placed in close proximity to a flap, additional pressure gradients are generated due to the curvature of the surface, which affect the aerodynamic coupling between the two components. Earlier research has shown that, in this case, the interaction between the propeller and the boundary layer can lead to a propeller-induced flow separation [149]. To analyze this interaction, the impact of the propeller on the flow field over the flap is described in Sec.7.3.1. The influence of propeller position is then addressed in Sec. 7.3.2. Again, the results are presented for high thrust and low tip clearance (BL_1, $V_\infty = 20$ m/s, $C_T = 0.35$, $\varepsilon/R = 0.037$), unless explicitly mentioned otherwise. However, since the increased velocity over the flap surface decreases propeller thrust, the rotational speed has to be increased to match the thrust coefficient C_T. This is reflected in Fig. 7.19, where additionally, contrary to the flat-wall configuration, the thrust of the propeller can be seen to increase with increasing tip clearance.

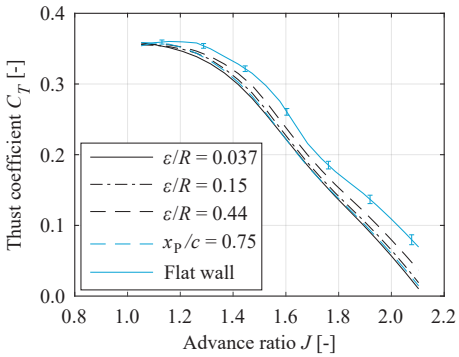

Figure 7.19: Propeller thrust curves, measured for $\delta_f = 20^o$, $\varepsilon/R = 0.037$, $x_P/c = 0.8$, unless otherwise specified by the legend (BL_1, $V_\infty = 20$ m/s).

7.3.1. PROPELLER-INDUCED FLOW SEPARATION

When the flap is deflected, the velocity over the flap hinge is increased, as shown in Fig. 7.20a. The boundary-layer thickness grows considerably over the flap surface, although no flow reversal is observed in the FOV. However, Fig. 7.20b shows that, when the propeller is installed and operated at a high thrust setting, the axial momentum of the flow

is increased and the flow separates over the flap. This indicates that the boundary layer cannot sustain the suction peak required on the flap surface to deflect the slipstream downwards, and leads to a region of reverse flow, delimited by the white contour line. This also confirms that, in high-lift conditions, an over-the wing propeller can cause flow separation, as identified in the work of Müller et al. [149].

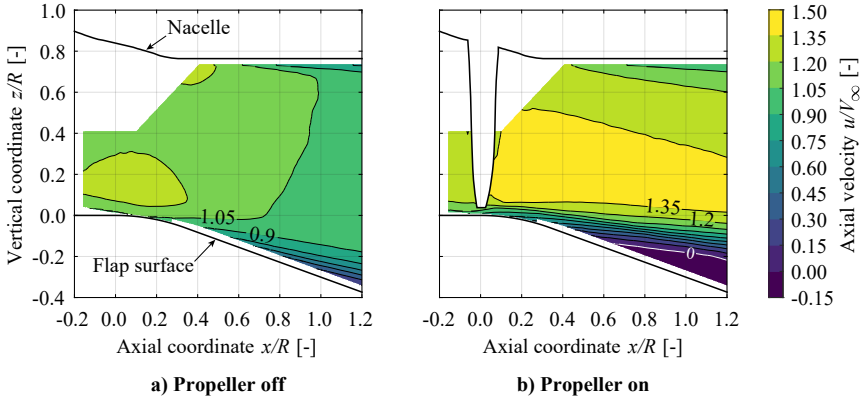

Figure 7.20: Time-averaged axial velocity distribution obtained from PIV measurements between the nacelle and the flap surface.

Due to the propeller-induced flow separation, the propeller slipstream does not follow the flap surface. This is visible in the flow field shown in Fig. 7.21. Although Fig. 7.21 presents the phase-averaged velocity distribution for $\phi = 5^o$, the $\tilde{u}/V_\infty = 0$ boundary is representative of the ensemble-averaged distribution. This was concluded by comparing the velocity fields in the $y/R = 0$ plane for different phase angles, which showed that the amount of flow reversal did not change significantly from one phase angle to another. Therefore, the severity of the propeller-induced flow separation is governed by the time-averaged influence of the propeller, and not by the periodic excitation of discrete tip-vortices. This is a consequence of the relatively high excitation frequency, when compared to a typical shedding frequency expected from the wing[1].

In this configuration, the tip vortices do not remain immersed in the wing boundary-layer—contrary to the flat-wall case—and hence they deform only slightly, without splitting into two. This is also visible in the propeller-induced surface-pressure fluctuations, shown in Fig. 7.22. The strong pressure fluctuations generated by the bound vorticity on the propeller blades are still visible beneath the propeller. However, the pressure fluctuations induced further downstream by the trailing vorticity in the slipstream have decreased considerably. Consequently, the "V" shaped pattern (Fig. 7.13) is no longer present, although weak pressure fluctuations are still visible downstream of the propeller disk in Fig. 7.22. An analysis of the pressure spectra, not included here, showed that the pressure fluctuations downstream of the propeller ($x/R > 1$) contained only weak tonal components, and a relatively strong broadband component. Therefore, the patches of

[1] Assuming a Strouhal number of 0.2, the natural shedding frequency a cylinder of diameter equal to the thickness of the wing at the point of separation would be around 45 Hz for the operating conditions considered, while the blade passage frequency is 531 Hz.

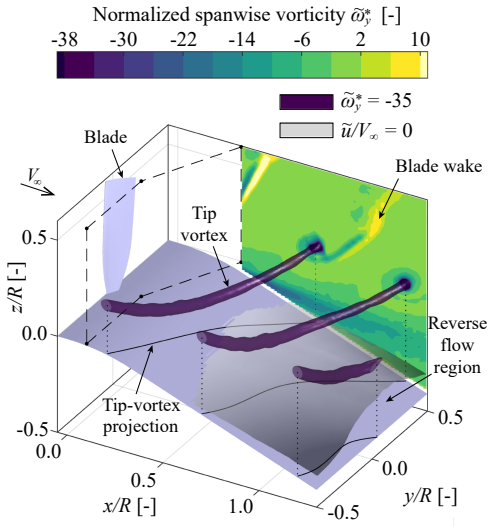

Figure 7.21: Phase-averaged vorticity distribution downstream of the propeller with flap deflected, including an axial-velocity isosurface which delimits the region of reverse flow ($\phi = 5^o$, $\varepsilon/R = 0.07$). Data only shown downstream of the plane indicated by dashed lines. Figure based on experimental data.

increased fluctuations in this area are not created by flow structures in the slipstream, but by unsteady flow behavior in the separated-flow region. These pressure fluctuations are more prominent in the upper-right quadrant of Fig. 7.22, indicating that there is a slight asymmetry in the reverse-flow region. This is also reflected in Fig. 7.21, where the most upstream point of the $\tilde{u}/V_\infty$ isosurface is located on the starboard side ($y/R > 0$) of the center plane. The cause of this minor asymmetry could not be confirmed with the data available.

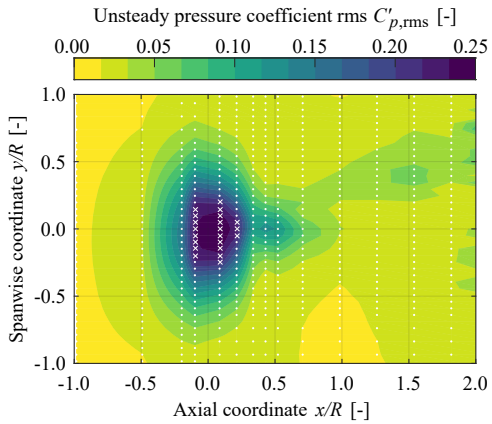

Figure 7.22: Unsteady pressure-coefficient rms contours on the wing surface with flap deflection. Dots indicate measurement locations, while crosses indicate locations where the maximum input level of the microphone was exceeded.

7.3.2. IMPACT OF PROPELLER POSITION

Finally, this section describes how the propeller-induced flow separation is affected by the position of the propeller. To this end, Fig. 7.23 presents the phased-locked vorticity fields for three different configurations: the baseline configuration discussed in the previous section, a configuration with increased tip clearance, and a configuration where the propeller has been moved upstream by $0.05c$ while maintaining a constant tip clearance. The figure also includes the propeller-induced velocity vectors, which indicate the difference between the velocity field with the propeller on, and the one obtained without the propeller. In the baseline configuration (Fig. 7.23a), the velocity vectors show how the velocity over the flap is significantly reduced, leading to the reverse-flow region shown in Fig. 7.20b. The region of strong (negative) vorticity around $z/R = -0.1$ indicates the edge of the reverse-flow region, where a strong shear layer exists.

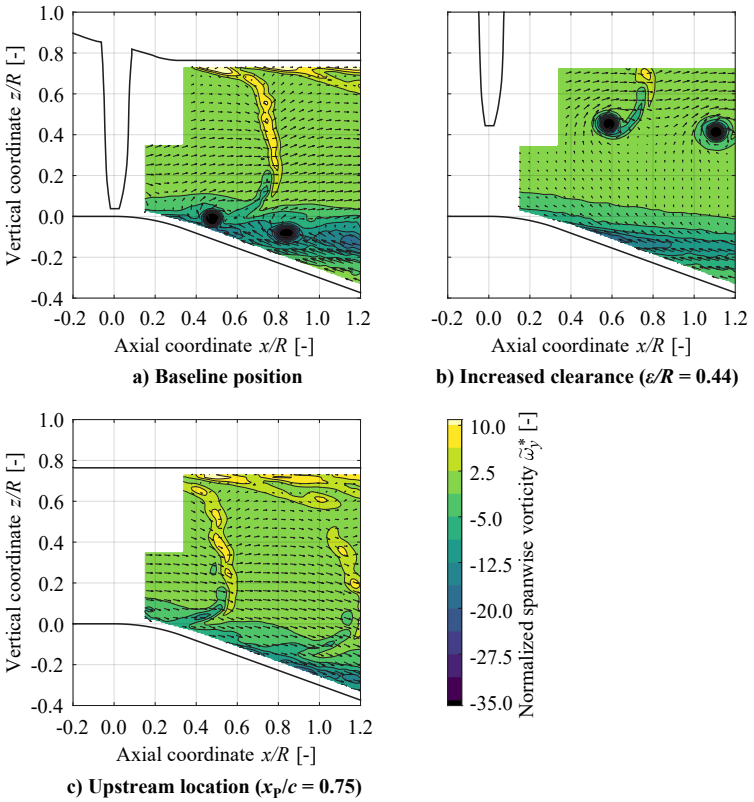

Figure 7.23: Phase-averaged spanwise vorticity distribution and in-plane propeller-induced velocity vectors, obtained from PIV data for three propeller positions.

A. EFFECT OF PROPELLER TIP-CLEARANCE

When the tip clearance is increased to $\varepsilon/R = 0.44$, the velocity over the flap surface is still reduced with respect to propeller-off conditions, as shown in Fig. 7.23b. The shear line is also detached from the surface, indicating that the boundary layer has separated.

Therefore, even though the blade tips are outside the boundary layer ($\varepsilon = 3\delta_{99}$), the propeller still causes flow separation. This occurs because the high-momentum slipstream acts as a boundary, and a divergent flow channel is created between the slipstream edge and the flap surface. The divergent flow channel increases the adverse pressure gradient and causes the flow to separate. This confirms that, for these test conditions and geometry, the time-averaged effect of the propeller is the dominant cause for flow separation, and not the periodic excitation caused by the tip vortices. An inspection of the flow fields obtained with other tip-clearances (Table 7.2), not included here, showed a similar effect. Increasing the tip clearance is therefore not an effective strategy to avoid propeller-induced flow separation.

B. EFFECT OF AXIAL POSITION RELATIVE TO THE FLAP HINGE

Figure 7.23c shows how the flow field is affected by placing the propeller further upstream. In this case, the velocity over the flap is increased with respect to propeller-off conditions, and the slipstream is locally parallel to the flap surface. Moreover, the tip vortices are not visible in the field-of-view. For this configuration, the boundary layer has slightly different thickness at the propeller location. However, this difference should play only a minor role, since the boundary-layer thickness does not significantly affect the propeller thrust or the pressure gradient generated on the wing surface, as discussed previously. The differences with respect to the baseline configuration can therefore be explained by referring to the findings of Sec. 7.2. In the baseline configuration, the flap curvature starts directly beneath the propeller disk. The axial-velocity distribution in the flat-wall configuration (Fig. 7.9b) showed that, at that location, the slipstream contraction leads to a region of reduced axial velocity at the wall surface. The associated adverse pressure gradient is the dominant trigger for flow separation in the baseline, flap-deflected configuration. However, further downstream of the propeller, the slipstream approaches the wall in the flat-wall configuration. This leads to a fuller boundary-layer profile with high-momentum flow near the surface (Fig. 7.9), and causes the tip vortices to split and move away from the $y/R = 0$ plane (Fig. 7.17). Therefore, when the flap is deflected half a radius ($0.05c \approx 0.5R$) downstream of the propeller, the boundary layer is able to withstand strong adverse pressure gradients, and the flow remains attached. Consequently, the suction on the flap surface generates a Coandă effect [279, 280] , exerting a vertical force on the fluid and deflecting the high-momentum flow in the slipstream downwards along the flap. This Coandă effect leads to an increase in system lift. Moreover, even though the tip vortices are not the dominant cause for flow separation, their absence from the flow field in the $y/R = 0$ region is beneficial for the boundary layer and further contributes to an attached flow over the flap.

7.3.3. COMPARISON BETWEEN NUMERICAL AND EXPERIMENTAL RESULTS

In order to assess the validity of the numerical results, they are compared to the experimental data for the flap-deflected configuration in this section. An important region for the propeller–wing interaction is the flowfield in the vicinity of the flap. Therefore, the measured flowfield at the flap is compared with the computed flowfield in Fig. 7.24. For these simulations, the wind-tunnel walls were also modeled to replicate the complete experimental setup (without propeller support sting). No significant difference between

the experimental and numerical results can be found in the propeller-off case, indicating that the numerical approach is capable of predicting the flow field over the flap of the isolated wing with reasonable accuracy. This is confirmed by the comparison of the pressure distributions for the propeller-off case in Fig. 7.25a. The experimental results, however, exhibit a slightly lower axial velocity compared to the numerical results, despite a more downstream onset of flow separation, indicated by the contour-line of zero velocity in Fig. 7.24b.

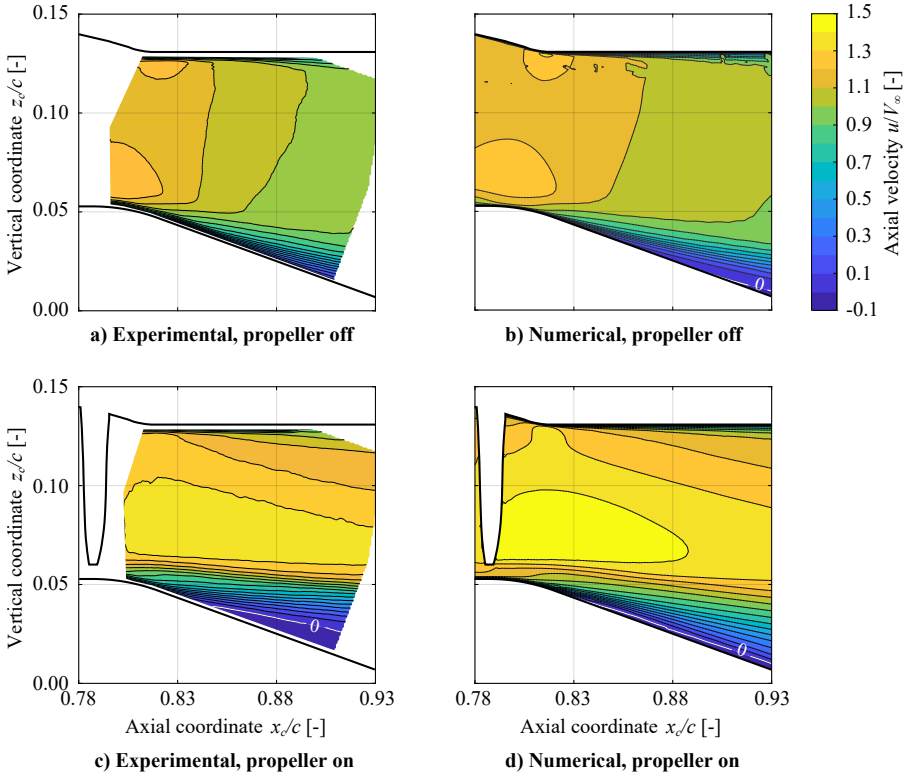

Figure 7.24: Comparison between the time-averaged PIV measurement and the time-averaged CFD RANS results for the axial velocity distribution over the flap.

Adding the propeller results in a stronger adverse pressure gradient at the propeller location that decreases the momentum in the boundary-layer over the flap and ultimately leads to earlier flow reversal than in the propeller-off case, as observed in the experiments. This effect of the propeller on flow separation, however, is more pronounced in the experimental results (Fig. 7.24c) than in the numerical ones (Fig. 7.24d). In the numerical results, the point of flow separation moves upstream when the propeller is included; however, the slipstream still deflects downwards and the flow remains more parallel to the flap surface than in the experiment. Consequently, the suction over the flap is stronger in the numerical results than in the experimental ones, as shown in Fig. 7.25b.

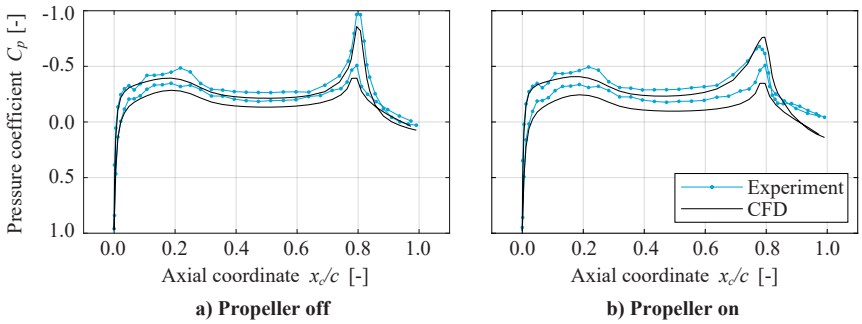

Figure 7.25: Comparison of wing pressure distributions obtained from the experimental and numerical results.

The differences in propeller-induced flow separation can be attributed to several factors. Firstly, all the turbulence in the flow is modeled, and not resolved—including the small turbulence scales close to the wing surface, where the flow reversal originates. Hence, the separation behavior is influenced by the selection of the turbulence model, and the ability of the model to predict flow separation can deteriorate when a propeller causes additional unsteady and highly-concentrated adverse pressure gradients. Secondly, numerical diffusion weakens the tip vortices, as shown in Fig. 7.26. This reduction in tip-vortex strength reduces the velocity deficits generated between the vortex core and the flap surface, therefore having a less detrimental effect on the boudary layer. The strong numerical diffusion can be encountered for various RANS turbulence models and is also indicative of an insufficient mesh resolution in the respective area [257]. Thirdly, the surface imperfections in the experiment, evident in Fig. 7.25, may weaken the boundary-layer and increase the magnitude of flow separation. Finally, the overset mesh can lead to a small delay in flow separation, due to increased velocity gradients near the wing surface, as established when discussing the overset mesh in previous sub-

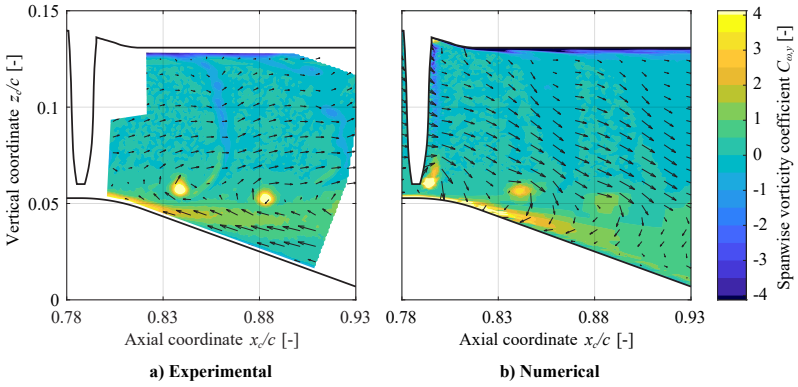

Figure 7.26: Comparison between the instantaneous CFD RANS results and the phase-locked PIV measurement for the out-of-plane vorticity over the flap, at the same phase angle ($\phi = 6°$). Vectors indicate the propeller-induced in-plane velocity.

sections. The overset interface may also further attenuate the influence of the blade tip vortices once the propeller is installed [281].

Tables 7.4 and 7.5 compare the resulting sectional pressure-lift and pressure-drag coefficients obtained below the propeller axis, as well as the propeller thrust coefficient. For the lift and drag coefficients,"uninstalled" refers to the propeller-off wing-configuration (i.e., with the nacelle present), whereas the uninstalled thrust coefficient is obtained from the isolated propeller. The thrust coefficients predicted by the CFD simulations show an acceptable agreement with the values obtained in the experiment, showing a difference of $\Delta C_T = -0.017$ (4.8%) and $\Delta C_T = -0.007$ (2.0%) in the uninstalled and installed cases, respectively. The discrepancy is larger in the uninstalled case because the propeller is operating in the non-linear region of the thrust curve (see Fig. 7.19), at which a larger portion of the blades have stalled in the isolated configuration than in the installed configuration. Hence, the numerical model captures the performance of the installed propeller measurement more accurately, due to less flow separation on the blades. The onset of blade stall at these high-thrust conditions also implies that the thrust coefficient varies only slightly with advance ratio, which explains why the differences in thrust between the installed and uninstalled cases are relatively small ($\Delta C_T = 0.005$) when compared to the reductions in propeller thrust that are typically obtained in over-the-wing configurations (see Sec. 6.1).

Table 7.4: Pressure-lift and -drag coefficients, and thrust coefficients from the experimental (Exp.) and numerical (CFD) results.

	c_{lp}	c_{dp}	C_T
Exp. (uninstalled)	0.097	0.0111	0.353
Exp. (installed)	0.110	0.0089	0.348
CFD (uninstalled)	0.101	0.0080	0.336
CFD (installed)	0.167	0.0051	0.341

Table 7.5: Difference in coefficients between installed (inst.) and uninstalled (uninst.), as well as numerical and experimental results.

	Δc_{lp}	Δc_{dp}	ΔC_T
CFD vs. exp. (uninst.)	0.004	-0.0031	-0.017
CFD vs. exp. (inst.)	0.052	-0.0038	-0.007
Inst. vs. uninst. (exp.)	0.013	-0.0022	-0.005
Inst. vs. uninst. (CFD)	0.066	-0.0029	0.005

The computed lift coefficient of the uninstalled case compares reasonably well with the measured one. The uninstalled drag coefficient from CFD, however, is $\Delta c_{dp} = -0.0031$ lower than in the experiment, which represents a reduction of approximately 28%. This is attributed to the higher pressures obtained over the flap, as reflected in Fig. 7.25a. When the propeller is installed, the more pronounced propeller-induced flow separation of the experimental results leads to a lower circulation than in the numerical

results. Consequently, the lift coefficient is $\Delta c_{lp} = 0.052$ (45%) higher in the numerical approach. Analogously, the difference in drag between numerical and experimental results increases to $\Delta c_{dp} = -0.0038$ (-43%) in the installed case, since lower pressures are obtained near the trailing edge in the experiment as a consequence of the increased flow separation. Hence, the lift enhancement and drag reduction due to the propeller installation is more pronounced in the numerical results than in the measurements. However, it should be noted that the relatively high percentage differences between experimental and numerical data is largely a consequence of the low reference lift and drag coefficients.

This comparison shows that no quantitative conclusions should be drawn based on the numerical results. Moreover, it indicates that the numerical model is likely to underestimate any propeller-induced flow-separation effects. Nevertheless, the objective of the numerical analysis is to investigate the effect of propeller inclination. By analyzing the results qualitatively, and keeping the aforementioned limitations in mind, the numerical evaluation of the problem can provide valuable insight into some of the interaction mechanisms that govern the performance of the system.

7.4. EFFECT OF PROPELLER INCLINATION ON FLOW SEPARATION

This section discusses the potential impact of propeller inclination with the flap on flow separation. For this, the results of the numerical simulations are analyzed. The reader is reminded that the numerical approach was found to under-predict the propeller-induced flow separation. Therefore, the effects of propeller inclination are assessed by comparing CFD results of the inclined configuration to those of the baseline configuration, rather than comparing them directly to the experimental results. These numerical results are obtained without wind tunnel walls, to remove their influence on the aerodynamic interaction.

7.4.1. FLOW-FIELD CHARACTERIZATION

The time-averaged flow field induced by the inclined propeller is compared to the one of the baseline configuration in Fig. 7.27. When the propeller is deflected together with the flap, not only the downwash over the wing surface introduces a vertical velocity component in the slipstream, but also the inclination of the propeller directs the slipstream along the propeller axis. Figures 7.27b and 7.27d show that the momentum deficit over the flap is filled by the slipstream and the velocity over the flap is increased. The additional momentum in the boundary layer of the flap due to propeller inclination is reflected in Fig. 7.28, which compares the velocity component parallel to the flap surface for the two configurations and the propeller-off reference case. These velocity profiles indicate that a stronger adverse pressure gradient can be tolerated in the inclined-propeller configuration, compared to the baseline configuration. From both Fig. 7.27b and Fig. 7.27d it can also be inferred that the propeller thrust and, therewith, the maximum induced velocity and minimum induced pressure, is shifted towards the upper half of the propeller disk, away from the wing.

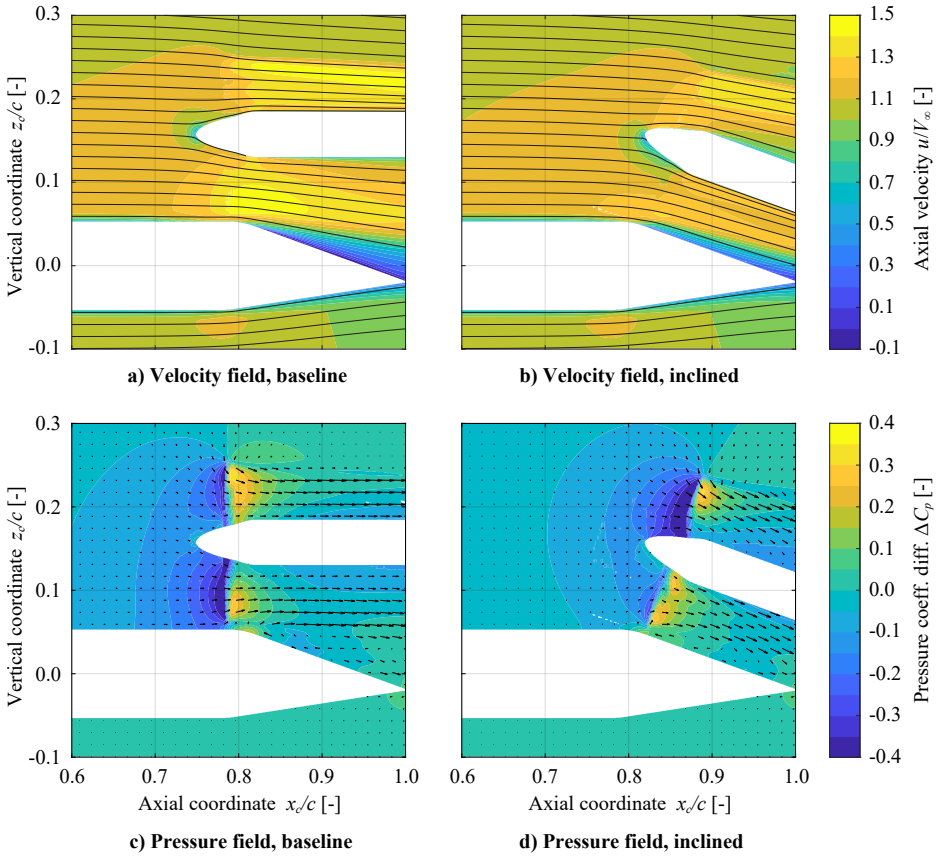

Figure 7.27: Time-averaged axial velocity with streamlines (top) and induced pressure and in-plane velocities (bottom) at $y/c = 0$ for the baseline and inclined configurations, obtained from the numerical simulations.

The influence of the inclined propeller on the sectional pressure distribution at $y/c = 0$ is shown in Fig. 7.30b. The main difference with respect to the baseline pressure distribution (Fig. 7.30a) is that the pressure reduction in front of the propeller is smaller in the inclined case. Moreover, while the suction peak over the flap is reduced in the baseline configuration due to the propeller-induced flow separation, in the inclined configuration the pressure peak over the flap is maintained. In both cases, a significant spread in the pressure coefficient due to the unsteady flow-field generated by the propeller blades can be observed. In the baseline configuration, the pressure fluctuations are centered around the axial position of the propeller ($x/c = 0.79$), and rapidly decay in both upstream and downstream directions. This is consistent with the pressure-fluctuation distributions obtained in the experimental analysis (see Fig. 7.22). However, in the inclined configuration, where the bottom of the propeller disk is located at $x/c \approx 0.82$, the pressure fluctuations persist more downstream. In this case, the slipstream is closer to the flap surface, and therefore the tip vortices induce more pronounced pressure fluctuations, comparable to the flat-wall measurements of Sec. 7.2.

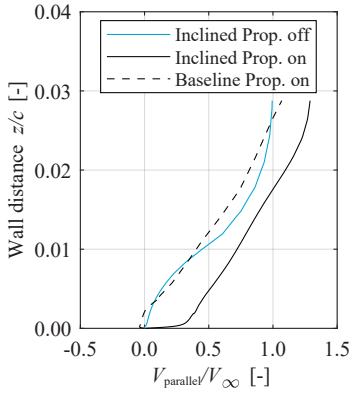

Figure 7.28: Time-averaged velocity component parallel to the flap surface at $x/c = 0.9$, below the propeller axis ($y/c = 0$).

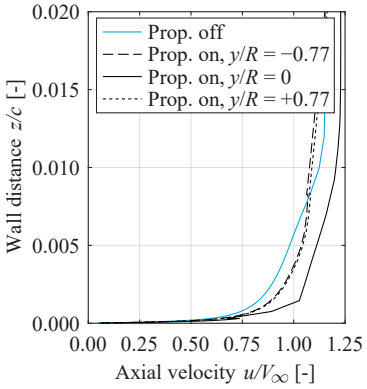

Figure 7.29: Axial-velocity profiles $0.5R$ ahead of the propeller in the baseline configuration, at three spanwise locations.

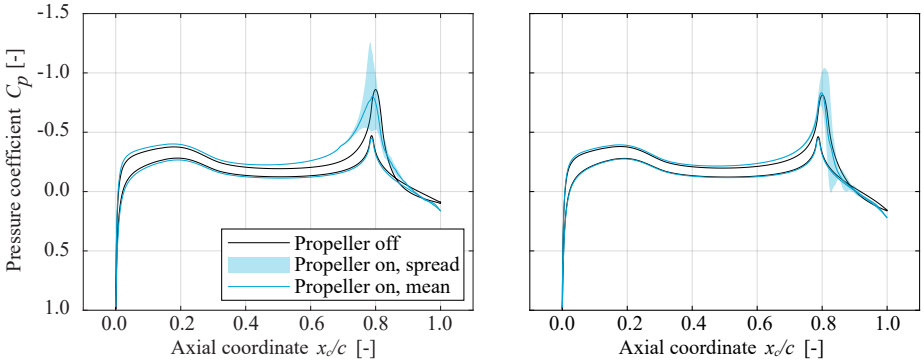

a) Baseline configuration **b) Inclined configuration**

Figure 7.30: Pressure distributions of the wing profile at $y/c = 0$, in the baseline and inclined configurations. Results obtained from numerical simulations.

The experimental results showed that the unsteady interaction between tip vortices and the wing boundary layer is not the dominant trigger for propeller-induced flow separation. This is reaffirmed in Figs. 7.31a–7.31c, which present the wall-shear lines and propeller-induced surface-pressure distributions of the baseline configuration. For the two unsteady flow fields, which correspond to blade-phase angles of $\phi = 0^o$ and $\phi = 30^o$ respectively, the spanwise vorticity component plotted in the center plane ($y/c = 0$) reveals the location of the tip vortices. The shear lines show that the flow reversal is centered directly beneath the propeller axis. However, the lobes visible along the separation line indicate that flow separation has locally been postponed away from the propeller axis. This is due to the increased velocity upstream of the propeller, which increases the momentum in the boundary-layer of the wing, as reflected in Fig. 7.29. This in turn increases its capability to withstand the adverse pressure gradient over the flap. In

any case, a comparison of Figs. 7.31a, 7.31b, and 7.31c shows that the most upstream location of flow separation varies by just ±1% chord, depending on the phase angle. Therefore, the time-averaged velocity and pressure effects caused by the propeller are the dominant cause of flow separation.

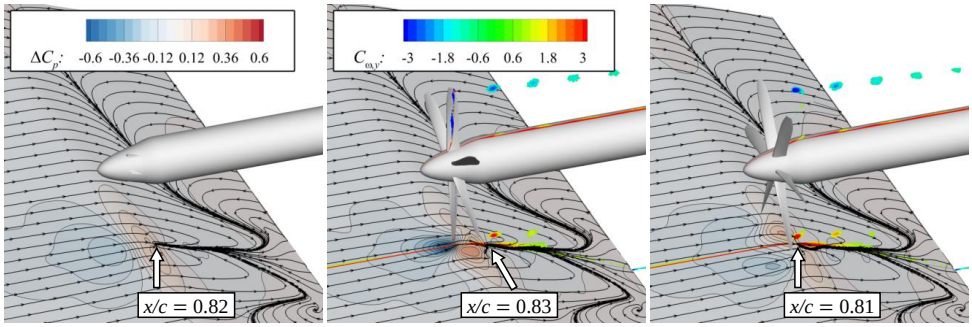

(a) Baseline, time-averaged (b) Baseline, $\phi = 0°$ (c) Baseline, $\phi = 30°$

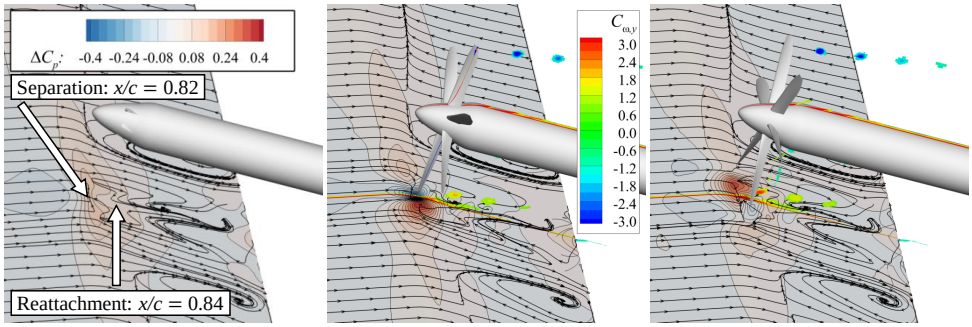

(d) Inclined, time-averaged (e) Inclined, $\phi = 0°$ (f) Inclined $\phi = 30°$

Figure 7.31: Time-averaged (left) and unsteady (middle, right) influence of the propeller on the surface-pressure distribution and wall-shear lines of the wing, in the baseline (top) and inclined (bottom) configurations. Vorticity contours shown in $y/c = 0$ plane for $|C_{\omega,y}| > 1.5$.

Figures 7.31d–7.31f present the wall-shear lines and propeller-induced pressure distributions for the inclined-propeller configuration. In a time-averaged sense, the flow is found to separate directly beneath the propeller ($x/c = 0.82$) and reattach soon after ($x/c = 0.84$). While the exact extent of this separation bubble is not clearly visible in Fig. 7.31d, additional skin-friction coefficient plots (not shown here) confirmed its presence [271]. This reattachment occurs because, in this configuration, the high-momentum flow in the slipstream is parallel to the flap surface, and the same effect as the one observed in the interaction with a flat wall (Sec. 7.2) takes place. Moreover, while in the baseline configuration the flow separation on the flap was only postponed below the outboard part of the slipstream, Fig. 7.31d indicates the possibility of completely attached flow in those regions for the inclined configuration. Since in this case the propeller already induces vertical momentum, less suction is necessary on the surface of the wing to deflect the flow downwards. Moreover, the adverse-pressure gradient

beneath the propeller is located slightly downstream of the suction peak over the flap hinge. Therefore, the boundary-layer can withstand the pressure gradients on the flap. The time-dependent results in Figs. 7.31e and 7.31f also show that the blade tip vortices merely vary the chordwise extent of the local separation bubble beneath the propeller. However, the overall flow field exhibits no significant dependency on the blade phase angle.

7.4.2. EFFECT ON PROPELLER AND WING LOADS

After having analyzed the aerodynamic interaction effects for an inclined propeller in the previous section, this section describes how the aerodynamic interaction influences the distribution of forces generated by the propeller and wing. First, the propeller loading distributions will be compared between the baseline and inclined configuration. Then, the spanwise distributions of lift and drag of the wing are compared for the two configurations.

A. PROPELLER LOADING DISTRIBUTIONS

The wing-induced flowfield results in a modified propeller loading and propeller thrust. Compared to the isolated thrust coefficient of $C_T = 0.336$, the baseline propeller thrust increases by $\Delta C_T = 0.005$, which is less than 2 % of the isolated thrust. The small increase obtained in this configuration can be explained by analyzing the thrust distribution on the propeller disk, shown in Fig. 7.32a. The wing induces a flowfield to the propeller such that there is higher axial velocity, as well as a vertical velocity component. The vertical component results in a net negative angle of the inflow to the propeller disk and, hence, a strong increase and moderate decrease of the blade angle of attack for the up-going and down-going blades, respectively. This causes the asymmetry in the thrust distribution in Fig. 7.32a. A higher axial velocity typically reduces the blade angle of attack and, therewith, the thrust, over the entire propeller disk. However, due to the low lift coefficient of the wing, this effect is small compared to the angle of attack effect. These trends are also reflected in the wake-pressure measurements of Sec. 6.1.

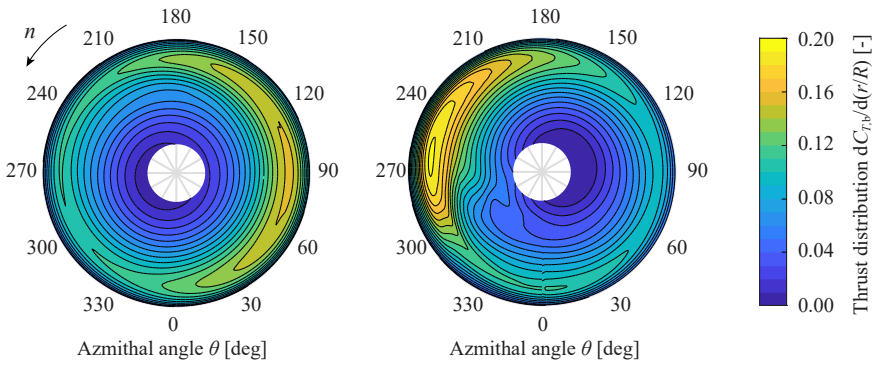

Figure 7.32: Thrust distributions on the propeller disk obtained from the numerical simulations.

In the inclined configuration (Fig. 7.32b), the propeller inclination is larger than the local flow angle induced by the wing. Therefore, the inclined propeller disk experiences a net positive angle of attack to the inflow, and the in-plane velocities increase the blade angle of attack for the down-going blades, contrary to the baseline case. The local thrust increase for the inclined propeller is larger in magnitude than for the baseline propeller, but confined to a smaller area on the disk. Consequently, the thrust coefficient, $C_T = 0.335$, of the inclined propeller is lower than that of the baseline propeller, but comparable to the isolated-propeller thrust. Close to the wing, the thrust augmentation fades as the inflow is more aligned with the propeller axis again and the axial velocity increases. Compared to the baseline configuration, the inclined propeller produces less thrust close to the wing.

Although the total thrust along the propeller axis exhibits only a small change when the propeller is inclined, the force in flight direction, F_x, changes considerably. Recall that the different propeller force components were defined in Fig. 2.6. When the propeller is inclined, not only the horizontal force F_x decreases, but also the vertical force F_z increases, effectively leading to a thrust-vectoring effect. A comparison of the individual time-averaged force components is given in Table 7.6. The coefficients in table 7.6 are normalized with the reference area $S_{\text{ref}} = 1.1cD_{\text{p}}$ to be comparable to the lift and drag coefficients of a wing segment of span $1.1D_{\text{p}}$, for a distributed propeller application where multiple propellers would be installed in close proximity—for example, with a hypothetical tip clearance of $0.1D_{\text{p}}$. The variable F_{c}^* refers to the total resultant force on the propeller. The results in Table 7.6 confirm that the thrust in the flight direction, $F_{x\text{c}}^*$, decreases, while the vertical component, $F_{z\text{c}}^*$, increases when the propeller is inclined. The vertical component becomes more pronounced for two reasons: firstly, because the thrust vector is tilted upwards, and secondly, because the normal force on the propeller is stronger due to the angle-of-attack effect.

Table 7.6: Comparison of the time-averaged forces for the different propeller installations.

Parameter	Baseline	Inclined	Isolated
C_T	0.341	0.335	0.336
T_{c}^*	0.094	0.093	0.093
N_{c}^*	-0.009	0.022	0
$F_{x\text{c}}^*$	-0.094	-0.080	-0.093
$F_{z\text{c}}^*$	-0.009	0.053	0
F_{c}^*	0.095	0.096	0.093

The torque and shaft power of the inclined propeller ($C_Q = 0.1029$, $C_P = 0.647$) change only slightly compared to both the baseline results ($C_Q = 0.1022$, $C_P = 0.642$) and the isolated values ($C_Q = 0.1023$, $C_P = 0.643$). In fact, the change in torque coefficient falls within the uncertainty band determined earlier. Since the shaft power required in the two configurations is comparable, the results of Table 7.6 indicate that the propulsive efficiency is highest in the baseline configuration, if the force component in the direction of flight is considered. The increase in efficiency with respect to the isolated propeller, albeit minor, is contradictory to the propulsive-efficiency penalties observed in Sec. 6.1. However, this is due to the relatively high angle of attack induced locally

on the propeller disk, and the relatively low axial-velocity increase generated above the low-lift-coefficient wing. This indicates that the effect on OTW propeller efficiency is highly dependent on the operating condition and geometry of the system, and may explain some of the contradictions observed in literature. The effect of the operational and geometrical parameters is discussed in more depth in Ch. 8.

B. WING LOADING DISTRIBUTIONS

The inclination of the propeller not only affects the pressure distribution of the wing at the propeller location, but also the distribution of lift and drag along the span. The time-averaged spanwise lift and drag distribution of the wing are shown in Fig. 7.33. As a reference, the same coefficients are also given for the isolated wing and the wing with nacelle, excluding the propeller blades. In the baseline configuration, the suction induced locally by the propeller results in a peak of the lift in the middle of the wing, below the propeller axis. Contrary to the centered lift peak, the lowest drag is shifted below the outboard part of the up-going blade. This is attributed to a higher blade loading on the up-going blade side, which increases the static pressure behind the propeller disk and consequently reduces the pressure drag. Below the down-going blade, the drag saved by the propeller merely compensates for the additional drag of the nacelle, resulting in a propeller-on drag coefficient close to the one of the isolated wing.

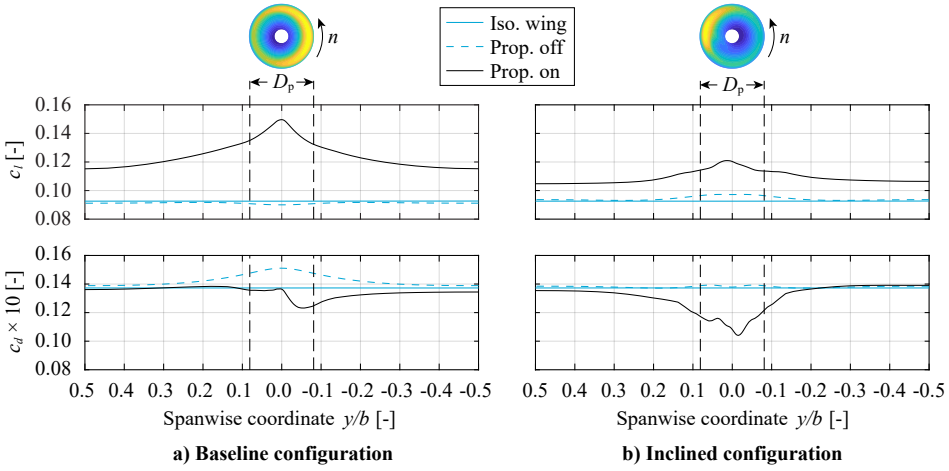

Figure 7.33: Sectional lift (top) and drag (bottom) coefficient distributions along the wingspan obtained from the numerical simulations in the baseline and inclined configurations.

Despite the delay of flow reversal on the flap, the lift distribution in the inclined configuration exhibits a smaller rise in lift coefficient than the baseline configuration, due to the relatively weak induced velocities close to the wing. The drag, however, shows a larger reduction, which is associated to the postponement of flow separation on the flap. Moreover, axial vorticity distributions in the wake (not shown here) indicate that the relative effect of trailing vorticity due to the non-uniform spanwise loading on the induced angle of attack is negligible. Hence, the inclined configuration presents larger drag reductions than the baseline case, while the baseline configuration shows a larger lift increase.

To evaluate the system forces in a hypothetical distributed-propulsion application where the tip clearance between adjacent propellers is 10% of the propeller diameter, the differences between the propeller-on and propeller-off lift and drag distributions are integrated over a wing segment of $1.1D_p$ span. The resulting force coefficients ΔC_L and ΔC_D can then be added to the lift and drag coefficients of the isolated wing, plus the thrust coefficient of the propeller in the respective direction (from Table 7.6), to obtain the total forces for an OTW propeller system. It should be noted, however, that this procedure does not account for interaction effects that would be present with multiple adjacent propellers. This leads to conservative results in terms of wing lift and drag, since the propeller also increases lift and decreases drag beyond the $1.1D_p$ interval, as reflected in Fig. 7.33. Table 7.7 shows that the additional vertical force component of the propeller in the inclined configuration compensates for the weaker lift increase of the wing segment (ΔC_L), such that the total force in the vertical direction is 24% larger than for the baseline propeller configuration. This effective lift increase due to propeller inclination can be even higher in terms of the maximum attainable lift coefficient, since the postponed flow separation over the flap is likely to shift the maximum lift coefficient to higher angles of attack. The inclination of the propeller, however, also leads to a weaker additional forward force, F^*_{xc}, to the system. This reduction in net thrust is not compensated by the decrease in drag of the wing (ΔC_D). Hence, the baseline configuration has a 20% larger installed thrust than the inclined configuration. Moreover, due to the comparable thrust in the x-direction for the baseline and isolated configuration, the drag saved on the baseline wing also leads to a larger installed thrust compared to the isolated configuration. It is also worth noting that, since the shaft power is comparable in the two cases, the propulsive efficiency of the baseline OTW system is slightly higher than for the isolated propeller. This shows that not only the lift-to-drag ratio, but also the propulsive efficiency can indeed be increased in some OTW configurations, as observed in Ref. [63].

Table 7.7: Balance of vertical (z) and horizontal (x) forces for a wing segment of span $b = 1.1D_p$, at approximately the same shaft power.

Config.	$C_{L,\text{iso}}$	ΔC_L	F^*_{zc}	Total, z	$C_{D,\text{iso}}$	ΔC_D	F^*_{xc}	Total, x
Isolated	0.093	0	0	0.093	0.0137	0	-0.093	-0.0793
Baseline	0.093	0.050	-0.009	0.134	0.0137	-0.0018	-0.094	-0.0821
Inclined	0.093	0.020	0.053	0.166	0.0137	-0.0025	-0.080	-0.0688

7.5. SUMMARY OF KEY FINDINGS

A combined numerical/experimental investigation has been performed to study the aerodynamic interaction between an over-the-wing propeller and the wing boundary-layer. Propeller inclination is investigated as a potential mitigation strategy for flow separation, using an unsteady RANS approach. A comparison to experimental data shows that the magnitude of propeller-induced flow separation is under-predicted in the numerical approach. The discrepancy is attributed to the influence of the overset interface on flow gradients in the boundary-layer, the modeling of turbulence used by the RANS solver, and an under-estimation of tip-vortex strength due to numerical diffusion

and dissipation. Therefore, although the selected numerical approach captures the phenomena and trends observed in the experimental data, predicting the exact point of flow separation in OTW systems with unsteady RANS simulations remains a challenge.

To understand the underlying flow phenomena, first the time-averaged impact of a propeller placed in close proximity to a flat wall is analyzed. Results show that a strong adverse pressure gradient is generated below the propeller disk which increases linearly with thrust, decreases with increasing tip clearance, and is practically independent of the boundary-layer thickness. The associated contraction of the slipstream generates a region of reduced axial velocity between the slipstream edge and the wall. This region of reduced velocity extends approximately half a radius downstream of the propeller disk, beyond which the slipstream adheres to the wall and the thickness of the boundary layer is significantly reduced. Consequently, when the propeller operates at a high thrust setting above the flap hinge and an adverse pressure gradient is imposed by deflecting the flap, the flow is found to separate from the flap surface for two reasons. Firstly, the strong adverse pressure gradient created beneath the propeller weakens the boundary layer (steady effect). Secondly, the periodic presence of the tip vortices leads to local axial velocity deficits and pressure perturbations in the boundary layer, further reducing its capability to withstand an adverse pressure gradient (unsteady effect). The results show that the former (steady effect) is the dominant cause for propeller-induced flow separation, while the unsteady effects play only a minor role. Additionally, an evaluation of different propeller positions indicates that increasing the tip clearance is not an effective mitigation strategy. However, if the propeller is placed half a radius upstream of the flap hinge, a Coandă effect is generated which allows the flow to remain attached and increase system lift, when compared to propeller-off conditions.

In the inclined-propeller configuration, the flow separation over the flap is postponed. In spite of this, the inclined case does not to enhance the lift over the flap more than the baseline case at the same angle of attack, because of the higher static pressure created on the flap surface behind the propeller. The higher static pressure does, however, decrease the pressure drag of the wing when compared to the baseline case. Furthermore, in the inclined configuration, the additional vertical-force component of the propeller results in a larger lift of the inclined OTW propeller–wing system, compared to the baseline system. However, the inclination of the propeller leads to a lower net axial thrust than the in the baseline configuration.

These findings illustrate that the high-lift performance of over-the-wing propellers is very sensitive to the design of the system, and that a careful design is not possible without high-fidelity aerodynamic analyses. Because of this and the lower Reynolds numbers evaluated in this study, the quantitative values obtained are not representative of an actual OTWDP application. However, the Coandă effect and delayed flow separation due to propeller inclination observed in this study confirm that over-the-wing propellers can indeed increase the high-lift performance of an aircraft. A series of assumptions regarding the aircraft performance is made in Ch. 10 based on these qualitative considerations, to investigate what the effect of a lift increase in high-lift conditions would imply for the aircraft. Nevertheless, more detailed investigations for realistic geometries and operating conditions are required to quantify the increase in the maximum (system) lift coefficient due to OTWDP.

8

System Performance in Cruise Conditions

The previous two chapters focused on some of the more fundamental aspects of the aerodynamic interaction between OTW propellers and the surrounding elements. However, at this stage, the overall performance benefits or penalties of the system are still unclear. While in general the effects of the propeller(s) on the wing are beneficial, the effect of the wing on the propeller appears to vary. For example, the studies of Ch. 6 showed a reduction in propulsive efficiency due to the interaction of each propeller with the wing and the adjacent propellers. However, the analysis of Ch. 7 suggests that there is no significant propulsive-efficiency penalty. Likewise, a comparison of the existing literature does not lead to conclusive results regarding the overall performance of the system, as discussed in Ch. 2. It appears therefore that the potential performance gain is highly dependent on the geometry and operating conditions of the system. Hence, this chapter aims to quantify the aerodynamic characteristics of an over-the-wing distributed-propulsion (OTWDP) system in terms of performance parameters such as the propulsive efficiency and lift-to-drag ratio.

For this, a simplified OTWDP system consisting of three propellers and a rectangular wing is analyzed in cruise conditions. The investigation focuses on the cruise condition because it contributes the most to the overall energy consumption of the aircraft. In this context, the "cruise condition" is interpreted as a flight condition with low to moderate lift and thrust coefficients. However, as mentioned in Ch. 1, most of the analyses will be performed in subsonic conditions and at lower Reynolds numbers than the ones encountered during cruise in real flight. Hence, the reader is reminded that, although the effect of Reynolds and Mach number will be accounted for to a certain extent, the values of the performance coefficients will differ from a full-scale application. Furthermore, the trends should not be extrapolated to high-lift conditions, since in that case the stall behavior is highly dependent on the Reynolds number and geometry of the system—as concluded from the previous chapter. Analogously, to limit the scope, the effect of the duct is not accounted for in the present analysis. As discussed in Sec. 6.2.4, if the purpose

of the duct is to increase the aero-propulsive efficiency of the system, then this can be considered a conservative approach, since the duct would only be used if it further enhanced the performance. If, on the other hand, the duct is required for different reasons (e.g., noise, fatigue, or blade containment), then it may also deteriorate the performance of the system, depending on the thrust setting and position of the OTW propellers. For this, a dedicated study into representative duct shapes would be required to quantify the effect the duct has on the overall efficiency of the system.

A combined experimental–numerical approach is used to analyze the performance of the system. The methods are described in Sec. 8.1, and are both used for two purposes. The experimental analysis is first used to investigate the performance of the system for a range of angles of attack and thrust settings, for a given geometry, in Sec. 8.2. The results of the experimental investigation are subsequently used to validate the numerical model in Sec. 8.3. The numerical approach, on the other hand, is used in the sensitivity study of Sec. 8.4 to gain an understanding of the effect of parameters which are difficult to vary in the experiment. The numerical method is then used to create an aero-propulsive model (see Appendix C.3) which can be employed to incorporate the changes in aerodynamic performance into the aircraft design process.

8.1. Analysis Methods

Two approaches are used to analyze the performance of the over-the-wing distributed-propeller system: an experimental approach and a numerical approach. The two methods are described in Secs. 8.1.1 and 8.1.2, respectively.

8.1.1. Experimental Setup

This section describes the experimental campaign performed to analyze the over-the-wing distributed-propeller setup. To this end, the following subsections present the test setup, measurement techniques, and test conditions, respectively.

A. Facility & Model Description

The experiments were performed in the DNW Low-Speed Tunnel (LST), a closed-circuit wind tunnel with a test section of 2.25 m × 3 m and a maximum freestream velocity of 80 m/s. The purpose of the experiments was two-fold: to analyze the aerodynamic performance of a LEDP configuration in high-lift conditions (not discussed here), and to analyze the aerodynamic performance of the OTWDP configuration in cruise conditions (discussed here). The wing model was designed in a modular fashion and comprised multiple CNC-machined aluminum segments with different features (pressure taps, junctions for the leading-edge propellers, etc.). It had a span b of approximately 1.25 m, and was installed vertically on the external balance located on the top side of the test section, as depicted in Fig. 8.1a. The wing featured the same NLF-MOD22B airfoil [236] used in Sec. 6.1, including the Fowler flap of 30% chord. Only the flap-retracted position was tested in the OTWDP configuration, since it focused on cruise conditions. For these measurements, the flap slot was sealed on the pressure side and transition strips with distributed roughness (carborundum) elements of grit size 60 were placed at 10% and 5% chord on the pressure and suction sides of the airfoil, respectively.

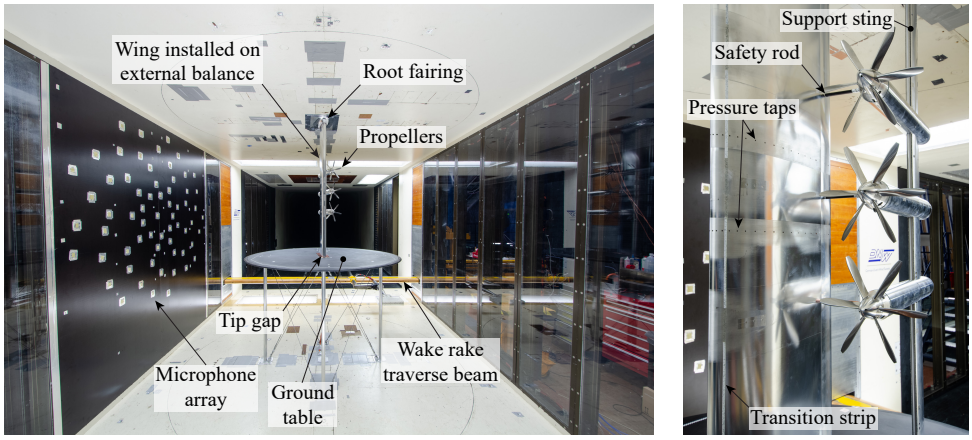

a) Test section seen from upstream **b) Close-up of model**

Figure 8.1: Overview of the test section and wind-tunnel model used in the LST campaign.

The existing XPROP-S propellers of $D_P = 0.2032$ m were used (see Sec. 6.3). The diameter-to-chord ratio of the model was selected as a compromise between the LEDP application, where larger diameter-to-chord ratios are expected (typically $D_P/c \sim 1$ or higher; see e.g. Refs. [61, 62]), and the OTWDP configuration, where lower diameter-to-chord ratios are envisioned ($D_P/c < 0.5$; see e.g. Refs. [52, 153]). This trade-off resulted in a diameter-to-chord ratio of $D_P/c = 0.6$, corresponding to a wing chord of $c = 0.3$ m. Given the modest aspect ratio of the model ($A = 4.16$), an end-plate was used to limit the tip effects and minimize the spanwise lift gradient at the location of the propellers. To this end, a ground table was positioned beneath the wing model, maintaining a gap of roughly 1.5 mm between the wing and the ground plate to prevent the transmission of forces. The ground table was produced from a wooden plate of 18 mm thickness and had a diameter of 1.45 m ($D_{table}/c \approx 5$), as shown in Fig. 8.2a. The plate was machined to present an elliptical edge of aspect ratio 5, and was positioned using five aluminum profiles of 30 mm thickness and 80 mm chord, which were reinforced using crossed stay wires. The wake-rake and microphone array visible in Fig. 8.1a were used mainly for the LEDP configuration and are not discussed here.

The propellers were installed without stagger on the suction side of the wing by means of the same nacelles and support sting described in Sec. 6.3. The support sting was clamped vertically in the ground table and top turntable of the test section, and could be installed at different vertical positions to sample the pressure distribution at various spanwise locations relative to the propellers, using the two rows of pressure taps shown in Fig. 8.1b. The position of the support sting was such that the propellers were located perpendicular to the local wing surface at $x_P/c = 0.8$, corresponding to an incidence angle relative to the wing chordline of $i_P = 10.2^o$ (see Fig. 8.2b). The tip clearance between the three propellers and between the propellers and wing surface were $d = 4.4$ mm ($d/R = 0.04$) and $\varepsilon = 5$ mm ($\varepsilon/c = 0.0167$), respectively. Additionally, a small rod, slightly larger than the propeller radius, was attached to each nacelle to act as a safety stop and prevent the wing from touching the propellers in case of wing deflection at

high angles of attack. A contact sensor attached to the tip of the rods confirmed that there was no contact in the measured angle-of-attack range, and thus the balance indeed registered the forces on the wing alone.

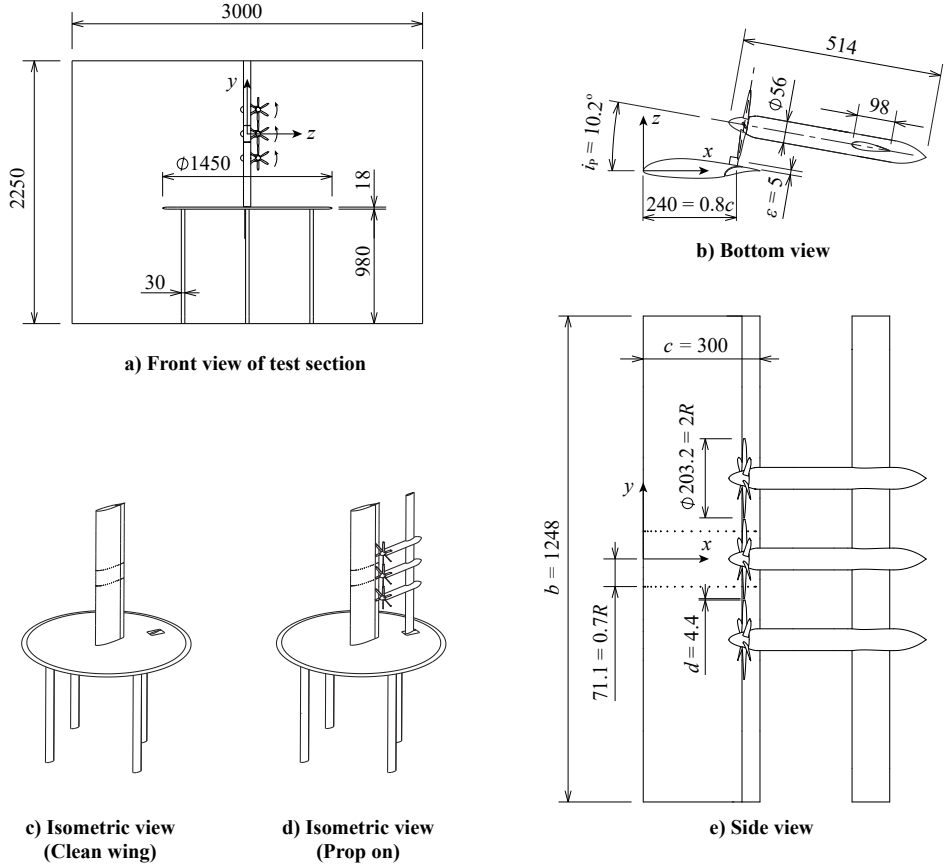

a) Front view of test section

b) Bottom view

c) Isometric view (Clean wing)

d) Isometric view (Prop on)

e) Side view

Figure 8.2: Isometric and 2D views of the LST setup, indicating the main dimensions, coordinate system ($\alpha = 0^o$), and rotation direction of the propellers. Safety rods not shown. Dimensions in mm.

B. MEASUREMENT TECHNIQUES

Three types of measurements were performed: external balance measurements, propeller force-sensor measurements, and wing surface-pressure measurements. These measurement techniques are described in the following subsections. No wind-tunnel wall corrections were applied to the measured data. The wing and ground table constituted approximately 1% and 2% of the cross-sectional area of the test section, respectively, and therefore blockage effects were expected to be minor. Moreover, the wing chord was small relative to the width of the test section, and only modest lift coefficients were evaluated in the OTWDP setup ($C_L < 1.1$). Therefore, the lift interference effects were also considered to be small. Consequently, given the complexity of accurately accounting for the effect of the wind-tunnel walls and ground table on the wing performance, it was decided to present the results in their uncorrected form.

External Balance

A six-component external balance was used to quantify the forces on the wing itself. The balance featured a measurement range of 2100 N in the directions of lift and drag, with a 0.1% calibration uncertainty on the full-scale range. Measurements were performed in a "clean wing" configuration (Fig. 8.2c), with the support sting and propellers ("Prop on", Fig. 8.2d), and with the support sting without propellers ("Prop off"). In this way, the effect of the support sting and the propellers on the wing loads could be determined separately. It is worth noting that, despite the efforts to reduce three-dimensional effects by means of the ground table and root fairing (Fig. 8.1), the lift and drag coefficients registered by the external balance are not fully representative of a 2D wing, particularly due to the interaction with the wind-tunnel wall boundary layer at the root.

Data were acquired at several angles of attack for each configuration and advance ratio. These angle-of-attack polars were recorded in the same order for each measurement run (i.e., without randomization), with one angle of attack being repeated several times to capture potential deviations throughout a given run due to e.g. hysteresis effects. Additionally, wind-off tare runs were performed to subtract non-aerodynamic forces recorded on the balance when varying the angle of attack. No systematic data fitting was applied to the polars, since the changes in lift and drag due to the propellers were found to be sensitive to the type of fitting applied. Instead, the mean of all measurements at a given angle of attack was taken as the "true" value at that angle of attack, and the scatter in data points and the residuals of the wind-off corrections were taken as an indicative measure of the uncertainty. These deviations were found to be small when compared to the effect of the propellers on the wing, and are included as errorbars in the following sections. The errorbars do not include the calibration uncertainty of the balance, since tare measurements were performed and the changes in forces with respect to the wind-off zero measurement were small compared to the full measurement range of the balance.

Propeller Internal Force Sensor

The same six-component force sensor employed in Sec. 6.3 was used to quantify the forces on the middle propeller. In these dedicated force-sensor measurements, the safety rod behind the middle propeller (see Fig. 8.1b) was removed to avoid any potential upstream effect on the propeller. The measurement procedure, temperature calibration, data fitting, and uncertainty quantification were performed analogously to the experiments described in Sec. 6.3. The isolated-propeller measurements of Sec. 6.3 were also used as an "uninstalled" reference case. A posterior analysis of the data revealed that the thrust component was not accurately captured, since it was appreciably higher than expected from the isolated-propeller measurements, and on occasions led to propeller efficiencies greater than one. The propeller torque and in-plane forces, on the other hand, were found to provide values which were in line with the trends observed in the previous chapters. Moreover, these components were accurately reproducible in repeated runs on different days. Since the torque and in-plane forces are predominantly dependent on different strain gauges than the ones used to determine thrust (and in-plane moments), the torque and in-plane force components were considered to provide reliable results.

Wing Pressure Taps

The wing model was instrumented with two rows of pressure taps, located $\pm 0.7R$ from the mid-span location of the wing, as shown in Fig. 8.2e. Each section contained 45 pressure taps, of which 10 were not used in the flap-retracted measurements because they were located inside the flap cove. Pressure taps up to 10% and 50% chord on the pressure and suction sides, respectively, were connected to 5 psi (34.5 kPa) pressure sensors, while the remaining pressure taps were connected to 1 psi (6.9 kPa) pressure sensors. The pressure sensors featured a calibration uncertainty of 0.25% of the full-scale range. The pressure at the trailing edge was estimated by taking the average of the extrapolated pressure values of the upper and lower sides of the airfoil. Therefore, the data point at $x/c = 1$ is an approximated value, and not a measured value. Pressure data were recorded with the propellers installed at four different vertical positions, thereby sampling the sectional pressure distribution at eight spanwise locations with respect to the middle propeller ($-1.0 < y/R < 1.4$). The deviations observed among repeated measurements were confirmed to be significantly smaller than the effect of the propeller on the wing pressure distribution. These deviations are indicated by error bars in the resulting sectional lift and drag polars, although the error bars do not include the pressure-sensor calibration uncertainty, since only gauge pressures were recorded which were small compared to the full range of the measurement device.

C. TEST CONDITIONS

Table 8.1 provides an overview of the operating conditions tested in the LST experiment. All measurements were performed at a freestream velocity of 30 m/s, a blade pitch of $\beta_{0.7R} = 30^{o}$, with co-rotating propellers, and without controlling the relative phase angle between the propellers. In these conditions, the wing-chord-based Reynolds number is $Re_c \approx 6 \cdot 10^5$. For the external balance measurements, angle-of-attack sweeps were performed at three different advance ratios, corresponding to high thrust ($J = 1.00$, $T_c \approx 0.45$), medium thrust ($J = 1.15$, $T_c \approx 0.17$), and near-zero thrust ($J = 1.35$, $T_c \approx 0$), respectively. For the propeller force-sensor measurements, advance-ratio sweeps were performed at $\alpha = 2^{o}$ and $\alpha = 8^{o}$.

Table 8.1: Overview of test conditions evaluated in the LST experiment.

Parameter	Values
Freestream velocity V_∞ [m/s]	30
Angle of attack α [deg]	$-4 < \alpha < 10$
Blade pitch $\beta_{0.7R}$ [deg]	30
Advance ratio J [-]	$0.8 < J < 1.35$
Relative blade-phase angle $\Delta\phi$ [deg]	random
Rotation direction	co-rotating

8.1.2. NUMERICAL SETUP

A numerical method is developed to investigate the effect of several design parameters on the performance of the OTWDP system. Since it is additionally intended for preliminary aircraft design purposes (see Ch. 10), the method is formulated to be sen-

sitive to top-level aircraft design parameters, without requiring a detailed geometrical description of the system. Several lower-order methods have also been developed for OTW propellers by other authors. Cooper et al. [80] used a panel method to model the wing and the axisymmetric streamtube enclosing the propeller slipstream, controlling the contraction and mass flow through the streamtube to account for different thrust settings. Veldhuis [68] studied the OTW propeller using both a vortex-lattice method and a panel-method approach, with a blade-element method (BEM) for the propeller, and representing the slipstream edge as a sheet of discretized vorticity elements to compute the effect of the propeller on the wing. More recently, the method developed by Marcus [231] combined a 3D panel method with a BEM adapted for non-uniform inflow, and a slipstream vortex lattice with non-uniform loading. The comparisons to experimental data performed by these authors showed that these lower-order methods can capture the changes in wing lift and pressure drag with reasonable accuracy, matching the trends observed in the experiment, but generally with slight offsets in the lift or drag values. Nonetheless, the level of fidelity is considered appropriate to examine the effect of the main design variables and provide a first performance estimate for conceptual aircraft design purposes. Therefore, the lower-order numerical method developed here for the OTWDP system is based on these earlier studies, though with two major differences. First, the change in profile drag due to propeller-induced variations in the boundary-layer thickness is accounted for by assuming independent 2D wing sections and designing an equivalent propeller-on airfoil (see following subsections). Second, the propeller efficiency in non-uniform inflow is estimated using an engineering method based on propeller sensitivity maps obtained from previously-run CFD calculations.

Figure 8.3 presents the three main components modeled in the numerical method: a propeller-performance model used to estimate the changes in loading on the propeller disk, a slipstream-vortex model used to estimate the velocities induced by the propeller-vortex system, and a series of wing sections represented with a 2D panel method. The three modules are described in the following subsections, respectively, and are coupled following the flowchart of Fig. 8.4. The implementation is performed in Matlab. The computational time required to estimate the performance of an OTW propeller and the wing segment beneath it, including viscous effects, ranges from several seconds to several minutes on a single core, depending on the discretization settings and the initial guess of the inverse airfoil-design process (described in the following sections). To limit the computational costs and input requirements of the model, several simplifying assumptions are made:

- Although the effect of the propeller on the wing and vice versa are accounted for, no iterative coupling is included. This assumption is based on the observations of previous chapters, which show that the changes in wing pressure coefficient due to the OTW propeller are typically significantly lower than the isolated-wing pressure coefficients ($C_p \sim 1$, $\Delta C_p \sim 0.1$).

- The unswept, high aspect-ratio wing is modeled as a series of independent 2D wing segments. Although each segment accounts for the velocities induced by the propellers in a 3D space, the spanwise velocity component is neglected and the effect of trailing vorticity due to spanwise variations in wing loading is not ac-

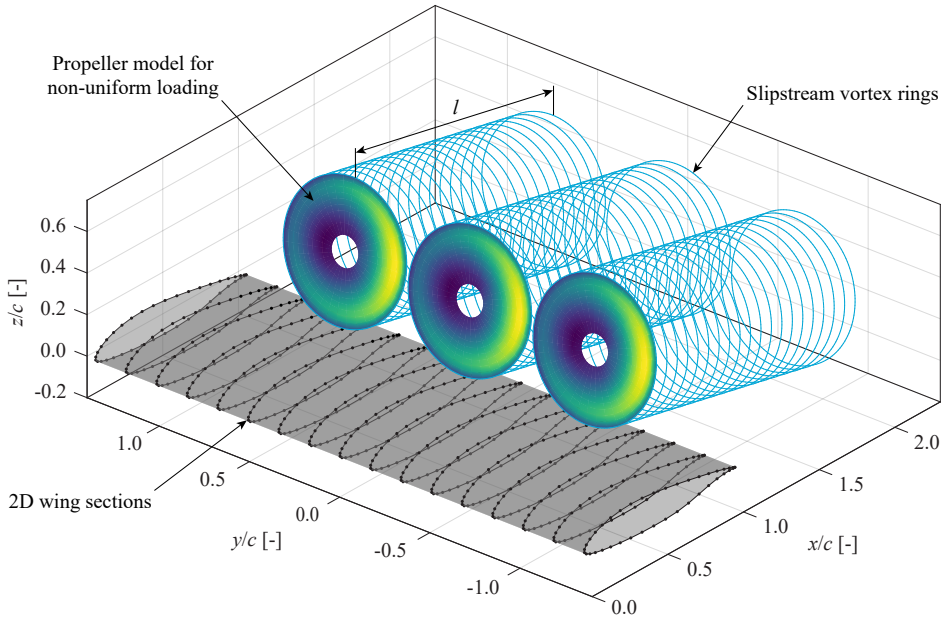

Figure 8.3: Overview of the three components modeled in the numerical method: wing section, propeller disk, and slipstream ring vortices.

counted for. This assumption is based on the experimental results (see Sec. 8.2), which show that the changes in lift and drag created beneath the distributed propellers are practically constant in spanwise direction.

- The propeller slipstream is modeled as a single tube of ring vortices of radius R, whose circulation strength is related to the average thrust on the propeller disk. In other words, the circulation is assumed to be constant along the propeller blade, and to be constant throughout a revolution. Although this is inconsistent with the non-uniform loading on the propeller, a more refined representation of the slipstream including radial and circumferential discretizations of different strengths was found to have no significant influence on the wing pressure distribution.

- The effect of propeller-propeller interaction is neglected, since the results of Sec. 6.3 showed that the effect on integral propeller performance is small.

- Additional elements such as ducts, nacelles, or pylons are not modeled. Although they may appreciably affect the performance of the system, they require a more detailed geometrical description. This would limit the ability to draw generalized conclusions regarding the effect of determined geometrical parameters, which is important to understand and be able to model the performance of the system in the conceptual design phase. Moreover, these elements would imply a more complex 3D modeling and an increased computational cost of the method. Hence, in this low-fidelity modeling approach, their effect is neglected.

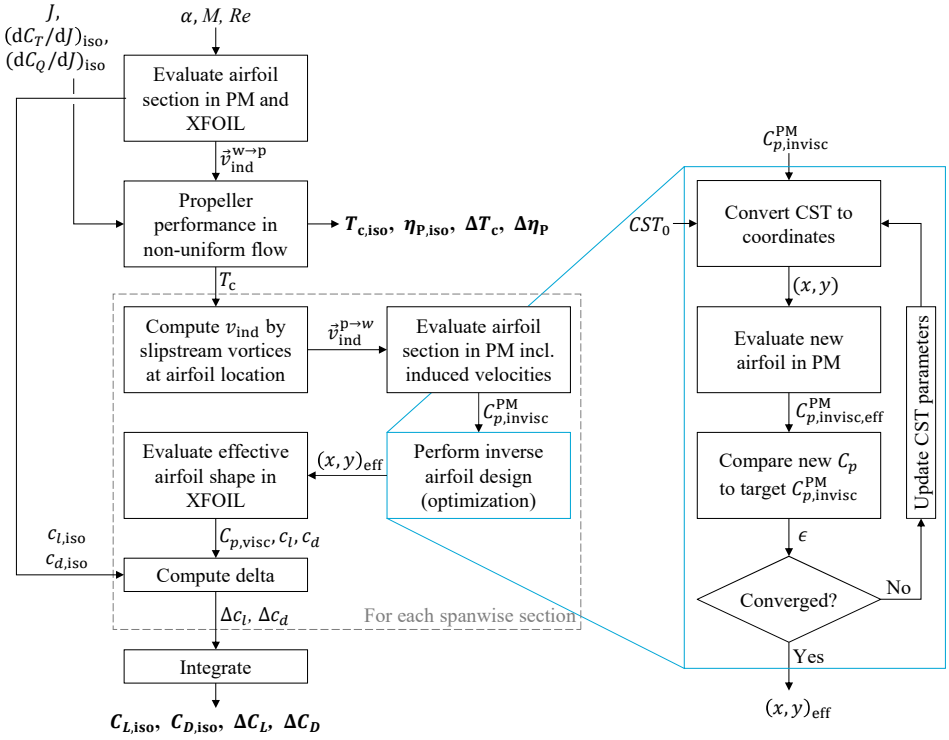

Figure 8.4: Top-level flowchart of the numerical method used to estimate cruise performance for a given geometry.

A. PROPELLER PERFORMANCE MODEL

The engineering method developed by van Arnhem [90] is used to estimate the performance of the propeller in the non-uniform inflow field generated by the wing. In the selected approach, the wing is unswept, the root and tip are assumed to be far from the propellers ($A \to \infty$), and no iterative coupling between the propeller and wing is included. Hence, the non-uniform inflow field induced by the wing at the propeller location $\vec{v}_{ind}^{w\to p}$ is two-dimensional, and can be estimated by sampling the velocity induced by the discrete vortex elements of the 2D panel method representing the wing. This first step is indicated in the top left-hand corner of Fig. 8.4. The propeller performance model then computes the thrust and torque distribution on the propeller disk for a generic inflow velocity distribution by decomposing the local perturbation into axial and azimuthal components. By obtaining the sensitivity of the blade loading to changes in axial and tangential inflow from CFD simulations of the isolated propeller [90], the change in blade loading can be computed for an arbitrary non-uniform inflow field. This change in loading is subsequently integrated over the complete propeller disk to provide the overall propeller forces and efficiency, and their difference with respect to an isolated propeller in uniform inflow at zero angle of attack. The sensitivity maps were created for a range of advance ratios for the same geometry and operating conditions as the experimental analysis (XPROP-S, $V_\infty = 30$ m/s) in earlier work [90].

Although the nacelle is not explicitly modeled in the numerical method, a correction to the in-plane velocity distribution at the propeller disk is included to account for the changes in propeller normal force due to the flow around the nacelle. For this, the cross-flow induced by the nacelle is estimated by taking the in-plane component of the velocity at the center of the propeller disk, $V_\mathrm{P} \sin\alpha_\mathrm{P}$ (including wing-induced velocities; see Fig. 2.6), and assuming that it evolves around the nacelle cross-section similarly to the potential flow around a 2D cylinder. In that case, the cylinder can be represented by a doublet and the in-plane velocities induced by the nacelle can be expressed in cylindrical coordinates as (see e.g. Ref. [282], Ch. 3):

$$v_r = (V_\mathrm{P} \sin\alpha_\mathrm{P}) \cos\theta \left(1 - \frac{R_\mathrm{hub}^2}{r^2}\right), \tag{8.1}$$

$$v_\theta = -(V_\mathrm{P} \sin\alpha_\mathrm{P}) \sin\theta \left(1 + \frac{R_\mathrm{hub}^2}{r^2}\right), \tag{8.2}$$

where r is the radial distance from the nacelle axis, θ is the azimuthal coordinate, R_hub is the radius of the nacelle at the propeller location. Analyses performed by van Arnhem [283] confirmed that the in-plane velocities estimated with this simplified approach are comparable to those estimated by RANS simulations of the nacelle at an angle of attack.

Though the selected propeller modeling method provides a rapid estimation of the changes in propeller performance due to the interaction with the wing, it presents some limitations when evaluating the propeller at higher freestream velocities. Most importantly, it is insensitive to changes in the freestream Mach number or Reynolds number, since the sensitivity maps correspond to $V_\infty = 30$ m/s. Therefore, although the influence of Re and M on the *changes* in propeller performance due to its interaction with the wing is considered a second-order effect, the true values in full-scale applications may differ from the estimated values. Although the method would also be applicable to such conditions if the corresponding isolated-propeller sensitivity maps were computed, this was not performed in the present work. The effect of Reynolds number on the changes in propeller performance are expected to be small, since an increase in Re leads to an offset in the propeller performance curves (see e.g. Ref. [90]), without significantly altering their slope. Hence, the response to a given ΔJ is not significantly affected by the Reynolds number. However, the absolute value of the force and torque coefficients predicted at a given J will be lower than in a full-scale application.

B. SLIPSTREAM VORTEX MODEL

Of the various elements that constitute the propeller vortex system, only the tangential-vorticity component in the slipstream has an effect on the velocities outside the slipstream, as discussed in Ch. 2. Therefore, the velocities induced by the propeller on the wing can be estimated by representing the propeller as a series of vortex rings, as shown in Fig. 8.3. As mentioned earlier, in this simplified approach, the radial and azimuthal variations in circulation on the propeller disk are neglected. If additionally the blade drag is assumed to be much smaller than the blade lift and the Kutta–Joukowski theorem is applied at the mid-span of the blade, it can be shown (see e.g. Ref. [284]) that

$$\Gamma_b \approx \frac{T/B}{\rho \pi n R^2}, \tag{8.3}$$

from which it follows that the total bound circulation can be expressed as a function of the thrust coefficient as

$$\Gamma \approx \frac{T_c V_\infty^2}{2n}. \tag{8.4}$$

The circulation strength of each ring vortex can then be calculated by considering the total amount of tangential circulation contained in the helical tip vortices between two subsequent vortex rings separated by a distance Δx, leading to

$$\Gamma_{ring} = \frac{\Delta x}{p}\Gamma, \tag{8.5}$$

where the helix pitch p can be estimated based on the axial induction at the propeller disk a from

$$p = \frac{(1+a)V_\infty}{n}, \tag{8.6}$$

$$a = \frac{1}{2}\left(\sqrt{1+T_c}-1\right). \tag{8.7}$$

In Eq. 8.6 it is assumed that the tip vortices translate in axial direction at a constant velocity $V_\infty(1+a)$. This simplified approach therefore neglects any downstream acceleration or contraction of the slipstream. The assumption of no contraction is considered valid for cruise conditions, in which case only low thrust coefficients are attained and the contraction is negligible. In fact, in these conditions, the slipstream often maintains a constant radius or even increases in radius due to the presence of the nacelle.

The velocities induced by each vortex ring can be computed by applying the Biot-Savart law to discretized vortex segments. However, since a constant circulation is assumed, an analytical expression can be used instead to provide a more continuous velocity field and decrease the computational costs. Yoon and Heister [285] showed that the velocities induced by a vortex ring located at the origin with its axis parallel to the x-axis can be calculated in cylindrical coordinates as

$$u(r,x) = \frac{\Gamma_{ring} R}{4\pi}\left[\left(R + \frac{a_0}{b_0}r\right)\frac{4E(m_0)}{c_0^3(1-m_0)} - \frac{4K(m_0)}{kb_0}r\right], \tag{8.8}$$

$$v_r(r,x) = \frac{\Gamma_{ring} R}{4\pi}\frac{x}{b_0}\left(\frac{4K(m_0)}{c_0} - \frac{4a_0E(m_0)}{c_0^3(1-m_0)}\right), \tag{8.9}$$

where $a_0 = x^2 + r^2 + R^2$, $b_0 = -2rR$, $c_0 = \sqrt{(r+R)^2 + x^2}$, $m_0 = 4rRc_0^{-2}$, and $K(m_0)$ and $E(m_0)$ are the complete elliptic integrals of the first and second kind, respectively. The velocities given by Eqs. 8.8 and 8.9 are subsequently converted into Cartesian coordinates, accounting for the location and inclination of the slipstream with respect to the x-axis. Finally, the contributions of all rings are summed to obtain the velocity induced by a single slipstream. This process is repeated for each of the N_P propellers to give the total induced velocity at a determined location on the wing.

Figure 8.5a shows an example of the velocity field induced in the $y/R = 0$ plane by a propeller at a low thrust setting. The figure shows the location of the wing for reference, although the velocities induced by the wing are not included. The velocity increase across the propeller disk is clearly visible. Moreover, the slipstream appears as a straight tube, since contraction is neglected and the gradual alignment of the slipstream center-line with the freestream velocity is not accounted for. Figure 8.5b presents the corresponding out-of-plane component of the curl of the velocity field. It can be seen that the magnitude is non-zero in the vicinity of the slipstream edge, particularly at the propeller location. Therefore, the flow is not irrotational everywhere in the domain. This effect grows with increasing thrust setting and has an effect on the solution of the panel method, as discussed in the following section.

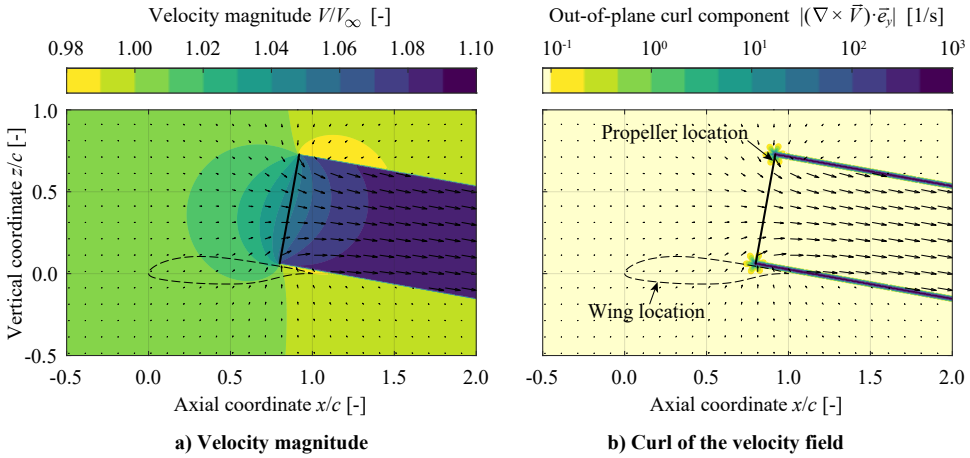

Figure 8.5: Example of the velocity magnitude (left) and curl of the velocity field (right) created by the propeller (including freestream velocity; excluding wing-induced velocities) at a low thrust setting. Velocity vectors indicate the in-plane induced velocities, i.e. $(u, w)_{\text{on}} - (u, w)_{\text{off}}$.

8

C. Wing Model: 2D Panel Methods

Two panel methods are used in the numerical model: a 2D panel method implemented directly in Matlab, and XFOIL [243]. The purpose of former (hereafter referred to as "PM" to distinguish it from XFOIL) is to compute the velocities induced by the (inviscid) wing at the propeller location, and to solve the (inviscid) pressure distribution on the wing when subjected to the propeller-induced velocities. It models the panels as linear-strength vortex distributions, following the procedure presented by Katz and Plotkin [282], and accounts for compressibility effects using the Karman-Tsien correction (see e.g. Ref. [286], Ch. 11). The propeller-induced velocities are added to the right-hand-side of the linear set of equations. In this way, the panel vortex strengths are such that they induce a normal velocity at each panel collocation point which is equal in magnitude but opposite in sign the normal component of the freestream velocity *plus* the propeller-induced velocity. The purpose of XFOIL, on the other hand, is to account for viscous effects. It must be combined with the PM because, on its own, it cannot account for the propeller-induced effects. The two panel methods were confirmed to produce the same results for an isolated airfoil in inviscid flow. While the friction drag was found

to not be significantly affected by the propeller, the change in boundary-layer thickness due to the propeller-induced pressure gradients was found to play a significant role in the lift and pressure drag. Therefore, neglecting the viscous effects would lead to an over-estimation of the lift enhancement and drag reduction.

The way in which these two methods are combined is shown in Fig. 8.4. XFOIL is first run for a determined set of operating conditions (α, M, Re) to provide the lift and drag of the isolated 2D wing. Boundary-layer transition is enforced at the location of the trip strips in the experiment, i.e. at 5% and 10% chord on the suction and pressure sides, respectively. The PM is then used to compute the velocities induced by the wing at the propeller location. This step does not account for changes in the wing-induced velocities at the propeller location due to viscous or compressibility effects. After computing the propeller performance, the velocities induced by the slipstream at the panel collocation points of a given spanwise wing section $\vec{v}_{\text{ind}}^{\text{p}\rightarrow w}$ are computed. The PM is subsequently solved including these velocities, thereby providing the inviscid pressure distribution on the wing section including propeller effects, $C_{p,\text{invisc}}^{\text{PM}}$. To account for viscous effects, the boundary layer has to be solved for this pressure distribution. For this, an equivalent or "effective" airfoil shape $(x, y)_{\text{eff}}$ has to be determined which produces the same pressure distribution in uniform inflow as the original airfoil shape in non-uniform flow.

Inverse Airfoil Design Procedure: Optimization

To account for the change in the wing boundary layer due to the propeller-induced velocities, the effective airfoil shape corresponding to a predetermined pressure distribution has to be found. For a wide range of representative pressure distributions this can be done explicitly, and XFOIL includes this functionality. However, the inverse-design routine of XFOIL was found to produce unreliable results, due to the sensitivity to noise in the curvature distribution of the airfoil, and because each time the input pressure distribution is modified slightly to satisfy the Lighthill constraints [287]. This suggests that, in fact, there is no mathematical solution which satisfies the Lighthill constraints[1] and exactly replicates a generic propeller-on pressure distribution. Hence, an optimization approach is taken instead to find an airfoil shape whose pressure distribution resembles the propeller-on pressure distribution as closely as possible. Although this significantly increases the computational time of the method, it provides more transparent results.

The steps of this inverse airfoil design optimization are shown on the right-hand-side of Fig. 8.4. For the optimization, the airfoil shape is parametrized using the class-function/shape-function transformation (CST) described by Kulfan [289]. In this parametrization, the upper and lower sides of the airfoil are represented by a series of Bernstein polynomials multiplied by scaling coefficients, referred to here as "CST coefficients". To reduce the number of design variables, and based on the conceptual breakdown of Fig. 2.7, it was hypothesized that the effect of the propellers on the wing pressure distribution could be replicated by changing the angle of attack of the airfoil, and modifying the curvature on only the suction side of the airfoil. Hence, the CST design variables are limited to the upper side. Moreover, to ensure a smooth leading edge, the first

[1] Lighthill [288] defined three integral constraints that have to be met to guarantee that an inverse-design solution exists; one condition requires the velocity at infinity to equal V_∞, and the other two impose that the airfoil must be a closed contour.

CST coefficient of the suction side is also kept constant. This does not suppose a major limitation to the design space, as long as the propeller is not placed close to the leading edge. Analogously, the lower bound of the last CST coefficient on the suction side is set to the value of the last CST coefficient on the pressure side, to avoid self-intersecting geometries. Therefore, for an airfoil parametrized with N_{CST} coefficients per side, the number of design variables in the optimization problem is N_{CST}: one design variable for the effective angle of attack, and $N_{\text{CST}} - 1$ design variables describing the upper surface of the airfoil. The initial guess for the design variables, CST_0, are the CST coefficients of the original airfoil shape[1]. No additional constraints are imposed, and a gradient-based optimization is performed to find the airfoil shape which minimizes the difference between the airfoil's pressure distribution $C^{\text{PM}}_{p,\text{invisc,eff},i}$ and the target pressure distribution $C^{\text{PM}}_{p,\text{invisc}}$. For this, the new airfoil created in each iteration is solved in the PM and the resulting error (objective function) is computed as

$$\epsilon = \frac{\sum_{i=1}^{N_{\text{panels}}} \left| C^{\text{PM}}_{p,\text{invisc},i} - C^{\text{PM}}_{p,\text{invisc,eff},i} \right| \cdot W_i}{\sum_{i=1}^{N_{\text{panels}}} W_i}, \tag{8.10}$$

where the summation operates over each of the N_{panels} panels of the discretized airfoil, and $W = 1 + k_1 \exp(-k_2 \cdot x/c)$ is a generic weighting function ($k_1 = 2$, $k_2 = 40$) that associates more weight to points near the leading edge in order to capture the suction peak and stagnation point more accurately.

An example of an inverse-design result is given in Fig. 8.6. The pressure distributions given by dashed and solid black lines correspond to the inviscid wing-pressure distribution without and with propeller-induced velocities, respectively. The wing shape is

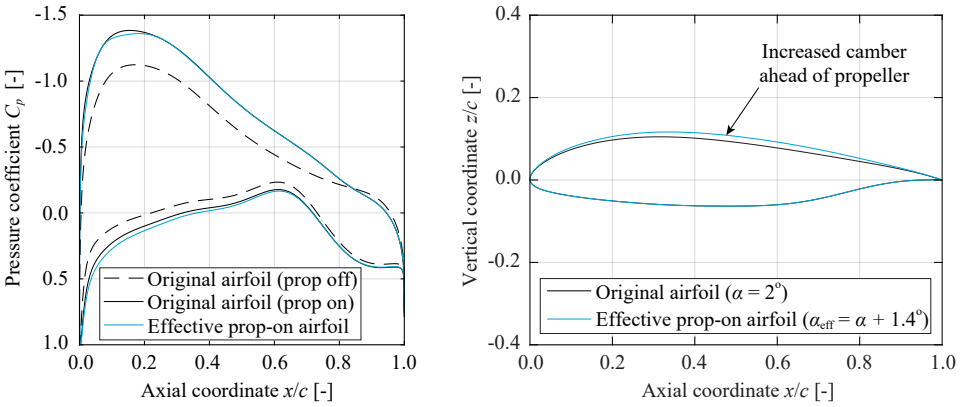

a) Pressure distribution **b) Airfoil shape**

Figure 8.6: Inverse airfoil design example ($J = 1.00$), comparing the pressure distributions obtained by the PM for the effective airfoil shape, and the original airfoil with propeller-induced velocities ($x_{\text{P}}/c = 0.8$).

[1] To reduce computational costs, each time the optimization converges to a solution, the resulting design variables and the associated pressure distribution are stored in a database. In subsequent optimizations for a different operating condition or spanwise location, the set of design variables in the database whose associated pressure distribution is most similar to the target pressure distribution is used as initial guess.

shown in black in Fig. 8.6b. The optimization results in the airfoil shape shown in blue, which presents an increase in camber on the suction side, mainly upstream of the propeller location. If this airfoil is solved at the effective angle of attack α_{eff} obtained from the optimization, the pressure distribution shown in blue in Fig. 8.6a is obtained. The pressure distribution closely resembles the propeller-on pressure distribution, confirming the earlier hypothesis that the effect of the propeller on the wing can be modeled as an increase in the effective angle of attack and a change in the upper-surface curvature. However, some difference between the actual prop-on pressure distribution and the effective airfoil's pressure distribution can be observed, particularly at the suction peak or on the pressure side for $x/c < 0.4$.

Calculation of Wing Lift and Drag

The sectional lift c_l and pressure drag c_{dp} of each wing section are estimated by integrating the pressure distribution given by

$$C_p = C_{p,\text{iso}} + \Delta C_p. \tag{8.11}$$

However, Fig. 8.6 shows how the effective airfoil gives only an approximation of the actual pressure distribution. Hence, the change in pressure, ΔC_p, is obtained from

$$\Delta C_p = \Delta C^{\text{PM}}_{p,\text{invisc}} + \left(\Delta C^{\text{XFOIL}}_{p,\text{visc}} - \Delta C^{\text{XFOIL}}_{p,\text{invisc}}\right), \tag{8.12}$$

with

$$\Delta C^{\text{PM}}_{p,\text{invisc}} = C^{\text{PM}}_{p,\text{invisc}} - C^{\text{PM}}_{p,\text{invisc,iso}}, \tag{8.13}$$

$$\Delta C^{\text{XFOIL}}_{p,\text{visc}} = C^{\text{XFOIL}}_{p,\text{visc,eff}} - C^{\text{XFOIL}}_{p,\text{visc,iso}}, \tag{8.14}$$

$$\Delta C^{\text{XFOIL}}_{p,\text{invisc}} = C^{\text{XFOIL}}_{p,\text{invisc,eff}} - C^{\text{XFOIL}}_{p,\text{invisc,iso}}. \tag{8.15}$$

Equation 8.12 shows that the ΔC_p obtained from the PM is corrected by the term in parenthesis, which is the ΔC_p due to the change in boundary-layer behavior between the propeller-on and propeller-off cases. Note that $\Delta C^{\text{XFOIL}}_{p,\text{visc}}$ is not equal to ΔC_p, since the "propeller on" pressure distribution evaluated in XFOIL is only an approximation of the actual propeller-on pressure distribution and therefore $\Delta C^{\text{PM}}_{p,\text{invisc}} \neq \Delta C^{\text{XFOIL}}_{p,\text{invisc}}$. The friction drag component c_{df}, on the other hand, is obtained directly from XFOIL.

The 3D aerodynamic force coefficients can be obtained by performing the previous steps for different spanwise locations along the wing. Assuming that the OTWDP contains many propellers, the lift and drag coefficients of the wing segment associated to one propeller located at $y/R = 0$ can be calculated from

$$C_L = \frac{1}{2R+d}\int_{-R-d/2}^{R+d/2} c_l \mathrm{d}y, \tag{8.16}$$

$$C_D = \frac{1}{2R+d}\int_{-R-d/2}^{R+d/2} (c_{dp} + c_{df})\mathrm{d}y. \tag{8.17}$$

An initial investigation of the spanwise lift and drag distributions, however, showed inconsistent local peaks at spanwise locations close to the propeller axis. This effect was

more pronounced for higher thrust settings and smaller tip clearances. At these locations, the propeller-on C_p distribution obtained from the PM was found to present a sharp spike at the trailing edge, with additional wiggles close to the trailing edge. A closer inspection of the PM with more elementary disturbances revealed that the pressure distribution was smooth if subjected to an infinite 2D vortex (which produces an irrotational velocity field everywhere except at the vortex location), while presenting the trailing-edge spike if subjected to a finite 2D vortex segment (which does not produce an irrotational velocity field[1]). Based on this analysis it was concluded that these spikes were an artifact of the rotational flow field, which violates the underlying assumption of potential flow models. As seen in Fig. 8.5b, the curl of the velocity field produced by Eqs. 8.8 and 8.9 is non-zero, particularly near the slipstream edge. Therefore, although a mathematical solution for the singularity strengths on the airfoil panels exists, the physical meaning of this solution is inaccurate if the panels are close to the slipstream edge.

To minimize the impact of this limitation of the selected numerical approach, two modifications were made to the loading distributions. Firstly, the estimated lift and drag values of airfoil sections with a chordline located at a distance of less than $1.2R$ from the center of the propeller disk were considered unreliable. There, the solutions were removed and replaced by interpolating the lift and drag coefficients of the adjacent wing sections. Interpolation was considered an acceptable approach because the experimental data showed that the lift and drag present smooth distributions (see Sec. 8.2), and therefore the sectional lift and drag values estimated beneath the edges of the propeller disk are also representative of the values beneath the propeller axis. For the baseline tip clearance, this meant that a significant portion ($\sim 50\%$) of the wing span covered by each propeller had to be interpolated. This highly conservative approach was selected such that the same $1.2R$ margin would be applied for all thrust settings and tip clearances investigated in this study. However, for larger tip clearances and lower thrust settings (including typical cruise thrust settings), the $1.2R$ margin could be reduced or even removed. And secondly, the ΔC_p values downstream of $x/c = 0.95$ were removed to neglect the effect any remaining (minor) spikes near the trailing edge, and the trailing-edge ΔC_p was estimated by taking the average of the extrapolated values from the top and bottom sides. Qualitatively, this modification resulted in ΔC_p distributions that resemble the effects observed in the experimental campaign and Ch. 6 more closely. In any case, these approximations further highlight the need for a dedicated validation study (Sec. 8.3).

8.2. BASELINE AERODYNAMIC PERFORMANCE

This section describes how the aerodynamic interaction between three over-the-wing propellers and a wing affects the forces produced by the system. For this, exclusively the results from the experimental campaign are discussed. These results are used as reference case for the validation of the numerical model in Sec. 8.3 and as a baseline for the sensitivity studies performed in Sec. 8.4. The effects are described in the following two subsections, which focus on the impact on propeller performance and on wing performance, respectively.

[1] The tangential velocity induced by a finite vortex filament of length $\mathrm{d}l$ scales with $1/r^2$, while the tangential velocity induced by an infinite 2D vortex scales with $1/r$. The curl of the velocity field generated by the latter is zero, while the curl of the former is not.

8.2.1. PROPELLER PERFORMANCE

Figures 8.7 and 8.8 present the thrust, torque, normal-force, and side-force coefficients of the middle propeller in the installed condition. Isolated propeller thrust and torque, obtained in Sec. 6.3, are included in Fig. 8.7 for reference. Since the isolated propeller is evaluated at zero angle of attack, the corresponding in-plane forces are zero. The reader is reminded that in these figures, and in the rest of this chapter, the forces are defined as indicated in Fig. 2.6. The propeller thrust T is therefore the force component parallel to the propeller axis, while the normal force N is an in-plane force component. In a general sense, both force components contribute to the vertical (lift) and horizontal ("drag") forces of the system.

As discussed in Sec. 8.1, the installed propeller thrust component could not be accurately measured in the experiment. The isolated-propeller thrust curve gives an indication of which advance ratios correspond to "high" or "low" thrust settings, since the thrust reduction of the installed propeller is small for this axial position (see Fig. 6.14). For this, the right-hand axis of Fig. 8.7a presents the thrust coefficient obtained if the thrust is non-dimensionalized with the wing reference area S_{ref} instead of the propeller disk area S_{p}, T_{c}^*. For example, at $J = 1.15$, the thrust produced by the propeller ($T_{\text{c}}^* \approx 0.1$) would be equal to the lift produced by a wing segment of span $d + D_{\text{P}}$, if it had a lift coefficient of approximately 0.1. These values suggest that the thrust produced by the propeller at $J = 1.15$ is significantly more than the drag of the wing segment that it covers (assuming $c_d \ll 0.1$), although it is unknown at this stage how much total aircraft drag each propeller would have to overcome.

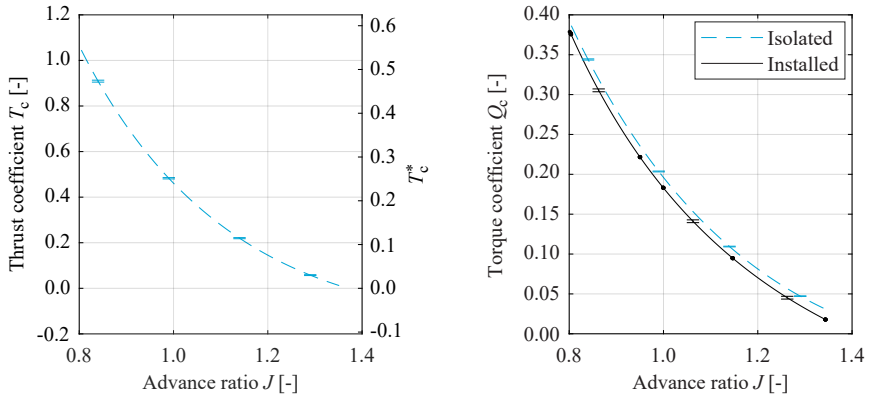

a) Thrust coefficient **b) Torque coefficient**

Figure 8.7: Comparison of propeller thrust and torque coefficients in isolated ($\alpha = 0^{\text{o}}$) and installed ($\alpha = 2^{\text{o}}$, $i_{\text{P}} = 10.2^{\text{o}}$) configurations. Experimental data ($x_{\text{P}}/c = 0.8$); markers indicate individual measurements.

A comparison of the torque coefficients in Fig. 8.7b shows that the torque produced for a given advance ratio is lower in the installed OTWDP configuration than in the isolated-propeller configuration. However, as found in Sec. 6.1, the thrust reduction due to increased inflow velocities at a given freestream-based advance ratio outweighs the reduction in torque, which overall would lead to a decrease in propulsive efficiency. Moreover, it should be noted that, although the influence of the wing is dominant, the

propeller is also affected by other surrounding elements such as the nacelles, support sting, or adjacent propellers. For example, the neighboring propellers and nacelles lead to a minor reduction in the torque of the middle propeller, as discussed in Sec. 6.3.

An examination of the in-plane forces, provided in Fig. 8.8, shows that the normal force is roughly three times larger in magnitude than the side force. This suggests that there is a larger difference in loading between left and right sides of the propeller disk (if the wing is viewed horizontally) than between the top and bottom sides of the propeller disk. In other words, the non-uniform loading on the disk is mainly caused by an angle-of-attack effect, and not so much by the axial-velocity gradient normal to the wing surface. Furthermore, the normal force decreases slightly with advance ratio, while the side force appears to be practically independent of advance ratio. At zero thrust ($J \approx 1.3$), both in-plane components are non-zero, due to the in-plane velocities induced by the wing, nacelles, and other elements. The magnitude of both components increases with angle of attack, since also the inflow angle and velocity gradients to the propeller disk increase. This increase in in-plane forces with angle of attack occurs not only due to the wing, but also due to the nacelle of the middle propeller and the adjacent ones, as discussed in Sec. 6.3.

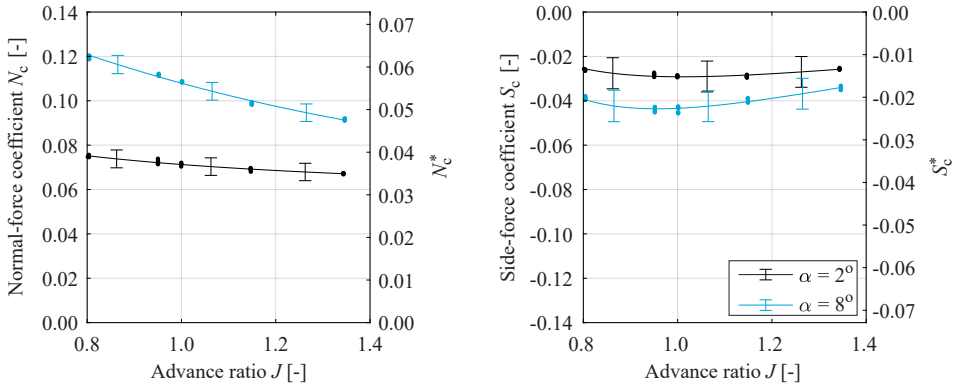

a) Normal-force coefficient **b) Side-force coefficient**

Figure 8.8: Propeller in-plane force coefficients in the installed configuration, for two angles of attack. Experimental data ($x_P/c = 0.8$); markers indicate individual measurements.

The side force generated on the propellers is of little relevance if the propellers are counter-rotating, or if the array of propellers on each semi-wing rotates in opposite direction. Though co-rotating propellers on either side of the fuselage have historically been preferred due to the reduced engine maintenance and production costs, with electrically-driven propellers it is likely that the aerodynamic benefits of having a symmetric aircraft with zero side force drives the selection of the rotation direction. In any case, the normal force is more relevant for the aerodynamic performance of the system, since it directly contributes to system lift and, to a lesser extent, to system drag (see Fig. 2.6). Figure 8.8a shows that, for an advance ratio of $J = 1.15$, the normal-force coefficient based on the wing reference area is approximately $N_c^* = 0.035$, for an angle of attack of 2^o. At this angle of attack, the sectional lift coefficient of the isolated wing is $c_l \approx 0.38$ (see

following paragraphs). Therefore, despite the low angle of attack and thrust coefficient the contribution of the propeller normal force to the total vertical force, $N \cdot \cos(\alpha + i_P)$, is approximately 9% of the isolated-wing lift contribution.

8.2.2. WING PERFORMANCE

Figure 8.9 presents the C_p distributions registered by the port row of pressure taps ($y/R = -0.7$) when the vertical position of the support sting is centered around the mid-span of the wing, as depicted in Fig. 8.2. The clean-wing pressure distribution is included in Fig. 8.9a for reference. This plot shows that the support sting and nacelles have a noticeable upstream effect on the wing pressure distribution. However, since the geometry of the nacelles and support sting are not representative of an actual OTWDP design, the effect of the propeller can be examined more properly by comparing the propeller-on to the propeller-off measurements, which both include the nacelles and support sting.

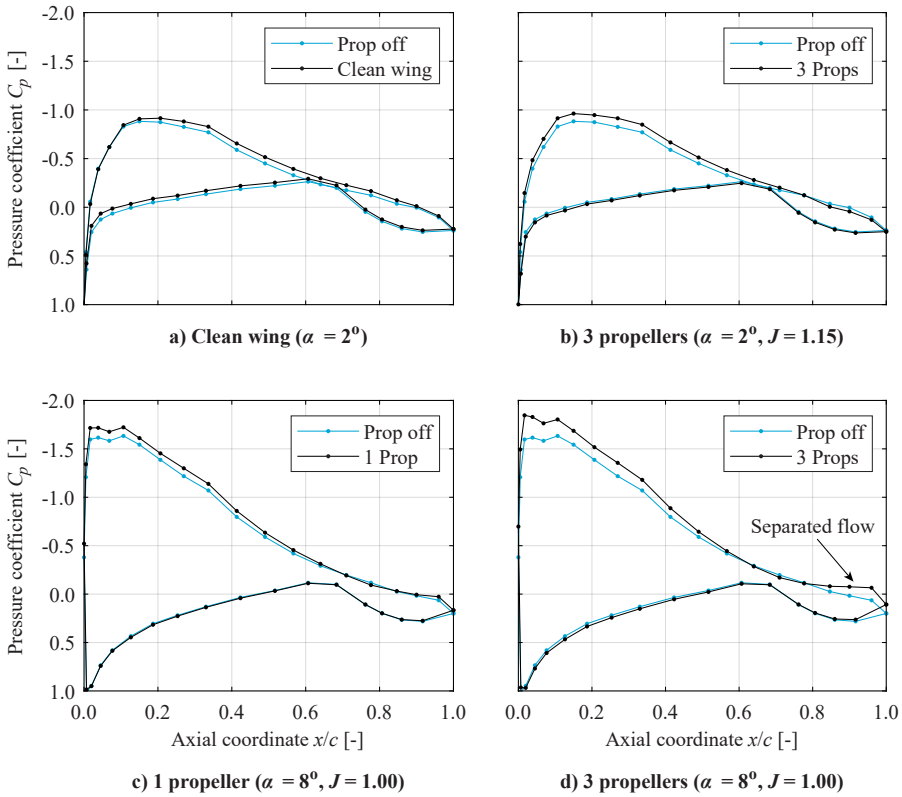

Figure 8.9: Pressure-coefficient distributions on the wing of the OTW system at $y/R = -0.7$, for various configurations and operating conditions. Experimental data ($x_P/c = 0.8$).

The comparison between propeller-on and propeller-off pressure distributions is shown in Fig. 8.9b, for a low lift and thrust setting ($c_{l,\text{off}} = 0.38$, $T_c \approx 0.17$). On the suction side, the pressure is reduced upstream of the propeller location ($x_p/c = 0.8$) and

increased downstream of it, as expected from literature [68, 80] and the observations of Ch. 6. At $x/c = 0.2$, the pressure difference induced by the propellers is approximately $\Delta C_p = -0.1$. This pressure difference is relatively small, since the advance ratio corresponds to a low thrust setting and the pressure is not sampled directly beneath the propeller axis. Moreover, on the pressure side, a minor increase in pressure is observed along the entire chord. This shows how the influence of the propeller on the C_p distribution can conceptually be decomposed into two main effects, as discussed in Ch. 2: an increase in the effective angle of attack, and a local change in pressure directly beneath the propeller—as long as the flow remains attached.

The upstream suction generated by the propellers is also visible at higher angles of attack and thrust settings, as shown in Figs. 8.9c and 8.9d. In these figures, the kink on the suction side near the leading edge is caused by the transition strip. Downstream of the propellers, the behavior is different than in Fig. 8.9b. The combination of a strong adverse pressure gradient on the airfoil and a strong adverse pressure gradient beneath the propeller disk leads to flow separation at the location of the propeller, as discussed in Ch. 7. The flow separation is especially evident in the three-propeller configuration (Fig. 8.9d), and less in the one-propeller configuration (Fig. 8.9c). In both cases, flow separation occurs directly beneath the propeller axis ($y/R = 0$; not shown here). However, while with a single propeller the adverse pressure gradient gradually reduces as one moves away from the centerline ($y/R = 0$), with multiple propellers this is not per se the case, since the adjacent propellers also create their own adverse pressure gradients.

The spanwise variations in lift and pressure drag can be obtained by integrating the C_p distributions for different spanwise positions of the propellers relative to the pressure taps. These loading distributions are shown in Fig. 8.10 for the same conditions as the pressure distribution of Fig. 8.9b. In Fig. 8.10, the horizontal axis is expressed relative to the spanwise location of the center of the middle propeller. Figure 8.10a shows that the lift is practically constant in the spanwise interval evaluated, in both the propeller-on and propeller-off conditions. The minor spanwise variations are attributed to differences between the two rows of pressure taps, which are interspersed in the sequence of

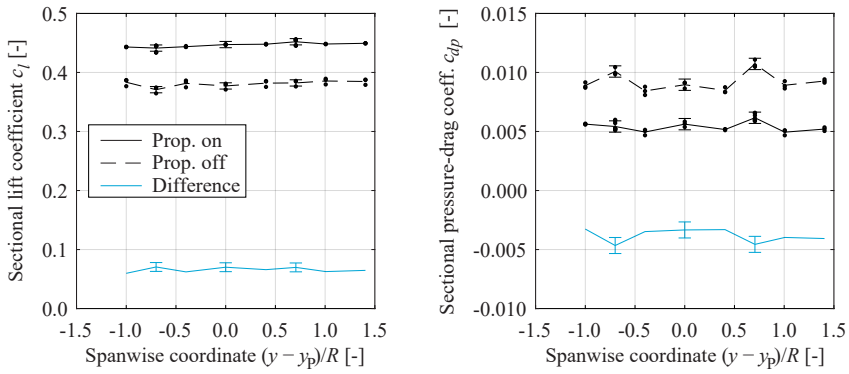

a) Lift distribution **b) Pressure drag distribution**

Figure 8.10: Spanwise loading distributions along the wing in the three-propeller configuration, for $\alpha = 2^o$, $J = 1.15$. Experimental data ($x_P/c = 0.8$); markers indicate individual measurements.

y-coordinates, and present slightly different pressure distributions due to 3D effects on the wing. Furthermore, the effect that the propeller has on wing lift (i.e., the difference between the propeller-on and propeller-off measurements, Δc_l) is also practically constant in spanwise direction. This is different than a single-propeller configuration, where the propeller creates a bell-shaped Δc_l distribution (see e.g. Fig. 7.33). In the distributed-propeller configuration, for the chosen propeller separation distance d, the superposition of these "bell-shaped" loading distributions created by each propeller leads to an approximately constant change in lift.

The spanwise drag distribution, provided in Fig. 8.10b, presents a slightly more distinguishable spanwise variation. The propeller provides a significant reduction in pressure drag; in this condition, the pressure drag is approximately half of the value corresponding to the propeller-off case. When moving from $(y - y_P)/R = \pm 1$ towards the propeller axis ($(y - y_P)/R = 0$), the drag reduction due to the propeller Δc_d first increases (in magnitude), as the pressure rise generated on the aft part of the airfoil (see Fig. 8.9b) increases. However, close to the propeller axis, the drag starts to increase. This occurs because the strong adverse pressure gradient beneath the propeller causes the boundary layer to thicken, reducing the effective camber near the trailing edge.

To analyze how the lift and drag of the wing vary with angle of attack and thrust setting, Fig. 8.11 presents the sectional lift and pressure-drag polars obtained beneath the middle propeller's axis. The lift polars show that the support sting and nacelles have a negligible effect on the sectional lift. The lift coefficients attained with the clean wing are lower than in the experiments of Boermans and Rutten [236], most likely due to the lower Reynolds number, the boundary-layer trips employed, and non-2D setup of the present experiment. In the propeller-on cases, the lift polars present an offset with respect to the propeller-off cases. This reinforces the earlier interpretation of the pressure distributions, where the increase in wing lift is associated to an increase in the effective angle of attack. In this sense, OTW propellers are very different from tractor propellers, since in the latter configuration the propellers increase the lift-curve slope of the wing due to increased dynamic pressure in the slipstream [68, 290].

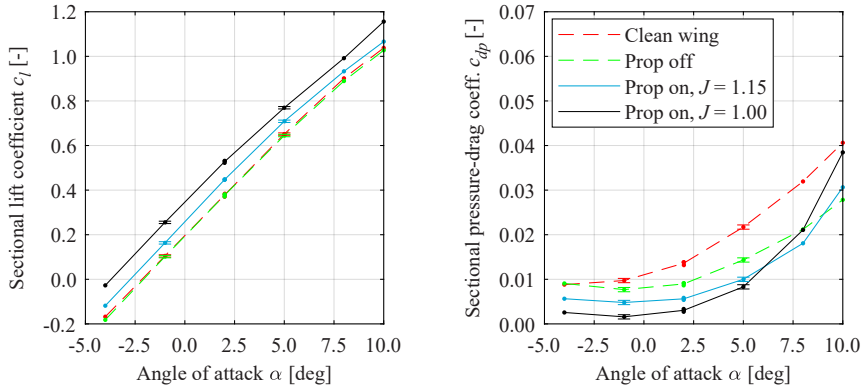

Figure 8.11: Sectional lift and pressure-drag polars at $(Y - Y_p)/R = 0$ (i.e. beneath the middle propeller's axis). Experimental data ($x_P/c = 0.8$); markers indicate individual measurements.

Figure 8.11b shows that the support sting and nacelles have a significant effect on the pressure drag of the wing segment directly beneath the propeller axis. When comparing the propeller-on and propeller-off cases, an appreciable drag reduction is observed, especially at low angles of attack. However, at higher angles of attack, the drag reduction is decreased, and the interaction eventually leads to a drag increase. This is especially evident at the high thrust setting ($J = 1.00$, $T_c \approx 0.41$), where the drag exceeds the propeller-off case above $\alpha = 8^o$ due to the propeller-induced trailing-edge separation observed in Fig. 8.9d.

In order to link the sectional pressure distributions and polars to the 3D characteristics of the wing, Fig. 8.12 presents the lift and drag characteristics of the complete wing, as obtained from the external balance. Since the forces correspond to the complete wing, the wing reference area $S_{ref} = b \cdot c$ is used for normalization, though only 50% of the wing span is covered by the three propellers. Therefore, the average changes in lift and drag for a full-span OTWDP system would be roughly double. The graphs include a single data point at a very high thrust setting ($J = 0.8$, $T_c \approx 1.0$), and present all results with the propeller installation located in its default mid-span position—except for the clean-wing configuration. The C_L values plotted in Fig. 8.12a are only slightly lower than the sectional c_l values of Fig. 8.11a. The wing drag coefficients C_D, on the other hand, are appreciably higher than the sectional drag coefficients c_d of 8.11b, since C_D includes the friction drag and induced drag of the wing. The increase in drag is most noticeable at high angles of attack for the clean-wing and propeller-off cases, due to the stall originating at the wing root.

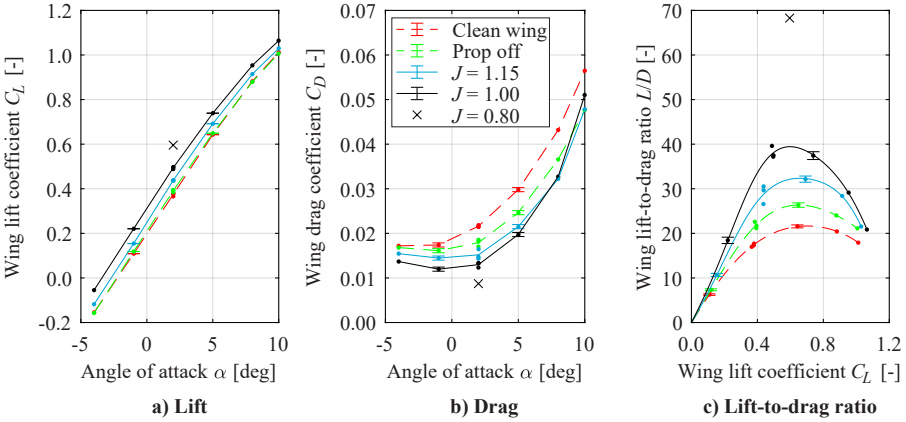

Figure 8.12: Wing lift, drag, and lift-to-drag ratio polars. Dots indicate individual measurements. Data obtained from external balance measurements ($S_{ref} = b \cdot c$, $x_P/c = 0.8$).

Finally, Fig. 8.12c provides the wing lift-to-drag ratio as a function of the lift coefficient. For this plot, polynomial fits were applied to the lift and drag data, to allow an approximate comparison of the different cases at a constant lift coefficient. As expected from the drag polars, the lift-to-drag ratio of the propeller-off configuration is higher than the one of the clean wing. However, these balance measurements do not include the forces on the support sting and nacelles. Since the support sting and nacelle geome-

tries are not representative of a practical application, the effect of the propellers themselves should be assessed by comparing the propeller-on to the propeller-off measurements, rather than to the clean-wing measurements. The increase in lift-to-drag ratio due to the OTW propellers is highest near the lift coefficient corresponding to maximum L/D, reaffirming that the OTWDP system is beneficial for cruise. At a lift coefficient of $C_L \approx 0.6$, the lift-to-drag ratio of the wing is increased by approximately 23% at a low thrust setting ($J = 1.15$), and by 51% at a high thrust setting ($J = 1.00$). This increase in L/D does not include the contribution of the propeller normal force to lift (see previous section), which would further increase the lift-to-drag ratio. The substantial increase in L/D at high thrust settings suggests that OTWDP may also be beneficial for aircraft whose propulsion system is sized for take-off conditions. As the thrust setting is further increased ($J = 0.8$), the drag approaches zero and the lift-to-drag ratio increases exponentially. This effect is comparable to the lip-thrust generated on ducts at high thrust settings (see Sec. 6.2). However, it is important to highlight that these values are inherent to this specific experimental setup. For example, a change in the span-fraction covered by the OTW propellers would directly affect the overall lift-to-drag ratio. Moreover, the OTWDP system used in the experiment had a diameter-to-chord ratio of $D_P/c = 0.6$. The L/D benefit is lower for smaller D_P/c values, which are likely to be encountered in practice due to other constraints in the design process. The influence of such geometrical parameters is discussed in Sec. 8.4.

8.3. VERIFICATION & VALIDATION OF NUMERICAL MODEL

This section aims to provide an indicative value of the uncertainty of the numerical model, and to identify potential limitations. For this, first a "grid" convergence study is performed, to verify that the numerical discretization has been performed correctly. This verification study focuses on the slipstream vortex model and the two panel methods, since the propeller-performance model has been subjected to a separate validation study in Ref. [90]. Then, the results are compared to the experimental data presented in the previous section, to validate the overall applicability of the model.

8.3.1. CONVERGENCE STUDY

The numerical method contains three modules which are sensitive to discretization error: the slipstream vortex model and the two panel methods (PM and XFOIL). For the slipstream vortex model, different slipstream-tube lengths and vortex-ring spacings are evaluated. For the panel methods, different numbers of panels and CST coefficients are compared. The results of this convergence study are provided in Appendix E.3. Here, only the key findings are summarized. Regarding the slipstream vortex model, a slipstream tube of 500 rings with a total length of $5c$ is selected. For the panel methods, 200 panels are selected to represent the airfoil. Moreover, 12 CST coefficients are used to parametrize the suction side of the airfoil in the inverse-design process. Although no systematic UQ is performed, the trends suggest discretization errors of the order of $\Delta c_l \sim 0.01$ and $\Delta c_{dp} \sim 0.0005$ for the changes in sectional lift and drag, respectively. The effect of this error on the wing-induced velocity field and subsequent changes in propeller performance is a second-order, negligible effect.

8.3.2. Comparison to Experimental Data

Although the model used to estimate propeller performance has already been validated for a generic non-uniform inflow in Ref. [90], Fig. 8.13 compares the propeller forces estimated by the model to those of the experiment to ensure a correct implementation of the method. The estimated thrust and torque curves (Figs. 8.13a and 8.13b) are qualitatively similar to the ones obtained in the experiment (Fig. 8.7), although the installed thrust—and therewith, propeller efficiency—could not be quantified in the experiment. When analyzing the change in propeller torque ΔQ_c (Fig. 8.13d), the experimental data suggests that the torque reduction is practically independent of the advance ratio, since the bumps in the curve are primarily an artifact of the polynomial fitting. The numerical model matches the experimental data at low advance ratios, though it under-estimates the torque difference at high advance ratios. The same effect was observed in terms of thrust in an over-the-wing configuration of a previous validation study [90]. Additional analyses of that validation study suggest that the error in the predicted propeller efficiency is of the order of $\Delta\eta_P \pm 0.01$, for an inflow comparable to the one encountered here (which is predominantly an angle-of-attack effect, since the propeller is placed near the trailing edge). Furthermore, the numerical model appears to under-estimate the normal force on the propeller (Fig. 8.13c), as expected from the aforementioned validation study. However, the normal-force discrepancy is slightly larger in this case, being under-predicted by 20% to 30% at high and low thrust settings, respectively. This can be attributed to the forces on the spinner (which are not included in the numerical model),

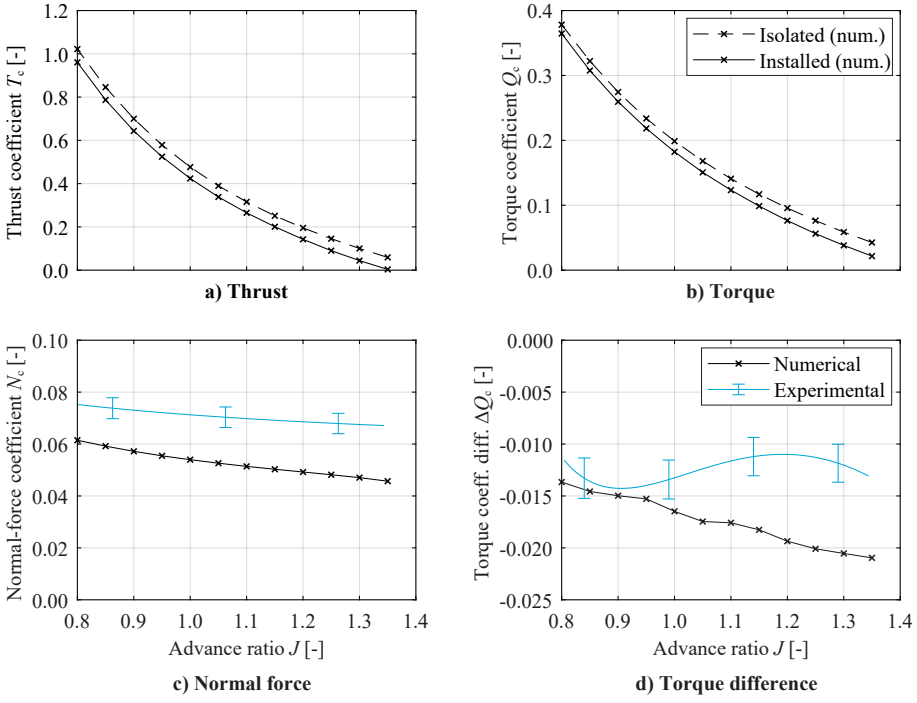

Figure 8.13: Isolated and installed ($\alpha = 2^o$) propeller performance curves obtained from the numerical method, compared to experimental results.

an incorrect modeling of the nacelle, or to an under-prediction of the wing-induced flow angle at the propeller location α_P. For the present configuration, an under-estimation of the normal force contributes to conservative results regarding the overall system performance.

To verify the estimated changes in wing performance, Fig. 8.14 presents the pressure distributions obtained on the wing at $y/R = -0.7$, for two operating conditions. In both cases (Figs. 8.14a and 8.14b), the C_p distributions are comparable to the ones obtained in the experiment (Fig. 8.9), though with higher suction peaks in both the propeller-on and propeller-off cases. This difference is attributed to tip and root effects on the wing in the experiment, as well as to the presence of the nacelles and support sting. However, Fig. 8.14c shows that differences between propeller-on and propeller-off conditions are comparable at low angles of attack and thrust settings. Therefore, the numerical method can capture the changes in the C_p distribution with reasonable accuracy for such conditions. However, the agreement deteriorates at higher angles of attack and thrust settings, as shown in Fig. 8.14d. In this case, the numerical model predicts a more downstream flow separation than the one recorded in the experiment, leading to a higher pressure near the propeller location ($x/c = 0.8$). As expected from Ch. 7, the flow separation trig-

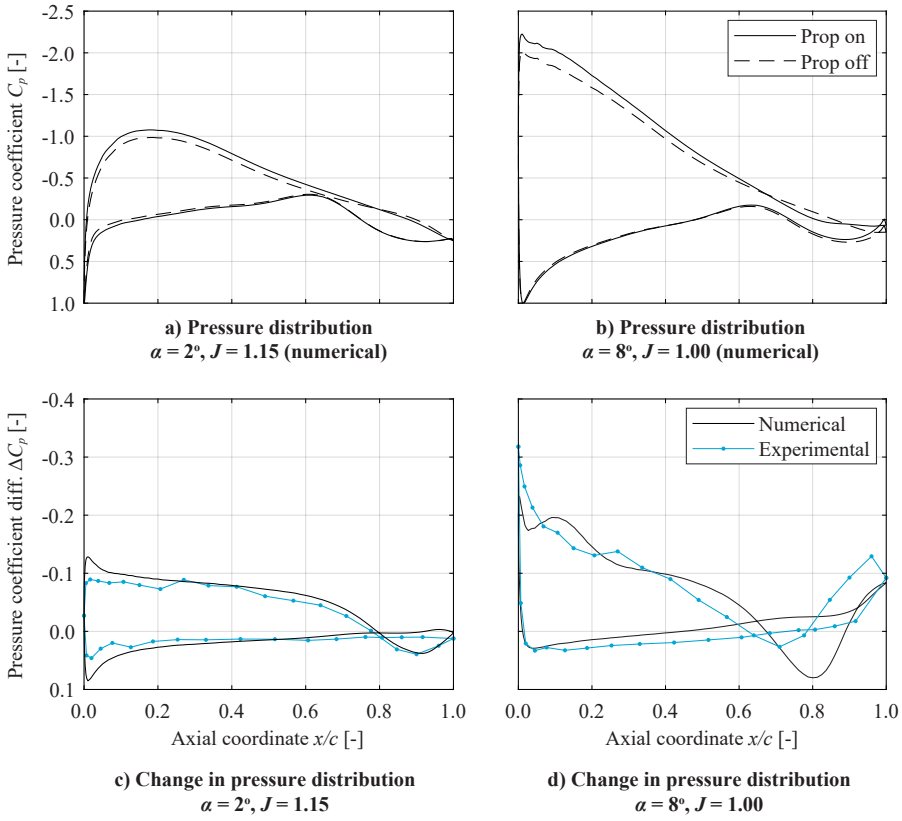

Figure 8.14: Pressure-coefficient distributions on the wing ($y/R = -0.7$). The experimental ΔC_p distributions correspond to the pressure distributions shown in Fig. 8.9b and 8.9d.

gered by the propeller-induced pressure gradients cannot be captured accurately with a 2D panel method such as XFOIL. Therefore, the numerical model is inaccurate if flow separation occurs beneath the propeller.

Figure 8.15 shows the sectional lift and pressure-drag distributions obtained by integrating the C_p distributions. Again, although the actual values of lift and drag differ from the experiment (Fig 8.10), the change in wing loading due to the propeller is accurately captured by the numerical model for $\alpha = 2^o$, $J = 1.15$. A slight deviation in pressure drag can be observed at $y/R = \pm 0.7$, where the numerical model does not capture the local reduction in pressure drag encountered in the experimental data.

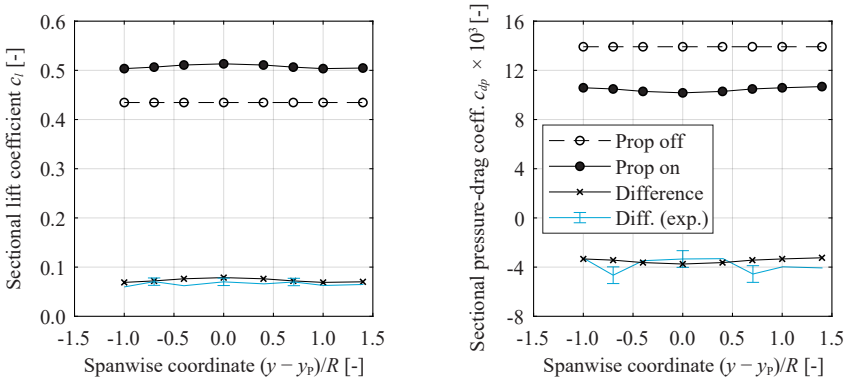

a) Lift distribution **b) Pressure drag distribution**

Figure 8.15: Spanwise loading distributions along the wing, for $\alpha = 2^o$, $J = 1.15$. Experimental "delta" replicated from Fig. 8.10 for reference.

Finally, Fig. 8.16 analyzes the change in c_l and c_d for a range of operating conditions. The lift polars of Fig. 8.16a show a similar offset to the ones of the experiment (Fig. 8.11), although in this case the offset reduces at higher angles of attack. This suggests that the de-cambering effect of the propeller on the wing boundary layer may be over-estimated in the numerical model. However, a more pronounced difference can be observed in the drag coefficient (Fig. 8.16b), which shows significantly lower drag values than in the experiment—particularly at high angles of attack and high thrust settings. This is a consequence of the increased suction peak and delayed flow separation predicted by the numerical model, as reflected in the pressure distributions. Nonetheless, the numerical method is intended to estimate the changes in performance at low or moderate angles of attack and thrust settings (cruise conditions). These changes in performance are shown in Figs. 8.16c and 8.16d. A comparison of the lift "deltas" shows that the numerical model predicts the lift enhancement reasonably well for $J = 1.15$, $\alpha > 2^o$. At lower angles of attack, the lift increase is over-estimated, as seen in Fig. 8.16c. This may be a result of the straight slipstream-tube approximation, although additional investigations would be required to confirm this. In any case, the corresponding c_l are lower than the ones that would typically be encountered throughout a flight profile ($c_l < 0.4$). At a higher thrust setting ($J = 1.00$, $T_c \approx 0.4$), the numerical model under-estimates the lift enhancement for $\alpha > 0^o$. This is a consequence of the aforementioned challenges with respect to pre-

dicting the boundary-layer evolution under strong adverse pressure gradients. Therefore, in these conditions, which are more representative of a climb phase, the model is less accurate, and provides conservative results in terms of lift.

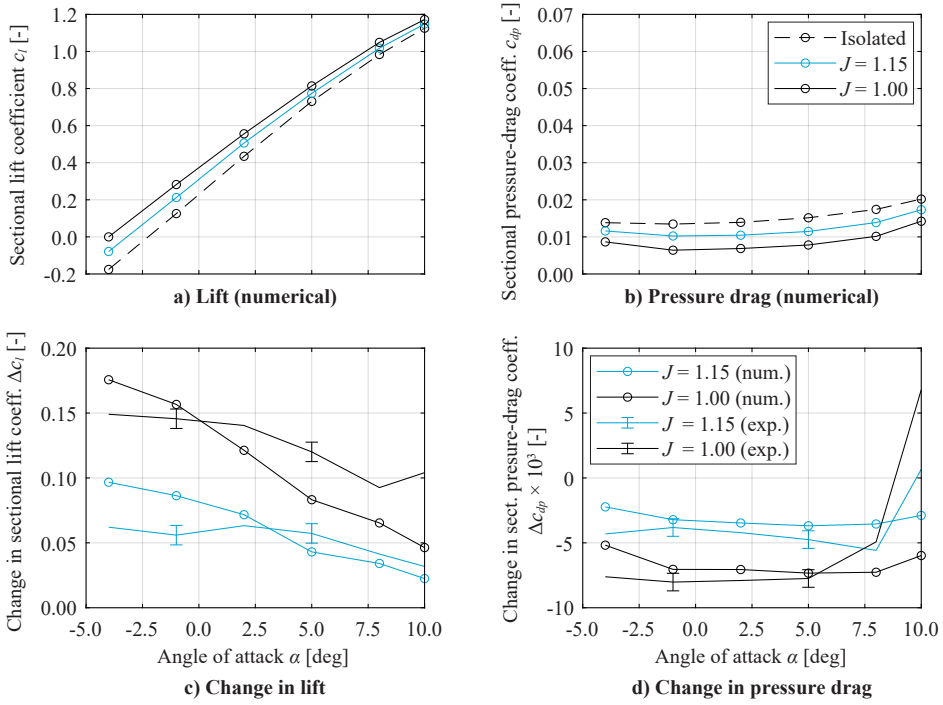

Figure 8.16: Sectional lift and pressure-drag polars at $y/R = -0.7$.

The changes in pressure drag are compared in Fig. 8.16d. This figure shows that the model under-estimates the drag reduction due to OTWDP for low to moderate angles of attack, in both low and high thrust settings. At high angles of attack, the model over-estimates the drag reduction, because in that case the trailing-edge flow separation that occurs in the experiment is not present to the same extent in the simulations. For the friction drag, no data is available for a direct comparison. However, given that it is estimated by a proven method (XFOIL), no significant errors are expected as long as the flow remains attached over the entire airfoil.

8.3.3. LIMITATIONS OF THE NUMERICAL METHOD

Based on this validation study, it appears that the numerical model provides acceptable but conservative results in terms of lift enhancement, drag reduction, and propeller normal-force increase, for typical cruise conditions ($T_c < 0.2$, $c_l \sim 0.5$). In these conditions, the predicted Δc_l and Δc_d values differ from the experimental data by approximately ± 0.02 and ± 0.001, respectively. The trends of the changes in lift, drag, and sectional pressure distributions also match the experiment and are in line with the observations of earlier studies [68, 80, 231]. Moreover, previous analyses [90] suggest that the

method may slightly over-estimate the changes in propeller efficiency, presenting deviations of the order of $\Delta\eta_P \pm 0.01$. The validation also shows that the model does not produce accurate results if flow separation occurs beneath the propellers.

These conclusions can be extrapolated to other geometries and operating conditions, with several limitations. Firstly, the operating conditions must be such that the flow remains attached. This imposes a limitation especially on the angle of attack and thrust-coefficient range, although the exact limit of attached flow depends on numerous factors. Given that the sensitivity of the boundary layer to the adverse pressure gradients induced by the propeller reduces with Reynolds number, the model can be used at higher Reynolds numbers, but should not be used at lower Reynolds numbers than the ones used for the validation study ($Re_c = 6 \cdot 10^5$). Higher subsonic Mach numbers can also be evaluated, though the compressibility correction loses accuracy as the transonic regime is approached. Moreover, the propeller model is not sensitive to changes in the Mach number, and is therefore likely to provide unreliable results in those conditions. Regarding the geometry of the system, the model is expected to be able to predict the interaction for a wide range of D_P/c values, since the velocities induced by the propeller on the wing and vice versa are predominantly caused by inviscid effects. The model is not accurate for cases where the size of the propeller is of the same order as the thickness of the wing boundary layer ($D_P/c \ll 1$). Furthermore, due to the violation of the assumption of irrotational flow at the slipstream edge, the accuracy of the solution cannot be guaranteed for lower tip clearances than the one used in the validation study. Thus, the combination of incidence angle, axial position, and tip clearance, should be such that the slipstream maintains a separation from the wing surface of at least $\varepsilon/R > 0.05$. Finally, the axial position of the propeller should not be close to the leading edge ($x_P > 0.2$), since the leading edge is not modified in the inverse-design process.

The numerical method should not be applied for geometries or operating conditions that exceed these bounds. It is particularly important to emphasize in this regard that the model does not include the effect of the duct. However, the validation study shows that, within these bounds, the method is capable of estimating the changes in wing and propeller performance with an accuracy that is appropriate of low-order methods for conceptual design purposes. Therefore, it is used in the following section to analyze the performance of the wing and propeller for different operating conditions and geometrical parameters of the OTWDP system.

8.4. EFFECT OF GEOMETRICAL DESIGN PARAMETERS & OPERATING CONDITIONS

Now that the verification and validation of the numerical method has been performed and its limitations are known, it is used in this section to understand how the performance of an OTWDP system is affected by various design parameters and operating conditions. For this, the results of a parameter sweep are briefly discussed in Sec. 8.4.1. A dedicated discussion is held for the effect of blade pitch in Sec. 8.4.2. Finally, the overall efficiency and force breakdown of the OTWDP system is compared to an isolated wing and propeller in Sec. 8.4.3, to provide an indication of the aero-propulsive efficiency benefits that can be obtained at subsystem level using OTWDP.

8.4.1. PARAMETER SWEEPS

A parameter sweep was performed to assess which operating conditions and geometrical parameters have a significant effect on the performance of the system, to determine how they affect the performance of the system, and to verify whether the trends match those of earlier studies. The geometrical parameters of the experiment were used as baseline, and the analyses were performed by varying one parameter at a time, while maintaining everything else constant. In other words, the sweeps were not performed at constant lift, thrust, or shaft power. This approach was selected to be able to trace the effect of each parameter, but can cause misleading conclusions regarding the performance changes due to the interaction, as shown by Veldhuis [68]. For this reason, only the most relevant findings are qualitatively summarized below. Additional information regarding the approach and the results obtained can be found in Appendix G.

- Axial propeller position, x_P: the lift enhancement is found to be maximum for a propeller placed around 85% chord. This is in line with the findings of Veldhuis [68], although other authors find a maximum lift increase for propellers placed at the trailing edge [80, 231]. The drag reduction is maximum for a propeller placed ahead of the mid-chord, and the propulsive-efficiency penalty is minimum for a propeller placed at the trailing edge, as observed in all the earlier studies. The optimum axial position depends on various factors, such as the thrust setting, or the relative contribution of lift, drag, and thrust of the OTWDP system to the lift, drag, and thrust of the complete aicraft.
- Propeller incidence angle, i_P: a slight nose-down incidence angle can be beneficial to reduce drag and increase the propulsive efficiency. The propulsive-efficiency gain is a result of an increased thrust component in the direction of flight and an angle-of-attack effect, since the flow direction above the wing does not coincide with the direction of flight.
- Diameter-to-chord ratio, D_P/c: larger diameter-to-chord ratios enhance the lift benefit, propeller normal-force contribution, and drag reduction. For the baseline axial position ($x_P/c = 0.8$), the effect on the propulsive efficiency is small.
- Tip clearance, ε: as the distance to the wing is increased, the lift benefit and the propulsive-efficiency penalty are reduced. This is line with the findings of Johnson and White [63], Veldhuis [68], and Müller et al. [69]. For the selected axial position ($x_P/c = 0.8$), the effect on drag is small.
- Separation distance, d: as the separation between propellers increases, the average lift-to-drag ratio of the wing segment associated to each propeller is reduced. This reduction in L/D is larger than the propeller-efficiency penalties due to propeller-propeller interaction observed in Ch. 6, and therefore, for a given fraction of wing span covered by the OTWDP system, a reduced separation distance is beneficial from an aero-propulsive perspective.
- Reynolds number, Re_c: the L/D benefits are higher at higher Reynolds numbers, since the de-cambering effect of the propeller on the wing boundary layer is reduced. The changes in lift-to-drag ratio are also less sensitive to Mach number at higher Reynolds numbers.

8.4.2. Impact of Blade Pitch Setting

The blade-pitch setting plays an important role in the propulsive-efficiency penalty of OTW propellers, particularly in off-design conditions. Therefore, a dedicated discussion is required for the effect of blade pitch on OTW propeller performance, especially since it has neither been addressed in previous chapters nor—to the best of the author's knowledge—in the existing literature. To this end, Fig. 8.17 presents the axial force, torque, and propulsive efficiency (in the direction of flight; see Eq. 2.2) of the propeller for two blade-pitch angles. The figure shows that, for this propeller position, its thrust, torque, and efficiency are reduced in installed conditions, for both blade-pitch settings. When installing the propeller over the wing while maintaining a constant advance ratio, the propulsive efficiency drops from point A to point B, in Figs. 8.17c and 8.17d. However, this is not a fair comparison. Instead, for a fixed blade pitch, a comparison at constant thrust is more representative. In this case, if the isolated propeller were operating at the advance ratio corresponding to maximum efficiency (point A), the propulsive-efficiency penalty (A→C) would be less than in the case of an installation at constant advance ratio. In other words, the propulsive-efficiency penalties obtained in the parameter sweeps of the previous section are conservative, since in practice the rotational speed of the propeller would have to increase to compensate the local increase in inflow velocity, and the corresponding propulsive-efficiency penalty would be lower (see also Ref. [68]).

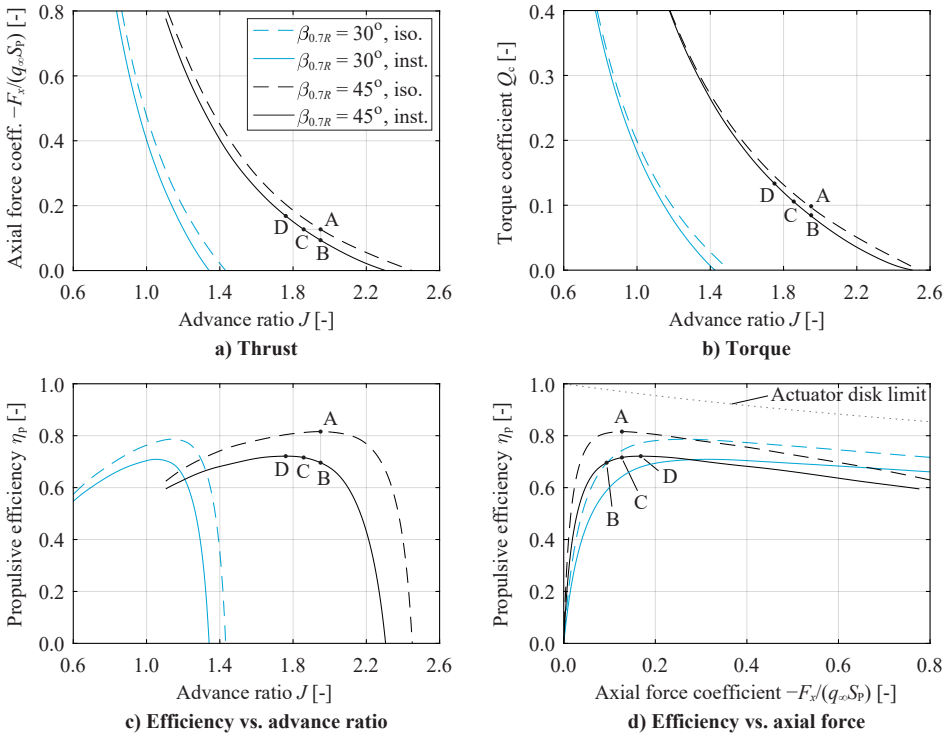

Figure 8.17: Comparison of propeller performance parameters in isolated and installed conditions, for two different blade-pitch settings.

This propulsive-efficiency penalty is further reduced if a variable-pitch propeller is considered. In that case, the reduction in propeller efficiency from point A to point D is more representative, since the blade pitch would be adjusted to always operate at the maximum efficiency for a given thrust setting. Although point D does not correspond to the same thrust setting as point A, a slight adjustment in the blade pitch to ensure equal thrust would lead to comparable propulsive-efficiency values. In fact, it can be shown that the ratio between the maximum efficiency of the isolated propeller and the maximum efficiency of the installed propeller, $\eta_{\mathrm{pA}}/\eta_{\mathrm{pD}}$, is practically independent of the blade-pitch setting [283]. Therefore, for a variable-pitch propeller, the propulsive-efficiency penalty can be computed for a given blade-pitch setting, and scaled to all other thrust settings, assuming that the propeller always operates at the optimum blade-pitch. From a design perspective, this implies that the efficiency of an installed variable-pitch propeller can, in first approximation, be computed assuming the ideal efficiency of an actuator disk as a function of the thrust coefficient—indicated with a dotted line in Fig. 8.17d—and correcting for two effects. First, a correction factor k_{P} has to be applied to account for the viscous and swirl losses of the isolated propeller (see Eq. 2.13). The efficiency should then be multiplied by a second correction factor, to account for the installation effects on the propeller. This second factor (i.e., the ratio $\eta_{\mathrm{p}}/\eta_{\mathrm{p,iso}}$) can be estimated for a given blade pitch and applied over the full range of thrust coefficients, if the effect of variations in Re and M with advance ratio are neglected. The numerical method developed in this chapter is used to estimate this factor in the aero-propulsive model described in Appendix C.3.

8.4.3. OVERALL PERFORMANCE COMPARISON

To conclude the performance analyses, Fig. 8.18 compares the overall performance breakdown of the baseline OTW configuration and a "modified" configuration to the isolated wing and propeller. The design-parameter values of the modified configuration do not represent the optimum combination of OTWDP parameters, but are merely selected to discuss what occurs if small propellers are placed near the trailing edge—a configuration that is encountered in the aircraft design studies of Ch. 10. For this, propellers of $D_{\mathrm{P}}/c = 0.2$ are positioned at 95% chord, with the axis aligned with the freestream direction. Furthermore, additional propellers are simulated on either side, to obtain the performance characteristics of an OTWDP system with $N_{\mathrm{P}} \gg 1$ propellers. Moreover, the distance between propellers d/R is increased to limit the potential acoustic or aerodynamic penalties due to the propeller–propeller interaction observed in Sec. 6.3. For the comparison, the advance ratio and angle of attack of each configuration are adjusted to maintain a constant total vertical force on the system equal to a lift coefficient of 0.5, as well as a constant axial force coefficient on the propeller of $F_X/(q_\infty S_{\mathrm{P}}) = 0.1$ ($\approx T_{\mathrm{c}}$). These settings are representative of the cruise conditions of a typical twin-turboprop aircraft (see Appendix G). The corresponding operating conditions and geometrical parameters are given in Table 8.2.

Figure 8.18a illustrates that the friction drag is practically constant among the different cases, which is expected since the friction drag of a given airfoil is not strongly dependent on the angle of attack [244]. The same was reported in the experiments of Johnson and White [63]. Moreover, in the baseline case, the propeller-induced veloci-

Table 8.2: Overview of design parameters and operating conditions used in the performance comparison. For all cases, $C_L = 0.5$ and $F_X/(q_\infty S_P) = 0.1$.

Parameter	**Isolated**	**Config. 1 (baseline)**	**Config. 2 (modified)**
Angle of attack α [deg]	1.69[a]/0[b]	0.87	1.62
Advance ratio J [-]	2.035	1.944	2.109
Reynolds number Re [-]	10^7	10^7	10^7
Mach number M [-]	0.4	0.4	0.4
Blade pitch $\beta_{0.7R}$ [deg]	45	45	45
Axial position x_P/c [-]	-	0.80	0.95
Incidence angle i_P [deg]	-	10	−1.63
Diameter-to-chord ratio D_P/c [-]	0.67	0.67	0.20
Tip clearance ε/c [-]	-	0.017	0.017
Number of props. modeled N_P [-]	1	3	7
Propeller separation d/R [-]	-	0.044	0.100

[a]Isolated wing
[b]Isolated propeller

ties reduce the wing pressure drag to nearly zero. In all cases, a net excess thrust can be observed, since the thrust coefficient is representative of the disk loading that would be required on a complete aircraft to offset the aircraft drag. For the modified configuration, the thrust contribution (normalized with the wing reference area) is significantly lower. Therefore, additional propellers would be needed along the wing to produce the same total thrust. A comparison of the vertical force components (Fig. 8.18b) shows that, in the baseline configuration, the propeller thrust and normal force both contribute to lift, due to the incidence angle of the propeller. For the modified configuration, the normal force counteracts lift since, in this case, the local flow angle relative to the propeller axis α_P is negative.

In the baseline configuration, the lift-to-drag ratio of the wing is increased by 45% with respect to the isolated wing, if the contribution of the propeller to system lift is considered. This benefit would be a few per cent higher if more than 3 propellers were modeled (see Appendix G). However, for this propeller location, the propulsive efficiency η_p is reduced by approximately 12%. The L/D benefit accompanied by a strong propulsive-efficiency drop is in line with the studies of Veldhuis [68] and Müller et al. [69]. In the modified configuration, on the other hand, the propulsive efficiency is increased by 14% due to the flow deceleration near the trailing edge and a local angle-of-attack effect, although the effective L/D is decreased by 1%. The increase in propulsive efficiency observed in the investigations of Johnson and White [63], which may seem contradictory to the findings of others, is likely caused by a similar effect. This shows that an OTW propulsion system can increase the aero-propulsive efficiency through an increase in the wing lift-to-drag ratio, *or* through an increase in the propulsive efficiency.

Based on the comparison of Fig. 8.18, it appears that the baseline configuration is the best alternative of the three, with a 29% increase in aero-propulsive efficiency, $\eta_p \cdot (L/D)$, relative to the isolated components. However, this figure can be misleading, since the

L/D values correspond to the wing segment covered by a propeller, and do not include the drag of the complete aircraft. If the OTWDP system covers part of the wing, and the lift and drag on the rest of the wing, fuselage, and other elements are included, the net L/D benefit can easily be outweighed by the propulsive-efficiency penalty. Therefore, the modified configuration appears to constitute a more reasonable design for transport aircraft. Nonetheless, in that case, the same applies to the propulsive efficiency: if the aircraft presents multiple propulsion systems, then the efficiency benefit only affects the fraction of the total thrust which is generated by the OTWDP system. This implies that the optimum design of the OTWDP system cannot be determined by looking at the subsystem alone, but has to be assessed at aircraft level.

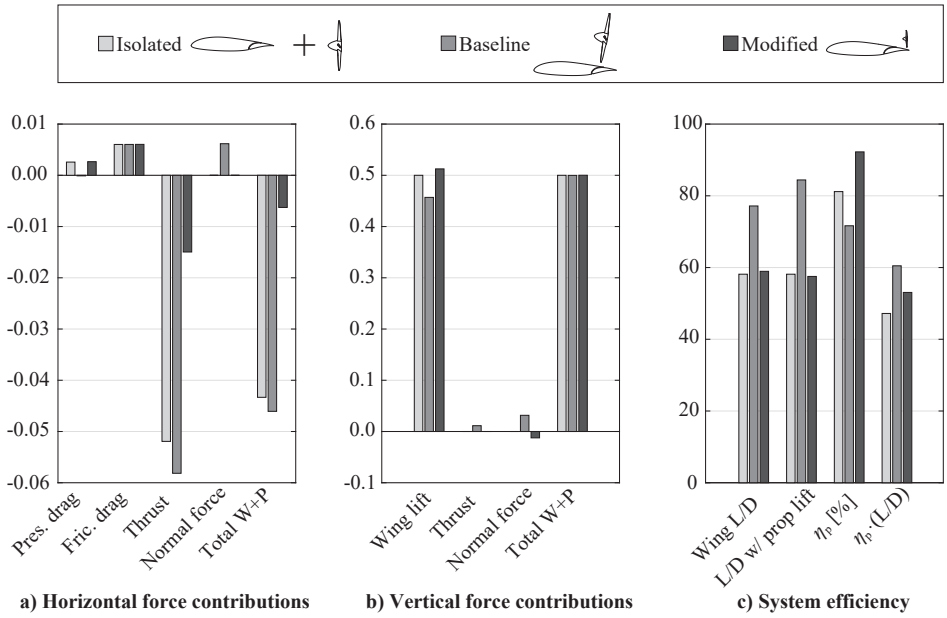

Figure 8.18: Comparison of system forces for the isolated and installed propeller/wing configurations. All forces non-dimensionalized with freestream dynamic pressure and planform area of the wing segment covered by a single propeller, $S_{\text{ref}} = c \cdot (D_P + d)$.

8.5. CONCLUDING REMARKS

The results of this chapter indicate that the aerodynamic benefits of OTWDP can be significant—at least at subsystem level. In the experimental setup, a wing L/D increase of at least 20% was observed, for a low thrust setting and with 50% of the wing span covered by propellers of diameter-to-chord ratio $D_P/c = 0.68$. The numerical model estimates that, for this configuration in cruise conditions, the average sectional lift-to-drag ratio beneath the propeller increases by 45%, at the expense of a 12% reduction in propulsive efficiency. For a small propeller placed near the trailing edge, a 14% increase in propulsive efficiency is predicted, without a significant change in L/D. The benefits

increase considerably with thrust setting, which can relief the take-off constraint of the aircraft and allow for a smaller powertrain size. Moreover, these benefits are relative to an isolated wing and propeller. Additional benefits may be considered when comparing the OTWDP system to alternative propulsion systems. For example, compared to a LEDP configuration, OTWDP has the advantage of not generating strong spanwise lift gradients, and thus having a much smaller effect on the lift-induced drag.

However, these values are estimated with a simplified geometrical description of the system. Although the main effects on wing and propeller performance can be explained with a simplified 2D analysis, there are several other factors which are neglected in the present analysis. These include contributions like the duct, nacelles, pylons, adjacent propellers, and the trailing vorticity due to spanwise lift gradients. The results so far indicate that the effect of the last two on overall performance is small. However, the same cannot be said regarding the duct. The parameter sweeps have shown that, in general, OTW configurations which lead to a significant L/D increase (large propellers placed ahead of the mid-chord) come with a strong propeller-efficiency penalty, while configurations which enhance the propeller efficiency (small propellers placed near the trailing edge) do not have an appreciable benefit in terms of L/D. Moreover, although a duct may lead to a decrease in system drag at high thrust settings (see Sec. 6.2), in cruise conditions it is likely to lead to an increase in drag due to the increased wetted area [291]. This indicates that the use of ducts is only beneficial to reduce the non-uniform inflow to propellers placed far from the trailing edge. Likewise, the effect of the nacelles and pylons has not been assessed. While the pylons would increase the wetted area of the system and lead to additional corner-flow effects, they may also act as stator vanes and enhance the propulsive efficiency at high thrust settings due to the swirl-recovery effect [240]. Since the overall effects are highly dependent on the operating conditions and shape of the components, further investigation is required to quantify how they affect the performance of the system for realistic geometries.

Finally, for a given geometry, the validation study of this chapter showed that the deviations of the numerical predictions from the experimental values are of the order of $\Delta c_l \pm 0.02$, $\Delta c_d \pm 0.001$, and $\Delta \eta_\mathrm{p} \pm 0.01$. While these deviations show that the model is applicable for preliminary estimations in the conceptual sizing phase, the effect of the uncertainty in the aerodynamic model should be analyzed. Furthermore, the question remains whether the L/D benefit is significant when including the forces acting on the rest of the airframe. Likewise, a propeller-efficiency benefit obtained from the OTWDP installation may be less significant at vehicle level, if multiple propulsion systems are considered. The variety of factors and unknowns involved evidences that a design-space exploration study has to be performed at the start of the aircraft design process, to investigate which OTW system design is most beneficial for the particular mission. In this trade-off process, acoustic considerations may also play an important role. Consequently, the following chapters aim to explore the design space from an aircraft perspective, to determine how the aerodynamic benefits at subsystem level affect the overall aerodynamic performance of the aircraft, and to investigate whether these benefits are sufficient to offset the weight penalty of the hybrid-electric powertrain.

Part IV

Hybrid-Electric Aircraft with Over-the-Wing Distributed Propulsion

9

DESIGN-SPACE EXPLORATION

The previous parts of this dissertation have looked into two key technologies: hybrid-electric propulsion (HEP), and over-the-wing distributed propulsion (OTWDP). Several key benefits, drawbacks, and challenges have been identified, but neither these investigations nor the ones encountered in literature have been able to properly assess a combination of these two technologies at aircraft level. Given the wide range of design choices involved, it is unclear for what sort of aircraft these technologies provide the greatest benefit, if any, or what a "good" OTWDP system would look like. Therefore, the purpose of this chapter is to explore the design space and gain an understanding of how different design parameters, assumptions, and requirements affect the take-off mass and energy efficiency of aircraft featuring hybrid-electric OTWDP.

The baseline configuration and sizing approach used for this study are described in Sec. 9.1. The design-space exploration is then performed in two steps. Firstly, a "direct" approach is taken in Sec. 9.2, where a sensitivity study is conducted to investigate how a determined input parameter $\mathbb{X}$ (e.g., battery specific energy) affects a figure of merit $\mathbb{Y}$ (e.g., energy consumption) of the aircraft. Based on this study, it becomes evident that, for passenger transport aircraft, hybrid-electric OTWDP does not lead to a benefit at aircraft level unless the propulsion system is designed to provide a significant aero-propulsive benefit. Thus, secondly, an "inverse" approach is taken in Sec. 9.3, to estimate the aero-propulsive benefit required in order to obtain a determined improvement in the figure of merit $\mathbb{Y}$. In other words, this reverse-engineering approach aims to answer questions such as: what are the technology-level requirements for an X% reduction in energy consumption, when compared to a conventional aircraft configuration? Or, for which mission are these technology requirements the lowest, i.e., for which mission will the OTWDP aircraft be competitive the "soonest"? Hence, the direct approach provides an understanding of the influence of the individual input variables, while the inverse approach provides a series of values for these input variables, that must be attained in order to achieve a determined performance gain at aircraft level.

Parts of this Chapter have been published in Refs. [292, 293].

9.1. SETUP

A brief overview of the approach taken in the design-space-exploration study is provided in this section. The aircraft configuration described in Sec. 9.1.1 is sized for different input and output parameters, as outlined in Sec. 9.1.2. Sections 9.1.3 and 9.1.4 then present how the aerodynamic characteristics of the aircraft are modeled in the "direct" and "inverse" approaches, respectively.

9.1.1. AIRCRAFT CONFIGURATION

For the design-space exploration, an initial aircraft configuration is selected based on several qualitative design considerations. The baseline mission requirements correspond to those of a 70-passenger regional turboprop: the aircraft must have a harmonic range of R = 850 nmi with a 7500 kg payload, and a baseline cruise altitude and Mach number of 17,000 ft and 0.41, respectively. The HEP concept, which aims for an entry-into-service year of 2035, is presented in Fig. 9.1, along with the conventional aircraft configuration used as reference. The hybrid-electric aircraft presents two distinct propulsion systems.

The first is a propulsive empennage (PE), which acts as the main source of thrust and is responsible for the control and stability of the aircraft [294]. The second is an over-the-wing distributed-propulsion system, which is attached to the flap mechanism in order to provide thrust vectoring in low-speed conditions. This propulsive-empennage arrangement is selected as a generic example of a hypothetical OTWDP aircraft where

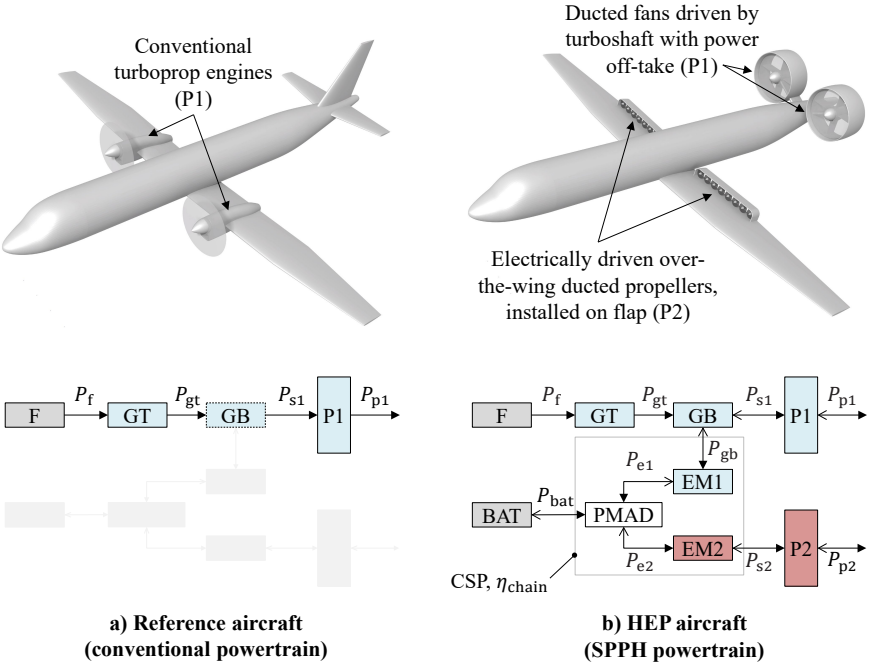

Figure 9.1: Notional representation of the reference (left) and HEP (right) aircraft concepts, indicating the external layout of the propulsion systems (top) and associated powertrain architecture (bottom).

the primary powertrain system is located at the rear of the fuselage to leave space for the OTWDP system on the wing. Note that the Class-I sizing process employed (see Sec. 9.1.2) does not consider empennage design, and therefore the findings of this study are equally applicable for other aft-mounted propeller arrangements such as tail- or pylon-mounted propeller configurations. Moreover, although previous design studies of the propulsive-empennage concept indicate that this propulsion system leads to a slightly higher maximum take-off mass (MTOM) than conventional turboprop configurations due to an increased center-of-gravity excursion [294], the combination of this system with over-the-wing (OTW) DP entails multiple benefits. Firstly, the placement and shielding of the propulsors may lead to a reduction in both cabin noise and flyover noise [74]. Secondly, the propulsion-airframe integration challenges in terms of ground clearance are removed, and thus a shorter landing gear is possible. Thirdly, since the total thrust is divided over two propulsion systems, the disk loading of each system can be reduced, effectively leading to an increase in bypass ratio [295] which increases the average propulsive efficiency. And, finally, given that only a fraction of the total power has to be diverted to the DP system, the weight of the electrical powertrain components is limited. In this sense, a fully serial architecture leads to significant weight penalties (see Ch. 5). The concept in Fig. 9.1b, on the other hand, presents a series/parallel partial-hybrid architecture. However, given that the SPPH powertrain is the most generic architecture, it allows the designer to analyze whether a small amount of batteries is beneficial and, if not, then the optimal result will automatically lead to a PTE architecture.

9.1.2. SIZING PROCEDURE

The top-level weight breakdown, installed power, and wing area of the aircraft are computed using the method described in Ch. 3. This section describes some of the assumptions made in order to represent the aircraft from a Class-I perspective. In the sensitivity study (Sec. 9.2), the changes in lift, drag, and propulsive efficiency due to OTWDP are approximated using the model described in Sec. 9.1.3. For the propulsive empennage and conventional propellers they are neglected, since the aerodynamic coupling is relatively weak. Moreover, both the reference aircraft and the HEP variant are sized for all mission requirements and technology assumptions, in order to provide a fair comparison. The baseline aircraft requirements and design parameters are provided in Appendix D.2. Several of these parameters are then varied and the sizing routine is applied successively to provide contour maps of the figures-of-merit. A subset of the evaluations are performed with both the reference and HEP aircraft each flying at the optimum cruise altitude. This is achieved by incorporating an external loop which evaluates different values of the independent variable h_{cr} and selects the one corresponding to minimum energy consumption throughout the nominal mission.

A. POWERTRAIN REPRESENTATION

In order to determine the complete behavior of the SPPH powertrain architecture, three power-control parameters must be specified: the gas turbine throttle (ξ_{GT}), the supplied power ratio (Φ), and the shaft power ratio (φ). It is important to recall that these three power-control parameters are time-dependent variables, whose profile throughout the mission must be chosen by the designer. The selected values have a direct impact on

the aircraft size, since they affect both the constraints in the power-loading diagram, and the energy consumption estimated during the mission analysis. In some mission segments, the flight condition is fully specified, and thus one of the parameters results from the propulsive power requirement (usually ξ_{GT}; see Appendix A). The degree-of-hybridization (of energy) of the aircraft DOH $= E_{bat}/(E_{bat} + E_f)$, meanwhile, is a scalar result of the sizing process. In the first part of the design-space exploration (Sec. 9.2), the three control parameters are assumed to vary linearly throughout each mission segment. Their evolution is therefore defined by their value at the start and end of each mission segment, e.g. $[\Phi_1, \Phi_2]$. After this initial exploration, in Sec. 9.3 the shaft power ratio is assumed to be constant throughout the entire mission to reduce the number of independent variables. It is evident that for $\varphi = 0$ the power transmitted by—and thus the weight of—the electrical components is zero, and therefore the conventional powertrain is the lightest. However, per definition this limit case also corresponds to zero aero-propulsive benefit, since there is no enhanced propulsion–airframe integration.

The powertrain description is further simplified by grouping all electrical components into a single "black box" which represents the electrical drivetrain and is characterized by two parameters, namely a *chain efficiency*, η_{chain}, and a *combined specific power* (CSP). These parameters are useful to interpret the results for (partial-) turboelectric configurations, in which case there are no batteries present (see Fig. 9.1). The former is defined as the ratio between the output power and input power of the electrical drivetrain, that is, it represents the combined transmission efficiency of all electrical components:

$$\eta_{chain} = \frac{P_{s2}}{P_{GB}} = \prod_{i=1}^{k} \eta_i, \tag{9.1}$$

where the index i covers all the k electrical components connected in series, each of which presents a determined transmission efficiency η_i. The combined specific power, meanwhile, is defined as the power introduced to the electrical drivetrain divided by the total mass of all components in said drivetrain, and is typically expressed in kW/kg:

$$\text{CSP} = \frac{P_{GB}}{\sum_{i=1}^{n} m_i}, \tag{9.2}$$

where m is the mass of each component in the electrical drivetrain and n the number of components. If the losses in the drivetrain are small ($\eta_{chain} \approx 1$), then the combined specific power can be computed based on the specific power (SP) of each component as:

$$\text{CSP} \approx \sum_{i=1}^{n} \frac{1}{(1/\text{SP}_i)}. \tag{9.3}$$

Although the "black box" simplification makes this approach unsuitable for detailed studies, it has several advantages. Firstly, it provides a more simplified, top-level understanding of the effect of powertrain technology levels, since it does not require information regarding every component in the powertrain. Secondly, the number of dimensions of the design space is significantly reduced, given that the electrical drivetrain is now parametrized by just two variables. Thirdly, the findings of this study are therefore independent of the design of the electrical system (AC vs. DC transmission, active vs. passive

cooling, redundant wiring, etcetera). The relation between the individual properties of each component and the global properties, CSP and η_{chain}, can be established ad-hoc on a case-to-case basis.

The baseline technology assumptions used here are based on those of Ch. 5. The values of specific energy and specific power assumed for the batteries at pack level are commonly used in design studies for the 2035 timeframe, even though these values are considered optimistic given that they approach the maximum theoretical values attainable with lithium-ion batteries at cell level [117]. For the batteries, a minimum state-of-charge of 20% is maintained. The values of specific power and transmission efficiency assumed for the electrical machines and inverters/rectifiers are based on the state-of-the-art research goals presented in Ref. [119]. The weight and efficiency contributions of the inverters/rectifiers are combined with those of the electrical machines to form an equivalent "EM". Since both the thermal management system and additional elements of the power management and distribution (PMAD) system can constitute a significant weight contribution (see e.g. Refs. [79, 114]), the weight of the electrical systems estimated by the design method—which only includes electromotors, generators, inverters and rectifiers—is increased by 30%. This generic weight penalty is assumed due to a lack of information in the preliminary sizing phase for an accurate estimation of the weight of components such as coolers, transformers, or cables. For this reason, Sec. 9.2.4 presents a sensitivity analysis of the assumed component properties. Finally, the thermal efficiency of the gas turbine is assumed to be 0.34 for the reference aircraft. An additional 20% improvement is hypothesized for the 2035 timeframe. Given that the thermal efficiency is kept constant throughout the sizing process, the potential benefit of improved gas turbine performance due to electrical assistance in off-design conditions is not accounted for. The weight of the gas turbines is estimated using the empirical correlation of Ref. [92].

Table 9.1: Powertrain component properties. Values assumed for 2035 timeframe, unless otherwise stated.

Parameter	**Value**
Battery specific energy at pack level e_{bat} [Wh/kg]	500
Battery specific power at pack level SP_{bat} [kW/kg]	1
Specific power of electrical machines [kW/kg]	13
Specific power of converters [kW/kg]	19
Weight penalty for PMAD and cooling elements	30%
Minimum battery state-of-charge	20%
Gas turbine efficiency η_{GT} (current) [-]	0.34
Gas turbine efficiency η_{GT} (2035) [-]	0.40
Electrical machine efficiency [-]	0.97
Converter efficiency [-]	0.99
PMAD efficiency η_{PMAD} [-]	0.99
Gearbox efficiency η_{GB} [-]	0.96

For the "inverse" approach, Table 9.2 presents the chain efficiency and CSP computed for the three hypothetical technology scenarios discussed in Sec. 9.3.2. The mid-

term scenario corresponds to the baseline values of Table 9.1. Again, the electrical drivetrain of the powertrain is assumed to be comprised of two sets of electrical machines (generators and motors) and two sets of power converters (rectifiers and inverters), to which an additional 30% weight penalty is added to account for additional elements of the power distribution and thermal management system.

Table 9.2: Specific power and transmission efficiency of the components and the complete electrical drivetrain, for three hypothetical technology scenarios.

Scenario	Electrical machines		Power converters		PMAD weight	Complete chain	
	[kW/kg]	η [-]	[kW/kg]	η [-]	penalty	CSP [kW/kg]	η_{chain} [-]
Near-term	9	0.92	13	0.97	30%	2	0.80
Mid-term	13	0.96	19	0.99	30%	3	0.90
Long-term	22	0.99	32	1.00	30%	5	0.98

B. DESIGN OF EXPERIMENTS

For the "inverse" approach (Sec. 9.3), a design-of-experiments (DoE) is performed to create a response surface of the design space, such that the results can be interpolated to constant output parameters such as the MTOM. The input parameters that are varied in the DoE are gathered in Table 9.3. Although the baseline reference aircraft is based on a regional turboprop, the mission parameters (harmonic range, payload mass and cruise Mach number) are also sampled at higher values to analyze the trends in the regional jet or short-haul market, comparable to recent research on high-capacity turboprop aircraft [296]. A payload mass of 100 kg is assumed per passenger, including luggage. The conventional, fuel-based reference aircraft is also sampled for the same range of mission requirements, in order to compare the performance of the HEP variant to a conventional aircraft sized for the same mission. In both cases, the optimum cruise altitude in terms of minimum energy consumption is computed and subsequently selected for each point. In addition to the mission requirements, the powertrain technology level is varied by modifying the combined specific power and chain efficiency of the powertrain. This is done by scaling the specific power and transmission efficiency of all electrical components included in the sizing method equally, such that the desired CSP and η_{chain} (see Table 9.2) are obtained. Furthermore, the shaft power ratio of the aircraft is varied, applying the same value to all mission segments and performance constraints. Finally, the impact of HEP on the aero-propulsive performance of the aircraft is simulated by scaling the zero-lift drag and lift-induced drag components equally.

A Latin-hypercube sampling of 20,000 points is performed for the input parameters given in Table 9.3, and the sizing routine is applied successively. In order to obtain continuous gradients in the resulting plots, a seven-dimensional, 7^{th} order polynomial fit is applied using a linear-least-squares algorithm, described in Appendix F.1. Of the 20,000 points, 95% are used to generate the surrogate model, while the remaining 5% are used to evaluate the accuracy of the fit and to ensure that no over-fitting occurs. Results are only analyzed in the intervals given in Table 9.3, i.e., no extrapolation is performed. The mean deviation of the surrogate model from the data points is found to be below 0.01%,

Table 9.3: List of input parameters varied in the DoE, including the range of values sampled.

Parameter	Minimum	Maximum
M	0.45	0.65
m_{PL} [t]	5 (50 pax)	20 (200 pax)
R [nmi]	500	2000
CSP [kW/kg]	1.5	6
η_{chain}	0.8	1.0
φ	0	1
$\Delta(\eta_{\text{p}} L/D)$	-50%	+50%

with a maximum deviation of 0.8% for MTOM, and 0.3% for PREE. Therefore, although these values lie well within the accuracy of a Class-I sizing routine, an additional uncertainty of approximately ±1% should be kept in mind when analyzing the results.

9.1.3. AERO-PROPULSIVE MODELING (DIRECT APPROACH)

When performing the sensitivity study for an OTWDP aircraft, an aero-propulsive model is required which estimates the change in aerodynamic performance of the vehicle due to aerodynamic interaction effects. Two contributions to lift, drag and propulsive efficiency are considered in the sizing method, as defined in Ch. 3:

$$C_L = C_{L,\text{airframe}} + \Delta C_L, \tag{9.4}$$

$$C_D = C_{D,\text{airframe}} + \Delta C_D, \tag{9.5}$$

$$\eta_{\text{p}} = \eta_{\text{p,isolated}} + \Delta\eta_{\text{p}}. \tag{9.6}$$

The first term of the right-hand side of Eqs. 9.4–9.6 corresponds to uninstalled conditions, that is, to the lift and drag of the airframe when no propulsion system is present, and to the propulsive efficiency of the propulsors if these were operating in freestream conditions. In the proposed OTWDP configuration, it is assumed that the airframe lift is generated entirely by the wing. For airframe drag, a parabolic lift polar is assumed, i.e. $C_{D,\text{airframe}} = C_{D0,\text{airframe}} + C^2_{L,\text{airframe}}/(\pi A e)$. Following the traditional Class-I sizing methods [85], a constant propulsive efficiency is assumed per mission segment for the propulsive empennage, since this propulsion system presents no strong aerodynamic interaction effects with the airframe[1]. For the DP system, on the other hand, it is necessary to estimate the isolated-propulsor efficiency, in order to account for the sensitivity to propulsor diameter. Given that the total disk area scales with the square of the propulsors' diameter but linearly with the number of propulsors, multiple small propulsors have a significantly lower total disk area than a single large fan or propeller for a given span of wing covered. Hence, if the DP system is responsible for a large fraction of the total thrust, high thrust coefficients are obtained, and consequently the propulsive

[1] The thrust of the propulsive empennage would, in practice, have a strong effect on trim drag, but preliminary sizing methods do not include this drag term.

efficiency deteriorates. Therefore, the propulsive efficiency of the DP system in uninstalled conditions is estimated using Eq. 2.13. Based on the empirical data presented in Ref. [297], a value of $k_P = 0.88$ is used to account for viscous, swirl, and induced losses.

The second contribution to lift, drag, and propulsive efficiency comprises the changes in uninstalled performance due to aerodynamic interaction between the propulsors and the airframe when these are integrated with each other. Since this investigation was performed prior to the development of the numerical method of Ch. 8, a simplified aero-propulsive model was created to estimate these terms using the method developed by Marcus [234]. In this method, a single propeller placed at $x_P/c = 0.85$ above a high aspect-ratio rectangular wing is simulated using a blade-element method, a vortex-lattice to represent the slipstream, and panel method to represent the wing. The superposed effect of multiple adjacent propellers is not considered, and the contributions of nacelles and ducts are neglected. Viscous effects are also neglected. Although the simplifications limit the applicability of the model, the trends it provides are considered accurate enough to gain an understanding of the effect of some key design variables in the preliminary sizing phase. However, it should be noted that the lift, drag, and propulsive-efficiency changes provided by this method were found to be conservative, partially due to the generic, un-optimized geometry of the wind-tunnel model on which it is based. Additional information regarding the approach can be found in Ref. [292].

The thrust coefficient and lift-coefficient values for which the aero-propulsive model was generated are representative of the cruise, descent, and (majority of the) climb segments of the mission. However, in low speed conditions (take-off and landing), the required thrust and lift coefficients are higher, and the numerical model is not capable of providing an accurate estimation (see Ref. [234]). In these conditions, ΔC_L, ΔC_D, and $\Delta\eta_p$ are limited to the values they obtain at the bounds of the model. This is considered a conservative approach, since the aero-propulsive benefits improve with increasing thrust coefficient (see Ch. 8). Furthermore, although the results of Ch. 7 studies indicate that the OTW propeller may adversely affect the maximum lift coefficient on the wing, they also suggest that inclining the propulsors for thrust vectoring may further increase lift and decrease drag without an appreciable propulsive efficiency penalty. In general, this shows that there is a large amount of uncertainty regarding the maximum lift coefficient attainable with these systems. For this reason, a separate sensitivity analysis is carried out with respect to the assumed low-speed characteristics in Sec. 9.2.2.

9.1.4. AERO-PROPULSIVE MODELING (INVERSE APPROACH)

In the inverse approach, the "delta" terms due to aero-propulsive interaction in the OTWDP system are not calculated. Instead, a generic increase in aero-propulsive efficiency is assumed, and the aircraft is sized without considering the specific propulsion-system layout. The results of Sec. 9.3 therefore indicate what aero-propulsive benefit is required to achieve a determined energy consumption, while it is up to the designer to determine *how* such benefits can be achieved: with over-the-wing propulsion, tip-mounted propellers, or any other type of propulsor arrangement.

Distributed propulsion can be used to increase the aero-propulsive efficiency in multiple ways. This is evidenced if a parabolic drag polar is assumed, in which case

$$\eta_{\mathrm{p}} \cdot \frac{L}{D} = \eta_{\mathrm{p}} \left(\frac{C_L}{C_{D0} + \dfrac{C_L^2}{\pi A e}} \right). \tag{9.7}$$

Equation 9.7 indicates four direct ways in which distributed propulsion can be used to enhance the aero-propulsive performance of the aircraft: by decreasing the zero-lift drag coefficient, reducing the lift induced drag (through an equivalent increase in aspect ratio or Oswald factor), increasing the propulsive efficiency, or by changing the lift coefficient. The lift coefficient varies throughout the mission, and depends on the flight condition (speed and altitude) and wing loading—which, in turn, depends on the maximum lift coefficient. Rather than studying the effect of each parameter separately, in this study, the effect of improved propulsion–airframe integration is simulated by varying the aero-propulsive efficiency $\eta_{\mathrm{p}}(L/D)$ as a whole (see Table 9.3). This simplifies the problem, decreasing the number of independent variables and leading to top-level conclusions which are independent of the type of propulsion system, analogously to the simplification made in Sec. 9.1.2 regarding the powertrain parametrization. The change in aero-propulsive efficiency can then be related to the effect of a determined propulsion system on a case-to-case basis. A more detailed discussion regarding this approach and how it differs from individually varying each parameter (C_{D0}, A, etc.) is given in Ref. [293].

9.2. DIRECT APPROACH: SENSITIVITY STUDY

The results are grouped into four sections. First, in Sec. 9.2.1 the conventional configuration is compared to reference aircraft data to verify that the assumed aircraft characteristics are reasonable, and to a baseline HEP variant. Sections 9.2.2, 9.2.3, Sec. 9.2.4 then analyze the sensitivity of the HEP design to different design parameters, mission requirements, and technology assumptions, respectively. In some cases, the optimum found in a sensitivity analysis is taken as starting point for subsequent analyses. Although this does not provide the optimum design, it ensures that insight is provided in the more relevant parts of the design space.

9.2.1. BASELINE DESIGN

Table 9.4 collects several top-level parameters of the conventional aircraft configuration and the baseline HEP configuration. Details regarding the selected design-parameter values and performance requirements can be found in Appendix D.2. The conventional configuration with current technology assumptions is compared to reference data of an ATR 72-600. The MTOM is underestimated by 2.5%, while the fuel energy is overestimated by 7%. These two characteristics are reduced by 6% and 23%, respectively, when evaluating the 2035-configuration. In this variant, only two modifications have been assumed. Firstly, the thermal efficiency of the gas turbine has been increased (see Table 9.1). Secondly, the design point corresponding to maximum wing loading has been selected, instead of a trade-off between maximum wing loading and maximum power loading, as reflected in Fig. 9.2a. This allows a fair comparison between the conventional and HEP architectures, since the point of maximum wing-loading leads to an im-

proved design, as discussed in Sec. 9.2.2. In the following sections, the conventional architecture evaluated for the 2035 timeframe will be taken as the reference aircraft for comparison with the HEP variant.

The design parameters selected for the baseline HEP concept are chosen manually without any prior knowledge of the optimal values. For the selected power-control variables (whose values can be found in Appendix D.2), the battery provides additional power during take-off. As a consequence, the power requirement for the gas turbine is reduced, and the take-off constraint is no longer its sizing constraint, as reflected in Fig. 9.2b. However, both the primary electrical machines (generators) and secondary electrical machines (electromotors) are sized for take-off conditions. Note that the one-engine-inoperative constraints do not influence the secondary electrical machines, since a total of 10 electromotors are used, and thus the failure of one of these elements does not con-

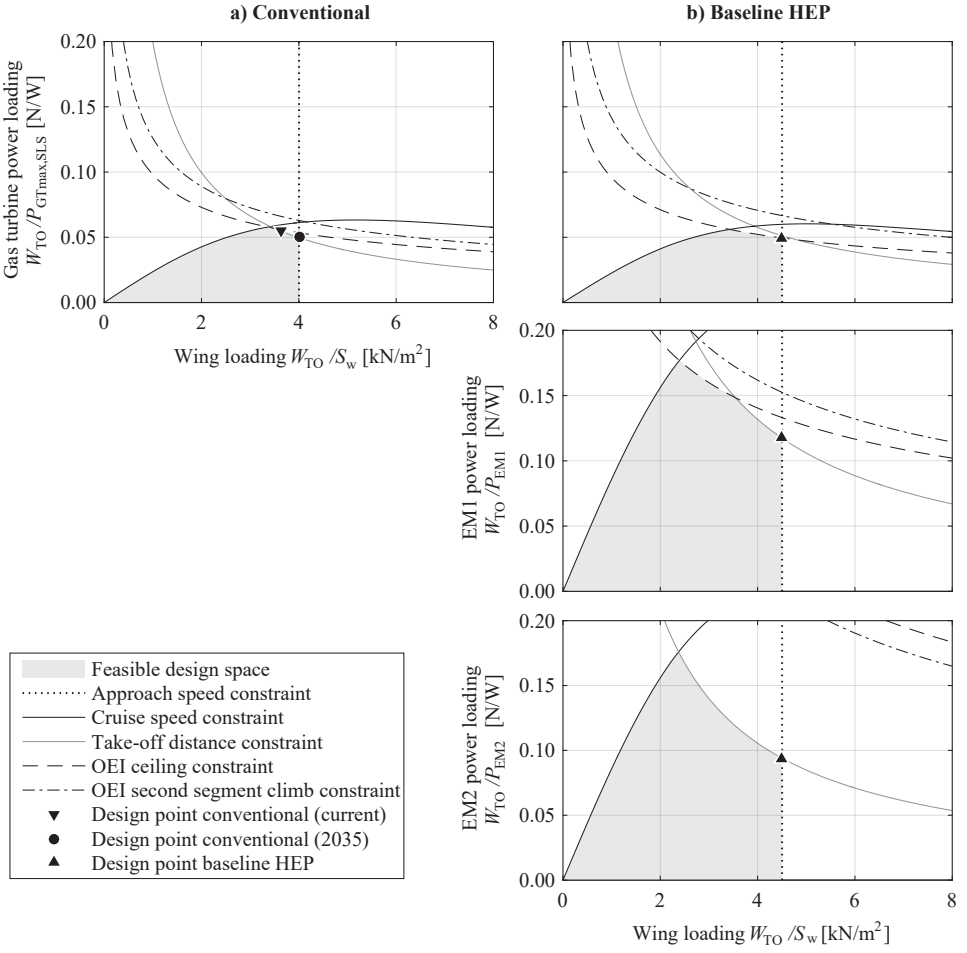

Figure 9.2: Power-loading constraint diagrams of the conventional (left) and baseline HEP (right) configurations.

Table 9.4: Summary of sizing results, comparing two conventional configurations and the baseline HEP configuration. Lift-to-drag ratio is presented as cruise-phase average. Fuel and battery energy include reserves.

	ATR 72-600 (Ref. [228])	**Conventional (current)**	**Conventional (2035)**	**Baseline HEP**
Take-off mass, m_{TO} [t]	22.8	22.2	20.9	24.1
W_{TO}/S [kN/m^2]	3.67	3.64	4.00	4.50
$W_{TO}/P_{GT,max,SL}$ [N/kW]	58.2	54.6	49.7	49.5
Wing area, S [m^2]	61.0	59.8	51.3	52.6
Fuel energy, E_f [GJ]	85.6	91.7	70.2	84.6
Battery energy, E_{bat} [GJ]	0	0	0	1.1
$(L/D)_{cr}$ [-]	-	17.3	17.9	18.4
PREE [-]	-	2.02	2.11	1.77

stitute a limitation to the remaining nine. Furthermore, the maximum wing loading of the HEP concept is increased due to thrust vectoring and aero-propulsive interaction in landing conditions. Consequently, it presents a small increase in cruise lift-to-drag ratio when compared to the reference aircraft, as shown in Table 9.4. Nevertheless, the hybrid-electric configuration is outperformed by the reference aircraft in terms of both MTOM and energy consumption. The main reasons for this are the increased weight due to the hybrid-electric powertrain components, and the reduced propulsive efficiency of the OTW propulsors in cruise conditions.

9.2.2. SENSITIVITY TO DESIGN PARAMETERS

The following subsections discuss how the take-off mass and energy efficiency depend on the chosen design point in terms of wing and power loading, on the assumed low-speed aerodynamic characteristics, and on the selected power-control parameters. The geometrical design parameters of the OTWDP system are not varied here since the aero-propulsive model employed is rudimentary, and thus those parameters are investigated in Ch. 10 instead. However, a dedicated discussion on the low-speed aerodynamic characteristics of the OTWDP system is required, since they cannot be estimated without high-fidelity analysis—as established in Ch. 7—but they have a significant effect on the overall efficiency of the aircraft.

A. DESIGN POINT SELECTION

In the preliminary sizing process, the designer must choose a design point in the power-loading diagram. Due to the large weight contribution of the powertrain to MTOM in the case of HEP, a priori it was hypothesized that the design point for maximum power loading might lead to a lighter aircraft than the design point for maximum wing loading. This is, however, not the case, as shown in Fig. 9.3a. This figure shows that the top-right corner of the design space leads to the lightest aircraft. The point of maximum (gas turbine) power loading can be misleading in this sense, since the associated wing-loading value corresponds to a minimum gas-turbine size per unit weight of the aircraft, but not to the minimum electrical-machine size, as visible in Fig. 9.2b.

For this aircraft, the point of minimum MTOM also corresponds to the point of maximum payload-range energy efficiency. The contours of PREE shown in Fig. 9.3 are more skewed than the MTOM contour lines, indicating that this parameter is relatively more sensitive to wing loading. This is a result of the direct effect of wing loading on aerodynamic efficiency and, consequently, on energy consumption. Although this design point has been identified as the optimal one in design studies of comparable HEP configurations as well [98], this is evidently not always the case for hybrid-electric aircraft [230].

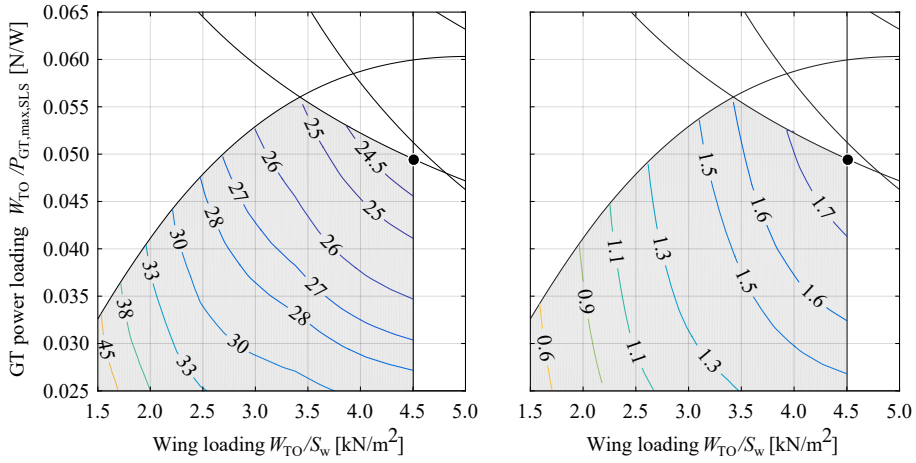

a) MTOM contours **b) PREE contours**

Figure 9.3: Gas-turbine power-loading diagram of the HEP concept, showing the feasible design space in gray together with contour lines of constant MTOM (left; values expressed in metric tons) and payload-range energy efficiency (right). The marker indicates the selected design point.

B. LOW-SPEED AERODYNAMIC PERFORMANCE

The low-speed performance of the aircraft is generally enhanced with a higher maximum lift coefficient. The effective maximum lift can be increased in three ways: by employing larger high-lift devices ($C_{L\text{max,airframe}} \uparrow$), exploiting aero-propulsive interaction effects to increase wing lift ($\Delta C_L \uparrow$), or increasing the vertical force contribution of the propulsors by means of, for example, thrust vectoring ($T \sin\delta_P \uparrow$). The three approaches are equivalent from a flight-performance perspective. Since there is no reliable estimation of the ΔC_L due to OTWDP in high-lift conditions, the effect of thrust vectoring is analyzed here to understand how an increase in system lift in take-off and landing conditions affects the energy consumption of the aircraft.

To this end, Fig. 9.4 shows the changes in MTOM and PREE obtained when varying the thrust-vectoring angle in take-off and landing. For all other flight phases, the angle is zero. Again, the HEP configuration presents a weight and PREE penalty for all combinations sampled. However, an improvement with respect to the baseline is possible. The contour plots show a minimum MTOM around $\delta_{P,TO} = 10^o$, $\delta_{P,L} = 55^o$. During take-off, a small degree of thrust vectoring is beneficial to enhance lift, although larger deflections are detrimental, since the axial component of thrust is reduced. During landing,

on the other hand, larger deflections lead to a lighter and more efficient aircraft. As $\delta_{\mathrm{P,L}}$ increases, so does the wing loading of the aircraft, and consequently the lift-to-drag ratio L/D in cruise is improved. However, for $\delta_{\mathrm{P,L}} > 55^{\mathrm{o}}$, two things occur. Firstly, the wing area is reduced so much that the lift coefficient in cruise approaches, and then exceeds, the value corresponding to maximum L/D, thus decreasing the overall aircraft performance. This key consideration has to be taken into account when sizing a DP system, and will be discussed in more detail in the following sections. Secondly, the wing loading surpasses the intersection of the OEI-ceiling constraint with the take-off constraint in the gas-turbine power-loading diagram, and thus the weight of the gas turbine increases more rapidly with increasing wing loading. This can be seen in the constraint curves of Fig. 9.2b for $W_{\mathrm{TO}}/S_{\mathrm{w}} > 4.5$ kN/m^2. The same effect is responsible for the discontinuity in gradient at, e.g., $(\delta_{\mathrm{P,TO}};\delta_{\mathrm{P,L}}) = (40;23)$: as the thrust-vectoring angle during take-off is increased past its optimum for a given $\delta_{\mathrm{P,L}}$, the take-off constraint descends in the gas-turbine power-loading diagram and starts limiting the size of the gas turbine.

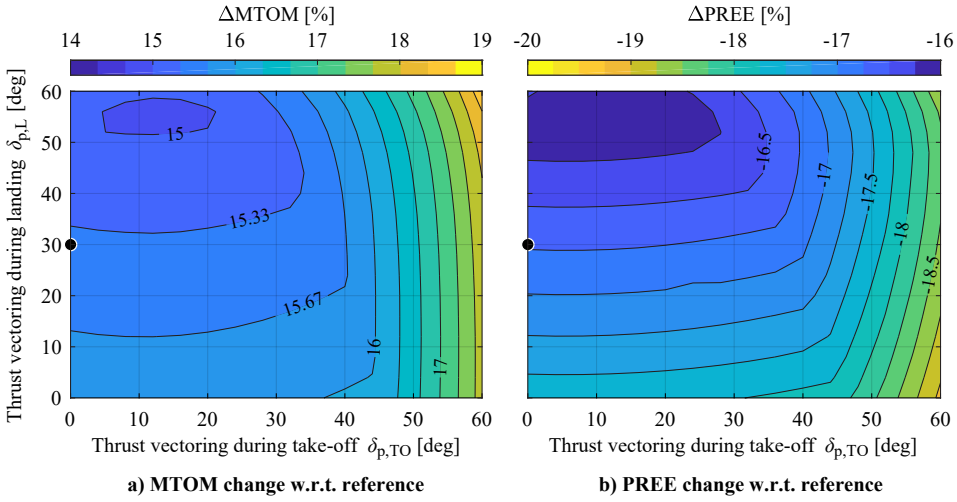

Figure 9.4: Change in MTOM (left) and PREE (right) with respect to the reference aircraft, as a function of the thrust-vectoring angle employed during take-off and landing. The marker indicates values used for the baseline design.

Figure 9.4 confirms that the effective system lift in low-speed conditions can have a noticeable impact on the overall aircraft energy consumption, due to the effect it has on the required powertrain size and, due to the associated change in wing loading, on the cruise lift-to-drag ratio. Additional investigations into the effect of the assumed $\Delta C_{L,\mathrm{max}}$ (not shown here; see Ref. [292]) during landing and take-off showed larger changes in MTOM and PREE. However, the conclusions were similar as those obtained from Fig. 9.4: it determines which performance constraints are limiting and, for a given set of cruise conditions and drag polar characteristics, there is a local optimum, beyond which a further increase in system lift is no longer beneficial in terms of energy consumption. Finally, it is worth noting that the drag coefficient in low-speed conditions can also have an

appreciable impact on the design. During take-off, a decrease in drag leads to a reduction of the required take-off power, which sizes most components. During landing, an increase in drag would increase the thrust required to maintain a determined approach speed. This would, in turn, increase ΔC_L and the effect of thrust vectoring, and therefore the maximum wing loading would be increased.

C. POWER-CONTROL STRATEGY

For the first stages of the sizing process, the designer must choose a set of power-control parameters. Given the relatively large amount of design variables, and the fact that—as suggested in the previous section—these variables can have a decisive impact on the aircraft's design, an optimization could be the way forward. However, since the objective of this study is to understand the effect of the different variables, a design-of-experiments (DOE) is performed. For the SPPH architecture, three power-control parameters have to be specified per performance constraint. For each of the six mission segments (climb, cruise, and descent of the nominal mission, plus diversion), a linear evolution of the control parameters is assumed. Since in cruise conditions one of them has to remain free in order to satisfy the flight condition, this leads to a total of 49 variables. By assuming the same profiles for the nominal mission and the diversion, using the same strategy during take-off and second-segment climb, and fixing the gas-turbine throttle for determined flight phases (maximum throttle in take-off, engine-idle in descent, etc.), the number of variables is reduced to 19. A latin-hypercube sampling technique is used to distribute 15,000 sample points in the design space. An upper and lower bound are imposed on each variable, in order to avoid energy harvesting ($\varphi < 0$ or $\varphi > 1$) or samples which are known to lead to poor results (e.g., a large supplied power ratio during cruise). The values of these bounds can be found in Appendix D.2.

The results of the DOE in terms of MTOM and PREE are collected in Fig. 9.5a, with the colormap indicating the degree-of-hybridization (of energy) the design. Figure 9.5a confirms three characteristics of HEP aircraft. Firstly, the power-control strategy is a driving factor in the design process, since a bad strategy may significantly over-size the aircraft (over 100 tons, in this case). Secondly, for a given PREE, the MTOM increases as the DOH increases. In other words, if the objective of a design is to minimize in-flight emissions, for example, then a slightly heavier aircraft carrying additional battery energy may be more beneficial. And thirdly, a lower DOH (i.e., low Φ values) leads to a lighter and more energy-efficient aircraft, as expected for the technology levels assumed. Inspection of the optimal point in terms of PREE revealed a similar strategy to the baseline configuration: the batteries are used during take-off and climb, and are charged during descent in order to keep enough energy in the batteries for a second take-off and climb in case of a diversion. Although this allows for a smaller gas turbine and a more efficient well-to-shaft energy transmission, the battery weight penalty outweighs these benefits. In a strict sense, however, this is not a fair comparison, since the potential benefit of improved gas-turbine efficiency through on-design sizing is not accounted for.

Based on the previous observations, a second DOE was carried out. In this case, all Φ values were set to zero, meaning that in essence a partial-turboelectric architecture was simulated. The results of this second DOE are plotted in Fig. 9.5b. As can be seen from the range of the axes, the MTOM and PREE obtained in this case are of the same order as the reference aircraft, although the HEP concept still performs worse than the

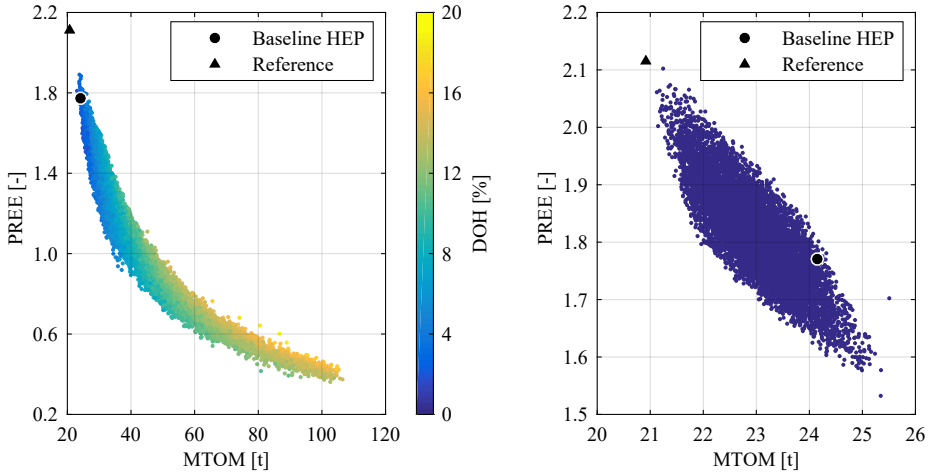

Figure 9.5: Results obtained from the power-control-parameter DOE carried out for the baseline HEP concept (left), together with the results obtained when the supplied power ratio is set to zero for all constraints and mission segments (right).

reference even in the most ideal scenario. It is also evident that, while Fig. 9.5a suggests that the control variables were appropriately selected for the baseline configuration, Fig. 9.5b shows that there is still room for improvement. In order to understand the main reasons for these differences, Fig. 9.6 presents the control-variable values corresponding to the optimum point in terms of PREE for both DOE's. The most notable difference between the baseline strategy and the improved strategy obtained for the PTE case is a reduction of the shaft power ratio, especially in take-off and cruise. Although the DP system increases the lift-to-drag ratio for a given wing loading, it leads to an appreciable propulsive-efficiency penalty due to the non-uniform inflow to the propeller in the rudimentary aero-propulsive model used here (see Ref. [231]). Furthermore, additional power is lost when converting the shaft power of the gas turbine to electrical power, distributing it along the airframe, and converting it back to mechanical power. Thus, in theory, distributed propulsion can improve propulsive efficiency through a decrease in disk loading [295], but this benefit can easily be counteracted by propulsive-efficiency penalties due to non-uniform inflow and losses in the components of the electrical system. For this reason, Fig. 9.6 suggests that the propulsive empennage should remain as the main source of thrust for all mission segments except during landing ($\varphi \approx 1$). In landing conditions, a large fraction of the total thrust should be diverted to the DP system, in order to enhance wing lift and provide an additional vertical force through thrust vectoring. However, the total thrust during landing is generally low, since the aircraft must maintain its approach speed. Consequently, the powertrain components are not sized by power requirements during landing, and thus ξ_{GT} and Φ were not varied in the DOE.

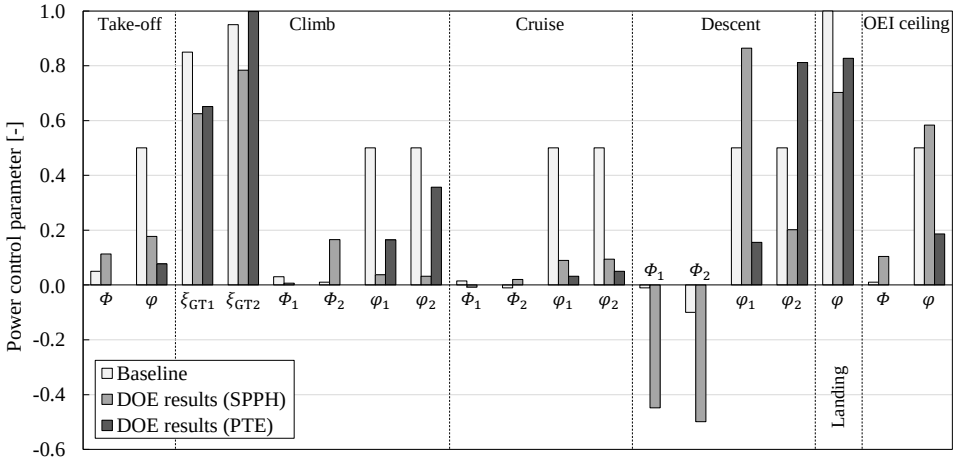

Figure 9.6: Comparison of between power-control parameter values used for the baseline HEP design and the ones corresponding to maximum PREE in the two DoE studies.

9.2.3. SENSITIVITY TO MISSION REQUIREMENTS

In this section, the performance of the HEP configuration is evaluated for a range of payload weights, harmonic ranges, and cruise Mach numbers. A distinction is made between evaluating the mission requirements at fixed altitude and at optimum altitude, in order to illustrate the importance of this design consideration. Two Mach numbers are considered: the cruise Mach number of the ATR 72 ($M_{cr} = 0.41$), and a "high-speed" case ($M_{cr} = 0.6$). For this sensitivity study, the best power-control strategy identified in the previous section is applied (i.e., no batteries are employed). Thus, during cruise, most thrust is generated by the propulsive empennage, and the propulsive efficiency is nearly constant. Furthermore, based on the findings of Sec. 9.2.2, thrust vectoring angles of 10^o and 55^o are used in take-off and landing, respectively.

A. SENSITIVITY AT A FIXED CRUISE ALTITUDE

Figures 9.7a–9.7d present the results of the payload–range sweep at the original cruise altitude of 17,000 ft. For each payload–range combination, ΔMTOM and ΔPREE are computed based on a HEP aircraft and a conventional aircraft which are both sized for the given mission requirements. Note that at $M_{cr} = 0.6$ the sizing routine does not converge for $R = 400$ nmi, since the climb and descent phases exceed the nominal mission range. The same occurs for $R > 1750$ nmi, in this case because the powertrain is heavily oversized, and consequently the aircraft presents a positive excess power during part of the descent phase, with the engine in idle conditions ($\xi_{GT} = 0.1$). This problem could be mitigated by changing the power-control variables, but it is considered preferable to obtain the trends without an additional variation of these variables.

With the newly selected design parameters, the HEP configuration presents a minor weight increase and PREE reduction for the baseline mission ($M_{cr} = 0.41$, Figs. 9.7a and Figs. 9.7b). However, the PREE improves with increasing range and, to a lesser extent, with increasing payload. The trend of PREE with range is attributed to an increased lift-to-drag ratio in cruise of the HEP configuration ($(L/D)_{cr} \approx 18.4$) when compared to the

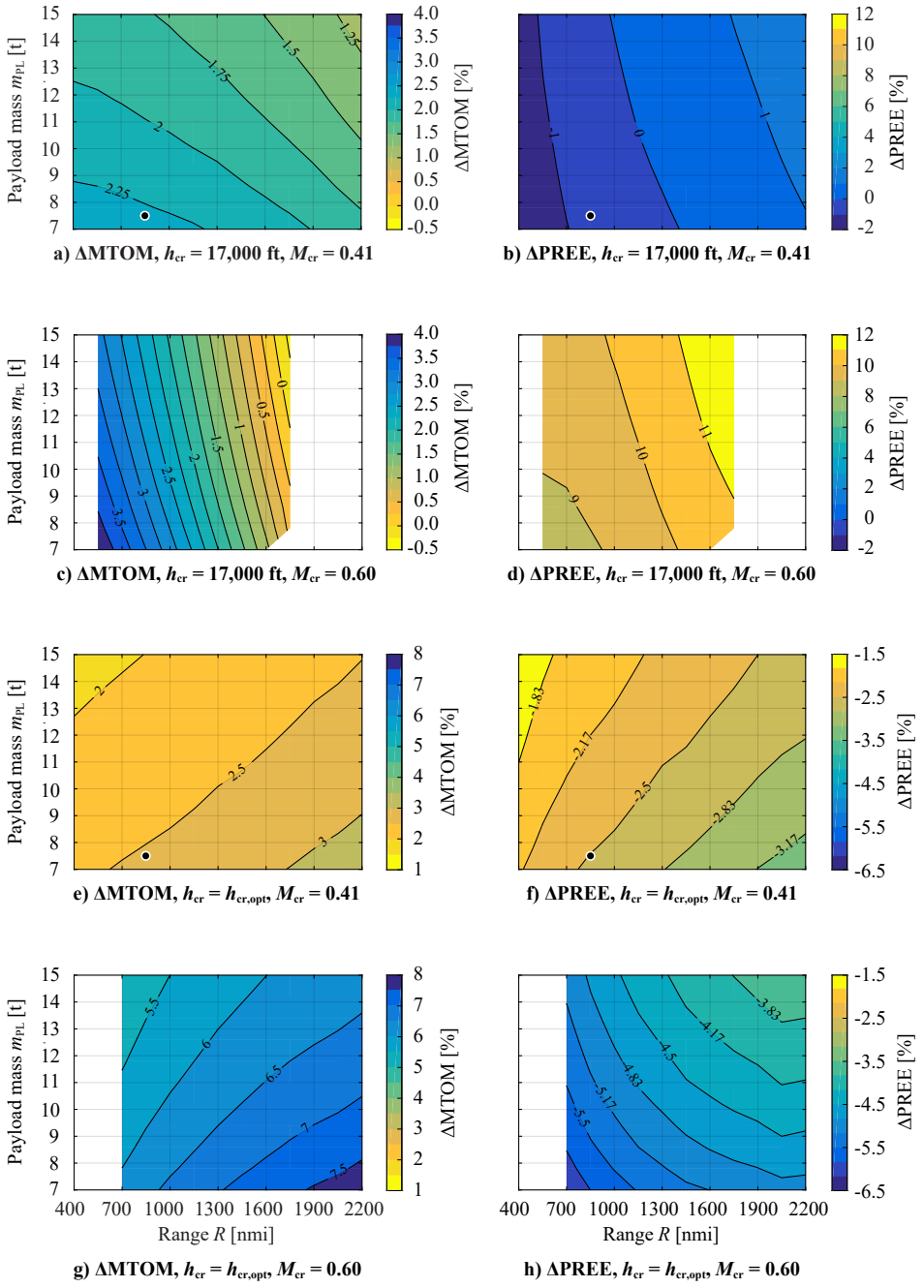

Figure 9.7: Change in MTOM (left) and PREE (right) of the PTE configuration with respect to the reference aircraft, for different mission requirements. Note that the colorbars of the results at constant (top) and optimum (bottom) cruise altitude present different ranges. The marker indicates values used for the baseline design.

reference aircraft ($(L/D)_{cr} \approx 17.7$). At $M_{cr} = 0.6$ (Figs. 9.7c and 9.7d), the PREE gain is increased to nearly 12% with respect to the reference aircraft, and the sensitivity of MTOM to mission range is larger than for the $M_{cr} = 0.41$ case. The flaw of this analysis becomes evident when comparing the lift-to-drag ratio of the reference and hybrid-electric aircraft, which attain values of approximately 10.9 and 12.6, respectively. The L/D benefit of the HEP configuration is larger in this case, and thus the sensitivity of ΔMTOM with respect to range increases. However, these L/D values clearly show that the combination of cruise altitude and Mach number are not adequate for the selected wing loading. In these conditions, the lift coefficient is significantly lower than the value corresponding to optimum L/D.

B. SENSITIVITY AT OPTIMAL CRUISE ALTITUDE

The payload–range maps are also evaluated at 45 equally spaced flight levels between 12,000 ft and 34,000 ft. The lower bound is equal to the OEI ceiling, while the upper bound corresponds to a typical cruise altitude for turbofan aircraft. For each payload–range combination, the optimum altitude in terms of PREE is selected for each aircraft. Thus, the two configurations are not necessarily sized at the same altitude. In this case, the results differ in trend and in value from the ones obtained at constant altitude, as can be observed in Fig. 9.7.

Figures 9.7e and 9.7f show that, at $M_{cr} = 0.41$, the hybrid-electric variant is approximately 2.5% heavier than the reference, and presents a 2.5% lower payload-range energy efficiency. For the conventional configuration, the optimum cruise altitude increases from 19,000 ft at short harmonic ranges, to 24,000 ft at long harmonic ranges. For the HEP aircraft, the optimum cruise altitude increases from 15,000 ft at short harmonic ranges, to 20,000 ft at long harmonic ranges. The optimum altitude increases with harmonic range, because the efficiency gain during cruise offsets the increase in energy required to climb to that altitude. In general, the hybrid-electric aircraft has a lower optimum altitude than the reference, due to the increased wing loading enabled by DP. At their optimum altitude, both aircraft configurations have a comparable lift-to-drag ratio. Therefore, the fact that the PREE and MTOM penalties of the HEP configuration reduce with decreasing range is attributed its lower cruise altitude. For example, at 400 nmi range, the optimum cruise altitude of the HEP configuration is 4,000 ft lower than the conventional configuration, and thus it requires less energy for climbing.

At $M_{cr} = 0.6$, the upper altitude bound was identified as optimum for both the reference and the HEP aircraft. At this flight speed, the weight and PREE penalties of the hybrid-electric configuration are greater than for $M_{cr} = 0.41$. Surprisingly, the weight penalty is minimized for high payloads and short ranges, while the PREE penalty is minimized for high payloads and high ranges. In this case, the lift-to-drag ratio of the reference aircraft is approximately 17.7, while for the HEP variant it is approximately 18.3. Based on these L/D values, it appears that the HEP configuration operates near its optimum altitude, and for this reason, ΔPREE improves with increasing range. On one hand, this indicates that additional altitudes must be evaluated for a fair comparison. On the other, this also shows that, if the cruise altitude of the aircraft is restricted by air traffic regulations or other requirements, the use of HEP provides an additional degree-of-freedom which can be used to tailor the wing loading such that an optimal L/D is achieved in cruise.

The main characteristics of the improved HEP design, evaluated for the baseline mission (m_{PL} = 7500 kg, R = 850 nmi, M_{cr} = 0.41) at optimum altitude, are summarized in Table 9.5. Additional variables can be found in Appendix D.2. The results show a significant improvement with respect to the baseline design in all aspects except power loading, which is decreased. However, the HEP configuration is still outperformed by the reference aircraft, which is also evaluated at its optimum altitude.

Table 9.5: Main characteristics of the improved HEP design, for the baseline mission at optimum cruise altitude. Lift-to-drag ratio is presented as cruise-phase average. Fuel and battery energy include reserves.

Parameter	Value	Diff. w.r.t. baseline HEP	Diff. w.r.t. reference
Take-off mass, m_{TO} [t]	21.4	-11.4%	+2.5%
W_{TO}/S_w [kN/m^2]	4.70	+4.4%	+17.4%
$W_{TO}/P_{GT,max,SLS}$ [N/W]	0.043	-13.1%	-13.5%
Wing area, S [m^2]	44.7	-15.1%	-12.6%
Fuel energy, E_f [GJ]	71.5	-15.4%	+3.3%
Battery energy, E_{bat} [GJ]	0	-100%	0%
Cruise altitude, h_{cr} [ft]	18,000	+5.9%	-16.3%
$(L/D)_{cr}$ [-]	18.4	+0.2%	+0.2%
PREE [-]	2.10	+18.5%	-2.5%

9.2.4. SENSITIVITY TO TECHNOLOGY ASSUMPTIONS

The results of Sec. 9.2.2 show that the use of batteries is detrimental for both figures of merit for the assumed mission and aircraft layout. In order to assess whether this conclusion is highly dependent on the battery's characteristics, Fig. 9.8 presents the sensitivity of MTOM and PREE to the specific energy and specific power of the batteries at pack level. Both properties are varied between 50% and 300% of the baseline value reported in Table 9.1. For this assessment, the baseline SPPH configuration was used. As expected, an improvement in battery technology leads to an appreciable reduction in MTOM and increase in PREE. However, even for the optimistic values of 3 kW/kg and 1500 Wh/kg, the concept performs worse than the one without batteries. For the baseline case, the battery mass is sized by power requirements, hence being insensitive to the assumed specific energy. In the top-left corners of Fig. 9.8, on the other hand, the battery mass is sized by energy requirements, and is therefore insensitive to specific power. The curve defined by the loci of points on the response map that present a discontinuity in gradient (i.e, at the kink of the contour lines) delimits these two regions. The location of this limit depends on the chosen power-control strategy. Modifying the power-control strategy such that the design point ends up on this discontinuity means that the full potential of the battery is used in terms of both energy and power. Logically, this simple distinction is an artifact of assuming constant battery properties at pack level. For a more accurate result, a battery model is required. With an appropriate design of the battery, the trade-off between energy requirements and power requirement can be tailored for the specific design.

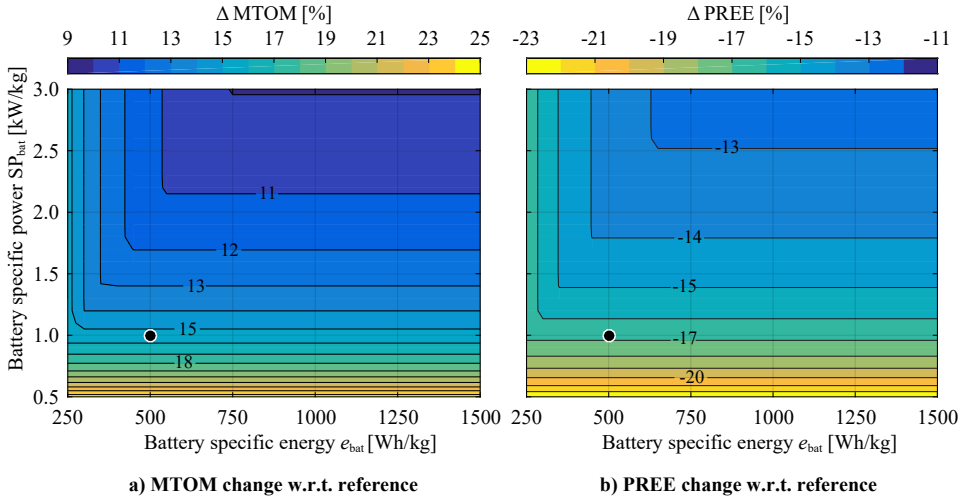

Figure 9.8: Change in MTOM (left) and PREE (right) of the baseline SPPH concept with respect to the reference aircraft, as a function of the specific energy and specific power of the batteries at pack level. The marker indicates values used for the baseline design.

In second place, the sensitivity of MTOM and PREE to the weight and efficiency of the electrical components of the powertrain (excluding batteries) is assessed. The resulting sensitivities are reflected in Fig. 9.9. Although both MTOM and PREE improve with increasing CSP or chain efficiency, PREE is more sensitive to the latter than MTOM is. In baseline conditions, the HEP aircraft presents an MTOM and PREE comparable to the reference, since this analysis is carried out at the original cruise altitude. The PREE benefit increases up to 6% if the CSP of the system is tripled, and the losses approach zero. In these conditions, the MTOM of the HEP aircraft is also 4% lower than the reference.

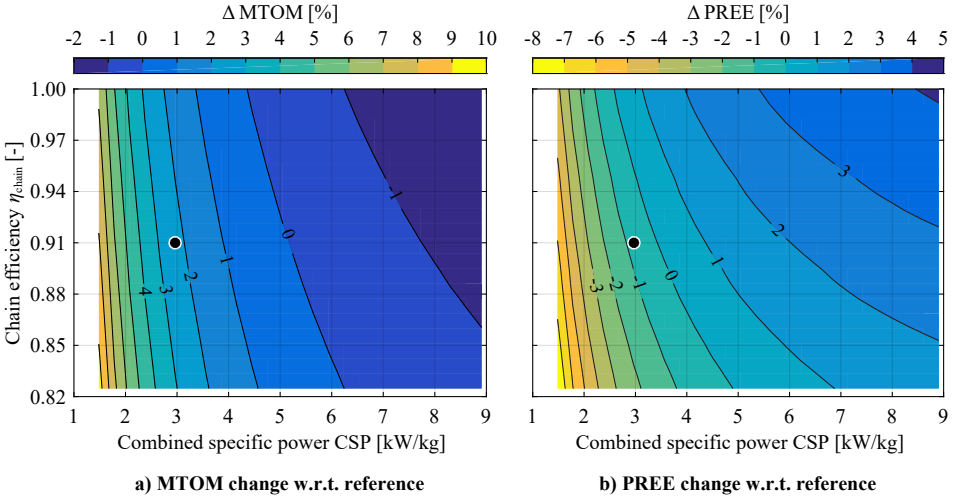

Figure 9.9: Change in MTOM (left) and PREE (right) of the PTE concept with respect to the reference aircraft, as a function of the combined specific power and efficiency of the electrical powertrain components. The marker indicates values used for the baseline design.

9.3. INVERSE APPROACH: AERO-PROPULSIVE EFFICIENCY REQUIREMENTS

The results are grouped into two sections. First, Sec. 9.3.1 describes how the aero-propulsive requirements depend on the mission parameters. Section 9.3.2 then describes how these requirements evolve with the powertrain technology level.

9.3.1. IMPACT OF MISSION REQUIREMENTS

Figure 9.10 presents the payload-range energy efficiency of the reference (fuel-based) aircraft and the turboelectric variant, as a function of the mission payload and range. For the turboelectric aircraft, a 10% increase in aero-propulsive efficiency (i.e., $(\eta_p L/D)_{HEP}/(\eta_p L/D)_{ref} = 1.1$) has been assumed, together with a shaft power ratio of $\varphi = 0.2$. The maps show that both the conventional and the turboelectric aircraft are most efficient at a range of approximately 650 nmi, with a payload of 20 t (Point A). Although the trends of the two aircraft are the same, the turboelectric variant presents a slightly higher PREE for the technology scenario and aero-propulsive benefit considered.

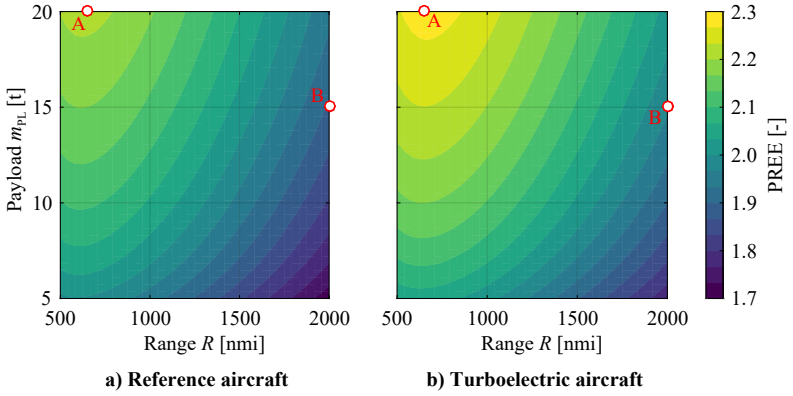

Figure 9.10: Payload-range energy efficiency as a function of mission requirements for the reference (left) and partial turboelectric (right) aircraft, assuming a 10% increase in aero-propulsive efficiency for the latter ($M = 0.55$, $\eta_{chain} = 0.9$, CSP = 3 kW/kg, $\varphi = 0.2$). Markers indicate the scenarios collected in Tables 9.6 and 9.7.

In order to further analyze the difference between the turboelectric and the conventional aircraft, Fig. 9.11 presents the aero-propulsive efficiency gain necessary for a 15% increase in PREE. The results are displayed for a generic value of ΔPREE = 15% because, from a commercial perspective, a significant energy saving is required to outweigh the additional complexity and development costs of such aircraft. Figure 9.11 shows that a significant increase in aero-propulsive efficiency of around 20% is required for a 15% energy reduction. The percentage change in aero-propulsive efficiency is larger than the percentage reduction in energy consumption, because the additional weight and efficiency losses of the hybrid-electric powertrain must be compensated. The required aero-propulsive benefit is practically independent of the payload considered, and decreases with increasing range. This occurs because, for longer ranges, the amount of fuel saved increases. This leads to a direct energy saving on one hand, and decreases the

weight penalty of the turboelectric aircraft on the other, since the fuel weight increases less with range for the turboelectric aircraft than for the conventional one. Therefore, while point A represents the combination of payload and range where the turboelectric aircraft is most efficient (within the m_{PL} and R intervals studied), point B—or any other point for $R = 2000$ nmi—represents the mission for which the turboelectric presents the greatest benefit when compared to the reference aircraft. This confirms that turboelectric configurations are most competitive for longer ranges, which is why many turboelectric aircraft design studies focus on medium- and long-haul flights [53, 114, 295], and not on the regional or thin-haul market. This also highlights an important difference compared to other hybrid-electric aircraft that make use of batteries, for which the extra battery weight generally implies that reduced ranges have to be flown (see e.g. Refs. [66, 204, 213, 298]).

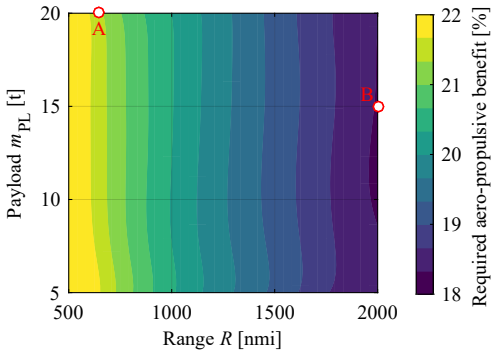

Figure 9.11: Aero-propulsive efficiency increase required in order to obtain a 15% increase in PREE, as a function of mission range and payload ($M = 0.55$, $\eta_{chain} = 0.9$, CSP = 3 kW/kg, $\varphi = 0.2$). Markers indicate the scenarios collected in Tables 9.6 and 9.7.

Finally, the effect of cruise Mach number is assessed in Fig. 9.12. This figure presents the same variables as Fig. 9.11, but at a constant payload of 15t (150 pax) and for three different Mach numbers. Again, the figure clearly shows that a 15% energy reduction is most easily achieved at long ranges. Furthermore, the required aero-propulsive efficiency benefit increases with Mach number. In other words, a determined energy saving is easier to achieve with a low-speed turboelectric aircraft than with a high-speed one. This occurs because, at high Mach numbers, the power required during cruise increases, and hence the cruise-speed constraint descends in the loading diagram. Given that, for the range of Mach numbers considered, the cruise-speed constraint is actively sizing the powertrain, this translates into a reduced power loading. Moreover, since the turboelectric powertrain is heavier than a gas turbine alone, the powertrain weight fraction increases much faster with Mach number for the turboelectric aircraft than for the reference aircraft. This leads to a larger difference in MTOM between the two configurations, and consequently, the turboelectric aircraft requires an additional aero-propulsive benefit to offset this weight increase at higher Mach numbers.

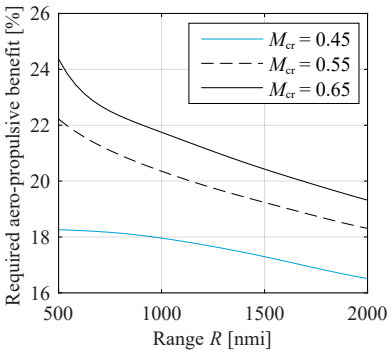

Figure 9.12: Influence of Mach number on the aero-propulsive efficiency increase required in order to obtain a 15% increase in PREE (m_{PL} = 15 t, η_{chain} = 0.9, CSP = 3 kW/kg, φ = 0.2).

9.3.2. IMPACT OF ELECTRICAL-COMPONENT TECHNOLOGY LEVEL

This section describes how the aero-propulsive requirements discussed in the previous section evolve as the technology of hybrid-electric powertrain components matures. To this end, Figs. 9.13 and 9.14 present the required aero-propulsive benefit for a 15% increase in PREE for missions A and B, respectively, as a function of the electrical drivetrain's chain efficiency and combined specific power. The required aero-propulsive benefit decreases with increasing chain efficiency and CSP, as expected. The trends of Figs. 9.13 and 9.14 are similar, although the aero-propulsive requirements are slightly less restrictive for the latter (R = 2000 nmi), as discussed previously. It is interesting to note that these figures also provide information regarding possible trade-offs between the weight and the transmission efficiency of the electrical components. For example, it may be possible to make a more efficient, but heavier, electrical drivetrain, by including active (cryogenic) cooling systems which enable superconductivity on determined components (see e.g. Refs. [119, 299]). Taking the circular marker of Fig. 9.13b (η_{chain} = 0.9, CSP = 3 kW/kg) as an example, it is evident that a 50% increase in weight of the electrical drivetrain (CSP = 2 kW/kg) is justifiable if it allows the chain efficiency to be increased beyond 95%. Therefore, although evidently a more mature technology will lead to a more competitive turboelectric aircraft, for a given point in time, a trade-off between the chain efficiency and CSP has to be performed to identify the most optimal combination.

Both Fig. 9.13 and Fig. 9.14 present the results for three different shaft power ratios, the third of which (φ = 1) corresponds to a fully-turboelectric powertrain. The figures show that higher aero-propulsive benefits are required to compensate higher shaft power ratios: for a fully-turboelectric architecture, the electrical drivetrain has to be able to absorb all the power produced by the gas turbine, leading to very heavy components. Moreover, the higher the shaft power ratio, the higher the amount of power lost in the electrical drivetrain[1]. Consequently, the aero-propulsive benefits required to offset these penalties and additionally lead to an energy reduction are practically infeasible—even for very advanced technology levels, as indicated in in Figs. 9.13c and 9.14c. It appears

[1]The power lost in the electrical powertrain branch is $P_{GB} - P_{s2}$, which can be shown to be equal to $\varphi(1-\eta_{chain})(\eta_{chain}+\varphi(1-\eta_{chain}))^{-1}P_{GT}$. Therefore, the losses range from zero, at $\varphi = 0$, to $(1-\eta_{chain})P_{GT}$, at $\varphi = 1$.

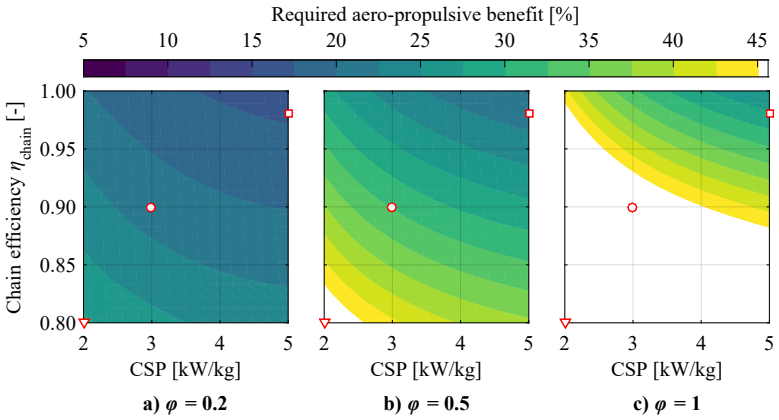

Figure 9.13: Aero-propulsive efficiency increase required in order to obtain a 15% increase in PREE for mission A, as a function of the assumed technology level ($M = 0.55$, $m_{PL} = 20$ t, $R = 650$ nmi). Markers indicate the technology scenarios collected in Tables 9.6 and 9.7.

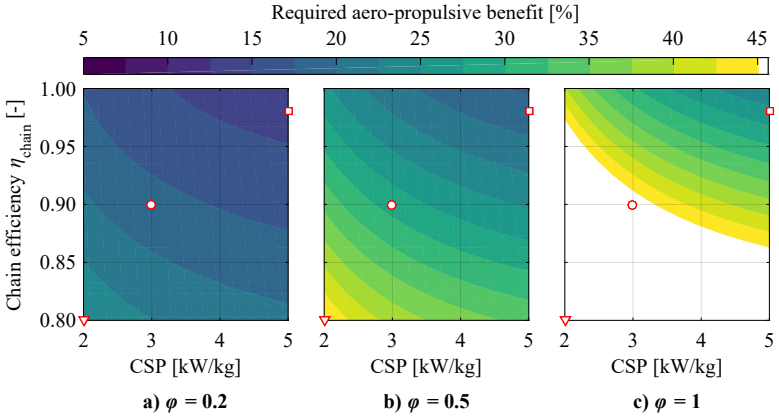

Figure 9.14: Aero-propulsive efficiency increase required in order to obtain a 15% increase in PREE for mission B, as a function of the assumed technology level ($M = 0.55$, $m_{PL} = 15$ t, $R = 2000$ nmi). Markers indicate the technology scenarios collected in Tables 9.6 and 9.7.

therefore that a lower shaft power ratio is beneficial. However, the question remains whether the required aero-propulsive benefit is achievable with low shaft power ratios. For example, the required aero-propulsive benefit in Figs. 9.13a and 9.14a is of the order of 15%–25%, but this increase in aerodynamic or propulsive efficiency would have to be achieved by means of a smart integration of only 20% of the total shaft power. For some propulsion system layouts this may not constitute a major challenge, if there is a local optimum in terms of shaft power ratio from an aerodynamic perspective. For example, for a BLI system, the benefit cannot exceed the amount of power dissipated in the fuselage boundary layer, and thus it is only beneficial to divert a fraction of the total shaft power to the fuselage-mounted propulsor [300]. However, if, for a deter-

mined propulsion-system arrangement, the aero-propulsive benefit grows indefinitely until $\varphi \to 1$, then most likely it will not be possible to take full advantage of the potential of the propulsion system, because of the associated weight penalty. Either way, most of the aero-propulsive efficiency values plotted in Figs. 9.13 and 9.14 are difficult, if not impossible, to achieve. This indicates that a 15% reduction in energy consumption is unlikely for the missions considered.

9.3.3. OVERVIEW OF AERO-PROPULSIVE EFFICIENCY REQUIREMENTS

A summary of the aero-propulsive efficiency requirements is gathered in Tables 9.6 and 9.7, for different missions, technology scenarios, and shaft power ratios. As discussed in Sec. 9.1.2, the "mid-term" scenario corresponds to state-of-the-art research goals, which is assumed to be applicable to the 2035-timeframe. The long-term scenario is expected to be applicable only beyond 2050, if ever. However, these timeframes have to be interpreted with caution, since there is no clear forecast. Tables 9.6 and 9.7 also categorize the aero-propulsive efficiency requirements into three qualitative groups. Green indicates an aero-propulsive efficiency gain which is considered to be feasible ($\Delta(\eta_p L/D) \leq 15\%$), though not necessarily easy to achieve. Orange indicates aero-propulsive benefits which are considered extremely difficult to attain ($15\% < \Delta(\eta_p L/D) \leq 25\%$), while the red numbers indicate benefits which are most likely impossible to achieve in practice ($\Delta(\eta_p L/D) > 25\%$). The reader is reminded that the values correspond exclusively to the aero-propulsive benefit enabled by turboelectric propulsion when compared to a conventional gas-turbine based aircraft designed for the same mission and timeframe. The results are shown for a cruise Mach number of $M = 0.55$; results at $M = 0.45$ and $M = 0.65$ can be found in Appendix D.2.

Table 9.6: Summary of the aero-propulsive efficiency increase necessary for a 15% increase in PREE with respect to a fuel-based reference aircraft.

			Mission A			**Mission B**		
		m_{PL} [t]	20			15		
		R [nmi]	650			2000		
	CSP	M [-]	0.55			0.55		
Scenario	[kW/kg]	η_{chain} [-]	$\varphi = 0.2$,	0.5,	1.0	$\varphi = 0.2$,	0.5,	1.0
Near-term	2	0.80	28%	>45%	>45%	25%	>45%	>45%
Mid-term	3	0.90	22%	32%	>45%	19%	29%	>45%
Long-term	5	0.98	17%	21%	28%	14%	19%	26%

Tables 9.6 and 9.7 show that, in the near term, a significant reduction in energy consumption by means of turboelectric propulsion is unfeasible. In the mid-term, a 5% reduction in energy consumption is possible if the aero-propulsive efficiency is increased by approximately 11%, although a 15% energy reduction is practically impossible. If the power density and transmission efficiency of the electrical components are further improved, then a 15% reduction in energy consumption may be possible in the long term, provided that the distribution of power leads to a 14%–17% increase in aero-propulsive efficiency. However, these conclusions all consider a shaft power ratio of $\varphi = 0.2$, implying that the aero-propulsive benefit must be gained by distributing around 20% of the

total power available. Since the primary powertrain branch (gas turbine and generators) is the dominant contributor to powertrain weight, from an aircraft design perspective, it is generally beneficial to keep it close to the center of gravity. This makes it difficult to reap benefits such as fuselage boundary-layer ingestion or tip-mounted propulsion with the primary propulsors, and thus a large fraction of the aero-propulsive benefit must be achieved by the smaller, electrically-driven propulsors. Obtaining a 7%–17% benefit in aero-propulsive efficiency is therefore not a trivial target. In any case, Tables 9.6 and 9.7 indicate that fully-turboelectric configurations ($\varphi = 1$) are not an effective solution to decrease the energy consumption of transport aircraft.

Table 9.7: Summary of the aero-propulsive efficiency increase necessary for a 5% increase in PREE with respect to a fuel-based reference aircraft.

			Mission A			**Mission B**		
		m_{PL} [t]	20			15		
		R [nmi]	650			2000		
	CSP	M [-]	0.55			0.55		
Scenario	[kW/kg]	η_{chain} [-]	$\varphi = 0.2$,	0.5,	1.0	$\varphi = 0.2$,	0.5,	1.0
Near-term	2	0.80	18%	38%	>45%	17%	37%	>45%
Mid-term	3	0.90	12%	22%	40%	11%	21%	39%
Long-term	5	0.98	8%	12%	18%	7%	11%	18%

9.4. DISCUSSION

The sizing method of Ch. 3 has been used to analyze the sensitivity of a hybrid-electric aircraft configuration to a series of design parameters, mission requirements, and technology assumptions. Several important conclusions can be drawn based on the sensitivity analyses. First, although literature suggests that hybrid-electric propulsion (HEP) can lead to significant improvements in terms of energy consumption, the results evidence that several theoretical benefits at subsystem level do not necessarily lead to an improvement at aircraft level when the relevant dependencies are included in the sizing process. As an example, the payload-range energy efficiency (PREE) of the best HEP configuration proposed in Sec. 9.2 is still 2.5% lower than a conventional aircraft. For this aircraft, the partial-turboelectric powertrain was found to be the best-performing architecture. In other words, for the battery specific-energy values envisioned for the coming decades, the use of battery power directly for propulsion purposes does not improve the energy efficiency of a regional transport aircraft.

In second place, when designing a hybrid-electric aircraft, it must be compared to a conventional configuration sized for the same mission, and each concept must be evaluated at its optimum cruise altitude. Not doing so can lead to an overestimation of the HEP aircraft's benefits. In this study, a comparison at constant cruise altitude suggests that the HEP aircraft can present up to a 12% increase in PREE, due to an increased wing loading. However, the efforts to increase wing loading are in vain if the conventional configuration can attain an equally efficient C_L in cruise by varying its altitude. In spite of this, there are several circumstances under which the increase in wing loading enabled by DP may still be beneficial. For example, if an appreciable amount of energy is

consumed during the climb segment, or if the maximum altitude is limited by air-traffic regulations, then the lower optimal altitude of the HEP aircraft is beneficial. Moreover, when the maximum wingspan is limited by gate constraints, a HEP aircraft can carry more payload or employ a higher aspect-ratio wing, for the same wing span. Furthermore, for the same aspect ratio and bending-relief effects, a smaller wing is less heavy.

In third place, the sensitivity studies confirm that the power-control strategy has a large impact on both the constraint diagram and the mission analysis, and therefore affects practically all characteristics of the aircraft. The optimal control strategy is also highly dependent on the aero-propulsive interaction effects. For example, the design-of-experiments of Sec. 9.2 has shown that a low shaft power ratio (i.e., low thrust share of the DP-system) is better in cruise, due to the propulsive-efficiency penalty of the DP system. However, if this penalty could be reduced by properly re-designing the over-the-wing propulsors, then it may be more beneficial to maximize the shaft power ratio in cruise. Given that the chain efficiency of the powertrain's electrical components is 91% in this study, a small improvement in propulsive efficiency would not have a noticeable impact at aircraft level, since the DP system is not used in cruise. If, on the other hand, the propulsive efficiency increases sufficiently to offset this 9% efficiency penalty, then the shaft power ratio would be maximized in cruise.

Finally, the results of the inverse approach (Sec. 9.3) indicate that the benefit of turboelectric propulsion increases with range and decreases with cruise Mach number, while being practically independent of the payload mass. Furthermore, the shaft power ratio, φ, is shown to have a large impact on the turboelectric aircraft, with high shaft power ratios ($\varphi \rightarrow 1$) demanding a large increase in aero-propulsive efficiency to offset the weight penalty of the powertrain. This highlights the importance of considering the relation between the achievable aero-propulsive benefit and the shaft power ratio required to achieve it, early in the design process. The results show that, when compared to a conventional, fuel-based aircraft designed for the same timeframe, a 5% reduction in energy consumption is possible in the mid-term (entry into service circa 2035) if an increase in aero-propulsive efficiency of 11% is achieved with a shaft power ratio of 0.2. The results also suggest that a 15% reduction in energy consumption is only possible with radical improvements in the specific power and transmission efficiency of the electric drivetrain, and if the aero-propulsive efficiency can be increased by 14% using a shaft power ratio of 0.2.

10

SYNTHESIS: AIRCRAFT PERFORMANCE

The aerodynamic analyses performed in Part II have shown that over-the-wing propellers can lead to a significant aerodynamic benefit at subsystem level. For example, the analyses of Ch. 8 show that the aero-propulsive efficiency $\eta_p(L/D)$ of an OTW propeller and the wing segment beneath it can increase by more than 30% with respect to the two components without aerodynamic coupling. However, this only considers a small part of the complete aircraft. The aircraft-level sensitivity analyses of Ch. 9, on the other hand, show that an average increase in aero-propulsive efficiency of at least 10% is required at vehicle level, to offset the HEP weight penalty and gain a 5% reduction in energy consumption. Hence, the question remains whether OTWDP can provide such a benefit at aircraft level, or whether it is not a practical solution for regional transport aircraft. The objective of this final chapter is therefore to combine the design method of Ch. 3, the aerodynamic model of Ch. 8, and the lessons learned in Chapters 5–9 to determine if, or how, a typical OTWDP application can lead to a reduction in energy consumption at aircraft level.

The following section (Sec. 10.1) describes a series of qualitative design considerations that should be taken into account when attempting to design a regional aircraft with OTWDP. These considerations are based on the findings of previous chapters. The mission requirements of the case study are subsequently presented in Sec. 10.2, along with the assumptions made in the sizing process. The aircraft-level performance indicators defined in Ch. 2 are then compared to a conventional reference aircraft sized for the same mission with the same method (Sec. 10.3). No explicit validation is performed; for the validation of the sizing method and the aerodynamic model, the reader is referred to Chapters 4 and 8, respectively. Finally, Sec. 10.4 shows how an appropriate selection of the geometrical OTWDP design parameters and power-control strategy can affect the aircraft-level performance metrics.

Parts of this Chapter have been published in Ref. [301].

10.1. DESIGN CONSIDERATIONS FOR OTWDP AIRCRAFT

The design-space exploration study of Ch. 9 demonstrated that a partial-turboelectric (PTE) powertrain is the most suitable HEP architecture for a regional transport aircraft. This powertrain layout is carried forward in this chapter, and therefore no batteries are used. It is worth noting that, though this architecture is found to be the best solution in terms of overall energy consumption, in practice a small amount of batteries could be beneficial or necessary for different reasons. For example, to enable electric taxiing, to reduce emissions in the vicinity of the airport, or to act as a buffer during transient power requirements throughout the mission. However, since the total battery energy capacity has to be minor compared to the total fuel energy to avoid an excessive weight increase, these effects are not considered for this Class-I analysis.

A key benefit of the PTE configuration is that a large amount of thrust can be provided by the primary propulsors in the sizing condition, and therefore the electrical components can remain relatively small and light. In the case of a subsonic regional aircraft, the propellers used as primary propulsors have to remain relatively large in order to ensure a low disk loading on both propulsion systems. For example, for an ATR 72-600 [228], the total propeller disk area (24 m^2) equals roughly 40% of the reference wing area (61 m^2). For an OTWDP system to present a comparable disk loading, large diameter-to-chord ratios would be required, which entail significant structural integration challenges. Therefore, in the PTE configuration, a large fraction of the total disk area corresponds to the primary propellers. Thus, the OTWDP system in essence supports the primary propellers with varying levels of power share throughout the mission.

An important consideration for the OTWDP system is which parts of the wing it covers. While the aerodynamic benefit increases with the span fraction covered, the installation of OTW propulsors in the outboard region comes with several drawbacks, such as an increased roll inertia, increased yawing moments in case of component failure, a potential wing weight increase (depending on the structural sizing condition), and interference with the control surfaces (ailerons). While the roll control could in principle be provided by means of control surfaces integrated in a duct or stator vane, this additional level of complexity is not considered for the present study. Therefore the OTWDP system is limited to the inboard portion of the wing, from the root until the outboard edge of the flap. This decision comes with its own challenges, since the OTWDP system must be integrated with the flap, and the primary propellers cannot be installed in a typical wing-mounted tractor configuration because their slipstream would cover part of the OTWDP system. Hence, they must be installed on the wing tip, tail, or fuselage. While each of these positions has its advantages and drawbacks, for the present study the propellers are placed in a pylon-mounted pusher configuration, similarly to the Embraer/FMA CBA-123 Vector [302] or some of the advanced propfan concepts investigated by NASA in the 1980s [86]. This arrangement is depicted in Fig. 10.1. At this location, the propellers do not significantly interfere with the horizontal tail, with the ground clearance of the aircraft, or with the wake of the OTWDP system. Moreover, the aft placement of the propellers leads to a reduction in cabin noise compared to wing-mounted configurations [86]. Although the overall noise levels of the propellers increase due to the impingement of the pylon wake, this penalty could be reduced with a pylon-blowing system [303]. However, this configuration presents a larger center-of-gravity excursion

than wing-mounted configurations, which may lead to an increase in tail size, trim drag, and aircraft weight [294]. While these effects are not accounted for in the Class-I sizing phase, they should be kept in mind when assessing the overall performance of the configuration.

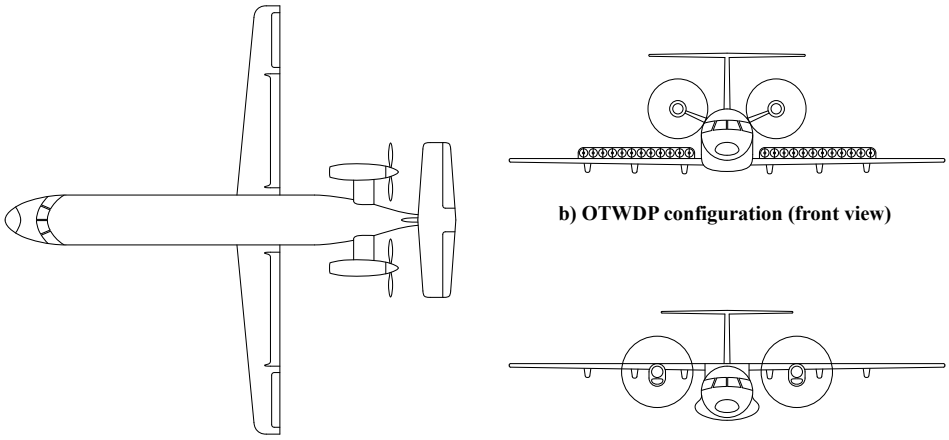

a) OTWDP configuration (top view)

b) OTWDP configuration (front view)

c) Conventional configuration (front view)

Figure 10.1: Conceptual sketch of a hybrid-electric regional transport aircraft with OTWDP. Conventional configuration with same total disk area included for reference.

Now that the approximate location and extent of the two propulsor systems has been presented, the size and axial position of the OTW propellers has to be decided. Chapters 6 and 8 showed that the lift-to-drag ratio benefit is higher for propellers placed near the location of maximum airfoil thickness. However, for forward locations, the propulsive efficiency of the propellers is reduced considerably. Therefore, for the present study, the OTW propellers are placed near the trailing edge. In this way, the propellers can additionally be installed on the flap. The deflection of the propeller in high-lift conditions can contribute to an effective lift increase due to thrust vectoring, as well as postpone flow separation, as discussed in Ch. 7. However, even for $0.75 < x_P/c < 1$, changes in the axial propeller location can appreciably affect the performance of the OTWDP system (see Appendix G). The incidence angle of the propeller relative to the wing also plays an important role in this regard: the previous analyses showed that the performance is improved if the propeller presents a slight nose-down installation angle. Furthermore, based on the investigations performed in previous chapters, it is unclear whether a duct is beneficial from an system-level aerodynamic perspective. Although it can, in principle, reduce the non-uniformity of the inflow to the propeller, this may not be required for small propellers placed near to the trailing edge. Moreover, while the duct itself contributes positively to thrust at high thrust settings (Ch. 6), in cruise it is likely to reduce the L/D of the system due to the increase in wetted area [291]. If a duct *is* required, then a two-dimensional "envelope" duct comparable to the concept of Fig. 10.1 is considered the best option. A two-dimensional duct is sufficient to reduce the non-uniform inflow,

since the inflow conditions to the propeller present no significant spanwise variations (Ch. 8), and it presents less wetted area and less corner-flow challenges than adjacent circular or square ducts, respectively (Ch. 6). In any case, further investigation into the effect of duct shape and position would be required if this configuration is selected.

Based on these criteria, two hypothetical OTWDP arrangements are shown in Fig. 10.2. In the first (Fig. 10.2a), the propeller is placed closer to the trailing edge, in order to maximize the propulsive efficiency. In that case, a duct is not required. However, the propeller must be installed in a pusher configuration[1]. The impingement of the pylon wake, together with the limited wing-shielding capabilities due to the proximity to the trailing edge, is likely to lead to an increase in both flyover and cabin noise. In the second configuration (Fig. 10.2b), the propeller is placed slightly further forward, to reduce wing drag. In this case, a duct becomes more advantageous, since the wing-induced velocity profile presents stronger gradients. Moreover, if the wavelength of the blade-passage frequency is small relative to the size of the duct or the distance to the wing trailing edge, then this configuration is likely to present lower noise levels than the former due to noise shielding [74]. In both cases, the flap presents a drooped hinge, such that a Fowler motion is achieved when rotating the flap. The rotation of the flap is such that, when deflected, the gap is minimized. This leads to a situation comparable to Ch. 8, where the propeller is located behind the suction peak over the flap hinge. It is assumed that, in this configuration, the suction induced upstream by the propeller allows the flow to remain attached without requiring a slot for a fresh boundary-layer on the flap. However, further analyses into the interaction effects in high-lift conditions at realistic Reynolds numbers are required to confirm this assumption.

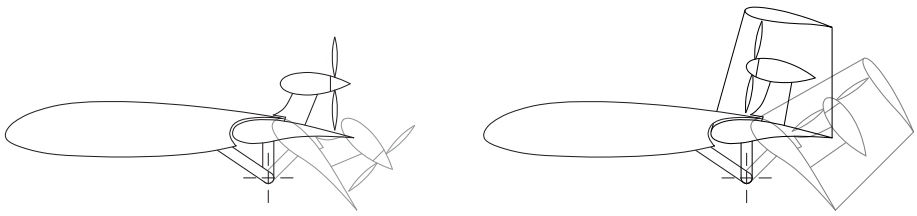

a) Unducted pusher configuration **b) Ducted tractor configuration**

Figure 10.2: Conceptual sketch of two OTWDP variants, including the position of the propeller in case of a $\delta_f = 45^o$ flap deflection.

Finally, a generic diameter-to-chord ratio of $D_P/c = 0.25$ is assumed for the sketches of Fig. 10.2. The previous chapters show that the wing L/D benefit increases significantly with the diameter-to-chord ratio. However, larger propellers require larger pylons and create a stronger nose-down pitching moment due to the vertical placement of the thrust vector, which can lead to higher actuator loads when installing them on a flap. Therefore, although the effect of D_P/c on the aerodynamic performance is accounted for in the following sections, the Class-I sizing process is not sensitive to such drawbacks.

[1]The terms "pusher" and "tractor" are used in this research to refer to the position of the propeller relative to the motor that drives it, not relative to the center of gravity of the aircraft.

10.2. TOP-LEVEL AIRCRAFT REQUIREMENTS & ASSUMPTIONS

To demonstrate the effect of OTWDP at aircraft level, a propeller transport aircraft is sized using the Class-I sizing method described in Ch. 3. The majority of the selected design parameters and assumptions are comparable to those used in the design-space exploration study of Ch. 9. The corresponding values can be found in Appendix D.2. In the following two subsections, the mission requirements and assumptions of the present study are described, focusing on the aspects that differ from the previous chapter.

10.2.1. MISSION REQUIREMENTS

The results of Ch. 9 highlight that a turboelectric aircraft with distributed propulsion presents a greater advantage over conventional fuel-based aircraft for long-range missions, and for low cruise Mach numbers. However, long-haul flights at subsonic cruise speeds are not a realistic scenario due to the significant increase in travel time. Therefore, two missions are considered here. The first is the same mission investigated in Chapters 5 and 9, which corresponds to the nominal mission of an ATR 72-600 (M_{cr} = 0.41, R = 825 nmi). The second corresponds to a high-subsonic turboprop aircraft for longer ranges (see e.g. the IRON project, Refs. [266, 296]), with a cruise Mach number of M_{cr} = 0.6 and a range of R = 1500 nmi. A range of 1500 nmi is selected because over 90% of the scheduled passenger flights have ranges below this value [56, 58], and such ranges could be covered with lower Mach numbers than those of turbofan aircraft, without a significant increase in door-to-door travel time. A conventional reference aircraft and the OTWDP configuration described in the previous section are both sized for these mission requirements. In both cases, the optimum cruise altitude is selected to avoid misleading conclusions regarding the potential of distributed propulsion, as learned from Ch. 9. The optimum cruise altitudes were found to lie in the intervals of 19,000 ft – 22,500 ft and 36,000 ft – 40,000 ft for the M_{cr} = 0.41 and M_{cr} = 0.60 missions, respectively. The optimum cruise altitudes of the M_{cr} = 0.60 mission are particularly high as a consequence of the assumed drag polar, which is more representative of low-speed turboprops, and therefore presents the optimum lift-to-drag ratio at an excessively high lift coefficient for the selected wing loading and cruise Mach number. While the optimum altitude could be reduced by assuming different drag-polar characteristics for the high-speed case, this was not done in the present study to keep the input variables identical among the two missions. Additionally, for both missions, a payload of 7.5 t (approximately 75 passengers) is considered. While an increased payload may be beneficial for the longer-range mission, the sensitivity studies of Ch. 9 showed that the *change* in aircraft performance due to hybrid-electric distributed propulsion is practically insensitive to the payload weight. Therefore, the potential benefits of OTWDP that are analyzed for the chosen payload are also representative for higher payloads.

Several criteria are added to the list of mission requirements considered in previous chapters to make the design study more representative. Firstly, in addition to the take-off, cruise, landing, OEI second-segment climb, and OEI ceiling performance constraints, an all-engines operative (AEO) constraint is added following the CS 25.119 regulations [227]. This additional constraint is incorporated because initial investigations

showed that the secondary electrical machines, which are not strongly limited by OEI constraints (see Ch. 5), typically required more power throughout the nominal mission than the value computed in the power-loading diagram. Note that this may even be the case if this additional constraint—or any other—is included, depending on the power-control strategy employed in each flight condition. Moreover, a 30 minute loiter at 6,000 ft and a 5% contingency fuel reserve is added. Furthermore, energy fractions are added to account for the fuel employed during start-up and take-off (1.5%) and landing (0.5%) (see Roskam [85], Part I). Finally, the take-off constraint is computed using the approach described by Torenbeek [304] instead of the take-off parameter (TOP) used previously, assuming that all engines are operating during take-off. In this way, the take-off constraint is sensitive to aerodynamic parameters such as the lift-to-drag ratio.

10.2.2. ASSUMPTIONS REGARDING OTWDP MODELING

The effect of OTWDP is investigated predominantly from an aerodynamic perspective. In this simplified Class-I design approach, it is assumed that the structural weight of the airframe is not significantly affected by the OTWDP system. On one hand, the OTWDP system would lead to an increase in wing weight, since the flap structure must be able to withstand the forces generated by the propellers, nacelles, pylons, and (potentially) ducts, which may constitute a limiting load case in some designs. Likewise, the large pylons supporting the aft-mounted propellers are likely to be heavier than in a fully fuel-based, aft-mounted propeller configuration, since the electrical generators are housed inside the nacelle, coupled to the turboshaft engines. On the other hand, previous studies suggest that distributed-propulsion systems can reduce the wing weight due to an alleviation of the root bending moment [305], as well as the vertical tail size due to reduced OEI yawing moments and the possibility to use thrust vectoring for yaw control [51]. Here, it is assumed that these counteracting effects approximately lead to a net zero effect on the structural weight of the airframe.

For the hybrid-electric powertrain, it is assumed that inverters and rectifiers are required for DC power transmission. Table 10.1 presents the properties assumed for the powertrain components for the 2035 timeframe. The values are based on current NASA technology development goals [119] and are similar to the values used in Ch. 9. Again, for this Class-I approach a generic 30% weight penalty is added to the mass of the electrical drivetrain to account for cooling, cables, switches, and other elements of the power distribution and thermal management systems.

Table 10.1: Assumed powertrain-component properties for the design study.

Parameter	Value
Gas turbine efficiency η_{GT} [-]	0.34
Gearbox efficiency η_{GB} [-]	0.96
Electrical machine efficiency [-]	0.98
Converter efficiency [-]	0.99
PMAD efficiency η_{PMAD} [-]	0.99
Specific power of electrical machines [kW/kg]	13
Specific power of converters [kW/kg]	19
PMAD/thermal management weight penalty	30%

The changes in lift, drag, and propulsive efficiency due to the aerodynamic interaction between the OTW propellers and the wing are estimated using the numerical method described in Ch. 8. The changes in lift ΔC_L and drag ΔC_D are then added to the lift and drag of the airframe, where the latter is modeled using a symmetric parabolic polar (see Eq. 4.4, with $C_{L,\text{min}D} = 0$). To incorporate the "delta" terms in the sizing process in a computationally efficient manner, a surrogate model is constructed, as described in Appendix C.3. However, as mentioned previously, this method has several limitations. For example, it does not account for the nacelles, pylons, or duct of the OTWDP system. While it is reasonable to assume that a duct would only be included in the design if it further improves the aerodynamic characteristics of the OTWDP system, the wetted area of the nacelles and pylons is likely to lead to an increase in drag. These considerations indicate that there is some uncertainty regarding the aerodynamic modeling, and therefore in Sec. 10.3 the sensitivity of the aircraft performance metrics to the potential uncertainty in the aerodynamic model is analyzed.

One key limitation of the aerodynamic model is that it cannot account for high-lift or high-thrust conditions. More specifically, it cannot simulate flap deflection, and provides inaccurate results if flow separation occurs beneath the propellers. Thus, based on the validation study of Ch. 8, the aerodynamic model given by $[\Delta C_L,\ \Delta C_D,\ \Delta\eta_\text{P}] = \boldsymbol{f}(C_{L,\text{airframe}}, T_\text{c}, Re, M, x_\text{P}/c, D_\text{P}/c, i_\text{P})$ is limited to airframe-only lift coefficients of $C_{L,\text{airframe}} < 1$, and thrust coefficients of $T_\text{c} < 0.4$. These values are typically exceeded during the mission analysis at the start of climb, as well as for several performance constraints. In that case, the model is likely to provide conservative estimates, since the lift and drag benefits increase significantly with thrust setting. While this implies that the "delta" terms are inaccurate in these conditions, the conservative approach ensures that the overall potential of OTWDP is not over-estimated in this regard.

Furthermore, for the flight-performance constraints that are performed with the flap deflected (take-off, approach, and balked landing), several simplifying assumptions have to be made. Firstly, it is assumed that the net force produced by the propeller is approximately aligned with the propeller axis. In that case, the thrust-vectoring component $T\cos\delta_\text{P}$ contributes to the effective lift increase. Secondly, it is assumed that the stall angle of the OTWDP wing is not lower than the stall angle of the wing alone. In other words, it is assumed that the inclined propeller postpones flow separation over the (unslotted) flap sketched in Fig. 10.2, such that the maximum lift coefficient of the wing is comparable to the maximum lift coefficient of the isolated wing with the original (slotted) flap. This assumption is based on the qualitative observations of Ch. 7, though these effects have not been quantified for a specific design of the system. And finally, it is assumed that the increase in wing lift and reduction in wing drag due to the propellers, for a given angle of attack and flap deflection, is similar to the value obtained at the bounds of the surrogate model (flap retracted, $C_{L,\text{airframe}} = 1$, $T_\text{c} = 0.4$). This is again considered a conservative assumption, since the experimental results of Ch. 6 showed that, when the propeller is deflected with the flap, the ΔC_L benefit is only reduced slightly, while the pressure drag is reduced significantly (see Fig. 6.12). Although these simplifying assumptions could not be verified within the scope of this research, they should be revisited once a more detailed investigation of the high-lift characteristics has been performed.

10.3. BASELINE AIRCRAFT PERFORMANCE

In this section, the aircraft-level performance metrics of a baseline OTWDP configuration are computed. The OTWDP aircraft is first compared to a conventional twin-turboprop reference aircraft in Sec. 10.3.1. The sensitivity of the aircraft performance to the uncertainty in the aerodynamic model is then assessed in Sec. 10.3.2. The values of the OTWDP-system design parameters (i.e., geometrical parameters and the power-split strategy) selected for this baseline are provided in Table 10.2. For both the reference aircraft and the OTWDP configuration, two primary propellers are used ($N_1 = 2$). The size of these propellers is set to $D_{P1}/b = 0.146$ and $D_{P1}/b = 0.126$ for the reference and OTWDP configurations, respectively, such that both configurations have the same ratio between total propeller disk area and wing area as an ATR 72-600. For the entire mission analysis, a shaft power ratio of $\varphi = 0.5$ is assumed. Note that the thrust-vectoring angle in low-speed conditions is treated as a design variable for illustrative purposes. However, in practice, the thrust-vectoring angle would be equal to the angle of attack plus the flap deflection angle, unless a more complicated mechanism is used to provide an additional degree of freedom. Therefore, the propeller-wing-flap system would have to be designed in more detail to ensure that the flap and propeller deflection together lead to a determined overall lift coefficient. The influence of some of these design parameters are discussed in Sec. 10.4.

Table 10.2: Design-parameter values assumed for the OTWDP system in the baseline configuration.

Parameter	Value
Propeller axial position x_P/c [-]	0.8
Span-fraction covered by DP system b_{dp}/b [-]	0.53
Number of secondary propulsors N_2 [-]	24
Propeller incidence angle i_P [deg]	0
Thrust-vectoring angle, take-off $\delta_{P,TO}$ [deg]	15
Thrust-vectoring angle, landing $\delta_{P,L}$ [deg]	45
Thrust-vectoring angle, balked landing $\delta_{P,bL}$ [deg]	45
Shaft power ratio, cruise φ_{cr} [-]	0.5
Shaft power ratio, take-off φ_{TO} [-]	0.2
Shaft power ratio, landing φ_L [-]	1.0
Shaft power ratio, OEI sec. seg. climb φ_{ssc} [-]	0.5
Shaft power ratio, OEI ceiling φ_{cI} [-]	0.5
Shaft power ratio, balked landing φ_{bL} [-]	0.5

10.3.1. COMPARISON TO REFERENCE AIRCRAFT

Figure 10.3 compares the propulsive-power constraint diagram of the OTWDP aircraft to the one of the conventional reference aircraft. A comparison of Figs. 10.3a and 10.3b shows how the approach-speed constraint corresponds to higher wing loadings in the OTWDP configuration, due to the effective lift enhancement in landing conditions. Moreover, the cruise constraint allows for slightly higher power loadings in the OTWDP configuration (as observed particularly in the top-right corner of the diagrams), due to

the drag reduction of the OTW system. This cruise constraint is performed at the optimum cruise altitude for an aircraft whose wing loading equals the maximum allowed wing loading: 4.0 and 4.5 kN/m^2 for the conventional and OTWDP configurations, respectively. The contours of PREE show that the energy consumption is lowest at the design point of maximum wing loading, as observed in Ch. 9.

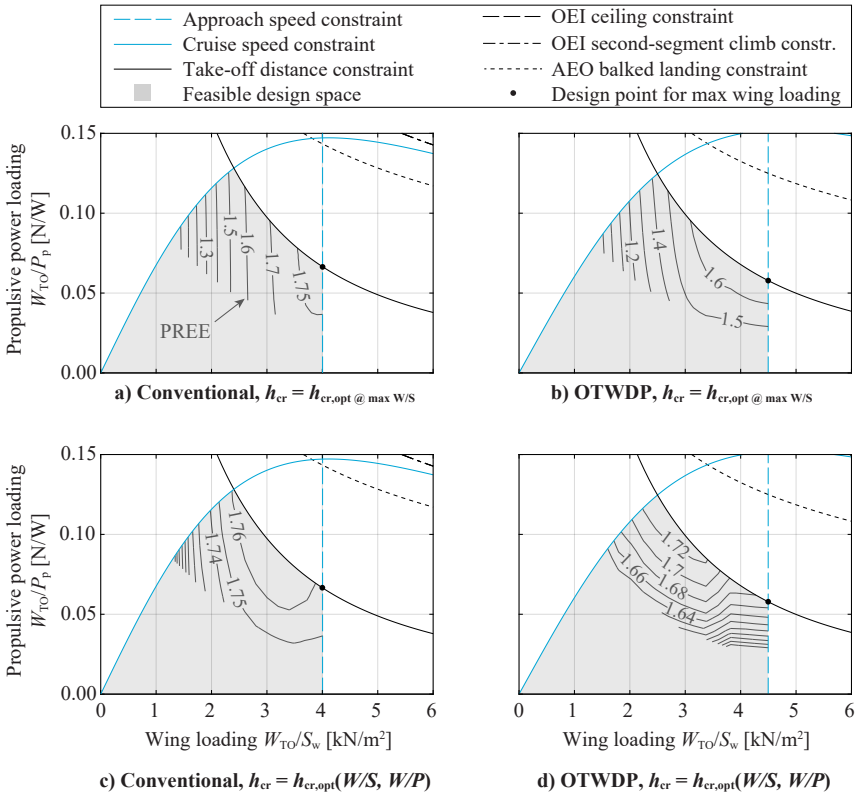

Figure 10.3: Propulsive power-loading constraint diagrams of the conventional reference aircraft (left) and the hybrid-electric OTWDP variant (right), including contours of PREE obtained in the feasible design space for a fixed (top) and optimized (bottom) cruise altitude ($M_{cr} = 0.41$).

However, if the optimum cruise altitude is selected for each feasible combination of wing- and power loading, the PREE contours of Figs. 10.3c and 10.3d are obtained instead. Note that the cruise constraint at the original cruise altitude of Figs. 10.3a and 10.3b is shown in the diagram, though in reality the constraint varies depending on the cruise altitude and, hence, on the selected combination of W_{TO}/S_w and W_{TO}/P_p. For lower wing-loading values, the optimum cruise altitude is higher, and thus the actual cruise constraint is less restrictive than the one depicted. In any case, the PREE contours show that the optimum design point changes significantly in this case. Since the cruise altitude is adapted for each wing loading such that the aircraft operates near the optimum lift-to-drag ratio, the power loading plays a larger role in the location of the op-

timum design point. This is especially evident for the OTWDP configuration (Fig. 10.3d), where the optimum design point in terms of PREE corresponds to a very low wing loading (i.e., a very large wing) and a very high power loading (i.e. a relatively small powertrain). This effect is more prominent in the OTWDP configuration due to the high powertrain weight fraction for this configuration. In practice, there would be a lower bound on the feasible wing loading, since the wing span is limited by the airport gate category, and the cruise altitude may be restricted by air-traffic constraints. In that case, the characteristics of the drag polar (e.g., $C_{L,\min D}$) would be adapted to ensure that optimum design point is found at feasible wing-loading values. Given that numerous factors play a role in the location of the optimum design point, the one corresponding maximum wing loading is selected here for further analysis of the baseline configuration. This design choice will be varied in Sec. 10.4.

The corresponding component power-loading diagrams of the gas turbine and electrical machines are shown in Fig. 10.4. For both the conventional and OTWDP aircraft,

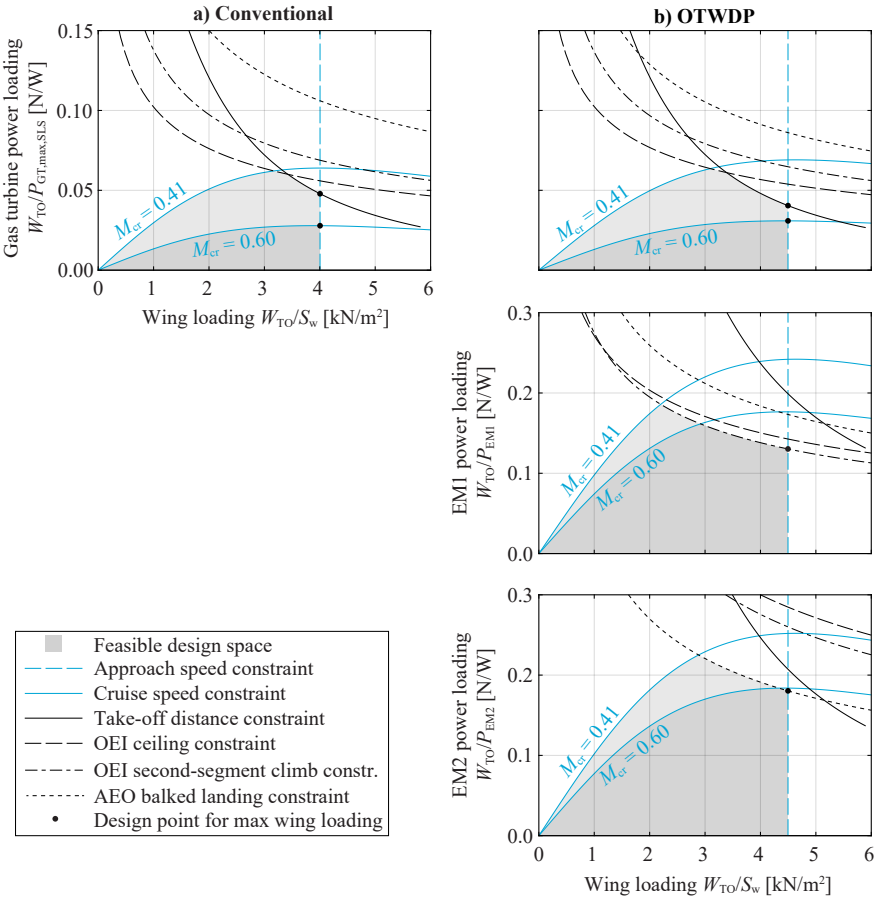

Figure 10.4: Component power-loading constraint diagrams of the conventional reference aircraft (left) and the hybrid-electric OTWDP variant (right).

the gas turbine is sized by the take-off requirement for the $M_{cr} = 0.41$ mission, but by the cruise-speed requirement for the $M_{cr} = 0.60$ mission. The gas-turbine power loading of the OTWDP configuration is lower than the conventional configuration because it has to compensate the power that is dissipated in the electrical drivetrain. This shows that the aerodynamic benefits of the OTWDP system during take-off do not outweigh the losses in the electrical components. For this reason, a relatively low power share is used during take-off ($\varphi_{TO} = 0.2$), and the electrical machines are not actively constrained by the take-off condition. Instead, Fig. 10.4b shows that the generators (EM1) are sized by the second-segment-climb constraint in case of component failure, since there are only two generators, and thus they have to be over-sized by a factor 2. The electrical motors (EM2), on the other hand, are not limited by the OEI constraints, since there are numerous motors, and in this simplified analysis it is assumed that only one of them fails in the OEI scenario. Hence, they are sized by the balked-landing constraint.

The aerodynamic, propulsive, and overall efficiency obtained throughout the nominal mission for the design point of maximum wing loading are shown in Fig. 10.5. Figure 10.5a shows that, for the selected OTWDP geometry, the interaction with the wing leads to an appreciable increase in lift-to-drag ratio during climb and cruise. The average propulsive efficiency of the OTWDP aircraft is comparable to the conventional one, being marginally higher during climb due to the higher thrust setting, while being slightly lower during cruise. Note that several factors play a role in the average propulsive efficiency: the efficiency of the primary (tail-mounted) propellers, the isolated-propeller efficiency of the OTWDP system, the change in efficiency of the OTWDP system due to interaction with the wing, and the power split between the two propulsion systems, φ. For this comparison, the same total disk area is assumed for the OTWDP and conventional configurations. Therefore, the primary propellers of the OTWDP aircraft are smaller than the ones of the conventional aircraft. If they would be the same size, then the overall disk loading of the OTWDP configuration would be lower, leading to a slight increase in propulsive efficiency. Finally, when considering the changes in lift-to-drag

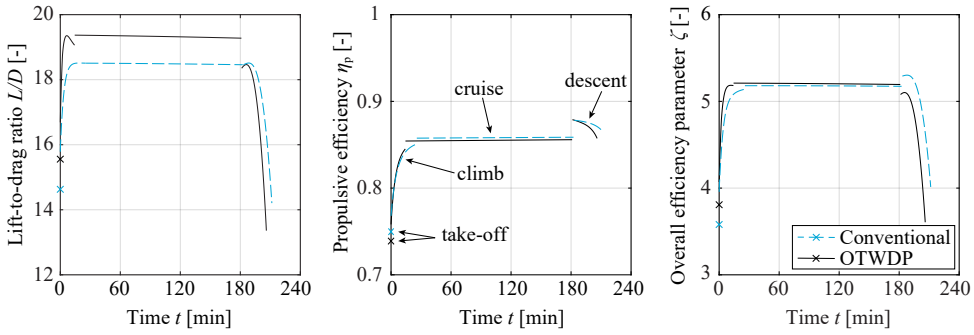

a) Lift-to-drag ratio **b) Propulsive efficiency** **c) Overall efficiency**

Figure 10.5: Aerodynamic, propulsive, and overall efficiencies throughout the nominal mission ($M_{cr} = 0.41$, $R = 825$ nmi). Take-off values correspond to V_2 (i.e., after liftoff). Diversion and loiter not shown.

ratio, propulsive efficiency, and powertrain efficiency, the overall efficiency benefit of OTWDP is marginal for the assumed design parameters and component technology levels (Fig. 10.5c). It is highest during climb, due to the increase in L/D and η_p at higher thrust settings.

The resulting weight breakdown of the two configurations is reflected in Fig. 10.6. The figure shows that, for both sets of mission requirements, the minor increase in overall efficiency due to OTWDP is insufficient to offset the increase in take-off weight, and thus the fuel consumption is slightly higher (in an absolute sense) for the OTWDP configuration. The weight increase is a result of adding the electrical components on one hand, and of requiring a larger gas turbine to offset the losses in the electrical drivetrain (see Fig. 10.4) on the other. Nevertheless, the differences in take-off mass and energy consumption between the baseline OTWDP aircraft and the reference aircraft are relatively small.

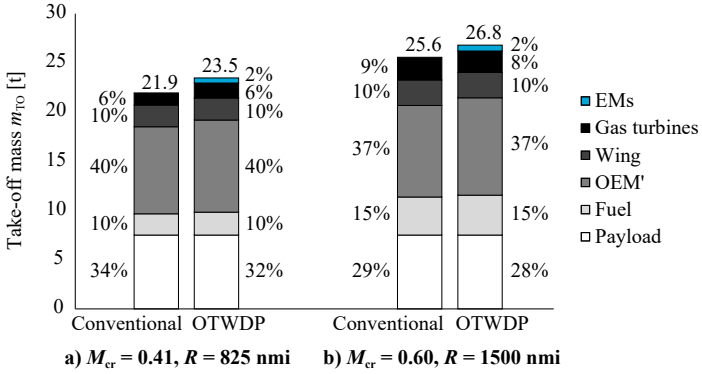

Figure 10.6: Mass breakdown of the conventional and OTWDP configurations, for the short and long-range missions. Values are expressed in metric tons and as a percentage of take-off mass.

10.3.2. SENSITIVITY TO UNCERTAINTY IN AERODYNAMIC MODELING

The changes in lift, drag, and propulsive efficiency present some uncertainty for several reasons. Firstly, for a given geometry of the wing and OTW propellers, the numerical model itself presents a determined uncertainty (see Ch. 8), due to the assumptions made in the formulation (modeling error) and the numerical implementation (discretization and convergence errors) of the method. A comparison to experimental data showed that it tends to under-estimate the lift and drag benefits, while over-estimating the propulsive efficiency. Secondly, to apply this numerical method, several simplifying assumptions have been made regarding the geometry of the system. Some of these simplifications are likely to contribute to optimistic results (e.g., neglecting nacelles or pylons), some contribute to conservative results (e.g., using a generic, un-optimized wing and propeller geometry), and for others the effect on overall performance is not fully clear (e.g., the incorporation of a duct). These simplifications are especially important in high-lift conditions, where several additional assumptions have to be made for the method to be applicable in the preliminary sizing phase (see Sec. 10.2).

Therefore, to understand how sensitive the aircraft-level performance metrics are to these uncertainties, two hypothetical limit cases are considered: a "conservative" scenario, and an "optimistic" scenario. For the former, the change in lift, drag, and propulsive efficiency are simultaneously decreased, increased, and decreased, respectively. For the optimistic scenario, the opposite is done. For the sectional changes in lift and drag, the deviations from experimental data (approximately $\Delta c_l \pm 0.02$, $\Delta c_d \pm 0.001$) and from the asymptotic value observed in the convergence study (approximately $\Delta c_l \pm 0.01$, $\Delta c_d \pm 0.0005$) are considered. These values are scaled by the factor b_{dp}/b (Table 10.2) to convert them into three-dimensional force coefficients, ΔC_L and ΔC_D. For the propulsive efficiency, the indicative error band of $\Delta\eta_{\text{p}} \pm 0.01$ discussed in Sec. 8.3 is used. An overview of these values is provided for the two scenarios in Table 10.3.

Table 10.3: Modifications made to the "delta" terms to analyze the sensitivity to uncertainty in the aero-propulsive model.

		Scenario 1 (conservative)	**Scenario 2 (optimistic)**
ΔC_L	=	$\Delta C_{L,\text{computed}} - 0.016$	$\Delta C_{L,\text{computed}} + 0.016$
ΔC_D	=	$\Delta C_{D,\text{computed}} + 0.0008$	$\Delta C_{D,\text{computed}} - 0.0008$
$\Delta\eta_{\text{p}}$	=	$\Delta\eta_{\text{p,computed}} - 0.01$	$\Delta\eta_{\text{p,computed}} + 0.01$

Figure 10.7 presents the aircraft performance indicators for the conservative, baseline, and optimistic scenarios. All values are normalized with the corresponding parameter of the conventional reference aircraft. The parameters L/D, η_{p}, and ζ correspond to average values obtained throughout nominal mission; i.e., diversion and loiter are not included in the metric. Fig. 10.7a shows that the L/D benefit at aircraft level is doubled and reduced to practically zero for the optimistic and conservative scenarios, respectively. For both sets of mission requirements, the average propulsive efficiency is

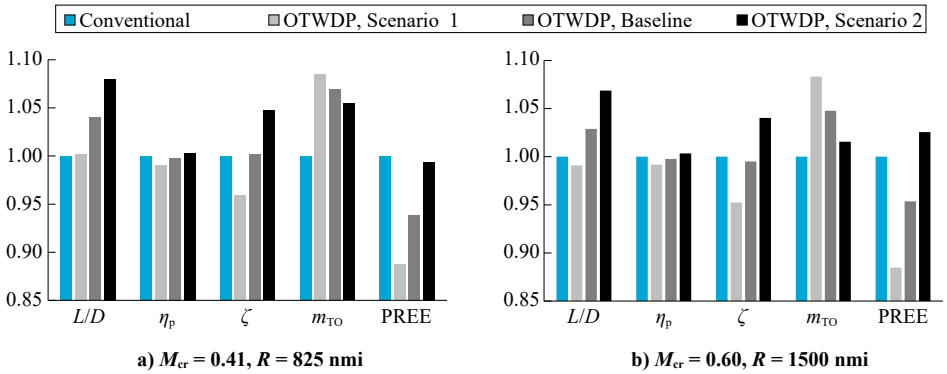

Figure 10.7: Effect of aerodynamic-model assumptions on aircraft performance parameters. All values are normalized with the corresponding reference-aircraft values.

slightly higher than the reference aircraft in the optimistic scenario, while being lower in the baseline and conservative scenarios. These differences cascade into an overall variation of the PREE of approximately ±5%, depending on the mission. The changes in PREE are higher for the long-range mission because the fuel-weight fraction is higher and the aero-propulsive benefit is exploited for a longer duration. Although these variations in PREE (±5%) and take-off mass (±3%) do not represent a specific confidence interval, they can be considered a conservative indication of the potential error due to uncertainty in the aerodynamic modeling.

10.4. INFLUENCE OF OTWDP DESIGN PARAMETERS

The OTWDP design-parameter values of the baseline configuration analyzed in the previous section were generically selected without any systematic sensitivity or optimization study. While they provide insight into some of the key effects of OTWDP at aircraft level, they do not indicate the actual benefit that can be obtained from these systems. The purpose of this section is to investigate how the aircraft-level performance metrics are affected by these parameters. The parameters are divided into two groups: those that define the geometry of the OTWDP system, and those that define the power-split strategy. These two categories are discussed in the two following subsections, respectively. Finally, in the last subsection, the overall performance of the aircraft with the best combination of OTWDP design-parameter values is discussed.

10.4.1. GEOMETRICAL PARAMETERS

To investigate the effect of the top-level parameters that describe the geometry of the OTWDP system, the first seven parameters of Table 10.2 are varied: the axial propeller position, the span-fraction covered, the number of propellers, the propeller incidence angle, and the thrust-vectoring angle in the take-off, landing, and AEO balked landing constraints. A design-of-experiments (DoE) is performed by distributing 1,000 points equally among all dimensions using a Latin-hypercube sampling. The OTWDP aircraft is then sized for the short-range mission ($M_{cr} = 0.41$, $R = 825$ nmi) for each combination of parameters. The values of these parameters are limited to the bounds specified in Table D.16 of the Appendix. The aerodynamic efficiency, propulsive efficiency, take-off weight, and payload-range energy efficiency of the resulting designs are gathered in Fig. 10.8. Note that L/D and η_p correspond to the average values obtained throughout the nominal mission.

Figure 10.8a shows that, even though the design parameters have been limited to "reasonable" bounds, changes in the design of the system can have a significant impact on the aero-propulsive efficiency of the aircraft. The trends observed at subsystem level (Ch. 8) also apply at aircraft level; for example, a more aft OTW propeller position increases the average η_p of the aircraft, but leads to a lower lift-to-drag ratio. Lower propeller incidence angles are also found to increase the average propulsive efficiency. An increase in the span fraction b_{dp}/b, meanwhile, increases the relative influence of the OTWDP system on the overall aerodynamic characteristics of the aircraft, and consequently has a clearly distinguishable effect on the overall energy consumption.

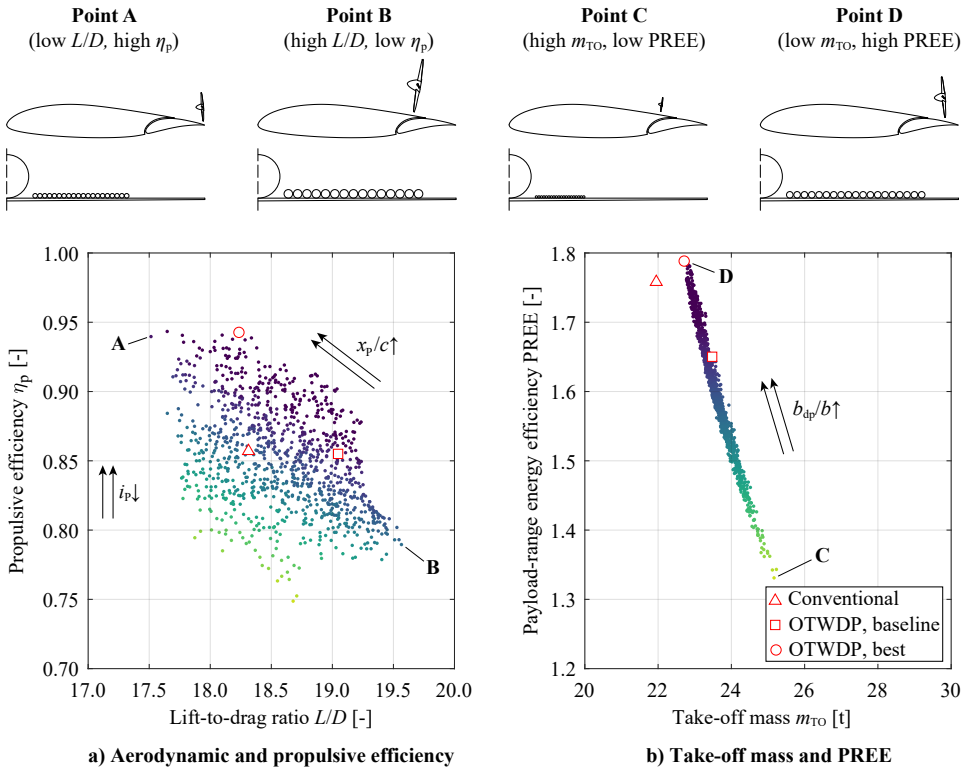

Figure 10.8: Top-level aircraft performance metrics for various combinations of OTWDP geometrical design-parameter values, as obtained from the DoE. Darker colors indicate higher PREE values. Top sketches indicate the size and position of the OTWDP array, for four specific data points. $M_{cr} = 0.41$, $R = 825$ nmi.

To illustrate these effects, four examples are shown on the top Fig. 10.8. The point with lowest L/D, Point A, also presents roughly the maximum η_p benefit. This design corresponds to a relatively small propeller placed near the trailing edge of the wing, with a small nose-down angle. In this case, a very high average propulsive efficiency can be achieved due to a combination of several factors: the reduction in local velocity near the trailing-edge stagnation point, a small angle-of-attack effect on the propeller which contributes to an increased thrust along the freestream direction, and a decreased disk loading due to a higher total disk area of the aircraft. The opposite occurs for Point B, where a series of larger propellers are placed further forward along the chord, and along a large fraction of the wing span. In this case, the lift-to-drag ratio is increased by 7% relative to the conventional aircraft, while the propulsive efficiency is reduced by approximately 9%. The design with the lowest PREE (Point C), on the other hand, corresponds to an array of small propellers placed upstream of the flap, covering a relatively small portion of the wing. Finally, the design which leads to the lowest energy consumption (Point D) corresponds to an array which covers a large portion of the wing, with propellers that present a negative incidence angle, and whose axial position is a compromise between the propulsive-efficiency gain obtained near the trailing edge, and the drag reduction obtained at more forward positions.

10.4.2. POWER-CONTROL STRATEGY

The power-control parameters of a PTE architecture are the gas-turbine throttle and the shaft power ratio. The former determines roughly how much thrust the propulsion system produces, while the latter determines the thrust share between the primary propellers and the OTWDP system. Therefore, for a given thrust setting, the shaft power ratio affects the aero-propulsive efficiency of the aircraft. To investigate the effect of the shaft power ratio φ, a DoE with 1,000 data points is performed similarly to the previous section. In this DoE, the φ values of the six performance constraints and of the climb, cruise, descent, and loiter phases of the mission analysis are varied between 0 and 1. A linear evolution of φ is assumed for each mission segment, and the same values are applied for the nominal mission and the diversion. The full list of variables is provided in the Appendix (Table D.16). In this analysis, the geometrical design parameters of the baseline configuration are maintained (i.e. the best results of the previous section are not used as starting point).

Figure 10.9 shows the aircraft performance metrics obtained for each combination of shaft power ratios. For this OTWDP system geometry, the propulsive efficiency of the aircraft does not vary significantly with φ, when compared to the effect of the geometrical design parameters (Fig. 10.8a). However, the lift-to-drag ratio does vary, and is particularly sensitive to the shaft power ratio during cruise. This occurs because higher φ_{cr} values lead to higher OTWDP-system thrust coefficients during cruise, and therefore to an increase in L/D during a large part of the mission. Nevertheless, the colors of the data points show that higher a L/D does not necessarily correspond to a more efficient aircraft in terms of the PREE. The reason for this is that the shaft power ratio not only affects the aero-propulsive efficiency throughout the mission, but also the power require-

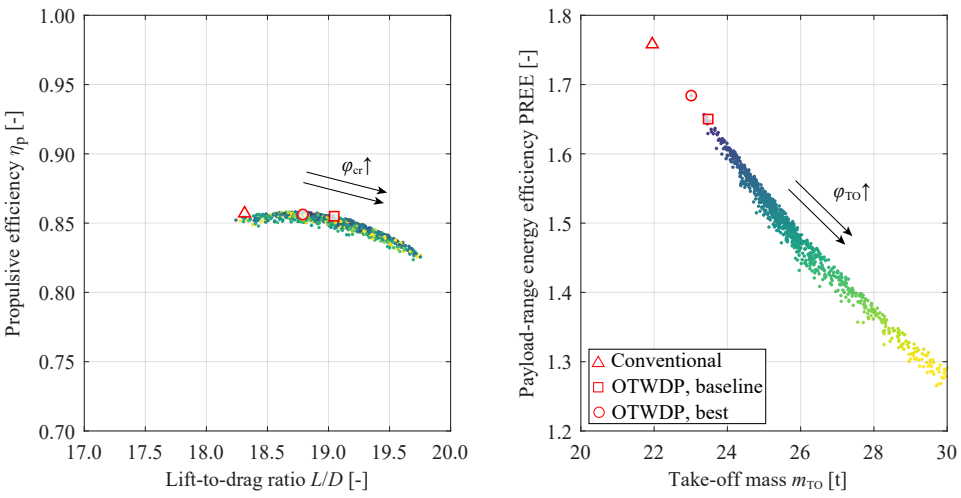

a) Aerodynamic and propulsive efficiency **b) Take-off mass and PREE**

Figure 10.9: Top-level aircraft performance metrics for various combinations of shaft power ratio φ, as obtained from the DoE. Darker colors indicate higher PREE values. $M_{cr} = 0.41$, $R = 825$ nmi.

ments of the powertrain components in the constraint diagrams. Therefore, the take-off mass of the aircraft is much more sensitive to changes in the power-control strategy (Fig. 10.9b) than to changes in the geometrical parameters of the OTWDP system (Fig. 10.8b). The shaft power ratio during take-off is found to have a particularly large influence on the take-off mass and, consequently, on the PREE, since in many cases the take-off is the limiting constraint for the powertrain components.

In Fig. 10.9a, the lift-to-drag ratio is more sensitive to the power-control strategy than the average propulsive efficiency. However, a different trend may be observed for a different geometry if, for example, small propellers are placed close to the trailing edge. To ensure that the overall performance comparison between the OTWDP configuration and the reference aircraft is representative, a third and final DoE is performed, where both the geometrical and power-control parameters are varied simultaneously. In this case, the wing loading is also treated as a design variable, since the results of Fig. 10.3 show that the OTWDP configuration may present a strongly sub-optimal performance at maximum wing loading. Additionally, the span-fraction of the OTWDP system is kept constant and equal to the baseline value, since in this Class-I approach the optimum would be $b_{dp}/b = 1$, but this is unfeasible due to the space required for the fuselage and ailerons. This leads to a total of 21 design variables, which can be found in Table D.16 of the Appendix. The resulting design with maximum PREE is selected for further analysis. For simplicity, that design is referred to as the "optimum" in subsequent paragraphs; however, it should be noted that this corresponds to a well-performing design (as was confirmed in posterior manual evaluations), and not to a global optimum. Also note that the conventional reference aircraft is kept constant, since all design variables are only applicable to the OTWDP system. One exception is the design wing loading, but a different wing loading would lead to only minor improvements in PREE for the conventional aircraft, as reflected in Fig. 10.3c.

The best-performing power-control strategy obtained from the DoE is shown in Fig. 10.10. The optimal shaft power ratio during take-off is comparable to the baseline value, remaining around 0.2 in order to limit the power required from the electrical components in the sizing condition. The shaft power ratio in the OEI second-segment climb, OEI ceiling, and balked landing constraints are lower than in the baseline configuration. This occurs because, in the baseline configuration, the electrical machines are sized by these performance constraints (see Fig. 10.4). However, these requirements can be alleviated by requesting more power from the primary propellers without affecting the gas-turbine size, which is limited by the take-off constraint. The shaft power ratio is also reduced in the landing constraint, which leads to a lower maximum wing loading. This does not adversely affect the aircraft performance because the optimum wing loading is below the maximum wing loading. In other words, the shaft power ratio and thrust vectoring angle during landing do not affect the overall aircraft performance. In practice, this would imply that a smaller high-lift system could be used without a reduction in aircraft performance, i.e. $C_{L\text{max,airframe}}$ can be reduced until the optimum design wing loading equals the maximum allowable wing loading. Analogously, since the powertrain is sized during take-off, the shaft power ratio in the cruise constraint does not actively limit the powertrain size. Consequently, during the climb and cruise phases of the mission analysis, the shaft power ratio can be increased slightly to enhance the aero-

propulsive benefits without exceeding the installed power of the electrical components. Finally, during descent, the shaft power ratio tends towards the upper bound, though it has a negligible impact on the overall energy consumption since the thrust setting, and therefore fuel consumption, is minimal during descent.

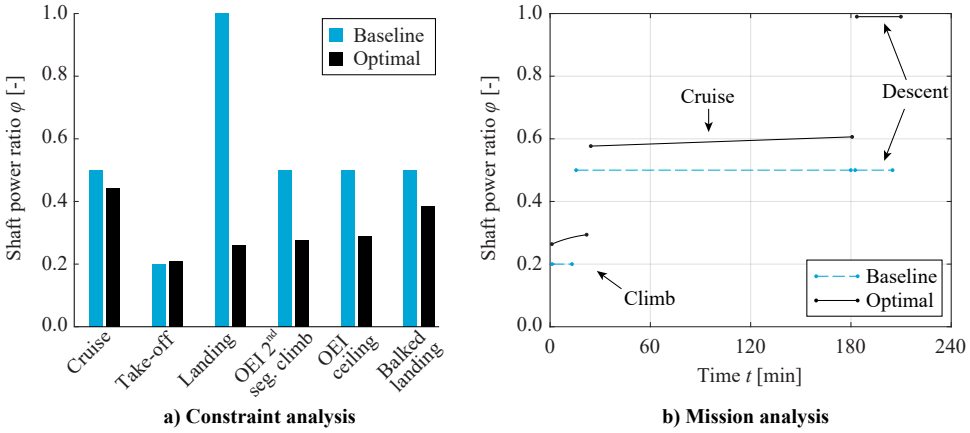

Figure 10.10: Comparison of shaft-power-ratio values obtained for the OTWDP configuration in the performance constraints (left) and throughout the nominal mission (right). $M_{cr} = 0.41$, $R = 825$ nmi.

10.4.3. OVERALL PERFORMANCE COMPARISON & DISCUSSION

To provide a concluding discussion regarding the potential of OTWDP systems for regional transport aircraft, Table 10.4 compares the design parameters and aircraft-level performance metrics of the baseline and optimized OTWDP configurations to the reference aircraft. Additional characteristics can be found in Table D.15 of the Appendix. The optimal axial position and number of OTW propellers do not lie on the variables' bounds ($0.75 < x_P/c < 1.00$, $20 < N_2 < 40$), indicating that the correct part of the design space has been explored in the DoE and in Ch. 8. This also suggests that larger OTW propellers are not necessarily better from an aero-propulsive perspective, contrary to what was initially hypothesized. While larger propellers would have a higher isolated-propeller efficiency for the same total thrust requirement, the higher thrust coefficients required from smaller propellers enhance the $\Delta\eta_p$, ΔC_L, and ΔC_D terms, which appears to outweigh the benefits associated to a lower disk loading. This is reflected in the average thrust coefficient of all propellers throughout the mission, $T_{c,mean}$: while in the baseline OTWDP configuration it is 4%–6% lower than the conventional aircraft due to the reduced drag, in the optimized configuration it is increased by roughly 3% because the OTW propellers are purposely operated at a higher thrust setting during cruise. Moreover, the results show that, for the given approach speed requirement and assumed $C_{Lmax,airframe}$, the thrust-vectoring during the (balked) landing is not necessary. This is a consequence of the higher HEP-component power loadings that can be achieved at lower wing loadings, as discussed earlier.

Table 10.4: Results of the OTWDP design-parameter optimization study. Percentages expressed relative to the conventional aircraft for the same mission.

	Conventional Aircraft		**Baseline OTWDP**		**Optimal OTWDP**	
M_{cr} [-]	0.41	0.60	0.41	0.60	0.41	0.60
R [nmi]	825	1500	825	1500	825	1500
x_P/c [-]	-	-	0.80	0.80	0.776	0.782
N_2 [-]	-	-	24	24	36	32
D_P/c [-]	-	-	0.25	0.25	0.17	0.19
i_P [deg]	-	-	0	0	-5	-5
$\delta_{P,TO}$ [deg]	-	-	15	15	0.2	27.9
$\delta_{P,L}$ [deg]	-	-	45	45	21.2	44.2
$\delta_{P,bL}$ [deg]	-	-	45	45	20.8	21.7
W_{TO}/S_w [kN/m^2]	4.00	4.00	4.50 (+12%)	4.50 (+12%)	4.04 (+0.9%)	3.91 (-2.4%)
$T_{c,mean} \times 10$ [-]	1.13	1.09	1.06 (-5.9%)	1.05 (-4.0%)	1.17 (+3.4%)	1.12 (+2.8%)
L/D [-]	18.3	18.4	19.0 (+4.0%)	18.9 (+2.9%)	19.4 (+5.8%)	19.0 (+3.4%)
η_P [-]	0.86	0.86	0.86 (-0.2%)	0.86 (-0.2%)	0.91 (+6.0%)	0.90 (+5.0%)
η_{PT} [-]	0.33	0.33	0.32 (-3.4%)	0.32 (-3.1%)	0.31 (-4.3%)	0.32 (-3.4%)
ζ [-]	5.12	5.14	5.13 (+0.2%)	5.11 (-0.5%)	5.50 (+7.3%)	5.39 (+4.8%)
m_{TO} [t]	21.9	25.6	23.5 (+7.0%)	26.8 (+4.8%)	22.4 (+2.1%)	25.5 (-0.5%)
PREE [-]	1.76	1.56	1.65 (-6.1%)	1.49 (-4.6%)	1.84 (+4.6%)	1.64 (+4.8%)

Table 10.4 shows that the average lift-to-drag ratio and propulsive efficiency of the "optimized" OTWDP aircraft are approximately 6% higher than the reference aircraft, for the short-range mission. The benefits are reduced to 3.4% and 5% respectively, for the long-range mission. Part of these benefits are forfeited in the transmission losses of the electric drivetrain, leading to an overall increase of 7.3% and 4.8% in ζ for the short- and long-range missions, respectively. For the short-range mission, a portion of this benefit is required to compensate the increase in aircraft weight due to the hybrid-electric powertrain. In total, this leads to a roughly 2% increase in take-off mass, while the PREE is improved by 4.6%. For the long-range mission, the increase in powertrain weight is compensated by the reduction in fuel weight, and therefore the take-off mass is similar to the reference aircraft. In this case, a PREE increase of approximately 5% is achieved. The range of shaft power ratios ($0.2 < \varphi < 0.5$), changes in aero-propulsive efficiency (9%–12%), and changes in PREE ($\sim 5\%$) obtained in this study are also in line with the values expected from Ch. 9, confirming that the additional simplifications made in the design-space exploration studies of the previous chapter are valid.

These results indicate that hybrid-electric configurations with OTWDP can reduce the energy consumption of regional transport aircraft for the 2035 timeframe. However, a 5% reduction in energy consumption is most likely insufficient to justify a radical change in the overall layout of the aircraft. Furthermore, the sensitivity analysis of Sec. 10.3.2 suggests a PREE uncertainty of approximately ±5% due to uncertainty in the aerodynamic modeling of the OTWDP system alone. Hence, additional detailed studies on a particular OTWDP-system design would be required to determine whether the PREE benefit lies closer to 0%, or to 10%. Moreover, the configuration analyzed in this study (Fig. 10.1) presents a relatively large center-of-gravity excursion, which is not

modeled in the present Class-I approach and may be a disadvantage compared to conventional, wing-mounted propeller configurations. Thus, a more detailed, Class-II design loop is required to assess the performance benefit more accurately. Nevertheless, the findings show that the aerodynamic benefits at subsystem level can indeed lead to a benefit at aircraft level. Based on these considerations and the lessons learned in the previous chapters, the following scenarios are identified as potential configurations where OTWDP may play a role in the future:

- **High-efficiency regional transport**: a regional aircraft with OTWDP could present a more significant reduction in energy consumption if the aero-propulsive benefits are increased beyond the ones estimated in this study. This may be achieved with a more optimal design of the OTWDP geometry, or if the full span of the wing can be covered without significant penalties in the structural weight or stability and control of the aircraft. Advancements in HEP-component technology also play an important role in this sense, since the PREE benefits increase significantly with the efficiency and specific power of the electrical components (see Ch. 9). Moreover, as the aviation industry gains experience with the operation and certification of (hybrid-) electric powertrain components for smaller aircraft, the entry barriers for such technologies for larger regional aircraft will be reduced.

- **Low-noise regional transport**: this is considered separately from the previous point, since the optimum OTWDP design in terms of aerodynamic efficiency (propellers near trailing edge) is likely to differ considerably from the optimum design in terms of community noise. However, if the propellers are ducted and placed more forward to exploit the shielding capabilities of the wing, a low-noise configuration may be achieved. In that case, the primary propellers would also have to be installed in a low-noise configuration; for example, above a U-tail [306] or as ducted propellers [175, 176]. Another advantage of OTWDP in this regard is the reduced diameter of the primary propellers when compared to a twin-turboprop with the same total disk area (see Table D.15), which can lead to lower blade-tip Mach numbers.

- **Small fully-electric aircraft**: if smaller, fully-electric aircraft are used in the future for inter- or intra-city transport due to lower operating costs or the absence of in-flight emissions, then considerations such as STOL capabilities or flyover noise will play a relatively larger role [307]. In that case, OTWDP can present several advantages over conventional or LEDP configurations, without significantly increasing the weight of the already electric powertrain. In addition to a potential increase in cruise performance, OTWDP can increase the high-lift capabilities by deflecting the propeller and flap and, in a limit case, enable VTOL operations. Furthermore, the noise shielding can be an important advantage over leading-edge configurations when operating close to urban areas. Depending on the type of runway, the improved shielding from foreign-object damage (FOD) may also constitute an additional benefit. Also for these applications it is important to keep in mind that the optimal OTWDP designs in terms of cruise performance, high-lift performance, and noise production are likely to differ considerably, and therefore not all benefits can be maximized simultaneously.

- **Long-haul transport**: the results of this chapter and the previous one confirm that the increased aero-propulsive benefit leads to a larger benefit at aircraft level for longer ranges. However, long-haul missions typically require transonic cruise speeds. In these conditions, OTWDP would require divergent ducts and present significant challenges due to shock formation on the upper side of the wing [152]. However, for very low diameter-to-chord ratios, it may still provide benefits. This may be possible, for example, in a blended-wing-body configuration [295]. However, in that case, the diameter of the propulsors is comparable to the height of the boundary layer, and many of the aerodynamic observations made in the present study no longer hold or are no longer dominant. Instead, more attention has to be paid to the boundary-layer ingestion effects.

11

CONCLUSIONS AND RECOMMENDATIONS

The objective of the research presented in this dissertation is to answer the question:

What are the effects of over-the-wing distributed-propulsion on the energy efficiency of hybrid-electric aircraft?

The previous chapters have presented a series of theoretical, experimental, and numerical investigations that aim to answer this question. Some of these investigations were more fundamental in nature, while others were more applied and focused on the particular combination of hybrid-electric propulsion, distributed propulsion, and over-the-wing propulsion. In this final chapter, the key findings of these investigations are summarized. Moreover, several open questions are highlighted, which serve as recommendations for future research.

11.1. CONCLUSIONS

The research performed to answer the question above is divided into three main blocks: the development of a conceptual sizing method for hybrid-electric distributed-propulsion (HEDP) aircraft, an investigation into the aerodynamic interaction effects between the components of an OTWDP system, and an aircraft-level assessment of the aerodynamic benefits of OTWDP. These blocks correspond to Parts II, III, and IV of this dissertation, and their main findings are presented in the following subsections, respectively.

11.1.1. THE SIZING PROCESS OF HYBRID-ELECTRIC AIRCRAFT

A sizing method for the conceptual design of aircraft with hybrid-electric or distributed-propulsion systems has been developed. The method is intended for fixed-wing aircraft, with a focus on tube-and-wing configurations. The formulation of this method shows that:

- The three main steps of traditional Class-I sizing methods (performance constraint analysis, mission analysis, and weight estimation) are also applicable to HEDP aircraft, though they have to be modified to account for two factors: aero-propulsive interaction effects, and the additional components of the hybrid-electric powertrain.
- The aero-propulsive interaction effects of distributed-propulsion systems can be accounted for by including a series of "delta" terms in the basic point-performance equations of the aircraft. These terms represent the changes in lift, drag, and propulsive efficiency of the aircraft due to the aerodynamic interaction between the propulsors and the airframe, and must be estimated as a function of top-level, non-dimensional parameters using simplified methods.
- Conventional, series, parallel, partial turboelectric, fully-turboelectric, and fully-electric propulsion-system architectures can all be represented as limit cases of a generic "series/parallel partial hybrid" architecture if the powers produced are specified by means of three power-control parameters: the supplied power ratio, the shaft power ratio, and the throttle setting.
- If constant transmission efficiencies are assumed for the powertrain components, the powers produced by each component of a generic HEP architecture can be computed for a given propulsive-power requirement or power-control strategy by inverting a single matrix representing a set of linear equations.
- Different components of a HEP powertrain are generally sized in different flight conditions, and therefore a power-loading diagram is required for each component, instead of the single power-loading diagram used in traditional sizing methods.
- The energy requirements of HEP aircraft can be estimated using an analytical range equation. However, for this, constant power-control parameters have to be assumed, which leads to unrealistic results. Therefore, a time-stepping mission analysis is recommended in the preliminary sizing phase.

To verify that the method was correctly formulated and implemented, a verification study was performed by comparing the results to a separate, independently-developed HEP aircraft sizing method. In this study, both methods were first used to size a 19-seater commuter aircraft, and results were compared to existing reference data. Then, a series of hybrid-electric variants, without distributed propulsion, were sized and the two methods were contrasted against each other. This comparison showed that:

- For the conventional aircraft, both methods deviate from the reference data by less than 4% in terms of maximum take-off mass.
- The trends in take-off mass and payload-range energy efficiency (PREE) obtained from the two methods when varying mission range, battery technology level, or the hybridization ratio, match each other and match the trends expected from literature.

- The results of the serial and parallel architectures tend towards those of the conventional, turboelectric, or fully-electric architectures in the limit cases of "0% hybridization" and "100% hybridization", confirming that the aforementioned matrix representation of a generic HEP powertrain is consistent.
- When comparing the hybrid- and fully-electric aircraft configurations obtained from the two methods, differences of up to 2% in take-off mass and 5% in PREE are found, relative to each other.

This verification study confirmed that the sizing method is capable of modeling hybrid-electric aircraft without aero-propulsive interaction effects. To ensure that the method also provides confident results for configurations with significant aero-propulsive coupling, the aero-propulsive models must be validated on a case-to-case basis. To understand how these interaction effects influence the design of the aircraft, a regional aircraft with leading-edge distributed propellers was sized and compared to a conventional twin turboprop. This demonstrated that:

- The shaft power ratio and supplied power ratio play a fundamental role in the weight of the propulsion system, since each component can be sized by a different flight condition, and the power required for each flight condition depends on these variables.
- The lift enhancement provided by leading-edge distributed propulsion during approach leads to a significant increase in wing loading (+50%). However, there is an optimum wing loading for a given cruise altitude, speed, and drag polar, and thus excessive lift enhancement during approach can be detrimental for the overall energy consumption.
- In this particular study, the serial and partial-turboelectric (PTE) configurations present an increase in cruise lift-to-drag ratio of roughly 6% due to the increased wing loading. However, the increase in powertrain weight—particularly for the serial configuration—leads to an increase in energy consumption of 40% and 3% for the serial and PTE configurations, respectively.

11.1.2. PROPELLER INTERACTION EFFECTS IN OTWDP SYSTEMS

The design considerations and typical operating conditions obtained from the previous HEDP aircraft design study were used as a starting point for the detailed aerodynamic analyses. The purpose of these analyses was to gain a more fundamental understanding of the flow phenomena that take place when a propeller operates in close proximity to other elements of an OTWDP system, such as the wing, duct, or adjacent propellers. Given that these interaction effects are unsteady, three-dimensional, and viscous in nature, a predominantly experimental approach was selected for these investigations. These investigations were complemented with high-fidelity numerical analyses to obtain more detailed information regarding the flow field in case of complex geometries, and with a low-fidelity numerical analysis to rapidly estimate the effect of geometrical parameters that could not be varied easily in an experiment. The key takeaways of these aerodynamic investigations are divided into four categories: propeller–wing interaction

in cruise conditions, propeller–wing interaction in high-lift conditions, propeller–duct interaction, and propeller–propeller interaction.

PROPELLER–WING INTERACTION IN CRUISE CONDITIONS

Three different experimental setups were employed to investigate the propeller–wing aerodynamic interaction in cruise lift and thrust settings: one focusing on the effect of a single propeller on the wing, one focusing on the effect of a wing on a single propeller, and one investigating the two-way interaction between a wing and three propellers. The experimental data were used to validate a low-fidelity numerical method, which was in turn used to perform sensitivity studies and complement the experimental data. The results showed that the OTW propeller(s) had the following effects on the wing:

- When a single propeller is placed above a wing, the velocities induced by the propeller on the wing can be decomposed into a change in the effective angle of attack, and a non-uniform velocity component along the wing surface. The former is more dominant for larger diameter-to-chord ratios, and leads to an increase in lift, as well as to a reduction in drag due to the reorientation of the lift vector.

- The non-uniform velocities induced locally by the propeller lead to an increase in suction immediately upstream of the propeller, an increase in pressure immediately downstream of it, and an adverse pressure gradient directly beneath the propeller disk. For a typical OTWDP configuration in cruise conditions, the magnitude of the changes in surface pressure is of the order of $\Delta C_p \approx \pm 0.1$. The effect of these changes in pressure on lift and drag is highly dependent on the axial position of the propeller: the lift increase is maximized if the propeller is placed towards the rear of the airfoil, while the drag reduction is maximized if the propeller is placed near the location of maximum airfoil thickness.

- Only the tangential vorticity component of the propeller vortex system induces velocities outside the slipstream. Therefore, in cruise conditions, the effect of the propeller on the wing is primarily a function of the relative size of the propeller and the thrust coefficient. The blade count, shape, and pitch angle do not play a major role.

- Propellers placed near the trailing edge have no significant upstream effect on the boundary-layer transition location. Propellers placed ahead of the natural transition location move the transition point upstream.

- The propeller-induced pressure gradients lead to an increase in boundary-layer thickness in cruise conditions, effectively de-cambering the airfoil and reducing the lift and drag benefits with respect to inviscid flow. This effect is more prominent at lower Reynolds numbers.

- In subsonic flight conditions ($M < 0.6$) and high Reynolds numbers ($Re \geq 10^7$), the Mach number has no significant impact on the changes in wing performance due to the propellers.

- For an array of OTW propellers ($N \gg 1$), the changes in sectional wing lift and drag beneath the array are approximately constant in spanwise direction.
- For an array of three propellers located at 80% chord, with a diameter equal to 67% of the wing chord, the average sectional lift-to-drag ratio beneath the middle propeller is found to increase by 45% in typical cruise conditions (effect of nacelle, duct, and pylons excluded). The lift-to-drag ratio benefit increases with thrust setting, diameter-to-chord ratio, and Reynolds number, and decreases with tip clearance and a more downstream position of the propeller.

Regarding the effect of the wing on the OTW propeller(s), the following conclusions can be drawn:

- The velocity profile induced by the wing at the propeller location can be decomposed into four contributions: a change in the effective advance ratio, a change in the effective angle of attack, a non-uniform velocity profile induced by the inviscid wing, and a non-uniform velocity profile caused by the wing boundary layer.
- For a propeller positioned near the trailing edge, the non-uniform loading is primarily caused by an angle-of-attack effect. This leads to differences in loading between the up-going and down-going blade sides. For a propeller positioned near the leading edge, the non-uniform loading is primarily caused by the vertical gradient of axial velocity. This leads to differences in loading between the top and bottom sides of the propeller disk.
- The propeller performance is strongly dependent on the incidence angle relative to the wing, i_P. On one hand, the non-uniform loading due to non-axial inflow reduces the efficiency along the propeller axis. On the other hand, given that the local flow direction above the wing is not aligned with the freestream direction, a small angle-of-attack effect can also increase the effective propulsive efficiency in the flight direction.
- For the typical diameter-to-chord ratios envisioned for regional OTWDP aircraft ($D_P/c \sim 0.2$), the wing boundary layer has a negligible effect on propeller performance.
- Downstream of the propulsion system, the propeller slipstream is stretched in vertical direction due to the vertical velocities induced by the wing. Moreover, for typical tip-clearance values ($\varepsilon/c < 0.1$), the bottom part of the slipstream deforms due to the interaction with the wing wake.
- For an array of three propellers located at 80% chord, with a diameter equal to 67% of the wing chord, the propulsive efficiency of the propeller is found to decrease by 12% in typical cruise conditions (effect of duct, nacelle, and pylons excluded).

PROPELLER–WING INTERACTION IN HIGH-LIFT CONDITIONS

The interaction between an OTW propeller and the wing in high-lift conditions was first analyzed in an exploratory test of a single propeller above a wing with a Fowler flap. Subsequently, a dedicated test with a simplified wing geometry was performed to investigate

the interaction between the propeller and the wing boundary layer with and without external pressure gradients. For this, the propeller was placed above the hinge line of a plain flap. Moreover, unsteady RANS simulations were performed to investigate the effect of inclining the propeller together with the flap for this particular geometry. These analyses showed that:

- When a propeller operates at a high thrust setting ($C_T = 0.35$) close to a flat surface (i.e, without external pressure gradients), a bubble of reduced axial velocity is generated near the wall immediately behind the propeller. Behind this bubble ($x/R > 0.6$), the slipstream approaches the wall and the boundary-layer thickness is reduced. The axial extent of the bubble increases with tip clearance and decreases at higher thrust settings.
- When a propeller is placed above the hinge line of a plain flap and operated at a high thrust setting, the propeller triggers flow separation over the flap. This is predominantly caused by the time-averaged adverse pressure gradient induced by the propeller. The unsteady interaction between the blade tip vortices and wing boundary layer is not the dominant cause for flow separation.
- Increasing the tip clearance between propeller and wing is not a practical solution to mitigate propeller-induced flow separation.
- Placing the propeller further upstream, such that the flap hinge is located immediately behind the low-velocity bubble generated behind the propeller, leads to a Coandă effect which postpones flow separation and increases system (i.e., wing + flap + propeller) lift.
- Inclining the propeller by rotating it together with the flap around the flap hinge delays the point of flow separation with respect to uninstalled conditions and leads to an increase in system lift, primarily due to the contribution of the propeller thrust and normal force to the net vertical force.
- For a propeller operating at a high thrust setting above a Fowler flap, deflecting the propeller with the flap is found to provide a stronger drag reduction ($\Delta C_{Dp} = -0.008$) than if the propeller is not deflected ($\Delta C_{Dp} = -0.005$), without an appreciable change in wing lift. In both cases, the magnitude of the non-uniform loading on the propeller is comparable.
- A comparison to experimental data shows that the magnitude of propeller-induced flow separation was under-predicted by unsteady RANS simulations.

PROPELLER–DUCT INTERACTION

A duct may be beneficial to reduce the non-uniform inflow to the propellers of an OTWDP system and provide additional noise shielding. However, based on the existing literature, it is not clear what a representative duct shape would look like. Therefore, two simplified limit cases were analyzed: a circular ducted propeller and a square ducted propeller. These simplified geometries were selected in order to draw more generalized, qualitative conclusions regarding the typical interaction effects that may occur with the

corners and flat walls of ducted OTWDP systems, and avoid conclusions inherent to a specific duct design. A numerical (RANS) approach was taken to obtain detailed information regarding the blade loading and flow field inside the duct. A high thrust setting was analyzed. The numerical analyses revealed that:

- The adverse pressure gradients created by the propeller inside the square duct lead to flow reversal in the corners of the duct and create a spanwise velocity component at the trailing edge which is oriented towards the corners. This contributes to the formation of a pair of counter-rotating vortices.
- In the square duct, the non-axisymmetric inflow and varying end-plate effect perceived by the propeller blades every 90^o leads to an unsteady blade loading which is especially prominent in the outboard part of the blade. For the setup analyzed, at the radial location of maximum loading, the amplitude of the blade thrust fluctuations is 9% of the mean blade thrust.
- For a given system (i.e., propeller plus duct) thrust setting, the contribution of the duct thrust to the total thrust is higher for the circular duct than for the square one: at $T_c \approx 1.0$, they constitute 15% and 2.5% of the total system thrust, respectively. In both cases, the ratio between duct thrust and system thrust increases with thrust setting.
- For the geometry, blade-pitch setting, and advance ratio ($J = 0.7$) analyzed in this study, the circular and square ducted propeller systems produce similar levels of thrust ($T_c \approx 1.0$), though approximately 7% less than the isolated propeller. In these conditions, the circular ducted propeller system was found to be slightly more efficient than the isolated propeller, while the square ducted propeller system was found to be slightly less efficient.
- Based on the two-dimensional disturbance created above the wing in an OTWDP configuration, the corner-flow effects encountered in the square duct, and the changes in wetted area when going from a single ducted propeller to multiple ducted propellers, a 2D envelope duct without walls between adjacent propellers appears to be more beneficial in terms of aerodynamic performance than an array of adjacent circular or square ducts.

PROPELLER–PROPELLER INTERACTION

If the propellers of an OTWDP array are placed in close proximity without a duct or with a 2D envelope duct, then their aerodynamic characteristics are affected by the neighboring propellers. To investigate this, an experiment was performed with three adjacent propellers (without a wing). An evaluation of the interaction effects for different geometrical design parameters and operating conditions showed that the performance of the middle propeller was affected in the following ways:

- At the thrust setting corresponding to maximum propeller efficiency, the efficiency of the propeller is reduced by 1.5% due to the presence of the additional propellers on each side. This performance loss is caused primarily by the presence of the adjacent nacelles.

- The minor efficiency reduction due to aerodynamic interaction is higher for a propeller placed slightly upstream of the neighbors (forward stagger), for a non-zero angle of attack, or for lower thrust settings. It decreases with increasing separation distance between the propellers and is independent of the rotation direction or the relative blade-phase angle.

- The velocities induced by each propeller's vortex system do not significantly affect the time-averaged performance of the adjacent propellers, but do lead to the appearance of in-plane velocity components that generate unsteady blade loading. The local changes in loading are of the order of 5%–10% of the average disk loading of the propeller. They are primarily caused by the time-averaged influence of each propeller slipstream on its neighbors, and not by discrete, unsteady blade-to-blade interactions.

- For typical operating conditions encountered during forward flight, the interaction does not lead to a significant deformation of the slipstreams: $1.2R$ behind the propellers, the slipstreams retain a quasi-circular cross section.

11.1.3. PERFORMANCE OF HYBRID-ELECTRIC AIRCRAFT WITH OTWDP

After gaining several insights into the sizing process of HEDP aircraft and the aerodynamic characteristics of OTWDP systems, the final part of this dissertation aims to determine if, or under which conditions, the combination of HEP and OTWDP can lead to a benefit at aircraft level. For this, first, a design-space exploration study was performed by sizing a generic OTWDP aircraft for different combinations of mission requirements, design parameters, and technology assumptions. These sensitivity studies revealed that:

- The benefit of OTWDP in terms of overall energy consumption increases with mission range, decreases with increasing cruise Mach number, and is practically independent of the payload weight.

- For a fair comparison between HEDP and conventional configurations, each aircraft should fly at the optimum cruise altitude, or the characteristics of the drag polar (e.g. $C_{L,\min D}$) should be adapted such that both configurations operate near the optimum lift coefficient for a predetermined cruise altitude. If not, the benefits of the increased wing loading enabled by the distributed-propulsion system may be significantly over- or under-estimated.

- For typical pack-level battery energy-density values envisioned for the coming decades (250 ~ 750 Wh/kg), the use of batteries for aircraft propulsion is detrimental for the energy consumption of a regional HEDP aircraft—unless a very small amount of batteries can appreciably increase the efficiency of the thermal engine or other powertrain components.

- Serial and fully-turboelectric powertrains are not beneficial for regional transport aircraft, due to the high weight of the electrical components. For this reason, a partial-turboelectric architecture is considered the most promising for distributed-propulsion applications.

- For the aerodynamic benefits of HEDP to lead to a 15% reduction in energy consumption for the 2035+ timeframe, an average increase of 17%–23% in aero-propulsive efficiency is required throughout the mission. However, this benefit must be achieved with low degrees of "hybridization" ($\varphi \sim 0.2$), and will therefore be extremely difficult to reach in practice.

Based on these analyses, a regional aircraft with OTWDP and a partial-turboelectric powertrain was sized for a short-range mission ($R = 825$ nmi, $M_{cr} = 0.41$) and a medium-range mission ($R = 1500$ nmi, $M_{cr} = 0.60$). The design study was intended for an entry-into-service of 2035, and focused on a configuration where the OTWDP system was installed on the flap. A simplified aero-propulsive model was used to estimate the effect of the OTW propellers on wing performance and vice versa. No duct is included in the modeling. This aero-propulsive model was applicable for cruise conditions, while for high-lift conditions, several simplifying assumptions had to be made. In this design study:

- The optimal wing loading of the OTWDP configuration in terms of PREE corresponds to the point of maximum power loading if the aircraft is sized at the optimal cruise altitude.
- The optimal shaft power ratio is 0.2–0.25 in the sizing condition (take-off), depending on the mission. For both missions, the shaft power ratio during cruise is increased to 0.5–0.6 in order to maximize the aero-propulsive benefits in this condition without exceeding the installed power of the powertrain components.
- For an OTWDP array covering 53% of the wing span, the best combination of axial propeller position and number of propellers is found to be $x_P/c = 0.78$ and $N_2 = 38$, respectively. In this simplified modeling approach, in which the propeller performance is not sensitive to Reynolds number, a negative propeller incidence angle (e.g. $i_P = -5^o$) is beneficial for the aero-propulsive efficiency.
- The average aero-propulsive efficiency gains due to OTWDP are found to be 12% and 9% for the short- and medium-range missions, respectively, compared to a twin-turboprop reference aircraft. Of these benefits, approximately 4% is required to offset the efficiency losses in the electric drivetrain.
- The uncertainties in take-off mass and PREE due to uncertainty in the aerodynamic modeling are, conservatively, estimated to be ±3% and ±5%, respectively.
- The take-off mass and PREE are found to increase by 2% and 4.6% for the short-range mission, respectively, compared to the reference aircraft. For the medium-range mission, the take-off mass is comparable to the reference aircraft, and the PREE is increased by approximately 5%.

11.2. DIRECTIONS FOR FUTURE RESEARCH

The research presented in this dissertation has shed a light on several aspects of hybrid-electric aircraft, distributed propulsion, over-the-wing propulsion, and the combination thereof. Nevertheless, there are still many aspects that require further investigation to

gain a true understanding of these complex systems. The following paragraphs present a series of topics that require further research, based on the limitations encountered in this study, and some concluding remarks regarding the potential applications of OTWDP.

REGARDING THE CONCEPTUAL DESIGN OF HYBRID-ELECTRIC AIRCRAFT

The conceptual design approach taken in this research has focused particularly on the aerodynamic characteristics of the distributed-propulsion system and the implications that it has in terms of aircraft performance. However, there are other aspects of distributed-propulsion systems that can make or break the design. For more sound conclusions, the level of fidelity of the hybrid-electric powertrain modeling has to be increased; for example, by accounting for the drag or weight penalties of the thermal management system, or by providing more realistic estimates of the weight and efficiency of the electrical machines and combustion engine. Such methods have already been developed by other authors, and can be combined with the approach presented here to obtain a more consistent level of fidelity across the different disciplines. Furthermore, several of the "secondary" benefits or drawbacks of OTWDP, which are not accounted for in the Class-I sizing phase, should be investigated in more detail. For example, the change in structural weight due to the installation of HEP or OTWDP components should be investigated. One particularly important aspect in this sense is the effect of distributed propulsion on stability and control. For example, the pitching moment created by the OTWDP system—particularly if deflected with the flap in landing conditions—may affect the required horizontal tail size and trim drag. On the other hand, the reduced moments in case of component failure and potential horizontal alignment of the thrust vector with the center-of-gravity of the aircraft may also have beneficial effects regarding tail sizing.

The design method formulated in this research can be used as a starting point for more advanced design routines that account for these effects, or it can act as an integrator and be coupled to higher-fidelity modules. Expanding the method in this manner will not only increase the accuracy of the modeling, but additionally open the door to a wider range of aircraft configurations. For example, the aft pylon-mounted propeller configuration that was combined with OTWDP in Chapter 10 may present disadvantages when compared to other primary-propeller locations, such as tail-mounted, wing-tip-mounted, or fuselage boundary-layer ingesting propellers. To be able to investigate such configurations and perform a fair comparison, it is vital that aero-propulsive models are developed for different integration strategies, following the parametrization and level of fidelity that is appropriate of a conceptual design process.

REGARDING THE AERODYNAMIC CHARACTERISTICS OF OTWDP SYSTEMS

A significant fraction of the work presented in this dissertation has focused on understanding the aerodynamic interaction between a wing and an OTW propeller. However, in this process, components such as the nacelles and pylons required to install the propellers have largely been ignored. The effect of these additional components on the interaction between the propeller and wing should be assessed to gain a more representative estimation and understanding of the performance of OTWDP systems. For example, the results of this research indicate that the nacelles have an influence on both the performance of the wing and the adjacent propellers, though the effect of nacelle shape and

position has not been investigated. A particularly relevant question in this regard is the effect of the duct: what is the effect of a properly-designed duct on the performance of the system? What is the optimal shape? Both fundamental aerodynamic investigations and more design-focused aerodynamic optimization studies would strongly support the development of OTWDP systems in this sense. For such studies, the effect of the Reynolds and Mach numbers encountered throughout the flight envelop should not be overlooked.

One of the most important limitations of the present research is, perhaps, the lack of actual high-lift performance predictions. The investigations have provided insight into some of the fundamental interaction effects between the propellers and the wing and its boundary layer, and have shown that OTW propellers can increase the high-lift capabilities of the system by either inducing a Coandă effect, or by deflecting the propellers with the flap. Moreover, the aircraft design studies have highlighted the tremendous impact that the increase in wing loading due to aero-propulsive interaction can have on the overall aircraft's efficiency. However, it is currently unclear how much the maximum lift coefficient or stall angle of the system can increase with OTWDP, or what a well-performing high-lift design would look like. Research on this topic is challenging due to the importance of additionally matching the Reynolds number in experimental approaches. Moreover, as demonstrated in this research, high-fidelity numerical approaches struggle to capture the propeller-induced flow separation over a flap. Hence, research into the high-lift performance for realistic Reynolds numbers and geometries is not only important from a design perspective, but also to further the capabilities of numerical methods. The datasets or prediction models stemming from such investigations can subsequently be applied to the sizing method described in this research to assess what the impact at aircraft level would be. It should be noted that, in this regard, not only the maximum lift coefficient is important, but especially the *trimmed* maximum lift coefficient. This may require dedicated research on its own, due to the coupling between thrust, lift, and pitching moment. Particularly the changes in pitching moment, which have not been analyzed in this work, require further investigation.

Furthermore, even though the potential noise shielding benefit of OTWDP has been mentioned several times throughout this dissertation, it has not been investigated as such. Previous studies have shown that the wing can, in theory, shield the ground from the noise produced by the propeller. However, the question remains whether this can be done effectively for an aerodynamically-efficient design of the OTWDP system. The aerodynamic interaction effects identified in this study lead to an appreciable unsteady blade loading and already hint that there is a trade-off between aerodynamic and acoustic performance; for example, regarding the axial position of the propellers, or the separation between adjacent propellers. A more detailed investigation of the acoustic interference effects in OTWDP systems can provide a more fundamental understanding of the problem, and potentially make room for a low-noise HEDP aircraft configuration.

FUTURE RESEARCH INTO NOVEL AIRCRAFT CONFIGURATIONS

The design studies of Chapter 10 conclude that OTWDP can lead to a 5% reduction in energy consumption for a regional turboprop aircraft, albeit with an uncertainty band of comparable amplitude. This 5% reduction alone is most likely insufficient to justify a

radical change in the design, production, operation, and maintenance of the aircraft—especially when considering that the Class-I sizing method used to estimate this value ignores some important factors such as tail sizing and trim drag. However, there at least are three scenarios that can foment the use of OTWDP for regional transport, which are not mutually exclusive. The first is if the efficiency and specific power of the electrical components are increased beyond the values assumed in this study. Though this is unlikely on the short term, an improvement in these components would have a non-linear effect on the aircraft: for a percentage increase in transmission efficiency, the benefits of OTWDP lead to more than a percent reduction in energy consumption. The second corresponds to a scenario where the aero-propulsive benefits of OTWDP are increased beyond the levels identified in this study. For example, by carefully integrating the OTWDP system with the wing structure and control surfaces, a full-span OTWDP system where the duct contributes to the cross-sectional inertia of the wing may be created. And thirdly, if the aforementioned noise-shielding effects can be demonstrated without hindering the aerodynamic performance, then the combined energy-consumption benefits and noise benefits will present a strong case for such aircraft configurations.

The application of OTWDP for other missions and market segments should also be explored. The recent developments in fully-electric general aviation are a good starting point in this sense. If in the future only small, fully-electric aircraft are allowed to operate in the proximity of urban areas, a reality which is becoming more and more common for ground transportation, then OTWDP can offer aerodynamic (and potentially, acoustic) benefits that conventional or leading-edge distributed propeller arrangements do not present. While such applications would not significantly reduce the environmental impact of the aviation sector as a whole, they can act as a seed to develop the technology and facilitate its posterior application for larger aircraft. Similarly, the long-haul market is a promising candidate for partial-turboelectric distributed propulsion, due to the large fuel weight fractions required for such missions. OTWDP could be used for such missions if the cruise speed is reduced slightly and highly swept propellers are employed. However, the use of OTWDP at transonic cruise speeds comes with its own challenges in terms of shock formation, which would require additional dedicated research into the interaction effects.

Finally, it should be noted that OTWDP can be combined with other advanced propulsion technologies. For example, the potential benefits of alternative fuels such as hydrogen could be superimposed to the aero-propulsive benefits provided by the OTWDP system. Likewise, the benefits of supporting the combustion engine with battery power in off-design conditions may lead to an overall increase in powertrain efficiency, since the batteries can also be used as a buffer or to directly power the OTWDP system in particular off-design cases. Furthermore, as evidenced in this research, the OTWDP system should be complemented by an additional propeller system. These additional propellers may also be placed at strategic locations on the airframe to further enhance the aerodynamic or propulsive efficiency of the aircraft; for example, in a boundary-layer ingestion configuration. More detailed research into these radical aircraft configurations will contribute to a better understanding of the underlying physics, a more accurate comparison of the different configurations, and, ultimately, to a more sustainable aviation industry.

PART V

APPENDICES

A

HYBRID-ELECTRIC POWERTRAIN OPERATING MODES

Chapter 3 presents a simple powertrain model for conceptual aircraft sizing purposes. For this highly simplified model, the components of the hybrid-electric powertrain are represented by "black boxes", each characterized by a constant transmission efficiency. The serial/parallel partial hybrid (SPPH) is taken as a generic hybrid-electric powertrain representation, since all other architectures can be obtained as limit cases of this architecture. In that case, the set of linear equations representing the power balances across each component (Eq. 3.21) can be complemented by three closing equations and expressed as

$$\boldsymbol{A} \cdot \boldsymbol{P} = \boldsymbol{b}, \tag{A.1}$$

where $\boldsymbol{A}$ is a coefficient matrix containing the transmission efficiencies and power-control variables, $\boldsymbol{P}$ is a column vector containing the unknowns (i.e., the ten powers indicated in the top schematic of Fig. A.1), and the right-hand-side column vector $\boldsymbol{b}$ depends on the constraints imposed to close the system of equations. This conceptually and mathematically simple representation of a generic hybrid-electric powertrain allows the designer to compute the power produced by each component by simply inverting the matrix $\boldsymbol{A}$.

For example, when both energy sources provide power, both propulsors generate thrust, and excess power is sent from the gearbox to the electrical system, the set of equations becomes (copied from Eq. 3.22):

$$\begin{bmatrix} -\eta_{GT} & 1 & 0 & 0 & 0 & 0 & 0 & 0 & 0 & 0 \\ 0 & -\eta_{GB} & 1 & 1 & 0 & 0 & 0 & 0 & 0 & 0 \\ 0 & 0 & 0 & -\eta_{P1} & 0 & 0 & 0 & 0 & 1 & 0 \\ 0 & 0 & -\eta_{EM1} & 0 & 1 & 0 & 0 & 0 & 0 & 0 \\ 0 & 0 & 0 & 0 & -\eta_{PMAD} & -\eta_{PMAD} & 1 & 0 & 0 & 0 \\ 0 & 0 & 0 & 0 & 0 & 0 & -\eta_{EM2} & 1 & 0 & 0 \\ 0 & 0 & 0 & 0 & 0 & 0 & 0 & -\eta_{P2} & 0 & 1 \\ \Phi & 0 & 0 & 0 & 0 & (\Phi-1) & 0 & 0 & 0 & 0 \\ 0 & 0 & 0 & \varphi & 0 & 0 & 0 & (\varphi-1) & 0 & 0 \\ 0 & 0 & 0 & 0 & 0 & 0 & 0 & 0 & 1 & 1 \end{bmatrix} \cdot \begin{bmatrix} P_f \\ P_{gt} \\ P_{gb} \\ P_{s1} \\ P_{e1} \\ P_{bat} \\ P_{e2} \\ P_{s2} \\ P_{p1} \\ P_{p2} \end{bmatrix} = \begin{bmatrix} 0 \\ 0 \\ 0 \\ 0 \\ 0 \\ 0 \\ 0 \\ 0 \\ 0 \\ P_p \end{bmatrix} \tag{A.2}$$

The last three rows of Eq. A.2 specify the supplied power ratio, shaft power ratio, and total propulsive power. Therefore, this formulation can be used to determine the power required from each component for an assumed Φ, φ, and a given total propulsive power. This is for example the case in the constraint diagram, where the propulsive power requirement stems from the flight-performance equations for the given flight condition. This formulation does not specify the throttle setting or the maximum power that system can produce.

On the other hand, once the powertrain size has been determined, it can be of interest to specify the throttle setting, while leaving the propulsive power as a dependent variable. This can occur, for example, during the climb phase of the mission analysis, when the engines are operated at maximum continuous power, and the excess power is used to accelerate or increase altitude. In that case, the set of equations can be solved as

$$\begin{bmatrix} -\eta_{GT} & 1 & 0 & 0 & 0 & 0 & 0 & 0 & 0 & 0 \\ 0 & -\eta_{GB} & 1 & 1 & 0 & 0 & 0 & 0 & 0 & 0 \\ 0 & 0 & 0 & -\eta_{P1} & 0 & 0 & 0 & 0 & 1 & 0 \\ 0 & 0 & -\eta_{EM1} & 0 & 1 & 0 & 0 & 0 & 0 & 0 \\ 0 & 0 & 0 & 0 & -\eta_{PMAD} & -\eta_{PMAD} & 1 & 0 & 0 & 0 \\ 0 & 0 & 0 & 0 & 0 & 0 & -\eta_{EM2} & 1 & 0 & 0 \\ 0 & 0 & 0 & 0 & 0 & 0 & 0 & -\eta_{P2} & 0 & 1 \\ \Phi & 0 & 0 & 0 & 0 & (\Phi-1) & 0 & 0 & 0 & 0 \\ 0 & 0 & 0 & \varphi & 0 & 0 & 0 & (\varphi-1) & 0 & 0 \\ 0 & \xi_{GT} & 0 & 0 & 0 & 0 & 0 & 0 & 0 & 0 \end{bmatrix} \cdot \begin{bmatrix} P_f \\ P_{gt} \\ P_{gb} \\ P_{s1} \\ P_{e1} \\ P_{bat} \\ P_{e2} \\ P_{s2} \\ P_{p1} \\ P_{p2} \end{bmatrix} = \begin{bmatrix} 0 \\ 0 \\ 0 \\ 0 \\ 0 \\ 0 \\ 0 \\ 0 \\ 0 \\ P_{GT,max} \end{bmatrix} \tag{A.3}$$

In this case, the total propulsive power $P_p = P_{p1} + P_{p2}$ is obtained for a given installed gas-turbine power $P_{GT,max}$ and throttle setting ξ_{GT}.

The coefficient matrices $\boldsymbol{A}$ of both Eqs. A.2 and A.3 assume that all elements of the solution vector $\boldsymbol{P}$ are positive. However, this is not necessarily the case, if for example the battery is being charged, or the propulsors are windmilling. In those cases, the elements of the coefficient matrix change depending on the so-called "operating mode" of the powertrain. Given that the gas turbine cannot produce a negative shaft power, and that not all powers can simultaneously flow into or out of a given component, a total of

nine operating modes exist. These are conceptually represented in Fig. A.1. While most of these operating modes may not be practical or feasible for a given powertrain design, they are, theoretically, possible. For example, Fig. A.1.7 shows a situation where the primary propulsors are extracting power from the flow, which is diverted—together with the gas-turbine power and battery power—to the secondary propulsors. This may be useful in a situation where a series of LEDP propellers are operated at high thrust to increase the wing lift as much as possible during landing, while the primary propulsors are windmilling to generate enough drag and maintain a sufficiently low approach speed. In that case, the gas turbine may still produce a residual amount of power because it remains in an idle setting. Another example may be the case depicted in Fig. A.1.9, where both propulsor systems are harvesting energy and all power is diverted to the battery. This scenario may be useful if drag has to be increased during the descent phase to allow a steeper approach. In this case, part of the kinetic and potential energy of the aircraft is stored in the batteries, which may lead to a (minor) reduction in overall energy consumption or a reduction in turnaround time, if limited by the battery charging process. This feature may also reduce the required spoiler size.

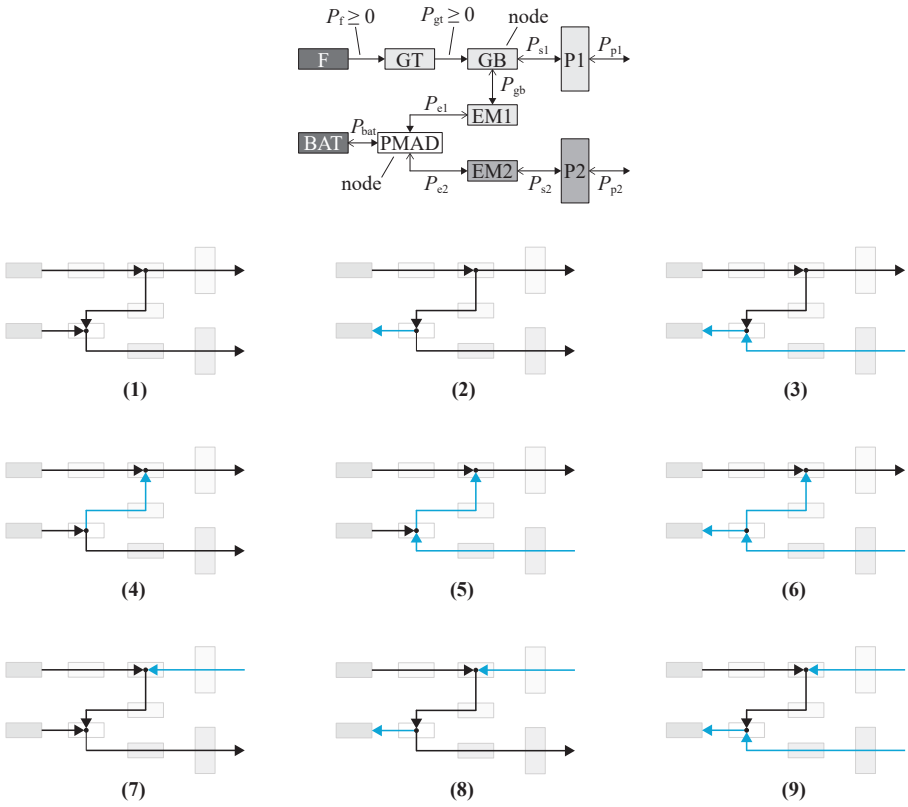

Figure A.1: Overview of the nine possible powertrain operating modes. Blue arrows indicate negative P_i values, following the convention defined as positive with the filled arrowheads in the top schematic.

The coefficient matrices corresponding to these nine operating modes are presented below. These matrices can be implemented in the sizing routine, and the designer can select the corresponding one depending on the operating mode of the powertrain. However, for a generic combination of Φ and φ, the operating mode is unknown a priori. In that case, the different options have to be probed, to find one where the assumed sign of each variable P_i (for that operating mode) matches the sign of the solution variables. It should be noted that, for powertrain architectures other than the SPPH configuration, one or more of the powers P_i is zero. This means that multiple coefficient matrices can provide the same physical solution. For example, for a serial configuration, $\varphi = 1$ (see Table 3.1), and $P_{s1} = P_{p1} = 0$. In that case, operating modes 7, 8, and 9 will provide the same solution as modes 1, 2, and 3, respectively. Also note that, while in the examples below the same three closing equations are used as in Eq. A.2, for each operating mode, alternative closing equations such as a specified throttle setting (Eq. A.3) can also be used instead.

1. Battery and gas turbine provide power, both propulsor systems create thrust, and excess power from the gas turbine is diverted to the electrical system (used in Eq. A.2):

$$\boldsymbol{A_1} = \begin{bmatrix} -\eta_{GT} & 1 & 0 & 0 & 0 & 0 & 0 & 0 & 0 & 0 \\ 0 & -\eta_{GB} & 1 & 1 & 0 & 0 & 0 & 0 & 0 & 0 \\ 0 & 0 & 0 & -\eta_{P1} & 0 & 0 & 0 & 0 & 1 & 0 \\ 0 & 0 & -\eta_{EM1} & 0 & 1 & 0 & 0 & 0 & 0 & 0 \\ 0 & 0 & 0 & 0 & -\eta_{PMAD} & -\eta_{PMAD} & 1 & 0 & 0 & 0 \\ 0 & 0 & 0 & 0 & 0 & 0 & -\eta_{EM2} & 1 & 0 & 0 \\ 0 & 0 & 0 & 0 & 0 & 0 & 0 & -\eta_{P2} & 0 & 1 \\ \Phi & 0 & 0 & 0 & 0 & (\Phi-1) & 0 & 0 & 0 & 0 \\ 0 & 0 & 0 & \varphi & 0 & 0 & 0 & (\varphi-1) & 0 & 0 \\ 0 & 0 & 0 & 0 & 0 & 0 & 0 & 0 & 1 & 1 \end{bmatrix} \tag{A.4}$$

2. The gas turbine provides power to the battery and both propulsor systems:

$$\boldsymbol{A_2} = \begin{bmatrix} -\eta_{GT} & 1 & 0 & 0 & 0 & 0 & 0 & 0 & 0 & 0 \\ 0 & -\eta_{GB} & 1 & 1 & 0 & 0 & 0 & 0 & 0 & 0 \\ 0 & 0 & 0 & -\eta_{P1} & 0 & 0 & 0 & 0 & 1 & 0 \\ 0 & 0 & -\eta_{EM1} & 0 & 1 & 0 & 0 & 0 & 0 & 0 \\ 0 & 0 & 0 & 0 & -\eta_{PMAD} & -1 & 1 & 0 & 0 & 0 \\ 0 & 0 & 0 & 0 & 0 & 0 & -\eta_{EM2} & 1 & 0 & 0 \\ 0 & 0 & 0 & 0 & 0 & 0 & 0 & -\eta_{P2} & 0 & 1 \\ \Phi & 0 & 0 & 0 & 0 & (\Phi-1) & 0 & 0 & 0 & 0 \\ 0 & 0 & 0 & \varphi & 0 & 0 & 0 & (\varphi-1) & 0 & 0 \\ 0 & 0 & 0 & 0 & 0 & 0 & 0 & 0 & 1 & 1 \end{bmatrix} \tag{A.5}$$

3. The gas turbine provides power to the battery and primary propulsors, while the secondary propulsors are harvesting energy:

$$\boldsymbol{A_3} = \begin{bmatrix} -\eta_{GT} & 1 & 0 & 0 & 0 & 0 & 0 & 0 & 0 & 0 \\ 0 & -\eta_{GB} & 1 & 1 & 0 & 0 & 0 & 0 & 0 & 0 \\ 0 & 0 & 0 & -\eta_{P1} & 0 & 0 & 0 & 0 & 1 & 0 \\ 0 & 0 & -\eta_{EM1} & 0 & 1 & 0 & 0 & 0 & 0 & 0 \\ 0 & 0 & 0 & 0 & -\eta_{PMAD} & -1 & \eta_{PMAD} & 0 & 0 & 0 \\ 0 & 0 & 0 & 0 & 0 & 0 & -1 & \eta_{EM2} & 0 & 0 \\ 0 & 0 & 0 & 0 & 0 & 0 & 0 & -1 & 0 & \eta_{P2} \\ \Phi & 0 & 0 & 0 & 0 & (\Phi-1) & 0 & 0 & 0 & 0 \\ 0 & 0 & 0 & \varphi & 0 & 0 & 0 & (\varphi-1) & 0 & 0 \\ 0 & 0 & 0 & 0 & 0 & 0 & 0 & 0 & 1 & 1 \end{bmatrix} \tag{A.6}$$

4. The battery provides power to both propulsor systems simultaneously:

$$\boldsymbol{A_4} = \begin{bmatrix} -\eta_{GT} & 1 & 0 & 0 & 0 & 0 & 0 & 0 & 0 & 0 \\ 0 & -\eta_{GB} & \eta_{GB} & 1 & 0 & 0 & 0 & 0 & 0 & 0 \\ 0 & 0 & 0 & -\eta_{P1} & 0 & 0 & 0 & 0 & 1 & 0 \\ 0 & 0 & -1 & 0 & \eta_{EM1} & 0 & 0 & 0 & 0 & 0 \\ 0 & 0 & 0 & 0 & -1 & -\eta_{PMAD} & 1 & 0 & 0 & 0 \\ 0 & 0 & 0 & 0 & 0 & 0 & -\eta_{EM2} & 1 & 0 & 0 \\ 0 & 0 & 0 & 0 & 0 & 0 & 0 & -\eta_{P2} & 0 & 1 \\ \Phi & 0 & 0 & 0 & 0 & (\Phi-1) & 0 & 0 & 0 & 0 \\ 0 & 0 & 0 & \varphi & 0 & 0 & 0 & (\varphi-1) & 0 & 0 \\ 0 & 0 & 0 & 0 & 0 & 0 & 0 & 0 & 1 & 1 \end{bmatrix} \tag{A.7}$$

5. The primary propulsors are powerd by the gas turbine, the battery, and the (windmilling) secondary propulsors:

$$\boldsymbol{A_5} = \begin{bmatrix} -\eta_{GT} & 1 & 0 & 0 & 0 & 0 & 0 & 0 & 0 & 0 \\ 0 & -\eta_{GB} & \eta_{GB} & 1 & 0 & 0 & 0 & 0 & 0 & 0 \\ 0 & 0 & 0 & -\eta_{P1} & 0 & 0 & 0 & 0 & 1 & 0 \\ 0 & 0 & -1 & 0 & \eta_{EM1} & 0 & 0 & 0 & 0 & 0 \\ 0 & 0 & 0 & 0 & -1 & -\eta_{PMAD} & \eta_{PMAD} & 0 & 0 & 0 \\ 0 & 0 & 0 & 0 & 0 & 0 & -1 & \eta_{EM2} & 0 & 0 \\ 0 & 0 & 0 & 0 & 0 & 0 & 0 & -1 & 0 & \eta_{P2} \\ \Phi & 0 & 0 & 0 & 0 & (\Phi-1) & 0 & 0 & 0 & 0 \\ 0 & 0 & 0 & \varphi & 0 & 0 & 0 & (\varphi-1) & 0 & 0 \\ 0 & 0 & 0 & 0 & 0 & 0 & 0 & 0 & 1 & 1 \end{bmatrix} \tag{A.8}$$

6. The secondary propulsors are harvesting energy, and the power is used to both charge the battery and support the primary propulsors:

$$\boldsymbol{A_6} = \begin{bmatrix} -\eta_{GT} & 1 & 0 & 0 & 0 & 0 & 0 & 0 & 0 & 0 \\ 0 & -\eta_{GB} & \eta_{GB} & 1 & 0 & 0 & 0 & 0 & 0 & 0 \\ 0 & 0 & 0 & -\eta_{P1} & 0 & 0 & 0 & 0 & 1 & 0 \\ 0 & 0 & -1 & 0 & \eta_{EM1} & 0 & 0 & 0 & 0 & 0 \\ 0 & 0 & 0 & 0 & -1 & -1 & \eta_{PMAD} & 0 & 0 & 0 \\ 0 & 0 & 0 & 0 & 0 & 0 & -1 & \eta_{EM2} & 0 & 0 \\ 0 & 0 & 0 & 0 & 0 & 0 & 0 & -1 & 0 & \eta_{P2} \\ \Phi & 0 & 0 & 0 & 0 & (\Phi-1) & 0 & 0 & 0 & 0 \\ 0 & 0 & 0 & \varphi & 0 & 0 & 0 & (\varphi-1) & 0 & 0 \\ 0 & 0 & 0 & 0 & 0 & 0 & 0 & 0 & 1 & 1 \end{bmatrix} \tag{A.9}$$

7. Primary propuslors are windmilling, and the power is diverted together with the gas-turbine power and battery power to the secondary propulsors:

$$\boldsymbol{A_7} = \begin{bmatrix} -\eta_{GT} & 1 & 0 & 0 & 0 & 0 & 0 & 0 & 0 & 0 \\ 0 & -\eta_{GB} & 1 & \eta_{GB} & 0 & 0 & 0 & 0 & 0 & 0 \\ 0 & 0 & 0 & -1 & 0 & 0 & 0 & 0 & \eta_{P1} & 0 \\ 0 & 0 & -\eta_{EM1} & 0 & 1 & 0 & 0 & 0 & 0 & 0 \\ 0 & 0 & 0 & 0 & -\eta_{PMAD} & -\eta_{PMAD} & 1 & 0 & 0 & 0 \\ 0 & 0 & 0 & 0 & 0 & 0 & -\eta_{EM2} & 1 & 0 & 0 \\ 0 & 0 & 0 & 0 & 0 & 0 & 0 & -\eta_{P2} & 0 & 1 \\ \Phi & 0 & 0 & 0 & 0 & (\Phi-1) & 0 & 0 & 0 & 0 \\ 0 & 0 & 0 & \varphi & 0 & 0 & 0 & (\varphi-1) & 0 & 0 \\ 0 & 0 & 0 & 0 & 0 & 0 & 0 & 0 & 1 & 1 \end{bmatrix} \tag{A.10}$$

8. The primary propulsors are windmilling, and the power produced is combined with the gas-turbine power to charge the battery and feed the secondary propulsors:

$$\boldsymbol{A_8} = \begin{bmatrix} -\eta_{GT} & 1 & 0 & 0 & 0 & 0 & 0 & 0 & 0 & 0 \\ 0 & -\eta_{GB} & 1 & \eta_{GB} & 0 & 0 & 0 & 0 & 0 & 0 \\ 0 & 0 & 0 & -1 & 0 & 0 & 0 & 0 & \eta_{P1} & 0 \\ 0 & 0 & -\eta_{EM1} & 0 & 1 & 0 & 0 & 0 & 0 & 0 \\ 0 & 0 & 0 & 0 & -\eta_{PMAD} & -1 & 1 & 0 & 0 & 0 \\ 0 & 0 & 0 & 0 & 0 & 0 & -\eta_{EM2} & 1 & 0 & 0 \\ 0 & 0 & 0 & 0 & 0 & 0 & 0 & -\eta_{P2} & 0 & 1 \\ \Phi & 0 & 0 & 0 & 0 & (\Phi-1) & 0 & 0 & 0 & 0 \\ 0 & 0 & 0 & \varphi & 0 & 0 & 0 & (\varphi-1) & 0 & 0 \\ 0 & 0 & 0 & 0 & 0 & 0 & 0 & 0 & 1 & 1 \end{bmatrix} \tag{A.11}$$

9. Both propulsor systems are windmilling, and all the power produced is used to charge the batteries.

$$\boldsymbol{A_9} = \begin{bmatrix} -\eta_{GT} & 1 & 0 & 0 & 0 & 0 & 0 & 0 & 0 & 0 \\ 0 & -\eta_{GB} & 1 & \eta_{GB} & 0 & 0 & 0 & 0 & 0 & 0 \\ 0 & 0 & 0 & -1 & 0 & 0 & 0 & 0 & \eta_{P1} & 0 \\ 0 & 0 & -\eta_{EM1} & 0 & 1 & 0 & 0 & 0 & 0 & 0 \\ 0 & 0 & 0 & 0 & -\eta_{PMAD} & -1 & \eta_{PMAD} & 0 & 0 & 0 \\ 0 & 0 & 0 & 0 & 0 & 0 & -1 & \eta_{EM2} & 0 & 0 \\ 0 & 0 & 0 & 0 & 0 & 0 & 0 & -1 & 0 & \eta_{P2} \\ \Phi & 0 & 0 & 0 & 0 & (\Phi - 1) & 0 & 0 & 0 & 0 \\ 0 & 0 & 0 & \varphi & 0 & 0 & 0 & (\varphi - 1) & 0 & 0 \\ 0 & 0 & 0 & 0 & 0 & 0 & 0 & 0 & 1 & 1 \end{bmatrix} \tag{A.12}$$

B

Range Equation for Hybrid-Electric Aircraft

Estimating the energy required to fly a determined range is one of the main steps of the conceptual aircraft design process. In most design studies, this is done by means of a time-stepping mission analysis [45, 99, 104, 108, 309, 310]. However, this already requires information regarding the aircraft layout and power-control strategy which may not be available at the very beginning of a clean-sheet design process. In that case, a more simplified approach can be used to estimate the energy consumption. For conventional aircraft, this is typically done in the Class-I sizing phase by means of the well-established Breguet range equation (see e.g. Refs. [85, 91, 92]), which can be expressed as:

$$R = \eta_{GT}\eta_p \left(\frac{L}{D}\right)\left(\frac{e_f}{g}\right)\ln\left(\frac{W_{OE}+W_{PL}+W_f}{W_{OE}+W_{PL}}\right), \tag{B.1}$$

where $W_{OE} + W_{PL} + W_f$ equals the take-off weight of the aircraft, W_{TO}. This equation shows that the range depends on the weight breakdown of the aircraft, the specific energy of the fuel used, and the propulsive efficiency (η_p), aerodynamic efficiency (L/D), and combustion-engine efficiency (η_{gt}) of the aircraft. There is a logarithmic dependency of range on fuel weight, since the fuel weight—and thus, the aircraft weight—decreases throughout the mission.

A range equation can also be derived for fully-electric aircraft in a similar fashion. In that case, the equation is simplified further, since the mass of the energy source (batteries) remains constant throughout the mission. Numerous studies (see e.g. Refs. [38, 105, 311, 312]) have already shown that, in this case, the range equation is given by:

$$R = \eta_{EM}\eta_p \left(\frac{L}{D}\right)\left(\frac{e_{bat}}{g}\right)\left(\frac{W_{bat}}{W_{OE}+W_{PL}+W_{bat}}\right). \tag{B.2}$$

Parts of this Appendix have been in published Ref. [308].

Here, the efficiency factor η_{EM} comprises the efficiencies of all electrical components connected in series between the energy source (batteries) and the propulsor shaft. Since the aircraft weight remains constant, there is no logarithmic dependency, and the range is directly proportional to the battery weight fraction W_{bat}/W_{TO} instead.

Multiple authors have also derived range equations for hybrid-electric aircraft, which combine the two energy sources. An overview of some existing works on this topic is provided in Ref. [308]. However, the formulations encountered in literature are often based on inaccurate assumptions, or are limited to a specific powertrain architecture and control strategy. The purpose of this section is therefore to derive a simple range equation for aircraft with hybrid-electric powertrain architectures that feature a single propulsion system. Architectures with two propulsion systems (SPPH, partial turboelectric, and dual-electric; see Sec. 3.2) are not considered for simplicity, although the same rationale could be followed to derive a more generic expression which is compatible with these architectures. In order to obtain a closed form of the range equation, a constant power-split throughout the mission is assumed. In practice, it is unlikely that a constant power-split will lead to the best design, and therefore it is important to analyze variable power-control strategies early in the design process, as indicated in Chapters 5 and 9. Nevertheless, a simplified range equation can be applied to discrete mission segments with constant power split, or to determine initial values for more advanced design methods. Moreover, the derivation and application of the range equation helps to understand the influence of some of the key parameters and design considerations involved in the sizing process of hybrid-electric aircraft.

B.1. SIMPLIFIED POWERTRAIN REPRESENTATION

The simplified schematic representation of the different powertrain architectures used in this study is based on the classification of Ch. 3. When considering hybrid-electric powertrain architectures with only one type of propulsion system, one can distinguish between powertrains with a mechanical node (a gearbox), and powertrains with an electrical node (a power management and distribution system). Parallel and serial powertrains are examples of such architectures, as shown in Fig. B.1a and B.1b, respectively. Conventional, turboelectric, and fully-electric powertrains, on the other hand, can be identified as simplified versions of these two architectures. Contrary to Ch. 3, for simplicity, a distinction is made here between the electrical motor (EM) and the generator (GEN), while the PMAD and GB boxes are not explicitly shown.

At this point the simplification is made that no power losses exist at the nodes. In this case, the two powertrain types can be further simplified and merged into a single schematic, shown in Fig. B.1c. This generic representation presents two energy sources (fuel and batteries) and one energy sink (the ambient air). The three branches which connect the node with the energy sources and sinks are labeled “1”, “2”, and “3” for simplicity. Each branch is modeled by a single constant transmission efficiency η, which encompasses different elements depending on the powertrain architecture. The relation between each branch and the different architectures is summarized in Table B.1.

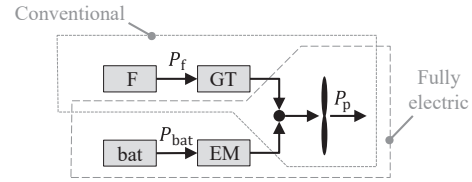

a) Mechanical node (parallel architecture)

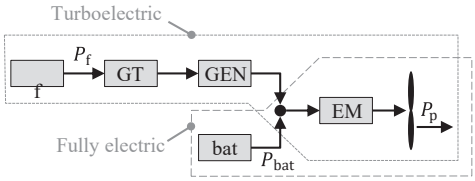

b) Electrical node (serial architecture)

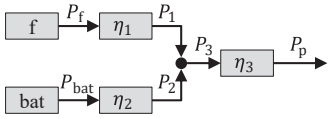

c) Simplified generic representation

Figure B.1: Simplified schematic representations of powertrain architectures.

Table B.1: Relation between powertrain branch efficiencies and component efficiencies for powertrains with mechanical (conventional, parallel, or fully-electric architectures) and electrical (turboelectric, serial, or fully-electric architectures) nodes.

Simplified representation	**Mechanical-node architectures**	**Electrical-node architectures**
$\eta_1 =$	η_{GT}	$\eta_{GT}\eta_{GEN}$
$\eta_2 =$	η_{EM}	1
$\eta_3 =$	η_p	$\eta_{EM}\eta_p$

Finally, the supplied power ratio can be used to define how the power coming from the two energy sources is shared at the node (see Sec. 3.2.2):

$$\Phi = \frac{P_{bat}}{P_{bat} + P_f}. \tag{B.3}$$

The supplied power ratio is assumed to be constant in the present analysis, as discussed earlier. Equation B.3 can be re-written as

$$P_{bat} = \frac{\Phi}{1-\Phi} P_f, \tag{B.4}$$

where, in an intermediate step, both sides of the equation have been divided by the term $(1-\Phi)$. This will lead to a singularity for $\Phi = 1$, as discussed in Sec. B.3.

B.2. DERIVATION OF THE RANGE EQUATION

The derivation starts by considering the power balance at the node of the powertrain, $P_3 = P_1 + P_2$, which can be written as

$$\frac{P_\mathrm{p}}{\eta_3} = \eta_1 P_\mathrm{f} + \eta_2 P_\mathrm{bat}. \tag{B.5}$$

The powers included on the right-hand side of Eq. B.5 are defined as positive when the energy sources are being depleted, such that

$$P_\mathrm{f} = -\frac{\mathrm{d}E_\mathrm{f}}{\mathrm{d}t}, \tag{B.6a}$$

$$P_\mathrm{bat} = -\frac{\mathrm{d}E_\mathrm{bat}}{\mathrm{d}t}. \tag{B.6b}$$

The propulsive power included on the left-hand side of Eq. B.5 can be related to the thrust required in the current flight condition, since $P_\mathrm{p} = T \cdot V$. Given that the weight of the aircraft decreases over time, the altitude of the aircraft will increase. However, the resulting flight path angle γ is approximately zero, and thus quasi-level flight is assumed. Under these conditions, the propulsive power can be expressed as

$$P_\mathrm{p} = \frac{W \cdot V}{(L/D)}. \tag{B.7}$$

By inserting Eqs. B.4, B.6, and B.7 into Eq. B.5 and reorganizing terms, one obtains

$$V = -\eta_3 \left(\frac{L}{D}\right) \frac{1}{W} \frac{\mathrm{d}E_\mathrm{f}}{\mathrm{d}t} \left(\eta_1 + \eta_2 \frac{\Phi}{1-\Phi}\right). \tag{B.8}$$

Since the flight speed is constant, the left-hand side of Eq. B.8 can be integrated to obtain the range covered during a mission segment that starts at a generic time instance t_1 and ends at t_2:

$$\int_{t_1}^{t_2} V \,\mathrm{d}t = R. \tag{B.9}$$

Equation B.8 can therefore be re-written as

$$R = \eta_3 \left(\frac{L}{D}\right) \left(\eta_1 + \eta_2 \frac{\Phi}{1-\Phi}\right) \int_{t_2}^{t_1} \frac{1}{W(t)} \frac{\mathrm{d}E_\mathrm{f}}{\mathrm{d}t} \mathrm{d}t, \tag{B.10}$$

where the integral limits have been swapped to remove the minus sign. The aircraft weight varies over time, since:

$$W(t) = W_\mathrm{OE} + W_\mathrm{PL} + W_\mathrm{bat} + W_\mathrm{f}(t). \tag{B.11}$$

Note that the battery weight W_bat is not considered part of the operating empty weight. When relating battery and fuel weight to battery and fuel energy, it is important to make a distinction between the total energy capacity of the aircraft, and the remaining energy at a given point along the mission. While the former is equal to the amount of energy

available at the beginning of the mission, the latter varies over time. With this in mind, the two weight components can be expressed as

$$W_f(t) = \frac{g}{e_f} E_f(t), \tag{B.12a}$$

$$W_{bat} = \frac{g}{e_{bat}} E_{0,bat}. \tag{B.12b}$$

In Eq. B.12b, e_{bat} refers to the specific energy of the battery at pack level when it is fully charged, which is constant and known a priori. This value should include a weight penalty of the order of 20% [78] to ensure a minimum state-of-charge during the mission and avoid detrimental effects on battery life.

Subsequently, by inserting Eqs. B.11, B.12a and B.12b into Eq. B.10, the following expression is obtained:

$$R = \eta_3 \left(\frac{L}{D}\right) \left(\eta_1 + \eta_2 \frac{\Phi}{1-\Phi}\right) \int_{t_2}^{t_1} \left(\frac{\frac{dE_f}{dt}}{W_{OE} + W_{PL} + \frac{g}{e_{bat}} E_{0,bat} + \frac{g}{e_f} E_f(t)} \right) dt. \tag{B.13}$$

The integral can be solved by recalling that $d(\ln(x))/dt = (1/x) \cdot dx/dt$, such that

$$R = \eta_3 \left(\frac{L}{D}\right) \left(\eta_1 + \eta_2 \frac{\Phi}{1-\Phi}\right) \int_{t_2}^{t_1} \frac{e_f}{g} \frac{d}{dt} \left(\ln \left(W_{OE} + W_{PL} + \frac{g}{e_{bat}} E_{0,bat} + \frac{g}{e_f} E_f(t) \right) \right) dt, \tag{B.14}$$

which, by evaluating the integral limits, leads to

$$R = \eta_3 \frac{e_f}{g} \left(\frac{L}{D}\right) \left(\eta_1 + \eta_2 \frac{\Phi}{1-\Phi}\right) \ln \left[\frac{W_{OE} + W_{PL} + \frac{g}{e_{bat}} E_{0,bat} + \frac{g}{e_f} E_f(t_1)}{W_{OE} + W_{PL} + \frac{g}{e_{bat}} E_{0,bat} + \frac{g}{e_f} E_f(t_2)} \right]. \tag{B.15}$$

Equation B.15 can be used to determine the range of a discrete mission segment, if the fuel energy E_f or fuel weight W_f (see Eq. B.12a) at the beginning and end of the segment are known. This allows an evaluation of different mission phases with different power splits or lift-to-drag ratios (e.g., cruise and diversion).

If all fuel is consumed, then $E_f(t_1) = E_{0,f}$ and $E_f(t_2) = 0$. Moreover, the fuel and battery energy carried on board at the start of the mission can be related to the total energy $E_{0,tot} = E_{0,f} + E_{0,bat}$ by combining Eqs. B.6a and B.6b with Eq. B.3 and integrating them over time, obtaining

$$E_{0,f} = (1-\Phi) E_{0,tot}, \tag{B.16a}$$

$$E_{0,bat} = \Phi E_{0,tot}. \tag{B.16b}$$

Equations B.16a and B.16b show that, because the supplied power ratio is constant throughout the mission, it is identical to the degree-of-hybridization of energy of the aircraft ($\Phi \leftrightarrow$ DOH). Equation B.15 is therefore reduced to

$$R = \eta_3 \frac{e_f}{g}\left(\frac{L}{D}\right)\left(\eta_1 + \eta_2 \frac{\Phi}{1-\Phi}\right) \ln\left[\frac{W_{OE} + W_{PL} + \frac{g}{e_{bat}} E_{0,tot}\left(\Phi + \frac{e_{bat}}{e_f}(1-\Phi)\right)}{W_{OE} + W_{PL} + \frac{g}{e_{bat}}\Phi E_{0,tot}}\right]. \tag{B.17}$$

This equation can be used to estimate the range of conventional, serial, parallel, turboelectric, and fully-electric aircraft, assuming that the supplied power ratio, flight speed, lift-to-drag ratio, and transmission efficiencies are constant. Note that the weight and energy components are expressed in their respective units to make the derivation easier to follow; however, when analyzing the range equation for different aircraft, the use of normalized variables such as weight fractions or energy fractions is recommended.

B.3. LIMIT CASES

A. FULLY FUEL-BASED CONFIGURATIONS

For fully fuel-based configurations, the supplied power ratio is equal to zero ($\Phi = 0$). Thus, Eq. B.17 is reduced to

$$R = \eta_1 \eta_3 \frac{e_f}{g}\left(\frac{L}{D}\right) \ln\left(\frac{W_{OE} + W_{PL} + \frac{g}{e_f} E_{0,tot}}{W_{OE} + W_{PL}}\right). \tag{B.18}$$

For a conventional powertrain, $(g/e_f) \cdot E_{0,tot}$ equals the fuel weight W_f of the aircraft and $\eta_1\eta_3 = \eta_{GT}\eta_p$ (see Table B.1), and hence the conventional Breguet range equation of Eq. B.1 is obtained. The same expression is applicable to turboelectric powertrains, although in that case the additional efficiency contributions of the electrical components are included ($\eta_1\eta_3 = \eta_{GT}\eta_{GEN}\eta_{EM}\eta_p$). This implies that, for the same aero-propulsive efficiency and weight breakdown, a conventional aircraft will always outperform a turboelectric variant.

B. FULLY ELECTRICAL CONFIGURATIONS

For fully battery-based configurations, the supplied power ratio is equal to one. However, when substituting $\Phi = 1$ in Eq. B.17, an indeterminate $\infty \cdot 0$ is obtained, as expected from Eq. B.4. Therefore, the limit $\Phi \to 1$ has to be analyzed. By performing a Taylor series expansion around $\Phi = 1$, the limit can be computed as

$$\lim_{\Phi \to 1} R(\Phi) = \frac{a_0 b_0 n_0}{c_0 + m_0} + \frac{a_0 n_0 (2(b_0 - 1)c_0 + b_0 n_0 - 2m_0)}{2(c_0 + m_0)^2}(\Phi - 1) + O\left((\Phi - 1)^2\right), \tag{B.19}$$

where the dummy variables a_0–n_0 are given by

$$a_0 = \eta_1 \eta_3 \frac{L}{D} \frac{e_f}{g}, \tag{B.20a}$$

$$b_0 = \frac{\eta_2}{\eta_1}, \tag{B.20b}$$

$$c_0 = W_{OE} + W_{PL}, \tag{B.20c}$$

$$m_0 = \frac{g}{e_{bat}} E_{0,tot}, \tag{B.20d}$$

$$n_0 = \frac{g}{e_f} E_{0,tot}. \tag{B.20e}$$

Therefore, by neglecting higher-order terms, in the limit of $\Phi \to 1$ the range is equal to

$$R = \eta_2 \eta_3 \left(\frac{L}{D} \right) \frac{E_{0,tot}}{W_{OE} + W_{PL} + \frac{g}{e_{bat}} E_{0,tot}}. \tag{B.21}$$

Given that $\eta_2 \eta_3 = \eta_{EM} \eta_p$, irrespective of the type of powertrain node considered (see Table B.1), in this case the range equation of the electrical architecture (Eq. B.2) is obtained. It is interesting to note that, although Eq. B.17 differs from the equations derived in literature (see Ref. [308]), in the limit $\Phi \to 1$, the different approaches result in the same expression. This is because, in the case of $\Phi = 1$, the aircraft weight remains constant and thus Eq. B.2 is valid for "hybrid-electric" aircraft. Moreover, in that case, the order in which the two energy sources is used is irrelevant, since one of them contains zero energy.

C

AERO-PROPULSIVE MODELS FOR CONCEPTUAL AIRCRAFT DESIGN

This appendix provides two aero-propulsive models which can be used to obtain a first estimate of the ΔC_L, ΔC_D, and $\Delta\eta_\mathrm{p}$ terms for wing-mounted distributed propellers in the conceptual design process, as outlined in Ch. 3. For this, the simplified geometrical parametrization of Sec. C.1 is used. The model employed for LEDP (Sec. C.2) is based on simplified analytical relations and an empirical correction for finite slipstream height, while for OTWDP (Sec. C.3) a surrogate model of numerical data is used.

C.1. GEOMETRICAL DESCRIPTION OF THE DP SYSTEM

A simplified geometrical layout of a wing-mounted distributed-propulsion system is shown in Fig. C.1. While the axial and vertical positions of the propeller array are defined differently for the leading-edge (Fig. C.1b) and over-the-wing (Fig. C.1c) arrangements, the propeller size, separation distance, and span fraction are defined in the same way (Fig. C.1a). This simplified representation assumes that the wing has a rectangular planform of span b and chord c, and that the propulsors are not located near the wing root or tip. The DP system is considered to be an array of N_dp propulsors of diameter D_P ($N_\mathrm{dp}/2$ propulsors per semi-wing, where N_dp is equal to N_1 or N_2 depending on whether the DP system corresponds to the primary or secondary powertrain, respectively), aligned in spanwise direction with a separation distance d. The propulsors are positioned at an incidence angle i_P relative to the wing chordline.

For a given number of propulsors and fraction of wingspan occupied by the DP array (b_dp/b), the diameter of the propulsors can be computed as

$$D_\mathrm{p} = \frac{(b_\mathrm{dp}/b)}{N_\mathrm{dp}(1 + d/D_\mathrm{P})} b. \tag{C.1}$$

Parts of this chapter have been published Ref. [203]

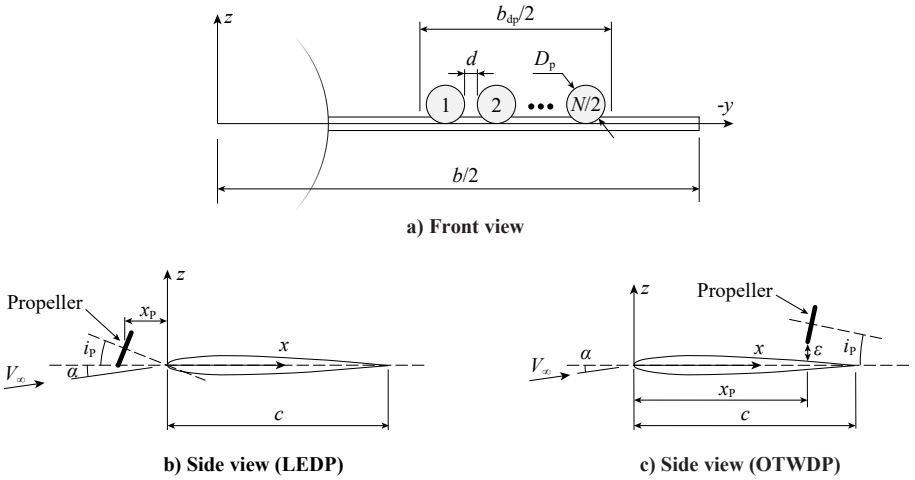

Figure C.1: Simplified representation of the LEDP (Sec. C.2) and OTWDP (Sec. C.3) systems, indicating the main geometrical parameters.

In Eq. C.1, N_{dp} and b_{dp}/b are selected as design variables, while the diameter of the propulsors is left as dependent variable. This approach is preferred since the span interval along which propulsors are installed can be limited by structural or geometrical constraints. Given that $b = \sqrt{S_w A}$ is an extensive parameter, and is therefore unknown in the sizing process, the propulsor diameter must be expressed in a normalized manner as

$$\frac{D_p^2}{W} = \left(\frac{(b_{dp}/b)}{N_{dp}(1 + d/D_P)} \right)^2 \frac{A}{(W/S_w)}, \tag{C.2}$$

hereby defining a parameter which indicates how much propulsor-disk area is needed per unit of aircraft weight W, as a function of geometrical parameters and the wing loading of the aircraft. This parameter has units of m^2/N, and can therefore be interpreted as the inverse of a weight-oriented disk loading. This parameter can be used to compute the thrust coefficient T_c[1] in the preliminary sizing phase without knowing the actual diameter of the propulsors, since

$$T_c = \frac{4}{\pi N_{dp}} \frac{\chi (T/W)}{q_\infty (D_p^2/W)}, \tag{C.3}$$

where T is the total thrust produced by the aircraft, including the non-DP system if present. Furthermore, Eq. C.2 is useful to compute the diameter-to-chord ratio of the propellers as a function of the aircraft-level design parameters, since

$$\frac{D_P}{c} = \sqrt{\left(\frac{D_p^2}{W} \right) \left(\frac{W}{S_w} \right) A}. \tag{C.4}$$

[1] Note that a different definition of the thrust coefficient was used when this method was initially published in Ref. [203].

C.2. LEADING-EDGE DISTRIBUTED PROPULSION

A series of "Delta" terms (ΔC_L, ΔC_{D_0}, ΔC_{D_i}, and $\Delta\eta_{dp}$) must be estimated in order to incorporate the aero-propulsive interaction effects in the design process. This section proposes a method to estimate these terms for distributed propellers mounted ahead of the wing leading-edge.

C.2.1. ESTIMATING THE CHANGES IN LIFT AND DRAG

Modeling the impact of tractor propellers on wing performance boils down to estimating the "Delta" terms of Eqs. 3.6, 3.4, and 3.5. Several assumptions are required in order to obtain a reasonable estimation with the information available in the preliminary sizing phase. Firstly, the propeller is modeled as an actuator disk in uniform axial inflow, and thus the upstream effect of the wing on the propeller is neglected ($\Delta\eta_{dp} = 0$). Secondly, the effect of each propeller on the adjacent ones is neglected. Thirdly, the wing is assumed to have a symmetric airfoil. Furthermore, the flow is attached, and the wing is fully immersed in the slipstream, i.e., half of the slipstream flows under the wing and half over the wing. And finally, the effect of the propellers on the wing is limited to the spanwise interval occupied by the disks (b_{dp}/b), and—within this spanwise interval—the effect on the wing is uniform in spanwise direction. Due to these strong simplifications, the accuracy of this approach requires further investigation, especially in high-lift conditions. Nonetheless, its simplicity and sensitivity to top-level design parameters make it suitable for the preliminary sizing phase and useful to demonstrate the applicability of the proposed sizing method.

The first step is to compute the axial induction factor at the propeller disk (a_P) as a function of the propeller thrust coefficient, given by Eq. C.3. From actuator disk theory it is known that (see also Eq. 8.7):

$$a_P = \frac{V_P - V_\infty}{V_\infty} = \frac{1}{2}\left(\sqrt{1+T_c} - 1\right), \tag{C.5}$$

where $V_P - V_\infty$ is the velocity increase at the propeller disk. Due to contraction, the slipstream velocity impinging on the wing is higher than at the propeller disk. Following to the derivation of Veldhuis [68], the contraction ratio of the slipstream at the wing leading-edge (R_w/R) can be expressed as

$$\frac{R_w}{R} = \sqrt{\frac{1+a_P}{1+a_P\left(1+\frac{x_P/R}{\sqrt{(x_P/R)^2+1}}\right)}}, \tag{C.6}$$

where x_P/R is the axial position of the propeller with respect to the wing leading edge, expressed as a fraction of its radius. From conservation of mass in incompressible flow it follows that

$$a_w = \frac{a_P + 1}{(R_w/R)^2} - 1. \tag{C.7}$$

With this, the velocity increase due to the thrust generated by the propellers at the wing leading-edge is known. Following the derivation of Patterson and German [313]

and modifying their equation to remove the singularity at $c_l = 0$, one can compute the sectional lift coefficient increase as

$$\Delta c_l = 2\pi \left[\left(\sin\alpha - a_w \beta \sin i_P \right) \sqrt{(a_w\beta)^2 + 2a_w\beta\cos(\alpha + i_P) + 1} - \sin\alpha \right], \tag{C.8}$$

where α is the geometric angle of attack of the wing and β is a finite-slipstream correction factor. Since in the sizing process the angle of attack of the wing is unknown, it has to be estimated using the three-dimensional lift coefficient. For this, the expression presented by Roskam [314] can be used:

$$\alpha \approx \frac{C_{L_{\text{airframe}}}}{2\pi A} \left[2 + \sqrt{A^2(1-M^2)\left(1 + \frac{\tan^2\Lambda_{c/2}}{1-M^2}\right) + 4} \right]. \tag{C.9}$$

In Eq. C.9, M is the freestream Mach number and $\Lambda_{c/2}$ the wing half-chord sweep angle. Since the aero-propulsive model assumes a rectangular wing, in this case the sweep angle is $\Lambda_{c/2} = 0$. With the aforementioned simplifications and assuming that $d/D_P \ll 1$, the sectional lift-coefficient increase obtained from Eq. C.8 can be related to the wing lift-coefficient increase through

$$\Delta C_L = \Delta c_l \cdot (b_{dp}/b). \tag{C.10}$$

Determining the finite-slipstream correction factor β of Eq. C.8 is a critical step in the process. If this term is neglected, the lift increase can be significantly over-estimated, especially for small ratios between the slipstream radius and wing chord [315]—as is the case for distributed propulsion. To this end, Patterson [61] generated a surrogate model based on CFD simulations of an actuator disk in front of a two-dimensional wing with a modified NACA 0012 airfoil. The surrogate model is used in this study to compute β as a function of a_P, x_P/c, and R/c (Eq. C.4). It is worth noting that this surrogate model uses the induced velocity far downstream of the disk as input, which according to actuator disk theory is equal to $(1 + 2a_P)V_\infty$.

In order to evaluate the impact of the propeller on wing drag, several contributions have to be analyzed. Firstly, the increase in zero-lift drag is related to the increase in friction drag on the wing surface due to increased dynamic pressure in the slipstream. This contribution can be calculated using

$$\Delta C_{D_0} = a_w^2 C_f (b_{dp}/b), \tag{C.11}$$

where C_f is the sectional skin friction coefficient, for which a typical value of 0.009 can be used [316]. Since at this stage of the design process not enough information is available to obtain a meaningful estimation of the change in wetted area when replacing one large nacelle by multiple smaller ones, this contribution to ΔC_{D_0} is neglected.

The increase in lift-induced drag can be attributed to an increase in C_L^2 on one hand, and to a change in the Oswald factor on the other. The former can be estimated by assuming a parabolic polar and expanding C_L^2 such that

$$\Delta C_{D_i} = \frac{\Delta C_L^2 + 2C_{L,\text{airframe}}\Delta C_L}{\pi A e}. \tag{C.12}$$

The change in Oswald factor due to aero-propulsive interaction, meanwhile, is assumed to be limited to a change in the span efficiency of the wing. However, the variation in span efficiency depends on a large number of design parameters and operating conditions, and is therefore difficult to estimate analytically. At high thrust settings, the increased velocity and swirl in the propeller slipstream lead to pronounced peaks in the spanwise loading distribution, decreasing the span efficiency. At low thrust settings, on the other hand, the trends are less clear. While some studies predict a decrease in span efficiency [61], others show an increase in span efficiency due to improved swirl recovery [65]. Since these effects cannot be quantified with the information available in the preliminary sizing phase, the change in span efficiency is neglected. This simplification is more accurate for DP systems than for single-propeller systems, since the increase in lift is distributed along the span of the wing instead of being concentrated at a determined spanwise station.

C.2.2. VALIDATION OF THE AERO-PROPULSIVE MODEL

In order to verify that the simplified aero-propulsive model captures the ΔC_L and ΔC_D trends correctly, the model is evaluated for a range of airframe lift coefficients and compared to CFD simulations of the NASA X-57 demonstrator. The geometrical parameters, operating conditions, and results are based on the studies of Deere et al. [317]. The CFD simulations analyzed the high-aspect ratio wing ($A = 15$) with 12 propellers in approach conditions, with a flap deflection of 30°. For the comparison, an Oswald factor of $e = 0.8$ was selected based on work of Patterson [61], and a propeller angle of attack of $\alpha_P = 0°$ was assumed. The changes in lift and drag coefficient predicted with the aero-propulsive model are presented in Fig. C.2a along with the CFD results. The results agree well in terms of ΔC_L. A slight deviation is visible for high airframe lift coefficients ($C_{L,\text{airframe}} > 2.5$) as the maximum airframe lift coefficient of 2.7 is approached. Figure C.2a also shows that the aero-propulsive model underestimates the increase in drag co-

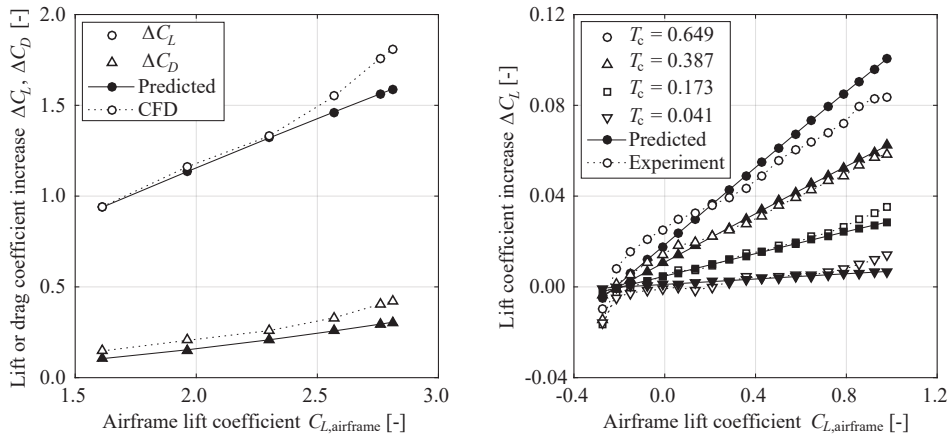

a) Distributed propulsion ($T_c = 1.56$, $i_P = 0°$) **b) Single propeller ($i_P = 2°$)**

Figure C.2: Comparison of the aero-propulsive model with a) CFD simulations of the NASA X-57 wing [317] and b) experimental data of a single tractor propeller [65].

efficient, which is expected since the impact of DP on the span efficiency is neglected[1]. Counterintuitively, for the aircraft considered in this study, this discrepancy leads to a conservative design. The main impact of DP on the aerodynamic performance of the aircraft is an increase in L/D due to increased wing loading, and not due to improved L/D for a given wing loading. The maximum wing loading is determined in landing conditions, for which a higher drag coefficient is beneficial since more thrust is required to maintain the same approach speed. This leads to an increase in ΔC_L, which in turn increases the maximum allowable wing loading.

The predictions are also compared to the experimental data of Sinnige et al. [65], to check whether the model is accurate for other propeller configurations. These experiments studied a single tractor propeller mounted on a low-aspect-ratio wing. The wing airfoil was cambered, and the performance was evaluated at low lift coefficients. Initial comparisons between the analytical model and experimental data showed that the model is not capable of directly capturing the performance trends. This is attributed to several reasons. Firstly, at low lift coefficients, the symmetric-airfoil assumption becomes less accurate: at $i_P = 0^o$, $\alpha = 0^o$, a symmetric airfoil generates zero lift independently of thrust, while a cambered airfoil produces more lift as thrust is increased. Secondly, the diameter of the propeller was not small when compared to the span of the wing ($D_P/b = 0.32$). Therefore, the propeller has a relatively larger impact on the lift distribution outside the slipstream. Furthermore, the swirl in the slipstream has a larger impact on the spanwise lift distribution. A more detailed analysis showed that the trends could be estimated with reasonable accuracy if the effect of airfoil camber was represented by means of a small propeller incidence angle; in this case, -2^o with respect to the wing. The resulting ΔC_L curves[2] are shown in Fig. C.2b for four thrust coefficients. With this correction, the trends predicted by the model can be applied to the preliminary sizing process. Therefore, in summary, the verification procedure shows that the model is applicable to high-aspect-wings at high lift coefficients and with a large number of propellers, while it is not accurate for wings at low angles of attack and with large propellers, unless experimental or numerical data are available to correct the model for the setup considered.

C.3. OVER-THE-WING DISTRIBUTED PROPULSION

This section presents a simplified aero-propulsive model to estimate the changes in lift, drag, and propulsive efficiency of an OTWDP system. The model is intended for preliminary aircraft-sizing purposes and is only applicable to moderate lift ($C_{L,\text{airframe}} < 1$) and thrust ($T_c < 0.4$) coefficients. Therefore, it cannot be used for take-off or landing conditions. Analogously to the previous section, this model considers a simplified geometrical representation shown in Fig. C.1, which assumes an array of $N_{dp} \gg 1$ propellers placed above an unswept, untapered wing. The propellers are assumed to be far from the root and tip, and the effect of nacelles, pylons, ducts, or other elements are not considered.

[1] Evaluation of the aero-propulsive model with an Oswald-factor penalty of -0.2 leads to a nearly perfect agreement between the predicted ΔC_D values and those obtained from CFD in Fig. C.2. However, this arbitrary value would not be justifiable for other configurations or thrust coefficients.

[2] Wing drag data were not representative for comparison, due to the effect of the slipstream on trailing-edge flow separation at low Reynolds numbers during the experimental campaign.

The numerical method developed in Ch. 8 is used to estimate the "delta" terms. For more information regarding the assumptions and accuracy of the method, the reader is referred to Ch. 8. However, while this method uses the angle of attack and advance ratio as independent variables, these variables are not known in the preliminary sizing phase. Therefore, a surrogate model is created to estimate the "delta" terms as a function of the airframe-only lift coefficient, wing-chord-based Reynolds number, Mach number, and the propellers' thrust coefficient, axial position, incidence angle, and diameter-to-chord ratio. For this surrogate model, the separation between propellers ($d/R = 0.1$) and tip clearance to the wing ($\varepsilon/c = 0.0167$) are selected based on Ch. 8 and kept constant. Moreover, since the wing chord is unknown in the preliminary sizing phase, a reference chord length must be assumed to obtain a rough estimate of the Reynolds number. The diameter-to-chord ratio and thrust coefficient, on the other hand, can be estimated based on top-level aircraft design parameters using Eqs. C.3 and C.4. Note that, as in the previous section, the number of propellers N_{dp} and the span fraction covered by the propeller array (b_{dp}/b) are taken as design variables, while the propeller size is computed. The surrogate model can be expressed as:

$$\Delta c_l,\ \Delta c_d,\ \Delta\eta_{\text{p}}/\eta_{\text{p,iso}} = f\left(C_{L,\text{airframe}}, T_{\text{c}}, Re, M, x_{\text{P}}/c, i_{\text{P}}, D_{\text{P}}/c\right). \tag{C.13}$$

The coefficients Δc_l and Δc_d represent the average change in lift and drag of the wing segment beneath a single propeller. Assuming that the OTW propellers have a negligible effect on aircraft lift and drag outside the interval b_{dp}, these "sectional" coefficients can be related to the 3D lift and drag coefficients through:

$$\Delta C_L = \Delta c_l \cdot (b_{\text{dp}}/b), \tag{C.14}$$

$$\Delta C_D = \Delta c_d \cdot (b_{\text{dp}}/b). \tag{C.15}$$

Moreover, the ratio $\Delta\eta_{\text{p}}/\eta_{\text{p,iso}}$ is taken as output from the surrogate model because the ratio between the installed and isolated propeller efficiencies is, for a given inflow disturbance, independent of the blade pitch angle, as discussed in Ch. 8 and Ref. [283]. Therefore, assuming a variable-pitch propeller, or a fixed-pitch propeller that operates near the advance ratio of maximum efficiency, the change in propulsive efficiency can be obtained from

$$\Delta\eta_{\text{p}} = \left(\frac{\Delta\eta_{\text{p}}}{\eta_{\text{p,iso}}}\right)\eta_{\text{p,iso}}, \tag{C.16}$$

where the propulsive efficiency of the isolated propeller $\eta_{\text{p,iso}}$ can be computed for a given thrust coefficient using e.g. Eq. 2.13.

Table C.1 provides an overview of the variables involved in the surrogate model. The "LHS bounds" columns present the lower and upper bounds of the input parameters that were varied in a design-of-experiments. The bounds were selected based on the limits established in Ch. 8. In this DoE, 2,000 points were defined using a Latin-hypercube sampling. The numerical model was then used to compute the isolated-wing lift coefficient (which is assumed to be equal to the airframe-only lift coefficient), the propeller thrust coefficient, and the three "delta" terms for each point. Subsequently, the changes

in lift and drag (Δc_l, Δc_d) were fitted to the independent variables x_1–x_7 using a (seven-dimensional) third-order polynomial fit. The ratio of the change in propulsive efficiency ($\Delta\eta_\mathrm{p}/\eta_\mathrm{p,iso}$) was also fitted to the independent variables x_1–x_5 using a (five-dimensional) third-order polynomial fit. Since the numerical method does not account for the effect of the Reynolds and Mach numbers on the propulsive efficiency (see Ch. 8), these dependencies are ignored. A third-order fit was selected because the parameter sweeps of Appendix G showed that the physical response is smooth and can be modeled with a relatively low-order polynomial. For simplicity, and given that it has a negligible effect on the overall computational cost of the aircraft sizing routine, the same order was applied for all variables. However, it should be noted that a better fit can be achieved if the dependency of each independent variable y on each dependent variable x is modeled using a polynomial order that is physically representative. In that case, some of the less significant terms of the polynomial will disappear.

For a third-order fit of $N = 7$ independent variables, the polynomial representing one of the "delta" terms contains $m = 120$ monomials (see Appendix F.1). As discussed in Appendix F.1, for a given dependent variable $\check{y}_i$, this polynomial can be expressed as[1]

$$\check{y}_i = \sum_{j=1}^{m} \left[\beta_{ij} \left(\prod_{k=1}^{N} \check{x}_k^{E_{jk}} \right) \right], \tag{C.17}$$

where β_{ij} is the linear coefficient of the j-th monomial, and E_{jk} the exponent of the k-th independent variable of the j-th monomial. For Eq. C.17, the dependent ($\check{y}_i$) and independent ($\check{x}_k$) variables are scaled from zero to one, in order to improve the quality of the fit. In other words, $\check{x}_k$ can be obtained from the input value x_k using

$$\check{x}_k = \frac{x_k - x_{\mathrm{L},k}}{x_{\mathrm{U},k} - x_{\mathrm{L},k}}, \tag{C.18}$$

where $x_{\mathrm{L},k}$ and $x_{\mathrm{U},k}$ correspond to the lowest and highest values of the independent variable x_k sampled in the DoE, respectively. These values are provided in the last two columns of Table C.1. Analogously, once the scaled variable $\check{y}_i$ has been calculated using Eq. C.17, it can be un-scaled to the actual value y_i with

$$y_i = y_{\mathrm{L},i} + \check{y}_i \cdot \left(y_{\mathrm{U},i} - y_{\mathrm{L},i} \right). \tag{C.19}$$

The values of the coefficients and exponents of Eq. C.17 are tabulated in Table C.2. These values can be used to compute Δc_l, Δc_d, and $\Delta\eta_\mathrm{p}/\eta_\mathrm{p,iso}$ with Eqs. C.17–C.19 and the scaling factors given in Table C.1. The coefficients β_{ij} were calculated with the procedure of Appendix F.1 using 90% of the data points. The remaining 10% were used to evaluate the accuracy of the fit. The mean deviation of the test points from the surrogate model was found to be below 0.04%, relative to the width of the interval $\left(y_{\mathrm{U},i} - y_{\mathrm{L},i}\right)$. The maximum deviation observed was of the order of 10% of this interval. However, a manual comparison of the surrogate model to the results of Sec. 8.4 showed that the trends were correctly captured. Moreover, to avoid potentially inaccurate fits near the variable bounds, the surrogate-model input was limited to the bounds indicated in Table C.1 ("SM bounds"). For the geometrical parameters and Reynolds number, this did

[1] The integers i, j, k are used as index variables here; i.e. no Einstein notation is employed.

not constitute any limitation in the design studies of Ch. 10. While the Mach number was exceeded in the cruise phase of the high-speed mission ($M_{\text{cr}} = 0.6$), the changes in lift and drag are practically insensitive to Mach number in those conditions (see Sec. 8.4). However, at the start of climb, the upper bounds of $C_{L,\text{airframe}}$ and T_{c} were exceeded. In that case, limiting the variables to their values at the bounds was considered to lead to conservative results, since the benefits generally increase with thrust setting.

Table C.1: Bounds and scaling factors of the independent (x_k) and dependent (y_i) variables used in the surrogate model (SM).

	Variable	**LHS bounds**		**SM bounds**		**SM scaling factos**	
		Lower	**Upper**	**Lower**	**Upper**	x_{L} / y_{L}	x_{U} / y_{U}
	α [deg]	-3	8	-	-	-	-
	J [-]	1.4	2.6	-	-	-	-
$x_1 =$	$C_{L,\text{airframe}}$ [-]	-	-	0	1.0	-0.0735	1.3248
$x_2 =$	T_{c} [-]	-	-	0	0.4	-0.0862	0.4516
$x_3 =$	x_{P}/c [-]	0.70	1.05	0.75	1.00	0.7006	1.0494
$x_4 =$	i_{P} [deg]	-7	12	-5	10	-6.9683	11.9683
$x_5 =$	D_{P}/c [-]	0.05	1.05	0.1	1.0	0.0517	1.0483
$x_6 =$	$\log_{10}(Re)$ [-]	5.9	8.1	6	8	5.9037	8.0963
$x_7 =$	M [-]	0	0.55	0.05	0.50	0.0009	0.5491
$y_1 =$	Δc_l [-]	-	-	-	-	-0.0627	0.3057
$y_2 =$	Δc_d [-]	-	-	-	-	-0.0316	0.0044
$y_3 =$	$\Delta\eta_{\text{p}}/\eta_{\text{p,iso}}$ [-]	-	-	-	-	-0.2441	0.2187

Table C.2: Coefficients and exponents of the OTWDP surrogate model.

Monomial	**Coefficients**			**Exponents**						
j	β_{1j}	β_{2j}	β_{3j}	E_{j1}	E_{j2}	E_{j3}	E_{j4}	E_{j5}	E_{j6}	E_{j7}
1	0.3229	0.8795	0.7364	0	0	0	0	0	0	0
2	-0.0671	-0.0055	0.4397	1	0	0	0	0	0	0
3	-0.2650	-0.0498	0.0499	0	1	0	0	0	0	0
4	-0.1335	-0.0617	0.5132	0	0	1	0	0	0	0
5	-0.3796	0.0141	-0.6382	0	0	0	1	0	0	0
6	-0.4409	0.0361	-0.9801	0	0	0	0	1	0	0
7	-0.1108	-0.0030	0.0000	0	0	0	0	0	1	0
8	-0.2895	0.1002	0.0000	0	0	0	0	0	0	1
9	-0.2015	0.0855	-0.2020	2	0	0	0	0	0	0
10	0.1068	-0.1460	0.0424	1	1	0	0	0	0	0
11	0.1422	0.0189	-0.1144	0	2	0	0	0	0	0
12	-0.0862	-0.0685	0.2866	1	0	1	0	0	0	0
13	0.5291	0.1641	0.0133	0	1	1	0	0	0	0
14	0.1280	0.1465	0.1777	0	0	2	0	0	0	0
15	0.2590	0.0130	-0.9746	1	0	0	1	0	0	0
16	0.3976	0.0624	-0.0185	0	1	0	1	0	0	0
17	0.0890	-0.0534	-0.3503	0	0	1	1	0	0	0
18	0.4128	-0.0086	0.1715	0	0	0	2	0	0	0
19	-0.0371	0.1441	-0.9151	1	0	0	0	1	0	0
20	1.3705	-0.5230	-0.0611	0	1	0	0	1	0	0
21	-0.1282	0.0050	-0.8925	0	0	1	0	1	0	0
22	0.4117	0.0066	1.3958	0	0	0	1	1	0	0
23	0.0974	0.0238	1.2465	0	0	0	0	2	0	0
24	0.2096	0.0591	0	1	0	0	0	0	1	0
25	0.1448	0.0465	0	0	1	0	0	0	1	0
26	0.1427	-0.0967	0	0	0	1	0	0	1	0
27	-0.1334	-0.0043	0	0	0	0	1	0	1	0
28	0.0271	0.0228	0	0	0	0	0	1	1	0
29	0.0117	-0.0127	0	0	0	0	0	0	2	0
30	0.1456	-0.0929	0	1	0	0	0	0	0	1
31	0.2779	-0.1222	0	0	1	0	0	0	0	1
32	0.1831	-0.0438	0	0	0	1	0	0	0	1
33	0.0732	-0.0375	0	0	0	0	1	0	0	1
34	0.1125	0.0016	0	0	0	0	0	1	0	1
35	0.1236	0.0705	0	0	0	0	0	0	1	1
36	0.2582	-0.1269	0	0	0	0	0	0	0	2
37	0.1755	-0.0423	0.1591	3	0	0	0	0	0	0
38	-0.1188	0.0297	-0.0012	2	1	0	0	0	0	0
39	-0.0043	0.1269	-0.0116	1	2	0	0	0	0	0
40	-0.0003	-0.0379	0.0763	0	3	0	0	0	0	0

Table C.2: (continued)

Monomial	**Coefficients**			**Exponents**						
j	β_{1j}	β_{2j}	β_{3j}	E_{j1}	E_{j2}	E_{j3}	E_{j4}	E_{j5}	E_{j6}	E_{j7}
41	0.1153	-0.0322	0.0009	2	0	1	0	0	0	0
42	-0.2546	0.3152	-0.0376	1	1	1	0	0	0	0
43	-0.1356	0.0226	-0.0125	0	2	1	0	0	0	0
44	0.0912	-0.0836	-0.0841	1	0	2	0	0	0	0
45	-0.3542	-0.1428	0.0271	0	1	2	0	0	0	0
46	-0.0567	-0.0273	-0.2520	0	0	3	0	0	0	0
47	-0.0286	-0.0330	-0.0004	2	0	0	1	0	0	0
48	-0.0729	0.0236	-0.0423	1	1	0	1	0	0	0
49	-0.2491	-0.0173	0.0181	0	2	0	1	0	0	0
50	-0.0255	0.0549	-0.0776	1	0	1	1	0	0	0
51	-0.0512	-0.0935	0.0013	0	1	1	1	0	0	0
52	-0.0392	-0.0185	0.1870	0	0	2	1	0	0	0
53	-0.1426	-0.0358	0.2453	1	0	0	2	0	0	0
54	-0.0197	-0.0696	0.0184	0	1	0	2	0	0	0
55	-0.0355	0.0848	0.0568	0	0	1	2	0	0	0
56	-0.1730	0.0206	-0.0130	0	0	0	3	0	0	0
57	0.0453	-0.0124	-0.0903	2	0	0	0	1	0	0
58	0.0461	-0.5625	0.0127	1	1	0	0	1	0	0
59	-0.2207	-0.0700	0.0083	0	2	0	0	1	0	0
60	-0.0276	0.1421	-0.0530	1	0	1	0	1	0	0
61	-0.4329	0.5980	-0.0090	0	1	1	0	1	0	0
62	0.0530	-0.0593	0.1722	0	0	2	0	1	0	0
63	0.0152	-0.0133	0.5887	1	0	0	1	1	0	0
64	0.3165	0.2618	-0.0113	0	1	0	1	1	0	0
65	-0.0066	0.0193	0.0670	0	0	1	1	1	0	0
66	-0.0572	-0.0706	-0.2745	0	0	0	2	1	0	0
67	0.1513	-0.0943	0.4352	1	0	0	0	2	0	0
68	-0.4350	-0.1056	0.0474	0	1	0	0	2	0	0
69	0.1645	-0.1444	0.3797	0	0	1	0	2	0	0
70	-0.0351	-0.0245	-0.7235	0	0	0	1	2	0	0
71	-0.0364	0.0818	-0.5347	0	0	0	0	3	0	0
72	-0.1993	-0.0171	0	2	0	0	0	0	1	0
73	0.1607	-0.1819	0	1	1	0	0	0	1	0
74	-0.0084	-0.0508	0	0	2	0	0	0	1	0
75	-0.1280	0.0508	0	1	0	1	0	0	1	0
76	0.0588	0.1111	0	0	1	1	0	0	1	0
77	-0.0685	0.0359	0	0	0	2	0	0	1	0
78	0.0422	0.0021	0	1	0	0	1	0	1	0
79	-0.0122	0.0277	0	0	1	0	1	0	1	0
80	-0.0374	-0.0042	0	0	0	1	1	0	1	0

Table C.2: (concluded)

Monomial	**Coefficients**			**Exponents**						
j	β_{1j}	β_{2j}	β_{3j}	E_{j1}	E_{j2}	E_{j3}	E_{j4}	E_{j5}	E_{j6}	E_{j7}
81	0.0888	-0.0228	0	0	0	0	2	0	1	0
82	0.0308	-0.0488	0	1	0	0	0	1	1	0
83	0.2149	-0.1672	0	0	1	0	0	1	1	0
84	-0.0271	0.0322	0	0	0	1	0	1	1	0
85	0.0563	0.0069	0	0	0	0	1	1	1	0
86	-0.0669	0.0042	0	0	0	0	0	2	1	0
87	0.0530	0.0207	0	1	0	0	0	0	2	0
88	-0.1153	0.0597	0	0	1	0	0	0	2	0
89	0.0612	-0.0154	0	0	0	1	0	0	2	0
90	0.0215	0.0183	0	0	0	0	1	0	2	0
91	-0.0322	0.0284	0	0	0	0	0	1	2	0
92	-0.0270	-0.0127	0	0	0	0	0	0	3	0
93	0.0611	0.0445	0	2	0	0	0	0	0	1
94	-0.2044	0.0472	0	1	1	0	0	0	0	1
95	-0.0012	0.0400	0	0	2	0	0	0	0	1
96	0.0130	0.0295	0	1	0	1	0	0	0	1
97	-0.2599	0.0969	0	0	1	1	0	0	0	1
98	0.0178	-0.0380	0	0	0	2	0	0	0	1
99	-0.0244	0.0163	0	1	0	0	1	0	0	1
100	-0.0228	0.0379	0	0	1	0	1	0	0	1
101	-0.0172	-0.0126	0	0	0	1	1	0	0	1
102	0.0071	-0.0014	0	0	0	0	2	0	0	1
103	-0.0900	-0.0161	0	1	0	0	0	1	0	1
104	-0.0582	-0.0542	0	0	1	0	0	1	0	1
105	-0.0695	0.0303	0	0	0	1	0	1	0	1
106	-0.0460	0.0289	0	0	0	0	1	1	0	1
107	0.0158	-0.0195	0	0	0	0	0	2	0	1
108	-0.1701	-0.0648	0	1	0	0	0	0	1	1
109	0.0997	-0.1279	0	0	1	0	0	0	1	1
110	-0.0831	0.0459	0	0	0	1	0	0	1	1
111	-0.0028	-0.0054	0	0	0	0	1	0	1	1
112	0.0070	-0.0356	0	0	0	0	0	1	1	1
113	0.0159	-0.0040	0	0	0	0	0	0	2	1
114	-0.0565	0.0664	0	1	0	0	0	0	0	2
115	-0.1771	0.0905	0	0	1	0	0	0	0	2
116	-0.0669	0.0214	0	0	0	1	0	0	0	2
117	-0.0402	0.0164	0	0	0	0	1	0	0	2
118	-0.0322	0.0192	0	0	0	0	0	1	0	2
119	-0.0414	-0.0187	0	0	0	0	0	0	1	2
120	-0.0746	0.0373	0	0	0	0	0	0	0	3

D

AIRCRAFT SIZING DATA

D.1. VALIDATION STUDY

This section lists the requirements, assumptions, design parameters, and results obtained in the validation study presented in Chapter 4. In the following tables, "Method A" refers to the method described in Ref. [104], while "Method B" refers to the method used in this dissertation.

Table D.1: Additional design parameters and assumptions which are not included in Tables 4.1, 4.2, and 4.5.

Parameter	Value	Parameter	Value
Number of propellers N_P [-]	2	Take-off lift coeff. $C_{L,TO}$ [-][a]	1.34
PMAD efficiency η_{PMAD} [-]	1.0	$\Delta C_{L,max}$, take-off flaps [-]	0.73
Gearbox efficiency η_{GB} [-]	1.0	$\Delta C_{L,max}$, landing flaps [-]	0.97
Fuel specific energy e_f [MJ/kg][b]	42.8	$\Delta C_{D,min}$, take-off flaps [-][b]	0.010
OEM/MTOM fraction [-][b]	0.600	$\Delta C_{D,min}$, landing flaps [-][b]	0.045
OEM'/MTOM fraction [-][a]	0.545	$\Delta C_{D,min}$, landing gear [-][b]	0.015
Ambient density ρ_∞ [kg/m^3]	ISA	$\Delta C_{L,minD}$, take-off flaps [-][b]	0
Ambient temperature T_∞ [^{o}C]	ISA	$\Delta C_{L,minD}$, landing flaps [-][b]	0
Coefficient of rolling friction [-][a]	0.04	Δe, take-off flaps [-][b]	0.040
Max. lift coeff. (clean) $C_{L,max}$ [-]	1.70	Δe, landing flaps [-][b]	0.125

[a] Parameters only required for Method A.
[b] Parameters only required for Method B.

Table D.2: Assumed aircraft properties per performance constraint and mission segment. A dash (-) indicates that the quantity is not an input, but a computed value.

		ξ [-]	Velocity [m/s]	m/m_{TO} [-]	Prop. eff. [-]	Flap setting	Landing gear
Constraints	Cruise	0.9	115	1	0.8	retracted	retracted
	Take-off	1	-[a] / $1.2V_s$[b,1]	1	0.7	take-off	extended
	Landing	0.9	34.6	1	0.8	landing	extended
	AEO ROC	0.9	$V_{\text{best climb}}$[a] / $1.2V_s$[b,1]	1	0.7	retracted	retracted
	OEI ROC	1	$V_{\text{best climb}}$[a] / $1.2V_s$[b,1]	1	0.65	retracted	retracted
Mission analysis	Climb	0.9	-	-	0.8	retracted	retracted
	Cruise	-	115	-	0.8	retracted	retracted
	Descent	0.10[a] / 0.05[b]	-	-	0.8	retracted	retracted
	Div. climb	0.9	-	-	0.8	retracted	retracted
	Div. cruise	-	82	-	0.8	retracted	retracted
	Div. des.	0.10[a] / 0.05[b]	-	-	0.8	retracted	retracted
	Loiter	-	53[a] / $V_{\text{max endurance}}$[b]	-	0.8	retracted	retracted

[a] Values used for Method A.
[b] Values used for Method B.
[1] Stall speed in the flight condition considered.

Table D.3: Component masses and wing area obtained in the reference aircraft comparison.

Mission	Method	m_{TO} [kg]	m_{OE} [kg]	m_{PL} [kg]	m_f [kg]	m_{GT} [kg]	S_w [m^2]
396 km	Reference	6400	3900	1960	540	349	32.0
	A	6641	3866	1960	615	356	32.3
	B	6416	3865	1960	591	354	32.2
1280 km	Reference	6400	3900	1325	1175	349	32.0
	A	6434	3862	1325	1247	356	32.2
	B	6403	3857	1325	1221	353	32.1
2361 km	Reference	6400	3900	547	1953	349	32.0
	A	6489	3895	547	2047	359	32.5
	B	6188	3728	547	1914	341	31.0

Table D.4: Taxi, take-off, and landing energy fractions assumed for Method B, based on the estimations of Method A, for the three missions considered. Energy fractions expressed as a percentage of total installed energy (including reserves). "N/A" indicates no converged design was obtained.

		Short range $R = 396$ km $m_{PL} = 1960$ kg	**Medium range** $R = 1280$ km $m_{PL} = 1280$ kg	**Long range** $R = 2361$ km $m_{PL} = 2361$ kg
Conv.	Taxi out & take-off	2.6%	1.3%	0.8%
	Landing & taxi in	1.6%	0.8%	0.5%
Parallel	Taxi out & take-off	2.1%	0.9%	0.6%
	Landing & taxi in	0.7%	0.3%	0.2%
Serial	Taxi out & take-off	2.2%	0.9%	N/A
	Landing & taxi in	0.7%	0.3%	N/A
Electric	Taxi out & take-off	1.6%	N/A	N/A
	Landing & taxi in	0.1%	N/A	N/A

Table D.5: Component masses and wing area obtained for the four different powertrain configurations in the HEP comparison study. "N/A" indicates no converged design was obtained.

Config.	***R* [km]**	**Method**	m_{TO} [kg]	m_{OE} [kg]	m_{PL} [kg]	m_f [kg]	m_{bat} [kg]	m_{GT} [kg]	m_{GEN} [kg]	m_{EM} [kg]	S_w [m^2]
Conv.	396	A	6216	3731	1960	525	0	343	0	0.0	31.1
		B	6259	3770	1960	529	0	345	0	0.0	31.4
	1280	A	6364	3820	1325	1219	0	352	0	0.0	31.9
		B	6446	3883	1325	1238	0	356	0	0	32.3
	2361	A	7083	4252	547	2285	0	391	0	0.0	35.5
		B	7182	4325	547	2310	0	396	0	0.0	36.0
Parallel	396	A	6361	3803	1960	486	113	316	0	19.7	31.9
		B	6385	3830	1960	481	115	317	0	18.9	32.0
	1280	A	7058	4219	1325	1222	292	351	0	21.8	35.4
		B	7102	4259	1325	1222	296	352	0	21	35.6
	2361	A	13472	8054	547	3924	947	670	0	41.6	67.5
		B	13363	8014	547	3863	939	663	0	39.5	66.9
Serial	396	A	8295	5490	1960	697	148	457	256	256	41.6
		B	8246	5452	1960	686	148	453	243	244	41.3
	1280	A	12518	8284	1325	2389	519	690	386	387	62.7
		B	12354	8168	1325	2348	513	679	364	365	61.9
	2361	A	N/A	N/A	N/A	N/A	N/A	N/A	N/A	N/A	N/A
		B	N/A	N/A	N/A	N/A	N/A	N/A	N/A	N/A	N/A
Electric	396	A	8168	4704	1960	0	1504	0	0	252	40.9
		B	8294	4784	1960	0	1550	0	0	245	41.6
	1280	A	N/A	N/A	N/A	N/A	N/A	N/A	N/A	N/A	N/A
		B	N/A	N/A	N/A	N/A	N/A	N/A	N/A	N/A	N/A
	2361	A	N/A	N/A	N/A	N/A	N/A	N/A	N/A	N/A	N/A
		B	N/A	N/A	N/A	N/A	N/A	N/A	N/A	N/A	N/A

D.2. DESIGN-SPACE EXPLORATION STUDY

This section lists the requirements, assumptions, design parameters, and results obtained in the sensitivity studies presented in Chapter 9.

Table D.6: Baseline aircraft requirements.

Parameter	Value
Payload, m_{PL} [kg]	7,500
Cruise altitude, h_{cr} [ft]	17,000
Cr. Mach number, M_{cr} [-]	0.41
Range, R [nmi]	825
Take-off field length [m]	1333
Approach speed [kts]	115
OEI ceiling [ft]	12,000
OEI s. s. climb gradient [-]	0.024
Diversion altitude [ft]	10,000
Div. Mach number [-]	0.3
Diversion range [nmi]	250

Table D.7: Baseline design-parameter values. Asterisks indicate parameters which are only applicable to the hybrid-electric configuration.

Parameter	Value
Aspect ratio, A [-]	12
Half-chord sweep [deg]	0
Taper ratio [-]	0.62
Wing root t/c [-]	0.18
N$^{\text{o}}$ of primary props., N_1 [-]	2
N$^{\text{o}}$ of secondary props.*, N_2 [-]	10
DP span fraction*, b_{dp}/b [-]	0.5
Spacing between props.* d/D_{P} [-]	0.01
Axial position of props.*, x_{P}/c [-]	0.85

Table D.8: Baseline aerodynamic and mission properties assumed per constraint. All parameters are non-dimensional. Asterisks indicate parameters which are only applicable to the hybrid-electric configuration.

	Cruise speed	Approach speed	Take-off distance	OEI ceiling	OEI s. s. c.
Flap configuration	clean	landing	take-off	clean	take-off
Landing gear position	retracted	extended	extended	retracted	retracted
Zero-lift drag coeff., C_{D_0}	0.022	0.087	0.037	0.022	0.027
Oswald factor, e	0.8	0.95	0.9	0.8	0.9
Max. lift coeff., $C_{L_{\text{max,airframe}}}$	-	3	2.1	1.6	2.1
Prop. eff. (primary), η_{p1}	0.85	0.8	0.7	0.8	0.75
Aircraft weight fraction	0.98	0.95	1	0.98	1
Gas turbine throttle, ξ_{GT}	0.8	0.5	1	1	1
Supplied power ratio*, Φ	0.01	0.01	0.05	0.1	0.05
Shaft power ratio*, φ	0.5	1	0.5	0.5	0.5

Table D.9: Values of the power-control parameters varied during the DOE. From left to right: baseline value, lower bound in DOE, upper bound in DOE, and the "optimum" value found in the DOE in terms of payload-range energy efficiency. Subscripts "1" and "2" indicate start and end of mission segment, respectively.

		Baseline	**Lower bound**	**Upper bound**	**Best value**
Take-off	Φ	0.05	0	0.5	0
	φ	0.5	0	1	0.032
Climb	ξ_{GT1}	0.85	0.5	1	0.651
	ξ_{GT2}	0.95	0.5	1	0.998
	Φ_1	0.03	0	0.5	0
	Φ_2	0.01	0	0.5	0
	φ_1	0.5	0	1	0.165
	φ_2	0.5	0	1	0.357
Cruise	Φ_1	0.015	-0.05	0.05	0
	Φ_2	-0.01	-0.05	0.05	0
	φ_1	0.5	0	1	0.032
	φ_2	0.5	0	1	0.050
Descent	Φ_1	-0.01	-0.5	0.05	0
	Φ_2	-0.1	-0.5	0.05	0
	φ_1	0.5	0	1	0.160
	φ_2	0.5	0	1	0.811
Landing	φ	1	0	1	0.827
OEI ceiling	Φ	0.01	0	0.5	0
	φ	0.5	0	1	0.187

Table D.10: Main characteristics of the reference aircraft (conventional configuration, 2035 timeframe), the reference aircraft evaluated at optimum altitude, the baseline HEP aircraft, and the improved HEP aircraft evaluated at optimum altitude. Powertrain properties refer to the total installed power or mass, not per component instance.

	Reference (2035)	**Reference (2035, opt. h_{cr})**	**HEP (baseline)**	**HEP (improved, opt. h_{cr})**
Take-off mass [t]	20.9	20.9	24.1	21.1
Operative empty mass [t]	11.8	11.8	14.1	12.0
Wing mass [t]	1.69	1.64	1.89	1.55
Gas turbine mass [t]	1.14	1.14	1.30	1.31
Generator mass [t]	0	0	0.16	0.11
Rectifier mass [t]	0	0	0.11	0.07
Electromotor mass [t]	0	0	0.19	0.10
Inverter mass [t]	0	0	0.13	0.07
Additional PMAD mass [t]	0	0	0.18	0.11
Fuel mass [t]	1.64	1.62	1.98	1.65
Batery mass [t]	0	0	0.61	0
Wing loading [kN/m^2]	4.00	4.00	4.50	4.68
Wing area [m^2]	51.3	51.1	52.6	44.3
Gas turbine W_{TO}/P [N/kW]	49.7	49.7	49.5	43.1
Generator W_{TO}/P [N/kW]	N/A	N/A	117.4	148.5
Electromotor W_{TO}/P [N/kW]	N/A	N/A	94.0	156.2
Battery W_{TO}/P [N/kW]	N/A	N/A	389.4	∞
Gas turbine power [MW]	4.13	4.12	4.79	4.81
Generator power [MW]	N/A	N/A	2.02	1.40
Electromotor power [MW]	N/A	N/A	2.52	1.33
Battery power [MW]	N/A	N/A	0.61	0
Average cruise L/D [-]	17.86	18.45	18.41	18.50
Average cruise η_p [-]	0.850	0.850	0.825	0.851
Cruise altitude [ft]	17,000	21,500	17,000	18,000
Thrust vec. angle, take-off [deg]	N/A	N/A	0	10
Thrust vec. angle, landing [deg]	N/A	N/A	30	55
Fuel energy [GJ]	70.2	69.2	84.6	70.6
Battery energy [GJ]	0	0	1.09	0
Degree-of-hybridization [-]	0	0	0.013	0
PREE [-]	2.11	2.15	1.76	2.13

Table D.11: Aeropropulsive efficiency increase necessary for a 15% increase in PREE with respect to a fuel-based reference aircraft, for a cruise Mach number of $M = 0.45$.

			Mission A			Mission B		
		m_{PL} [t]	20			15		
		R [nmi]	650			2000		
	CSP	M [-]	0.45			0.45		
Scenario	[kW/kg]	η_{chain} [-]	$\varphi = 0.2$,	0.5,	1.0	$\varphi = 0.2$,	0.5,	1.0
Near-term	2	0.80	24%	>45%	>45%	23%	44%	>45%
Mid-term	3	0.90	18%	28%	>45%	17%	27%	>45%
Long-term	5	0.98	15%	18%	24%	13%	17%	23%

Table D.12: Aeropropulsive efficiency increase necessary for a 5% increase in PREE with respect to a fuel-based reference aircraft, for a cruise Mach number of $M = 0.45$.

			Mission A			Mission B		
		m_{PL} [t]	20			15		
		R [nmi]	650			2000		
	CSP	M [-]	0.45			0.45		
Scenario	[kW/kg]	η_{chain} [-]	$\varphi = 0.2$,	0.5,	1.0	$\varphi = 0.2$,	0.5,	1.0
Near-term	2	0.80	15%	34%	>45%	15%	34%	>45%
Mid-term	3	0.90	10%	18%	36%	9%	18%	37%
Long-term	5	0.98	6%	9%	15%	6%	9%	15%

Table D.13: Aeropropulsive efficiency increase necessary for a 15% increase in PREE with respect to a fuel-based reference aircraft, for a cruise Mach number of $M = 0.65$.

			Mission A			Mission B		
		m_{PL} [t]	20			15		
		R [nmi]	650			2000		
	CSP	M [-]	0.65			0.65		
Scenario	[kW/kg]	η_{chain} [-]	$\varphi = 0.2$,	0.5,	1.0	$\varphi = 0.2$,	0.5,	1.0
Near-term	2	0.80	32%	>45%	>45%	27%	>45%	>45%
Mid-term	3	0.90	23%	37%	>45%	20%	33%	>45%
Long-term	5	0.98	18%	24%	33%	15%	20%	30%

Table D.14: Aeropropulsive efficiency increase necessary for a 5% increase in PREE with respect to a fuel-based reference aircraft, for a cruise Mach number of $M = 0.65$.

			Mission A			Mission B		
		m_{PL} [t]	20			15		
		R [nmi]	650			2000		
	CSP	M [-]	0.65			0.65		
Scenario	[kW/kg]	η_{chain} [-]	$\varphi = 0.2$,	0.5,	1.0	$\varphi = 0.2$,	0.5,	1.0
Near-term	2	0.80	22%	>45%	>45%	20%	44%	>45%
Mid-term	3	0.90	13%	27%	>45%	12%	25%	>45%
Long-term	5	0.98	8%	14%	24%	8%	13%	22%

D.3. OTWDP AIRCRAFT PERFORMANCE STUDY

This section lists the some of the design parameters and results obtained in the design studies presented in Chapter 10.

Table D.15: Powertrain and wing characteristics obtained in the OTWDP aircraft performance study. Powertrain properties refer to the total installed power or mass, not per component instance.

	Conventional aircraft		**Baseline OTWDP**		**Optimal OTWDP**	
M_{cr} [-]	0.41	0.60	0.41	0.60	0.41	0.60
R [nmi]	825	1500	825	1500	825	1500
h_{cr} [ft]	22,400	39,800	19,100	36,900	22,100	40,000
N^o of primary propulsors	2	2	2	2	2	2
N^o of secondary propulsors	N/A	N/A	24	24	36	32
Take-off mass [t]	21.9	25.6	23.5	26.8	22.4	25.5
Payload mass [t]	7.5	7.5	7.5	7.5	7.5	7.5
Operative empty mass [t]	12.3	14.2	13.7	15.2	12.8	14.3
Wing mass [t]	2.2	2.6	2.3	2.6	2.3	2.6
Gas turbine mass [t]	1.2	2.3	1.5	2.2	1.2	2.2
Generator mass [kg]	N/A	N/A	98	112	72	96
Rectifier mass [kg]	N/A	N/A	93	106	51	68
Electromotor mass [kg]	N/A	N/A	136	155	75	100
Inverter mass [kg]	N/A	N/A	67	77	49	65
Additional PMAD mass [kg]	N/A	N/A	118	135	74	98
Fuel mass [t]	2.1	3.9	2.3	4.1	2.1	3.7
Wing loading [kN/m^2]	4.0	4.0	4.5	4.5	4.0	3.9
Wing area [m^2]	53.8	62.7	51.2	28.5	54.4	64.0
Wing span [m]	25.4	27.4	24.8	26.5	25.5	27.7
Diameter primary props. [m]	3.7	4.0	3.1	3.3	3.2	3.5
Diameter secondary props. [m]	N/A	N/A	0.52	0.56	0.36	0.44
Gas turbine W_{TO}/P [N/kW]	47.9	27.8	40.4	30.9	48.2	29.1
Generator W_{TO}/P [N/kW]	N/A	N/A	130	130	226	193
Electromotor W_{TO}/P [N/kW]	N/A	N/A	180	180	235	201
Gas turbine power [MW]	4.5	9.0	5.7	8.5	4.6	8.6
Generator power [MW]	N/A	N/A	1.8	2.0	1.0	1.3
Electromotor power [MW]	N/A	N/A	1.3	1.5	0.9	1.2

Table D.16: Overview of the OTWDP design parameters varied in the DoE. The gas-turbine throttle setting is included for reference, though it was not varied. Subscripts "1" and "2" indicate start and end of mission segment, respectively. Climb, cruise, and descent φ and ξ_{GT} settings are applied to both the nominal mission and the diversion.

		Bounds		**Baseline**		**Optimal**	
		Lower	**Upper**	**OTWDP**		**OTWDP**	
Mission	M_{cr} [-]	-	-	0.41	0.60	0.41	0.60
requirements	R [nmi]	-	-	825	1500	825	1500
Geometry	x_P/c [-]	0.75	1.00	0.80	0.80	0.776	0.782
	b_{dp}/b [-][a]	0.25	0.75	0.53	0.53	0.53	0.53
	N_2 [-]	20	40	24	24	36	32
	i_P [deg]	-5	10	0	0	-5	-5[b]
	$\delta_{P,TO}$ [deg]	0	45	15	15	0.2	27.9
	$\delta_{P,L}$ [deg]	0	45	45	45	21.2	44.2
	$\delta_{P,bL}$ [deg]	45	45	45	45	20.8	21.7
Design point	$(W_{TO}/S_w)/(W_{TO}/S_w)_{max}$	0.4	1	1.00	1.00	0.99	0.88
Performance	φ_{cr}	0	1	0.50	0.50	0.44	0.44
constraints	φ_{TO}	0	1	0.20	0.20	0.21	0.25
	φ_L	0	1	1.00	1.00	0.26	0.99
	φ_{ssc}	0	1	0.50	0.50	0.28	0.38
	φ_{cI}	0	1	0.50	0.50	0.29	0.40
	φ_{bL}	0	1	0.50	0.50	0.38	0.47
	$\xi_{GT,cr}$	-	-	0.90	0.90	0.90	0.90
	$\xi_{GT,TO}$	-	-	1.00	1.00	1.00	1.00
	$\xi_{GT,L}$	-	-	0.90	0.90	0.90	0.90
	$\xi_{GT,ssc}$	-	-	1.00	1.00	1.00	1.00
	$\xi_{GT,cI}$	-	-	1.00	1.00	1.00	1.00
	$\xi_{GT,bL}$	-	-	1.00	1.00	1.00	1.00
Climb	φ_1	0	1	0.50	0.50	0.26	0.18
	φ_2	0	1	0.50	0.50	0.29	0.21
	$\xi_{GT,1}$	-	-	0.80	0.80	0.80	0.80
	$\xi_{GT,2}$	-	-	0.90	0.90	0.90	0.90
Cruise	φ_1	0	1	0.50	0.50	0.58	0.50
	φ_2	0	1	0.50	0.50	0.61	0.53
Descent	φ_1	0	1	0.50	0.50	0.99	0.99[b]
	φ_2	0	1	0.50	0.50	0.99	0.99[b]
	$\xi_{GT,1}$	-	-	0.05	0.05	0.05	0.05
	$\xi_{GT,2}$	-	-	0.05	0.05	0.05	0.05
Loiter	φ_1	0	1	0.50	0.50	0.38	0.43
	φ_2	0	1	0.50	0.50	0.42	0.45

[a] This parameter was varied in the geometry-oriented DoE, but kept constant in the final DoE.
[b] These parameters were kept constant in the final DoE of the long range mission, since previous results showed that they would tend towards the bounds.

E

VERIFICATION OF NUMERICAL APPROACHES

Three numerical investigations are performed in this research to assess the aerodynamic interaction effects and performance of different components of the OTWDP system: two RANS simulations, and one lower-order, panel/vortex-based method. For such computational approaches, a grid convergence study is an important step of the verification process, used to quantify the discretization error. Since this step generally requires an elaborate investigation and description but, once the characteristics of the "converged" discretization settings are known, does not directly contribute to the interpretation of results, it has been omitted in the main body of the dissertation. Nevertheless, it is included here for transparency. Hence, the following three sections present the convergence studies of the investigations performed in Sec. 6.2, Ch. 7, and Ch. 8, respectively.

E.1. PROPELLER–DUCT INTERACTION (RANS)

This section addresses the mesh convergence study performed for the RANS simulations of Sec. 6.2. Additional information of this study can be found in Ref. [245]. The numerical discretization error was estimated for the steady simulations of the isolated circular duct, isolated square duct, and isolated propeller. The numerical error of the isolated circular duct computations was estimated for both the 2D axisymmetric and the 3D setups. The discretization error was analyzed by a performing grid convergence study for each isolated configuration. The grids were modified by changing the cell size settings in ANSYS meshing software so that each finer or coarser mesh would have the specified refinement ratio with respect to the previous mesh, while keeping all the grids geometrically similar (for each case), as recommended in Ref. [259]. The cell sizings relative to inflation zones were chosen in order to keep the total height of each inflation zone height constant, for the different grids. As the first cell height was also kept constant (in order to maintain the same y^+), the growth rate of the inflation layers had to be modified in order to increase or decrease the number of layers inside each inflation zone.

Table E.1 shows, for each grid, the number of elements and the grid refinement ratio with respect to the finest grid, (h_i/h_1). The refinement ratios shown in Table E.1 were calculated based on the number of generated cells, and differ from the ratios estimated based on the specified sizings. The differences are assumed to be associated with the grid generation algorithm used by ANSYS meshing. For the square duct and propeller, less grids were considered than for the circular duct, due to convergence issues with the remaining generated grids. Eça and Hoekstra [259] recommend the usage of at least 3 geometrically similar grids, in order to perform a convergence study.

Table E.1: Grids used in the convergence studies circular duct, square duct and propeller, in their isolated configurations. "2D*" refers to a two-dimensional (axisymmetric) simulation in cylindrical coordinates.

Grid	2D* circ. duct		3D circ. duct		Square duct		Propeller	
	# of cells	h_i/h_1	# of cells	h_i/h_1	# of cells	h_i/h_1	# of cells	h_i/h_1
6	7.92×10^3	2.89	2.32×10^6	1.76	-	-	-	-
5	14.18×10^3	2.16	2.60×10^6	1.70	-	-	-	-
4	19.86×10^3	1.82	3.30×10^6	1.60	5.23×10^6	1.33	-	-
3	28.46×10^3	1.52	4.61×10^6	1.40	7.08×10^6	1.20	4.01×10^6	1.59
2	42.88×10^3	1.24	7.00×10^6	1.22	9.26×10^6	1.10	7.96×10^6	1.27
1	65.95×10^3	1.00	12.7×10^6	1.00	12.3×10^6	1.00	16.2×10^6	1.00

Grids 4, 3, 1, and 2 were selected for the 2D axisymmetric duct, 3D circular duct, square duct, and propeller cases, respectively. Grids 4 and 3, respectively for the 2D and 3D circular duct simulations, have similar cell size settings. The results from the different grids were then used to estimate the numerical uncertainty based on the method described in Ref. [259]. The method was adapted for the 3rd order discretization scheme used in this study. Thus, the theoretical order of convergence of the studied quantities was assumed to be 3. Considering this difference, the numerical uncertainty U of a given quantity ϕ was estimated from:

$$U = \begin{cases} 3\Delta_\phi & \text{for } p \le 0 \text{ or oscillatory} \\ \min(1.25\epsilon_\phi + \sigma, 1.25\Delta_\phi) & \text{for } 0 < p < 0.95 \\ 1.25\epsilon_\phi + \sigma & \text{for } 0.95 \le p < 3.05 \\ \max(1.25\epsilon^*_\phi + \sigma^*, 1.25\Delta_\phi) & \text{for } p \ge 3.05 \end{cases} \tag{E.1}$$

where ϵ_ϕ is the difference between the estimated exact solution and the solution obtained with the considered grid, σ is the standard deviation of the fit, p is the observed order of convergence of the quantity and Δ_ϕ is the maximum difference between all the solutions obtained. ϵ^*_ϕ and σ^* are relative to the fits obtained considering p to be equal to the theoretical order of convergence, p^*. The quantities analysed during the convergence study were the drag coefficient, C_D, for the isolated ducts, and the thrust, T_c, and torque, Q_c, coefficients for the isolated propeller. The fits obtained for the duct and propeller cases can be seen in Figs. E.1, E.2 and E.3. Table E.2 shows the values of the

observed order of convergence, standard deviation of the best fit and fit with $p = 3$, and the overall uncertainties calculated from each convergence study. For each case, the standard deviation and the overall uncertainties are shown as a percentage of the value corresponding to the grid which was finally selected.

The uncertainties gathered in Table E.2 suggest a low discretization error, ranging from 0.1% for propeller loads, to 1%–2% for duct loads. However, when analyzing the

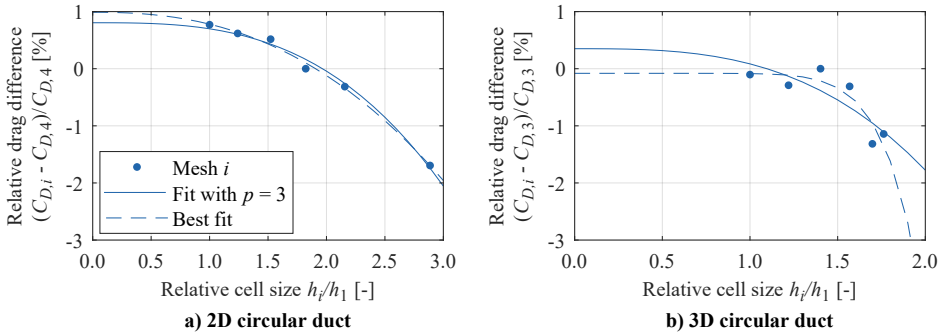

Figure E.1: Circular duct grid convergence study.

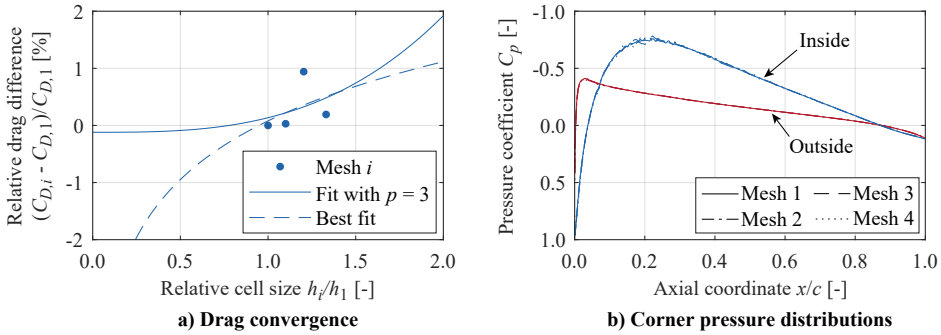

Figure E.2: Square duct grid convergence study.

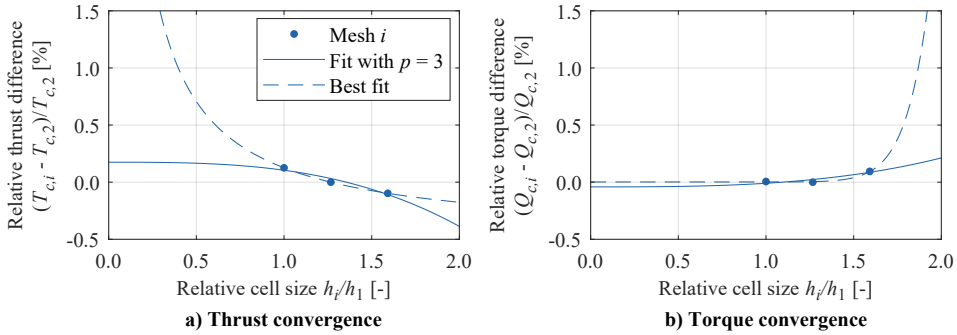

Figure E.3: Propeller grid convergence study.

convergence of the pressure- and friction-drag components of the ducts separately, these quantities were found to converge in opposite directions, with friction drag increasing and pressure drag decreasing with grid refinement. In fact, the uncertainty-estimation method described above predicted a 25% and 21% uncertainty in pressure drag for the (3D) circular and square ducts, respectively, and a 9.5% and 6.8% uncertainty for the friction drag. Hence, when considering the relative impact of these two drag contributions, the total drag uncertainty would be approximately 13% and 10% for the circular and square ducts, respectively. To verify whether these high uncertainties were the consequence of a poorly resolved flow field or simply an artifact of the uncertainty-estimation method, the pressure distributions on the ducts were monitored, and the 3D circular-duct convergence was compared to the 2D one. For the 2D case, a wider range of cell sizes could be evaluated due to the reduced computational costs, and in this case the pressure drag, friction drag, and total drag all presented low uncertainties. Moreover, the observed order of convergence corresponded closely to the theoretical order of convergence ($p = 3$), as visible in Fig. E.1a. While this was not the case for the 3D circular duct (Fig. E.1b), the drag values obtained matched closely with the ones obtained from the 2D case (see Fig. 6.18), suggesting that the high uncertainties in pressure and friction drag were an artifact of an over-conservative uncertainty estimation. For the 3D square duct, no analogous 2D simulation could be performed, and the observed order of convergence differed considerably from the theoretical one ($p = 3$), as can be observed in Fig. E.2a. However, the pressure distribution over the duct surface was found to be sufficiently converged for the selected grid (Grid 1), as shown in Fig. E.2b. The fluctuations visible around $x/c = 0.2$ for the coarser grids were much higher in the corner region, shown in the figure, than along the rest of the duct, due to the unstructured mesh in the corner. Based on these observations, the pressure- and friction-drag uncertainty estimates were considered to be extremely conservative, and thus the overall grid uncertainty was considered acceptable for this study.

Table E.2: Estimated grid convergence uncertainties for the isolated circular duct, square duct and propeller configurations. "2D*" refers to a two-dimensional (axisymmetric) simulation in cylindrical coordinates.

	2D* circ. duct	**3D circ. duct**	**Square duct**	**Propeller**	
Quantity	C_D	C_D	C_D	T_c	Q_c
p	2.41	9.85	0.015	-0.94	14.96
σ [%]	0.086	0.30	0.70	0	0.0064
σ^* [%]	0.12	0.40	0.72	0.040	0.029
U [%]	1.32	1.64	1.18	0.095	0.0088

E.2. PROPELLER–BOUNDARY-LAYER INTERACTION (RANS)

This section analyzes the influence of the overset mesh and presents the mesh convergence study of the RANS simulations of Ch. 7. Additional information of this verification process can be found in Ref. [271]. In the following subsection, the effect of the overset interpolation procedure on the velocity and pressure distributions is described qualitatively. Subsequently, a mesh refinement study is performed to estimate the discretization error.

OVERSET GRID

The overset mesh used in this investigation features a structured wing mesh that serves as the background (Fig. E.4a) and a separate propeller mesh (Fig. E.4b) that is inserted into the background mesh. On the inside, the propeller mesh is the same unstructured mesh as in Fig. 7.6 for consistency. Towards the outside of the mesh, however, a structured grid is used for a sufficient overlap and transition to the structured wing mesh. The resulting OTW configuration is depicted in Fig. E.4c. The overlap is minimized on cells of similar volume where the propeller mesh has a higher grid priority to enforce a constant position of the overset interface when the propeller rotates.

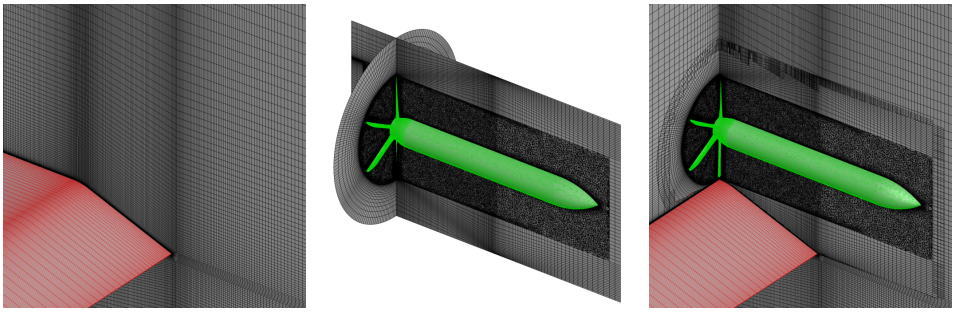

(a) Wing. (b) Propeller. (c) Wing + propeller.

Figure E.4: Overset mesh assembly of the baseline configuration.

The overset interface is in close proximity with the wing's boundary-layer, and thus the interpolation that is required between the stationary and rotating mesh may affect the boundary-layer profile. To determine the potential error due to the overset implementation, simulations were run with the wing and an "empty" overset mesh. Figure E.5a shows that the overset interface indeed results in a kink in the boundary-layer profile at a distance of approximately $z/c = 0.002$ to the wing-surface. Hence, close to the wing surface, the overset interface can cause an increase in wall shear due to an increased vertical velocity gradient. However, this has a negligible influence on the boundary-layer thickness δ_{99} indicated by the dots in Fig. E.5a, which increases by less than 2%. The presence of the overset boundary also slightly affects the pressure distribution on the suction side of the wing, as shown in Fig. E.5b. This is because the increased velocity gradient at the wing surface (Fig. E.5a) leads to a slight delay in flow separation. Therefore, although the influence on integral lift and drag values is small, the observed irregularities in the boundary-layer profile should be taken into account when analyzing the interaction between the propeller and the wing's boundary-layer in the propeller-on configuration.

GRID CONVERGENCE & UNCERTAINTY QUANTIFICATION

The convergence history of the steady simulations of the wing geometry was such that the residuals dropped at least five orders of magnitude and the change in lift and drag over the last 100 iterations was less than 0.001%. Analogously, the isolated propeller simulations were run until the iterative error of the thrust and torque coefficients over

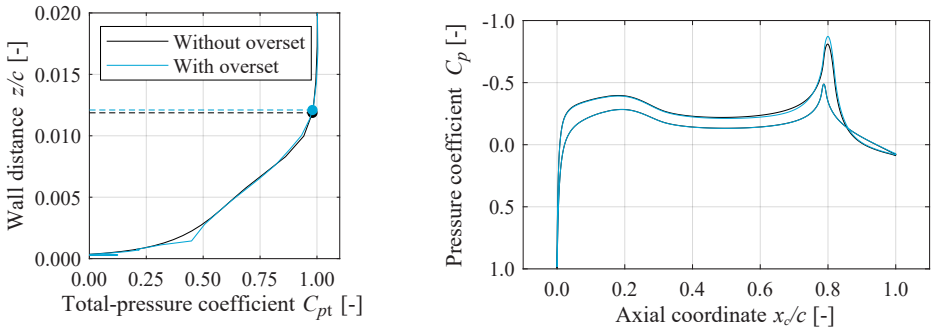

(a) Boundary-layer profile.

(b) Pressure distribution.

Figure E.5: Influence of the overset interface on the boundary-layer profile and pressure distribution of the wing at the propeller location ($x_c/c = 0.79$).

the last 100 iterations was less than 0.001% and the residuals dropped at least five orders of magnitude. Therefore, the iterative error is relatively small, when compared to the discretization error. The discretization errors for the wing and propeller were estimated with four systematically refined grids by using a grid refinement ratio of 1.3. For each of the meshes, the first-layer height and number of layers in inflation layers were kept constant. The grids are denoted h_1 to h_4, where h_1 is the finest one, as shown in Table E.3.

Table E.3: Grids of the mesh refinement study.

Grid	Wing		Propeller	
	h_i/h_1	Cells	h_i/h_1	Cells
Grid 1	1	208,212	1	14,463,300
Grid 2	1.27	128,342	1.25	7,346,487
Grid 3	1.62	79,404	1.55	3,909,325
Grid 4	2.04	50,224	1.87	2,192,981

In these simulations, the discretization error is determined by using an updated procedure by Eça and Hoekstra [276], which is similar to the one used in Appendix E.1. The discretization error ϵ, is calculated by a power series expansion as $\epsilon = \alpha h_i^p$ where α is a constant to be determined, h_i is the representative grid cell size, and p is the observed order of grid convergence. The lift and drag values appear to diverge as the grid is refined, as shown in Figs. E.6a and E.6b. However, the resulting fits with the observed order converges towards finer grids and results in a low standard deviation σ, as shown in Table E.4 for grid 3. Moreover, the observed order of convergence is very close to the theoretical order of two for both lift and drag. Although the observed order of convergence for drag is larger than two, it is within the range $0.5 \leq p < 2.1$. Therefore, it is considered as acceptable for monotonic convergence. The uncertainty in the numerical results indicated by the errorbars in Figures E.6a and E.6b is then estimated for a general quantity ϕ as:

$$U = \begin{cases} 1.25 \cdot \epsilon_\phi + \sigma + |\phi_i - \phi_{\text{fit}}| & \text{for } \sigma < \Delta_\phi \\ 3\dfrac{\sigma}{\Delta_\phi}(\epsilon_\phi + \sigma + |\phi_i - \phi_{\text{fit}}|) & \text{for } \sigma \geq \Delta_\phi \end{cases} \tag{E.2}$$

where Δ_ϕ is a data range parameter defined in Ref. [276]. The resulting uncertainty estimation has a confidence level of 95%. For grid 3, the relative discretization error and uncertainty in lift and drag from Table E.4 are relatively large. However, this is due to the low absolute lift and drag coefficients of the airfoil used in this investigation ($c_\sim 0.1$). Figures E.6a and E.6b show that the absolute values of all four grids are already very close to each other and the accuracy is only marginally improved with a finer mesh. Furthermore, Fig. E.6c shows that the velocity profile at the propeller location deviates hardly between grid 3 and grid 1. Therefore, grid 3 is selected for the wing.

Table E.4: Results of the mesh refinement study for grid 3.

Parameter	Wing		Propeller	
	c_l	c_d	C_T	C_Q
p	1.98	2.05	1.72	1.98
ϵ [%]	-2.4	4.2	0.9	-0.5
σ [%]	0.28	0.44	0.04	0.07
U [%]	4.0	6.1	1.1	0.8

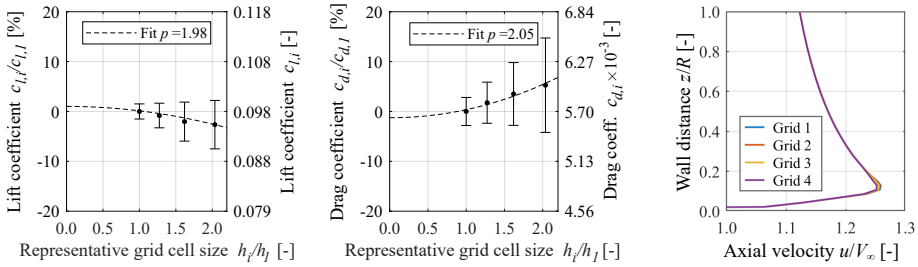

(a) Lift coefficient. (b) Drag coefficient. (c) Inflow velocity.

Figure E.6: Results of mesh refinement study of the two-dimensional wing section.

Figures E.7a and E.7b show that both the thrust and torque coefficients of the isolated propeller converged with an observed order in the acceptable range. The thrust distribution in Fig. E.7c shows no clear trend with grid refinement. Figure E.8a, however, shows that at a distance to the propeller tip equal to the tip clearance used in the OTW configuration, only grid 4 results in considerably weaker velocity fluctuations, caused by the blade tip vortices, compared to the finer grids. This is attributed to an inaccurate capture of flow gradients, close to the blade tip vortices, with the refinement level of grid 4. Moreover, the total pressure in the slipstream varies with mesh refinement only in the region of the blade tip vortex, as is shown by the radial total pressure distributions in Fig. E.8b. Only above $r/R = 0.8$ differences in total pressure can be found in the form of a

stronger total pressure gradient for the finer grids, due to reduced numerical diffusion. Therefore, the propeller grid 3 is used to keep the number of cells acceptable. This corresponds to a discretization error and uncertainty of the thrust and drag coefficients of the order of 1%, as listed in Table E.4.

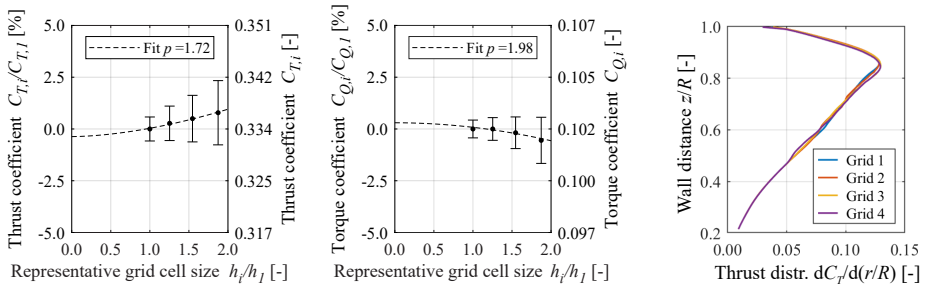

(a) Thrust coefficient. (b) Torque coefficient. (c) Thrust distribution.

Figure E.7: Results of the mesh refinement study for the isolated propeller.

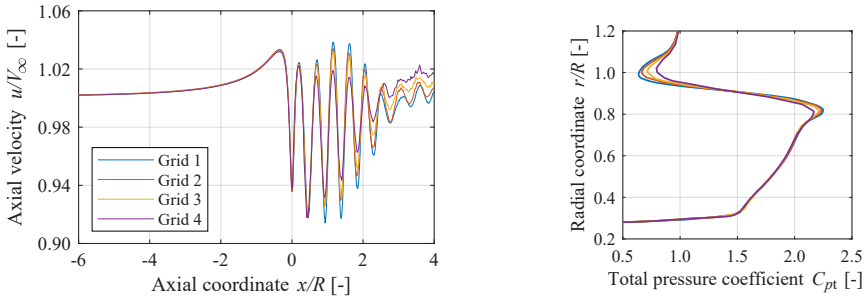

(a) Axial velocity profile. (b) Total pressure distribution.

Figure E.8: Axial velocity and total-pressure profiles in the isolated propeller slipstream, extracted from (a) axial ($r/R = 1.0738$) and (b) radial ($x/R = 1$) survey lines passing through the tip vortex.

E.3. CRUISE PERFORMANCE (VORTEX/PANEL METHODS)

A slipstream vortex model and two panel methods are used in Ch. 8 model the interaction between propeller and wing. To obtain an indicative estimate of the discretization error of these components, Fig. E.9 presents the changes in sectional lift and pressure drag estimated by the numerical model, for a series of discretization parameters. This process was performed iteratively, and therefore the effect of each discretization parameter is presented while maintaining all other parameters constant and equal to the value that was finally chosen. The geometrical parameters and operating conditions used for this figure correspond to the ones of the experiment of Ch. 8.

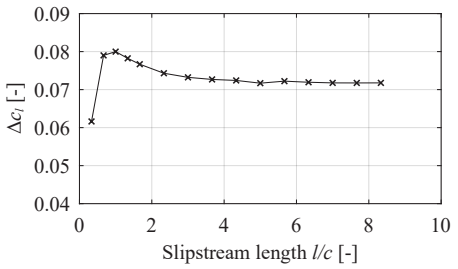

a) Slipstream tube length (lift)

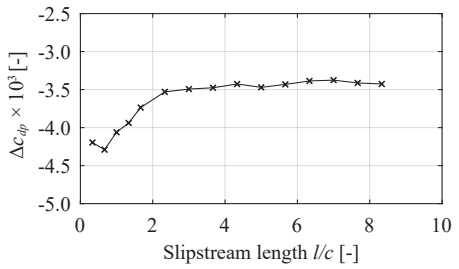

b) Slipstream tube length (drag)

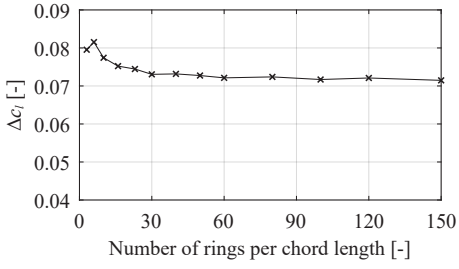

c) Vortex ring spacing (lift)

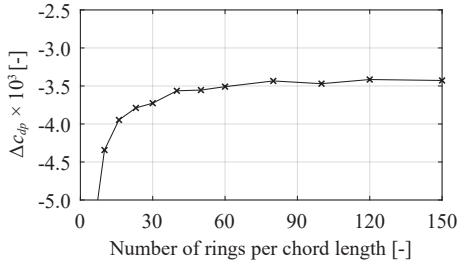

d) Vortex ring spacing (drag)

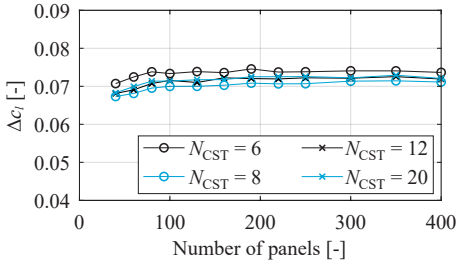

e) PM airfoil discretization (lift)

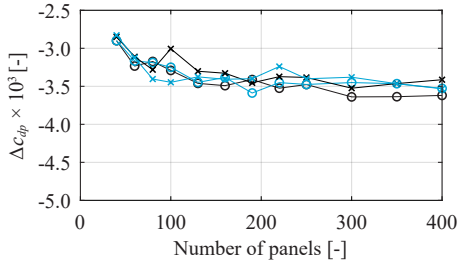

f) PM airfoil discretization (drag)

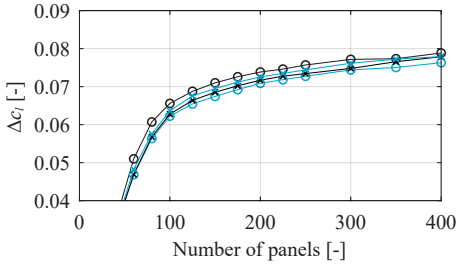

g) XFOIL airfoil discretization (lift)

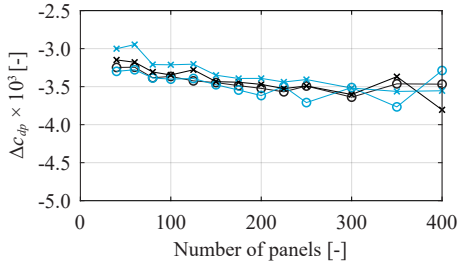

h) XFOIL airfoil discretization (drag)

Figure E.9: Convergence behavior of the change in sectional wing lift and pressure drag coefficients due to the propeller ($\alpha = 2^o$, $J = 1.15$, $y/R = -0.7$), for various discretization parameters.

Regarding the discretization of the slipstream vortex model, Figs. E.9a and E.9b show that the change in wing performance is captured for a slipstream length l (see Fig. 8.3) above four times the wing chord. To ensure that this would also be the case if the propeller were placed further upstream, a slipstream length of $5c$ was selected. The effect of the vortex ring density in axial direction, meanwhile, is shown in Figs. E.9c and E.9d. Based on these results, a density of 100 rings per chord length was selected, corresponding to a spacing of $0.01c$, or 500 rings in total per propeller slipstream.

The convergence behavior is less smooth when analyzing the discretization of the wing sections. In Figs. E.9e and E.9f, the changes in lift and drag are plotted versus the number of panels used in the PM, for four different numbers of CST coefficients. In all cases, Δc_l appears to converge to a steady value above approximately 100 panels, while Δc_d gradually levels out beyond 200 panels. Based on this evolution, a panel density of 200 elements was selected for further investigation. However, even beyond 200 panels, there are fluctuations in the lift and, especially, drag values. This is predominantly attributed to the inverse design process, whose exact solution depends on the initial guess for the design variables, the finite tolerance of the convergence criterion, and potentially on the presence of local minima. The fluctuations in lift and drag appear to be of the order of 10^{-4}, and are therefore acceptable given the overall fidelity and accuracy of the method.

Regarding the number of CST coefficients used to describe the airfoil shape, no clear effect can be observed in terms of Δc_d (Fig. E.9f). However, the Δc_l values obtained with 6 and 8 CST coefficients lie above and below the values obtained with 12 or 20 coefficients, respectively. Additional values of $N_{\text{CST}} > 12$ were evaluated (not shown here) and were all found to produce similar results to the case with 20 CST coefficients. Therefore, to limit the computational time, $N_{\text{CST}} = 12$ was selected to represent the suction side of the airfoil. Since the shape of the pressure side was not varied in the inverse design process (see Sec. 8.1.2), 20 CST coefficients were employed to model the pressure side of the original airfoil accurately, without an increase in computational cost.

Finally, the effect of the paneling density in XFOIL is shown in Figs. E.9g and E.9h. In this case, the Δc_l values do not converge to a constant value, but appear to increase gradually as the number of panels is increased. This was found to be a result of the viscous analysis—even if the baseline airfoil was evaluated manually without any propeller effects—while in the inviscid analysis the lift converged to a constant value at higher panel densities. Since XFOIL has an upper bound on the number of panels that it can model ($N_{\text{panels}} \leq 494$), a value of 200 panels was selected for further analyses. This panel density was selected because the slope of Δc_l and the value of Δc_d appear to be constant beyond this value. Moreover, in this way, the number of panels in the PM and XFOIL are identical. Nonetheless, Fig. E.9g suggests that the changes in lift predicted by the model may differ from their converged value by $\Delta c_l \sim 0.01$. The changes in drag differ by up to $\Delta c_{dp} \sim 0.0005$, depending on the number of CST coefficients selected. While this error is not excessive given the level of detail of the modeling, it should be taken as an indication of the potential uncertainty band when analyzing the results.

F

ENGINEERING METHODS FOR DATA PROCESSING

The following sections present some of the data processing and data reduction techniques used in this research. The methods described here are not based on an exhaustive review of the existing literature or theory, and are therefore most likely neither the only nor the optimal approach. Nevertheless, they are briefly summarized here to provide transparency regarding some of the more complex data-processing steps taken in this research, and to serve as a starting point for anyone encountering similar challenges.

F.1. *N*-DIMENSIONAL POLYNOMIAL FITTING

To reduce computational time and create a continuous response surface, it is often useful to create a surrogate model which provides an estimate $\hat{y}$ of a dependent variable y (e.g., ΔC_L, ΔC_D, or $\Delta\eta_\mathrm{p}$) as a function of N independent parameters $x_1, x_2, \ldots, x_N$ (e.g. T_c, α, D_P/c,...). A conceptually simple approach to this problem is to create an N-dimensional polynomial fit. The order of the fit, P, must be selected based on criteria such as the expected order of the underlying physical effects, or the number of available data points. For example, in the case of a 2$^{\text{nd}}$ order fit ($P = 2$) of three variables ($N = 3$), the model can be expressed as

$$\hat{y} = \hat{\beta}_0 + \hat{\beta}_1 x_1 + \hat{\beta}_2 x_2 + \hat{\beta}_3 x_3 + \hat{\beta}_4 x_1^2 + \hat{\beta}_5 x_1 x_2 + \hat{\beta}_6 x_1 x_3 + \hat{\beta}_7 x_2^2 + \hat{\beta}_8 x_2 x_3 + \hat{\beta}_9 x_3^2. \tag{F.1}$$

In a general sense, this can be written as

$$\hat{y} = \sum_{j=1}^{m} X_j \hat{\beta}_j = \boldsymbol{X}\hat{\boldsymbol{\beta}}, \tag{F.2}$$

where $\boldsymbol{X}$ and $\hat{\boldsymbol{\beta}}$ are row and column vectors of length m, respectively, and X_j is the j-th monomial, given by

$$X_j = \prod_{k=0}^{N} x_k^{E_{jk}}. \tag{F.3}$$

The exponents of the m monomials, $E_{jk} \in \mathbb{Z} \mid 0 \leq E_{jk} \leq P$, can be obtained as all possible combinations of N repetitions of the set $[1,2,...P]$ that satisfy $\sum_{k=1}^{N} E_{jk} \leq N$. It can be shown that the number of monomials of order l in N variables is

$$m_l = \binom{l+N-1}{N-1} = \frac{(l+N-1)!}{l!(N-1)!}. \tag{F.4}$$

Since the surrogate model a priori includes all terms from 0-th order (a constant) to P-th order, the total number of monomials is equal to

$$m = \sum_{l=0}^{P} \binom{l+N-1}{N-1}. \tag{F.5}$$

To create the surrogate model, the coefficients $\hat{\boldsymbol{\beta}}$ of Eq. F.2 must be found. For a sample of $n > m$ data points determined by $y_i = f(X_{1i}, X_{2i}, \ldots, X_{mi})$, the true response of the function f can be modeled with a linear regression as

$$\boldsymbol{y} = \boldsymbol{X}\boldsymbol{\beta} + \boldsymbol{\epsilon}, \tag{F.6}$$

where $\boldsymbol{\epsilon}$ is a column vector of length n which accounts for random error not captured by the model. Note that, in this case, $\boldsymbol{y}$ and $\boldsymbol{X}$ are matrices of size $n \times 1$ and $n \times m$, respectively, unlike the scalar equation given in Eq. F.2. Since in general there is no exact solution for the model fit, an ordinary-least-squares approach is taken to find $\hat{\boldsymbol{\beta}}$, which are the values of the coefficients $\boldsymbol{\beta}$ that minimize the residual sum-of-squares:

$$\text{RSS} = \left|\left|\boldsymbol{y} - \boldsymbol{X}\boldsymbol{\beta}\right|\right|^2 \tag{F.7}$$

By differentiating Eq. F.7 with respect to $\boldsymbol{\beta}$ and equating it to zero, it can be shown that the minimum S is achieved for

$$\hat{\boldsymbol{\beta}} = \left(\boldsymbol{X}^{\mathrm{T}}\boldsymbol{X}\right)^{-1}\boldsymbol{X}^{\mathrm{T}}\boldsymbol{y}. \tag{F.8}$$

Note that, for this, the inverse of $\boldsymbol{X}^{\mathrm{T}}\boldsymbol{X}$ must exist, for which the regressors $X_1, X_2, \ldots, X_m$ must be linearly independent. This is generally the case (except for the null solution), since each monomial X_j is a distinct product of the original independent variables $x_1, x_2, \ldots, x_N$, and can therefore not be expressed as a linear combination of the other monomials.

By computing the monomials $\boldsymbol{X}$ as a function of the original input variables using Eq. F.3 and subsequently solving Eq. F.8 for a given data set, an estimate of the independent variable $\hat{y}$ can be made using Eq. F.2. To ensure that the surrogate model is accurate, some of the fit statistics should be monitored. The quality of the fit can be improved by, e.g., scaling the input parameters or computing the p-value of the $\hat{\boldsymbol{\beta}}$ coefficients to verify which ones are statistically significant. In Ch. 9 and Appendix C.3, for simplicity, all coefficients are included, irrespective of their statistical significance. This is considered

acceptable because it is known a priori that all the independent variables $x_1, x_2, \ldots, x_N$ have an effect on the dependent variable y. Nevertheless, to verify the quality of the fit and ensure that no significant over-fitting occurs, only a fraction of the data points (e.g., 90%) is used to compute the coefficients of the surrogate model. The remaining (10%) is used to evaluate metrics such as the mean or maximum deviation of the predicted values from the actual values, or the coefficient of determination, given by

$$R^2 = \frac{\sum_{i=1}^{n} \left(\hat{y}_i - y_{\text{mean}}\right)^2}{\sum_{i=1}^{n} \left(y_i - y_{\text{mean}}\right)^2}, \tag{F.9}$$

where y_{mean} is the sample mean. The "testing points" are selected randomly from the complete data set, to verify that repeated fitting procedures produce comparable results.

An example of a polynomial fitting result of Appendix C.3 is illustrated in Fig. F.1. The scatter cloud presents a dependent variable versus two of the seven independent variables. Note that two points which appear to lie close to each other in Fig. F.1 do not necessarily lie close to each other in the N-dimensional space. Moreover, all variables are scaled to the interval $[0, 1]$. Circular markers indicate the original data points, while dots indicate the values estimated by the polynomial fit. The blue data points are used to create (or "train") the model, while the red points are used to test the accuracy of the model. In general, the differences between the true values and the predicted values are comparable for both the training points and the test points, indicating that no significant under- or over-fitting takes place. The statistics show a relatively high coefficient of determination ($R^2 = 0.989$) and that, on average, the values predicted by the polynomial model deviate by 0.03% from the actual value at a determined location. However, the maximum observed deviation is 0.075, indicating that at some locations the model may present errors of up to 7.5% of the full-scale range. The model is more prone to such errors if the input data present outliers, if the chosen order of the fit does not match the physical trends, or if the data points are not properly distributed across the space and some regions have less points (e.g. at the edges of the domain).

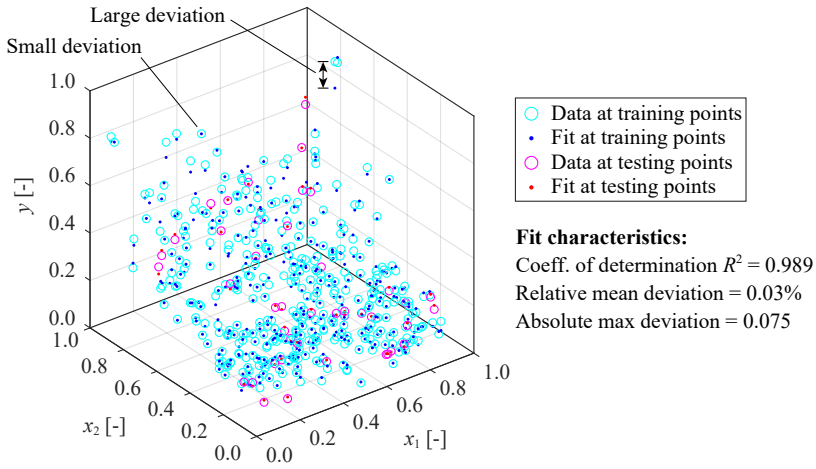

Figure F.1: Example of the training and testing points used to create a surrogate model with 7 variables ($N = 3$). Only 20% of the points used to create and test the model are shown.

F.2. 3D VELOCITY-FIELD INTERPOLATION OF PIV DATA

In Ch. 7, phase-locked PIV measurements are performed on several parallel y-planes in the slipstream of the propeller. The data of these planes is combined to provide a three-dimensional velocity field for a given blade phase angle. However, due to the relatively large spacing between planes, the out-of-plane resolution (2.5 mm vector spacing) is much lower than the in-plane resolution (0.3 mm vector spacing). This can generate misleading visualizations of the flow field, since in most processing software the default interpolations used to produce isosurfaces are computed along the three components of the Cartesian grid.

If it is known beforehand that the dominant flow features (e.g., a tip vortex) are continuous between subsequent measurement planes, the data can be interpolated onto additional intermediate planes to improve the quality of the isosurfaces. For this, it is assumed that the flow structures present in a measurement plane y_1 are also present in the adjacent measurement plane y_2, but with an in-plane displacement $(\Delta x, \Delta z)$, as shown in Fig. F.2. This displacement vector is estimated by performing 2D cross-correlation in an evaluation window surrounding each point (x, z) on a pair of subsequent measurement planes. The evaluation window should be large enough to capture the dominant flow feature on both planes. The flow-field quantities can then be computed on a series of intermediate query planes y_q by linearly interpolating between y_1 and Z_2 along the interpolation direction obtained from the cross-correlation. However, the displacement vector obtained at (x, z) on the plane y_1 does not apply to that same (x, z) point on the query plane, but to a slightly different location (x_q, z_q) given by

$$x_q = x_1 + \Delta x \left(\frac{y_q - y_1}{y_2 - y_1} \right), \tag{F.10}$$

$$z_q = z_1 + \Delta z \left(\frac{y_q - y_1}{y_2 - y_1} \right). \tag{F.11}$$

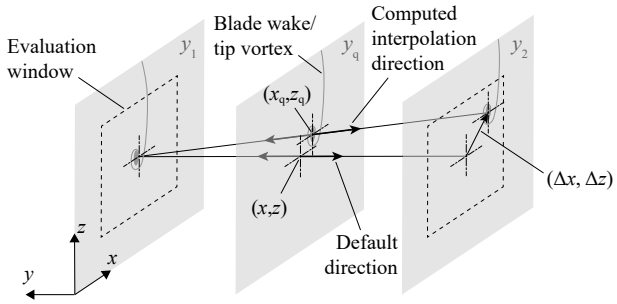

Figure F.2: Schematic representation of the interpolation process between two parallel measurement planes y_1 and y_2, for the volumetric reconstruction of PIV data.

Therefore, the components of the displacement vector $(\Delta x, \Delta z)$ at the location (x, z) on the query plane y_q must themselves be interpolated from the surrounding (x_q, z_q) points, at which the displacement vectors are defined. Since the positions of these points depend on the direction of each displacement vector, they do not form a Cartesian grid.

Although the cross-correlation usually provides erratic or inaccurate results in the absence of distinct flow features (e.g. in uniform flow), this is generally not an issue since these flow regions present weak gradients, and therefore an interpolation along a slightly different direction still provides roughly the same values. An example of the results of this interpolation procedure is given in Fig. F.3. In the default isosurface generation (Fig. F.3a), without any additional interpolation, the spacing of the PIV planes is clearly visible in the disconnected iso-vorticity surfaces of the blade wake. Since the blade wake is oblique relative to the y-plane, the region of high vorticity in the blade wake at a determined (x, z) location is not present at the same (x, z) location on the adjacent plane, and thus the default out-of-plane interpolation suggests that the flow feature ends on either side of the plane. However, by applying the interpolation procedure described above (Fig. F.3b), the continuity of the isosurfaces representing the vortex filaments and blade wakes is ensured.

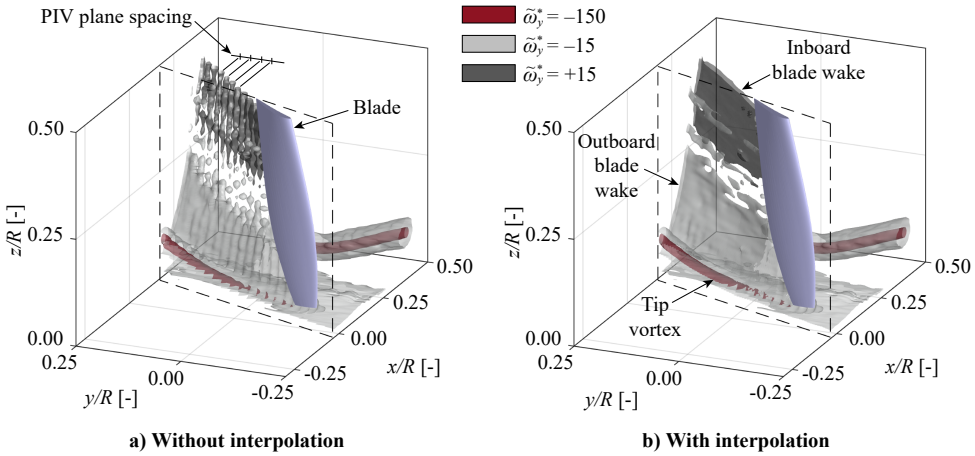

Figure F.3: Comparison of vorticity isosurfaces obtained from PIV data with and without interpolation. Data is only shown downstream of the plane indicated with a dashed line, and is used for Fig. 7.16.

F.3. SURFACE-PRESSURE RECONSTRUCTION USING MICROPHONE DATA

If the general behavior of the dominant flow structures in the vicinity of a surface is known beforehand, then the data acquired using multiple adjacent unsteady-pressure sensors (e.g. microphones) can be combined to provide a more detailed description of the instantaneous surface-pressure distribution. This processing procedure takes advantage of the temporal information available at each location, and predicts the pressure at a nearby location at a given time instance t_q based on the pressure recorded at the original measurement location at a different time instance t_1. This procedure can be used to artificially increase the measurement "resolution", thus providing more informative visualizations of the flow field, and allowing more accurate computations of unsteady loads [239].

A schematic representation of this process is shown in Fig. F.4. Assume that the pressure history is known at two measurement locations x_1 and x_2 along the direction in which the dominant flow structures move. These measurement locations must be sufficiently close to each other for the pressure perturbations induced by the flow structures to be recognizable in the two time (or in this case, phase angle ϕ) histories without an excessive loss of coherence. In that case, the pressure at an intermediate query location x_q can be estimated for each "time" instance ϕ_q using a linear interpolation. For this, the convection velocity of the pressure perturbation must be known,

$$V_{conv} = 2\pi n \frac{x_2 - x_1}{\phi_2 - \phi_1}, \tag{F.12}$$

such that the instants ϕ_1, ϕ_q, and ϕ_2 at which a given pressure perturbation is recorded at the locations x_1, x_q, and x_2, respectively, can be estimated. If the data at x_1 and x_2 are recorded synchronously, then the convective velocity can be obtained from the cross-power spectral density function of the two signals, as described in Ref. [144].

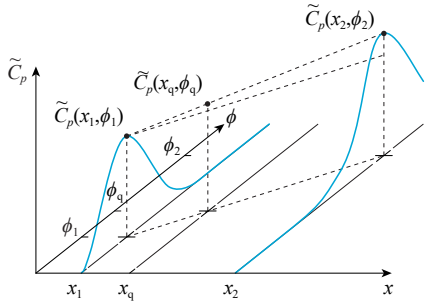

Figure F.4: Notional representation of the interpolation procedure between two consecutive microphones. Figure adapted from Ref. [239].

This procedure is applied in Ch. 7 to compute the instantaneous pressure distribution on a flat wall beneath the propeller. However, as suggested by Fig. 7.13, in this case the pressure perturbations do not necessarily travel in axial direction. Since the different spanwise locations were sampled by traversing the propeller relative to the microphones, the data were not acquired synchronously, and thus only the phase-averaged waveforms are considered here, while random components are neglected. As discussed in Sec. 7.2.2, upstream of the propeller ($x/R < 0$), the dominant pressure fluctuations follow the movement of the blade tips, displacing in the negative y direction. Therefore, in this region, the pressure at a generic x-coordinate is computed by linearly interpolating between the upstream and downstream measurement location, without considering any time delays. No interpolation is performed in y-direction, since the spanwise resolution is sufficiently high to capture the pressure peaks. For $x/R > 0.7$, on the other hand, the pressure fluctuations are caused by the blade wakes and tip vortices, and therefore they displace mainly in axial direction. For each measurement location in this region, a cross-correlation of the phase-averaged waveforms is performed with three downstream measurement locations: one at the same y-coordinate, and one additional point on each side in y direction. Of the three candidates, the point with the strongest correlation is then selected as the direction of the local convective velocity, which presents a weak spanwise

component in the "V"-shaped path of the tip vortices. Since this procedure can present outliers, particularly in the absence of strong periodic features, the convective velocity (i.e., the phase delay $\phi_2 - \phi_1$) is first computed for all points, and then a smoothing filter is applied and outliers are removed. The resulting phase-delay distribution is then used in the interpolation procedure of Fig. F.4 to, in this case, increase the number of axial points by a factor ten. Finally, in the overlap region ($0 < x/R < 0.7$), a sigmoid weighting function $W(x)$ is applied to provide a smooth transition between the two regions, as shown in Fig. 7.13.

Fig. F.5 compares the instantaneous (phase-averaged) pressure distributions obtained for three time instances. While the values at the measurement locations are iden-

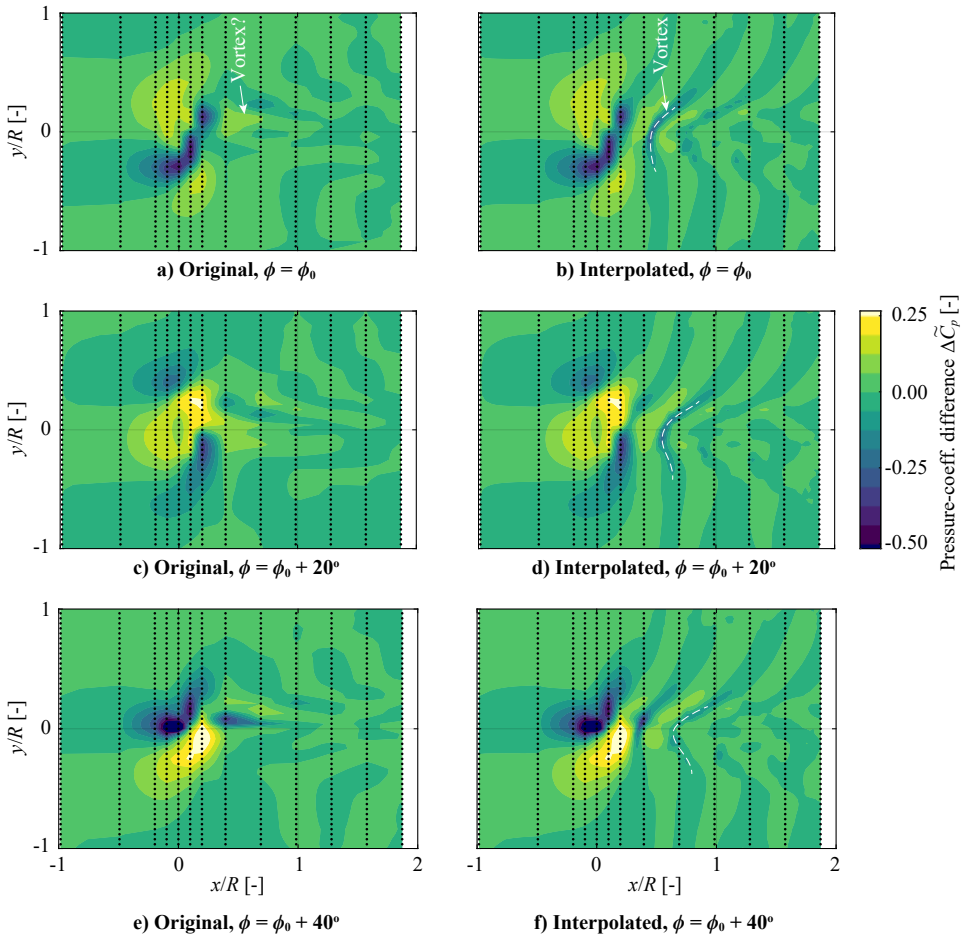

Figure F.5: Comparison of phase-averaged unsteady surface-pressure distributions obtained from microphone data on a flat wall beneath the propeller. Data presented with and without interpolation, for three time instances. Dots indicate measurement locations.

tical in the original and interpolated fields, the general pressure distributions are significantly different downstream of the propeller. In the interpolated pressure distributions, the evolution of the tip vortex can clearly be identified, as indicated by the white dashed line. However, in the original pressure distributions, the low axial resolution does not allow for a meaningful interpretation of the pressure field in the propeller slipstream. Nevertheless, even though the interpolated pressure fields match the expected physical effects, the convective-velocity estimation can provide inaccurate results if the correlations are weak, or if the phase delay estimated by the cross-correlation does not correspond to the correct blade passage (i.e, if instead of estimating the correct $\phi_2 - \phi_1$, it estimates $\phi_2 - \phi_1 + 2\pi/B$). For this reason, a cross-validation of the interpolated pressure distribution with PIV data is performed in Fig. 7.15.

G

AERODYNAMIC PERFORMANCE IN CRUISE CONDITIONS: PARAMETER SWEEPS

A parameter sweep is performed using the numerical method of Ch. 8 to investigate the sensitivity of the changes in propeller and wing loads to the operating conditions and design parameters of an OTWDP system. For this analysis, the geometrical parameters of the experimental setup of Ch. 8 are used as baseline. Several changes are made to the operating conditions to ensure that the conclusions are more representative for full-scale applications. Based on reference data of an ATR 72-600 [228], a typical cruise lift coefficient can vary between $C_L = 0.45$ and $C_L = 0.7$, while the wing chord-based Reynolds and Mach number are of the order of 10^7 and 0.4, respectively. Assuming aircraft lift-to-drag ratios of 15 and 17 for cruise at max speed and "economy" speed respectively, a propeller thrust coefficient of $0.076 < T_c < 0.103$ would be required for steady flight. Based on these figures, a propeller blade pitch of $\beta_{0.7R} = 45^o$ and an advance ratio fo $J = 2.0$ are selected as baseline. In these conditions, the propeller operates near to maximum efficiency and produces a thrust coefficient of approximately $T_c = 0.1$ when installed over the wing. The baseline angle-of-attack of $\alpha = 2^o$ is maintained, corresponding to propeller-on lift coefficients on the order of $C_L \approx 0.6$. Furthermore, the Reynolds and Mach number are set to 10^7 and 0.4, respectively. For the sensitivity analyses, one parameter is varied at a time. Therefore, the sweeps are not performed at constant total lift, thrust, or shaft power. The results obtained here should therefore not be used to quantify the actual performance changes attainable with an OTWDP system.

For reference, Table G.1 provides the force coefficients of the isolated wing and propeller in these conditions. For the isolated propeller, zero angle of attack is assumed. Therefore, the axial force F_x is equal to $-T$, while the vertical force F_z is equal to the normal force $+N$ (see Fig. 2.6). Note, however, that the coefficients F^*_{xc} and F^*_{zc} are normalized with the wing reference area S_{ref}, and not with the propeller disk area S_P,

unlike T_c and N_c. The reader is also reminded that, for these aerodynamic force coefficients, the wing area covered by one propeller of the DP array is used as reference, $S_{ref} = c \cdot (D + d)$, and not a complete wing. In this way, the results are representative of the average changes in lift and drag on a generic portion of a high aspect-ratio, rectangular wing with many OTW propellers ($N_P \gg 1$), and are not inherent to the specific aspect ratio of the wing.

The results are presented for four parameters representing the operating conditions (angle of attack, advance ratio, Reynolds number, and Mach number) and eight geometrical design parameters (axial propeller position, incidence angle, diameter-to-chord ratio, tip clearance, number of propellers modeled, separation distance, airfoil thickness, and airfoil camber) in Figs. G.1–G.3. The first two rows of these figures present the changes in vertical and horizontal forces acting on the system as a result of the aerodynamic coupling between propellers and wing. Note that a positive ΔF^*_{xc} indicates a thrust *reduction*. The third and fourth row present how wing lift-to-drag ratio and the propeller's propulsive efficiency are affected, relative to the isolated wing and propeller operating in that same condition. The reader is reminded that the propulsive efficiency considers the net force produced on the propeller alone in the direction of flight, $|F_x|$, and not the thrust along the propeller axis. The lift-to-drag ratio in installed conditions includes the contribution of the vertical forces on the propeller to the total system lift, i.e.

$$(L/D)_{tot} = \frac{C_{L,iso} + \Delta C_L + F^*_{zc}}{C_{D,iso} + \Delta C_D}. \tag{G.1}$$

Table G.1: Aerodynamic coefficients of the isolated wing and propeller, in the baseline operating conditions selected for the parameter sweeps.

Parameter	Value	Parameter	Value
Lift coefficient $C_{L,iso}$	0.537	Thrust coefficient $T_{c,iso}$	0.111
Pressure drag coeff. $C_{Dp,iso}$	0.0027	Normal-force coefficient $N_{c,iso}$	0
Friction drag coeff. $C_{Df,iso}$	0.0060	Prop. axial force coeff. F^*_{xc}	-0.058
Drag coefficient $C_{D,iso}$	0.0087	Prop. vertical force coeff. F^*_{zc}	0
Lift-to-drag ratio $(L/D)_{iso}$	62.0	Propeller efficiency $\eta_{P,iso}$	0.81

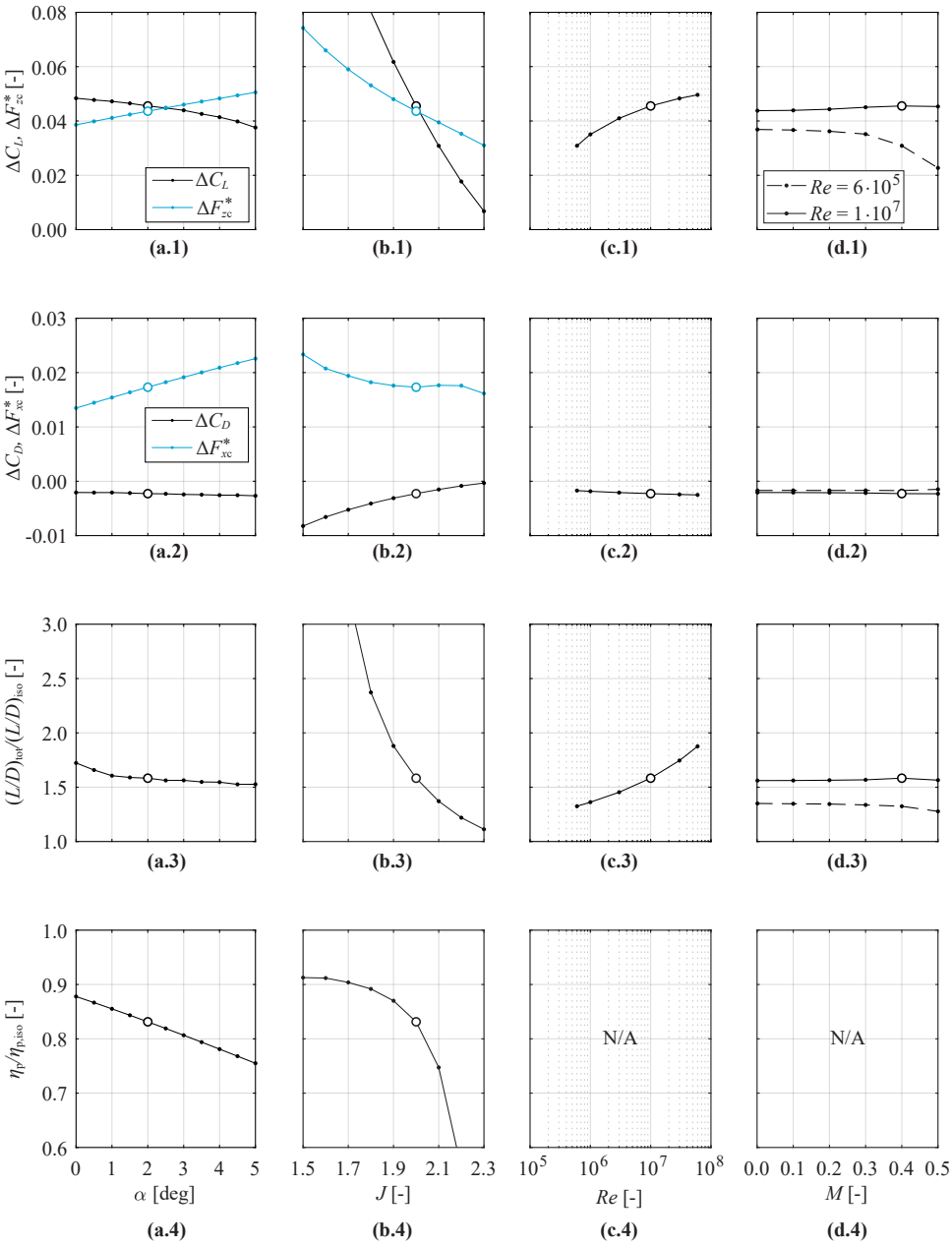

Figure G.1: Sensitivity of the changes in propeller/wing forces and efficiency to the angle of attack, advance ratio, Reynolds number, and Mach number. Large markers indicate baseline values. "N/A" indicates that the effect of a given parameter on propeller performance is not accounted for in the numerical method.

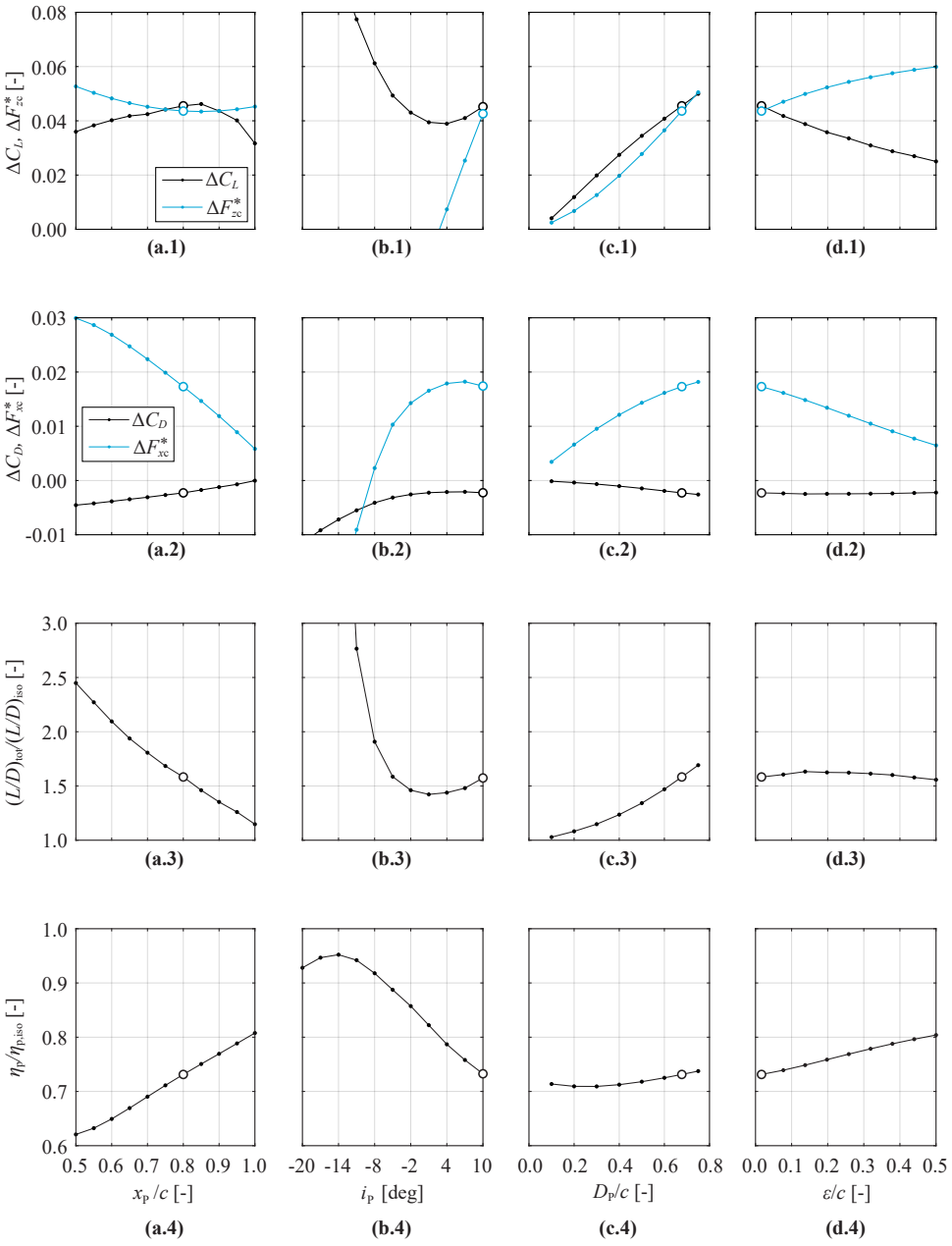

Figure G.2: Sensitivity of the changes in propeller/wing forces and efficiency to the propeller axial position, propeller incidence angle, diameter-to-chord ratio, and tip clearance. Large markers indicate baseline values.

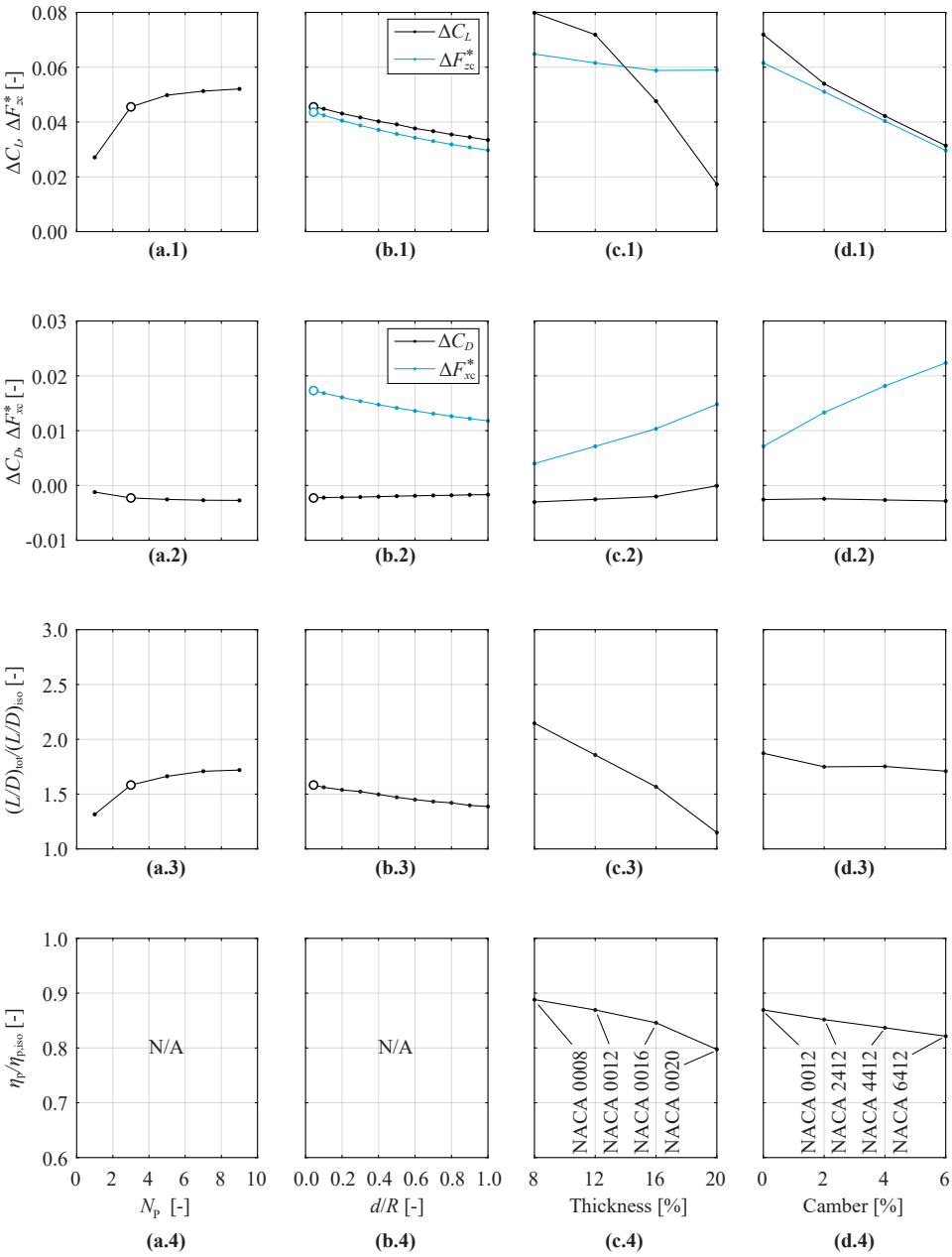

Figure G.3: Sensitivity of the changes in propeller/wing forces and efficiency to the number of propellers, separation between propellers, airfoil thickness, and airfoil camber. Large markers indicate baseline values. "N/A" indicates that the effect of a given parameter on propeller performance is not accounted for in the numerical method.

REFERENCES

[1] United Nations, "World Population Prospects 2019: Highlights," United Nations, Department of Economic and Social Affairs, New York, NY, USA, 2019.

[2] Vollset, S. E., Goren, E., Yuan, C.-W., Cao, J., Smith, A. E., Hsiao, T., Bisignano, C., et al., "Fertility, mortality, migration, and population scenarios for 195 countries and territories from 2017 to 2100: a forecasting analysis for the Global Burden of Disease Study," *The Lancet*, Vol. 396(10258), 2020, pp. 1285–1306. doi:10.1016/S0140-6736(20)30677-2.

[3] United Nations, "Sustainable Development Goals Report," United Nations, New York, NY, USA, 2020.

[4] Bolt, J., Timmer, M., and van Zanden, J., "GDP per capita since 1820," in van Zanden, J., et al. (eds.), How Was Life?: Global Well-being since 1820, OECD Publishing, Paris, France, 2010. doi:10.1787/9789264214262-7-en.

[5] Schafer, A., and Victor, D. G., "The future mobility of the world population," *Transportation Research Part A: Policy and Practice*, Vol. 34(3), 2000, pp. 171–205. doi:10.1016/S0965-8564(98)00071-8.

[6] Lee, J. J., Lukacho, S. P., Waitz, I. A., and Schafer, A., "Historical and future trends in aircraft performance, cost, and emissions," *Annual Review of Energy and the Environment*, Vol. 26(1), 2001, pp. 167–200. doi:10.1146/annurev.energy.26.1.167.

[7] International Air Transport Association, "Vision 2050 Report," IATA, Montreal, Canada, 2011.

[8] Grewe, V., Rao, A. G., Grönstedt, T., Xisto, C., Linke, F., Melkert, J., Middel, J., et al., "Evaluating the climate impact of aviation emission scenarios towards the Paris agreement including COVID-19 effects," *Nature Communications*, Vol. 12(3841), 2021. doi:10.1038/s41467-021-24091-y.

[9] Iacus, S. M., Natale, F., Santamaria, C., Spyratos, S., and Vespe, M., "Estimating and projecting air passenger traffic during the COVID-19 coronavirus outbreak and its socio-economic impact," *Safety Science*, Vol. 129, 2020, pp. 1–11. doi:10.1016/j.ssci.2020.104791.

[10] Lee, D. S., Fahey, D. W., Forster, P. M., Newton, P. J., Wit, R. C. N., Lim, L. I., Owen, B., et al., "Aviation and global climate change in the 21st century," *Atmospheric Environment*, Vol. 43(22-23), 2009, pp. 3520–3537. doi:10.1016/j.atmosenv.2009.04.024.

[11] Lee, D. S., Fahey, D., Skowron, A., Allen, M. R., Burkhardt, U., Chen, Q., J., D. S., et al., "The contribution of global aviation to anthropogenic climate forcing for 2000 to 2018," *Atmospheric Environment*, Vol. 244, 2021. doi:10.1016/j.atmosenv.2020.117834.

[12] Skeie, R. B., Fuglestvedt, J., Berntsen, T., Lund, M. T., Myhre, G., and Rypdal, K., "Global temperature change from the transport sectors: Historical development and future scenarios," *Atmospheric Environment*, Vol. 43(39), 2009, pp. 6260–6270. doi:10.1016/j.atmosenv.2009.05.025.

[13] Intergovernmental Panel on Climate Change, "Aviation and the global atmosphere," IPCC Special Report, 1999.

[14] Lee, D. S., Pitari, G., Grewe, V., Gierens, K., Penner, J. E., Petzold, A., Prather, M. J., et al., "Transport impacts on atmosphere and climate: Aviation," *Atmospheric Environment*, Vol. 44(37), 2010, pp. 4678–4734. doi:10.1016/j.atmosenv.2009.06.005.

[15] Le Quéré, C., Jackson, R. B., Jones, M. W., Smith, A. J. P., Abernethy, S., Andrew, R. M., De-Gol, A. J., et al., "Temporary reduction in daily global CO_2 emissions during the COVID-19 forced confinement," *Nature Climate Change*, Vol. 10, 2020, pp. 647–653. doi:10.1038/s41558-020-0797-x.

[16] Liu, Z., Ciais, P., Deng, Z., Lei, R., Davis, S. J., Feng, S., Zheng, B., et al., "Near-real-time monitoring of global CO_2 emissions reveals the effects of the COVID-19 pandemic," *Nature Communications*, Vol. 11, 2020. doi:10.1038/s41467-020-18922-7.

[17] Forster, P. M., Forster, H. I., Evans, M. J., Gidden, M. J., Jones, C. D., Keller, C. A., Lamboll, R. D., et al., "Current and future global climate impacts resulting from COVID-19," *Nature Climate Change*, Vol. 10, 2020, pp. 913–919. doi:10.1038/s41558-020-0883-0.

[18] Advisory Council for Aviation Research and Innovation in Europe (ACARE), "Realising Europe's vision for aviation: Strategic research & innovation agenda, Vol. 1," Advisory Council for Aviation Research and Innovation in Europe, 2012.

[19] Bonet, J. T., Schellenger, H. G., Rawdon, B. K., Elmer, K. R., Wakayama, S. R., Brown, D. L., and Guo, Y., "Environmentally Responsible Aviation (ERA) Project - N+2 Advanced Vehicle Concepts Study and Conceptual Design of Subscale Test Vehicle (STV): Final Report," Technical Report NASA/CR-2011-216519, December 2011.

[20] Advisory Council for Aviation Research and Innovation in Europe (ACARE), "Strategic research & innovation agenda, 2017 Update, Vol. 1," Advisory Council for Aviation Research and Innovation in Europe, 2017.

[21] Green, J. E., "Air Travel-Greener by Design. Mitigating the environmental impact of aviation: opportunities and priorities," *The Aeronautical Journal*, Vol. 109(1099), 2005, pp. 361–418. doi:10.1017/S0001924000000841.

[22] National Academies of Sciences, Engineering, and Medicine, *Commercial Aircraft Propulsion and Energy Systems Research: Reducing Global Carbon Emissions*, National Academies Press, 2016. doi:10.17226/23490.

[23] Bradley, M. K., and Droney, C. K., "Subsonic Ultra Green Aircraft Research Phase II: N+4 Advanced Concept Development," NASA/CR-2012-217556 Technical Report, 2012.

[24] "Strategic research and innovation agenda: The proposed European Partnership for Clean Aviation," available online, July 2020, accessed July 2020. URL `http://www.clean-aviation.eu/`.

[25] Fuel Cells and Hydrogen Joint Undertaking, Clean Sky 2 Joint Undertaking, "Hydrogen-powered aviation: A fact-based study of hydrogen technology, economics, and climate impact by 2050," , May 2020.

[26] International Civil Aviation Organization, "Destination Green: The Next Chapter," 2019 Environmental Report, Aviation and Environment, 2019.

[27] World Economic Forum, "Clean Skies for Tomorrow: Sustainable Aviation Fuels as a Pathway to Net-Zero Aviation," Insight Report, November 2020.

[28] BBC News, "'World's first' fully-electric commercial flight takes off," , December 2019, accessed January 2021. URL `https://www.bbc.com/news/business-50738983#:~:text=An%20all%2Delectric%20powered%20seaplane,fitted%20with%20an%20electric%20motor.`

[29] European Union Aviation Safety Agency, "EASA certifies electric aircraft, first type certification for fully electric plane world-wide," , June 2020, accessed January 2021. URL `https://www.easa.europa.eu/newsroom-and-events/news/easa-certifies-electric-aircraft-first-type-certification-fully-electric`.

[30] Baumeister, S., Leung, A., and Ryley, T., "The emission reduction potentials of First Generation Electric Aircraft (FGEA) in Finland," *Journal of Transport Geography*, Vol. 85, 2020. doi:10.1016/j.jtrangeo.2020.102730.

[31] Lueckhof, J., and Stumpf, E., "Well-to-Prop - A Holistic Analysis of Emerging Powertrain Concepts for On-Demand Air Mobility Vehicles," 2019 AIAA Aerospace Sciences Meeting, San Diego, CA, USA, January 7-11 2019. doi:10.2514/6.2019-1586.

[32] Epstein, A. H., and O'Flarity, S. M., "Considerations for Reducing Aviation's CO_2 with Aircraft Electric Propulsion," *Journal of Propulsion and Power*, Vol. 35(3), 2019, pp. 572–582. doi:10.2514/1.B37015.

[33] Cooper, T., Reagan, I., Porter, C., Green, K., and Franzoni, C., "Global Fleet and MRO Market Forecast 2020-2030," Oliver Wyman, 2020.

[34] Gnadt, A. R., Speth, R. L., Sabnis, J. S., and Barrett, S. R. H., "Technical and environmental assessment of all-electric 180-passenger commercial aircraft," *Progress in Aerospace Sciences*, Vol. 105, 2019, pp. 1–30. doi:10.1016/j.paerosci.2018.11.002.

[35] Schafer, A. W., Barrett, S. R. H., Doyme, K., Dray, L. M., Gnadt, A. R., Self, R., O'Sullivan, A., Synodinos, A. P., and Torija, A. J., "Technological, economic and environmental prospects of all-electric aircraft," *Nature Energy*, Vol. 4, 2019, pp. 160–166. doi:10.1038/s41560-018-0294-x.

[36] Hall, D. K., Greitzer, E. M., Dowdle, A. P., Gonzalez, J. J., Hoburg, W. W., Lang, J. H., Sabnis, J. S., et al., "Feasibility of Electrified Propulsion for Ultra-Efficient Commercial Aircraft Final Report," NASA Report CR–2019-220382, 2019.

[37] Hoogreef, M. F. M., de Vries, R., Sinnige, T., and Vos, R., "Synthesis of Aero-Propulsive Interaction Studies applied to Conceptual Hybrid-Electric Aircraft Design," 2020 AIAA Aerospace Sciences Meeting, Orlando, FL, USA, January 6-10 2020. doi:10.2514/6.2020-0503.

[38] Hepperle, M., "Electric Flight – Potential and Limitations," *NATO Report STO-MP-AVT-209*, 2012.

[39] Zhao, X., Sahoo, S., Kypriandis, K., Rantzer, J., and Sielemann, M., "Off-design performance analysis of hybridised aircraft gas turbine," *The Aeronautical Journal*, Vol. 123(1270), 2019, pp. 1999–2018. doi:10.1017/aer.2019.75.

[40] Lents, C., and Hardin, L., "Fuel Burn and Energy Consumption Reduction s of a Single Aisle Class Parallel Hybrid Propulsion System," AIAA Propulsion and Energy 2019 Forum, Indianapolis, IN, USA, August 19-22 2019. doi:10.2514/6.2019-4396.

[41] Chapman, J. W., "Utilizing Electrical Power Extraction for Stability Bleed Reduction within Gas Turbine Engines," AIAA Propulsion and Energy 2021 Forum, Virtual Event, August 9-11 2021. doi:10.2514/6.2021-3477.

[42] Seitz, A., Nickl, M., Stroh, A., and Vratny, P. C., "Conceptual study of a mechanically integrated parallel hybrid electric turbofan," *Proceedings of the Institution of Mechanical Engineers, Part G: Journal of Aerospace Engineering*, 2018. doi:10.1177/0954410018790141.

[43] Gladin, J. C., Trawick, D., Mavris, D., Armstrong, M., Bevis, D., and Klein, K., "Fundamentals of Parallel Hybrid Turbofan Mission Analysis with Application to the Electrically Variable Engine," 2018 AIAA/IEEE Electric Aircraft Technologies Symposium, Cincinnati, OH, USA, July 9-11 2018. doi:10.2514/6.2018-5024.

[44] Lammen, W., and Vankan, J., "Energy Optimization of Single Aisle Aircraft with Hybrid Electric Propulsion," 2020 AIAA Aerospace Sciences Meeting, Orlando, FL, USA, January 6-10 2020. doi:10.2514/6.2020-0505.

[45] Voskuijl, M., van Bogaert, J., and Rao, A. G., "Analysis and design of hybrid electric regional turboprop aircraft," *CEAS Aeronautical Journal*, Vol. 9, 2018, pp. 15–25. doi:10.1007/s13272-017-0272-1.

[46] Finger, D. F., Bil, C., and Braun, C., "Mass, primary energy, and cost: the impact of optimization objectives on the initial sizing of hybrid-electric general aviation aircraft," *CEAS Aeronautical Journal*, Vol. 11, 2020, pp. 713–130. doi:10.1007/s13272-020-00449-8.

[47] Sarlioglu, B., and Morris, C. T., "More Electric Aircraft: Review, Challenges, and Opportunities for Commercial Transport Aircraft," *IEEE Transactions on Transportation Electrification*, Vol. 1(1), 2015, pp. 54–64. doi:10.1109/TTE.2015.2426499.

[48] Borer, N. K., Patterson, M. D., Viken, J. K., Moore, M. D., Clarke, S., Redifer, M. E., Christie, R. J., et al., "Design and Performance of the NASA SCEPTOR Distributed Electric Propulsion Flight Demonstrator," 16th AIAA Aviation Technology, Integration, and Operations Conference, Washington, DC, USA, June 13-17 2016. doi:10.2514/6.2016-3920.

[49] Moore, K. R., and Ning, A., "Takeoff and Performance Trade-Offs of Retrofit Distributed Electric Propulsion for Urban Transport," *Journal of Aircraft*, Vol. 56(5), 2019, pp. 1880–1892. doi:10.2514/1.C035321.

[50] Pfeifle, O., Frangenberg, M., Notter, J., S. ad Denzel, Bergmann, D., Schneider, J., Fichter, W., and others., "Distributed Electric Propulsion for Yaw Control: Testbeds, Control Approach, and Flight Testing," AIAA Aviation 2021 Forum, Virtual Event, August 2-6 2021. doi:10.2514/6.2021-3192.

[51] Nguyen Van, E., Alazard, D., Döll, c., and Pastor, P., "Co-design of aircraft vertical tail and control laws with distributed electric propulsion and flight envelop constraints," *CEAS Aeronautical Journal*, Vol. 12, 2021, pp. 101–113. doi:10.1007/s13272-020-00481-8.

[52] Hermetz, J., Ridel, M., and Döll, C., "Distributed electric propulsion for small business aircraft: A concept-plane for key-technologies investigations," 30th ICAS Congress, Daejeon, South Korea, 2016.

[53] Schmollgruber, P., Döll, C., Hermetz, J., Liaboeuf, R., Ridel, M., Cafarelli, I., Atinault, O., François, C., and Paluch, B., "Multidisciplinary Exploration of DRAGON: an ONERA Hybrid Electric Distributed Propulsion Concept," 2019 AIAA Aerospace Sciences Meeting, San Diego, CA, USA, January 7-11 2019. doi:10.2514/6.2019-1585.

[54] Seitz, A., Habermann, A. L., Peter, F., Troeltsch, F., Castillo Pardo, A., Della Corte, B., van Sluis, M., et al., "Proof of Concept Study for Fuselage Boundary Layer Ingesting Propulsion," *Aerospace*, Vol. 8(1), 16, 2021. doi:10.3390/aerospace8010016.

[55] Babikian, R., Lukachko, S. P., and Waitz, I. A., "The historical fuel efficiency characteristics of regional aircraft from technological, operational, and cost perspectives," *Journal of Air Transport Management*, Vol. 8, 2002, pp. 389–400. doi:10.1016/S0969-6997(02)00020-0.

[56] Kenway, G. K. W., Henderson, R., Hicken, J. E., Kuntawala, N. B., Zingg, D. W., Martins, J. R. R. A., and McKeand, R. G., "Reducing Aviation's Environmental Impact Through Large Aircraft For Short Ranges," 48th AIAA Aerospace Sciences Meeting, Orlando, FL, USA, January 4-7 2010. doi:10.2514/6.2010-1015.

[57] Eisenhut, D., Moebs, N., Windels, E., Bergmann, D., Geiß, I., Reis, R., and Strohmayer, A., "Aircraft Requirements for Sustainable Regional Aviation," *Aerospace*, Vol. 8(61), 2021. doi:10.3390/aerospace8030061.

[58] Randt, N. P., "Perspectives of turboprop aircraft: A stakeholder-oriented evaluation using scenario planning," 63rd German Aerospace Congress, Augsburg, Germany, September 16-18 2014.

[59] Rosskopf, M., Lehner, S., and Luetjens, K., "Impact of single-aisle aircraft with reduced design range on airline operations and dynamics of fleet composition," *Journal of Aerospace Operations*, Vol. 2, 2013, pp. 99–113. doi:10.3233/AOP-130036.

[60] Langhans, S., Linke, F., Nolte, P., and Gollnick, V., "System Analysis for an Intermediate Stop Operations Concept on Long Range Routes," *Journal of Aircraft*, Vol. 50(1), 2013, pp. 29–37. doi:10.2514/1.C031446.

[61] Patterson, M. D., "Conceptual Design of High-Lift Propeller Systems for Small Electric Aircraft," PhD Dissertation, Georgia Institute of Technology, 2016.

[62] Biser, S., Filipenko, M., Boll, M., Kastner, N., Atanasov, G., Hepperle, M., Keller, D., et al., "Design Space Exploration Study and Optimization of a Distributed Turbo-Electric Propulsion System for a Regional Passenger Aircraft," AIAA Propulsion and Energy Forum (virtual event), August 24-28 2020. doi:10.2514/6.2020-3592.

[63] Johnson Jr., J. L., and White, E. R., "Exploratory Low-Speed Wind-Tunnel Investigation of Advanced Commuter Configurations Including an Over-the-Wing Propeller," AIAA Aircraft Design, Systems and Technology Meeting, Fort Worth, TX, USA, October 17-19 1983. doi:10.2514/6.1983-2531.

[64] Lv, P., Ragni, D., Hartuç, T., Veldhuis, L., and Rao, A. G., "Experimental Investigation of the Flow Mechanisms Associated with a Wake-Ingesting Propulsor," *AIAA Journal*, Vol. 55(4), 2017, pp. 1332–1342. doi:10.2514/1.J055292.

[65] Sinnige, T., van Arnhem, N., Stokkermans, T. C. A., Eitelberg, G., and Veldhuis, L. L. M., "Wingtip-Mounted Propellers: Aerodynamic Analysis of Interaction Effects and Comparison with Conventional Layout," *Journal of Aircraft*, Vol. 56(1), 2018, pp. 295–312. doi:10.2514/1.C034978.

[66] Antcliff, K. R., and Capristan, F. M., "Conceptual Design of the Parallel Electric-Gas Architecture with Synergistic Utilization Scheme (PEGASUS) Concept," 17th AIAA/ISSMO Multidisciplinary Analysis and Optimization Conference, Denver, CO, USA, June 5-9 2017. doi:10.2514/6.2017-4001.

[67] Müller, L., Heinze, W., Kožulović, D., Hepperle, M., and Radespiel, R., "Aerodynamic Installation Effects of an Over-the-Wing Propeller on a High-Lift Configuration," *Journal of Aircraft*, Vol. 51(1), 2014, pp. 249–258. doi:10.2514/1.C032307.

[68] Veldhuis, L. L. M., "Propeller Wing Aerodynamic Interference," PhD Dissertation, Delft University of Technology, 2005.

[69] Müller, L., Kožulović, D., Hepperle, M., and Radespiel, R., "The influence of the propeller position on the aerodynamics of a channel wing," Deutscher Luft-und Raumfahrt Kongress, Berlin, Germany, September 2012.

[70] Howard, R. M., and Miley, S. J., "An investigation of the effects of the propeller slipstream on a laminar wing boundary layer," SAE Technical Paper Series, 850859, 1985.

[71] Nathen, P., "Architectural performance assessment of an electric vertical take-off and landing (e-VTOL) aircraft based on a ducted vectored thrust concept," , April 2021.

[72] Sleeman Jr., W. C., and Hohlweg, W. C., "Low-speed wind-tunnel investigation of a four-engine upper surface blown model having a swept wing and rectangular and D-shaped exhaust nozzles," NASA Technical Note D-8061, 1975.

[73] Beck, S. C., Müller, L., and Langer, S. C., "Numerical assessment of the vibration control effects of porous liners on an over-the-wing propeller configuration," *CEAS Aeronautical Journal*, Vol. 7(2), 2016, pp. 275–286. doi:10.1007/s13272-016-0186-3.

[74] Broadbent, E. G., "Noise shielding for aircraft," *Progress In Aerospace Sciences*, Vol. 17, 1977, pp. 231–268. doi:10.1016/0376-0421(76)90009-9.

[75] Dornier, C., "The Dornier Do.X. Seaplane: Full Technical Details of the Design and Construction of the Largest Flying Boat Yet Built," *Aircraft Engineering and Aerospace Technology*, Vol. 1(10), 1929, pp. 339–341. doi:10.1108/eb029211.

[76] Müller, L., Kožulović, D., and Radespiel, R., "Aerodynamic performance of an over-the-wing propeller configuration at increasing Mach number," *CEAS Aeronautical Journal*, Vol. 5, 2014, pp. 305–317. doi:10.1007/s13272-014-0108-1.

[77] Seitz, A., Bijewitz, J., Kaiser, S., and Wortmann, G., "Conceptual investigation of a propulsive fuselage aircraft layout," *Aircraft Engineering and Aerospace Technology: An International Journal*, Vol. 86(6), 2014, pp. 464–472. doi:10.1108/AEAT-06-2014-0079.

[78] Isikveren, A. T., Pornet, C., Vratny, P. C., and Schmidt, M., "Optimization of Commercial Aircraft Using Battery-Based Voltaic-Joule/Brayton Propulsion," *Journal of Aircraft*, Vol. 54(1), 2017, pp. 246–261. doi:10.2514/1.C033885.

[79] Pornet, C., and Isikveren, A. T., "Conceptual design of hybrid-electric transport aircraft," *Progress in Aerospace Sciences*, Vol. 79, 2015, pp. 114–135. doi:10.1016/j.paerosci.2015.09.002.

[80] Cooper, R. K., McCann, W. J., and Chapleo, A. Q., "Over wing propeller aerodynamics," *ICAS Proceedings (AIAA)*, Vol. 18, 1992, pp. 266–273.

[81] RINGO: Identification of Aviation Research Infrastructure - Needs, Gaps, and Overlaps, "What aviation research infrastructures does Europe need to meet Flightpath 2050 challenges?" RINGO Final Report, 2020.

[82] Hoogreef, M. F. M., Vos, R., de Vries, R., and Veldhuis, L. L. M., "Conceptual Assessment of Hybrid Electric Aircraft with Distributed Propulsion and Boosted Turbofans," 2019 AIAA Aerospace Sciences Meeting, San Diego, CA, USA, January 7-11 2019. doi:10.2514/6.2019-1807.

[83] Zill, T., Iwanizki, M., Schmollgruber, P., Defoort, S., Döll, C., Hoogreef, M., de Vries, R., Vankan, J., and Lammen, W., "An overview of the conceptual design studies of hybrid propulsion air vehicles in the frame of Clean Sky 2 Large Passenger Aircraft," Aerospace Europe Conference 2020, Bordeaux, France, February 25-28 2020.

[84] Netherlands Aerospace Center and Delft University of Technology, "NOVAIR: Novel Aircraft Configurations and Scaled Flight Testing Instrumentation," Description of Action JTI-CS2-2015-CPW03-LPA-01-09, 2016.

[85] Roskam, J., *Airplane Design*, DARcorporation, 1985.

[86] Goldsmith, I. M., "A study to define the research and technology requirements for advanced turbo/propfan transport aircraft," NASA Contractor Report 166138, February 1981.

[87] van Zante, D. E., Collier, F., Orton, A., Arif Khalid, S., Wojno, J. P., and Wood, T. H., "Progress in open rotor propulsors: The FAA/GE/NASA open rotor test campaign," *The Aeronautical Journal*, Vol. 118(1208), 2014, pp. 1181–1213. doi:10.1017/S0001924000009842.

[88] Groeneweg, J. F., and Bober, L. J., "NASA Advanced Propeller Research," NASA Technical Memorandum 101361, 1988.

[89] Mitchell, G. A., "Experimental Aerodynamic Performance of Advanced 40^{o}-Swept, 10-Blade Propeller Model at Mach 0.6 to 0.85," NASA Technical Memorandum 88969, 1988.

[90] van Arnhem, N., de Vries, R., Sinnige, T., Vos, R., Eitelberg, G., and Veldhuis, L. L. M., "Engineering Method to Estimate the Blade Loading of Propellers in Nonuniform Flow," *AIAA Journal*, Vol. 58(12), 2020, pp. 5332–5346. doi:10.2514/1.J059485.

[91] Torenbeek, E., *Synthesis of Subsonic Airplane Design*, Delft University Press, 1982.

[92] Raymer, D. P., *Aircraft design: A conceptual approach*, AIAA Education Series, 2002. doi:10.2514/4.869112.

[93] Stückl, S., "Methods for the Design and Evaluation of Future Aircraft Concepts Utilizing Electric Propulsion Systems," PhD Dissertation, Technische Universität München, 2016.

[94] Pornet, C., "Conceptual Design Methods for Sizing and Performance of Hybrid-Electric Transport Aircraft," PhD Dissertation, Technical University of Munich, 2018.

[95] Kreimeier, M., "Evaluation of On-Demand Air Mobility Concepts with Utilization of Electric Powered Small Aircraft," PhD Dissertation, RWTH Aachen University, Lehrstuhl und Institut für Luft-und Raumfahrtsysteme (ILR), 2018.

[96] Çinar, G., "A Methodology for Dynamic Sizing of Electric Power Generation and Distribution Architectures," PhD Dissertation, Georgia Institute of Technology, 2018.

[97] Chakraborty, A. A., Mishra, "Generalized Energy-Based Flight Vehicle Sizing and Performance Analysis Methodology," *Journal of Aircraft*, Vol. 58(4), 2021, pp. 762–780. doi:10.2514/1.C036101.

[98] Zamboni, J., Vos, R., Emeneth, M., and Schneegans, A., "A Method for the Conceptual Design of Hybrid Electric Aircraft," 2019 AIAA Aerospace Sciences Meeting, San Diego, CA, USA, January 7-11 2019. doi:10.2514/6.2019-1587.

[99] Riboldi, C. E. D., "An optimal approach to the preliminary design of small hybrid-electric aircraft," *Aerospace Science and Technology*, Vol. 81, 2018, pp. 14–31. doi:10.1016/j.ast.2018.07.042.

[100] Geiß, I., and Voit-Nitschmann, R., "Sizing of the energy storage system of hybrid-electric aircraft in general aviation," *CEAS Aeronautical Journal*, Vol. 8(1), 2017, pp. 53–65. doi:10.1007/s13272-016-0220-5.

[101] Iwanizki, M., Arzberger, M. J., Plohr, M., Silberhorn, D., and Hecken, T., "Conceptual Design Studies of Short Range Aircraft Configurations with Hybrid Electric Propulsion," AIAA Aviation 2019 Forum, Dallas, TX, USA, June 17-21 2019. doi:10.2514/6.2019-3680.

[102] Isikveren, A. T., Kaiser, S., Pornet, C., and Vratny, P. C., "Pre-design strategies and sizing techniques for dual-energy aircraft," *Aircraft Engineering and Aerospace Technology: An International Journal*, Vol. 86(6), 2014, pp. 525–542. doi:10.1108/AEAT-08-2014-0122.

[103] Isikveren, A. T., "Method of Quadrant-Based Algorithmic Nomographs for Hybrid/Electric Aircraft Predesign," *Journal of Aircraft*, Vol. 55(1), 2018, pp. 394–403. doi:10.2514/1.C034355.

[104] Finger, D. F., "Methodology for Multidisciplinary Aircraft Design under Consideration of Hybrid-Electric Propulsion Technology," PhD Dissertation, RMIT University, 2020.

[105] Brelje, B. J., and Martins, J. R. R. A., "Electric, hybrid, and turboelectric fixed-wing aircraft: A review of concepts, models, and design approaches," *Progress in Aerospace Sciences*, Vol. 104, 2019, pp. 1–19. doi:10.1016/j.paerosci.2018.06.004.

[106] Sahoo, S., Zhao, X., and Kyprianidis, K., "A Review of Concepts, Benefits, and Challenges for Future Electrical Propulsion-Based Aircraft," *Aerospace*, Vol. 7(44), 2020. doi:10.3390/aerospace7040044.

[107] Isikiveren, A. T., et al., "Guidelines for Analysis of Hybrid Electric Aircraft System Studies: Nomenclature, Pictographic Representations, Standalone and Combined Properties and Attributes, Metrics, and Figures of Merit," AIAA Aircraft Electrified Propulsion and Power (AEPP) Working Group, 2019.

[108] Hoelzen, J., Liu, Y., Bensmann, B., Winnefeld, C., Elham, A., Friedrichs, J., and Hanke-Rauschenbach, R., "Conceptual Design of Operation Strategies for Hybrid Electric Aircraft," *Energies*, Vol. 11(1), 2018, p. 217. doi:10.3390/en11010217.

[109] Perullo, C., and Mavris, D., "A review of hybrid-electric energy management and its inclusion in vehicle sizing," *Aircraft Engineering and Aerospace Technology: An International Journal*, Vol. 86(6), 2014, pp. 550–557. doi:10.1108/AEAT-04-2014-0041.

[110] Moore, M. D., and Fredericks, B., "Misconceptions of Electric Propulsion Aircraft and their Emergent Aviation Markets," 52nd AIAA Aerospace Sciences Meeting, National Harbor, MD, USA, January 13-17 2014. doi:10.2514/6.2014-0535.

[111] Patterson, M. D., and Borer, N. B., "Approach Considerations in Aircraft with High-Lift Propeller Systems," 17th AIAA Aviation Technology, Integration, and Operations Conference, Denver, CO, USA, June 5-9 2017. doi:10.2514/6.2017-3782.

[112] Schefer, H., Fauth, L., Kopp, T. H., Mallwitz, R., Friebe, J., and Kurrat, M., "Discussion on Electric Power Supply Systems for All Electric Aircraft," *IEEE Access*, Vol. 8, 2020, pp. 84188–84216. doi:10.1109/ACCESS.2020.2991804.

[113] Cinar, G., Mavris, D. N., Emeneth, M., Schneegans, A., Riediger, C., Fefermann, Y., and Isikveren, A. T., "Sizing, Integration and Performance Evaluation of Hybrid Electric Propulsion Subsystem Architectures," 55th AIAA Aerospace Sciences Meeting, Grapevine, TX, USA, January 9-13 2017. doi:10.2514/6.2017-1183.

[114] Schiltgen, B., Freeman, J. L., and Hall, D. W., "Aeropropulsive Interaction and Thermal System Integration within the ECO-150: A Turboelectric Distributed Propulsion Airliner with Conventional Electric Machines," 16th AIAA Aviation Technology, Integration and Operations Conference, Washington, DC, USA, June 13-17 2016. doi:10.2514/6.2016-4064.

[115] Stoll, A. M., and Mikić, G. V., "Design Studies of Thin-Haul Commuter Aircraft with Distributed Electric Propulsion," 16th AIAA Aviation Technology, Integration, and Operations Conference, Washington, DC, USA, June 13-17 2016. doi:10.2514/6.2016-3765.

[116] Bruce, P. G., Freunberger, S. A., Hardwick, L. J., and Tarascon, J.-M., "Li-O_2 and Li-S batteries with high energy storage," *Nature Materials*, Vol. 11, 2012, pp. 19–29. doi:10.1038/nmat3191.

[117] Gerssen-Gondelach, S. J., and Faaij, A. P. C., "Performance of batteries for electric vehicles on short and longer term," *Journal of Power Sources*, Vol. 212, 2012, pp. 111–129. doi:10.1016/j.jpowsour.2012.03.085.

[118] Badwal, S. P. S., Giddey, S. S., Munnings, C., Bhatt, A. I., and Hollenkamp, A. F., "Emerging electrochemical energy conversion and storage technologies," *Frontiers in Chemistry*, Vol. 2, 2014, 79. doi:10.3389/fchem.2014.00079.

[119] Jansen, R. H., Bowman, C., Jankovsky, A., Dyson, R., and Felder, J., "Overview of NASA Electrified Aircraft Propulsion Research for Large Subsonic Transports," 53rd AIAA/SAE/ASEE Joint Propulsion Conference, Atlanta, GA, USA, July 10-12 2017. doi:10.2514/6.2017-4701.

[120] Sirimanna, S., Thanatheepan, B., Lee, D., Agrawal, S., Yu, Y., Wang, Y., Anderson, A., et al., "Comparison of Electrified Aircraft Propulsion Drive Systems with Different Electric Motor Topologies," *Journal of Propulsion and Power*, 2021. doi:10.2514/1.B38195.

[121] Filipenko, M., Biser, S., Boll, M., Corduan, M., Noe, M., and Rostek, P., "Comparative Analysis and Optimization of Technical and Weight Parameters of Turbo-Electric Propulsion Systems," *Aerospace*, Vol. 7(107), 2020. doi:10.3390/aerospace7080107.

[122] Chapman, J. W., Hasseeb, H., and Schnulo, S., "Thermal Management System Design for Electrified Aircraft Propulsion Concepts," AIAA Propulsion and Energy 2020 Forum, Virtual Event, August 24-28 2020. doi:10.2514/6.2020-3571.

[123] Duffy, M., Sevier, A., Hupp, R., Perdomo, E., and Wakayama, S., "Propulsion Scaling Methods in the Era of Electric Flight," 2018 AIAA/IEEE Electric Aircraft Technologies Symposium, Cincinnati, OH, USA, July 9-11 2018. doi:10.2514/6.2018-4978.

[124] Clarke, M., and Alonso, J. J., "Lithium–Ion Battery Modeling for Aerospace Applications," *Journal of Aircraft*, Vol. 58(6), 2021, pp. 1323–1335. doi:10.2514/1.C036209.

[125] Ibrahim, K., Sampath, S., and Nalianda, D., "Optimal Voltage and Current Selection for Turboelectric Aircraft Propulsion Networks," *IEEE Transactions on Transportation Electrification*, Vol. 6(4), 2020, pp. 1625–1637. doi:10.1109/TTE.2020.3004308.

[126] Byahut, S., and Uranga, A., "Propulsion Powertrain Component Modeling for an All-Electric Aircraft Mission," AIAA Scitech 2020 Forum, Orlando, FL, USA, January 6-10 2020. doi:10.2514/6.2020-0015.

[127] Nangia, R. K., "Efficiency parameters for modern commercial aircraft," *The Aeronautical Journal*, Vol. 110(1110), 2006, pp. 495–510. doi:10.1017/S0001924000001391.

[128] Hileman, J. I., Katz, J. B., Mantilla, J. G., and Fleming, G., "Payload fuel energy efficiency as a metric for aviation environmental performance," 26th International Congress of the Aeronautical Sciences, Anchorage, AK, USA, September 14-19 2008.

[129] Seitz, A., Schmitz, O., Isikveren, A. T., and Hornung, M., "Electrically powered propulsion: Comparison and contrast to gas turbines," Deutscher Luft-und Raumfahrt Kongress, Berlin, Germany, September 2012.

[130] Kruger, M., Byahut, S., Uranga, A., Dowdle, A., Gonzalez, J., and Hall, D. K., "Electrified Aircraft Trade-Space Exploration," 2018 Aviation Technology, Integration, and Operations Conference, Atlanta, GA, USA, June 25-29 2018. doi:10.2514/6.2018-4227.

[131] Bijewitz, J., Seitz, A., and Hornung, M., "A review of recent aircraft concepts employing synergistic propulsion-airframe integration," 30th Congress of the International Council of the Aeronautical Sciences, Daejeon, Korea, September 25-30 2016.

[132] Smith Jr., L. H., "Wake Ingestion Propulsion Benefit," *Journal of Propulsion and Power*, Vol. 9(1), 1993, pp. 74–83. doi:10.2514/3.11487.

[133] Torenbeek, E., *Optimum Cruise Performance of Subsonic Transport Aircraft*, Delft University Press, 1998.

[134] Betz, A., "The Theory of the Screw Propeller," NACA Technical Note TN-83, reprint from "Die Naturwissenschaften", 1922.

[135] van Kuik, G. A. M., Sørensen, J. N., and Okulov, V. L., "Rotor theories by Professor Joukowsky: Momentum theories," *Progress in Aerospace Sciences*, Vol. 73, 2015, pp. 1–18. doi:10.1016/j.paerosci.2014.10.001.

[136] Okulov, V. L., Sørensen, J. N., and Wood, D. H., "The rotor theories by Professor Joukowsky: Vortex theories," *Progress in Aerospace Sciences*, Vol. 73, 2015, pp. 19–46. doi:10.1016/j.paerosci.2014.10.002.

[137] Wald, Q. R., "The aerodynamics of propellers," *Progress in Aerospace Sciences*, Vol. 42(2), 2006, pp. 85–128. doi:10.1016/j.paerosci.2006.04.001.

[138] Durand, W. F., *Aerodynamic Theory*, Vol. IV, Julius Springer, Berlin, 1935.

[139] Marte, J. E., and Kurtz, D. W., "A Review of Aerodynamic Noise From Propellers, Rotors, and Lift Fans," NASA Technical Report 32-1462, 1970.

[140] Magliozzi, B., Hanson, D. B., and Amiet, R. K., "Propeller and Propfan Noise," *NASA. Langley Research Center, Aeroacoustics of Flight Vehicles: Theory and Practice*, Vol. 1: Noise Sources, 1991, pp. 1–64.

[141] Sinnige, T., "Aerodynamic and Aeroacoustic Interaction Effects for Tip-Mounted Propellers: An Experimental Study," PhD Dissertation, Delft University of Technology, 2018.

[142] Metcalfe, M. P., "On the Modelling of a Fully-Relaxed Propeller Slipstream," AIAA/SAE/ASME/ASEE 21th Joint Propulsion Conference, Monterey, CA, USA, July 8-10 1985. doi:10.2514/6.1985-1262.

[143] Miranda, L. R., and Brennan, J. E., "Aerodynamic effects of wingtip-mounted propellers and turbines," 4th Applied Aerodynamics Conference, San Diego, CA, USA, June 9-11 1986. doi:10.2514/6.1986-1802.

[144] de Vries, R., "Unsteady Pylon Loading for Pylon-Mounted Tractor Propellers," MSc thesis, Delft University of Technology, 2016.

[145] Carlton, J., *Marine propellers and propulsion*, 4th ed., Butterworth-Heinemann, 2019. doi:10.1016/B978-0-7506-8150-6.X5000-1.

[146] Traub, L. W., "Simplified propeller analysis and design including effects of stall," *The Aeronautical Journal*, Vol. 120(1227), 2016, pp. 796–818.

[147] Pasamanick, J., "Langley full-scale-tunnel tests of the Custer Channel wing airplane," NACA Research Memorandum L53A09, 1953.

[148] Blick, E. F., and Homer, V., "Power-on Channel Wing Aerodynamics," *Journal of Aircraft*, Vol. 8(4), 1971, pp. 234–238. doi:10.2514/3.44260.

[149] Müller, L., Friedrichs, J., and Kožulović, D., "Unsteady Flow Simulations of an Over-the-wing Propeller Configuration," 50th AIAA/ASME/SAE/ASEE Joint Propulsion Conference, Cleveland, OH, USA, July 28-30 2014. doi:10.2514/6.2014-3886.

[150] Wang, H., Gan, W., and Li, D., "An Investigation of the Aerodynamic Performance for a Fuel Saving Double Channel Wing Configuration," *Energies*, Vol. 12(20), 2019, pp. 1–16. doi:10.3390/en12203911.

[151] Wang, H., Gan, W., and Li, D., "An investigation of the aerodynamic performance for a propeller-aided lift-enhancing double wing configuration," *Aerospace Science and Technology*, Vol. 105, 2020. doi:10.1016/j.ast.2020.105991.

[152] Wick, A. T., Hooker, J. R., Hardin, C. J., and Zeune, C. H., "Integrated Aerodynamic Benefits of Distributed Propulsion," 53rd AIAA Aerospace Sciences Meeting, Kissimmee, FL, USA, January 5-9 2015. doi:10.2514/6.2015-1500.

[153] Perry, A. T., Ansell, P. J., and Kerho, M. F., "Aero-Propulsive and Propulsor Cross-Coupling Effects on a Distributed Propulsion System," *Journal of Aircraft*, Vol. 55(6), 2018, pp. 2414–2426. doi:10.2514/1.C034861.

[154] Perry, A. T., Bretl, T., and Ansell, P. J., "Aeropropulsive Coupling Effects on a General-Aviation Aircraft with Distributed Electric Propulsion," *Journal of Aircraft*, 2021. doi:doi.org/10.2514/1.C036048.

[155] Liu, C., Doulgeris, G., Laskaridis, P., and Singh, R., "Thermal cycle analysis of turboelectric distributed propulsion system with boundary layer ingestion," *Aerospace Science and Technology*, Vol. 27, 2013, pp. 163–170. doi:10.1016/j.ast.2012.08.003.

[156] Leifsson, L., Ko, A., Mason, W. F., Schetz, J. A., Grossman, B., and Haftka, R. T., "Multidisciplinary design optimization of blended-wing-body transport aircraft with distributed propulsion," *Aerospace Science and Technology*, Vol. 25, 2013, pp. 16–28. doi:10.1016/j.ast.2011.12.004.

[157] Savoni, L., and Rudnik, R., "Aerodynamic Assessment of Pylon-Mounted Over-the-Wing Engine Installations on a STOL Commercial Aircraft Concept," In: Dillmann, A. et al. (eds), New Results in Numerical and Experimental Fluid Mechanics XI. Notes on Numerical Fluid Mechanics and Multidisciplinary Design, Vol. 136, Springer, 2018. doi:10.1007/978-3-319-64519-3_5.

[158] Szodruch, J., and Kotschote, J., "Wind Tunnel Tests of Over-the-Wing Nacelles," *Journal of Aircraft*, Vol. 20(7), 1973, pp. 606–611. doi:10.2514/3.44918.

[159] Fujino, M., and Karamura, y., "Wave-Drag Characteristics of an Over-the-Wing Nacelle Business-Jet Configuration," *Journal of Aircraft*, Vol. 40(6), 2003, pp. 1177–1184. doi:10.2514/2.7207.

[160] Phelps, A. E., Letko, W., and Henderson, R. L., "Low-speed wind-tunnel investigation of a semispan STOL jet transport wing-body with an upper-surface blown jet flap," NASA Technical Note D-7183, 1973.

[161] Wimpress, J. K., "Upper Surface Blowing Technology as Applied to the YC-14 Airplane," *SAE Transactions*, Vol. 82, Section 4: Papers 730669–730990, 1973, pp. 3049–3056.

[162] Peridier, V. J., Smith, F. T., and Walker, J. D. A., "Vortex-induced boundary-layer separation. Part 2. Unsteady interacting boundary-layer theory," *Journal of Fluid Mechanics*, Vol. 232, 1991, pp. 133–165. doi:10.1017/S0022112091003658.

[163] Sengupta, T. K., and Sarkar, S., "Vortex-induced instability of an incompressible wall-bounded shear layer," *Journal of Fluid Mechanics*, Vol. 493, 2003, pp. 277–286. doi:10.1017/S0022112003005822.

[164] Doligalski, T. L., Smith, C. R., and Walker, J. D. A., "Vortex interactions with walls," *Annual Review of Fluid Mechanics*, Vol. 26(1), 1994, pp. 573–616. doi:10.1146/annurev.fl.26.010194.003041.

[165] Chuang, F.-S., and Conlisk, A. T., "The effect of interaction on the boundary layer induced by a convected rectilinear vortex," *Journal of Fluid Mechanics*, Vol. 200, 1989, pp. 337–365. doi:10.1017/S0022112089000686.

[166] Doligalski, T. L., and Walker, J. D. A., "The boundary layer induced by a convected two-dimensional vortex," *Journal of Fluid Mechanics*, Vol. 139, 1984, pp. 1–28. doi:10.1017/S0022112084000240.

[167] Murray IV, H. H., Devenport, W. J., Alexander, W. N., Glegg, S. A. L., and Wisda, D., "Aeroacoustics of a rotor ingesting a planar boundary layer at high thrust," *Journal of Fluid Mechanics*, Vol. 850, 2018, pp. 212–245. doi:10.1017/jfm.2018.438.

[168] Yang, Y., Sciacchitano, A., Veldhuis, L. L. M., and Eitelberg, G., "Analysis of propeller-induced ground vortices by particle image velocimetry," *Journal of Visualization*, Vol. 21(1), 2018, pp. 39–55. doi:10.1007/s12650-017-0439-1.

[169] Martio, J., Sipilä, T., Sanchez-Caja, A., Saisto, I., and Siikonen, T., "Evaluation of the Propeller Hull Vortex Using a RANS Solver," Second International Symposium on Marine Propulsors, Hamburg, Germany, June 15-17 2011.

[170] Sato, R., Tasaki, R., and Nishiyama, S., "Observation of flow on a horizontal flat plate above a working propeller and physics of propeller-hull vortex cavitiation," Proceedings of the International Symposium on Propeller and Cavitation, Wuxi, China, April 8-12 1986.

[171] Williams, M. H., Cho, J., and Dalton, W. N., "Unsteady Aerodynamic Analysis of Ducted Fans," *Journal of Propulsion and Power*, Vol. 7(5), 1991, pp. 800–804. doi:10.2514/3.23394.

[172] Sgueglia, A., Schmollgruber, P., Bartoli, N., Atinault, O., Benard, E., and Morlier, J., "Exploration and Sizing of a Large Passenger Aircraft with Distributed Ducted Electric Fans," 2018 AIAA Aerospace Sciences Meeting, Kissimmee, FL, USA, January 8-12 2018. doi:10.2514/6.2018-1745.

[173] Black, D., Wainauski, H., and Rohrbach, C., "Shrouded propellers - A comprehensive performance study," AIAA 5th Annual Meeting and Technical Display, Philadelphia, PA, USA, October 21-24 1968. doi:10.2514/6.1968-994.

[174] Zhang, T., and Barakos, G. N., "Review on ducted fans for compound rotorcraft," *The Aeronautical Journal*, Vol. 124(1277), 2020, pp. 941–974. doi:10.1017/aer.2019.164.

[175] Hubbard, H. H., "Sound measurements for five shrouded propellers at static conditions," NACA Technical Note 2024, 1950.

[176] Dittmar, J. H., "An Estimate of the Noise Shielding on the Fuselage Resulting From Installing a Short Duct Around an Advanced Propeller," NASA Technical Memorandum 100262, 1988.

[177] Stokkermans, T. C. A., "Aerodynamics of Propellers in Interaction Dominated Flowfields," PhD Dissertation, Delft University of Technology, 2020.

[178] Stokkermans, T. C. A., Usai, D., Sinnige, T., and Veldhuis, L. L. M., "Aerodynamic Interaction Effects between Propellers in Typical eVTOL Vehicle Configurations," *Journal of Aircraft*, Vol. 58(4), 2021, pp. 815–833. doi:doi.org/10.2514/1.C035814.

[179] Sweet, G. E., "Hovering measurements for twin-rotor configurations with and without overlap," NASA Technical Note D-534, 1960.

[180] Ramasamy, M., "Hover Performance Measurements Toward Understanding Aerodynamic Interference in Coaxial, Tandem, and Tilt Rotors," *Journal of the American Helicopter Society*, Vol. 60(3), 2015. doi:10.4050/JAHS.60.032005.

[181] Bagai, A., and Leishman, J. G., "Free-Wake Analysis of Tandem, Tilt-Rotor and Coaxial Rotor Configurations," *Journal of the American Helicopter Society*, Vol. 41(3), 1996, pp. 196–207. doi:10.4050/JAHS.41.196.

[182] Sheng, C., and Narramore, J. C., "Computational Simulation and Analysis of Bell Boeing Quad Tiltrotor Aero Interaction," *Journal of the American Helicopter Society*, Vol. 54(4), 2009. doi:10.4050/JAHS.54.042002.

[183] Lee, H., and Lee, D.-J., "Rotor interactional effects on aerodynamic and noise characteristics of a small multirotor unmanned aerial vehicle," *Physics of Fluids*, Vol. 32, 2020. doi:10.1063/5.0003992.

[184] Alvarez, E. J., and Ning, A., "High-Fidelity Modeling of Multirotor Aerodynamic Interactions for Aircraft Design," *AIAA Journal*, Vol. 58(10), 2020. doi:10.2514/1.J059178.

[185] Alvarez, E. J., Schenk, A., Critchfield, T., and Ning, A., "Rotor-on-Rotor Aeroacoustic Interactions of Multirotor in Hover," Brigham Young University Faculty Publications 4053, 2020.

[186] Yoon, S., Lee, H. C., and Pulliam, T. H., "Computational Analysis of Multi-Rotor Flows," 54th AIAA Aerospace Sciences Meeting, San Diego, CA, USA, January 4-8 2016. doi:10.2514/6.2016-0812.

[187] Zhou, W., Ning, Z., Li, H., and Hu, H., "An Experimental Investigation on Rotor-to-Rotor Interactions of Small UAV," 35th AIAA Applied Aerodynamics Conference, Denver, CO, USA, June 5-9 2017. doi:10.2514/6.2017-3744.

[188] Ning, Z., "Experimental investigations on the aerodynamic and aeroacoustic characteristics of small UAS propellers," PhD Dissertation, Iowa State University, 2018.

[189] Shukla, D., and Komerath, N., "Multirotor Drone Aerodynamic Interaction Investigations," *Drones*, Vol. 4(2), 43, 2018. doi:10.3390/drones2040043.

[190] Shukla, D., and Komerath, N., "Low Reynolds number multirotor aerodynamic wake interactions," *Experiments in Fluids*, Vol. 60(77), 2019. doi:10.1007/s00348-019-2724-3.

[191] Tinney, C. E., and Sirohi, J., "Multirotor Drone Noise at Static Thrust," *AIAA Journal*, Vol. 56(7), 2018. doi:10.2514/1.J056827.

[192] Veismann, M., and Gharib, M., "High Fidelity Aerodynamic Force Estimation for Multirotor Crafts in Free Flight," AIAA Scitech 2020 Forum, Orlando, FL, USA, January 6-10 2020. doi:10.2514/6.2020-0303.

[193] Bernardini, G., Centracchio, F., Gennaretti, M., Iemma, U., Pasquali, C., Poggi, C., Rossetti, M., and Serafini, J., "Numerical Characterisation of the Aeroacoustic Signature of Propeller Arrays for Distributed Electric Propulsion," *Applied Sciences*, Vol. 10, 2020. doi:10.3390/app10082643.

[194] Roger, M., and Moreau, S., "Tonal-Noise Assessment of Quadrotor-Type UAV Using Source-Mode Expansions," *Acoustics*, Vol. 2, 2020. doi:10.3390/acoustics2030036.

[195] Pascioni, K. A., and Rizzi, S. A., "Tonal Noise Prediction of a Distributed Propulsion Unmanned Aerial Vehicle," 2018 AIAA/CEAS Aeroacoustics Conference, Atlanta, GA, USA, June 25-29 2018. doi:10.2514/6.2018-2951.

[196] Pascioni, K. A., Rizzi, S. A., and Aumann, A. R., "Auralization of an unmanned aerial vehicle under propeller phase control," *INTER-NOISE and NOISE-CON Congress and Conference Proceedings*, Vol. 258(7), 2018, pp. 421–431.

[197] Pascioni, K. A., Rizzi, S. A., and Schiller, N. H., "Noise Reduction Potential of Phase Control for Distributed Propulsion Vehicles," AIAA Scitech 2019 Forum, San Diego, CA, USA, January 7-11 2019. doi:10.2514/6.2019-1069.

[198] Magliozzi, B., "Synchrophasing for cabin noise reduction of propeller-driven airplanes," 8th Aeroacoustics Conference, Atlanta, GA, USA, April 11-13 1983. doi:10.2514/6.1983-717.

[199] Johnston, J. F., Donham, R. E., and Guinn, W. A., "Propeller Signatures and Their Use," *Journal of Aircraft*, Vol. 18(11), 1981, pp. 934–942. doi:10.2514/3.57583.

[200] Rizzi, S. A., Palumbo, D. L., Rathsam, J., Christian, A., and Rafaelof, M., "Annoyance to Noise Produced by a Distributed Electric Propulsion High-Lift System," 23rd AIAA/CEAS Aeroacoustics Conference, Denver, CO, USA, June 5-9 2017. doi:10.2514/6.2017-4050.

[201] Patterson, A., Gahlawat, A., and Hovakimyan, N., "Propeller Phase Synchronization for Small Distributed Electric Vehicles," AIAA Scitech 2019 Forum, San Diego, CA, USA, January 7-11 2019. doi:10.2514/6.2019-1458.

[202] Patterson, A., Ackerman, K., Gahlawat, A., Hovakimyan, N., Schiller, N. H., and Gregory, I., "Controller Design for Propeller Phase Synchronization with Aeroacoustic Performance Metrics," AIAA Scitech 2020 Forum, Orlando, FL, USA, January 6-10 2020. doi:10.2514/6.2020-1494.

[203] de Vries, R., Brown, M., and Vos, R., "Preliminary Sizing Method for Hybrid-Electric Distributed-Propulsion Aircraft," *Journal of Aircraft*, Vol. 56(6), 2019, pp. 2172–2188. doi:10.2514/1.C035388.

[204] Wroblewski, G. E., and Ansell, P. J., "Mission Analysis and Emissions for Conventional and Hybrid-Electric Commercial Transport Aircraft," 2018 AIAA Aerospace Sciences Meeting, Kissimmee, FL, USA, January 8-12 2018. doi:10.2514/6.2018-2028.

[205] Dean, T. S., Wroblewski, G. E., and Ansell, P. J., "Mission Analysis and Component-Level Sensitivity Study of Hybrid-Electric General Aviation Propulsion Systems," 2018 AIAA Aerospace Sciences Meeting, Kissimmee, FL, USA, January 8-12 2018. doi:10.2514/6.2018-1749.

[206] ESDU, "Thrust and drag accounting for propeller/airframe interaction," ESDU 85017, 1985.

[207] Seitz, A., and Gologan, C., "Parametric design studies for propulsive fuselage aircraft concepts," *CEAS Aeronautical Journal*, Vol. 6(1), 2015, pp. 69–82. doi: 10.1007/s13272-014-0130-3.

[208] Mikić, G. V., Stoll, A. M., Bevirt, J., Grah, R., and Moore, M. D., "Fuselage Boundary Layer Ingestion Propulsion Applied to a Thin Haul Commuter Aircraft for Optimal Efficiency," 16th AIAA Aviation Technology, Integration, and Operations Conference, Washington, DC, USA, June 13-17 2016. doi:10.2514/6.2016-3764.

[209] Drela, M., "Power Balance in Aerodynamic Flows," *AIAA Journal*, Vol. 47(7), 2009, pp. 1761–1771. doi:10.2514/1.42409.

[210] Ang, A. W. X., Gangoli Rao, A., Kanakis, T., and Lammen, W., "Performance analysis of an electrically assisted propulsion system for a short-range civil aircraft," *Proceedings of the Institution of Mechanical Engineers, Part G: Journal of Aerospace Engineering*, 2018. doi:10.1177/0954410017754146.

[211] Finger, D. F., Bil, C., and Braun, C., "Initial Sizing Methodology for Hybrid-Electric General Aviation Aircraft," *Journal of Aircraft*, Vol. 57(2), 2019, pp. 245–255. doi: 10.2514/1.C035428.

[212] Ruijgrok, G. J. J., *Elements of airplane performance*, Delft University Press, 1996.

[213] Kreimeier, M., and Stumpf, E., "Benefit evaluation of hybrid electric propulsion concepts for CS-23 aircraft," *CEAS Aeronautical Journal*, Vol. 8, 2017, pp. 691–704. doi:10.1007/s13272-017-0269-9.

[214] Nam, T., Soban, D. S., and Mavris, D. N., "Power Based Sizing Method for Aircraft Consuming Unconventional Energy," 43rd AIAA Aerospace Sciences Meeting and Exhibit, Reno, NV, USA, January 10-13 2005. doi:10.2514/6.2005-818.

[215] Finger, D. F., de Vries, R., Vos, R., Braun, C., and Bil, C., "A Comparison of Hybrid-Electric Aircraft Sizing Methods," 2020 AIAA Aerospace Sciences Meeting, Orlando, FL, USA, January 6-10 2020. doi:10.2514/6.2020-1006.

[216] IHS Markit, "Jane's All the World's Aircraft: Development & Production: RUAG (Dornier) 228 NG," , accessed 7 November 2019. URL `https://janes.ihs.com/JAWADevelopmentProduction/Display/jawaa704-jawa`.

[217] Juretzko, P. G., Immer, M., and Wildi, J., "Performance analysis of a hybrid-electric retrofit of a RUAG Dornier Do 228NG," *CEAS Aeronautical Journal*, Vol. 11, 2020, pp. 263–275. doi:10.1007/s13272-019-00420-2.

[218] Hofmann, J., Stumpf, E., Weintraub, D., Köhler, J., Pham, D., Schneider, M., Dickhoff, J., Burkhart, B., Reiner, G., Spiller, M., and Werner, E. A., "A Comprehensive Approach to the Assessment of a Hybrid Electric Powertrain for Commuter Aircraft," 2019 AIAA Aviation Technology, Integration and Operations Conference, Dallas, TX, USA, June 17-21 2019. doi:10.2514/6.2019-3678.

[219] Dornier GmbH, Logistic, "Pilot's Operating Handbook Including the LBA Approved Airplane Flight Manual - Dornier 228-100," Dornier GmbH, Munich, Germany, 1983.

[220] RUAG Aerospace Services GmbH, "Dornier 228 Advanced Commuter (AC) Facts & Figures," Wessling, Germany, 2015.

[221] Honeywell, "TPE331-10 Turboprop Engine Brochure," Honeywell Aerospace, Phoenix, TX, USA, 2016.

[222] International Civil Aviation Organization, "Annex 6, Operation of Aircraft, Part I: International Commercial Air Transport — Aeroplanes," ICAO, Montreal, Canada, 2016.

[223] European Aviation Safety Agency, "Acceptable Means of Compliance and Guidance Material to Certification Specifications for Normal-Category Aeroplane (CS-23)," European Aviation Safety Agency, Cologne, Germany, 2017.

[224] ASTM F3179/F3179M-16, "Standard Specification for Performance of Aeroplanes," ASTM International, West Conshohocken, PA, USA, 2016.

[225] Gudmundsson, S., *General Aviation Aircraft Design: Applied Methods and Procedures*, Butterworth-Heinemann, Oxford, Great Britain, 2014. doi:10.1016/C2011-0-06824-2.

[226] Keller, D., "Towards higher aerodynamic efficiency of propeller-driven aircraft with distributed propulsion," *CEAS Aeronautical Journal*, 2021. doi:10.1007/s13272-021-00535-5.

[227] European Aviation Safety Agency, "Certification Specifications and Acceptable Means of Compliance for Large Aeroplanes," CS-25/Amendment 21, 2018.

[228] Lambert, M., and Jane, F. T., *Jane's All The World's Aircraft*, eighty-first ed., Jane's Information Group, 1990-91.

[229] Lents, C., Hardin, L., Rheaume, J., and Kohlman, L., "Parallel Hybrid Gas-Electric Geared Turbofan Engine Conceptual Design and Benefits Analysis," 52nd AIAA/SAE/ASEE Joint Propulsion Conference, Salt Lake City, UT, USA, July 25-27 2016. doi:10.2514/6.2016-4610.

[230] Finger, D. F., Braun, C., and Bil, C., "An Initial Sizing Methodology for Hybrid-Electric Light Aircraft," 2018 Aviation Technology, Integration, and Operations Conference, Atlanta, GA, USA, June 25-29 2018. doi:10.2514/6.2018-4229.

[231] Marcus, E. A. P., de Vries, R., Raju Kulkarni, A., and Veldhuis, L. L. M., "Aerodynamic Investigation of an Over-the-Wing Propeller for Distributed Propulsion," 2018 AIAA Aerospace Sciences Meeting, Kissimmee, FL, USA, January 8-12 2018. doi:10.2514/6.2018-2053.

[232] Bento, H. F. M., de Vries, R., and Veldhuis, L. L. M., "Aerodynamic Performance and Interaction Effects of Circular and Square Ducted Propellers," AIAA Scitech 2020 Forum, Orlando, FL, USA, January 6-10 2020. doi:10.2514/6.2020-1029.

[233] de Vries, R., van Arnhem, N., Sinnige, T., Vos, R., and Veldhuis, L. L. M., "Aerodynamic Interaction Between Propellers of a Distributed-Propulsion System in Forward Flight," *Aerospace Science and Technology*, Vol. 118, 2021. doi:10.1016/j.ast.2021.107009.

[234] Marcus, E. A. P., "Aerodynamic modelling and performance analysis of over-the-wing propellers: A combined numerical and experimental study," MSc thesis, Delft University of Technology, 2018.

[235] Serpieri, J., "Cross-Flow Instability: Flow diagnostics and control of swept wing boundary layers," PhD Dissertation, Delft University of Technology, 2018.

[236] Boermans, L. M. M., and Rutten, P. B., "Two-dimensional Aerodynamic Characteristics of Airfoil NLF-MOD22 with Fowler Flap," TU Delft Internal Report LSW-95-3, 1995.

[237] Broek, J. J., "The use of the total-head rise across the propeller of the De Havilland Canada DHC-2 Beaver as a similarity parameter to simulate power-on flight in the wind tunnel," TU Delft Report VTH-190, 1976.

[238] Garner, H. C., Rogers, E., Acum, W., and Maskell, E., *Subsonic wind tunnel wall corrections*, Advisory Group for Aerospace Research and Development (AGARDograph, AG-109), 1966.

[239] Sinnige, T., de Vries, R., Della Corte, B., Avallone, F., Ragni, D., Eitelberg, G., and Veldhuis, L. L. M., "Unsteady Pylon Loading Caused by Propeller-Slipstream Impingement for Tip-Mounted Propellers," *Journal of Aircraft*, Vol. 55(4), 2018, pp. 1605–1618. doi:10.2514/1.C034696.

[240] Li, Q., "Towards optimum swirl recovery for propeller propulsion systems," PhD Dissertation, Delft University of Technology, 2019.

[241] Stokkermans, T. C. A., and Veldhuis, L. L. M., "Propeller Performance at Large Angle of Attack Applicable to Compound Helicopters," *AIAA Journal*, Vol. 59(6), 2021, pp. 2183–2199. doi:10.2514/1.J059509.

[242] Nahuis, B. R., and Sinnige, T., "Design, manufacture and commissioning of a new NLR six-component rotating shaft balance for Delft University of Technology," 10th International Symposium on Strain-Gauge Balances, Mianyang, China, 2016.

[243] Drela, M., "XFOIL: An Analysis and Design System for Low Reynolds Number Airfoils," In: Mueller T.J. (eds) Low Reynolds Number Aerodynamics. Lecture Notes in Engineering, Vol. 54, Springer, Berlin, Germany, 1989. doi:10.1007/978-3-642-84010-4_1.

[244] Phillips, W. H., "Studies of Friction Drag and Pressure Drag of Airfoils Using the Eppler Program," *SAE Transactions*, Vol. 97(1): Journal of Aerospace, 1988, pp. 1020–1035.

[245] Bento, H. F. M., "Aerodynamic interaction effects of circular and square ducted propellers," MSc thesis, Delft University of Technology, 2019.

[246] Rubin, S., and Grossman, B., "Viscous flow along a corner: numerical solution of the corner layer equations," *Quarterly of Applied Mathematics*, Vol. 29(2), 1971, pp. 169–186.

[247] Tokuda, N., "Viscous flow near a corner in three dimensions," *Journal of Fluid Mechanics*, Vol. 53(1), 1972, pp. 129–148. doi:10.1017/S0022112072000072.

[248] Ansys Inc., "Ansys Fluent 12.0 Theory Guide," , 2009.

[249] van Leer, B., "Towards the Ultimate Conservative Difference Scheme. V. A Second-Order Sequel to Godunov's Method," *Journal of Computational Physics*, Vol. 32(1), 1979. doi:10.1016/0021-9991(79)90145-1.

[250] Menter, F., "Two-Equation Eddy-Viscosity Turbulence Models for Engineering Applications," *AIAA Journal*, Vol. 32(8), 1994, pp. 1598–1605. doi:10.2514/3.12149.

[251] Ortun, B., Boisard, R., and Gonzalez-Martino, I., "In-plane airloads of a propeller with inflow angle: prediction vs. experiment," 30th AIAA Applied Aerodynamics Conference, New Orleans, LA, USA, June 25-28 2012. doi:10.2514/6.2012-2778.

[252] Falissard, F., Boisard, R., and Delattre, G., "Aeroacoustic computation of a contra rotating open rotor model with test rig installation effects," 18th AIAA/CEAS Aeroacoustics Conference (33rd AIAA Aeroacoustics Conference), Colorado Springs, CO, USA, June 4-6 2012. doi:10.2514/6.2012-2218.

[253] Méheut, M., "Thrust and Torque Far-field Analysis of Propeller and Counter Rotating Open Rotor Configurations," 31st AIAA Applied Aerodynamics Conference, San Diego, CA, USA, June 24-27 2013. doi:10.2514/6.2013-2803.

[254] Ruiz-Calavera, L., and Perdones-Diaz, D., "CFD computation of in-plane propeller shaft loads," AIAA/ASME/SAE/ASEE Joint Propulsion Conference, San Jose, CA, USA, June 14-17 2013. doi:10.2514/6.2013-3798.

[255] Bardina, J., Huang, P., and Coakley, T., "Turbulence modeling validation," 28th Fluid dynamics conference, Snowmass Village, CO, USA, June 29 - July 2 1997. doi:10.2514/6.1997-2121.

[256] Mannini, C., Soda, A., and Schewe, G., "Unsteady RANS modelling of flow past a rectangular cylinder: Investigation of Reynolds number effects," *Computers & Fluids*, Vol. 39(9), 2010. doi:10.1016/j.compfluid.2010.05.014.

[257] Stokkermans, T., van Arnhem, N., Sinnige, T., and Veldhuis, L. L. M., "Validation and Comparison of RANS Propeller Modeling Methods for Tip-Mounted Applications," *AIAA Journal*, Vol. 57(2), 2019, pp. 566–580. doi:10.2514/1.J057398.

[258] Spalart, P., and Rumsey, C., "Effective Inflow Conditions for Turbulence Models in Aerodynamic Calculations," *AIAA Journal*, Vol. 45(10), 2007, pp. 2544–2553. doi:10.2514/1.29373.

[259] Eça, L., and Hoekstra, M., "Discretization Uncertainty Estimation Based on a Least Squares Version of the Grid Convergence Index," Proceedings of the Second Workshop on CFD Uncertainty Analysis, Instituto Superior Técnico, Lisbon, Pprtugal, October 2006.

[260] Jacobs, E., and Sherman, A., "Airfoil section characteristics as affected by variations of the Reynolds number," NACA Technical Report 586, 1937.

[261] Traub, L., "Preliminary Investigation of the Effects of Stagger on an Annular Wing," *Journal of Aircraft*, Vol. 54(6), 2017, pp. 2386–2392. doi:10.2514/1.C034310.

[262] Drela, M., and Youngren, H., "XROTOR User Guide," , accessed March 2016. URL `http://web.mit.edu/drela/Public/web/xrotor/xrotor_doc.txt`.

[263] Küchemann, D., and Weber, J., *Aerodynamics of Propulsion*, McGraw-Hill, 1953.

[264] Bogdański, K., Krusz, W., Rodzewicz, M., and Rutkowski, M., "Design and optimization of low speed ducted fan for a new generation of joined wing aircraft," 29th Congress of International Council of the Aeronautical Sciences, Saint Petersburg, Russia, September 7-12 2014.

[265] Gand, F., Monnier, J., Deluc, J., and Choffat, A., "Experimental Study of the Corner Flow Separation on a Simplified Junction," *AIAA Journal*, Vol. 53(10), 2015, pp. 2869–2877. doi:10.2514/1.J053771.

[266] van Arnhem, N., de Vries, R., Sinnige, T., Vos, R., and Veldhuis, L. L. M., "Aerodynamic Performance and Static Stability Characteristics of Tail-Mounted Propeller Aircraft," *Journal of Aircraft*, 2021. doi:10.2514/1.C036338.

[267] Ewald, B. F. R., *Wind Tunnel Wall Corrections (la Correction des effets de paroi en soufflerie)*, Advisory Group for Aerospace Research and Development (AGARD-AG-336), 1998.

[268] Wieneke, B., "PIV uncertainty quantification from correlation statistics," *Measurement Science and Technology*, Vol. 26, 074002, 2015. doi:10.1088/0957-0233/26/7/074002.

[269] de Vries, R., van Arnhem, N., Avallone, F., Ragni, D., Vos, R., Eitelberg, G., and Veldhuis, L. L. M., "Experimental Investigation of Over-the-Wing Propeller–Boundary-Layer Interaction," *AIAA Journal*, Vol. 59(6), 2021, pp. 2169–2182. doi:10.2514/1.J059770.

[270] Bölk, S. A., de Vries, R., van Arnhem, N., and Veldhuis, L. L. M., "Numerical Investigation of Propeller–Flap Interaction in Inclined Over-the-Wing Distributed-Propulsion Systems," AIAA Scitech 2021 Forum, Virtual Event, January 11-15 & 19-21 2021. doi:10.2514/6.2021-0603.

[271] Bölk, S. A., "Aerodynamic interaction effects present in tiltable over-the-wing propeller systems," MSc thesis, Delft University of Technology, 2020.

[272] Lin, N., Reed, H. L., and Saric, W. S., "Effect of leading-edge geometry on boundary-layer receptivity to freestream sound," *Instability, Transition, and Turbulence*, Springer, New York, NY, 1992, pp. 421–440. doi:10.1007/978-1-4612-2956-8_42.

[273] Schlichting, H., *Boundary-Layer Theory*, 7th ed., New York: McGraw-Hill, 1979.

[274] Wallin, S., and Johansson, A. V., "An explicit algebraic Reynolds stress model for incompressible and compressible turbulent flows," *Journal of Fluid Mechanics*, Vol. 403, 2000, pp. 89–132. doi:10.1017/S0022112099007004.

[275] Rhie, C. M., and Chow, W. L., "Numerical study of the turbulent flow past an airfoil with trailing edge separation," *AIAA journal*, Vol. 21(11), 1983, pp. 1525–1532. doi:10.2514/3.8284.

[276] Eça, L., and Hoekstra, M., "A procedure for the estimation of the numerical uncertainty of CFD calculations based on grid refinement studies," *Journal of Computational Physics*, Vol. 262, 2014, pp. 104–130. doi:10.1016/j.jcp.2014.01.006.

[277] Yang, Y., "Aerodynamic Interaction between Propeller and Vortex," PhD Dissertation, Delft University of Technology, 2017.

[278] Levy, H., and Forsdyke, A. G., "The steady motion and stability of a helical vortex," *Proceedings of the Royal Society of London, Series A*, Vol. 120(786), 1928, pp. 670–690. doi:10.1098/rspa.1928.0174.

[279] Wille, R., and Fernholz, H., "Report on the first European Mechanics Colloquium, on the Coanda effect," *Journal of Fluid Mechanics*, Vol. 23(4), 1965, pp. 801–819. doi:10.1017/S0022112065001702.

[280] Reba, I., "Applications of the Coanda effect," *Scientific American*, Vol. 214(6), 1966, pp. 84–93.

[281] Hariharan, N., "Rotary-Wing Wake Capturing: High-Order Schemes Toward Minimizing Numerical Vortex Dissipation," *Journal of aircraft*, Vol. 39(5), 2002, pp. 822–829. doi:10.2514/2.3002.

[282] Katz, J., and Plotkin, A., *Low-speed aerodynamics*, 13th ed., Cambridge University Press, 2001. doi:10.1017/CBO9780511810329.

[283] van Arnhem, N., "Unconventional Propeller–Airframe Integration for Transport Aircraft Configurations," PhD Dissertation, Delft University of Technology, in preparation.

[284] de Vaal, J. B., Hansen, M. O. L., and Moan, T., "Validation of a vortex ring wake model suited for aeroelastic simulations of floating wind turbines," *Journal of Physics: Conference Series*, Vol. 555, 012025, 2014. doi:10.1088/1742-6596/555/1/012025.

[285] Yoon, S. S., and Heister, S. D., "Analytical formulas for the velocity field induced by an infinitely thin vortex ring," *International Journal for Numerical Methods in Fluids*, Vol. 44, 2004, pp. 665–672. doi:10.1002/d.666.

[286] Anderson, J. D., *Fundamentals of Aerodynamics*, 2nd ed., McGraw-Hill, 1991.

[287] Drela, M., and Youngren, H., "XFOIL 6.94 User Guide," , 2001.

[288] Lighthill, M. J., "A New Method of Two-Dimensional Aerodynamic Design," Aeronautical Research Council, Reports and Memoranda, No. 2112, April 1945.

[289] Kulfan, B. M., "Universal Parametric Geometry Representation Method," *Journal of Aircraft*, Vol. 45(1), 2008, pp. 142–158. doi:10.2514/1.29958.

[290] Witkowski, D. P., Johnston, R. T., and Sullivan, J. P., "Propeller/Wing Interaction," 27th AIAA Aerospace Sciences Meeting, Reno, NV, USA, January 9-12 1989. doi:10.2514/6.1989-535.

[291] Dekkers, N. M., "Aero-Propulsive Analysis of an Over-the-Wing Distributed Propulsion System: A Numerical Investigation Into the Effect of Propeller Position and Wing Shape," MSc Thesis, Delft University of Technology, 2021.

[292] de Vries, R., Hoogreef, M. F. M., and Vos, R., "Preliminary Sizing of a Hybrid-Electric Passenger Aircraft Featuring Over-the-Wing Distributed-Propulsion," 2019 AIAA Aerospace Sciences Meeting, San Diego, CA, USA, January 7-11 2019. doi:10.2514/6.2019-1811.

[293] de Vries, R., Hoogreef, M. F. M., and Vos, R., "Aeropropulsive Efficiency Requirements for Turboelectric Transport Aircraft," AIAA Scitech 2020 Forum, Orlando, FL, USA, January 6-10 2020. doi:10.2514/6.2020-0502.

[294] Vos, R., and Hoogreef, M. F. M., "System-level assessment of tail-mounted propellers for regional aircraft," 31st International Congress of the Aeronautical Sciences, Belo Horizonte, Brazil, September 09-14 2018.

[295] Felder, J. L., Kim, H. D., and Brown, G. V., "Turboelectric Distributed Propulsion Engine Cycle Analysis for Hybrid-Wing-Body Aircraft," 47th AIAA Aerospace Sciences Meeting, Orlando, FL, USA, January 5-8 2009. doi:10.2514/6.2009-1132.

[296] Nicolosi, F., Corcione, S., Trifari, V., Cusati, V., Ruocco, M., and Della Vecchia, P., "Performance Evaluation and DOC Estimation of an Innovative Turboprop Configuration," 2018 Aviation Technology, Integration, and Operations Conference, Atlanta, GA, USA, June 25-29 2018. doi:10.2514/6.2018-3662.

[297] Filippone, A., *Advanced aircraft flight performance*, Cambridge University Press, 2012. doi:10.1017/CBO9781139161893.

[298] Spierling, T., and Lents, C., "Parallel Hybrid Propulsion System for a Regional Turboprop: Conceptual Design and Benefits Analysis," AIAA Propulsion and Energy 2019 Forum, Indianapolis, IN, USA, August 19-22 2019. doi:10.2514/6.2019-4466.

[299] Luongo, C. A., Masson, P. J., Nam, T., Mavris, D., Kim, H. D., Brown, G. V., Waters, M., and Hall, D., "Next Generation More-Electric Aircraft: A Potential Application for HTS Superconductors," *IEEE Transactions on Applied Superconductivity*, Vol. 19(3), 2009, pp. 1055–1068. doi:10.1109/TASC.2009.2019021.

[300] Seitz, A., Habermann, A. L., and van Sluis, M., "Optimality considerations for propulsive fuselage power savings," *Proceedings of the Institution of Mechanical Engineers, Part G: Journal of Aerospace Engineering*, 2020. doi:10.1177/0954410020916319.

[301] de Vries, R., and Vos, R., "Aerodynamic Performance Benefits of Over-the-Wing Distributed Propulsion for Hybrid-Electric Transport Aircraft," AIAA SciTech 2022 Forum, San Diego, CA, USA, January 3-7 2022.

[302] Reuland, R. S., "Pusher Turboprop Installation Technology for the Embraer CBA-123 Vector," *SAE Transactions*, Vol. 100(1): Journal of Aerospace, Part I, 1991, pp. 222–228.

[303] Sinnige, T., Ragni, D., Eitelberg, G., and Veldhuis, L. L. M., "Mitigation of Pusher-Propeller Installation Effects by Pylon Trailing-Edge Blowing," *Journal of Aircraft*, Vol. 54(1), 2017, pp. 292–300. doi:10.2514/1.C034000.

[304] Torenbeek, E., *Advanced aircraft design: conceptual design, analysis and optimization of subsonic civil airplanes*, John Wiley & Sons, 2013.

[305] Habermann, A. L., "Effects of Distributed Propulsion on Wing Mass in Aircraft Conceptual Design," AIAA Aviation 2020 Forum, Virtual Event, June 15-19 2020. doi:10.2514/6.2020-2625.

[306] Sanders, L., Mincu, D.-C., Vitagliano, P. L., Minervino, M., Kennedy, J., and Bennett, G., "Prediction of the acoustic shielding by aircraft empennage for contrarotating open rotors," *International Journal of Aeroacoustics*, Vol. 167(7-8), 2017, pp. 626–648. doi:10.1177/1475472X17734334.

[307] Antcliff, K., Borer, N., Sartorius, S., Saleh, P., Rose, R., Gariel, M., Oldham, J., et al., "Regional Air Mobility: Leveraging Our National Investments to Energize the American Travel Experience," NASA Report, April 2021.

[308] de Vries, R., Hoogreef, M. F. M., and Vos, R., "Range Equation for Hybrid-Electric Aircraft with Constant Power Split," *Journal of Aircraft*, Vol. 57(3), 2020. doi:10.2514/1.C035734.

[309] Friedrich, C., and Robertson, P. A., "Hybrid-Electric Propulsion for Aircraft," *Journal of Aircraft*, Vol. 52(1), 2015, pp. 176–189. doi:10.2514/1.C032660.

[310] Wroblewski, G. E., and Ansell, P. J., "Mission Analysis and Emissions for Conventional and Hybrid-Electric Commercial Transport Aircraft," *Journal of Aircraft*, Vol. 56(3), 2019, pp. 1200–1213. doi:10.2514/1.C035070.

[311] Traub, L. W., "Range and endurance estimates for battery-powered aircraft," *Journal of Aircraft*, Vol. 48(2), 2011, pp. 703–707. doi:10.2514/1.C031027.

[312] Avanzini, G., and Giulietti, F., "Maximum range for battery-powered aircraft," *Journal of Aircraft*, Vol. 50(1), 2012, pp. 304–307. doi:10.2514/1.C031748.

[313] Patterson, M. D., and German, B. J., "Simplified Aerodynamics Models to Predict the Effects of Upstream Propellers on Wing Lift," 53rd AIAA Aerospace Sciences Meeting, Kissimmee, FL, USA, January 5-9 2015. doi:10.2514/6.2015-1673.

[314] Roskam, J., *Methods for estimating drag polars of subsonic airplanes*, Roskam Aviation and Engineering Corporation, 1971.

[315] Ting, L., Liu, C. H., and Kleinstein, G., "Interference of Wing and Multipropellers," *AIAA Journal*, Vol. 10(7), 1972, pp. 906–914. doi:10.2514/3.50244.

[316] Biber, K., "Estimating Propeller Slipstream Drag on Airplane Performance," *Journal of Aircraft*, Vol. 48(6), 2011, pp. 2172–2174. doi:10.2514/1.C031458.

[317] Deere, K. A., Viken, J. K., Viken, S. A., Carter, M. B., Cox, D., Wiese, M. R., and Farr, N., "Computational Component Build-up for the X-57 Distributed Electric Propulsion Aircraft," 2018 AIAA Aerospace Sciences Meeting, Kissimmee, FL, USA, January 8-12 2018. doi:10.2514/6.2018-1275.

ACKNOWLEDGEMENTS

When I was offered the opportunity to do a PhD five years ago, I was doubting whether this would be something for me. But looking back now... What a fantastic journey it has been. I consider myself extremely fortunate with the company that I have had throughout these years, and want to express my gratitude to several people who, directly or indirectly, contributed to this piece of work.

First of all, I want to thank Roelof and Leo. In practically every meeting I have had with Roelof over the past years, I have learned something new about aircraft design or aircraft performance. He also provided me with room to establish my own research path, encouraged me to participate in conferences and working groups, and made sure I never forgot the bigger picture. And just like I could count on Roelof's expertise for aircraft-design related questions, I could count on Leo's expertise for anything related to propellers, aerodynamics, or wind-tunnel testing. Apart from the more detailed discussions, I also appreciate Leo's interpersonal skills as a promotor and his ability to ask the just the right questions to ensure that the research moves in the right direction. If I had to re-do this all over, I would choose this supervisory team again without hesitation.

Without any doubt, I also have to thank Nando and Tomas for helping me out on countless occasions. Their patience and willingness to help, Nando's knowledge of numerical and experimental research, and Tomas' relentlessly sharp interpretation of data have contributed substantially to the quality of my work, among many others. Moreover, if it weren't for Nando's magic soldering skills and Tomas' crazy phase-controlling software, all my experiments would have featured stationary propellers.

I also received support from many others throughout my experimental research. Thank you Biagio and Sumit for helping out, giving good advice, and, most importantly, your dry sense of humor. This is a seriously undervalued skill in the research world. I would also like to thank Daniele and Francesco for their help with PIV measurements, microphone measurements, and for their enthusiasm in general. Also, a big thanks to Leandro and Pedro for assisting with the LST experiment. And thank you Georg for insightful discussions on the more fundamental aspects of aerodynamics and wind-tunnel testing, and for reminding me to distinguish propeller efficiency from propulsive efficiency. Furthermore, I would like to thank Peter, Ed, Rob, Steve, Frank, and Leon from DEMO for producing the wind-tunnel models used in this research, and Stefan and Emiel for their help with wind-tunnel campaigns at the low-speed laboratory.

I was also lucky with my colleagues on the aircraft-design side of things. Thank you Maurice for being an excellent project manager and not going berserk while implementing my code in the Initiator. Another big thanks goes to the original crew of Office 6.12, not only for productive discussions regarding aircraft design, but also for showing us how to book hotels (Tarik), a code that can do anything (Martijn), and the occasional rant about societal and political matters (Malcom). Also, thank you Felix for a very fruitful and enjoyable collaboration, and for good laughs at conferences.

During the PhD, I had the opportunity to supervise some amazing master thesis students. Pepijn, Hugo, Sören, Nick, Pedro, and Alexandros, I hope that you learned at least as much as I did from your work, and that you look back on it with the same positivity as I do. Special thanks to Pepijn, Hugo, and Sören, who have directly contributed to significant portions of this thesis.

Furthermore, I want to thank my colleagues of FPP and other departments—Adam, Nitish, Beto, Roberto, Sonia, Tom, Akshay, André, Pieter-Jan, Anne-Liza, Carmine, Imco, Fabrizio, Arvind, Joris, Gianfranco, Martijn van Sluis, Ramon, Robert, Jatinder, Sarah, Sebastian, Francesco, Federica, and many others—for providing a very fun and relaxed environment. The jokes during coffee breaks and dinners out, barbecues at Adam's and Nitish's places, and occasional group excursion are perhaps the main reasons why I look back on the PhD as a very enjoyable work experience.

Of course, I also want thank my parents and my brother Leonard, who have shaped me to this day and of whom I am extremely grateful and proud. I'd also like to give a shout-out to my friends in Spain, who in fact often defy the distinction between friend and family, and who made sure that I came back fully re-charged after a summer holiday.

And, last but not least, thank you Alejandra—my fiancée, cooking companion, travel companion, sporting companion, couch potato, and favorite aerospace engineer—for your support and patience throughout these years, particularly during the questionable working hours of wind-tunnel testing and thesis writing. Without you, this journey would have been much more boring and much more difficult, and I am very happy to have gone through it together with you.

Reynard de Vries
Delft, December 2021

CURRICULUM VITÆ

Reynard de Vries was born in 1992 in Amsterdam, the Netherlands. Together with his family he moved to Singapore in 2002, and to San Pedro de Alcántara, Spain, in 2004. There he completed his high school education and baccalaureate in Science & Technology at I.E.S. Salduba. In 2010 he moved to Madrid, Spain to start a BSc degree in Aerospace Engineering at the Technical University of Madrid (UPM), specializing in Propulsion Systems. He subsequently returned to the Netherlands to follow an MSc degree in Flight Performance & Propulsion at the Faculty of Aerospace Engineering of Delft University of Technology, which he obtained with distinction in 2016. During his studies, Reynard performed internships at ITP Aero (Madrid, Spain) and KLM Engineering & Maintenance (Schiphol, the Netherlands), worked as a teaching assistant for several courses on aircraft design and CAD modeling, and achieved 2nd place in the 2014–2015 AIAA Graduate Team Design Competition together with his teammates.

In 2017 he started his PhD at the Flight Performance & Propulsion section of TU Delft, under the supervision of Roelof Vos and Leo Veldhuis. He performed his PhD research within the EU Clean Sky 2 research framework, focusing on conceptual design methods for hybrid-electric aircraft and propeller aerodynamic interaction in distributed-propulsion systems. Throughout the PhD trajectory, he carried out aircraft design studies in collaboration with academic and industrial institutions, performed numerous wind-tunnel tests, supervised six MSc thesis students, and completed various technical and non-technical courses as a part of the Doctoral Education Program. He received two best-presentation awards at the 2018 AIAA/IEEE Electrified Aircraft Technologies Symposium and has taught several lectures on the conceptual design of hybrid-electric aircraft. He has been a member of the AIAA Electrified Aircraft Propulsion & Power working group from 2018 to 2021, and a board member of the PhD Council of the Faculty of Aerospace Engineering from 2019 to 2021.

Reynard is currently a post-doctoral researcher at the Flight Performance & Propulsion section, where he continues to perform research in the fields of conceptual design and propulsion integration for (hybrid-) electric aircraft. Reynard enjoys cooking, bouldering, traveling, and—of course—sharing a beer with his friends and family.

List of Publications

Journal Papers

8. de Vries, R., Sinnige, T., and Veldhuis, L. L. M., "Aerodynamic Performance of an Over-the-Wing Distributed-Propeller System in Cruise Conditions", *under review*, 2022.

7. van Arnhem, N., de Vries, R., Sinnige, T., Vos, R., and Veldhuis, L. L. M., "Aerodynamic Performance and Static Stability Characteristics of Aircraft with Tail-Mounted Propellers", *Journal of Aircraft*, 2021. doi:10.2514/1.C036338.

6. de Vries, R., van Arnhem, N., Sinnige, T., Vos, R., and Veldhuis, L. L. M., "Aerodynamic Interaction Between Propellers of a Distributed-Propulsion System in Forward Flight", *Aerospace Science and Technology*, Vol. 118, 2021. doi:10.1016/j.ast.2021.107009.

5. de Vries, R., van Arnhem, N., Avallone, F., Ragni, D., Vos, R., Eitelberg, G., and Veldhuis, L. L. M., "Experimental Investigation of Over-the-Wing Propeller–Boundary-Layer Interaction", *AIAA Journal*, Vol. 59(6), 2021, pp. 2169–2182. doi:10.2514/1.J059770.

4. van Arnhem, N., de Vries, R., Sinnige, T., Vos, R., Eitelberg, G., and Veldhuis, L. L. M., "Engineering Method to Estimate the Blade Loading of Propellers in Nonuniform Flow", *AIAA Journal*, Vol. 58(12), 2020, pp. 5332-5346. doi:10.2514/1.J059485.

3. de Vries, R., Brown, M., and Vos, R., "Preliminary Sizing Method for Hybrid-Electric Distributed-Propulsion Aircraft," *Journal of Aircraft*, Vol. 56(6), 2019, pp. 2172–2188. doi:10.2514/1.C035388.

2. Sinnige, T., Della Corte, B., de Vries, R., Avallone, F., Merino-Martínez, R., Ragni, D., Eitelberg, G. and Veldhuis, L. L. M., "Alleviation of Propeller-Slipstream-Induced Unsteady Pylon Loading by a Flow-Permeable Leading Edge", *Journal of Aircraft*, Vol. 56(3), 2019, pp. 1214-1230. doi:10.2514/1.C035250.

1. Sinnige, T., de Vries, R., Della Corte, B., Avallone, F., Ragni, D., Eitelberg, G. and Veldhuis, L. L. M., "Unsteady Pylon Loading Caused by Propeller-Slipstream Impingement for Tip-Mounted Propellers", *Journal of Aircraft*, Vol. 55(4), 2018, pp. 1605-1618. doi:10.2514/1.C034696.

Engineering Notes

1. de Vries, R., Hoogreef, M. F. M., and Vos, R., "Range Equation for Hybrid-Electric Aircraft with Constant Power Split," *Journal of Aircraft*, Vol. 57(3), 2020, pp. 552-557. doi:10.2514/1.C035734.

CONFERENCE PAPERS

15. de Vries, R., and Vos, R., "Aerodynamic Performance Benefits of Over-the-Wing Distributed Propulsion for Hybrid-Electric Transport Aircraft", AIAA Scitech 2022 Forum, San Diego, CA, USA, January 3-7 2022.

14. Bölk, S. A., de Vries, R., van Arnhem, N., and Veldhuis, L. L. M., "Numerical Investigation of Propeller–Flap Interaction in Inclined Over-the-Wing Distributed-Propulsion Systems", AIAA Scitech 2021 Forum, Virtual Event, January 11-15 & 19-21 2021. doi:10.2514/6.2021-0603.

13. Zill, T., Iwanizki, M., Schmollgruber, P., Defoort, S., Hoogreef, M. F. M., de Vries, R., Vankan, J. and Lammen, W., "An Overview of the Conceptual Design Studies of Hybrid Electric Propulsion Air Vehicles in the Frame of Clean Sky 2 Large Passenger Aircraft", Aerospace Europe Conference 2020, Bordeaux, France, February 25-28 2020. doi:10.5281/zenodo.3899710.

12. de Vries, R., Hoogreef, M. F. M., and Vos, R., "Aeropropulsive Efficiency Requirements for Turboelectric Transport Aircraft", AIAA Scitech 2020 Forum, Orlando, FL, USA, January 6-10 2020. doi:10.2514/6.2020-0502.

11. Finger, D. F., de Vries, R., Vos, R., Braun, C., and Bil, C., "A Comparison of Hybrid-Electric Aircraft Sizing Methods", AIAA Scitech 2020 Forum, Orlando, FL, USA, January 6-10 2020. doi:10.2514/6.2020-1006.

10. Hoogreef, M. F. M., de Vries, R., Sinnige, T., and Vos, R., "Synthesis of Aero-Propulsive Interaction Studies applied to Conceptual Hybrid-Electric Aircraft Design", AIAA Scitech 2020 Forum, Orlando, FL, USA, January 6-10 2020. doi:10.2514/6.2020-0503.

9. Bento, H. F. M., de Vries, R., and Veldhuis, L. L. M., "Aerodynamic Performance and Interaction Effects of Circular and Square Ducted Propellers", AIAA Scitech 2020 Forum, Orlando, FL, USA, January 6-10 2020. doi:10.2514/6.2020-1029.

8. de Vries, R., van Arnhem, N., Avallone, F., Ragni, D., Vos, R., Eitelberg, G., and Veldhuis, L. L. M., "Aerodynamic Interaction Between an Over-the-Wing Propeller and the Wing Boundary-Layer in Adverse Pressure Gradients", AIAA Aviation 2019 Forum, Dallas, TX, USA, June 17-21 2019. doi:10.2514/6.2019-3035.

7. van Arnhem, N., de Vries, R., Vos, R., and Veldhuis, L. L. M., "Aerodynamic Performance of an Aircraft Equipped with Horizontal Tail Mounted Propellers", AIAA Aviation 2019 Forum, Dallas, TX, USA, June 17-21 2019. doi:10.2514/6.2019-3036.

6. de Vries, R., Hoogreef, M. F. M., and Vos, R., "Preliminary Sizing of a Hybrid-Electric Passenger Aircraft Featuring Over-the-Wing Distributed-Propulsion", 2019 AIAA Aerospace Sciences Meeting, San Diego, CA, USA, January 7-11 2019. doi:10.2514/6.2019-1811

5. Hoogreef, M. F. M., Vos, R., de Vries, R., and Veldhuis, L. L.M., "Conceptual Assessment of Hybrid Electric Aircraft with Distributed Propulsion and Boosted Turbofans", 2019 AIAA Aerospace Sciences Meeting, San Diego, CA, USA, January 7-11 2019. doi:10.2514/6.2019-1807

4. de Vries, R., Brown, M., and Vos, R., "A Preliminary Sizing Method for Hybrid-Electric Aircraft Including Aero-Propulsive Interaction Effects", 2018 Aviation Technology, Integration, and Operations Conference, Atlanta, GA, USA, June 25-29 2018. doi:10.2514/6.2018-4228

3. Marcus, E. A. P., de Vries, R., Raju Kulkarni, A., and Veldhuis, L. L. M., "Aerodynamic Investigation of an Over-the-Wing Propeller for Distributed Propulsion", 2018 AIAA Aerospace Sciences Meeting, Kissimmee, FL, USA, January 8-12 2018. doi:10.2514/6.2018-2053

2. Della Corte, B., Sinnige, T., de Vries, R., Avallone, F., Ragni, D., Eitelberg, G., and Veldhuis, L. L. M., "Tractor Propeller-Pylon Interaction, Part II: Mitigation of Unsteady Pylon Loading by Application of Leading-Edge Porosity", 55th AIAA Aerospace Sciences Meeting, Grapevine, TX, USA, January 9-13 2017. doi:10.2514/6.2017-1176

1. de Vries, R., Sinnige, T., Della Corte, B., Avallone, F., Ragni, D., Eitelberg, G., and Veldhuis, L. L. M., "Tractor Propeller-Pylon Interaction, Part I: Characterization of Unsteady Pylon Loading", 55th AIAA Aerospace Sciences Meeting, Grapevine, TX, USA, January 9-13 2017. doi:10.2514/6.2017-1175